Rational functionalization of molecular materials : towards magnetic liquids and liquid crystals

Elena Darbinean

THÈSE PRÉSENTÉE

POUR OBTENIR LE GRADE DE

DOCTEUR DE

L'UNIVERSITÉ DE BORDEAUX

École doctorale des sciences chimiques

SPÉCIALITÉ : Physico-Chimie de la Matière Condensée

Par Elena DARBINEAN

Fonctionnalisation rationnelle de matériaux moléculaires: vers des liquides et des cristaux-liquides magnétiques

Sous la direction de: Rodolphe CLÉRAC

Soutenue le 10 Mars 2017

Membres du jury :

Mme ZAKRI Cécile	Professeur, Université de Bordeaux	Président
M. LUNEAU, Dominique	Professeur, Université Bernard Lyon1	Rapporteur
M. SHATRUK, Michael	Professeur, The Florida State University	Rapporteur
M. CLÉRAC, Rodolphe	Directeur de recherche, CNRS	Directeur de thèse

- 2017 -

These three years of PhD taught me that scientific work cannot be accomplished without the help and support from many people. Herein, I wish to thank everybody who guided and encouraged me, and who was involved in the evolution of this work.

Firstly, I would like to thank ***Philippe Richetti***, ***Cécile Zakri*** *for welcoming me at the Centre de Recherche Paul Pascal.*

I would like to thank ***Prof. Michael Shatruk*** *and* ***Prof. Dominique Luneau*** *for their time and consideration to review this thesis work;* ***Prof. Cécile Zakri*** *for her participation in my thesis defense jury. Thank you all for your time to evaluate this manuscript.*

I am deeply grateful to my supervisor, ***Rodolphe Clérac****, for showing me an interesting research field, molecular magnetic materials. Thank you for the guidance, encouragement and support during this work. Thank you for you constructive criticism and good advices in difficult situations. His meticulousness showed me a model of a great scientist. Thank you for patience and understanding in the last moments of my PhD.*

I wish to dedicate special thanks to ***Daniel Rosario-Amorin*** *for help during this thesis. Besides the experimental work, scientific advices and research analyses, I thank you for your contribution, guidance and patience during the writing of this manuscript. Thank you for the time you took to explain and advise me during these three years, especially during the last months. I wish also dedicate special thanks to* ***Dmitri Mitcov****, who helped me in the first months of the PhD and introduced me to* Mn_{12} *and* $\{Co_2Fe_2\}$ *chemistry and, always, found time for discussion and help even after his departure from the lab.*

I would like to express my gratitude to many people, who actively contributed to this work: ***Yunnan Guo****, who initiated the project on spin crossover during his post-doctoral stay in our team,* ***Vincent Montigaud****, who helped me to reproduce and characterise some of the spin crossover and electron transfer systems during the last months of the thesis when I was busy with the preparation of the manuscript,* ***Abhishake Mondal****, who helped me for the synthesis of Fe(III) precursors and to solve, with* ***David Aguilà****, some crystallographic problems as well as* ***Maria Asensio*** *for providing some of organic precursors used for the synthesis of ligands. I would like to strongly acknowledge* ***Ahmed Bentaleb****, who was very often solicited for SAXS measurements and was always ready to schedule these experiments as soon as possible, even during the week-ends or vacations. Thank you for your positive energy and the time you dedicate to this work. I would like to thank* ***Pierre Dechambenoit*** *for teaching me the crystallography. Thank you for your help with single crystal X-ray diffraction experiments and to explain me how to solve the crystal structures. I appreciated your advices and fruitful discussions. I thank* ***Mathieu Rouzières*** *for setting up the magnetic measurements and help on the treatment of the data.*

I would like to mention many people who helped with scientific expertise and technical support: I thank ***Harald Bock*** *and* ***Fabien Durola*** *for the discussions in organic chemistry and liquid-crystals;* ***Elizabeth Hillard*** *for advices in coordination chemistry and crystallization and* ***Claude Coulon*** *for making magnetism more easy to understand. I would like to thanks* ***François Dole****,* ***Stéphanie Exiga, Xavier Brilland*** *and* ***Alain Derré*** *for the training on DSC, NMR, mass spectroscopy, FTIR and Vis-UV instruments and their availability when there were technical problems. Finally I would like to thank* ***Anne Facq****,* ***Jaon-***

***Luc Laborde**, **Natalie Touzé**, **Corine Amengual**, **Elisabeth Hortolland**, **Béatrice Dupin**, **Fréderic Louerat**, **Mbolotiana Rajaoarivelo**, **Stéphane Bechemin** and **Lionel Chevalier** for the administration, informatics, chemical and security support.*

*I would like also to thanks our dear neighbours from the Institut de Chimie de la Matière Condensée de Bordeaux (ICMCB) for their participation in our studies. Especially, I wish to thank **Corine Mathonière**, who has been collaborating with our team for many years on electron transfer and photomagnetic systems. I thank you for the time you spent on photomagnetic measurements and for your precious help on optical studies. I would like to thank **Alain Wattiaux**, who kindly proposed to characterise some of our compounds by Mössbauer spectroscopy, **Patrick Rosa**, for giving us access to VSM magnetometer, needed for high-temperature measurements and **Laeticia Etienne** for elemental analysis.*

*I would like to address many thanks to **Dmitri Mitcov**, **Mihail Secu** and **Evangelia Koumousi** for their help during my installation in France and precious guidance to deal with French administration. Thank you for your and friendly support and encouragement. Thank you to all my colleagues, who contributed to the development of a warm atmosphere at work: **Kasper Steen Pedersen**, **Matias Urdampilleta**, **Daniel N. Woodruff, Vivien Pianet, Yoann Prado**, **Jun-Liang Liu, Anandi Srinivasan, Vianney Grau, Miguel Cortijo**, **Xiaozhou Ma, Marli Ferreira, Edivandro Girotto, Deise Santos, Gabi Cabral, Guillame Naulet** and **Antoine Robert.** We had the opportunity to learn from each other not only science, but the traditions and interesting things about the countries from where we are coming. Thank you to my dear friends and collegues since bachelor **Vladimir Bulicanu, Petru Apostol** and **Dumitru Samohvalov** for being avaible to help and encourage me in difficult moments.*

*I would like to thank **Erasmus Mundus MID** program for financial support.*

*Finally, my hearty thanks are express to my family. I thank my loving, encouraging and patient husband, **Gheorghe.** Even if we were far away from each other during my PhD, he always understood and found time to listen to me. Thank to my darling parents: my father **Razmic** and my mother **Vasilisa.** Thank you my brother **David** and his wife **Irina**, my lovely niece **Bianca** and my mother-in-law **Maria**.*

Merci à tous!

Elena Darbinean
Pessac, January 2017

TABLE OF CONTENTS

General Introduction

The humanity knows about magnetism more than millennia. Nowadays, the interest to development of new magnetic materials and their interesting properties increased significantly. The first uses of magnetism are dating from 1060 in China, when Shen Kua found a process to magnetize the iron needles and in this respect he invented the compass.[1] This invention gave a rise to a number of devices that are based on magnetic compounds. The theoretical basis was drafted by Curie, Weiss, and Langevin. By 80s, the majority of the magnetic systems were studied as inorganic materials that are surrounded by metals or metal oxides. Later, the magnetism science developed with molecules that brought out novel properties. All these gave an opportunity to a new field that was called *molecular magnetism*. Molecular magnetism is the main discipline discussed in this thesis work. Our research is focused on functionalization of new magnetic materials and study of their physical and chemical properties.

The main motivation in this area of research is the magnetic properties that give the opportunity to multi-functionality of the magnetic material. Thus, we tried to develop hybrid magnetic material in order to obtain soft systems that can be easy-processable. Regarding this, we functionalize interesting molecule-based magnetic material by known groups that can induce liquid crystalline behavior or have a better solubility. Not at least, the original magnetic properties of the functionalized materials must be preserved.

Therefore, the main research objective in the "Molecular Materials and Magnetism" (M3) group at the Centre de Recherche Paul Pascal (CRPP) is focused on the functionalization of molecular magnetic materials towards hybrid systems possessing liquid crystalline properties and/or increased solubility. During her PhD thesis (2004-2007), Pauline Grondin developed the idea of grafting linear long alkyl chains onto triazole ligands, in order to obtain new $[Fe^{II}(R\text{-}trz)_3]A_2$ compounds (where R-trz is a functionalized triazole ligand and A is a counter-anion) that showed, in addition to spin crossover, liquid crystalline properties and/or the ability to gelate various solvents. Following the same aims, the thesis work of Diana Siretanu (2008-2011) was dedicated to functionalization of Mn_{12}-based SMMs, various Fe^{II}-based spin crossover (SC) systems and cyanido-bridged $\{Fe_2Co_2\}$ electron-transfer complexes. Continuing in this direction, the thesis work of Dmitri Mitcov (2010-2014) was focused in further functionalization of Mn_{12}-based SMMs and cyanido-bridged $\{Fe_2Co_2\}$ electron-transfer complexes via anion exchange.

Taking into account the foregoing works, in this thesis we are focused on rational functionalization of molecule-based magnetic materials such as Mn_{12}-based SMMs, Fe^{II}-based SC systems and cyanido-bridged $\{Fe_2M_2\}$ ($M = Co^{2+}$, Ni^{2+}) molecular squares. In Chapter I of this thesis, the reader can find general information about the three classes of magnetic complexes (single-molecule magnets, spin crossover complexes and electron transfer systems) chosen for functionalization, followed by several examples of already reported hybrid magnetic materials. In Chapter II, rational ligand functionalization of single-molecule magnets towards liquid crystalline phases is discussed. The third Chapter is focused on two strategies of functionalization of Fe^{II}-based SC systems. Chapter IV describes the cyanido-bridged $\{Fe_2M_2\}$ ($M = Co^{2+}$, Ni^{2+}) molecular squares and the influence of various functionalizations and solvation on the occurrence of the thermally, photo-induced electron transfer in solutions or liquid crystalline behaviour. All chapters present a conclusion with a summarized overview of the obtained results. Finally, general

conclusion with some future perspectives of this manuscript is provided to continue and complete the area of hybrid molecule-based materials.

1. Martis, D. C. *The theory of magnetism, Berlin*, Springer-Verlag, Vol. I, **1981**.

Chapter I

Generalities and Context

Table of Contents for Chapter I:

I.1. Introduction

Molecular magnetism is a relatively young research field, which has nonetheless grown fairly quickly with considerable advance, thanks to the possible interdisciplinary research between chemistry, physics and materials science. Materials in this field are built through the bottom-up approach using well-defined building blocks (metals and ligands, or the coordination complexes). This approach not only allows to predict and control the structural dimensionalities and architectures of the materials, but also sometimes their related magnetic properties. One of the most important advantages of molecular materials is that molecules are all identical, therefore allowing relatively easy experiments on large assemblies of them, while still being able to probe, for example, quantum effects. This means that we can relate macroscopic and microscopic properties through studying the simple quantum mechanics and thermodynamics. These remarkable physical properties are often rare or unknown in traditional inorganic materials. For example, molecular systems displaying spin crossover phenomenon (SCO),[1] photomagnetism,[2] single-molecule magnet (SMM)[3] or single-chain magnet (SCM)[4] behaviors and metal-to-metal electron transfer (ET)[2,5] process have been discovered. Independently of their academic interest, these molecular systems could potentially overcome some of the limitations of inorganic magnetic materials and find a place of choice in various technological areas. In this respect, a great challenge concerns their processing, which need to be easy and efficient without altering their intrinsic properties, and one of the possible options would be their integration in soft matter.

In the first part of this chapter, we will provide general information and basic theoretical concepts on three classes of molecule-based magnetic materials, namely SMM, SCO and ET systems that were investigated along this PhD work. The second part will provide a short bibliographic survey on molecule-based magnetic soft materials, which will help the reader to understand the motivations of our work.

I.2. Molecule-based magnetic materials

I.2.1. Single-Molecule Magnets (SMMs)

A single-molecule magnet (SMM) is a molecule that is able to retain magnetization at low temperature, giving rise to a magnetization *versus* field hysteresis loop. Therefore, a SMM behaves as bulk magnet but the bistability displayed is purely originating from the molecular level. The phenomenon was first observed in the early 90's on the now very well-known dodecamanganese complex $[Mn_{12}O_{12}(CH_3COO)_{16}(H_2O)_4]$ (Mn_{12}-OAc for short),[6] which synthesis and preliminary magnetic characterization were reported by Lis a decade before.[7] The prerequisites for a molecule to act as an SMM are a high value of the spin ground state (S_T), a high uniaxial magnetic anisotropy with a magnetic easy axis and negligible magnetic interactions between the molecules.[3,6,8] Because of their small size, SMMs can be truly placed at the interface between the quantum and classical worlds. These objects made possible experimental observation of theoretically predicted quantum phenomena, such as quantum tunneling of the magnetization[9] and quantum phase interference.[10] Furthermore, these molecules could be potentially used in

applications such as information storage,[6,8b] quantum computation[11] or as low-temperature refrigerants via the magnetocaloric effect.[11c,12]

Since the discovery of SMM behavior in Mn_{12}-OAc, a very fruitful research has been performed on the improvement of SMM characteristics and extraordinary advances have been made resulting in the development of large number of SMMs. Thus, coordination chemists were able to construct homo- or heterometallic complexes of various nuclearity exhibiting SMM behavior for *3d*,[6-8,13] *4d*,[14] *5d*,[14a,15] *4f*,[16] and 5*f*.[17] Moreover, in recent years, organometallic chemistry has produced many interesting developments that account for notable "records" in terms of magnetic hysteresis and anisotropy barriers.[18]

In the following paragraphs of Section I.2.1, basic theory of SMM physics is described to understand how these complexes are capable to show not only the classical magnet-like behavior but also the quantum properties.

I.2.1.1. Theoretical aspects illustrated by Mn_{12}-OAc complex

Single-molecule magnet compounds are composed of the metal ion that are bonded together by various ligands that help to isolate and protect the molecular core from its neighbors and ensure their cohesion. The intramolecular magnetic interactions between metal centers are significantly larger than the intermolecular interactions. Thus, the macroscopic magnetic properties of the material reflect the properties of a single molecule.

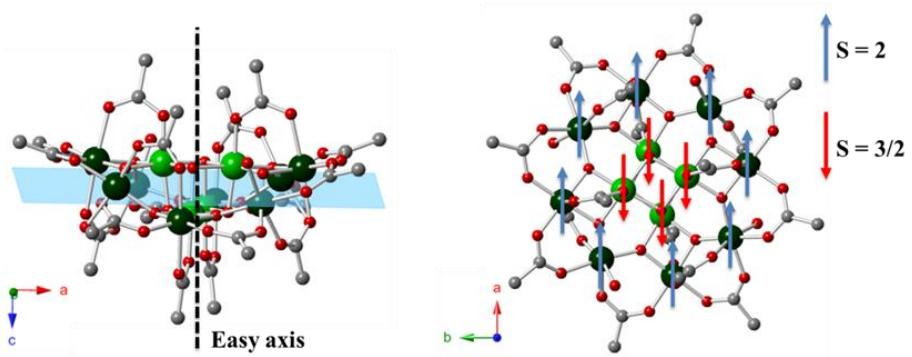

Figure I-1. Crystallographic structure of the Mn_{12}-OAc molecule (left) along the crystal *a*-axis and (right) along the crystal *c*-axis. Mn(IV) light green, Mn(III) dark green, O red, C grey. Hydrogens has been omitted for clarity.[6,7]

The Mn_{12}-OAc molecule,[6,7] which is used along Chapter II as precursor for the synthesis of metallomesogenic materials, is chosen to illustrate the theoretical aspects of the SMM behavior. The structure of Mn_{12}-OAc can be described as a $[Mn_{12}(\mu\text{-}O)_{12}]$ roughly planar disk containing a central $[Mn^{IV}{}_4O_4]^{8+}$ cube-like core surrounded by a non-planar ring of eight Mn^{III} ions that are connected to the central core *via* eight $\mu_3\text{-}O^{2-}$ ions and four bridging carboxylates perpendicular to the plane of the disk (Figure I-1). The SMM property of this molecule is due to the association of a large spin ground state value and strong uniaxial magnetic anisotropy. The spin ground state S_T value in Mn_{12}-OAc arises from a situation in which the spins of the four central Mn^{IV} centers are all aligned anti-parallel to the spins of the eight outer Mn^{III} centers, to give $S_T = |(4 \times 3/2) + (8 + (-2))| = 10$. The strong uniaxial anisotropy can be explained by the nearly parallel alignment of the eight Mn^{III} Jahn-Teller (JT) axes along the molecular *z*-axis.

I.2.1.2. Magnetic properties in the absence of external field

Taking into account the ground spin state, S_T = 10, and considering the three directions of magnetization are described as *x* – hard, *y* – intermediate, *z* – easy axis, the spin quantum number S_T is described by $2S_T + 1$ sublevels, each of them characterized by a projection quantum number m_S, where $-S_T \leq m_S \leq S_T$. At low temperature, when the magnetic coupling is larger than the thermal energy, the SMM behavior is defined by the following Hamiltonian (eq.1):

$$H = DS_{Tz}^2 + E\left(S_{Tx}^2 - S_{Ty}^2\right) \quad \text{(eq.1)}$$

where S_T is the total spin ground state: $S_{Tx}^2, S_{Ty}^2, S_{Tz}^2$ spin operators along the three principal directions of magnetization (*x* – hard, *y* – intermediate, *z* – easy axis), *D* and *E* are easy axis and transverse anisotropy parameters (that arise due to geometrical deviations from the ideal uniaxial symmetry for which *E* = 0). Hence in the absence of magnetic field and in the presence of a strong uniaxial anisotropy (*D* is negative and $|D| >> E$) the Hamiltonian can be described as:

$$H = DS_{Tz}^2 \quad \text{(eq.2)}$$

and the spin sublevels change their energy according to:

$$E_{m_s} = Dm_s^2 \quad \text{(eq.3)}$$

Hence, considering the S_T = 10 of Mn_{12}-OAc, the spin splits into 21 discrete energy levels ($-S_T \leq m_S \leq S_T$) with a strong uniaxial anisotropy energy barrier (Δ_A) of about 70 K (in Mn_{12}-based complexes) and a doubly degenerated ground state $m_S = \pm 10$ in zero field (Figure I-2).

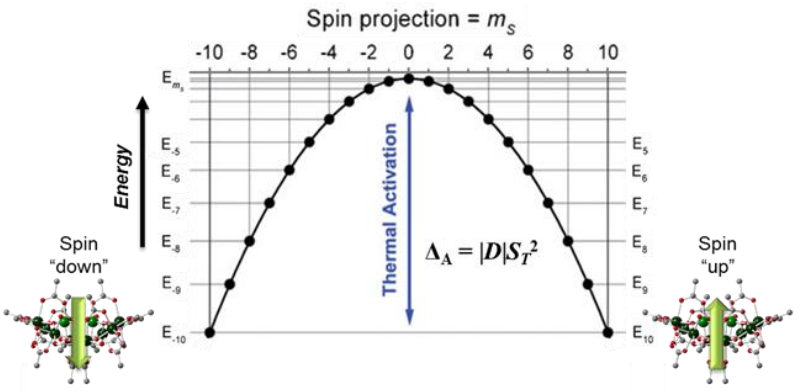

Figure I-2. Potential-energy diagram for Mn_{12}-OAc with an S_T = 10 ground state experiencing axial zero-field splitting, $\Delta_A = |D|S_T^2$. At low temperature SMMs are blocked in the fundamental state $m_S = \pm S_T$.

The spin corresponds to different projections (Figure I-2) of the total spin along the easy axis of the molecule (in the case of Mn_{12}-OAc, it corresponds to the *c*-axis of the crystal Figure I-1, left). The highest sublevel m_S corresponds to the lowest energy level. The energy barrier Δ_A, representing the difference between highest and lowest energy levels of the S_T ground state, is equal to $\Delta_A = |D| \cdot S_{T_z}^2$ for integer spins and $\Delta_A = |D| \cdot S_{T_z}^2 - 1/4$ for non-integer spins. The pathway to reverse the magnetization over the top of the energy barrier can only be reached by thermal energy.

I.2.1.3. Magnetic properties in longitudinal magnetic field

In the presence of an applied magnetic field the previous Hamiltonian (eq.**1**) is described as followed:

$$H = DS_{Tz}^2 - g\mu_B \overrightarrow{S_T} \cdot \vec{H} \qquad \text{(eq.4)}$$

where the last term is the Zeeman contribution resulting from the interaction of spin $\overrightarrow{S_T}$ with external magnetic field $\vec{H}$. When an external longitudinal magnetic field H_z is applied (along to easy axis), the spin sublevels change their energy according to the Zeeman coupling (Figure I-3):

$$E = Dm_z^2 - g\mu_B m_s \cdot H_z \qquad \text{(eq.5)}$$

According to eq.**5**, the spin sublevels with positive m_s value are energetically stabilized, while the sublevels with negative m_s value become energetically destabilized (Zeeman effect). Consequently, the population of the m_s = +10 sublevel is preferred. Thus, the favored orientation of the magnetic moments in the same direction as the applied field, gives rise to the magnetization $M \neq 0$ of the macroscopic sample.

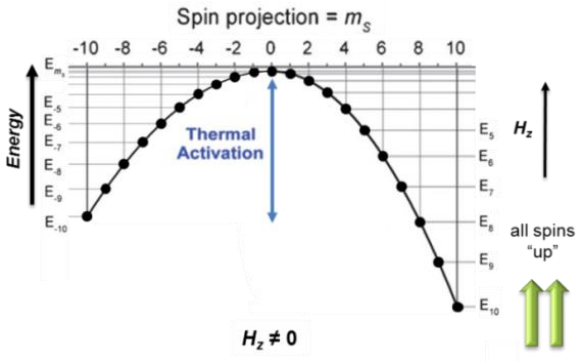

Figure I-3. Potential energy-diagram in the presence of a longitudinal magnetic field (Zeeman effect).

I.2.1.4. Relaxation of the magnetization

Upon removal of the external magnetic field, the initial energy spectrum is restored and spins recovered their thermodynamic energy levels with a certain dynamics and thus a magnetization relaxation is observed. In a classical paramagnetic system, the relaxation into the unmagnetized equilibrium initial state is often too fast to be observed (<< 1 s, even at low temperature).[19] In contrast, SMMs display a slow relaxation of magnetization due to the strong anisotropy barrier shown earlier (Figure I-2). The relaxation process is taking place through the coupling of the spin system with the environment. The molecule can absorb heat from the vibrational modes of the lattice (phonon) in the case where there is sufficient thermal energy (k_BT). Because of the selection rules of spin-phonon interaction, Δm_s = ±1 and ±2 are the only paths possible. In order to relax into the equilibrium state, the system must absorb phonon until it reaches m_s = 0, where it can thereafter reach m_s = -10 through phonon emission.

There are two methods used to monitor the relaxation process. First method consists to measure the time decay of the magnetization (*M(t)*) in a zero field. For that, a large *dc* field is first applied to the sample at a fixed temperature in order to saturate the magnetization in the easy direction. After removal of the magnetic field, the magnetization is then measured as a function of time (Figure I-4). As the decay of

magnetization is an exponential function of time, the relaxation time τ can be determined for every temperature by considering $\tau = t$ when the magnetization reaches 1/e.

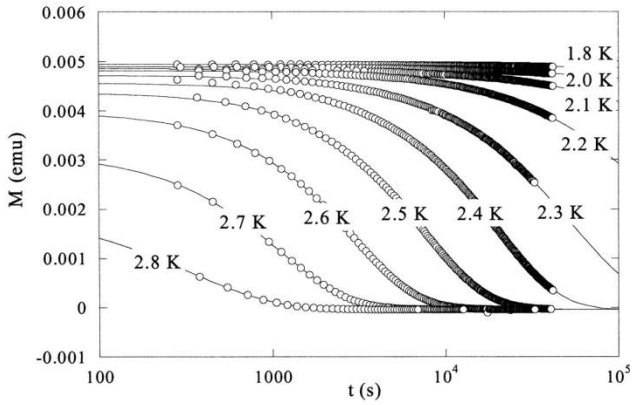

Figure I-4. Relaxation of the magnetization for Mn_{12}-OAc at different temperatures, measured at zero applied field for a single crystal after saturation at 5 T field applied along the easy axis of magnetization.[20]

In the simplest cases, the magnetization decreases exponentially with the time at fixed temperature according to the relation:

$$M(t) = M_0 \cdot \exp(-t/\tau) \qquad \text{(eq.}\mathbf{6}\text{)}$$

where M_0 or M_s (t = 0) is the saturated magnetization, $M(t)$ is the magnetization at given time t and τ is the relaxation time. The relaxation time is temperature dependent and it follows the Arrhenius law:

$$\tau = \tau_0 \cdot exp\left(\frac{\Delta_A}{k_B T}\right) \qquad \text{(eq.}\mathbf{7}\text{)}$$

where Δ_A is the energy barrier, k_B is the Boltzmann constant, and τ_0 is the pre-exponential factor, a constant that can be experimentally determined and depends on the nature of the SMM and its crystal packing. For Mn_{12} analogues, the relaxation time (τ_0) varies in the range of 10^{-8} – 10^{-10} s. From the eq.**7**, we can conclude that higher temperature means faster relaxation time.

The second method used to determine the relaxation time and give information about magnetization dynamics of a SMM is the alternating current (*ac*) magnetic susceptibility measurements (with a weak field, typically 1 – 5 Oe, oscillating at a given frequency, ν_{exp}). The alternating magnetic susceptibility produces two quantities: an in-phase or real, component χ' and an out-of-phase or imaginary, component χ'' as:

$$\chi_{ac} = \chi' + i\chi'' \qquad \text{(eq.}\mathbf{8}\text{)}$$

The relaxation time (τ) depends on the characteristic experimental time τ_{exp} ($\tau_{exp} = (2\pi\nu_{exp})^{-1}$). Consequently, when τ of the compound is shorter than τ_{exp}, the magnetization vector is oscillating with the *ac* field, and only a static behavior is observed (only the real component χ'). In the other case, when the τ is longer, the magnetization vector is dephased and non-zero χ'' signal can be measured. The χ'' versus temperature at a given frequency $\chi''(T)$ and/or χ'' versus frequency at fixed temperature $\chi''(\nu)$ can be measured. The temperature or frequency at which the χ'' signal reaches it maximum value correspond to the blocking temperature (T_B) or blocking frequency (ν_B) (Figure I-5, left). The relaxation time (τ) can be deduced from the maxima of the $\chi''(T)$ and / or $\chi''(\nu)$ curves at T_B and / or ν_B. In the case of Mn_{12}-OAc, the experimental thermally activated energy barrier is fitted by the Arrhenius law (τ vs 1/T plot, eq.9) as Δ_A/k_B = 62 K, with $\tau_0 = 2.1 \cdot 10^{-7}$ s (Figure I-5, right).[3a]

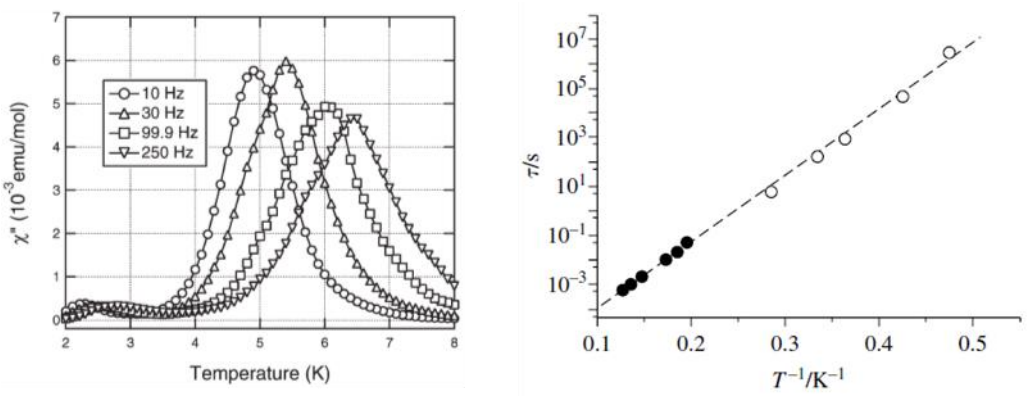

Figure I-5. (left) Imaginary component of the ac susceptibility of Mn_{12}-OAc measured with frequency ranging from 10 Hz to 250 Hz.[21a] (right) Temperature dependence of the relaxation time on a log scale of Mn_{12}-OAc extracted from *ac* susceptibility data (solid symbols) in the frequency range 1-270 Hz and from time decay of the magnetization (empty symbols), the line is the fit to the Arrhenius law (Eq. I.9) with Δ_A/k_B = 62 K, with $\tau_0 = 2.1 \cdot 10^{-7}$ s.[3a]

Below the blocking temperature, the magnetization versus field curves show hysteresis which depends on the sweeping rate of the magnetic field and becomes larger with temperature decreasing. A series of steps are also detected in the hysteresis loops of the Mn_{12}-OAc (Figure I-6, left). The observed steps in the hysteresis loop correspond to a faster rate of magnetization relaxation occurring when the energy levels on opposite parts of the double-well potential are at the same energy (Figure I-6, right). For these particular field values, tunneling of the magnetization is enabled, and an evident increase in the relaxation rate is observed.

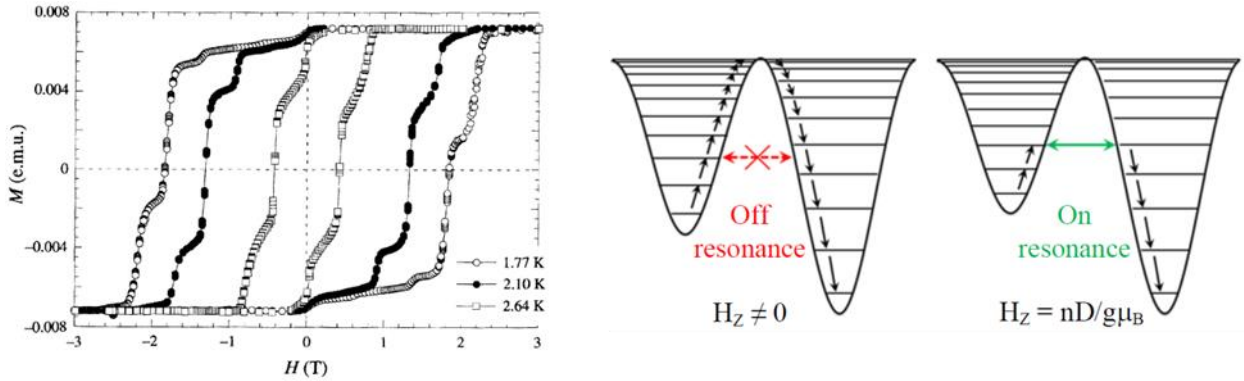

Figure I-6. (left) Magnetization vs. field plots for Mn_{12}-OAc emphasizing the stepwise hysteresis loop at low temperature. (right) Double-well potential diagram in the presence of a longitudinal field.[9b] Resonant magnetization corresponding to vertical "steps" occurs when the energy levels are aligned between of two halves of the diagram.

More recently, a multifaceted magnetization dynamics was observed in the mononuclear complex salt $(Bu_4N)_2[Re^{IV}Cl_4(CN)_2]\cdot 2DMA$(DMA = N, N-dimethylacetamide) by invoking Orbach, direct and Raman-type processes (Figure I-7, left).[21b] The Orbach relaxation process is characterized by an energy barrier of 39 K (29 cm^{-1}) based on high-field electron paramagnetic resonance (EPR). Slow relaxation of magnetization has not been observed due to the very short relaxation time. Therefore, a small static field was applied and *ac* signals were observed (Figure I-7, right). The spectroscopy gives the opportunity to access the energy levels involved in the Orbach relaxation.

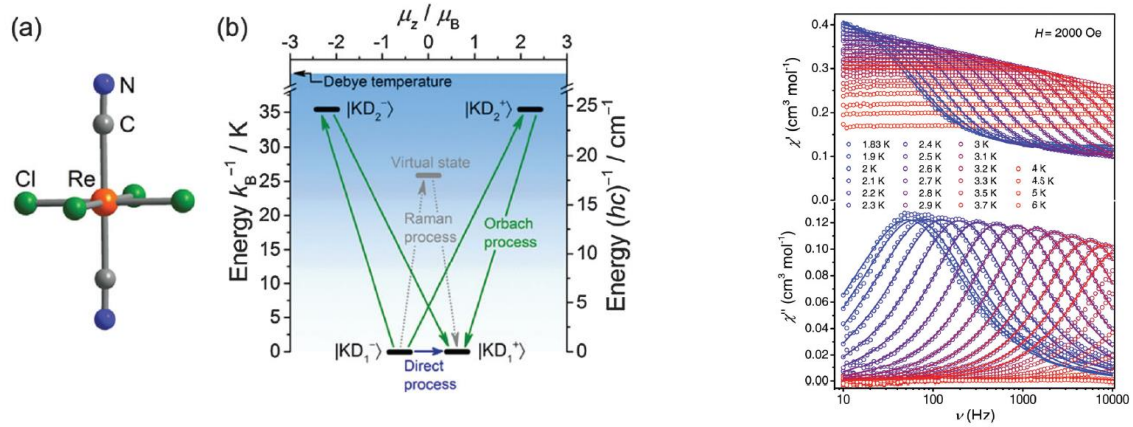

Figure I-7. (left) (a) Structure of the trans-$[Re^{IV}Cl_4(CN)_2]^{2-}$ complex. (b) Energy level diagram: The blue shading is schematic representation of the acoustic phonon density with the cut-off at the Debye temperature. The arrows indicate direct (blue), Raman (grey) and Orbach (green) relaxation pathways from state $|KD_1^-\rangle$ to $|KD_1^+\rangle$. (right) Frequency dependence of the in-phase (χ', top) and out-of-phase (χ'', bottom) components of the ac magnetic susceptibility at different temperatures of a polycrystalline sample $(Bu_4N)_2[Re^{IV}Cl_4(CN)_2]\cdot 2DMA$ under a 2000 Oe dc field. The solid line are the best fits to the generalized Debye model.[21b]

I.2.2. Spin Crossover Complexes (SCOs)

I.2.2.1. Generalities

The term spin crossover (SCO) design the phenomenon or complexes that exhibit a change of electronic configuration of its/their metal center(s) as function of an external physical or eventually chemical stimuli.[1] Spin-crossover phenomenon involves drastic change in magnetic properties, color, vibrational and structural properties, dielectric constant and electrical resistance.[1,22] For instance, in Fe(II) complexes, the SCO is associated with paramagnetic-to-diamagnetic switching. The ability of these materials to switch their physical properties may have interest for numerous practical applications such as sensors, switches, data storage and display devices.[23]

The field was initiated more than eighty years ago by the pioneering work of Cambi and Szegö, who reported anomalous magnetic susceptibilities on a series of Fe^{III} dithiocarbamate $[Fe(R_2NCS_2)_3]$ complexes.[24] However, it is only much later that the comprehension of the phenomenon began. Thus, the notion of spin equilibrium has been mentioned for the first time by Griffith in 1956.[25] Stoufer and co-workers.[26] demonstrated shortly later for the first time that the temperature can induce spin conversion phenomenon on a cobalt (II) compound, namely $[Co(L)_2]I_2$ (with L = bis-(2,6-pyridinedialdihydrazone ligand). This was followed by the discovery of the first iron(II) $[Fe(phen)_2(NCS)_2]$ (where phen = 1,10-phenanthroline) spin-crossover compound by Madeja and König.[27] At the same period, the concept of switching between two different states, namely the high-spin state (HS) and the low-spin state (LS), has been introduced by A. H. Ewald and co-workers,[28] who reinvestigated more in detail the magnetic properties of Fe^{III} dithiocarbamate complexes reported earlier by Cambi and Szegö. Since then, SCO phenomenon has been observed in many complexes of Fe^{II},[1] Fe^{III},[29] Co^{II},[30] Co^{III},[31] Cr^{II},[32] Mn^{II},[33] Mn^{III},[34] and Mo^{II}.[35] Examples of dinuclear,[36] trinuclear,[37] tetranuclear[38] or polymer[39] SCO systems have been also described. In most common situation,

the SCO is triggered by the change of temperature[1] or irradiation with light[40,41] but other stimuli such as pressure,[42] magnetic[43] or electric[44] fields can be used.

I.2.2.2. Ligand field theory

In octahedral symmetry, the five *d* orbitals of a transition metal ion are split into two sets of orbitals, namely t_{2g} and e_g orbitals. The set of lower energy corresponds to t_{2g} and is composed by the three d_{yz}, d_{yz} and d_{zx} orbitals, while e_g level of higher energy corresponds to the two d_{z^2} and $d_{x^2-y^2}$ orbitals (Figure I-8). Therefore, metal ions with d^4 to d^7 configuration may exist in either high-spin (HS) or low-spin (LS) states, depending of the energy separating the t_{2g} and e_g levels. For instance, octahedral Fe^{II} metal ion ($3d^6$), which are the most represented in SCO systems, can be found in either t_{2g}^6 LS state or in the $t_{2g}^4 e_g^2$ HS state. The crystal field spitting, Δ, between the t_{2g} and e_g levels, corresponds to the ligand field spitting (Dq) and is related to the ligand field strength as:

$$\Delta = 10D_q \qquad \text{(eq.9)}$$

where $D_q \propto \frac{\mu}{r^n}$, n = 5-6, μ is the dipole moment and *r* is the metal to ligand distance.

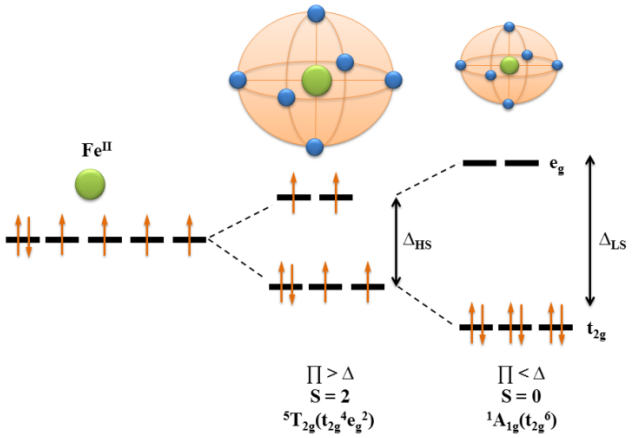

Figure I-8. Splitting of *d* orbitals in an octahedral field created by six ligands for Fe^{II} (d^6) ion with the spectroscopic terms associated with each configuration.

The energy of crystal field depends on the nature of ligands or more generally on the environment of the metal center.[45] The magnitude of the crystal field spitting along with the pairing energy (Π) of the complex determine whether the LS or HS configuration are stabilized.

- when Π > Δ, the energy required to populate the e_g orbitals is inferior to the one required for pairing the spins and the electrons will populate both levels accordingly to the Hund's rule, leading therefore to the high spin (HS) situation. In Fe^{II} metal ion, the spin value is S = 2 and the ground state is a paramagnetic HS state with a fundamental spectroscopic term $^5T_{2g}$.
- when Π < Δ, the energy to overcome the gap is too high and the electrons will fill only the orbitals t_{2g} according to Pauli's rule, leading to the low spin (LS) situation. For Fe^{II}, all the electrons are paired, giving rise to the diamagnetic (S = 0) ground state with a fundamental spectroscopic term $^1A_{1g}$.
- when Π ~ Δ, the two spin configurations are possible. The stabilization of either LS or HS states is then very sensitive to external perturbations such as temperature and spin crossover may occur.

The pairing energy Π does not change significantly from one complex to another and it is worth about 15000 cm^{-1} for Fe^{II} complexes.[46] In contrast, the crystal field is strongly dependent of the environment. Therefore, to predict the spin configuration of a complex and determine whether spin crossover is possible, it is necessary to know the crystal field. Such information can be assessed by optical measurements and explained using Tanabe-Sugano diagram (Figure I-9).[46,47] For example, the $[Fe(H_2O)_6]^{2+}$ complex has a Δ of about 10400 cm^{-1}, which is much lower than the pairing energy and the complex is HS whatever the temperature. The presence of cyanide ligands, is known to lead to high ligand field strength and for example $[Fe(CN)_6]^{4-}$ complex is characterized by Δ = 33000 cm^{-1} and is diamagnetic. The compound $[Fe(ptz)_6]^{2+}$ (ptz = 1-propyltetrazole) is HS at room temperature and becomes LS at low temperature. The study of its optical spectra at 295 K and 10 K gives Δ_{HS}/k_B = 16990 K and Δ_{LS}/k_B = 27940 K.[46]

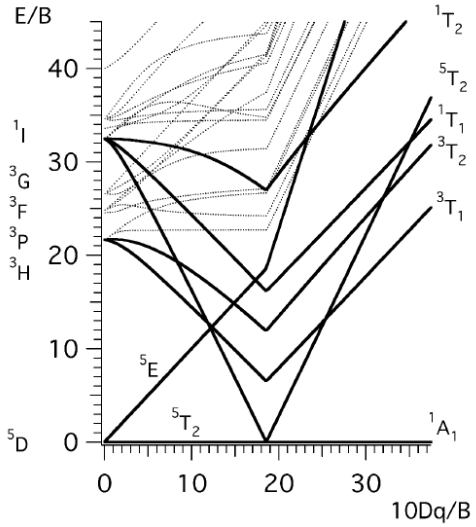

Figure I-9. Tanabe-Sugano diagram for a transition metal ion with six *d* electrons, showing the energy of the excited ligand-field states in units of the Racah parameter of electron-electronic repulsion B relative to the respective ground state, versus the ligand-field strength 10Dq also in units of B. The calculation was performed using the electrostatic matrices in the strong-field.[46,47]

Beside the changes of the magnetic and optical properties that can be respectively monitored by magnetic susceptibility measurements and vis-UV or reflectivity spectroscopies, other critical changes of the physical features are occurring during SCO. Especially, the change of the spin configuration is accompanied by a change of the vibrational modes giving the possibility to probe the SCO phenomenon by infrared or Raman spectroscopies. These methods are particularly relevant when complexes contains cyanides or thiocyanate ligands since their characteristic stretching vibrations (~ 2100-2150 cm^{-1}) are usually well isolated in the spectra. The SCO also affects the nuclear spin density of the metal center, giving access to ^{57}Fe Mössbauer spectroscopy, which can differentiate the LS and HS configurations though their differing isomer shifts and quadrupole splitting, as well as NMR characterization methods. Crystallography and more particularly single-crystal X-ray diffraction analysis is also a very useful tool to probe SCO. Indeed, the conversion from LS into HS configuration involves an expansion of the coordination sphere resulting from the elongation of the coordination bond distance of about 0.25 Å.[46,48] This phenomenon can be explained by the population of the anti-bonding e_g orbitals in the HS state, which reduce the σ character of the bond and limit overlapping between the t_{2g} orbitals from metal ion and vacant π* orbitals from the ligand (retro-

donating π interactions).[49] For Fe^{II} metal ion, the typical bond length values are 1.8 - 2.0 Å for the LS phase and 2.0 – 2.2 Å for the HS state. Beside the local changes of the coordination sphere, the SCO process might affect significantly the overall crystal packing leading sometime to a crystallographic phase transition.[50] The single-crystal X-ray diffraction analysis is therefore essential to correlate the properties originating from the molecular level to the macroscopic behavior observed in solid-state.

I.2.2.3. Conversion versus transition: thermodynamic aspects

As described above, SCO complexes show an interconversion between two different states. In this section we describe the mechanism of spin crossover based on simple thermodynamic models for binary systems.[51] As SCO complexes are essentially isolated paramagnetic species that exhibit Curie paramagnetism, the measurement of the molar magnetic susceptibility multiplied with the temperature as a function of temperature (χT vs T) is the principal technique used to characterize spin crossover phenomenon. The χT product corresponds to the Curie constants of each state and is related to their molar fraction x, according to the equation:

$$\chi T = x_{HS} \cdot (\chi T)_{HS} + x_{LS} \cdot (\chi T)_{LS} \qquad \text{(eq.}\mathbf{10}\text{)}$$

Considering $x_{HS} = x$, then eq.**10** becomes:

$$\chi T = x \cdot (\chi T)_{HS} + (1- x) \cdot (\chi T)_{LS} \qquad \text{(eq.}\mathbf{11}\text{)}$$

For the HS and LS states, $(\chi T)_{HS}$ and $(\chi T)_{LS}$ products are in most of cases temperature independent (Curie law). Therefore $\chi T = f(T)$ gives access to $x = f(T)$. In the following, the model for the temperature dependence of x is described for both ideal and regular solution models. Spin crossover may be described as equilibrium between two states:

$$LS \rightleftarrows HS$$

with Gibbs energy change:

$$\Delta G = \Delta H - T\Delta S \qquad \text{(eq.}\mathbf{12}\text{)}$$

This energy is positive below a temperature named T^* and negative above it. When $T = T^*$, the following relationship is verified:

$$\Delta H = T^*\Delta S \qquad \text{(eq.}\mathbf{13}\text{)}$$

Considering the ideal solution model, it is assumed that the HS and LS states are mixed without any interaction. If N is the total number of molecules, then $N_{HS} = x_{HS} \cdot N = x \cdot N$ is the number of molecules in the HS state and $N_{LS} = x_{LS} \cdot N = (1-x) \cdot N$ is the number of molecule in the LS state. In statistical thermodynamics, the Gibbs energy of the system can be described as:

$$G = N_{HS}G_{HS} + N_{LS}G_{LS} + G_{mix} \qquad \text{(eq.}\mathbf{14}\text{)}$$

where, G_{HS} and G_{LS} are the molar Gibbs energy for HS and LS molecules, and the G_{mix} is the energy of the mixture:

$$G_{mix} = - TS_{mix} = Nk_BT[x\ln x + (1-x)\ln(1-x)] \qquad \text{(eq.}\mathbf{15}\text{)}$$

hence:

$$G = xN(H_{HS} - k_BT\ln g_{HS}) + (1 - x)N(H_{LS} - k_BT\ln g_{LS}) + Nk_BT\,[x\ln x + (1-x)\ln(1-x)] \qquad \text{(eq.}\mathbf{16}\text{)}$$

This relationship allows describing the Gibbs energy per molecule, g_N, as following:

$$g_N = \frac{G}{N} = x\left[\Delta H - k_B T \ln\frac{g_{HS}}{g_{LS}}\right] + k_B T[x\ln x + (1-x)\ln(1-x)] + G_{LS} \quad \text{(eq.}\mathbf{17}\text{)}$$

Introducing the logarithmic degeneracy ratio, $a = \ln\left(\frac{g_{HS}}{g_{LS}}\right)$:

$$g_N = \frac{G}{N} = x[\Delta H - k_B T a] + k_B T[x\ln x + (1-x)\ln(1-x)] + G_{LS} = g'_N(x) + G_{LS} \quad \text{(eq.}\mathbf{18}\text{)}$$

The condition for equilibrium requires:

$$\left(\frac{\partial g'_N}{\partial x}\right)_{T,N} = 0 \quad \text{(eq.}\mathbf{19}\text{)}$$

As G_{LS} is a constant, the relation becomes:

$$\left(\frac{\partial g'_N}{\partial x}\right)_{T,N} = \Delta H - k_B T a + k_B T \ln\frac{x_{min}}{1-x_{min}} = 0 \quad \text{(eq.}\mathbf{20}\text{)}$$

The equation can be rearranged in the form of:

$$\frac{1-x_{min}}{x_{min}} = exp\left(\frac{\Delta H}{k_B T} - a\right) \quad \text{(eq.}\mathbf{21}\text{)}$$

or:

$$x_{min} = \frac{1}{1+exp\left(\frac{\Delta H}{k_B T} - a\right)} \quad \text{(eq.}\mathbf{22}\text{)}$$

For $T = T^*$, $x_{HS} = x_{LS} = x^* = 0.5$ and thus $\ln\frac{x^*}{1-x^*} = 0$. Then, $\Delta H - k_B T^* \cdot a = 0$ and $a = \frac{\Delta H}{k_B T^*}$.

The expression eq.**22** changes in:

$$x_{min} = \frac{1}{1+exp\left(\frac{\Delta H}{k_B}\left(\frac{1}{T} - \frac{1}{T^*}\right)\right)} = \frac{1}{1+exp\left(a\left(\frac{T^*}{T} - 1\right)\right)} \quad \text{(eq.}\mathbf{23}\text{)}$$

or

$$\frac{T}{T^*} = \frac{a}{a + \ln\frac{1-x_{min}}{x_{min}}} \quad \text{(eq.}\mathbf{24}\text{)}$$

This allows the plotting of the $\frac{T}{T^*} = f(x_{min})$ dependence (Figure I-10), where $T^* = \frac{\Delta H}{k_B \cdot a}$. Whatever is the value of a, the function x_{min} increases when T/T^* increases. This model predicts that at low temperature ($T/T^* << 1$), the system is in diamagnetic (LS) state, so $x_{min} = 0$. We can observe that all curves pass through a common point, $T/T^* = 1$, and $x_{min} = 0.5$. So we can conclude that T^* is a characteristic temperature of the system. At this point, the system contains 50 % of molecules in state HS and 50 % of molecules in state LS. Note that in the literature, T^* is often noted $T_{1/2}$ to reflect the composition of the system.

Let's consider now a real example of Fe^{II} octahedral system. The paramagnetic state (HS) corresponds to the $^5T_{2g}$ spectroscopic term, giving the spin degeneracy of 5 and the orbital degeneracy ($2L_{HS} + 1$) of 3. The diamagnetic state (LS) corresponds to the $^1A_{1g}$ spectroscopic term for which spin degeneracy is 1, and the orbital degeneracy is 1. Therefore, g_{HS} = (5×3), g_{LS} = (1×1) or g = 15, which gives $a = ln15 = 2.71$. According to the simulation plot provided in Figure I-9, the most similar case is for $a = 3$, where x_{min} tends to 0.95 at $T/T^* > 2$. But in real systems, the limit of x is very close to 1. The entropy change in Fe^{II} system can be experimentally measured by calorimetric methods or deduced from optical and/or magnetic measurements, thus the value of a could be experimentally estimated between 4.2 and 9.6.[52,53] This shows that in real complexes not only the electronic contributions to the degeneracy are present, but also the

vibrational contributions for paramagnetic and diamagnetic states, which are different due to the different geometry in both states.

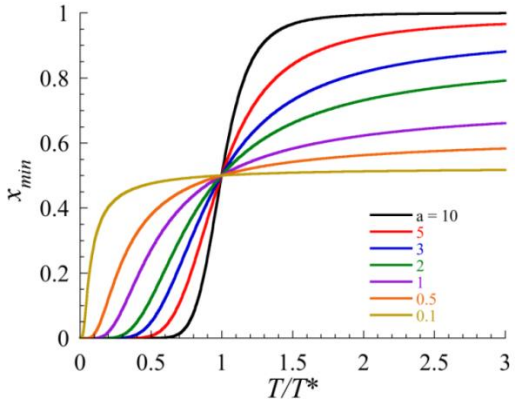

Figure I-10. Temperature dependence of the paramagnetic molar fraction x_{min} for different values of degeneracy, a (ideal solution model).

In a solid state the spin crossover is directly influenced by intermolecular interactions (mostly of elastic origin), which play an important role in the macroscopic properties of the systems. Therefore we can add the interaction energy, which is responsible for the cooperative effects, in the regular solution model. Hence, the Gibbs energy of the system can be written as:

$$G = N_{HS}G_{HS} + N_{LS}G_{LS} + G_{\text{mix}} + I \qquad \text{(eq.25)}$$

where, the interaction energy term $I(x)$ is defined as:

$$I(x) = Wx(1-x) \qquad \text{(eq.26)}$$

where W is the intermolecular interaction parameter (in units of energy) that is independent of temperature. Note that $I(x)$ is a simple exchange term in the mean-filed approximation: $Wx(1-x) = Wx_{HS}x_{LS}$. Thus, the insertion of this term in the molar Gibbs energy gives:

$$G = xN(H_{HS} - k_{\text{B}}T\ln g_{LS}) + (1-x)N(H_{LS} - k_{\text{B}}T\ln g_{LS}) + Nk_{\text{B}}T[x\ln x + (1-x)\ln(1-x)] + Wx(1-x) \qquad \text{(eq.27)}$$

then:

$$g'_N(x) = x[\Delta H - k_{\text{B}}Ta] + k_{\text{B}}T[x\ln x + (1-x)\ln(1-x)] + Wx(1-x) \qquad \text{(eq.28)}$$

and from the condition of equilibrium (eq. **19**):

$$\Delta H - k_{\text{B}}Ta + k_{\text{B}}T\ln\frac{x_{min}}{1-x_{min}} + W(1-2x_{min}) = 0 \qquad \text{(eq.29)}$$

or

$$k_{\text{B}}T = \frac{\Delta H + W(1-2x_{min})}{a + \ln\frac{1-x_{min}}{x_{min}}} \qquad \text{(eq.30)}$$

The dependence $\frac{T}{T_*} = f(x_{min})$ can be plotted and the function is defined by:

$$\frac{T}{T^*} = \frac{a + \frac{W}{k_{\text{B}}T^*}(1-2x_{min})}{a + \ln\frac{1-x_{min}}{x_{min}}} \qquad \text{(eq.31)}$$

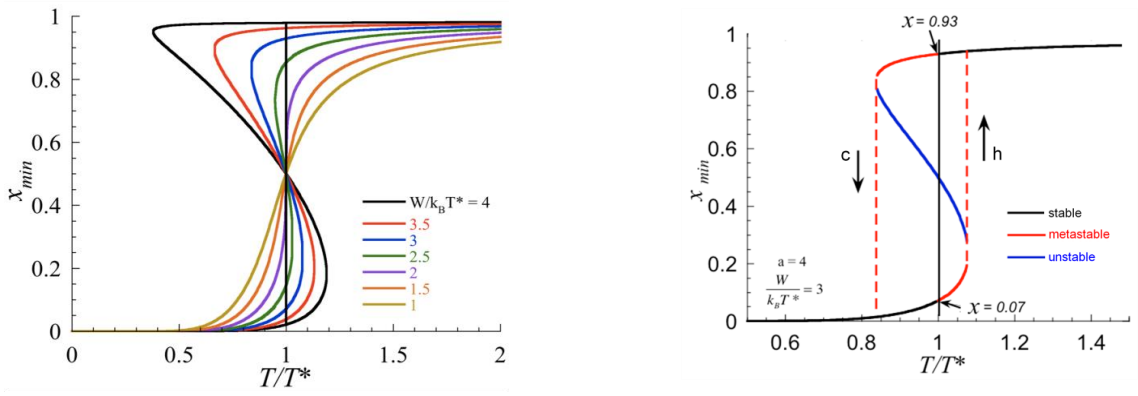

Figure I-11. (left) Temperature dependence of the paramagnetic molar fraction x for different values of $W/(k_BT^*)$ at fixed a = 4, in a regular solution model; (right) thermal hysteresis when a = 4 and $W/(k_BT^*)$ = 3, c – cooling mode, h – heating mode.

Three cases are possible:

- $W/k_BT^* < 2$, so x_{min} is increasing when T/T^* increases, and the corresponding curves are more and more steep for higher values of W/k_BT^* but possess the same inflection point given by $T/T^* = 1$ and $x_{min} = 0.5$. This phenomenon is a spin conversion.
- $W/k_BT^* = 2$, there is an abrupt curve corresponding to x_{min} at $T/T^* = 1$. This gives a first-order transition at $T/T^* = T_c$ and the spin transition temperature is given by the expression $W/k_BT^* = T_c$ This phenomenon is a spin transition at the critical point.
- $W/k_BT^* > 2$, the curve has an "S" shape, and for $T/T^* = 1$, not only the $x_{min} = 0.5$ solution is possible, but the Gibbs energy adopts two other local minimum values. A spin transition corresponding to a first transition is observed. In this case, a first order transition is associated with thermal hysteresis (Figure I-11, right).

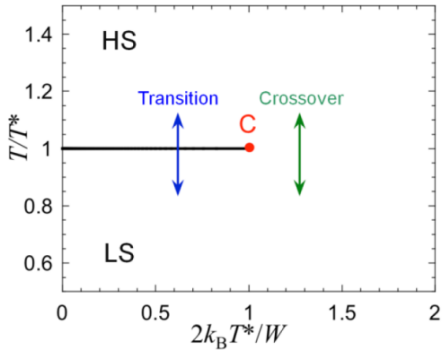

Figure I-12. Phase diagram for the regular solution mode with $W > 0$ in the plane $\left(\frac{T}{T_*}, \frac{2k_BT_*}{W}\right)$

The blue branch of the curve corresponds to unstable points, but actually the system describes a hysteresis, drawn in dashed lines (Figure, I-11, right). The hysteresis width does not depend on the thermodynamics but on kinetic criteria and thus on experimental scanning rate of the temperature. From this analysis, we can construct a phase diagram that describes the system at any temperature and any value of W. The phase diagram consists in a line of first order phase transition at $T/T^* = 1$ that ends with a critical point, C (red point from Figure I-12). From this phase diagram, we can predict if real system will present a conversion or a transition. If $2k_BT^*/W \leq 1$, the system crosses the transition line (blue arrow from Figure I-

11) and we will observe a spin transition; otherwise if $2k_BT^*/W > 1$, the system is beyond the critical point (green arrow from Figure I-12) and spin conversion will be observed.

I.2.2.4. Light-induced spin crossover

The discovery of a light-induced spin crossover by Gütlich and co-workers in 1984,[40] had an enormous impact in the field of spin switchable materials. In this seminal work, the authors reported that $[Fe(ptz)_6](BF_4)_2$ (ptz = 1-propyltetrazole) complex can be converted at 10 K from the stable LS ($^1A_{1g}$) state to the metastable HS ($^5T_{2g}$) state by irradiating with green light. This phenomenon, known as Light-Induced Excited Spin-State Trapping (LIESST), can be followed by optical and magnetic measurements.

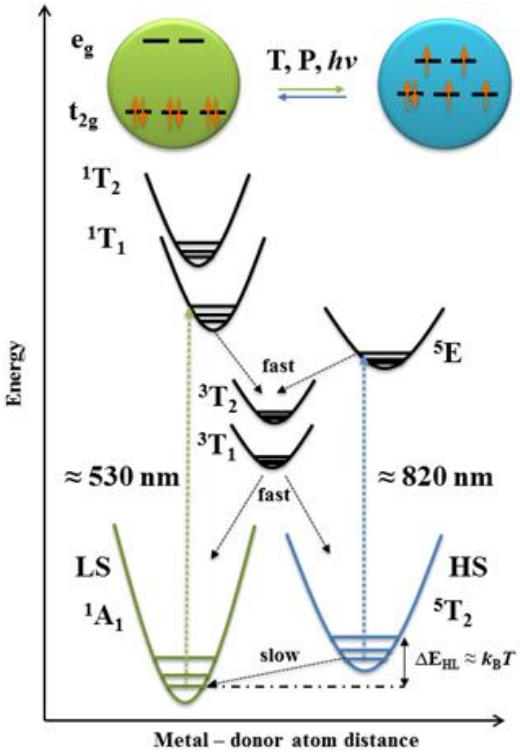

Figure I-13. Jablonski-type diagram representing the mechanism for LIESST,[40] and reverse-LIESST[54] of d^6 octahedral transition metal complex (e.g. $[Fe(ptz)_6](BF_4)_2$). The first step is a spin-allowed excitation via green light (≈ 530 nm) or red light (≈ 820 nm), followed by two intersystem crossing processes ending at the HS or LS, respectively.

The proposed mechanism for light-induced spin crossover is represented by Jablonski-type energy diagram (Figure I-13). The excitation with green light (≈ 530 nm) at low temperature induces a transition from the $^1A_1$ ground state into a $^1T_1$ excited state, which relaxes rapidly descending over two successive steps, $^1T_1 \rightarrow {}^3T_1 \rightarrow {}^5T_2$, populating the $^5T_2$ metastable state. When the temperature is low enough, the system remains trapped in same state since the energy barrier associated to the transition into the $^1A_1$ state is greater than the thermal energy of the system. At cryogenic temperature, the relaxation process can be very slow and a life time of about eleven days was for example found when the $[Fe(ptz)_6](BF_4)_2$ complex is maintained at 20 K.[54] When the temperature is increasing, the system can overcome the energy barrier and thus relaxes into the thermodynamic diamagnetic phase. In 1986, Hauser reported a reversed photomagnetic effect, referred as reverse-LIESST,[53] using a near-infrared (≈ 820 nm) light to convert the same $[Fe(ptz)_6](BF_4)_2$ compound from its photo-induced metastable HS state into the LS state. Recently, Long, Clérac and co-workers reported in the same compound that the metastable paramagnetic phase behave as a SMM, introducing

therefore the concept of magnetic tristability between a diamagnetic (S = 0) and a photo-activated SMM (S = 2) with either up (*Ms* = +2) or down (*Ms* = -2) polarities.[55a] This particular feature linking SCO and SMM fields, was confirmed shortly later in another example of SCO.[55b]

I.2.3. Electron Transfer Complexes (ET)

I.2.3.1. Generalities

During the past half-century, the interest in electron transfer (ET) systems has undergone a remarkable expansion.[2,5,56] Indeed, electron transfer phenomenon is one the most fundamental processes in physics, chemistry and biology.[57] The ET is a redox process between two units, one being the reductant (donor) and the second one being the oxidant (acceptor). In 1956, Rudolph A. Marcus developed the first generally accepted theory of outer-sphere (intermolecular) ET based on a transition state theory approach.[58] Then, Hush extended the theory to the problem of inner sphere (intramolecular) ET reactions.[59] Since then, several other models have been proposed to complete existing ones.[60]

The first reported synthetic molecular system showing metal-to-metal electron transfer is the well-known mixed valence Creutz–Taube ion of general formula $[(H_3N)_5Ru^{II}(pyr)Ru^{III}(NH_3)_5]^{5+}$ (pyr = pyrazine).[61] Such ET processes have been also observed in heterometallic compounds[62] as well as in purely organic systems.[63]

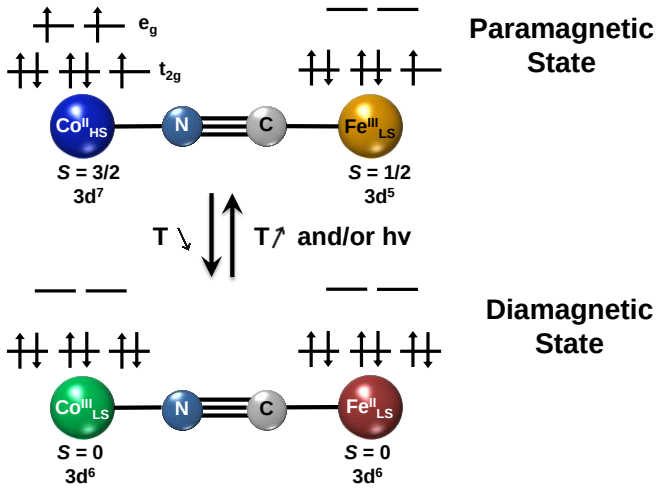

Figure I-14. Interconversion between the paramagnetic (Fe^{III}_{LS}-CN-Co^{II}_{HS}) and diamagnetic (Fe^{II}_{LS}-CN-Co^{III}_{LS}) electronic configurations due to thermally and photo-induced metal-to-metal electron transfer processes.

The first example of 3D coordination polymer, namely $K_{0.2}Co_{1.4}[Fe(CN)_6]\cdot 6.9H_2O$, featuring thermally or photo-induced ET was described by Hashimoto's group in 1996.[56a] This material, belonging to the family of Prussian Blue analogues (PBA), generated a great research interest due to the possibility to control magnetic properties at molecular level as the result of the metal-to-metal ET within the {Fe(μ-CN)Co} elemental motif. The ET is occurring through the cyanido-bridge and is accompanied by a diamagnetic-to-paramagnetic switching between the {Fe^{II}_{LS}(μ-CN)Co^{III}_{LS}} pair (Fe^{II}_{LS} *S* = 0; Co^{III}_{LS} *S* = 0) and {Fe^{III}_{LS}(μ-CN)Co^{II}_{HS}} pair (Fe^{III}_{LS} *S* = 1/2; Co^{II}_{HS} *S* = 3/2) (Figure I-14).

Cyanido-bridged hetero-bimetallic molecular complexes, exhibiting switching of their magnetic and optical properties *via* ET process, are another class of molecules proposed during this thesis work to develop hybrid materials. In this regard, the following Section I.2.3.2 is dedicated to a more detailed description of these interesting systems.

I.2.3.2. Examples of molecular Fe^{III}/M^{II} cyanide-based complexes

The discovery of Prussian blue and their analogues has raised much interest in many fields, including magnetism.[64] Prussian blue (PB) and their analogues have the general formula $A_xM_y[M'(CN)_6]_i \cdot nH_2O$ (A = alkaline ion, M and M' = transition metals). Certain M/M' couples of these materials can exhibit metal-to-metal electron transfer through the cyanide bridges. Moreover, ET process has been found to occur under the influence of temperature,[65] pressure,[66] visible light[65,67] and X-rays[68] in different PBAs.

As mentioned above, the first example that shows light-induced reversible magnetization changes was $K_{0.2}Co_{1.4}[Fe(CN)_6]\cdot 6.9H_2O$ (Figure I-15, left).[56a] In the visible region of its electronic absorption spectra, this material exhibits an intense metal-to-metal charge transfer absorption at 550 nm, ascribed to the conversion of $\{Fe^{II}_{LS}(\mu\text{-CN})Co^{III}_{LS}\}$ ($Fe^{II}_{LS} - t^6_{2g}$, $S = 0$ and $Co^{III}_{LS} - t^6_{2g}$, $S = 0$) into paramagnetic $\{Fe^{III}_{LS}(\mu\text{-CN})Co^{II}_{HS}\}$ ($Fe^{III}_{LS} - t^5_{2g}$, $S = 1/2$ and $Co^{II}_{HS} - t^5_{2g}e^2_g$, $S = 3/2$) units *via* metal-to-metal ET. Before irradiation, the system contains both pairs, $Co^{II} - NC - Fe^{III}$ and $Co^{III} - NC - Fe^{II}$, and behaves like magnet with a temperature T_c = 16 K. By irradiating with red light (660 nm), an increase of the ferrimagnetic ordering temperature (Curie temperature) from 16 to 19 K is observed (Figure I-15, right). The initial state of the compound can be recovered by irradiating with blue light (450 nm) or heating the sample above 150 K.

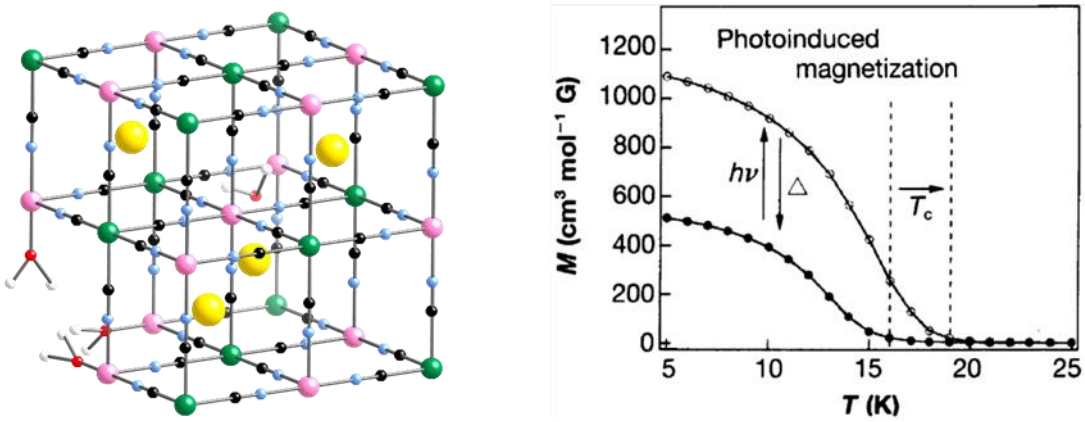

Scheme I-15. (left) General structure of Prussian blue analogues, $A_xM_y[M'(CN)_6]_l\cdot nH_2O$ (A = alkaline ion, yellow; M and M′ = transition metals, M green and M' pink ; C, black; N, blue; O, red; H, white). (right) Temperature dependence of the field-cooled magnetization at H = 5 G, before and after red light irradiation for $K_{0.2}Co_{1.4}[Fe(CN)_6]\cdot 6.9H_2O$.[56a]

Photomagnetic behavior and thermally induced ET of Fe/Co Prussian Blues analogues can be modulated by modifying the Co/Fe ratio present in the nonstoichiometric $A_xCo_y[Fe(CN)_6]\cdot nH_2O$ (A = alkaline ion) lattices.[56b,69] Considering x < 0.5, the Fe sites are fractionally occupied and the Co centers consequently contain one or more water molecules to complete their coordination spheres (Figure I-15). The number of water molecules tunes the ligand field strength and redox potential of the Co centers. It was indeed found that an average CoN_5O coordination environment and adjacent $[Fe(CN)_6]_n^-$ sites are primary to

result reversible thermally and photo-induced magnetization changes in the material. For example, Hashimoto and co-workers reported that $Na_{0.07}Co_{1.50}[Fe(CN)_6]\cdot 6.3H_2O$ and $Na_{0.94}Co_{1.15}[Fe(CN)_6]\cdot 3.0H_2O$ do not display ET and remain paramagnetic and diamagnetic, respectively, while $Na_{0.60}Co_{1.37}[Fe(CN)_6]\cdot 3.9H_2O$, $Na_{0.53}Co_{1.32}[Fe(CN)_6]\cdot 4.4H_2O$ and $Na_{0.37}Co_{1.37}[Fe(CN)_6]\cdot 4.8H_2O$ systems display photo-induced ET as well as thermally-induced first-order transition with a thermal hysteresis of about 40 K.[69e]

The Fe/Mn PBAs were also reported to exhibit photo- and/or thermally-induced ET with a large thermal hysteresis of 116 K between 147 and 263 K.[70,71] $Rb_{0.88}Mn[Fe(CN)_6]_{0.96}\cdot nH_2O$ system exhibits both thermally and photo-induced ET between $\{Fe^{III}_{LS}(\mu\text{-CN})Mn^{II}_{HS}\}$ pair (Fe^{II}, S = 1/2; Mn^{II}, S = 5/2) and $\{Fe^{II}_{LS}(\mu\text{-CN})Mn^{III}_{HS}\}$ pair (Fe^{II}, S = 0; Mn^{III}, S = 2). A structural transformation from cubic to tetragonal is also accompanying the ET due to Jahn-Teller distortion on the Mn^{III} sites. A ferromagnetic order was shown at low temperatures (T_C = 11 K) due to interactions between Mn^{III} ions through the diamagnetic $[Fe^{II}(CN)_6]$ units. A ferrimagnetic phase can be induced after irradiation at 532 nm as a result of metal-to-metal charge transfer, therefore showing a decrease of magnetization. By irradiating at 410 nm the initial state can be recovered. The ability Fe/Mn PBAs to exhibit ET phenomenon is known to be intimately coupled to the exact system stoichiometry.[72] Beside this systems, other PB analogues like V/Cr,[73] Mn/Cr,[74] Co/Os,[75] as well as many polycyanometalates-based compounds,[76] i.e. Co/W,[77] Cu/Mo,[78] featuring ET properties were reported.

As shown above in the Co/Fe PBAs, the variation of the amount of $[Fe(CN)_6]^{3-}$ vacancies greatly influences the cobalt ion coordination sphere, which is completed by water molecules, and consequently the structural, magnetic and optical features of materials. Although the control of vacancy amount is quite well mastered through the nature and concentration of alkaline ions (Na^+, K^+, Rb^+, Cs^+), their repartitions in the material is not homogeneous, limiting a systematic study of structure-property relationships. Furthermore, the low solubility of these 3D polymers limits their processability, even though some interesting strategies involving nanoparticles synthesis[79] or dipping techniques[80] have been explored. In this context, the development of molecular systems with lower structural dimensionality such as 2D or 1D polymers[81] or discrete molecules emerged as an appealing strategy to overcome these limitations.[5c,82-92] The first non-polymeric cyanide-bridged Fe/Co system exhibiting thermally-induced ET, was reported by Dunbar, Achim and co-workers.[83] A non-stoichiometric pentanuclear $\{[Co(tmphen)_2]_3[Fe(CN)_6]_2\}$ complex (tmphen = 3,4,7,8-tetramethyl-1,10-phenanthroline) was obtained by the self-assembly of $[Fe(CN)_6]^{3-}$ and $[Co(tmphen)_2]^{2+}$ building blocks. The ET was found to occur between the $\{Co_3^{II}Fe^{III}_2\}$ high-temperature phase and $\{Co_2^{II}Co^{III}Fe^{II}Fe^{III}\}$ low-temperature phase with a statistical disorder of Co^{III} and Fe^{II} in two positions. After exposition to moisture, the new phase was generated and the authors reported the occurrence of ET from $\{Co_3^{II}Fe^{III}_2\}$ phase into $\{Co^{II}Co_2^{III}Fe^{II}_2\}$ by cooling below 200 K. This latter was photo-active (generating the $\{Co_3^{II}Fe^{III}_2\}$ metastable phase) in contrast to previous $\{Co_2^{II}Co^{III}Fe^{II}Fe^{III}\}$ low-temperature phase.[83c]

After this seminal work, our team developed in collaboration with Mathonière and Holmes's groups the first molecular fragment that mimics not only the properties (thermal and photo-induced ET) but also the structure of 3D Fe/Co Prussian Blue analogue (cubic elementary unit; Figure I-16).[84] This octanuclear

complex, $\{[(pzTp)Fe^{III}(CN)_3]_4[Co^{II}(pz_3CCH_2OH)]_4\}(ClO_4)_2{\cdot}4H_2O{\cdot}13DMF$ (pzTp = tetrapyrazolylborate, pz_3CCH_2OH = 2,2,2-tris(pyrazolyl)ethanol) was obtained by a rational building block approach using capping ligands. The complex exhibits a reversible first-order transition between $\{Fe^{III}_4Co^{II}_4\}$ high temperature and $\{Fe^{II}_4Co^{III}_4\}$ low-temperature phase as a result of thermally-induced intramolecular ET occurring at 255 K. The ET process is accompanied by a paramagnetic-to-diamagnetic switching as a result of the conversion from paramagnetic $\{Fe^{III}_{LS}(\mu\text{-CN})Co^{II}_{HS}\}$ (Fe^{III}_{LS}, S = 1/2; Co^{II}_{HS}, S = 3/2) pairs into the diamagnetic $\{Fe^{II}_{LS}(\mu\text{-CN})Co^{III}_{LS}\}$ (Fe^{II}_{LS}, S = 0; Co^{III}_{LS}, S = 0) ones (Figure I.15, right). A metastable $\{Fe^{III}_4Co^{II}_4\}$ paramagnetic phase can be also generated by irradiation with white-light at low temperature or simply by a thermal quenching of the paramagnetic phase. These metastable phases were found remarkably stable in temperature (relaxation time estimated at 210 K with a sweeping rate 0.3 K/min) and a life time of about 10 years was found at 120 K, which is much longer than any reported 3D PBA materials (for example $Na_{0.32}Co[Fe(CN)_6]_{0.74}{\cdot}3.4H_2O$ has a life time of 33 hours at 120 K).

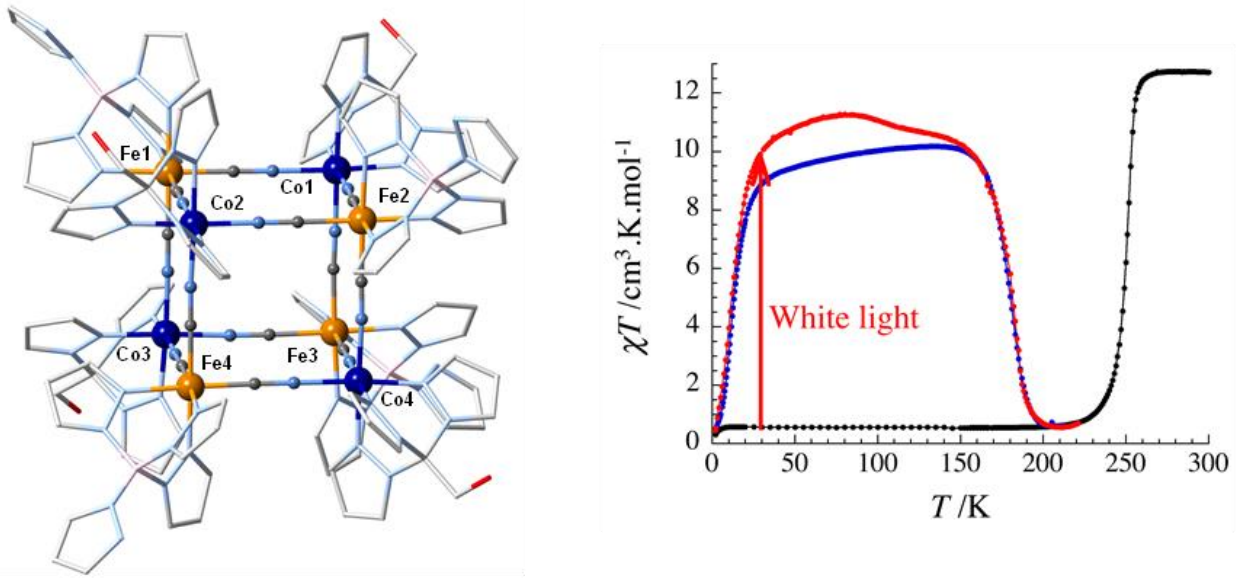

Scheme I-16. (left) View of the molecular $\{[(pzTp)Fe^{III}(CN)_3]_4[Co^{II}(pz_3CCH_2OH)]_4\}(ClO_4)_2{\cdot}4H_2O{\cdot}13DMF$ cube at 250 K. Color scheme: Fe(III) orange, Co(II) blue, C grey, O red, N light blue and B pink. Lattice solvents, anions, and hydrogen atoms are omitted for clarity. (right) Temperature dependence of the χT product for the $\{Fe_4Co_4\}$ cube before (black) and after (red) irradiation, and after thermal quenching (blue).[84]

Shortly latter, the same research teams consortium reported the first tetranuclear square, namely $\{[(Tp^*)Fe(CN)_3]_2[Co(bpy)_2]_2\}(OTf)_2{\cdot}2H_2O{\cdot}4DMF$ (Tp^* = tris(3,5-dimethylpyrazol-1-yl)hydroborate, bpy = 2,2′-bipyridine, OTf = trifluoromethanesulfonate, Figure I-17), that represents the elementary face of the cubic unit in PBAs and displays reversible thermally and photo-induced ET.[85a] The material exhibits a first-order phase transition with a thermal hysteresis of 18 K (at 0.4 K) between 186 and 168 K, associated with an electron transfer process between paramagnetic $\{Fe^{III}_2Co^{II}_2\}$ and diamagnetic $\{Fe^{II}_2Co^{III}_2\}$ states (Figure I-17, right).

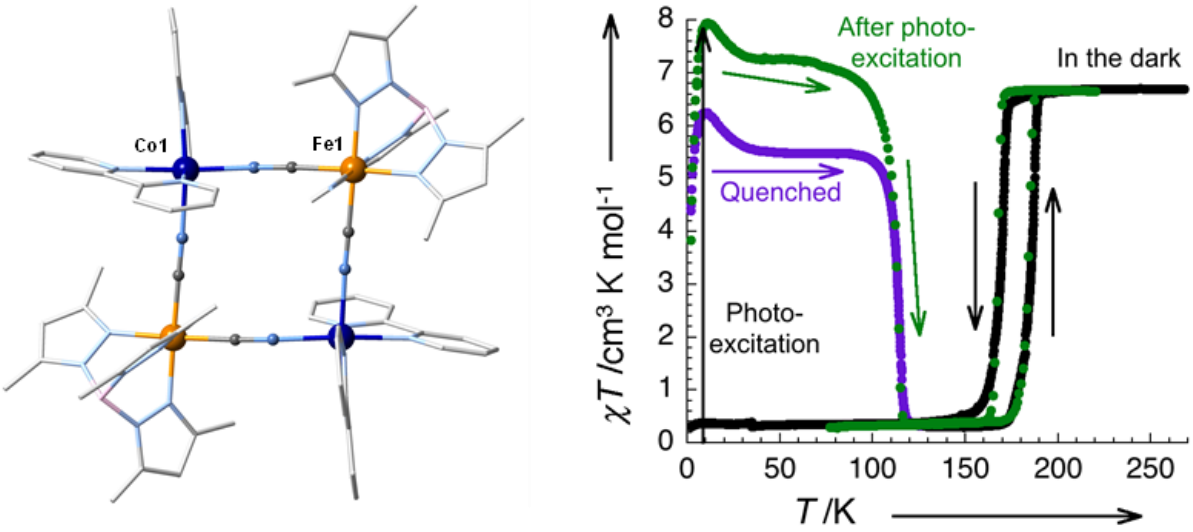

Figure I-17. (left) View of $\{[(Tp^*)Fe(CN)_3]_2[Co(bpy)_2]_2\}(OTf)_2\cdot 2H_2O\cdot 4DMF$ square at 230 K. Color scheme: C, grey; Co, blue; Fe, orange; N, light blue; B, pink. Lattice solvent molecules, anions, and hydrogen atoms are omitted for clarity. (right) χT vs. T data for $\{[(Tp^*)Fe(CN)_3]_2[Co(bpy)_2]_2\}[OTf]_2\cdot 2H_2O\cdot 4DMF$ (at 0.4 $Kmin^{-1}$): in the dark (black, 0.1 T), after thermal quench (dark blue, 0.1 T), and after irradiation (green, 1 T, 3 $mWcm^{-2}$).[85a]

Tetranuclear $\{Fe_2Co_2\}$ squares are currently the most widely molecular ET systems investigated.[85-90] Among these interesting studies, we should cite Prof. Oshio's work that revealed for the first time that the ET is not only occurring in solid-state but also in solution.[88b] They revealed that the ET process of $\{[(Tp^*)Fe(CN)_3]_2[Co(dtbbpy)_2]_2]\}(PF_6)_2$ (dtbbpy = 4,4'-ditertbutyl-2,2'-bipyridine) in butyronitrile can be triggered by the change of pH. Mathonière, Clérac, Holmes and co-workers showed that the ET process of $\{Fe_2Co_2\}$ squares in solution is strongly dependent of the nature of the solvent and the $T_{1/2}$ increases with the polarity index.[85b,86,87] Therefore, they showed the possibility to finely tune the ET temperature by using mixture of solvents.

Strong research efforts have been also devoted to develop dinuclear analogues of the Fe/Co PBA materials. During her thesis, Jeon showed that $[(bbp)Fe(CN)_3Co(PY5Me_2)](OTf)\cdot 2.5MeOH$ complex (bbp = 2,6-bis(benzimidazol-2-yl)pyridine; $PY5Me_2$ = 2,6-bis(1,1-bis(2-pyridyl)ethyl)pyridine) displays intramolecular ET in solution induced by the change of pH, which was explained by the protonation of the bbp ligand that affects the redox potential of the iron ion site.[91] In solid state, no ET was displayed but only a SCO from Co^{II}_{HS} into Co^{II}_{LS} was observed. The absence of ET in solid state was explained by the large difference between the redox potentials of the two building blocks. By a close examination of previous fails in obtaining ET in dinuclear complexes, it was predicted that the difference between the redox potential of the two building blocks should be close to 1 V to expect ET in the resulting pair. In this respect, it was proposed to replace the $[(bbp)Fe(CN)_3]^-$ building block of the previous pair by $[(Tp)Fe(CN)_3]^-$ precursor, which afford a $\Delta_{Fe/Co}$ of ca. 0.96 V. The resulting $[(Tp)Fe(CN)_3Co(PY5Me_2)](OTf)$ pair was the first example of a dinuclear molecule featuring thermally and photo-induced ET in solid state.[92] Despite this rational and successful strategy, the design and prediction ET process in molecular systems is far to be trivial, due to the strong and unpredictable crystal packing effects that might affect the redox potential of both Fe and Co sites and annihilate the metal-to-metal redox process.

I.3. Soft magnetic hybrid materials

As seen in the previous sections molecule-based materials may exhibit fascinating physical properties including magnetic, optical and other like (super)conductivity originating from the molecular level. Beside their academic interest, which allowed to understand some of the most fundamental concepts of magnetism (including both classical or quantum physics), these materials may be considered for numerous practical applications covering various fields ranging from biomedicine[93] to spintronics.[94] In particular, the almost limitless demand for increasing data storage capacities and at the same time for miniaturization of the devices push progressively the magnetic recording technologies toward the superparamagnetic frontier. With conventional materials, this limit could be reached for a storage capacity of about 400 Gbit/in^2,[94] while a capacity of about 200 Tbit/in^2 could be theoretically achieved using single-molecule magnets.[94,95] However, there are still huge breakthroughs to achieve, before such materials can be utilized in applications. This will require improvements and/or innovations of both molecular materials and technologies. Among them, one of the great challenges will be to develop efficient ways to process these molecules and control their organization, especially on surfaces.[96,97] In this scope, intensive research has been dedicated to the deposition of these compounds and multiple approaches based on self-assembled monolayers (SAM),[98] Langmuir-Blodgett films,[99] thermal sublimation,[100] electrospray[101] or lithographic[102] methods have been explored. An emerging approach to facilitate their deposition is to implement the molecules within soft phases such as gels or liquid-crystals, or to develop materials with low-melting point and enhanced solubility.[95, 103]

The following sections are mainly dedicated to liquid-crystal systems, which constitute the main approach developed in the thesis. Before the discussion on few representative examples of SCO and SMM complexes with liquid-crystal properties (Section I.3.2), the reader can find general information about liquid-crystals and metallomesogens. In the last section, we will describe several other soft-matter-based systems.

I.3.1. Generalities on liquid-crystals and metallomesogens

I.3.1.1. Liquid-crystals

Since their first observation in the late 19th century,[104] liquid-crystals (also known as mesogens) have been subject of important scientific curiosity and extensive industrial applications.[105] A liquid crystalline phase (or mesophase) is an intermediate state between a crystalline solid and a liquid. In contrast to a crystalline phase which is characterized by an order in the three directions and absence of mobility of their constituents (atoms, ions, molecules) and with a liquid phase in which, there is no order but motion of their constituents, a liquid crystalline phase combines both of them. Indeed, the molecules are free to move around as in a liquid but tend to be oriented and organized as in a crystal. As illustrated in Figure I-18, the molecule tend to orients themselves in the same direction and form, for example, layers (smectic phase), while no positional order is present within and between the layers.

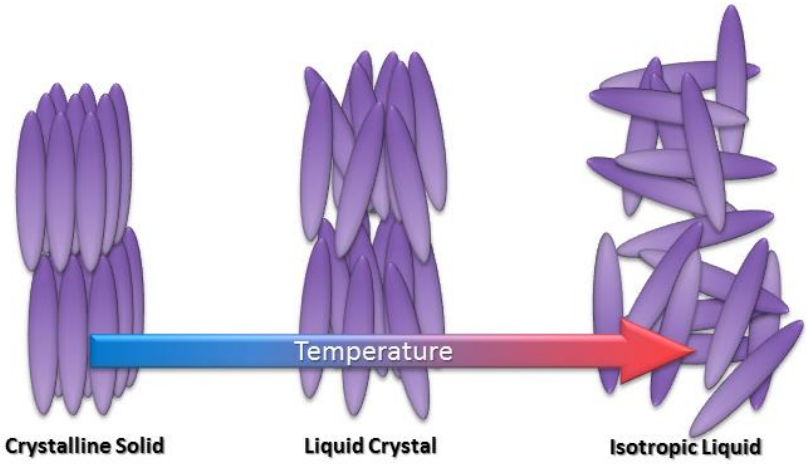

Figure I-18. (left) Schematic representation of a crystalline, (center) liquid crystalline phase and (right) isotropic liquid.

To behave as a liquid-crystal, the molecules have to be geometrically anisotropic in the sense that their physical properties are not identical in all the directions. Thus, the molecules must be composed by two antagonist parts: one rigid core or head and one or multiple flexible arms. Also, to generate a mesophase a microsegregation between the flexible and rigid parts is required.

There are three types of liquid-crystals: thermotropic, lyotropic and amphitropic.[105] A thermotropic liquid-crystal is a material that exhibits liquid crystalline properties as a function of the temperature. The temperature at which the material transits from a solid into a mesophase is referred as melting point and corresponds to the melting of the flexible parts, while the transition from a mesophase into the isotropic liquid phase is designed as clearing point. In the other hand, lyotropic materials are able to form mesophases by addition of a solvent, and their physical features are therefore strongly dependent of the formulation (nature of solvent, concentration, etc.). Amphitropic liquid-crystals are compounds which display characteristics of both thermotropic and lyotropic materials.

Thermotropic liquid-crystals can be divided into three principal types of mesophases, namely nematic, smectic and columnar phases. The organization in either type of mesophases is dictated by the geometry of the molecules and interactions between them. Therefore, it is not rare to have successively different types of phases by increasing the temperature. The molecules can be classed in two categories according to their shape: rod-like, also called calamitic molecules or disk-like, also known as discotic molecules (Figure I-19). It should be noticed that molecular systems without such geometry (globular) may also display liquid crystalline features and lead to unconventional cubic mesophases.[106-108]

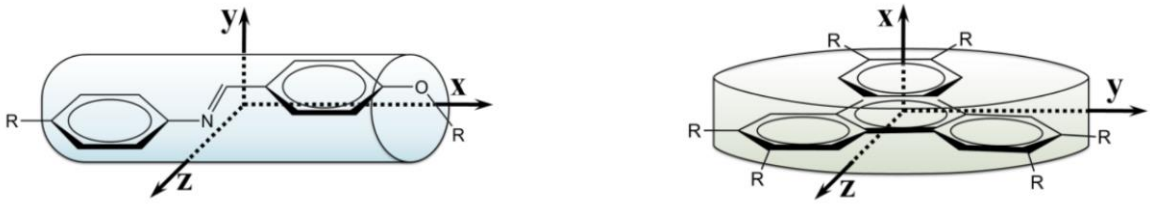

Figure I-19. Examples of calamitic (*N*-(4-alkoxybenzylidene)-4-alkylaniline) (left) and discotic (triphenylene derivatives) (right) molecules.

The nematic (abbreviated by N) phase has the simplest structure of all of the mesophases and is also the least ordered. The nematic phase is characterized by molecules that have a tendency to align parallel to each other with an organization following a preferred direction vector $\vec{n}$, parallel to the longitudinal axis (Figure I-20). The nematic phase can be found for both calamitic and discotic liquid-crystals.

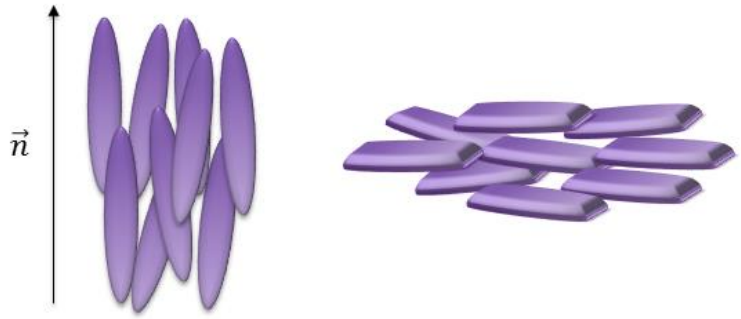

Figure I-20. Schematic representation of nematic phase for calamitic molecules (left) and discotic molecules (right).

Smectic phases are more highly ordered than the nematic phases and are characterized by partial translational order of the molecules in layers, in addition to the orientational order found in nematic phases (Figure I-21). There are numerous types of smectic phases $Sm_{A,B,C,E,F,I,J,K}$, with subcategories such as Sm_{A1} for monolayer and Sm_{A2} for bilayer. The simplest one is the smectic A (Sm_A) phase in which the molecules are oriented on average in the same direction and perpendicular to the layer plane (Figure I-21, left). The molecules of smectic C phase (Sm_C) have an organization similar to the Sm_A, but the longitudinal axis of the molecules is tilted in respect to the layer plane (Figure I-21, right). In both cases, there is no positional order within the layers.

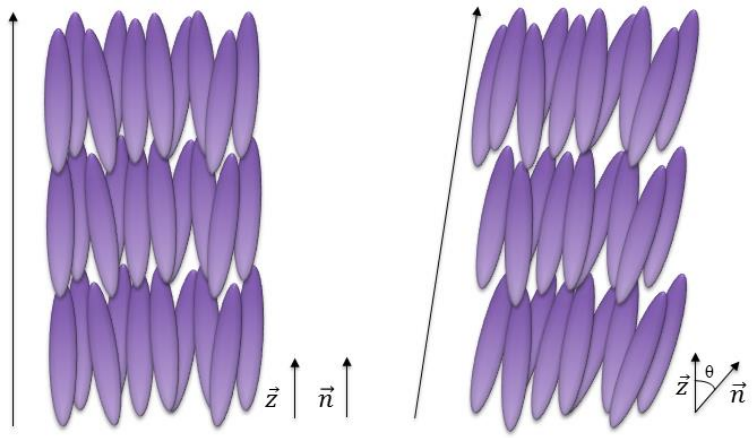

Figure I-21. (left) Schematic representation of a smectic A phase (Sm_A) and (right) a smectic C (Sm_C) mesophase.

The columnar mesophases are formed only for discotic molecules and results from the stacking of rigid cores in columns. The arrangement of columns forms a bidimensional organization. The symmetry of this 2D organization can be hexagonal (Col_h) (Figure 4c), rectangular (Col_r) and oblique (Col_o) (Figure I-22). In some cases, columns can arrange themselves into smectic layers and are referred as lamellar columnar Col_L or form nematic phases (N_{col}).

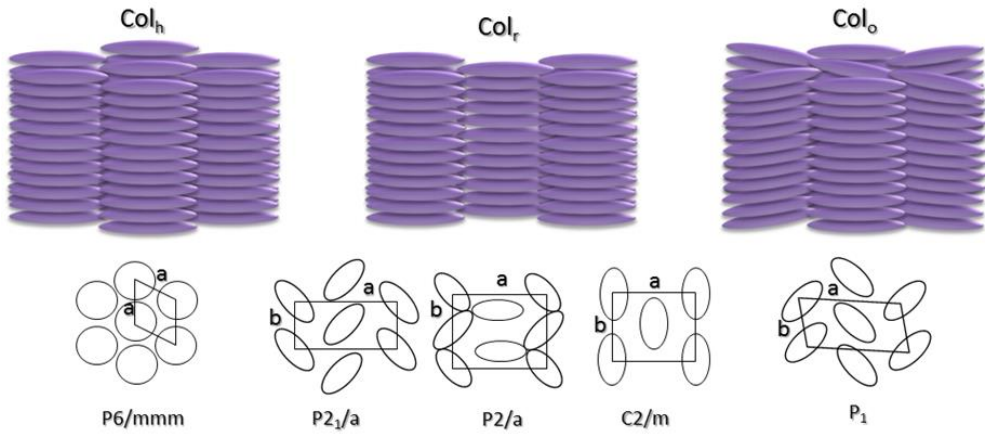

Figure I-22. (left) Schematic representation of columnar hexagonal (Col_h) phase, (center) columnar rectangular (Col_r) phase and (right) columnar oblique (Col_o) phase.

Thermotropic cubic phases (also known as smectic D) are 3D ordered supramolecular systems with a multi-continuous,[106] or a discrete micellar structure,[106,107] that depends on the molecular self-organization in the cubic cell (Figure I-23).[108] Cubic phases are a special type of mesophases as their physical properties are not anisotropic due to the cubic symmetry. Therefore, the detection of cubic phases is complicated because of their optically isotropic (black) texture when observed under polarized light. Nonetheless, cubic mesophases can be evidenced by small-angle X-ray scattering measurements. Cubic mesophases of lyotropic liquid-crystals are more common and two distinct organization symmetries have been described. In the simplest case, molecules organize themselves into micellar assemblies, leading to symmetries with the $Pn\bar{3}m$ and $Im\bar{3}m$ space groups (Figure I-23, top).[107b] Bicontinuous organization with $Ia\bar{3}d$, $Im\bar{3}m$ and $Pn\bar{3}m$ symmetries can be also observed.[106b] These can be described as two interwoven networks as shown in Figure I-23 (bottom). However, thermotropic cubic phases are not so well understood since their observation is not so usual.

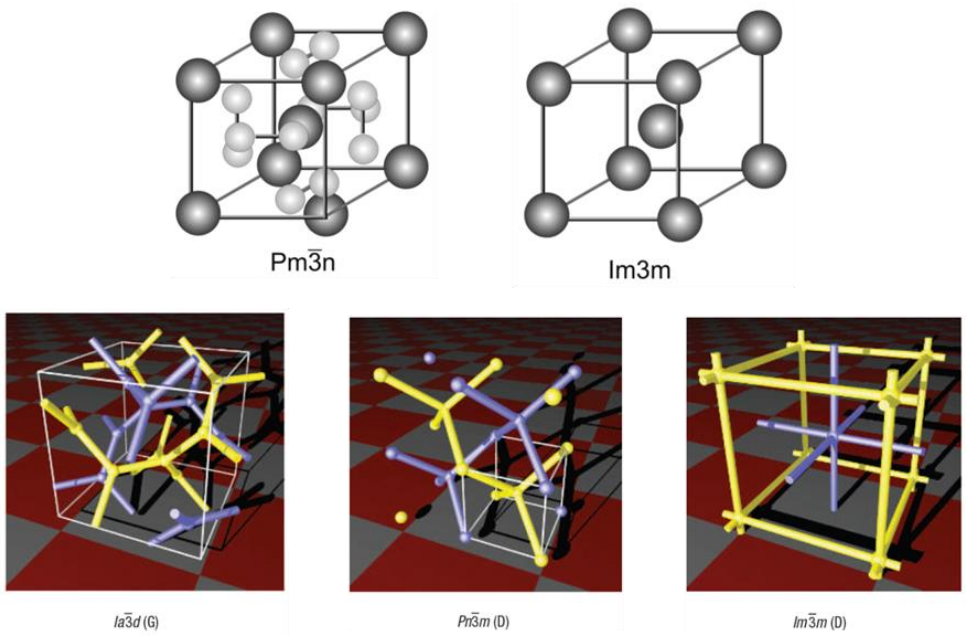

Figure I-23. (top) Schematic representation of (left) Primitive cubic and (right) Body centred cubic phase.[107b] (bottom) Network models of the three known biscontinuous cubic phases in soft matter: (left) $Ia\bar{3}d$; (center) $Pn\bar{3}m$; (right) $Im\bar{3}m$. The two interpenetrating networks are coloured blue and yellow. White lines delineate the unit cell.[106b]

The properties of a liquid-crystal are generally characterized by differential scanning calorimetry (DSC), polarized optical microscopy (POM), and X-ray scattering in small and wide angle (SAXS and WAXS). The DSC is used to determine the temperature of different phase transitions and establishes the phase diagrams. The different transitions can be identified based upon the POM observations and X-ray scattering investigations. The POM is used to detect the presence of birefringence textures, which can be characteristic of a specific type of mesophase (N, Sm, Col). These characteristic textures are generally observed after the first heating into the isotropic liquid phase. The exact nature of the organization is usually accessible thanks to X-ray scattering.

I.3.1.2. Metallomesogens

Metallomesogens are metal complexes that exhibit liquid crystalline properties.[109] The field emerged in the late 70s. At the origin, the main interest was to introduce paramagnetic metal centers in order to facilitate the orientation of liquid crystal with electrical or magnetic fields.[109,110] Indeed the orientation of traditional (organic) liquid crystals requires strong magnetic or electric fields, which become a major issue for miniaturization purpose. The strategy was therefore to functionalize existing mesogens with coordinating functions in order to bind metal ions.[109,110]

The philosophy of metallomesogen field has been rapidly extended; Metallomesogenic systems were developed not only to facilitate liquid-crystal alignment but to facilitate the processing and eventually improve the physical properties of existing complexes, leading to multifunctional materials of interest for various fields of material science, including molecular magnetism.[95,103] Examples of metallomesogens based on molecular magnetic materials are discussed later in section I-3.2. The strategy to design metallomesogens consists to functionalize or eventually the counter ions with functions able to induce liquid crystalline properties on the resulting materials. The design of liquid crystalline materials containing metal ions is not trivial. The stability of the complexes needs to be considered since the formation of liquid crystalline phases requires temperature and/or addition of solvents. The thermal properties and organization depend on the overall structure and shape of the complexes and not only on the mesogenic ligands/counter ions. Thus a functionalized complex may exhibit liquid crystalline properties while the ligands do not, and *vice versa*. The organization of mesophases is not always easy to predict especially for octahedral metal ions (which is the most common environment for spin crossover compounds) or polynuclear systems and can be even more complicated by the presence of counter ions, which might play a role on the self-organization through intermolecular interactions. However in some cases a prediction can be achieved considering the shape of ligand(s), the preferred coordination sphere symmetry of the metal center or the global architecture of the rigid core of the parent complex.[109] For example, numerous studies have been reported on metalloporphyrines[111] and metallophthalocyanines (Figure I-24).[112] These macrocycle ligands have discotic shape forming columns thanks to π-π stacking and it is well-known that these general features are maintained upon coordination of a metal center. Also, considering the trend of certain metal to adopt a square planar symmetry, the geometry of the complex can be adapted through a rational design of the ligands.[113] For instance, the ligand Pzpy illustrated in Figure I-24 has a calamitic geometry but it was rationally designed to

form discotic complex with Pt^{II} metal ion (square planar). In the last example of Figure I-24 (right), tetra(alkanoato)dimetal derivatives are known to have a *paddle wheel* architecture, and the functionalization of carboxylate ligands will preserve the discotic geometry, leading therefore preferentially to columnar phases.[114]

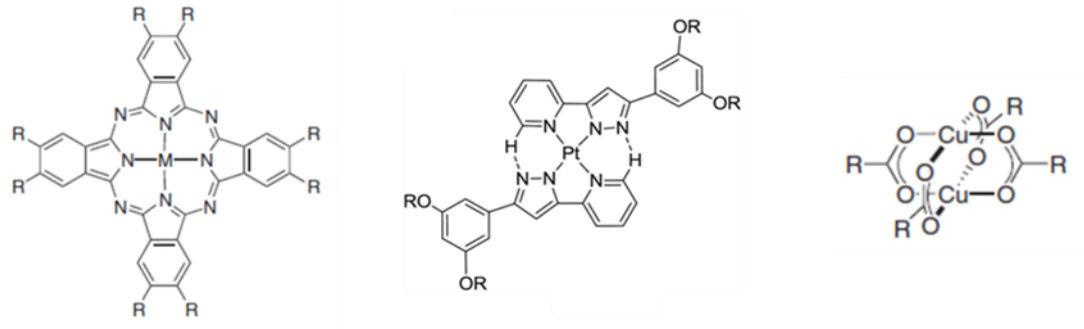

Figure I-24. Chemical structure of metallomesogens with predictable columnar organizations: (left) metallophthalocyanine,[112] (center) $[Pt(Pzpy)_2](Cl)_2$ (with Pzpy = 3-(3,5-bis(alkyloxy)phenyl)-(5-pyridin-2-yl)pyrazole)[113] and (right) tetra(alkanoato)-dicopper(II).[114]

I.3.2. Metallomesogens based on molecular magnetic materials

Researchers from both molecular magnetism and liquid-crystal communities progressively realize that the association of the interesting physical properties of their respective molecular systems in a same material might provide numerous advantages for these two fields of material science. For instance, peoples from liquid-crystal community will find in the development of SCO-based metallomesogens, the opportunity to introduce photo- or thermochromic properties and then, generate optically active liquid crystals or to align liquid crystals thanks to the paramagnetic ions. In the other hand, researchers from molecular magnetism field will find in liquid-crystals a way to shape and process their materials by forming self-organized thin films and concomitantly the opportunity to study the effect of soft matter in the magnetic behavior of their complexes. However, this pluridisciplinar research field is relatively young and the number of examples remains limited.

I.3.2.1. Metallomesogenic materials based on spin crossover complexes

Among molecular materials with interesting magnetic properties, SCO compounds were the first and are still the most widely studied metallomesogenic systems.[103] Indeed, beside the reasons cited just above, they received much consideration because the SCO phenomenon can be tuned to occur around room temperature. Thus, through a judicious design of the ligands, there is a possibility to synchronize in temperature the SCO and crystal-to-mesophase transitions and eventually generate an interplay between the two properties.[103] An eventual goal is to control of the spin switching using the sensitivity of liquid crystalline phases to external electric and/or magnetic fields.

The first complex combining liquid crystal and SCO properties was reported by Galyametdinov and co-workers.[115] In this study, a Schiff base ligand functionalized with a dodecyl tail was used to generate a Fe^{III} complex $[Fe(L)_2](PF_6)$ (with L = N-dodecyloxysalicylidenyl-N'-ethyl-N-ethylenediamine; Figure I-25). The complex has a calamitic geometry, therefore inducing smectic mesophase (Sm_A) above 388 K. Due to

the presence of paramagnetic ions, the material exhibits improved magnetic anisotropy and the authors demonstrated the possibility to align the liquid-crystal by applying magnetic field. The thermally-induced SCO was found to be gradual and appears at a much lower temperature than crystal-to-mesophase transition in such a way that no synergy between the two phenomena can be expected. The same conclusion was found for the first mononuclear Fe^{II} complex .[116]

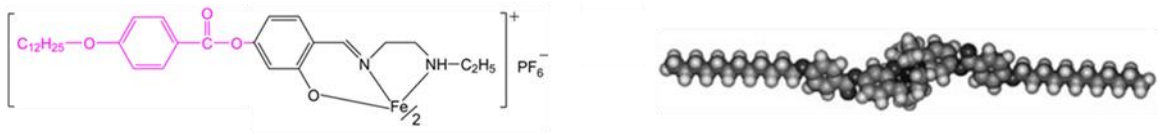

Figure I-25. (left) Chemical structure for $[Fe(L)_2](PF_6)$ and (right) Computational simulation of $[Fe(L)_2]^+$ emphasizing the calamitic shape of the metallomesogen.[115]

Gaspar and co-workers, have shown that a synchronization of the SCO and liquid-crystal transitions could be achieved by using complexes known for exhibiting SCO in the range of temperature where the solid-to-mesophase transition is usually observed.[117] Thus, they reported that the thermally-induced SCO in $[Fe(C_n\text{-tren})](Cl)_2$ starts exactly after the onset of the Cr ↔ Sm_A phase transition, suggesting that the structural changes associated with the Cr ↔ Sm_A transition trigger the spin crossover (Figure I-26). There are also systems where both transitions coexist in the same temperature region but are not coupled, so liquid-crystal phase transition is not the driving force of the spin state conversion.[118]

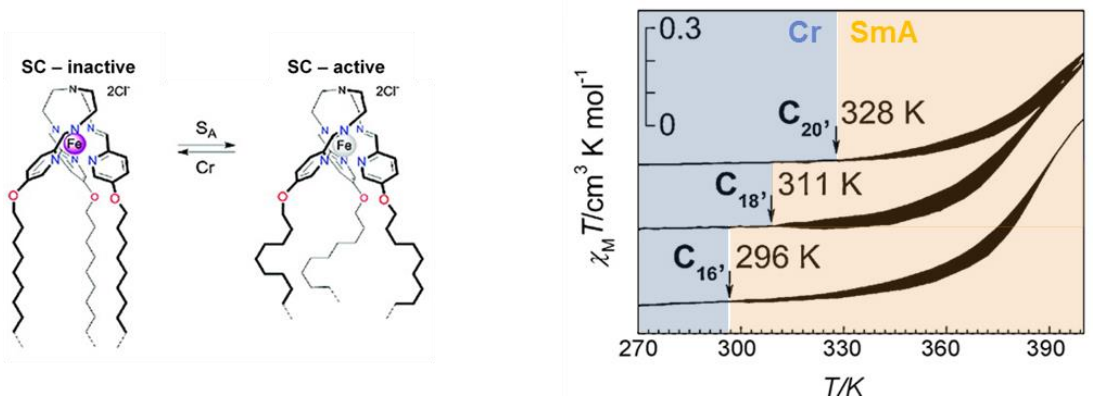

Figure I-26. (left) Schematic representation of structural changes associated with the Cr↔LC transition triggering the spin crossover in $[Fe(C_n\text{-tren})](Cl)_2$ (with C_n-tren = tris[3-aza-4-((alkoxy)-2-pyridyl))but-3-enyl]amine). (right) χT *vs.* T for n = 16, 18, 20., the black areas indicate the hysteresis loops, blue domain indicates crystalline phase and yellow domain indicates liquid crystal phase.[117]

Triazole-based Fe^{II} 1D coordination polymers of general formula $[Fe(RTrz)_3](A)_2 \cdot xH_2O$ (with RTrz = 4-substitued-1,2,4-triazole; A = monovalent anion, Figure I-27) have been the most widely studied SCO in metallomesogens.[86,119-122] Firstly, because these molecular systems are very well-known and have been already investigated for the preparation of hybrid systems[103b] including nanoparticles, Langmuir-Blodgett films, and gels, and secondly, because they have an appropriate geometry to induce liquid-crystalline features. Indeed, the scaffold formed by the triazole ligands can be seen as a succession of paddle wheels

(discotic) interconnected to each other by the Fe^{II} metal ions, and the formation of columnar mesophases can be therefore predicted.

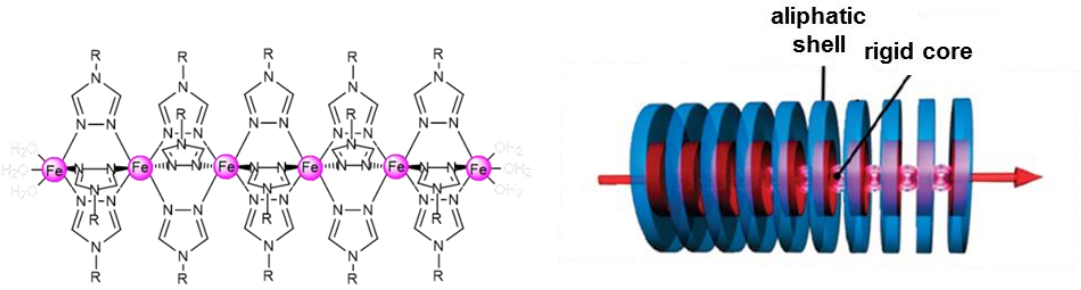

Figure I-27. (left) Chemical structure of $[Fe(R\text{-}Trz)_3]^{2+}$. (right) Schematic representation of the column formed by triazole ligands. The red disks represent the rigid core, blue disks represent the flexible shell and pink balls represent the Fe(II) sites.

Fujigaya's group[119] and Gaspar's group[120] reported the formation of hexagonal Col_h and lamellar columnar Col_L mesophases on $[Fe(R\text{-}Trz)_3](A)_2$ (with RTrz = 5-bis(alkoxyloxy)-*N*-(4*H*-1,2,4-triazol-4-yl)benzamide A = OTs^-, OTf^-, ClO_4^-, BF_4^-) and showed in some cases interplays between the liquid-crystal and SCO behaviors. Unfortunately, the modification of ligands in these systems also induced a gradual and incomplete SCO, while the clearing temperatures are near or above decomposition temperatures. Our team has been also interested in this molecule-based system. Thus, modifications of the triazole ligand with long linear alkyl chains were proposed ($[Fe(R\text{-}Trz)_3](A)_2$ with $R = C_nH_{2n+1}$ (n = 10 to 18) and A = OTs^-, Cl).[86,121] In many cases, cooperative and complete SCO were observed near room temperature, while liquid crystalline domains were unfortunately found to form at higher temperatures. Typical optical textures of lamellar phases were observed in the case of diamagnetic materials $[Zn(R\text{-}Trz)_3](A)_2$, which are thermally more stable than their Fe(II) analogues. In the latter systems, mesophases were present, but the appearance of oxidation/degradation processes occurring at high temperature, did not allow a detailed characterization of these systems.[121]

I.3.2.2. Metallomesogenic materials based on single-molecule magnets

Single-molecule magnets (SMMs) displaying mesomorphism are extremely rare in the literature and only two different molecular systems, namely $[Mn_{12}O_{12}(RCOO)_{16}(H_2O)_4]$ (Mn_{12} for short) and terbium(III) double decker phtalocyanine ($TbPc_2$) complexes, have been reported so far.[86,87,123,124] Similarly to spin crossover system, the implementation of SMMs within liquid crystalline materials is an alternative strategy to control their organization and potentially a facile route toward surface deposition. Beside this aspect, the formation of metallomesogenic systems may provide additional advantages. As mentioned earlier, one of the prerequisite for a complex to behave as a SMM is the absence of intermolecular magnetic interaction. Thus the decoration of these complexes with a bulky organic shell (alkyl chains) may afford the insulation required to prevent interactions between magnetic cores or surface upon deposition. Additionally, taking into account the fluidity in liquid-crystals and the paramagnetic nature of SMMs, this may give the opportunity to orient at will these molecular magnets along their easy axis by applying a magnetic field. This latter aspect remains only conceptual since no attempt to align SMM-based liquid crystals has been reported to date.

The first examples of mesomophic SMMs were described by Terazzi and co-workers.[123] Mesomorphic Mn_{12} complexes were obtained by substitution of the sixteen acetate ligands by benzoate moieties bearing three dodecyloxy or one to three cyanobiphenyloxyundecyloxy mesogenic substituents.[123a,c] When strongly lipophilic 3,4,5-tris-(dodecyloxy)benzoate ligand was employed, the Mn_{12} complex adopts a globular shape and the resulting mesophase organization was found cubic (body centred). In contrast, complexes containing pending calamitic smectogen units (cyanobiphenyl) were found to self-organise into bilayer lamellar-like mesophases with a short-ranged 2D arrangement, whose exact nature (hexagonal or square) could not be determined unambiguously (Figure I-28). The SMM properties were preserved upon the ligand exchange reaction and the authors reported a significant enhancement of their thermal stability in comparison to the original Mn_{12}-OAc. Unfortunately, the clearing point of these systems is close or above decomposition temperature, compromising their use for a proper surface deposition.

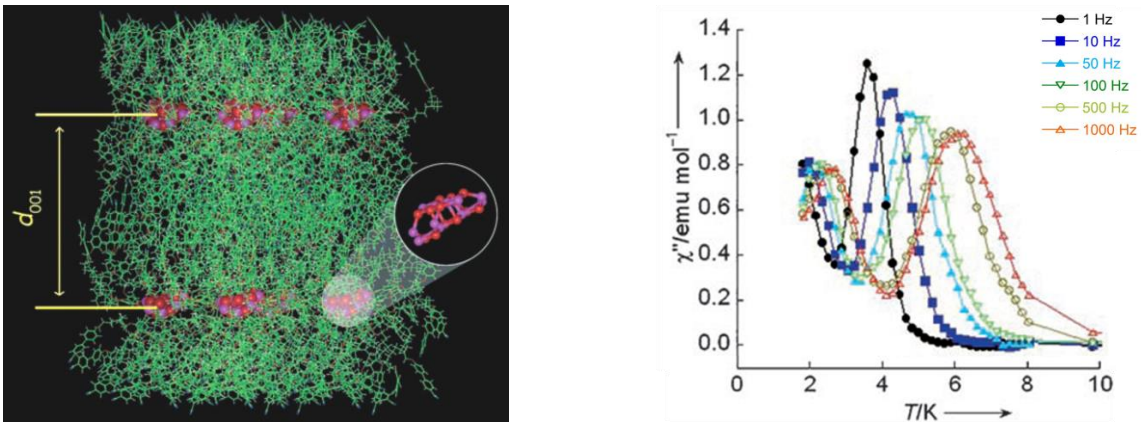

Figure I.28. (left) Computational simulation emphasizing the bilayer lamellar-like mesomorphic organization of Mn12 complexes containing calamitic smectogen units (right) Unaltered magnetic behavior of SMM: temperature dependence of out-of-phase ac susceptibility, χ''.[123a]

During their PhD theses in our team, Siretanu[86] and Mitcov[87] confirmed the formation of crystalline or mesomorphic cubic phases when benzoate ligands are functionalized by linear alkyl chains, whatever the number or length (nonyl to hexadecyl). They revealed that the replacement of cyanobiphenyl smectogen unit by biphenyl analogue was a successful approach to decrease significantly the clearing temperature of the resulting liquid-crystal material and therefore the isotropic liquid phase can be reached without any degradation of the Mn_{12} core. In addition, the existence of a smectic phase with a 2D hexagonal order was clearly evidenced by X-ray scattering measurements.

Besides Mn_{12}-based systems, the possibility to induce liquid-crystal phases in a double-decker terbium phtalocyanine complex with chiral (*S*)-2-(dodecyloxy)propoxy groups was reported (Figure I-29, left).[124] The functionalized complex exhibits hexagonal columnar mesophase at room temperature, while at low temperature, it behaves as a SMM. Moreover, this complex showed the possibility to reversibly control its magnetic properties by simple thermal treatment. Thus, the thermally trapped disordered phase (prepared by a very rapid cooling from 333 to 150 K) and the ordered crystalline state (slowly cooled from isotropic point) show different temperature dependences of the in-phase (χ') and out-of-phase (χ'') susceptibilities measured at several frequencies (Figure I-29, right). This system is one of the first examples of lanthanide double-

decker complex showing two different relaxation processes and it is the only system in which the ratio between these responses has been shown to be reversibly modified by simple thermal treatments.

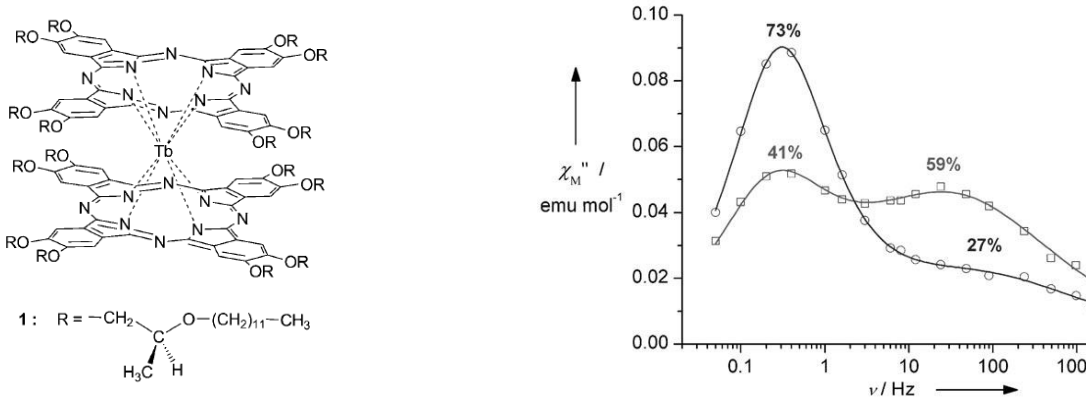

Figure I-29. (left) The structure of the functionalized Tb double-decker phthalocyanine complex. (right) The frequency dependence of the out-of-phase (χ'') susceptibility at 25 K for the quenched disordered phase (open squares) and for the crystalline phase (open circles).[124]

I.3.3. Other soft magnetic systems

As seen in the previous section, one of the favorite methods to promote mesomorphic complexes consists to decorate the ligands with flexible alkyl chains. Independently, this approach may afford additional interesting features for processing purposes such as the increase of solubility, the lowering of melting temperature, etc., and also in term of magnetic properties or for the study of the magnetism itself.[95,103] With few examples, we describe in the following sections some of the benefits provided by the functionalization with alkyl chains.

I.3.3.1. Magnetic gels

The grafting of alkyl chains onto the ligand might give to the resulting complex the ability to gelate solvents. This characteristic is particularly interesting with SCO systems to produce eventual thermochromic gels or to help their processing thought the formation of xerogel film (dried gel).[103] The first physical SCO-based physical gels were developed by our team on a series of polymeric compound $[Fe(R\text{-}Trz)_3](OTs)_2$ (with R = C_nH_{2n+1}, n = 13, 16, 18; see (b) in Figure I-27).[121a,125] These complexes, which exhibit thermotropic liquid-crystal properties, are able to efficiently gelate toluene, various alkanes and mixtures with chloroform even at low concentration (< 1 wt%). The magnetic and optical properties of the complexes were found likely unchanged in the gel phase whatever the composition. By studying their phase diagrams, it has been possible to tune the formulation of the gel and to synchronize the SCO temperature ($T_{1/2}$) with gelation/melting transition (Figure I-30).

Kuroiwa et co-workers reported a gel-like phase of Co^{II}/R-Trz (R = $C_{12}H_{25}OC_3H_6$) coordination polymer in chloroform.[126] The blue gel-like phase turns into a pink solution by cooling at 0 °C. This molecular system is not properly speaking a SCO. Indeed, a reversible dissociation/assembly of a polymeric aggregate of Co^{II} in tetrahedral symmetry (T_d) into mononuclear complexes with symmetry octahedral (O_h) is observed at 25 °C. At lower temperature 0 °C, these complexes self-assemble into oligomeric or polymeric species.

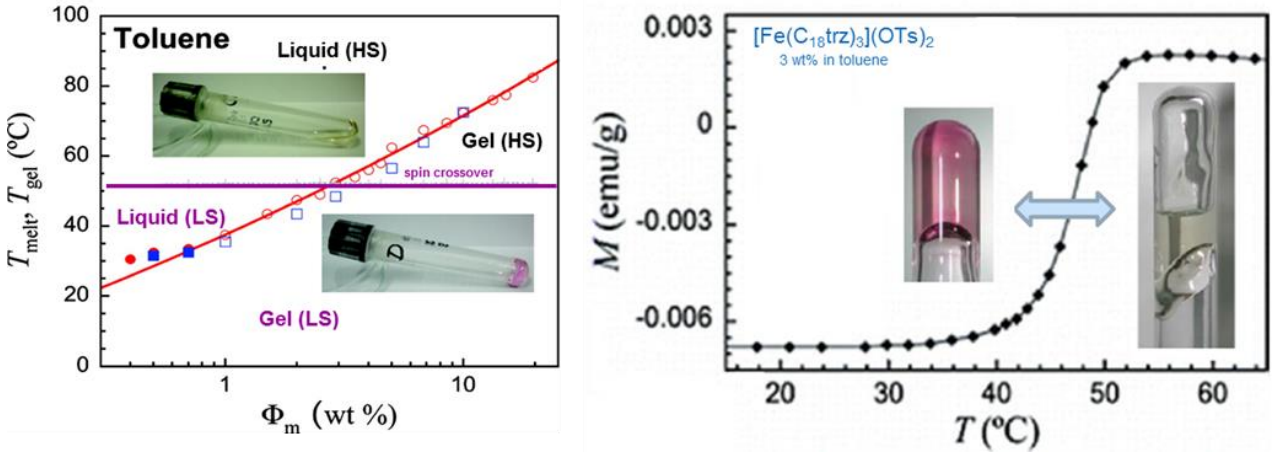

Figure I-30. (left) Temperature-composition pseudo-phase diagram for binary [Fe(R-Trz)$_3$](OTs)$_2$/toluene (R = $C_{18}H_{37}$). red circle: melting observed in heating; blue square: gelation observed on cooling; violet line: $T_{1/2}$; (right) Thermal dependence of the magnetization for [Fe^{II}(C_{18}trz)$_3$](OTs)$_2$/toluene (3 wt%). For this composition condition, the $T_{1/2}$ and melting temperature are synchronized. Inset: pictures corresponding to LS gel (pink) and HS liquid (colorless).[125]

I.3.3.2. Soluble systems

Ligand functionalization with lipophilic chains can help to improve the solubility of the resulting complexes in various organic solvents, giving access to low or non-polar solvents like alkanes. Systems with enhanced solubility are quite important for nanostructuration processes based on wet-methods.

For example, Langmuir-Blodgett (LB) is a very commonly used technique to shape molecular objects in well-organized multilayer films.[99] This method does not need necessarily the functionalization of the complexes and was for example used as the first approach to deposit Mn_{12}-OAc on surface.[99b] However, for non-modified complexes, addition of surfactants is required, while this role can be played in a more controllable way by the functionalization of the ligand(s) with lipophilic chains. The first example of SCO in LB film was reported by Kahn and co-workers on the [Fe^{II}(OP_3)$_2$(NCS)$_2$] complex where OP_3 is a 1,10-phenanthroline onto which three long aliphatic chains were grafted.[99a] The authors confirmed by infrared spectroscopy that the occurrence SCO in the 2D system in the same fashion as the bulk sample. Delhaès and co-workers reported the first example of SCO LB film characterized by means of magnetometry, namely [Fe^{II}(R-bpy)$_2$(NCS)$_2$] (with R,R-bpy = 4,4-bipyridine derivative; R = $(CH_2)_{12}(CF_2)_5CF_3$)).[127] By comparing the results with the one obtained for the bulk sample, they revealed a strong impact of the lamellar organization in LB film on the SCO phenomenon. Nonetheless, after several annealing at high temperature, the magnetic behavior was found barely identical to the one in bulk.

Another use of alkyl-chain-functionalized ligands is the formation of emulsions. Wu and co-workers reported the dispersion of stearic acid modified Mn_{12} complex (Mn_{12}-C_{18}) in water through an emulsion-assisted self-assembly (Figure I-31).[128] For that, they prepared an oil-in-water emulsion by ultrasonic treatment of a solution complex in hexane and a water solution containing an alkyl/poly(ethylene oxide) surfactant ($C_{18}EO_{10}$). The complexes were isolated from water by $C_{18}EO_{10}$ surfactant, forming stable water-dispersed Mn_{12}-C_{18}/$C_{18}EO_{10}$ aggregates. The molecule-based assemblies were found compatible with physiological media and were proposed as potential MRI contrast agent. The same group showed the possibility to form vesicular assemblies of Mn_{12}-C_{14} (C_{14} = pentadecanoate) complex in organic media.[129]

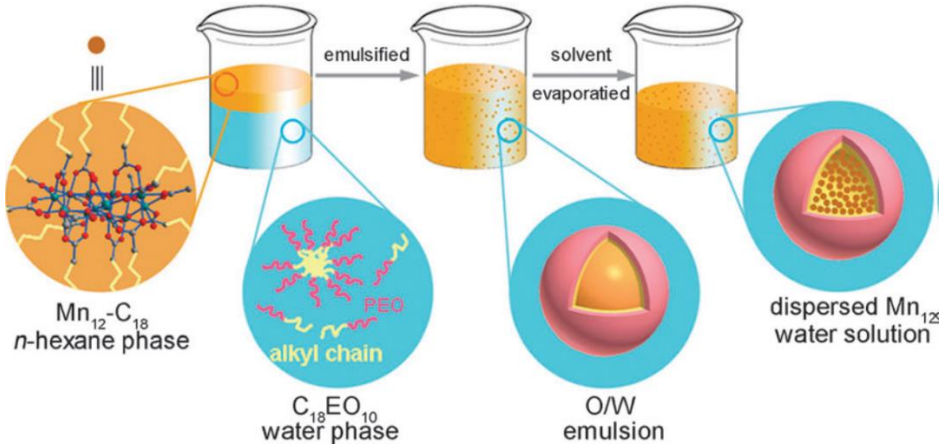

Figure I-31. Formation of Mn_{12}-C_{18}/$C_{18}EO_{10}$ aggregates through emulsion-assisted self-assembly method.[128]

For more academic purposes, the enhancement of the solubility of magnetic complexes gives also the opportunity to study their magnetic/optical properties of complexes in solution.

The ligand functionalization by a lipophilic chain of a known Fe^{III} SCO complex, [Fe^{III} (sal_2-OR_2trien)] (sal = salicylaldehyde, trien = triethylenetetramine, R = C_6H_{13}, C_8H_{17}, $C_{18}H_{37}$), led to a self-assembly of the complex in solution and the spin crossover behavior was found to be preserved (Figure I-32).[130] When the alkyl chains are long enough (R = $C_{18}H_{37}$), self-assembly of the complexes in solution forms discrete (microsize and submicrosize) aggregates. Compared to the original spin crossover system, the functionalized one presents an optimization in crossover temperature.

Extensive efforts have been devoted to explore the influence of anions and/or salts on the SCO properties, especially in the solid state.[131] The presence or absence of solvate molecules and packing effects often restrain the clear observation of host-anion interactions and the effects on SCO properties. Investigation of SCO in solution becomes obvious, as it could give information of substituent effects since in solution, crystal packing effects are excluded.[132] Same considerations have led to the exploration of electron transfer phenomenon in solution.[88b]

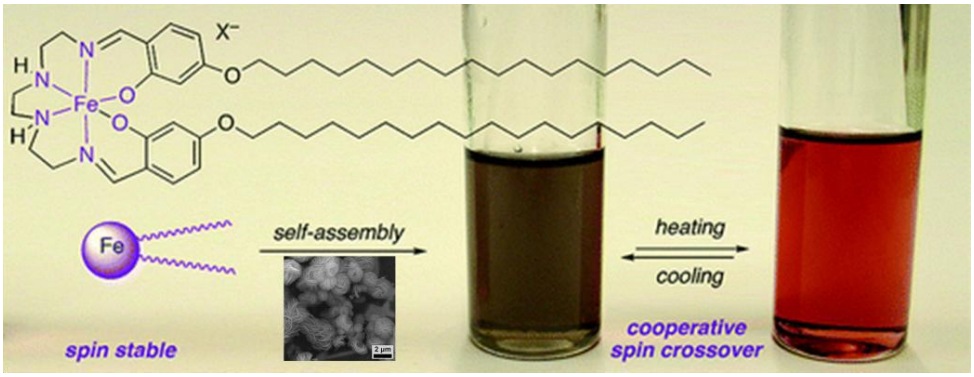

Figure I-32. Schematic representation of [Fe^{III}_{HS}(sal_2-OR_2trien)] complex in solid state, and self-assembly in solution that induce temperature dependence spin crossover in solution.[130]

As mentioned earlier, {[(Tp*)Fe(CN)$_3$]$_2$[Co(R,R-bpy)$_2$]$_2$}$^{2+}$ molecular squares (Tp* = tris(3,5-dimethylpyrazol-1-yl)hydroborate, R,R-bpy = 4,4'-disubstituent-2,2′-bipyridine with R = H or Me) have been studied in solution and the strong influence of the solvent on the $T_{1/2}$ was shown.[85b] More recently, the

bpy ligand was functionalized with extended alkyl chains (hexyl or tridecyl), which allowed investigations in a larger range of solvents including non-polar media like hexane or toluene.[86,87] These two new compounds did not revealed any ET ability in solid-state, while ET was almost systematically found in solution, highlighting the role of crystal packing in the annihilation of the ET phenomenon. The comparison with previous complexes in the same media allowed to reveal the influence of the substituents (CH_3 vs. C_6H_{13} vs. $C_{13}H_{27}$) on the ET temperature and an increase of the $T_{1/2}$ was observed when the electro-donating character increase.

I.3.3.3. Unconventional magnetic behaviors

As illustrated for metallomesogenic systems the implementation of molecule-based magnetic systems in soft matter may promote unusual situations. This is particularly prevalent for spin switchable compounds, whose behavior is strongly dependent of solid-state effects. Especially, it was shown that the occurrence of a phase transition from a solid phase into a mesophase, and the resulting change of the molecule arrangements might affect the metal ion coordination sphere and provoke spin switching.[103] Independent of metallomesogens, such phase transitions are quite common in systems containing flexible alkyl chains. This includes phase transitions resulting from change of the alkyl chain conformations or phase transition (melting) due to reducing cohesion this material.

Hayami and co-workers reported examples of $[Co(C_n\text{-terpy})_2](BF_4)_2$ complexes (terpy = 2,2':6,2"-terpyridine) functionalized with long alkyl chains (n = 14 and 16).[133] While the parent $[Co(terpy)_2](A)_2$ (A = ClO_4^-, NO_3^-) complexes are known to exhibit gradual SCO,[134] they reported in these complexes reverse-SCO. When the material is cooled from 300 or 400 K, a decrease of the χT products is observed down to ca. 190 K (n = 14) or 220 K (n = 16) as expected for a gradual SCO (Figure I-32, center and right). However, on further cooling, an increase of χT products is observed showing a non-natural transition into the HS phase. In heating the reverse process is observed at higher temperature, revealing wide thermal hysteresis. In the case of $[Co(C_{14}\text{-terpy})_2]^{2+}$ complex, a second SCO is observed at low temperature from the HS1 phase into the LS phase without showing any hysteretic behavior. The reverse-SCO phenomena were attributed to crystal-to-crystal phase transitions involving strong changes of configuration of the alkyl chains (Figure I-33, left). Such effects in less pronounced fashion were also revealed in few examples of Fe^{II} SCO liquid-crystals.[121,135]

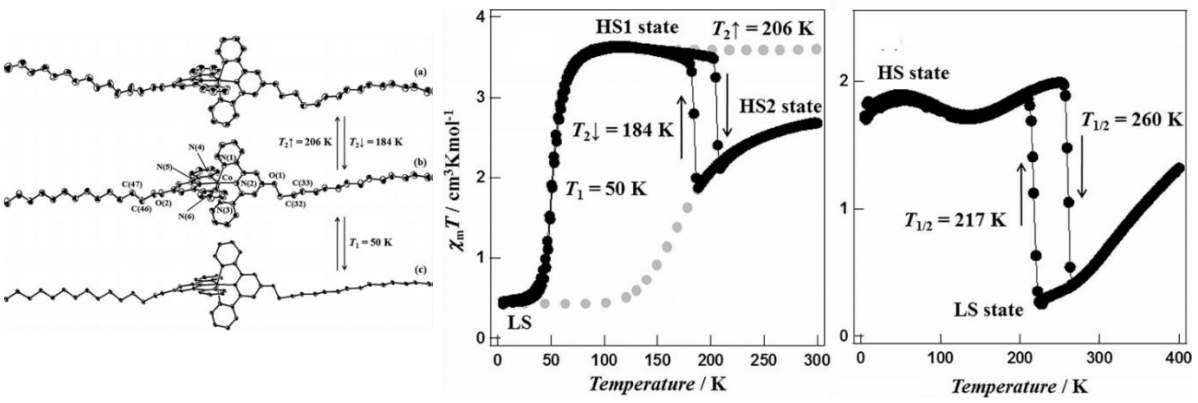

Figure I-33. Structures of the $[Co(C_{14}\text{-terpy})_2](BF_4)_2\cdot$MeOH in the HS2 phase at 190 K (a), the HS1 phase at 190 K (b), and the LS phase at 10 K (c). Lattice solvent and counter-anion are omitted for clarity. (center) χT *vs.* T plots for $[Co(C_{14}\text{-terpy})_2](BF_4)_2\cdot$MeOH. (right) χT *vs.* T plots for $[Co(C_{16}\text{-terpy})_2](BF_4)_2$.[133]

Real and co-workers recently reported a series of neutral Fe^{II} complexes based on pyridylbenzohydrazone ligands functionalized with long alkyl chains (Figure I-34).[136] Interestingly, all the materials melt at low temperature (below 400 K) and this transition is accompanied by a change of the spin state, suggesting therefore for the first time an interplay between SCO and a crystal-to-liquid transition. In addition, due to the natural hysteresis between the melting/crystallization transitions, the SCO itself was found hysteretic. The authors explained that the SCO temperature can be modulated by the melting point which is directly related to the alkyl chain length. This study that appeared during this thesis, utilizes the same SCO compounds that we had initially targeted for investigation in metallomesogen systems and we will show some additional interesting effects of the functionalization with alkyl chains in Chapter III.

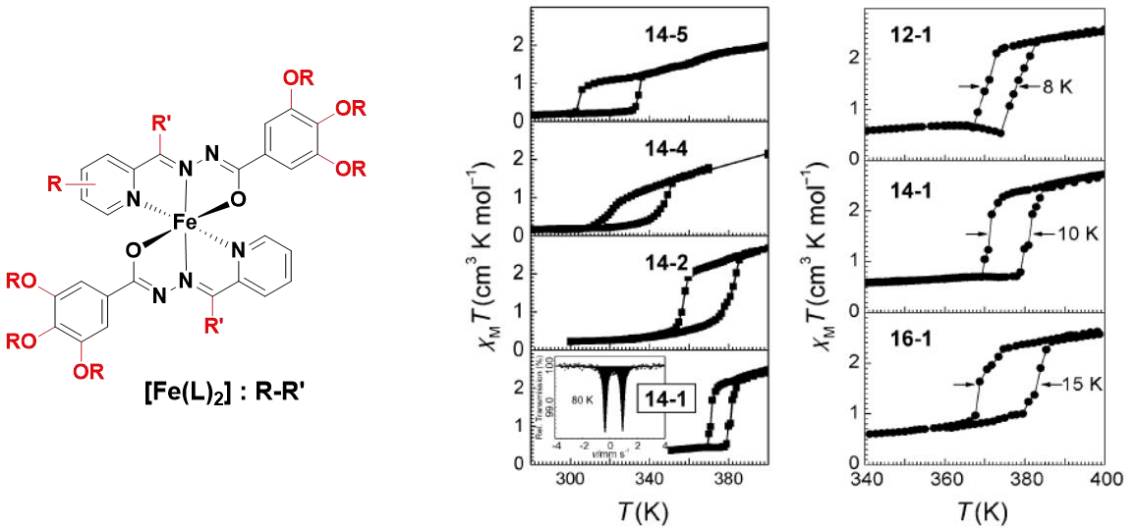

Figure I-34. (left) Chemical structure of $[Fe(L)_2]$ (L = pyridylmethylbenzohydrazone functionalized by alkyl chains (R = $C_nH_{2n+1}$with n = 12, 14, 16; R' = C_nH_{2n+1} with n = 1, 2, 4, 5) (right) χT *vs.* T plots for various $[Fe(L)_2]$ complexes showing SCO/melting synchronism.[136]

I.4. Conclusions and motivation of the thesis

Throughout this chapter, we have shown that molecular materials, including single-molecule magnets (SMMs), spin crossover (SCO) compounds and electron transfer (ET) systems present fascinating physical properties with interest for both academic research and potential applications. Even though the design of novel molecular magnetic materials and the study of their physical features represent a major activity in the field of molecular magnetism, it is also essential to devote a part of the efforts to shape and process the existing molecular materials. As shown in the second part of the chapter, soft materials present high versatility in physico-chemical properties. The implementation of these molecules in soft matter might afford interesting advantages for their processing, which include (i) self-organization abilities in liquid crystalline or gel phases, (ii) the increase of the solubility in conventional solvents facilitating their deposition on surface using wet-methods and (iii) the lowering of the melting temperature giving the opportunity to form thin films using spin-coating technique. In addition, this approach may afford some interesting features regarding their magnetic/optical properties. For example, the functionalization of SMMs with strongly lipophilic ligand may help to isolate and protect the magnetic cores and therefore prevent intermolecular

magnetic interactions between the molecules, while the alignment of their easy magnetic axes with a magnetic field may be potentially assessed in a fluid phase. It was also shown that interplays between structural phase transitions inherent to the soft matter and the SCO process can be eventually promoted, while the increase of the solubility gives access to fundamental studies of the spin switching phenomenon excluding crystal packing effects and conversely check the influence of the solvatosphere.

All these reasons have motivated our team along the years to design molecule-based magnetic soft materials *via* a rational ligand functionalization. The employed strategy consists in selection of known complexes from different magnetic classes and modification of their organic ligands with various functional groups known to induce liquid crystalline properties or, simply, improve the solubility. This PhD work aimed to contribute to these efforts by continuing the work achieved during the theses of Siretanu and Mitcov on metallomesophic Mn_{12} complexes and $\{Fe^{III}_2Co^{II}_2\}$ ET systems with improved solubility or by extending the same strategy to promote liquid-crystal properties in Fe^{II} SCO compounds and $\{Fe^{III}_2M^{II}_2\}$ (M^{II} = Co^{II}, Ni^{II}) molecular squares.

I.5. References

1. (a) Gütlich, P.; Goodwin, H. A. *Spin Crossover in Transition Metal Compounds*, Topics in Current Chemistry, Springer, Wien New York, vol. 233-235, **2004**. (b) Halcrow, M. A. *Spin-Crossover Materials: Properties and Applications*, John Wiley & Sons, Ltd., Chichester, **2013**.

2. Bleuzen, A.; Marvaud, V.; Mathonière, C.; Sieklucka, B.; Verdaguer, M. *Inorg. Chem.* **2009**, *48*, 3453.

3. (a) Gatteschi, D.; Sessoli, R.; Villain, J., Molecular Nanomagnets, Oxford University Press, **2006**. (b) Winpenny, R., Ed. Single-Molecule Magnets and Related Phenomena. *Structure and Bonding*; Springer: Berlin, **2006**; Vol. 122. (c) Pedersen, K. S.; Bendix, J.; Clérac, R. *Chem. Commun.* **2014**, *50*, 4396.

4. (a) Caneschi, A.; Gatteschi, D.; Lalioti, N.; Sangregorio, C.; Sessoli, R.; Venturi, G.; Vindigni, A.; Rettori, A.; Pini, M. G.; Novak, M. A. *Angew. Chem., Int. Ed.* **2001**, *40*, 1760. (b) Clérac, R.; Miyasaka, H.; Yamashita, M.; Coulon, C. *J. Am. Chem. Soc.* **2002**, *124*, 12837. (c) Coulon, C.; Miyasaka, H.; Clérac, R. *Struct. Bond*. **2006**, *122*, 163.

5. (a) Sato, O.; Tao, J.; Zhang, Y.-Z. *Angew. Chem. Int. Ed.* **2007**, *46*, 2152. (b) Ohkoshi, S.-I.; Tokoro, H. *Acc. Chem. Res.* **2012**, *45*, 1749. (c) Aguilà, D.; Prado, Y.; Koumousi, E. S.; Mathonière, C.; Clérac, R. *Chem. Soc. Rev*. **2016**, 45, 203.

6. (a) Caneschi, A.; Gatteschi, D.; Sessoli, R.; Barra, A. L.; Brunel, L. C.; Guillot, M. *J. Am. Chem. Soc.* **1991**, *113*, 5873. (b) Sessoli, R.; Tsai, H. L.; Schake, A. R.; Wang, S. Y.; Vincent, J. B.; Folting, K.; Gatteschi, D.; Christou, G. Hendrickson, D. N. *J. Am. Chem. Soc.* **1993**, *115*, 1804. (c) Sessoli, R.; Gatteschi, D.; Caneschi, A.; Novak, M. A. *Nature* **1993**, *365*, 141.

7. Lis, T. *Acta. Crystallogr. B* **1980**, *36*, 2042.

8. (a) Verdaguer, M. (Eds) *Molecular Magnets Recent Highlights*, Springer-Verlag Wien: New York, **2003**. (b) Gatteschi, D.; Cornia, A.; Mannini, M.; Sessoli, R. *Inorg. Chem.* **2009**, *48*, 3408.

9. (a) Friedman, J. R.; Sarachik, M. P.; Tejada J.; Ziolo, R. *Phys. Rev. Lett.* **1996**, *76*, 3830. (b) Thomas, L.; Lionti, F.; Balou, R.; Gatteschi, D.; Sessoli, R.; Barbara, B. *Nature* **1996**, *383*, 145.

10. Wernsdorfer W.; Sessoli, R. *Science* **1999**, *284*, 133.

11. (a) Leuenberger, M. N.; Loss D. *Nature* **2001**, *410*, 789. (b) Tejada, J.; Chudnovsky, E. M.; del Barco, E.; Hernandez, J. M.; Spiller, T. P. *Nanotechnology* **2001**, *12*, 181. (c) Tejada, J. *Polyhedron* **2001**, *20*, 1751.

12. Torres, F.; Hernández, J. M.; Bohigas, X.; Tejada J. *Appl. Phys Lett.* **2000**, *77*, 3248.

13. (a) Winpenny, R. E. P. *J. Chem. Soc*., *Dalton Trans*. **2002**, 1. (b) Ferko, P. J.; Holmes, S. M. *Curr. Inorg. Chem.* **2013**, *3*, 172.

14. (a) Wang, X.-Y.; Avendañoa, C.; Dunbar, K. R. *Chem. Soc. Rev.* **2011**, *40*, 3213. (b) Pedersen, K. S.; Dreiser, J.; Nehrkorn, J.; Gysler, M.; Schau-Magnussen, M.; Schnegg, A.; Holldack, K.; Bittl, R.; Piligkos, S.; Weihe, H.;

Tregenna-Piggott, P.; Waldmann, O.; Bendix, J. *Chem. Commun*. **2011**, *47*, 6918. (c) Qian, K.; Huang, X.-C.; Zhou, C.; You, X.-Z.; Wang, X.-Y.; Dunbar, K. R. *J. Am. Chem. Soc.* **2013**, *135*, 13302.

15. (a) Martínez-Lillo, J.; Mastropietro, T. F.; Lhotel, E.; Paulsen, C.; Cano, J.; De Munno, G.; Faus, J.; Lloret, F.; Julve, M.; Nellutla, S.; Krzystek, J. *J. Am. Chem. Soc.* **2013**, *135*, 13737. (b) Pedersen, K. S.; Sigrist, M.; Sørensen, M. A.; Barra, A.-L.; Weyhermüller, T.; Piligkos, S.; Thuesen, C. A.; Vinum, M. G.; Mutka, H.; Weihe, H.; Clérac, R.; Bendix J. *Angew. Chem., Int. Ed*. **2014**, *53*, 1351.

16. (a) Woodruff, D. N.; Winpenny, R. E. P.; Layfield, R. A. *Chem. Rev.* **2013**, *113*, 5110. (b) Dhers, S.; Feltham, L. C.; Rouzières, M., Clérac, R.; Brooker, S. *Dalton Trans*. **2016**, *45*, 18089-18093. (c) Feltham, L. C.; Dhers, S.; Rouzières, M., Clérac, R.; Powell, A. K.; Brooker, S. *Inorg. Chem.* **2015**, 2, 982-990.

17. (a) Mougel, V.; Chatelain, L.; Pecaut, J.; Caciuffo, R.; Colineau, E.; Griveau, J. C.; Mazzanti, M. *Nat. Chem*. **2012**, *4*, 1011. (b) Antunes, M. A.; Pereira, L. C. J.; Santos, I. C.; Mazzanti, M.; Marcalo, J.; Almeida, M. *Inorg. Chem*. **2011**, *50*, 9915. (c) Mills, D. R.; Moro, F.; McMaster, J.; van Slageren, J.; Lewis, W.; Blake, A. J.; Liddle, S. T. *Nat. Chem*. **2011**, *3*, 454. (d) Rinehart, J. D.; Meihaus, K. R.; Long, J. R. *J. Am. Chem. Soc.* **2010**, *132*, 7572. (e) Magnani, N.; Apostolidis, C.; Morgernstern, A.; Colineau, E.; Griveau, J. C.; Bolvin, H.; Walter, O.; Caciuffo, R. *Angew. Chem., Int. Ed*. **2011**, *50*, 1696.

18. Layfield, R. A. *Organometallics*, **2014**, *33*, 1084.

19. Abragam, A.; Bleaney, B. *Electron Paramagnetic Resonance of Transition Ions*, Clarendon Press, Oxford, UK, **1970**.

20. Thomas, L.; Barbara, B. *J. Low Temp. Phys.* **1998**, *113*, 1055.

21. (a) Awaga, K.; Suzuku, Y.; Hachisuka, H.; Takeda, K. *J. Mater. Chem.* **2006**, *16*, 2516. (b) Feng, X.; Liu, J.-L.; Pedersen, K. S.; Schnegg, A.; Holldack, K.; Bendix, J.; Sigrist, M.; Mutka, H.; Samohvalov, D.; Aguilà, D.; Tong, M.-L.; Long, J. R.; Clérac, R. *Chem. Commun.*, **2016**, *52*, 12905.

22. Bousseksou, A.; Molnár, G.; Demont, P.; Menegotto, J. *J. Mater. Chem.* **2003**, *13*, 2069.

23. (a) Létard, J.-F. Guionneau, P. Goux-Capes, L. *Top. Curr. Chem.* **2004**, *235*, 221. (b) Bousseksou, A.; Molnár. G.; Salmon. L.; Nicolazzi. W. *Chem. Soc. Rev.* **2011**, *40*, 3313.

24. Cambi, L.; Szego, L.; Cagnasso, A. *Atti accad. Lincei* **1931**, *13*, 809. (b) L. Cambi, L. Szego, *Ber. Dtsch. Chem. Ges.* **1931**, *64*, 2591.

25. Griffith, J. S. *Proc. Roy. Soc. A.* **1956**, *235*, 23.

26. Stoufer, R. C.; Busch, D. H.; Hadley, W. B. *J. Am. Chem. Soc.* **1961**, *83*, 3732.

27. Madeja, K.; König, E. *Inorg. Nucl. Chem.* **1963**, *25*, 377.

28. Ewald, A. H.; Ross, I.; White, A. H.; Martin, R. L. *Proc. Roy. Soc.* **1964**, *280*, 235.

29. (a) Reeder, K.; Dose, E.; Wilson, L. J. *Inorg. Chem.* **1978**, *17*, 1071. (b) Haddad, M.; Federer, W.; Lunch, M.; Hendrickson, D. *Inorg. Chem*. **1981**, *20*, 131. (c) Schenker, S.; Hauser, A.; Dyson, R. *Inorg. Chem*. **1996**, *35*, 4676.

30. (a) Zarembowitch, J.; Kahn, O. *Inorg. Chem*. **1984**, *23*, 589. (b) Heinze, K.; Huttner, G.; Zsolnai, L.; Schober, P.; *Inorg. Chem*. **1997**, *36*, 5457.

31. (a) Gütlich, P.; McGarvey, B. R.; Kläui, W. *Inorg. Chem*. **1980**, *19*, 3704. (b) Eberspach, W.; Murr, N. E.; Kläui, W. *Angew. Chem., Int. Ed*. **1982**, *21*, 915. (c) Kläui, W.; Eberspach, W.; Gütlich, P. *Inorg. Chem*. **1987**, *26*, 3977.

32. Halepoto, D.; Holt, D.; Larkworthy, L.; Leigh, G.; Povey, D.; Smith, W. *J. Chem. Soc. Chem. Comm*. **1989**, 1322.

33. (a) Ammeter, J.; Bucher, R.; Oswald, N. *J. Am. Chem. Soc.* **1974**, *96*, 7833. (b) Switzer, M. E.; Wang, R.; Rettig, M. F.; Maki, A. H. *J. Am. Chem. Soc*. **1974**, *96*, 7669.

34. (a) Sim, P. G.; Sinn, E. *J. Am. Chem. Soc*. **1981**, *103*, 241. (b) Kaustov, L.; Tal, M. E.; Shames, A. I.; Gross, Z. *Inorg. Chem*. **1997**, *36*, 3503.

35. Chisholm, M. H.; Kober, E. M.; Ironmonger, D. J.; Thornton, P. *Polyhedron* **1985**, *4*, 1869.

36. (a) Real, J. A.; Gaspar, A. B.; Muñoz, M. C.; Gütlich, P.; Ksenofontov, V.; Spiering, H. *Top. Curr. Chem.* **2004**, *233*, 167. (b) Bousseksou, A.; Molnár, G.; Real, J. A.; Tanaka, K. *Coord. Chem. Rev*. **2007**, *251*, 1822.

37. (a) Kolnaar, J. J. A.; van Dijk, G.; Kooijman, H.; Spek, A. L.; Ksenofontov, V. G.; Gütlich, P.; Haasnoot, J.; Reedijk, J. *Inorg. Chem.* **1997**, *36*, 2433. (b) Clérac, R.; Cotton, F. A.; Daniels, L. M.; Dunbar, K. R.; Murillo, C. A.; Wang, X. *Inorg. Chem.* **2001**, *40*, 1256.

38. Ruben, M.; Breuning, E.; Lehn, J.-M.; Ksenofonotv, V.; Renz, F.; Gütlich, P.; Vaughan, G. B. M. *Chem. Eur. J.* **2003**, *9*, 4422.

39. Muñoz, M. C.; Real, J. A. *Coord. Chem. Rev*. **2011,** 255, 2068.

40. (a) Decurtins, S.; Gütlich, P.; Köhler, C. P.; Spiering, H.; Hauser, A. *Chem. Phys. Lett.* **1984**, *105*, 1. (b) Decurtins, S.; Gütlich, P.; Hasselbach, A. P.; Hauser, A.; Spiering, H. *Inorg. Chem.* **1985**, *24*, 2174.

41 (a) Boillot, M. L.; Roux, C.; Audière, J. P.; Dausse, A.; Zarembowitch, J. *Inorg. Chem*. **1996**, *35*, 3975. (b) Real, J. A.; Gaspar, A. B.; Muñoz, M. C. *Dalton. Trans.* **2005**, 2062.

42. Gütlich, P.; Gaspar, A.B.; Ksenofontov, V.; Garcia, Y. *J. Phys. Condens. Matter* **2004**, *16*, 1087.

43 Bousseksou, A.; Boukheddaden, K.; Goiran, M.; Consejo, C.; Boillot, M. L.; Tuchagues, J. P. *Phys. Rev. B* **2002**, *65*, 172412.

44. (a) Renz, F.; Hasegawa, M.; Hoshi, T.; El-Ayaan, U.; Linert, W.; Fukuda, Y. *Mol. Cryst. Liq. Cryst.* **1999**, *335*, 1243. (b) Baadji, N. Piacenza, M.; Tugsuz, T.; Sala, F. D.; Maruccio, G.; Sanvito, S. *Nature Mater.* **2009**, *8*, 813.

45. James, R.; Parris, M.; Williams, R. J. P. *J. Chem. Soc.* **1961**, 4630.

46. A. Hauser, *Top. Curr. Chem.* **2004**, *233*, 49.

47. (a) Tanabe, Y.; Sugano, S. *J. phys. Soc. Japn*. **1956**, *11*, 864. (b) Sugano, S.; Tanabe, Y.; Kamimura, H. *Multiplets of transition metal ions*, Pure and applied physics, Vol.33, Academic, New York, **1970**.

48. Guionneau, P.; Marchivie, M.; Bravic, G.; Létard, J.-F.; Chasseau, D. *Top. Curr. Chem.* **2004**, *234*, 97.

49. Thuéry, P.; Zarembowitch, J.; Michalowicz, A.; Kahn, O. *Inorg. Chem.* **1987**, *26*, 851.

50.(a) Shatruk, M.; Phan, H.; Chrisostomo, B. A.; Suleimenova, A.; *Coord. Chem. Rev.* **2015**, *289–290*, 62. (b) Brooker, S. *Chem. Soc. Rev.* **2015**, *44*, 2880. (c) Ortega-Villar, N.; Muñoz, M. C.; Real, J. A. *Magnetochemistry* **2016**, *2*, 16.

51. Atkins, P.; De Paula, J. *Physical Chemistry*, 8th Ed., Oxford University Press, **2006**.

52. Boca, R. *"Theoretical Foundations of Molecular Magnetism in Current Methods in Inorganic Chemistry",* Elsevier, 1, **1999**.

53. Köng, E. *"Nature and dynamics of the spin-state interconversion in metal complexes"*, Structure and Bonding, Springer-Verlag, Berlin 76, 51, **1991**.

54. (a) Hauser, A. *Chem. Phys. Lett.* **1986**, *124*, 543. (b) Hauser, A. *Coord. Chem. Rev.* **1991**, *111*, 275.

55. (a) Feng, X.; Mathonière, C.; Jeon, I.-R.; Rouzières, M.; Ozarowski, A.; Aubrey, M. L.; Gonzalez, M. I.; Clérac, R.; Long, J. R. *J. Am. Chem. Soc.* **2013**, *135*, 15880. (b) Mathonière, C.; Lin, H.-J.; Siretanu, D.; Clérac, R.; Smith, J. M. *J. Am. Chem. Soc.* **2013**, *135*, 19083.

56. (a) Sato, O.; Iyoda, T.; Fujishima, A.; Hashimoto, K. *Science* **1996**, *272*, 704. (b) Sato, O.; Einaga, Y.; Fujishima, A.; Hashimoto, K. *Inorg. Chem.* **1999**, *38*, 4405.

57. Prassides, K. *Mixed Valency Systems Applications in Chemistry, Physics and Biology*, Kluwer Academic Publishers: Dordrecht, **1991**.

58. Marcus, R. A. *J. Chem. Phys.* **1956**, *24*, 966.

59. (a) Hush, N. S. *Prog. Inorg. Chem.* **1967**, *8*, 391. (b) Hush, N. S. *Electrochim. Acta* **1968**, *13*, 1005. (c) Hush, N. S. *Coord. Chem. Rev.* **1985**, *64*, 135.

60. Piepho, S. B.; Krausz, E. R.; Schatz, P. N. *J. Am. Chem. Soc.* **1978**, *100*, 2996.

61. (a) Creutz, C.; Taube, H. *J. Am. Chem. Soc.* **1969**, *91*, 3988. (b) Creutz, C.; Taube, H. *J. Am. Chem. Soc.* **1973**, *95*, 1086.

62. (a) Hankache, J.; Wenger, O. S. *Chem. Rev.* **2011**, *111*, 5138. (b) Cowan, D. O.; Le Vanda, C.; Park, J.; Kaufman, F. *Acc. Chem. Res.* **1973**, *6*, 1.

63. Guasch, J.; Grisanti, L.; Souto, M.; Lloveras, V.; Vidal-Gancedo, J.; Ratera, I.; Painelli, A.; Rovira, C.; Veciana, J. *J. Am. Chem. Soc.* **2013**, *135*, 6958.

64. Verdaguer, M.; Girolami, G. S. *Magnetism - Molecules to Materials* Miller, *V*, J. S.; Drillon, M.; Eds., Wiley-VCH: Weinheim, Germany, **2005**, 283.

65. Ohkoshi, S.-I.; Tokoro, H.; Hashimoto, K. *Coord. Chem. Rev.* **2005**, *249*, 1830.

66. (a) Ksenofontov, V.; Levchenko, G.; Reiman, S.; Güttlich, P.; Bleuzen, A.; Escax, V.; Verdaguer, M. *Phys. Rev. B* **2003**, *68*, 024415. (b) Morimoto, Y.; Hanawa, M.; Ohishi, Y.; Kato, K.; Takata, M.; Kuriki, A.; Nishibori, E.; Sakata, M.; Ohkoshi, S.-I.; Tokoro, H.; Hashimoto, K. *Phys. Rev. B* **2003**, *68*, 144106.

67. Sato, O. *J. Photochem. Photobiol. C: Photochem. Rev.* **2004**, *5*, 203.

68. Margadonna, S.; Prassides, K.; Fitch, A. N. *Angew. Chem. Int. Ed.* **2004**, *43*, 6316.

69. (a) Bleuzen, A.; Lomenech, C.; Escax, V.; Villain, F.; Varret, F.; Cartier dit Moulin, C.; Verdaguer, M. *J. Am. Chem. Soc.* **2000**, *122*, 6648. (b) Cartier dit Moulin, C.; Villain, F.; Bleuzen, A.; Arrio, M.-A.; Sainctavit, P.; Lomenech, C.; Escax, V.; Baudelet, F.; Dartyge, E.; Gallet, J.-J.; Verdaguer, M. *J. Am. Chem. Soc.* **2000**, *122*, 6653. (c) Escax, V.; Bleuzen, A.; Cartier dit Moulin, C.; Villain, F.; Goujon, A.; Varret, F.;Verdaguer, M. *J. Am. Chem. Soc.* **2001**, *123*, 12536. (d) Campion, G.; Escax, V.; Cartier dit Moulin, C.; Bleuzen, A.; Villain, F.; Baudelet, F.; Dartyge,

E.; Verdaguer, M. *J. Am. Chem. Soc.* **2001**, *123*, 12544. (e) Shimamoto, N.; Ohkoshi, S.; Sato, O.; Hashimoto, K. *Inorg. Chem*. **2002**, *41*, 678.

70. (a) Tokoro, H.; Ohkoshi, S.-I. *Dalton Trans.* **2011**, *40*, 6825. (b) Tokoro, H.; Matsuda, T.; Nuida, T.; Moritomo, Y.; Ohoyama, K.; Dangui, E. D. L.; Boukheddaden, K.; Ohkoshi, S.-I. *Chem. Mater.* **2008**, *20*, 423. (c) Tokoro, H.; Miyashita, S.; Hashimoto, K.; Ohkoshi S.-I. *Phys. Rev. B* **2006**, *73*, 172415. (d) Tokoro, H.; Ohkoshi, S.-I.; Matsuda, T.; Hashimoto, K. *Inorg. Chem.* **2004**, *43*, 5231. (e) Tokoro, H.; Ohkoshi, S.-I.; Hashimoto, K. *Appl. Phys. Lett.* **2003**, *82*, 1245. (f) Ohkoshi, S.-I.; Tokoro, H.; Utsunomiya, M.; Mizuno, M.; Abe, M.; Hashimoto, K. *J. Phys. Chem. B* **2002**, *106*, 2423. (g) Yokoyama, T.; Tokoro, H.; Ohkoshi, S.-I.; Hashimoto, K. *Phys. Rev. B* **2002**, *18*, 4111.

71. (a) Lummen, T. T. A.; Gengler, R. Y. N.; Rudolf, P.; Lusitani, F.; Vertelman, E. J. M.; van Koningsbruggen, P. J.; Knupfer, M.; Molodtsova, O.; Pireaux, J.-J.; van Loosdrecht, P. H. M. *J. Phys. Chem. C* **2008**, *112*, 14158. (b) Salmon, L.; Vertelman, E. J. M.; Murgui, C. B.; Cobo, S.; Molnár, G.; van Koningsbruggen, P. J.; Bousseksou, A. *Eur. J. Inorg. Chem.* **2009**, 760.

72. (a) Ohkoshi, S.-I.; Matsuda, T.; Tokoro, H.; Hashimoto, K. *Chem. Mater.* **2005**, *17*, 81. (b) Vertelman, E. J. M.; Maccallini, E.; Gournis, D.; Rudolf, P.; Bakas, T.; Luzon, J.; Broer, R.; Pugzlys, A.; Lummen, T. T. A.; van Loosdrecht, P. H. M.; van Koningsbruggen, P. J. *Chem. Mater*. **2006**, *18*, 1951. (c) Cobo, S.; Fernández, R.; Salmon, L.; Molnár, G.; Bousseksou, A. *Eur. J. Inorg. Chem.* **2007**, 1549.

73. Ohkoshi, S.-I.; Einaga, Y.; Fujishima, A.; Hashimoto, K. *J. Electroanal. Chem.* **1999**, *473*, 245.

74. (a) Bozdag, K. D.; Yoo, J.-W.; Raju, N. P.; McConnell, A. C.; Miller, J. S.; Epstein, A. J. *Phys. Rev. B* **2010**, *82*, 094449. (b) Holmes, S. M.; Girolami, G. S. *J. Am. Chem. Soc.* **1999**, *121*, 5593. (c) Hatlevik, Ø.; Bushmann, W. E.; Zhang, J.; Manson, J. L.; Miller, J. S. *Adv. Mater.* **1999**, *11*, 914. (d) Ferlay, S.; Mallah, T.; Ouahes, R.; Veillet, P.; Verdaguer, M. *Nature* **1995**, *378*, 701.

75. Dong, W.; Zhang, W.; Ou-Yang, Y.; Zhu, L.-N.; Liao, D.-Z.; Yoshimura, K.; Jiang, Z.-H.; Yan, S.-P.; Cheng, P. *J. Magn. Magn. Mater.* **2007**, *309*, 7.

76. Avendano, C.; Hilfiger, M. G.; Prosvirin, A.; Sanders, C.; Stepien D.; Dunbar, K. R. *J. Am. Chem. Soc.* **2010**, *132*, 13123.

77. (a) Ohkoshi, S.-I.; Tokoro, H.; Hozumi, T.; Zhang, Y.; Hashimoto, K.; Mathonière, C.; Bord, I.; Rombaut, G.; Verelst, M.; Cartier dit Moulin, C.; Villain, F. *J. Am. Chem. Soc.* **2006**, *128*, 270. (b) Rombaut, G.; Verelst, M.; Golhen, S.; Ouahab, L.; Mathonière, C.; Kahn, O. *Inorg. Chem.* **2001**, *40*, 1151. (c) Zhang, W.; Sun, H.-L.; Sato, O. *Dalton Trans*. **2011**, *40*, 2735. (d) Brossard, S.; Volatron. F.; Lisnard, L.; Arrio, M-A.; Catala, L.; Mathonière, C.; Mallah, T.; Cartier dit Moulin, C.; Rogalev, A.; Wilhelm, F.; Smekhova, A.; Sainctavit, P. *J. Am. Chem. Soc.* **2012**, *134*, 222.

78. (a) Ohkoshi, S.-I.; Hamada, Y.; Matsuda, T.; Tsunobuchi, Y.; Tokoro, H. *Chem. Mater.* **2008**, *20*, 3048. (b) Ozaki, N.; Tokoro, H.; Hamada, Y.; Namai, A.; Matsuda, T.; Kaneko, S.; Ohkoshi, S. *Adv. Func. Mater.* **2012**, *22*, 2089.

79. (a) Moulik, S. P.; De, G. C.; Panda, A. K.; Bhowmik, B. B.; Das, A. R. *Langmuir* **1999**, *15*, 8361. (b) Vaucher, S.; Li, M.; Mann, S. *Angew. Chem., Int. Ed.* **2000**, *39*, 1793.

80. (a) Pyrasch, M.; Toutianoush, A.; Jin, W. Q.; Schnepf, J.; Tieke, B. *Chem. Mater.* **2003**, *15*, 245. (b) Culp, J. T.; Park, J.-H.; Benitez, I. O.; Huh, Y.-D.; Meisel, M. W.; Talham, D. R. *Chem. Mater.* **2003**, *15*, 3431. (c) Culp, J. T.; Park, J.-H.; Frye, F.; Huh, Y.-D.; Meisel, M. W.; Talham, D. R. *Coord. Chem. Rev.* **2005**, *249*, 2642. (d) Frye, F. A.; Pajerowski, D. M.; Park, J. H.; Meisel, M. W.; Talham, D. R. *Chem. Mater.* **2008**, *20*, 5706.

81. (a) Liu, T.; Zhang, Y.-J.; Kanegawa, S.; Kang, S.; Sato, O. *Angew. Chem., Int. Ed.* **2010**, *49*, 8645. (b) Liu, T.; Zhang, Y.-J.; Kanegawa, S.; Kang, S.; Sato, O. *J. Am. Chem. Soc.* **2010**, *132*, 8250. (c) Hoshino, N.; Iijima, F.; Newton, G. N.; Yoshida, N.; Shiga, T.; Nojiri, H.; Nakao, A.; Kumai, R.; Murakami, Y.; Oshio, H. *Nat. Chem.* **2012**, *4*, 921. (d) Dong, D.-P.; Liu, T.; Kanegawa, S.; Kang, S.; Sato, O.; He, C.; Duan, C.-Y. *Angew. Chem., Int. Ed.* **2012**, *51*, 5119. (e) Coulon, C.; Pianet, V.; Urdampilleta, M.; Clérac, R. *Struct. Bond.* **2015**, *164*, 143. (f) Yang, J.; Zhou, L.; Cheng, J.; Hu, Z.; Kuo, C.; Pao, C.-W.; Jang, L.; Lee, J.-F.; Dai, J.; Zhang, S.; Feng, S.; Kong, P.; Yuan, Z.; Yuan, J.; Uwatoko, Y.; Liu, T.; Jin, C.; Long, Y. *Inorg. Chem.* **2015**, *54*, 6433.

82. (a) Herrera, J. M.; Marvaud, V.; Verdaguer, M.; Marrot, J.; Kalisz, M.; Mathonière, C. *Angew. Chem. Int. Ed*. **2004**, *43*, 5468. (b) Mathonière, C.; Podgajny, R.; Guionneau, P.; Labrugère, C.; Sieklucka, B. *Chem. Mater.* **2005**, *17*, 442. (c) Bleuzen, A.; Marvaud, V.; Mathonière, C.; Sieklucka, B.; Verdaguer, M. *Inorg. Chem.* **2009**, *48*, 3453. (d) Hilfiger, M.; Chen, M.; Brinzari, T.; Nocera, T.; Shatruk, M.; Petasis, D.; Musfeldt, J.; Achim, C.; Dunbar, K. R. *Angew. Chem., Int. Ed.* **2010**, *49*, 1410. (e) Mondal, A.; Chamoreau, L.-M.; Li, Y.; Journaux, Y.; Seuleiman, M.; Lescouëzec, R. *Chem. Eur. J.* **2013**, *19*, 7682.

83. (a) Berlinguette, C. P.; Dragulescu-Andrasi, A.; Sieber, A.; Galán-Mascarós, J. R.; Güdel, H.-U.; Achim, C.; Dunbar, K. R. *J. Am. Chem. Soc.* **2004**, *126*, 6222. (b) Berlinguette, C. P.; Dragulescu-Andrasi, A.; Sieber, A.; Güdel, H.-U.; Achim, C.; Dunbar, K. R. *J. Am. Chem. Soc.* **2005**, *127*, 6766. (c) Funck, K. E.; Prosvirin, A. V.; Mathonière, C.; Clérac, R.; Dunbar, K. R. *Inorg. Chem.* **2011**, *50*, 2782.

84. Li, D.; Clérac, R.; Roubeau, O.; Harté, E.; Mathonière, C.; Le Bris, R.; Holmes, S. M. *J. Am. Chem. Soc*. **2008**, *130*, 252.

85. (a) Zhang, Y.; Li, D.; Clérac, R.; Kalisz, M.; Mathonière, C.; Holmes, S. M. *Angew. Chem., Int. Ed.* **2010**, *49*, 3752. (b) Siretanu, D.; Li, D.; Buisson, L.; Bassani, D. M.; Holmes, S. M.; Mathonière, C.; Clérac, R. *Chem. Eur. J.* **2011**, *17*, 11704. (c) Zhang, Y.-Z.; Ferko, P.; Siretanu, D.; Ababei, R.; Rath, N. P.; Shaw, M. J.; Clérac, R.; Mathonière, C.; Holmes, S. M. *J. Am. Chem. Soc.* **2014**, *136*, 16854.

86. Siretanu, D. *PhD Thesis*, Univ. of Bordeaux, **2011**.

87. Mitcov, D. *PhD Thesis*, Univ. of Bordeaux, **2014**.

88. (a) Nihei, M.; Sekine, Y.; Suganami, N.; Oshio, H. *Chemistry Chem. Lett.* **2010**, 978. (b) Nihei, M.; Sekine, Y.; Suganami, N.; Nakazawa, K.; Nakao, A.; Nakao, H.; Murakami, Y.; Oshio, H. *J. Am. Chem. Soc*. **2011**, *133*, 3592. (c) Newton, G. N.; Nihei, M.; Oshio, H. *Eur. J. Inorg. Chem.* **2011**, *20*, 3031. (d) Sekine, Y.; Nihei, M.; Oshio, H. *Chem. Lett.* **2014**, 1029. (e) Sekine, Y.; Nihei, M.; Kumai, R.; Nakao, H.; Murakami, Y.; Oshio, H. *Inorg. Chem. Front.* **2014**, *1*, 540. (f) Sekine, Y.; Nihei, M.; Kumai, R.; Nakao, H.; Murakami, Y.; Oshio, H. *Chem. Commun.* **2014**, *50*, 4050. (g) Kitagawa, Y.; Asaoka, M.; Miyagi, K.; Matsui, T.; Nihei, M.; Oshio, H.; Okumura, M.; Nakano, M. *Inorg. Chem. Front.* **2015**, *2*, 771.

89. (a) Mercurol, J.; Li, Y.; Pardo, E.; Risset, O.; Seuleiman, M.; Rousselière, H.; Lescouëzec, R.; Julve, M. *Chem. Commun.* **2010**, *46*, 8995. (b) Mondal, A.; Li, Y.; Seuleiman, M.; Julve, M.; Toupet, L.; Buron-Le Cointe, M.; Lescouëzec, R. *J. Am. Chem. Soc*. **2013**, *135*, 1653.

90. (a) Cao, L.; Tao, J.; Gao, Q.; Liu, T.; Xia, Z.; Li, D. *Chem. Commun*. **2014**, *50*, 1665. (b) Zheng, C.; Xu, J.; Yang, Z.; Tao, J.; Li, D. *Inorg. Chem*. **2015**, 54, 9687.

91. (a) Jeon, I.-R.; Calancea, S.; Panja, A.; Piñero Cruz, D. M.; Koumousi, E. S.; Dechambenoit, P.; Coulon, C.; Wattiaux, A.; Rosa, P.; Mathonière, C.; Clérac, R. *Chem. Sci*. **2013**, *4*, 2463. (b) Jeon, I.-R. *PhD Thesis*, Univ. of Bordeaux, **2012**.

92. (a) Koumousi, E. S.; Jeon, I.-R.; Gao, Q.; Dechambenoit, P.; Merzeau, P.; Buisson, L.; Jia, B.; Li, D.; Woodruff, D. N.; Voltaron, F.; Mathonière, C.; Clérac, R. *J. Am. Chem. Soc*. **2014,** *136*, 15461. (b) Koumousi, E. S. *PhD Thesis*, Univ. of Bordeaux, **2015**.

93. (a) Shokouhimehr, M.; Soehnlen, E. S.; Khitrin, A.; Basu, S.; Huang, S. D. *Inorg. Chem. Commun.* **2010**, *13*, 58. (b) Mo, R.; Yang, J.; Wu, E.; Lin, S. *J. Magn Magn Mat.* **2011**, *323*, 2287. (c) Fu, G.; Liu, W.; Li, Y.; Jin, Y.; Jiang, L.; Liang, X.; Feng, S.; Dai Z. *Bioconjugate Chem.* **2014**, *25*, 1655.

94. (a) Roch, N.; Florens, S.; Bouchiat, V.; Wernsdorfer, W.; Balestro, F. *Nature* **2008**, *453*, 347. (b) Bogani, L.; Wernsdorfer W. *Nat. Mater.* **2008**, *7*, 179. (c) Lehmann, J.; Gaita-Arino, A.; Coronado, E.; Loss, D. *J. Mater. Chem.* **2009**, *19*, 1672. (d) Sanvito, S. *Chem. Soc. Rev.* **2011**, *40*, 3336. (e) Aromí, G.; Aguilà, D.; Gamez, P.; Luis, F.; Roubeau, O. *Chem. Soc. Rev.* **2012**, *41*, 537.

95. Rogez, G.; Donnio, B.; Terazzi, E.; Gallani, J.-L.; Kappler, J.-P.; Bucher, J.-P.; Drillon, M. *Adv. Mater.* **2009**, *21*, 4323.

96. (a) Gómez-Segura, J.; Veciana, J.; Ruiz-Molina, D. *Chem. Commun.* **2007**, 3699. (b) Domingo, N.; Bellido, E.; Ruiz-Molina, D. *Chem. Soc. Rev.* **2012**, *41*, 258. (c) Holmberg, R. J.; Murugesu, M. *J. Mat. Chem. C* **2015**, *3*, 11986.

97. (a) Cavallini, M.; Bergenti, I.; Milita, S.; Kengne, J. C.; Gentili, D.; Ruani, G.; Salitros, I.; Meded, V.; Ruben M. *Langmuir* **2011**, *27*, 4076. (b) Bonhommeau, S.; Molnár, G.; Galet, A.; Zwick, A.; Real, J. A.; McGarvey, J. J.; Bousseksou, A. *Angew. Chem., Int. Ed.* **2005**, *44*, 4069.

98. (a) Mannini, M.; Pineider, F.; Sainctavit, P.; Danieli, C.; Otero, E.; Sciancalepore, C.; Talarico, A. M.; Arrio, M-A.; Cornia, A.; Gatteschi, D.; Sessoli, R. *Nat. Mater.* **2009**, *8*, 194. (b) Glebe, U.; Weidner, T.; Baio, J. E.; Schach, D.; Bruhn, C.; Buchholz, A.; Plass, W.; Walleck, S.; Glaser, T.; Siemeling, U. *ChemPlusChem* **2012**, *77*, 889. (c) Moro, F.; Biagi, R.; Corradini, V.; Evangelisti, M.; Gambardella, A.; De Renzi, V.; del Pennino, U.; Coronado, E.; Forment-Aliaga, A.; Romero, F. M. *J. Phys. Chem. C* **2012**, *116*, 14936.

99. (a) Ruaudel-Teixier, A.; Barraud, A.; Coronel, P.; Kahn, O. *Thin Solid Films* **1988**, *160*, 107. (b) Clemente-León, M.; Soyer, H.; Coronado, E.; Mingotaud, C.; Gómez-García, C. J.; Delhaès, P. *Angew. Chem., Int. Ed.* **1998**, *37*, 2842. (c) Bogani, L.; Cavigli, L.; Gurioli, M.; Novak, R. L.; Mannini, M.; Caneschi, A.; Pineider, F.; Sessoli, R.; Clemente-León, M.; Coronado, E.; Cornia, A.; Gatteschi, D. *Adv. Mater.* **2007**, *19*, 3906. (d) Roubeau, O.; Natividad, E.; Agricole, B.; Ravaine, S. *Langmuir* **2007**, *23*, 3110.

100. (a) Malavolti, L.; Poggini, L.; Margheriti, L.; Chiappe, D.; Graziosi, P.; Cortigiani, B.; Lanzilotto, V.; Buatier de Mongeot, F.; Ohresser, P.; Otero, E.; Choueikani, F.; Sainctavit, P.; Bergenti, I.; Dediu, V. A.; Mannini, M.; Sessoli, R. *Chem. Commun.* **2013**, *49*, 11506. (b) Malavolti, L.; Lanzilotto, V.; Ninova, S.; Poggini, L.; Cimatti, I.; Cortigiani, B.; Margheriti, L.; Chiappe, D.; Otero, E.; Sainctavit, P.; Totti, F.; Cornia, A.; Mannini, M.; Sessoli, R. *Nano Lett.* **2015**, *15*, 535.

101. (a) Saywell, A.; Britton, A. J.; Taleb, N.; del Carmen Giménez-López, M.; Champness, N. R.; Beton, P. H.; O'Shea, J. N. *Nanotechnology* **2011**, *22*, 075704. (b) Handrup, K.; Richards, V. J.; Weston, M.; Champness, N. R.; O'Shea, J. N. *J. Chem. Phys.* **2013**, *139*, 154708.

102. (a) Mannini, M.; Bonacchi, D.; Zobbi, L.; Piras, F. M.; Speets, E. A.; Caneschi, A.; Cornia, A.; Magnani, A.; Ravoo, B. J.; Reinhoudt, D. N.; Sessoli, R.; Gatteschi, D. *Nano Lett.* **2005**, *5*, 1435. (b) Molnár, G.; Cobo, S.; Real, J. A.; Carcenac, F.; Daran, E.; Vieu, C.; Bousseksou, A. *Adv. Mater.* **2007**, *19*, 2163. (c) Cavallini, M.; Bergenti, I.; Milita, S.; Ruani, G.; Salitros, I.; Qu, Z. R.; Chandrasekar, R.; Ruben, M. *Angew. Chem., Int. Ed.* **2008**, *47*, 8596. (d) Bellido, E.; González-Monje, P.; Repollés, A.; Jenkins, M.; Sesé, J.; Drung, D.; Schurig, T.; Awaga, K.; Luis, F.; Ruiz-Molina, D. *Nanoscale* **2013**, *5*, 12565.

103. (a) Gaspar, A. B.; Seredyuk, M.; Gütlich, P. *Coord. Chem. Rev.* **2009**, *253*, 2399. (b) Roubeau, O. *Chem. Eur. J.* **2012**, *18*, 15230. (c) Gaspar, A. B.; Seredyuk, M. *Coord. Chem. Rev.* **2014**, *268*, 41.

104. (a) Reinitzer, F. *Monatsch. Chem.* **1888**, *9*, 421. (b) Lehmann, O.; *Z. Physikal. Chem.* **1889**, *4*, 462.

105. (a) Collings, P. *Introduction to Liquid Crystals, Chemistry and Physics*, Taylor & Francis: London, **1997**. (b) Tschierske, C. *Curr. Opin. Colloid Interface Sci.* **2002**, *7*, 355-370. (c) Bushby, R. J.; Kelly, S. M.; O'Neill, M.; *Liquid Crystalline Semiconductors*, Springer Series in Materials Science, Springer,Wien Dordrecht, vol. 169, **2013**.

106. (a) Levelut, A. M.; Clerc, M.; *Liq. Cryst.* **1998**, *24*, 105. (b) Zeng, X. B.; Ungar, G.; Impéror-Clerc, M. *Nat. Mater.* **2005**, *4*, 562. (b) Impéror-Clerc, M. *Curr. Opin. Colloid Interface Sci.* **2005**, *9*, 370.

107. (a) Kutsumizu, S. *Curr. Opin. Solid State Mater. Sci.* **2002**, *6*, 537. (b) Diele, S. *Curr. Opin. Colloid Interface Sci.* **2002**, *7*, 333.

108. (a) Percec, V.; Mitchell, C. M.; Cho, W. D.; Uchida, S.; Glodde, M.; Ungar, G.; Zeng, X.; Liu, Y.; Balagurusamy, V. S. K.; Heiney, P. A. *J. Am. Chem. Soc.* **2004**, *126*, 6078. (b) Percec, V.; Glodde, M.; Bera, T. K.; Miura, Y.; Shiyanovskaya, I.; Singer, K. D.; Balagurusamy, V. S. K.; Heiney, P. A.; Schnell, I.; Rapp, A.; Spiess, H. W.; Hudson, S. D.; Duan, H. *Nature* **2002**, *419*, 384. (c) Percec, V.; Peterca, M.; Sienkowska, M. J.; Ilies, M. A.; Aqad, E.; Smidrkal, J.; Heiney, P. A. *J. Am. Chem. Soc.* **2006**, *128*, 3324.

109. (a) Donnio, B.; Bruce, D. W. *Liquid Crystal II*, Structure & Bonding, Springer, Mingos. D. M. P.; Ed.; Wien New York, vol. 95, **1999**. (b) Donnio, B.; Guillon, D.; Deschenaux, R.; Bruce, D. W.; *Comprehensive Coordination Chemistry II*; McCleverty, J. A.; Meyer, T. J.; Eds.; Elsevier: Oxford,Vol. 7, **2003**, Chapter 7.9.

110. Binnemans, K.; Galyametdinov, Y. G.; Van Deun, R.; Bruce, D. W.; Collinson, S. R.; Polishchuk, A. P.; Bikchantaev, I.; Haase, W.; Prosvirin, A. V.; Tinchurina, L.; Litvinov, I.; Gubajdullin, A.; Rakhmatullin, A.; Uytterhoeven, K.; Van Meervelt, L. *J. Am. Chem. Soc.* **2000**, *122*, 4335.

111. Shimizu, Y. *Mol. Cryst. Liq. Cryst.* **2001**, *370*, 83.

112. Piechocki, G.; Simon, J.; Skoulios, A.; Guillon, D.; Weber, P. *J. Am. Chem. Soc.* **1982**, *104*, 5245.

113. Cuerva, C.; Campo, J. A.; Ovejero, P.; Rosario Torres, M.; Oliveira, E.; Santos, S. M.; Lodeiro, C.; Cano, M. *J. Mater. Chem. C* **2014**, *2*, 9167.

114. Ghermani, N. E.; Lecomte, C.; Rapin, C.; Steimetz, P.; Steimetz, J.; Malaman, B. *Acta Cryst. B* **1994**, 50, 157.

115. Galyametdinov, Y.; Ksenofontov, V.; Prosvirin, A.; Ovchinnikov, I.; Ivanova, G.; Gütlich, P.; Haase, W. *Angew. Chem. Int. Ed*. **2001**, *40*, 4269.

116. (a) Hayami, S.; Danjobara, K.; Inoue, K.; Ogawa, Y.; Matsumoto, N.; Maeda, Y. *Adv. Mater*. **2004**, *16*, 869. (b) Hayami, S.; Motokawa, N,; Shuto, A.; Masuhara, N; Someya, T.; Ogawa, Y.; Inoue, K.; Maeda, Y. *Inorg. Chem.* **2007**, *46*, 1789.

117. Seredyuk, M.; Gaspar, A. B.; Ksenofontov, V.; Galyametdinov, Y.; Kusz, J.; Gütlich, P. *J. Am. Chem. Soc.* **2008**, *130*, 1431.

118. Lee, Y. H.; Komatsu, Y.; Yamamoto, Y.; Kato, K.; Shimizu, T.; Ohta, A.; Matsui, T.; Hayami, S. *Inorg. Chem. Commun.* **2011**, *14*, 1498.

119. Fujigaya, T.; Aida, T. *J. Am. Chem. Soc.* **2003**, *125*, 14690.

120. (a) Seredyuk, M.; Gaspar, A. B.; Ksenofontov, V.; Reiman, S.; Galyametdinov, Y.; Haase, W.; Rentschler, E.; Gütlich, P. *Chem. Mater.* **2006**, *18*, 2513. (b) Seredyuk, M.; Gaspar, A. B.; Ksenofontov, V.; Galyametdinov, Y.; Verdaguer, M.; Villain, F.; Gütlich, P. *Inorg. Chem.* **2008**, *47*, 10232.

121. (a) Grondin, P. *PhD Thesis*, Univ. of Bordeaux, **2007**. (b) Grondin, P.; Siretanu, D.; Roubeau, O.; Achard, M.-F.; Clérac, R. *Inorg. Chem.* **2012**, *51*, 5417.

122. Lee, Y. H.; Komatsu, Y.; Yamamoto, Y.; Kato, K.; Shimizu, T.; Ohta, A.; Matsui, T.; Hayami, S. *Inorg. Chem. Commun.* **2011**, *14*, 1498.

123. (a) Terazzi, E.; Bourgogne, C.; Welter, R.; Gallani, J.-L.; Guillon, D.; Rogez, G.; Donnio, B. *Angew. Chem., Int. Ed*. **2008**, *47*, 490. (b) Terazzi, E.; Jensen, T. B.; Donnio, B.; Buchwalder, K.; Bourgogne, C.; Rogez, G.; Heinrich, B.; Gallani, J.-L.; Piguet, C. *Dalton Trans.* **2011**, *40*, 12028. (c) Terazzi, E.; Rogez, G.; Gallani, J.-L.; Donnio, B. *J. Am. Chem. Soc.* **2013**, *135*, 2708.

124. Gonidec, M.; Luis, F.; Vílchez, Á.; Esquena, J.; Amabilino, D. B.; Veciana, J. *Angew. Chem., Int. Ed.* **2010**, *49*, 1623.

125. (a) Roubeau, O.; Colin, A.; Schmitt, V.; Clérac, R. *Angew. Chem. Int. Ed.* **2004**, *43*, 3283. (b) Grondin, P.; Roubeau, O.; Castro, M.; Saadaoui, H.; Colin, A.; Clérac, R. *Langmuir*, **2010**, *26*, 5184.

126. Kuroiwa, K.; Shibata, T.; Takada, A.; Nemoto, N.; Kimizuka, N. *J. Am. Chem. Soc.* **2004**, *126*, 2016.

127. (a) Soyer, H.; Mingotaud, C.; Boillot, M.-L.; Delhaès, P. *Langmuir* **1998**, *14*, 5890. (b) Soyer, H.; Depart, E.; Gómez-García, C. J.; Mingotaud, C.; Delhaès, P. *Adv. Mat.* **1999**, *11*, 382.

128. Wang, Y.; Li, W.; Zhou, S.; Kong, D.; Yang, H.; Wu, L. *Chem. Commun.* **2011**, *47*, 3541.

129. Li, W.; Li, B.; Wang, Y.; Zhang, J.; Wang, S.; Wu, L. *Chem. Commun.* **2010**, *46*, 6548.

130. Gandolfi, C.; Moitzi, C.; Schurtenberger, P.; G. Morgan, G. G.; Albrecht, M. *J. Am. Chem. Soc.* **2008**, *130*, 14434.

131 (a) Hostettler, M.; Törnroos, K. W.; Chernyshov, D.; Vangdal, B.; Bürgi, H.-B. *Angew. Chem., Int. Ed.* **2004**, *43*, 4589. (b) Yamada, M.; Hagiwara, H.; Torigoe, H.; Matsumoto, N.; Kojima, M.; Dahan, F.; Tuchagues, J.-P.; Re, N.; Iijima, S. *Chem. Eur. J.* **2006**, *12*, 4536.

132. (a) Ni, Z.; Fiedler, S. R.; Shores, M. P. *Dalton Trans.* **2011**, *40*, 944. (b) Ni, Z.; McDaniel, A.M.; Shores, M. P. *Chem. Sci.* **2010**, *1*, 615.

133. (a) Judge, J. S.; Baker, W. A. *Inorg. Chim. Acta* **1967**, *1*, 68. (b) Kremer, S.; Henke, W.; Reinen, D. *Inorg. Chem.* **1982**, *21*, 3013.

134. (a) Hayami, S.; Shigeyoshi, Y.; Akita, M.; Inoue, K.; Kato, K.; Osaka, K.; Takata, M.; Kawajiri, R.; Mitani, T.; Maeda, Y. *Angew. Chem. Int. Ed.* **2005**, *44*, 4899. (b) Hayami, S.; Murata, K.; Urakami, D.; Kojima, Y.; Akita, M.; Inouea, K. *Chem. Commun.* **2008**, 6510.

135. (a) Lee, Y. H.; Ohta, A.; Yamamoto, Y.; Komatsu, Y.; Kato, K.; Shimizu, T.; Shinoda, H.; Hayami, S. *Polyhedron* **2011**, *30*, 3001. (b) Seredyuk, M.; Gaspar, A.B.; Ksenofontov, V.; Galyametdinov, Y.; Kusz, J.; Gütlich, P. *Adv. Funct. Mater.* **2008**, *18*, 2089.

136. Romero-Morcillo, T.; Seredyuk, M.; Muñoz, M. C.; Real, J. A. *Angew. Chem. Int. Ed.* **2015**, *54*, 14777.

Chapter II

Rational Functionalization of Single-Molecule Magnets: Towards Liquid Crystalline (LC) Phases

Table of Contents for Chapter II:

II.1. Introduction

The discovery of the first single-molecule magnet (SMM),[1] in the early 90's has opened an important research field at the interface of classical and quantum worlds. Single-molecule magnets are complexes which are able to retain magnetization at low temperature, acting therefore as a "nano" magnet.[2] These molecular objects appear as promising units for potential applications in molecular memories, quantum computing and spintronic devices.[3,4]

One of the important steps towards possible applications is to develop efficient methods to organize and process these nanomagnets. The organization of these systems has been reported on surfaces, in mesoporous materials or in coordination networks.[5] Another promising strategy towards their controlled organization is the development of the new hybrid materials with liquid crystal (LC) properties.[6] Indeed, metallomesogens (metal complexes which exhibit liquid crystalline properties) are very convenient materials in term of processability: they self-organize and are able to form suitable thin films for surface deposition. Moreover, taking into account the fluidity of liquid crystals, they can be eventually oriented with magnetic fields and this could be useful in order to position the easy axes of SMMs in the same direction (Figure II-1). Additionally, the organic shell provided by the mesogenic ligands may play an important role to isolate and protect the magnetic core and thus to prevent from interactions between objects (Figure II-1).

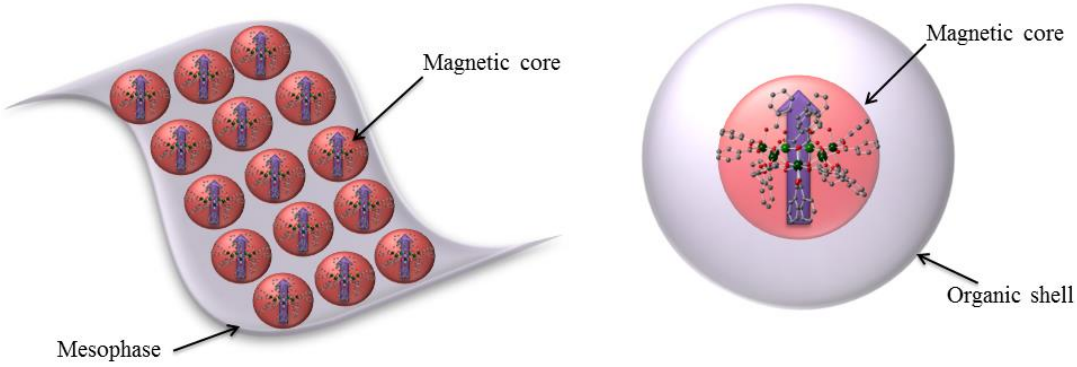

Figure II-1. Schematic representation emphasizing the advantages of SMM-based hybrids: (left) the formation of fluid phases that can help to organize, align and orient SMMs and (right) the isolation/protection of magnetic cores by an organic shell.

A part of this PhD work aimed to develop and study new metallomesogens based on SMMs and more precisely based on the well-known dodecanuclear manganese Mn_{12}-OAc. This chapter starts by short description of general aspects on Mn_{12}-based complexes and previous studies of these complexes in metallomesogens. Then the general functionalization strategy used in this work to promote liquid crystalline properties will be presented. The synthesis, analytical characterizations, magnetic and thermotropic properties of the complexes prepared during this work will be then discussed and compared with previous examples described in the literature.

II.2. Selected SMM: Mn_{12}-based complexes

II.2.1. Why Mn_{12}?

The dodecamanganese complex with general formula $[Mn_{12}O_{12}(CH_3COO)_{16}(H_2O)_4]$ (Mn_{12}-OAc) was the first SMM discovered.[1] It was synthesized in 1980 by Lis et al,[1a] while the evidences of slow relaxation of magnetization at low temperature were reported in 1993 by Sessoli et al.[1b,d,f,g] Despite the discovery of thousands new SMMs, Mn_{12}-OAc remains one of the most popular and widely studied system. Indeed, it displays a large energy barrier against thermal relaxation (ca. 60 K)[2] allowing to retain magnetization for months in absence of a magnetic field. Moreover, its synthesis is straightforward and inexpensive, and it is possible to replace easily the acetate ligands by other bidentate ligands to generate new Mn_{12} derivatives. Such chemical modifications allow for a relative control of the solubility, redox potentials and magnetic properties of the Mn_{12} core.[7]

II.2.2. Structure of Mn_{12}-based complexes

The Mn_{12}-OAc molecule and its derivatives are mixte-valence polyoxymetallate complexes of Mn^{III} and Mn^{IV} ions. The general structure is composed by a cubane core $Mn^{IV}{}_4O_4$ connected to a non-planar crown of eight Mn^{III} ions through eight μ_3-O^{2-} ions and four bridging carboxylates in axial positions (two in each side of the Mn^{III} crown; see the structure of Mn_{12}-OAc in Figure II-2). The eight Mn^{III} ions from crown are interconnected by twelve bridging carboxylate ligands (eight in equatorial positions and four in axial positions).

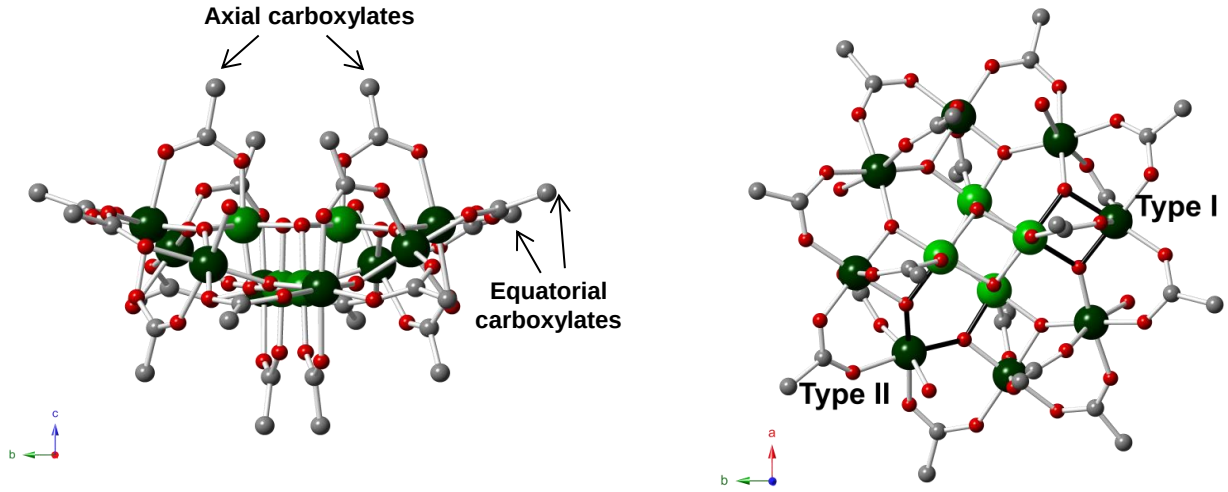

Figure II-2. Structure of Mn_{12}-OAc: (left) along the crystal a-axis and (right) along the crystal c-axis. Color Scheme: Mn(IV) light green, Mn(III) dark green, O red, C grey. Hydrogens are omitted for clarity.

The crown consists in an alternation of two types of Mn^{III} ions which are referred as type I or type II according to their connectivity with Mn^{IV} ions: Mn^{III} ions of type I are bridged to only one Mn^{IV} *via* two μ-O^{2-} ions while Mn^{III} ions of type II are connected to two different Mn^{IV} ion *via* μ_3-O^{2-} bridges (Figure II-2, right). Also, the structures contain usually four water ligands, which are always coordinated on type II Mn^{III}

sites. In the original Mn_{12}-OAc, these water ligands are equivalently distributed over the four Mn^{III} sites of type II and the complex is then referred as 1:1:1:1 isomer (Figure III-3(a)). The exact number and disposition of the water molecules can vary from one Mn_{12} complex to another. For example, the four water molecules in $[Mn_{12}O_{12}(CF_3COO)_{16}(H_2O)_4]$ are arranged in a 2:0:2 fashion (Figure III-3(b)),[8] while the compound $[Mn_{12}O_{12}(CHCl_2COO)_8(t\text{Bu-}CH_2COO)_8(H_2O)_3]$ contains only three water molecules with a 2:0:1 arrangement (Figure III-3(c)).[9]

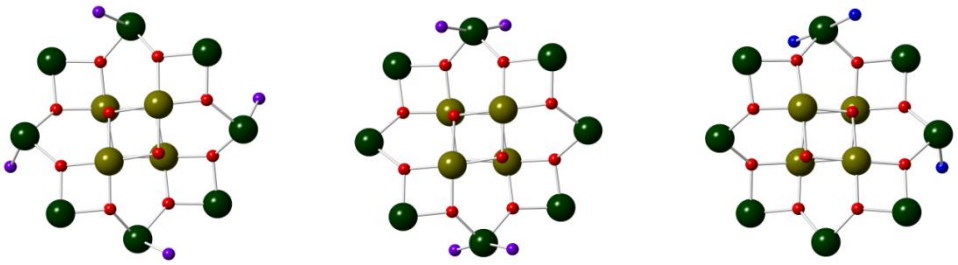

(a) (b) (c)

Figure II-3. Schematic representation of Mn_{12} cores with different numbers and positions of H_2O ligands: (a) $[Mn_{12}O_{12}(CH_3COO)_{16}(H_2O)_4]$, 1:1:1:1 isomer,[1a] (b) $[Mn_{12}O_{12}(CF_3COO)_{16}(H_2O)_4]$, 2:0:2 isomer,[8] (c) $[Mn_{12}O_{12}(CHCl_2COO)_8(t\text{Bu-}CH_2COO)_8(H_2O)_3]$, 2:0:1 isomer.[9] Color scheme: Mn(IV) light green, Mn(III) green, O red, O_{water} blue.

Mn_{12}-based complexes have a high spin ground state $S_T = 10$, which can be understood by analysis of magnetic core's structure. Indeed, the Mn^{IV} ions from cubane core ($S = 3/2$) are ferromagnetically coupled to each other and are antiferromagnetically coupled with the outer Mn^{III} ions ($S = 2$) giving an $S_T = 10$.

The magnetic anisotropy of the ground state in Mn_{12}-OAc is mainly due to the anisotropy of the eight outer Mn^{III} ions. The coordination sphere around each Mn^{III} ion is not perfect octahedron, but is axially distorted, since two Mn^{III}-O bonds are longer than the other ones. This distortion can be explained by the Jahn-Teller (JT) effect. The JT theory states that "any non-linear molecule with a spatially degenerate electronic ground state will undergo a geometrical distortion that removes that degeneracy, because the distortion lowers the overall energy of the species".[10]

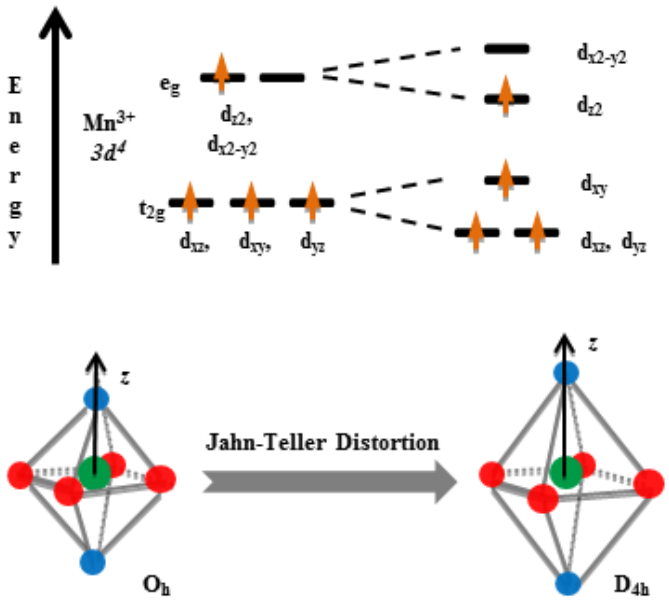

Figure II-4. (top) *d* orbital electronic configurations of distorted d^4 high spin complexes; (bottom) Schematic representation of regular octahedral complex (O_h) and the influence of the Jahn-Teller distortion with axial elongation.

In the case of Mn^{III} ion (d^4) in high spin configuration (S = 2), the fourth electron occupy either one of the e_g oribitals causing a JT distortion associated with a tetragonal elongation of trans Mn^{III}-O bonds (Figure II-4).[11] These distortions do not involve the Mn^{III}-μ_3-O^{2-} bonds, as they are the strongest bonds in the molecule. The JT elongation axes are nearly perpendicular to the plane of the $[Mn_{12}O_{12}]$ disk-like core (Figure II-5 (a)). Their nearly-parallel alignment along the molecular *z*-axis is the origin of the uniaxial magnetic anisotropy that greatly influences the magnetic properties of Mn_{12}-based systems.

In some Mn_{12}-based structures, one of the JT elongation axes can be oriented equatorially rather than axially in regard to the Mn_{12} core (Figure II-5 (b)). This abnormal orientation is energetically less favorable than the previous one but can be nonetheless stabilized by multiple structural (ie. nature of carboxylate ligands or number of water ligands) and crystal packing effects (eg. intermolecular interactions between complexes or with lattice solvents). A change on the crystal packing such as solvent loss may induce a conversion of this abnormal JT orientation to the normal one and vis-versa.[11]

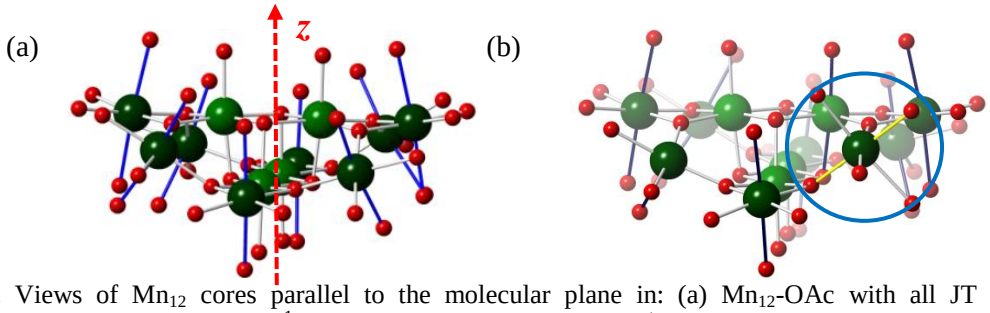

Figure II-5. Views of Mn_{12} cores parallel to the molecular plane in: (a) Mn_{12}-OAc with all JT axes nearly perpendicular to the molecular plane;[1c] (b) $[Mn_{12}O_{12}(CHCl_2COO)_8(Bu^t\text{-}CH_2COO)_{16}(H_2O)_3]$ with one abnormally oriented JT axis.[12] Color scheme: normally oriented JT axes are shown in blue and the abnormally oriented JT axis is shown in light green; Mn^{III} green, Mn^{IV} green, O red.

It is common to found samples in which both forms coexist. The ability of Mn_{12}-based molecules to exist in two different forms is known as Jahn-Teller isomerism.[10] The existence of two JT isomers is the origin of two distinct slow relaxation modes of the magnetization. Indeed, the abnormal orientation on one JT axis affect the uniaxial magnetic anisotropy and, thus, the slow relaxation of magnetization (around 10^{-3} - 1 s) occurs at lower temperature (ca, 2 – 3 K) in respect with the isomer with normal JT orientation (4 – 7 K).

II.2.3. Chemistry of Mn_{12}-based complexes

One of the advantages of the Mn_{12}-based molecules is their ability to undergo carboxylate substitution *via* ligand exchange reactions.[7,13] This characteristic provides a convenient and efficient approach to get new Mn_{12}-based derivatives with improved properties, in term of solubility, stability in solution, thermal stability or magnetism. The ligand substitution is driven by the greater acidity of added carboxylic acids and/or the ability to remove the acetate ligands. It was emphasized that the ligand substitution is actually a reversible process (eq.**1**), and in order to shift the reaction equilibrium towards the formation of desired products, the synthesis requires the use of an excess of the substituting ligands as well as the removal of the produced acetic acid by an azeotropic distillation with toluene.

$$[Mn_{12}O_{12}(CH_3COO)_{16}(H_2O)_4] + 16\ RCO_2H \rightleftharpoons [Mn_{12}O_{12}(RCO_2H)_{16}(H_2O)_4] + 16\ CH_3COOH \quad \text{(eq.1)}$$

Due to the presence of JT elongation in the axial Mn^{III}-O bonds, the reactivity of carboxylate ligands is different depending to their occupation in axial or equatorial positions (See Figures II-2). Indeed, the Mn^{III}-O bonds with JT distortion are weaker than the other ones making the axial positions more sensitive to nucleophilic substitutions. Also, the JT elongations maintain a greater electron density on the oxygen atoms and will favor therefore the presence of ligands with low basicity. Taking into account the difference of reactivity between axial and equatorial positions, it is possible to make regioselective substitutions on the Mn_{12} core and few examples of mixed-ligand complexes $[Mn_{12}O_{12}(RCOO)_8(L)_8(H_2O)_4]$ (with RCOO = carboxylate and L = carboxylate or sulfonate ligands) have been reported.[9,14] Two synthetic approaches have been explored.

The first method involves the direct addition of 8 equivalents of ligand HL (in its protonated form) to a pre-formed $[Mn_{12}O_{12}(RCOO)_{16}(H_2O)_4]$ complex to generate a mixed-ligand complex $[Mn_{12}O_{12}(RCOO)_8(L)_8H_2O)_4]$ (eq.**2**).[14]

$$[Mn_{12}O_{12}(RCOO)_{16}(H_2O)_4] + 8\ HL \rightleftharpoons [Mn_{12}O_{12}(RCOO)_8(L)_8(H_2O)_4] + 8\ RCOOH \qquad \text{(eq.2)}$$

This method is nonetheless not very efficient to prepare mixed-carboxylate complexes and yields to mixtures of complexes. In contrast, this method was found to be the only possible way to produce the mixed-ligands complex $[Mn_{12}O_{12}(OAc)_8^{eq}(PhSO_3)_8^{ax}(H_2O)_4]$ in which the benzene sulfonate ligands occupy exclusively the axial sites due to its very low basicity.[14a] The second approach is more successful to obtain the desired products. The synthesis involves an equimolar reaction of two homoleptic Mn_{12} complexes containing carboxylate ligands with significantly different pKa (eq.**3**).

$$[Mn_{12}O_{12}(RCOO)_{16}(H_2O)_4] + [Mn_{12}O_{12}(R'COO)_{16}(H_2O)_4] \rightleftharpoons 2[Mn_{12}O_{12}(RCOO)_8(R'COO)_8(H_2O)_4] \text{ (eq.3)}$$

This results in an 8:8 product in which the ligands with lower basicity are in the axial positions while the ligands with stronger basicity occupy the equatorial positions. To the best of our knowledge, only two examples of mixed-carboxylate complexes, namely $[Mn_{12}O_{12}(CHCl_2COO)_8^{ax}(^tBuCH_2COO)_8^{eq}(H_2O)_4]$ and $[Mn_{12}O_{12}(CHCl_2COO)_8^{ax}(C_2H_5COO)_8^{eq}(H_2O)_4]$ have been reported so far.[9] It is worthwhile to mention that the electronic discrimination between axial and equatorial positions can be overcome by steric effects. This is the case in the mixed-ligands complex $[Mn_{12}O_{12}(OAc)_8(Ph_2PO_2)_8(H_2O)_4]$, in which the eight bulky diphenyl phosphonate ligands are not exclusively on the axial positions as it is expected, but are equivalently distributed over the axial and equatorial positions.[14b] However, when only four bulky $(PhO)_2PO_2^-$ ligands are used, the previous rule is respected and the product $[Mn_{12}O_{12}(PhCOO)_{12}((PhO)_2(PO_2)_4(H_2O)_4]$ contains the four non-carboxylate ligands in axial positions.[14c]

All these synthetic methods could be useful in order to design hybrid molecular materials, eventually with functional groups able to induce liquid crystalline properties.

II.2.4. Mn_{12}-based complexes with liquid crystal properties

There are only few examples of coordination compounds combining SMM and mesomorphic properties.[15,16] The first SMM-containing metallomesogens were reported in 2008 on Mn_{12}-based systems.[15a] In this study, Terazzi and co-workers obtained two hybrids complexes by replacing the sixteen acetate ligands of the Mn_{12}-OAc by gallate ligands bearing three dodecyl or (cyanobiphenyloxy)undecyl chains. The SMM behavior was preserved in both cases, and mesomorphic properties were found to be significantly different according to the ligand functionalization strategy employed. The complex containing strongly lipophilic ligands, ie. tris(dodecyloxy)benzoate, self-organizes into a body-centered cubic mesophase.[15a] This unusual liquid crystal organization can be explained by the globular shape (spherulitic) of the complex, induced by the large number (48) of long alkyl chains, which favors such cubic organizations.[16,17]

On the other hand, the complex containing cyanobiphenyl units forms bilayer lamellar-like mesophases in which the magnetic cores display an intralayer short-ranged 2D organization. More recently they extended this strategy by varying the number and position of (cyanobiphenyloxy)undecyl substituents attached on the benzoate moieties and confirmed the ability of these complexes to generate smectic-like organizations. In these materials, the lamellar organization mainly results from the intermolecular π-π interactions between the cyanobiphenyl units, which are well-known calamitic smectogens, while the number of attached mesogenic groups or ligand symmetry have only a minor influence on the mesophase organization (variations only on periodicity and the compactness). The 2D organization displayed by the magnetic cores was found to be in all cases short-ranged, while its exact nature (rectangular or hexagonal) could not be unambiguously determined experimentally. One of the main drawbacks of these systems is their high clearing point temperatures, which are near or above the decomposition temperature, limiting their potential use for surface deposition. Indeed, the formation of thin film would require first the melting into the isotropic liquid phase and then the homogenization of the surface deposition, eventually by spin-coating methods.

Scheme II-1. Chemical structure of benzoate derivatives used by Terazzi et al.[15a,c]

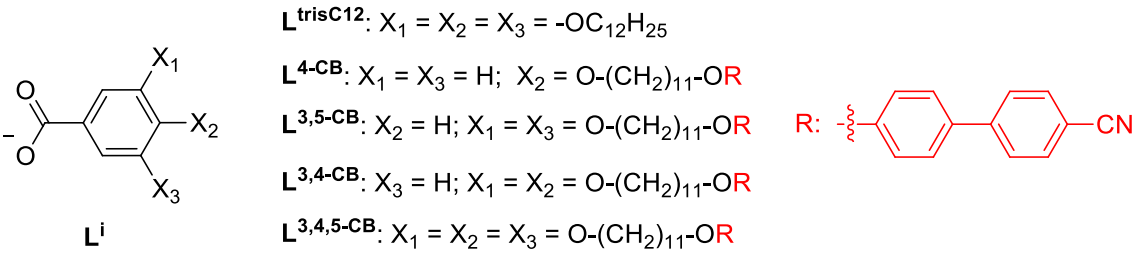

Our team in CRPP has been interested on the design of Mn_{12}-based metallomesogens since 2008.[16,18] Similarly to Terazzi and co-workers' studies, our first strategy was to develop Mn_{12} complexes containing strongly lipophilic carboxylate ligands. Thus, a series of complexes functionalized with 16 benzoate ligands bearing one, two or three alkyl chains ($L^{1\text{-}4}$, Scheme II-2) was prepared by Diana Siretanu and Dmitri Mitcov during their PhD thesis.[16,18] The study aimed to determine how the number and length size of lipophilic substituents influence the mesomorphic properties of final complexes. More precisely, we sought to determine whether a reduction of the number of lipophilic groups (one or two chains) would afford a less

globular bulkiness than the previously reported complexes and ultimately would provide mesophases with lower symmetry (nematic or smectic). This study emphasized that, despite the reduction of the number of alkyl chains, the overall geometry of the complexes remains pseudo-spherical leading therefore to cubic or pseudo-cubic organizations. Additionally, when benzoate ligands containing only one alkyl chain were used, the ratio between the rigid and flexible counterparts does not favor the formation of mesophases and only crystalline or amorphous phases were detected. Nonetheless, it have been shown that the variation of the lipophilic density around the Mn_{12} core has a significant influence on the thermal (strong difference on the melting and clearing temperatures) and cubic self-organization (different symmetries) of resulting complexes.

As previously reported,[15] our team also investigated a second strategy consisting in the introduction of pending calamitic smectogens on the Mn_{12} molecule. In addition to the cyanobiphenyl units proposed by Terazzi and co-workers, a complex containing biphenyl groups was also prepared (L^7, Scheme II.2).[16] This latter was found particularly interesting since it allows for a significant decrease of the clearing temperature (ca. 350 K) that is about 70 K below the decomposition temperature, making of this compound a more suitable system for surface deposition purpose. Additionally, small modifications of the ligand were found very efficient to control the liquid crystal organization. Indeed, small-angles X-ray scattering investigations revealed for the first time the formation bilayer lamellar mesophases in which the intralayer Mn_{12} cores form a long-range 2D order with hexagonal symmetry.

Scheme II-2. Chemical structure of benzoate derivatives used in our team for the functionalization of the Mn_{12} complex.[16,18]

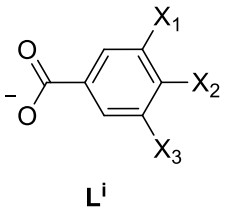

L^i

L^1: $X_1 = X_3 = H$; $X_2 = -OC_9H_{19}$

L^2: $X_1 = X_3 = H$; $X_2 = -OC_{10}H_{21}$

L^3: $X_1 = X_3 = H$; $X_2 = -OC_{12}H_{25}$

L^4: $X_1 = X_3 = H$; $X_2 = -OC_{16}H_{33}$

L^5: $X_2 = H$; $X_1 = X_3 = -OC_{12}H_{25}$

L^6: $X_1 = X_2 = X_3 = -OC_{12}H_{25}$

L^7: $X_2 = H$; $X_1 = X_3 =$ 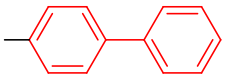

L^8: $X_2 = H$; $X_1 = X_3 =$ 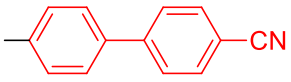

II.2.5. Functionalization strategy used in the thesis

In continuation with these promising investigations, we attempted a new functionalization strategy to induce liquid crystalline features on the Mn_{12} complex. In contrast with previous studies in which the sixteen acetate groups were replaced by mesogenic ligands, we alternatively introduced these ligands only on certain positions of the Mn_{12} core using the regioselective functionalization methodology (see section II.2.3). Here, the goal is to induce more structural anisotropy on the Mn_{12} core in order to facilitate the self-organization and eventually promote unprecedented mesomorphs. Two approaches can be envisaged: the

functionalization with mesogenic ligands on the equatorial or on the axial positions of the Mn_{12}. Using a selective functionalization of the equatorial positions with mesogenic ligand; we can expect that the complexes will adopt a discotic geometry, which will lead to nematic or columnar mesophases according to the intermolecular cohesion, (Figure II-6, left). In the second case, we can expect that the complexes which should have a rod-like shape (calamitic) will favor the formation of smectic or eventually nematic phases at high temperature (Figure II-6, right).

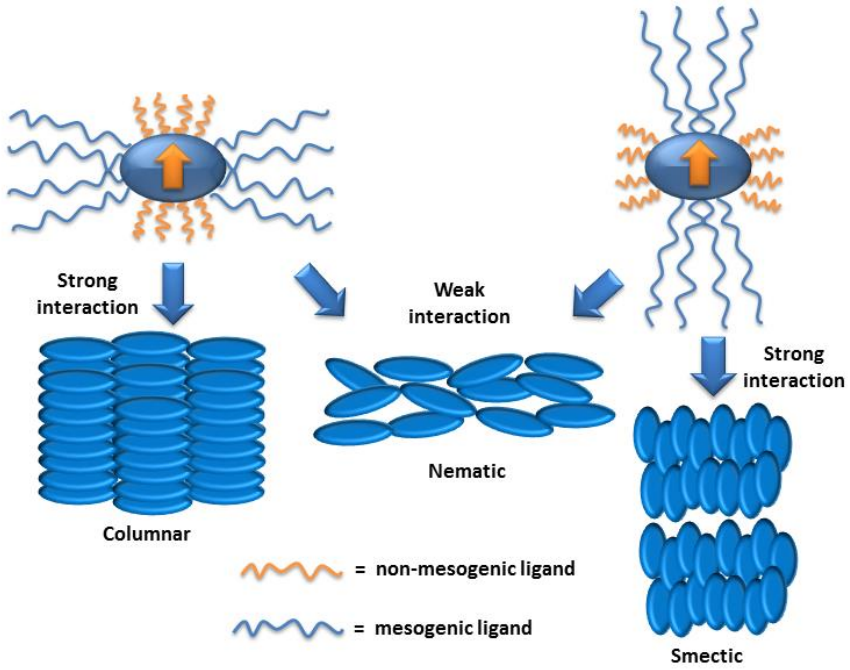

Figure II-6. Schematic representation and correlation between the molecular geometry and expected supramolecular organization

For this work, we have been mainly focused on the first approach. In order to achieve the desired site-selective functionalization, non-mesogenic ligands with low pK_a are required to occupy the axial positions of Mn_{12} molecule (see section II.2.3). Several ligands, including benzene sulfonate, dichloroacetate, trichloro- or trifluoroacetate have been tested in our preliminary studies, and the latter one was found to be the most convenient and efficient for the preparation of hybrids. For the equatorial positions, we selected ligands based on benzoate platforms since the pK_a of such ligands (pK_a ~ 4.2 – 4.4) is significantly higher than the one of the trifluoroacetate (pK_a = 0.3) (Scheme II-3). Additionally, the functionalization of this platform by one or multiple mesogenic substituents is easily accessible from a synthetic point of view.[15,16]

In order to highlight the effect of our functionalization strategy on magnetic and self-organization properties, we selected the ligands used in the thesis of D. Mitcov.[16] Indeed, this will allow for a direct comparison with the homo-substituted analogues $[Mn_{12}O_{12}(L^{i})_{16}(H_2O)_4]$ previously reported. Also, for a better understanding of the site-selective substitution and in order to validate our synthetic strategy, we also prepared a complex containing non-mesogenic ligands $[Mn_{12}O_{12}(CF_3COO)_8(L^{1})_8(H_2O)_4]$.

Scheme II-3. Chemical structure of ligands $\mathbf{L^{1-4}}$ used for the functionalization of equatorial positions of Mn_{12} complex.

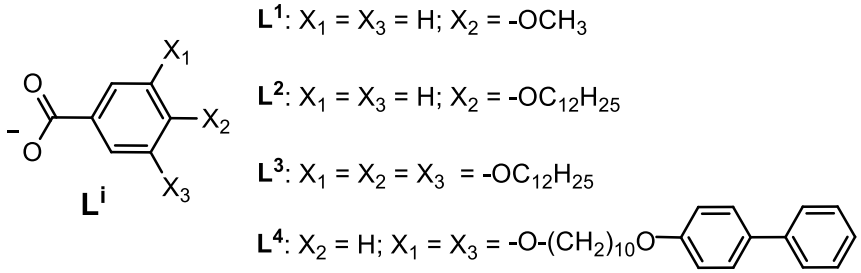

II.3. Functionalization of Mn_{12}-based SMMs: Synthesis and Characterizations

Accordingly to previous studies,[9] the most efficient way to obtain mixed-carboxylate complexes $[Mn_{12}O_{12}(RCOO)_8(R'COO)_8(H_2O)_4]$ involves an equimolar reaction of the corresponding homo-substituted complexes. All the carboxylate ligands and Mn_{12} precursors required for the preparation of the $[Mn_{12}O_{12}(CF_3COO)_8^{ax}(L^i)_8^{eq}(H_2O)_4]$ have been previously reported in D. Mitcov's thesis[16] or elsewhere[8,9,12,13] and their synthesis and characterization are concisely recalled in sections II.3.1 and II.3.2.

III.3.1. Synthesis of carboxylate ligands

The compounds $\mathbf{HL^3}$ and $\mathbf{HL^4}$ are not commercially available and were prepared, in two and three steps synthesis, respectively.[15c,16] In the case $\mathbf{HL^3}$, the first step is the synthesis of the precursor methyl tris(dodecyloxy)benzoate **1** by a Williamson reaction (Scheme II-4).

Scheme II-4. Synthetic pathway for $\mathbf{HL^i}$ (i=3-4)

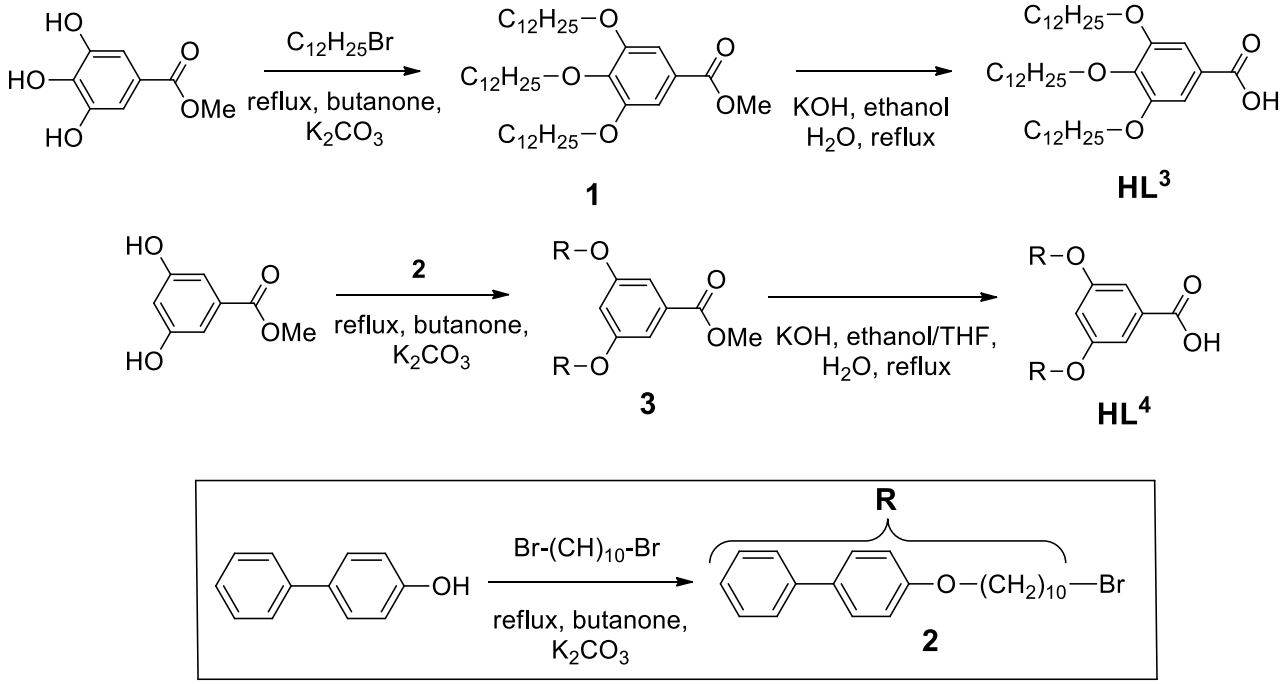

The etherification coupling between the 1-bromododecane and the methyl 3,4,5-trihydroxybenzoate requires potassium carbonate K_2CO_3 to deprotonate the phenolic positions and a catalytic amount of potassium iodide was used to promote the reaction by halide exchanges. A saponification of the compound is thereafter performed using KOH to produce **HL^3**. For **HL^4**, the first step involve the preparation of 4-((10-bromodecyl)oxy)-1,1'-biphenyl **2** by a Williamson reaction between 1,10-dibromodecane and 4-hydroxybiphenyl (Scheme II-4). A large excess of 1,10-dibromodecane is necessary to insure a mono-coupling of the aliphatic spacer, and it is removed at the end by column chromatography. The ligand **HL^4** is then obtained following the same reactional sequence used for **HL^3** by ether coupling reaction between **2** and methyl 3,5-dihydroxybenzoate followed by a saponification of the precursor **3** (Scheme II-4).

II.3.2. Synthesis and characterization of homo-substituted Mn_{12} complexes

As mentioned in Section II.2.3, homo-substituted complexes $[Mn_{12}O_{12}(\mathbf{L^i})_{16}(H_2O)_4]$ were prepared by ligand exchange reactions starting from $[Mn_{12}O_{12}(CH_3COO)_{16}(H_2O)_4]$ (eq. 4). This latter was obtained accordingly to the procedure described by Lis et al.[1a] by reaction of $KMnO_4$ with $Mn(CH_3COO)_2$ in acetic acid solution. The complex was isolated as black crystals, for which the unit cell was consistent with the reported structure of $[Mn_{12}O_{12}(CH_3COO)_{16}(H_2O)_4]\cdot 2CH_3COOH\cdot 4H_2O$.[1]

The replacement of the acetate ligands was carried out using an excess (~28 equiv) of **HL^i** in order to shift the reaction equilibrium toward the formation of desired complexes. Also, to prevent from reaction reversal, the out coming acetic acid was removed by several successive distillations as an azeotropic mixture with toluene.

$$[Mn_{12}O_{12}(CH_3COO)_{16}(H_2O)_4] + 16\ \mathbf{HL^i} \rightleftharpoons [Mn_{12}O_{12}(\mathbf{L^i})_{16}(H_2O)_4] + 16\ CH_3COOH \quad (\mathbf{eq.\ 4})$$

$[Mn_{12}O_{12}(\mathbf{L^1})_{16}(H_2O)_3]$ was purified and isolated as brownish-black crystals by slow diffusion of Et_2O vapor into a CH_2Cl_2 solution of complex at 4 °C. The verification of the unit cell parameters by single-crystal X-ray diffraction confirmed the composition $[Mn_{12}O_{12}(\mathbf{L^1})_{16}(H_2O)_3]\cdot 0.5Et_2O\cdot H_2O$ as previously reported.[16] $[Mn_{12}O_{12}(\mathbf{L^{2\text{-}4}})_{16}(H_2O)_4]$, which are not suitable for crystallization due to the presence of flexible and "greasy" moieties, were purified by size exclusion column chromatography, using Bio-Beads S-X3 beads (neutral, porous styrene divinylbenzene copolymer beads) as stationary phase. The removal of ligand excess or partially substituted Mn_{12} complexes from the fully substituted one was monitored by FTIR (*vide infra*). The separation is nonetheless not very easy to control and at least two successive purifications by column chromatography are required to isolate the desired products.

The formation of the expected complexes is established by FTIR and ^{1}H NMR measurements, which were found essentially identical to those previously reported.[15,16,18] The IR spectra display strong absorptions in the 1577 – 1604 cm^{-1} and 1370 – 1412 cm^{-1} ranges (Figures II-7), which are assigned respectively to $\nu_{OCO(as)}$ and $\nu_{OCO(s)}$ stretching vibrations of coordinated benzoate in bridging mode. The $\nu_{OCO(s)}$ stretching band associated to the acetate groups at 1381 cm^{-1} in the $[Mn_{12}O_{12}(CH_3COO)_{16}(H_2O)_4]$ spectrum (Figure S.II-1),

does not appear anymore, confirming the replacement of all acetate ligands by the desired ligands. Furthermore, the C=O stretches at ~ 1700 cm^{-1} and ~ 1680 cm^{-1} ascribed to molecules of acetic acid and benzoic acid derivatives, respectively, were not observed, in agreement with a complete removal of acetic acid by azeotropic distillation and ligand excess by recrystallization or column chromatography. The removal of the acetate ligands is also supported by the disappearance, in ^{1}H NMR, of the three singlet resonances found at δ 13.7, δ 40.9 and δ 47.8, in the parent complex Mn_{12}-OAc and attributed to acetate groups on non-equivalent binding sites (Figure S.II-5, top left).[13a] The ^{1}H NMR spectra show also broad signals corresponding to the aliphatic shell and pending biphenyl units, while the proton signals associated to the benzoate ring are completely extinguished (from the expected range ca. 6-8 ppm) due to their close proximity with the paramagnetic core (Figure S.II-5, bottom). This assignment confirms that the complexes remain intact in solution and no free ligand is present after the purification.

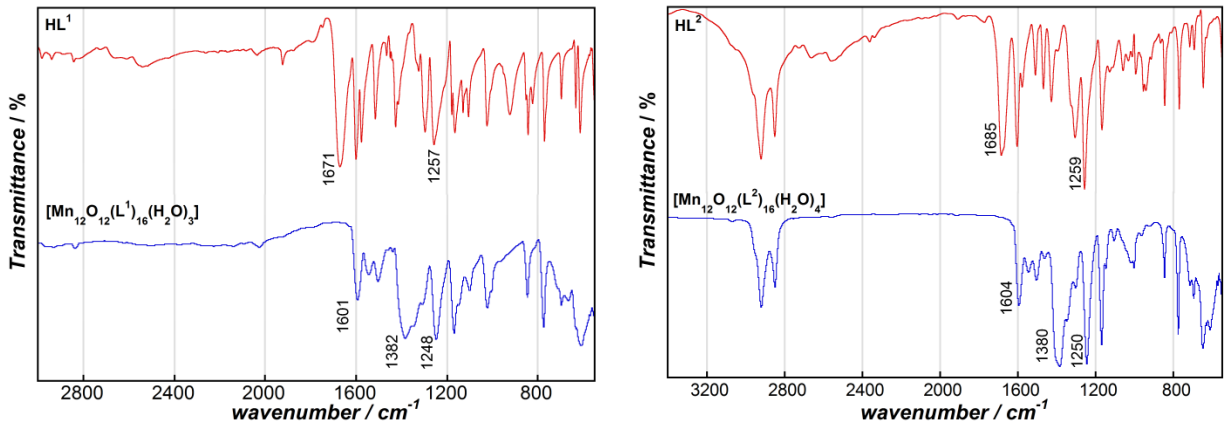

Figure II-7. FTIR spectra at room temperature: (left) of **HL^{1}** and $[Mn_{12}O_{12}(\mathbf{L^{1}})_{16}(H_2O)_3]$; (right) of **HL^{2}** and $[Mn_{12}O_{12}(\mathbf{L^{2}})_{16}(H_2O)_4]$.

The complex $[Mn_{12}O_{12}(CF_3COO)_{16}(H_2O)_4]$ required for the preparation of mixed-carboxylate Mn_{12} complexes was synthetized as reported by Zhao et al.[8] by treatment of a $[Mn_{12}O_{12}(CH_3COO)_{16}(H_2O)_4]$ solution in DCM with a large excess of trifluoroacetic acid. After filtration, the solution was layered with hexane, leading after few days, to the formation of black crystals of $[Mn_{12}O_{12}(CF_3COO)_{16}(H_2O)_4]\cdot 2CF_3COOH\cdot 4H_2O$ (based on the unit cell parameters). The FTIR spectrum is also consistent with the formation of the targeted complex and shows two strong absorption bands at 1601 and 1426 cm^{-1} ascribed to $\nu_{OCO(as)}$ and $\nu_{OCO(s)}$ stretching vibrations, respectively, as well as a band at 1797 cm^{-1}, which is characteristic for free trifluoroacetic acid present in the packing (Figure S.II-2). ^{19}F NMR spectroscopy shows, beside the presence of trifluoroacetic acid at -75.5 ppm, four peaks (-54.4; -26.6; 8.90; 60.0 ppm) corresponding to trifluoroacetate ligands in different binding modes (Figure S.II-5, top right). However, a proper assignment of these signals remains difficult.[13b]

II.3.3. Synthesis and characterization of mixed-carboxylate Mn_{12} complexes

The mixed-carboxylate compounds $[Mn_{12}O_{12}(CF_3COO)_8(\mathbf{L^i})_8(H_2O)_4]$ were prepared by reacting an equimolar amount of the two types of homo-substituted Mn_{12} complexes in CH_2Cl_2 (eq.**5**). After a filtration to remove minor decomposition products, the complexes were isolated as brownish powder or glassy solids.

$$[Mn_{12}O_{12}(CF_3COO)_{16}(H_2O)_4] + [Mn_{12}O_{12}(\mathbf{L^i})_{16}(H_2O)_4] \rightleftharpoons 2[Mn_{12}O_{12}(CF_3COO)_8(\mathbf{L^i})_8(H_2O)_4] \text{ (eq.5)}$$

The formation of mixed-carboxylate complexes by NMR and IR is not trivial to confirm and proving the expected regioselectivity with these techniques is likely impossible. In order to facilitate interpretations and validate the synthetic strategy, an important effort was first made to isolate the model compound $[Mn_{12}O_{12}(CF_3COO)_8(\mathbf{L^1})_8(H_2O)_4]$, as crystals and to determine its structure by single-crystal X-ray diffraction analysis.

II.3.3.1. Single-crystal X-ray diffraction analyses of $[Mn_{12}O_{12}(CF_3COO)_8(\mathbf{L^1})_8(H_2O)_4]$

Single crystals suitable for X-ray diffraction experiments were obtained by slow evaporation of a solution of the complex in THF:DCM (1:1). The X-ray diffraction analysis reveals that the polyoxometallic Mn_{12} core is preserved after reaction and its structure is similar to previously reported Mn_{12}-based complexes.[8-12] Views of the complex are shown in Figure II-8 and X-ray data parameters are summarized in Table S.II-1.

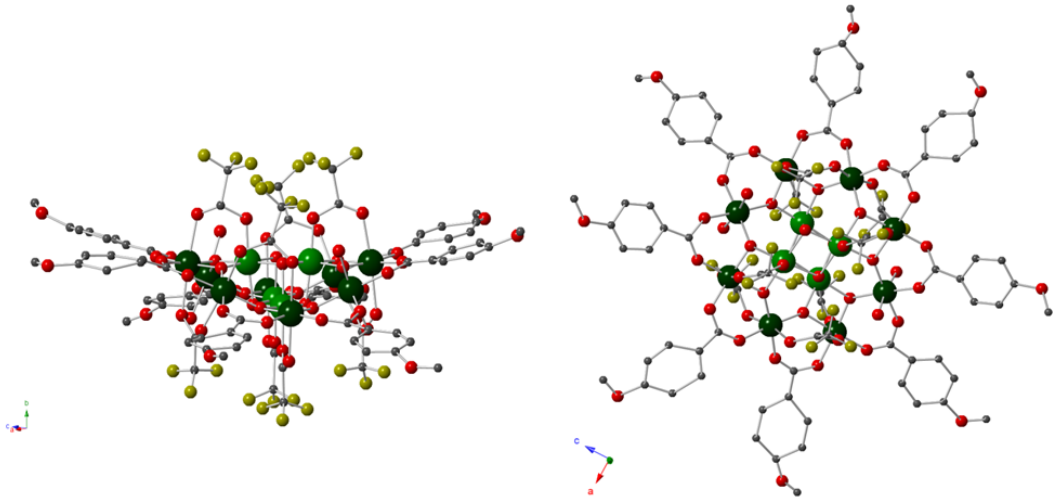

Figure II-8. Crystal structure of $[Mn_{12}O_{12}(CF_3COO)_8(\mathbf{L^1})_8(H_2O)_4]$ at 120 K viewed in the *bc* plane (left) and in the *ac* plane (right). Hydrogen atoms are omitted for clarity. Color scheme: Mn^{IV} green, Mn^{III} dark green, O red, C grey, F yellow.

The molecule contains eight methoxybenzoate and eight trifluoroacetate ligands in equatorial and axial positions, respectively, confirming that the ligand exchange was complete and the expected selectively was successfully achieved. The compound crystallizes in an orthorhombic C222 space group. The unit cell contains two Mn_{12} molecules and no co-crystallized solvent or ligand could be detected in the lattice void space. The molecule presents three orthogonal 2-fold rotation axes, which cross each other at the center of the pseudo-cubane Mn^{IV} core. Therefore, the molecule can be described by one crystallographic unique Mn^{IV}

(Mn1) and three Mn^{III} ions (one of type I, Mn3, and two of type II Mn2 and Mn4). The four water ligands are on the two Mn2 sites giving rise to a 2:0:2 isomer as it was previously reported for $[Mn_{12}O_{12}(CF_3COO)_{16}(H_2O)_4]\cdot CF_3COOH\cdot 7H_2O$ (Figure II-9, left).[8] It is worth noting that water ligands in the structure of the precursors $[Mn_{12}O_{12}(CF_3COO)_{16}(H_2O)_4]\cdot 2CF_3COOH\cdot 4H_2O$ and $[Mn_{12}O_{12}(\mathbf{L^1})_{16}(H_2O)_3]\cdot 0.5Et_2O\cdot H_2O$ are arranged in 1:1:1:1 and 2:0:1 fashion,[8,16] respectively, meaning that a reorganization of water ligands is also occurring during the reaction or crystallization.

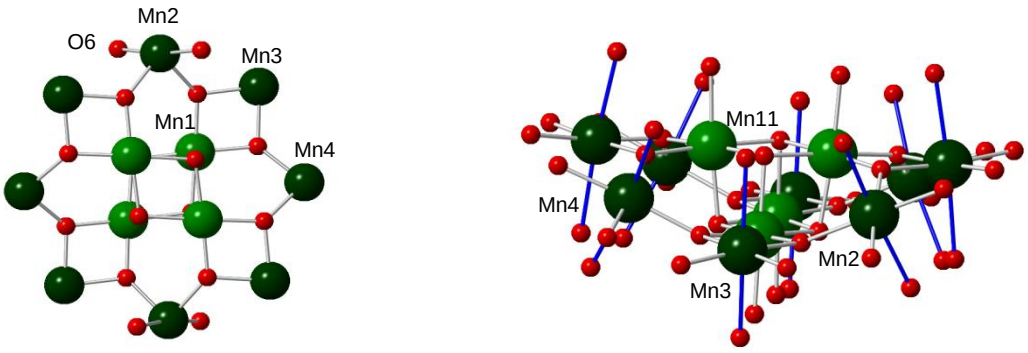

Figure II-9. Views of the Mn_{12} core in $[Mn_{12}O_{12}(CF_3COO)_8(\mathbf{L^1})_8(H_2O)_4]$ illustrating: (left) the arrangement of the four H_2O ligands (2:0:2 isomer), (right) the orientation of JT axes (in blue). Color scheme: Mn^{IV} green, Mn^{III} dark green, O red.

The analysis of bond length distances and charge balance confirms unambiguously the oxidation state +IV for the Mn ions from the cube-like core, while the surrounding Mn ions are +III. Indeed, the Mn-O bonds (1.832(7) – 1.881(9) Å) from the cubane Mn sites are on average shorter than the other ones (1.914-2.300 Å). The axial Mn^{III}-O bonds (2.140(1) – 2.300(1) Å) are significantly longer than the equatorial Mn^{III}-O bonds (1.880(1) – 1.947(1) Å), which is indicative of the expected JT elongation nearly perpendicular to the molecular plane as classically found in the original Mn_{12}-OAc complex (Figure II-9, right). The same observation was also found in the precursor $[Mn_{12}O_{12}(CF_3COO)_{16}(H_2O)_4]$,[8] while the precursor $[Mn_{12}O_{12}(\mathbf{L^1})_{16}(H_2O)_3]$ displays one abnormally oriented JT axis, almost perpendicular to the other ones.[16] Thus, considering the strong impact of these JT axes on the magnetic anisotropy, we can predict that the magnetic behavior of $[Mn_{12}O_{12}(CF_3COO)_8(\mathbf{L^1})_8(H_2O)_4]$ will be closer to $[Mn_{12}O_{12}(CF_3COO)_{16}(H_2O)_4]$ than $[Mn_{12}O_{12}(\mathbf{L^1})_{16}(H_2O)_3]$.

The methoxybenzoate ligands bridging the Mn3 and Mn4 centers were found strongly distorted. In order to improve the quality of the structure, many different crystallization conditions were tested. Recrystallization using diethyl ether vapor diffusion into a dichloromethane solution of complex at 4 °C gave after few days black crystal of $[Mn_{12}O_{12}(CF_3COO)_8(\mathbf{L^1})_8(H_2O)_4]$, which co-crystallizes with one molecule of diethyl ether. Although the quality of the crystal remained poor due to rapid loss of solvent, the data collection confirmed the expected composition of the complex and minor changes on the structure were found in respect to the previous one. In this case, the compound crystallizes in a tetragonal $I4_1/a$ space group in which the unit cell contains four Mn_{12} molecules. Views of the complex are shown in Figure II-10 and X-ray data parameters are summarized in Table S.II-1. By symmetry, the Mn_{12} complex is composed of a crystallographic unique Mn^{IV} (Mn3) center and only two Mn^{III} metal ions (one Mn^{III} of type I, Mn1, and one

Mn^{III} of type II, Mn2). Consequently, the water ligands are equivalently distributed over the four Mn^{III} sites of type II, giving rise to the 1:1:1:1 isomer instead of the 2:0:2 isomer described earlier. This illustrates, as previously described in the literature,[8] the versatility of these molecular systems to undergo isomerization in solution and highlights the importance of the reaction/crystallization conditions. Nonetheless, the magnetic behavior of these two compounds is expected to be very similar since no major, changes were found between the structures.

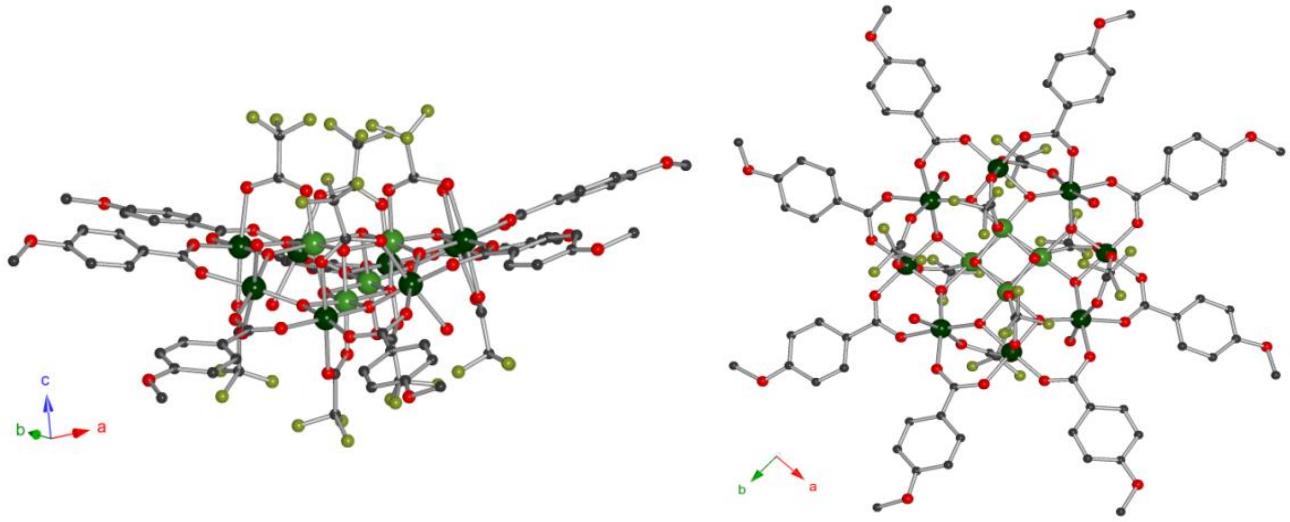

Figure II.10. Crystal structure of $[Mn_{12}O_{12}(CF_3COO)_8(\mathbf{L^1})_8(H_2O)_4]\cdot Et_2O$ at 120 K viewed in the *ac* plane (left) and in the *ab* plane (right). Lattice solvent molecules and hydrogen atoms are omitted for clarity. Color scheme: Mn^{IV} green, Mn^{III} dark green, O red, C grey, F yellow.

II.3.3.2. FTIR spectroscopy

Similarly to the homo-substituted complexes, the FTIR measurement performed on a single crystal of $[Mn_{12}O_{12}(CF_3COO)_8(\mathbf{L^1})_8(H_2O)_4]$ shows the characteristic absorption bands of bridging carboxylate ligands at 1603 ($\nu_{OCO(as)}$) and 1393 cm^{-1} ($\nu_{OCO(s)}$) (Figure II-11, left).

However, some absorption bands (1673 and 1426 cm^{-1} of the $[Mn_{12}O_{12}(CF_3COO)_8(H_2O)_4]$ precursor) found in the spectra of the homo-substituted precursors (Figure II-11, left), are not present anymore suggesting the removal of benzoate and trifluoroacetate ligands from the axial and equatorial positions, respectively, and confirming the absence of these precursors in the sample. The same features were also observed for the three mixed-carboxylate complexes containing mesogenic ligands (Figures II-11, right and S.II.2-4).

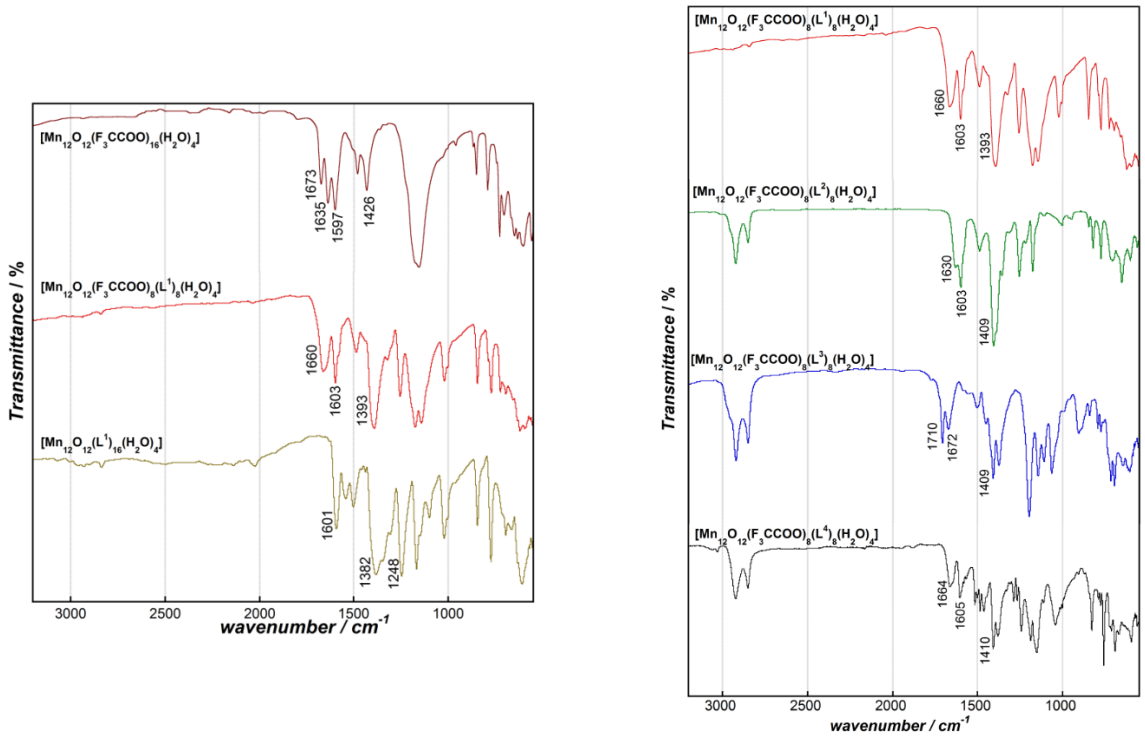

Figure II-11. (left) FTIR spectra for $[Mn_{12}O_{12}(CF_3COO)_8(\mathbf{L^1})_8(H_2O)_4]$ and its precursors; (right) FT-IR spectra for $[Mn_{12}O_{12}(CF_3COO)_8(\mathbf{L^i})_8(H_2O)_4]$ (i = 1-4).

II.3.3.3. ^{1}H NMR and ^{19}F NMR spectroscopies

^{1}H NMR spectroscopy for mixed-carboxylate compound is not very informative to illustrate the formation of expected complexes since the spectra were found essentially identical to those measured for the precursors $[Mn_{12}O_{12}(\mathbf{L^i})_{16}(H_2O)_4]$. The spectra show the presence of broad proton signals corresponding to the aliphatic shell or biphenyl units (Figure S.II-5), while the protons close to the Mn_{12} core (benzoate ring) are missing from the expected chemical shift range 6-8 ppm. Characterization of the mixte-carboxylate complexes was also performed by ^{19}F NMR. The spectra were in all case very similar, suggesting that the trifluoroacetate are coordinated in the same fashion for all the complexes, although complete attribution of the peaks was not possible due to the close proximity of trifluoroacetate ligands with the paramagnetic core. Some peaks observed in the spectrum of the precursor $[Mn_{12}O_{12}(CF_3COO)_{16}(H_2O)_4]$ were not present anymore in agreement with replacement of trifluoroacetate ligands in equatorial positions by benzoates ligands. The ^{1}H and ^{19}F NMR spectra also confirm the absence of co-crystallized ligand in the samples (Figure S.II-5, top right).

II.3.3.4. Elemental and thermogravimetric analyses

The composition of the complexes was confirmed by the complementary elemental and thermogravimetric analysis (TGA). The results for the elemental analysis are gathered in the Table II-1 and the TGA thermograms are given in the Figure S.II-6. The elemental analyses, performed on powder for all the samples, are in fair agreement with the proposed formula $[Mn_{12}O_{12}(CF_3COO)_8(\mathbf{L^i})_8(H_2O)_4]$, although,

best agreements require addition of water molecules (for $\mathbf{L^1}$ – x = 5; $\mathbf{L^2}$ – x = 5.5; $\mathbf{L^3}$ – x = 2; $\mathbf{L^4}$ – x = 5, as co-crystallized solvent. The presence of co-crystallized water molecules was confirmed by TGA, which show the corresponding weight losses in the range 350-400 K. It should be nonetheless mentioned that the exact number of water molecule cannot be determined accurately since the weight of water molecules correspond to less than 1% of the overall sample weight.

Table II-1. Elemental analyses of $[Mn_{12}O_{12}(CF_3COO)_8(\mathbf{L^{1\text{-}4}})_8(H_2O)_4]\cdot xH_2O$ (x = co-crystallized water molecules)

Compound	%C (found)	%H (found)	%C (calc.)	%H (calc.)
$[Mn_{12}O_{12}(CF_3COO)_8(\mathbf{L^1})_8(H_2O)_4]\cdot 5H_2O$ $C_{80}H_{74}F_{24}Mn_{12}O_{61}$	30.11	2.07	30.73	2.39
$[Mn_{12}O_{12}(CF_3COO)_8(\mathbf{L^2})_8(H_2O)_4]\cdot 5.5H_2O$ $C_{168}H_{251}F_{24}Mn_{12}O_{61.5}$	46.75	5.92	46.17	5.79
$[Mn_{12}O_{12}(CF_3COO)_8(\mathbf{L^3})_8(H_2O)_4]\cdot 2H_2O$ $C_{360}H_{644}F_{24}Mn_{12}O_{74}$	58.62	8.94	59.46	8.93
$[Mn_{12}O_{12}(CF_3COO)_8(\mathbf{L^4})_8(H_2O)_4]\cdot 5H_2O$ $C_{424}H_{506}F_{24}Mn_{12}O_{85}$	62.86	6.67	63.04	6.31

II.4. Magnetic measurements

In general, the replacement of the peripheral acetates of the Mn_{12}-OAc complex by other carboxylate ligands, and eventually by non-carboxylate ligands, allows for the preservation of SMM behavior. However, the distortions and deformations caused to Mn_{12} core by these chemical modifications may change some features including the spin ground state, blocking temperature or energy barrier. The magnetic properties of the four new complexes $[Mn_{12}O_{12}(CF_3COO)_8(\mathbf{L^i})_8(H_2O)_4]$ (i = 1 – 4), were fully characterized by magnetic measurements in both *dc* and *ac* modes and the results were compared with their precursors.

II.4.1 Magnetic measurements in ac mode

The presence of frequency dependent out-of-phase *ac* signal (χ'') is considered to be the characteristic feature of superparamagnetic-like or SMM behavior. In these molecular systems, a non-zero frequency dependent χ'' signal can be measured when the rate at which the magnetic moment of a molecule flips and the operating frequency of the ac magnetic field are very close. The system is not able to follow the ac field due to the presence of slow relaxation of the magnetization.

The temperature dependence of the in-phase (χ') and out-of-phase (χ'') components of the *ac* susceptibility were measured in a zero static external field with frequencies ranging from 1 to 1500 Hz. For all the complexes, an abrupt decrease of the $\chi'T$ product is systematically observed on lowering temperature below 8 K, which is indicative of a blocking process of magnetization (Figure II-12 and II-13). Accordingly, χ'' signals appear at the corresponding temperatures, confirming that all the samples display a SMM behavior.

For $[Mn_{12}O_{12}(CF_3COO)_8(\mathbf{L^1})_8(H_2O)_4]$, the $\chi'T$ value measured at the plateau 8 – 12 K, ca. 54 cm^3/mol, is favorably comparable to the value of $[Mn_{12}O_{12}(CF_3COO)_{16}(H_2O)_4]$, ca. 58 cm^3/mol and in good accordance with S_T = 10 with Landé factor g = 1.96 as typically found for the parent Mn_{12}-OAc (Figure II-

12, Table II-2). It is worth noting that these values are significantly higher than the precursor $[Mn_{12}O_{12}(\mathbf{L^1})_{16}(H_2O)_3]$ for which a S_T = 9 with g = 1.93 was found in agreement with previous investigations.[16]

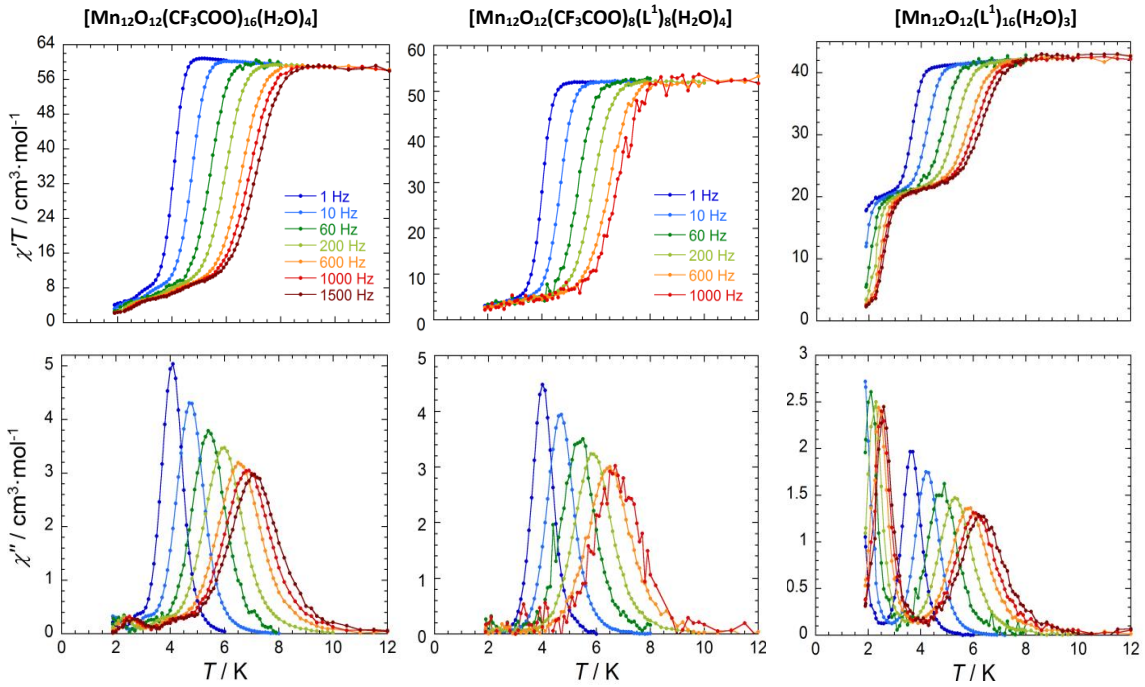

Figure II-12. Temperature dependence of $\chi'T$ and χ'' for $[Mn_{12}O_{12}(CF_3COO)_{16}(H_2O)_4]$ (left), $[Mn_{12}O_{12}(CF_3COO)_8(\mathbf{L^1})_8(H_2O)_4]$ (center) and $[Mn_{12}O_{12}(\mathbf{L^1})_{16}(H_2O)_3]$ (right) measured under various oscillating frequencies (1-1500 Hz) with H_{dc} = 0 Oe.

The χ'' vs. T plots for $[Mn_{12}O_{12}(CF_3COO)_8(\mathbf{L^1})_8(H_2O)_4]$ and $[Mn_{12}O_{12}(CF_3COO)_{16}(H_2O)_4]$ show only a single signal, with maxima ranging from 7 K to 4 K (between 1500 and 1 Hz, respectively), indicating that the complexes display only one magnetization relaxation mode, in contrast with the two relaxation modes found in the Mn_{12}-OAc complex. As well contrast, $[Mn_{12}O_{12}(\mathbf{L^1})_{16}(H_2O)_3]$ displays two χ'' signals in the low temperature region, 2 – 3 K, and in the high temperature range, 4 – 7 K, corresponding to the fast relaxation mode (FR) and slow relaxation mode (SR), respectively (Figure II-12). As mentioned in section II.2.2, the presence of two relaxation modes is attributed to the coexistence of two Mn_{12} JT isomers. The FR mode is associated with the distorted isomeric form in which one of the JT axes is abnormally oriented and almost orthogonal to the other JT elongations, as reported in the structure of $[Mn_{12}O_{12}(\mathbf{L^1})_{16}(H_2O)_3]$.[16] In this case, the occurrence of SMM behavior at lower temperature can be explained by the lower symmetry and magnetic anisotropy which involve a significant rhombic term within the structure. On the other hand, the SR mode is related to the second JT isomer involving nearly uniaxial JT elongations along the main molecular axis as shown in the structures of $[Mn_{12}O_{12}(CF_3COO)_8(\mathbf{L^1})_8(H_2O)_4]$ described above. The isomeric composition of the bulk sample can be estimated by the ratio of the two plateaus present in $\chi'T$ vs T plots and correspond to FR/SR = 51/49. These assignments confirms that the magnetic behavior of $[Mn_{12}O_{12}(CF_3COO)_8(\mathbf{L^1})_8(H_2O)_4]$ is much closer to the parent $[Mn_{12}O_{12}(CF_3COO)_{16}(H_2O)_4]$ than $[Mn_{12}O_{12}(\mathbf{L^1})_{16}(H_2O)_3]$ as predicted by the analysis of their crystallographic structures.

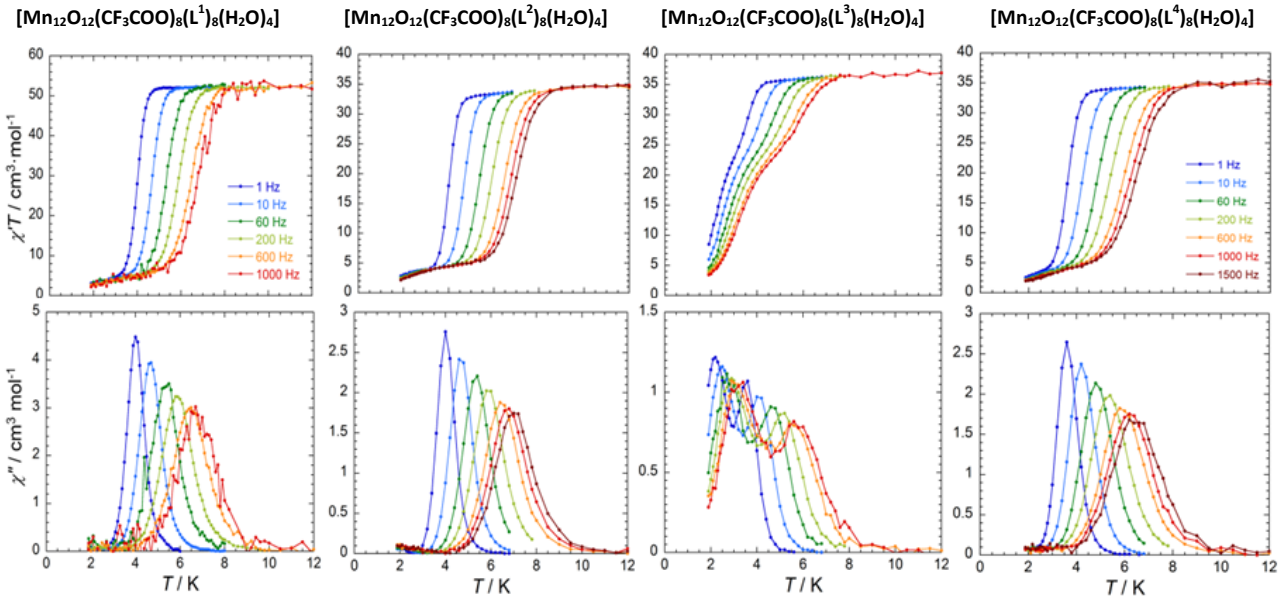

Figure II-13. Temperature dependence of $\chi'T$ and χ'' for $[Mn_{12}O_{12}(CF_3COO)_8(\mathbf{L}^{1\text{-}4})_8(H_2O)_4]$ measured under various oscillating frequencies (1-1500 Hz) with H_{dc} – 0Oe.

For $[Mn_{12}O_{12}(CF_3COO)_8(\mathbf{L}^{2\text{-}4})_8(H_2O)_4]$ complexes, the $\chi'T$ values in the plateau 8-12 K range from 35 to 37 $cm^3 \cdot mol^{-1}$ (Figure II-13), which is consistent with $S_T = 9$ with g factors of 1.72 – 1.86, as previously reported for their respective homo-substituted precursors $[Mn_{12}O_{12}(\mathbf{L}^{2\text{-}4})_{16}(H_2O)_4]$,[16] and relatives systems.[1c,13,19] Similarly to the model complex, $[Mn_{12}O_{12}(CF_3COO)_8(\mathbf{L}^{1})_8(H_2O)_4]$, the χ'' vs. T plots reveal that $[Mn_{12}O_{12}(\mathbf{L}^{2})_{16}(H_2O)_4]$ and $[Mn_{12}O_{12}(\mathbf{L}^{4})_{16}(H_2O)_4]$ display only one relaxation mode (SR) suggesting that only one JT isomer (with normal orientation of JT axes) is present in the bulk samples while their respective precursors $[Mn_{12}O_{12}(\mathbf{L}^{i})_{16}(H_2O)_4]$ contain systematically the two isomers.[16] Surprisingly, the complex $[Mn_{12}O_{12}(CF_3COO)_8(\mathbf{L}^{3})_8(H_2O)_4]$ does not follow the same trend and reveals two relaxation modes with a predominance of the FR mode, ca. 65 %, while the FR mode is only about 35 % for the precursor $[Mn_{12}O_{12}(\mathbf{L}^{3})_{16}(H_2O)_4]$. It is difficult to rationalize the origin of this behavior as no crystallographic structure can be reasonably obtained. However, Terazzi and co-workers suggested that the ratio FR/SR in mesomorphic Mn_{12} systems is directly related to the compactness of the supramolecular organization: The fast relaxation phase increase when the Mn_{12} cores are closer.[15]

The relaxation times (τ) at different temperatures can be determined from the position of peak maxima in χ'' vs T plots (Figure II-12-13) as $\tau = (2\pi\nu_{max})^{-1}$ (where ν_{max} is the frequency of the oscillating magnetic field). In all the samples, the thermally activated relaxation process of the magnetization follows the Arrhenius law (Orbach process) as typically observed in Mn_{12} derivatives. By fitting the τ vs. $1/T$ plots, the energy barrier Δ_{eff}/k_B can be calculated using the relation $\tau = \tau_0 \cdot \exp(\Delta_{eff}/k_B T)$, where, k_B is the Boltzmann constant, and τ_0 a pre-exponential factor (Figure II-14, Table II-2). The Δ_{eff}/k_B for the SR species are in the range 64 – 70.1 K, as typically found in Mn_{12}-OAc and its derivatives (Table II-2). Similarly, the value for FR phase in $[Mn_{12}O_{12}(CF_3COO)_8(\mathbf{L}^{3})_8(H_2O)_4]$ is 51.1 K which is in good agreement with values found in Mn_{12} analogues displaying FR process.[20]

Table II-2. Magnetic Properties for $[Mn_{12}O_{12}(CF_3COO)_8(\mathbf{L}^{1\text{-}4})_8(H_2O)_4]$ complexes and its precursors.

Compound	*S*	*g*	JT isomers ratios SR (%) / FR (%)	Fast relaxing (FR) JT isomer		Slow relaxing (SR) JT isomer		$\mu_0 H_C$ (T)
				Δ_{eff}/k_B (K)	τ_0 (s)	Δ_{eff}/k_B (K)	τ_0 (s)	
$[Mn_{12}O_{12}(CF_3COO)_8(\mathbf{L}^1)_8(H_2O)_4]$	10	1.86	100	-	-	70.1	4.8×10^{-9}	1.28
$[Mn_{12}O_{12}(CF_3COO)_8(\mathbf{L}^2)_8(H_2O)_4]$	9	1.75	100	-	-	69.1	6.0×10^{-9}	1.37
$[Mn_{12}O_{12}(CF_3COO)_8(\mathbf{L}^3)_8(H_2O)_4]$	9	1.80	35/65	51.1	1.64×10^{-11}	62.4	3.8×10^{-9}	0.17
$[Mn_{12}O_{12}(CF_3COO)_8(\mathbf{L}^4)_8(H_2O)_4]$	9	1.72	100	-	-	69	6.0×10^{-9}	0.97
$[Mn_{12}O_{12}(CF_3COO)_{16}(H_2O)_4]$	10	1.96	100	-	-	71.0	5.3×10^{-9}	1.16
$[Mn_{12}O_{12}(\mathbf{L}^1)_{16}(H_2O)_3]$	9	1.93	49/51	29.6	1.28×10^{-9}	63.7	4.7×10^{-9}	0.3
$[Mn_{12}O_{12}(\mathbf{L}^2)_{16}(H_2O)_4]^*$	9	1.91	70/30	34.7	2.7×10^{-10}	59.1	9.7×10^{-9}	0.55
$[Mn_{12}O_{12}(\mathbf{L}^3)_{16}(H_2O)_4]^*$	9	1.93	60/40	37.6	4.1×10^{-10}	58.0	2.0×10^{-8}	0.53
$[Mn_{12}O_{12}(\mathbf{L}^4)_{16}(H_2O)_4]^*$	9	1.86	65/35	31.7	1.9×10^{-9}	60.8	1.1×10^{-8}	0.72

*from ref. 16. *S*: spin ground state; *g*: Landé factor of ground state; Δ_{eff}: potential energy barrier; k_B: Boltzmann constant; τ_0: pre-exponential factor; $\mu_0 H_C$ (T): coercive field.

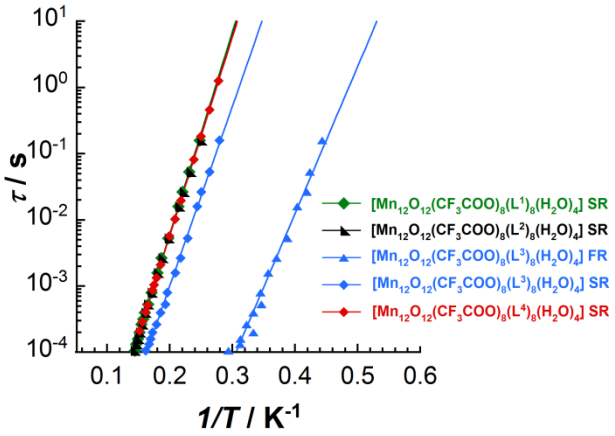

Figure II-14. Inverse temperature dependence of the relaxation time in semi-logarithmic scale for $[Mn_{12}O_{12}(CF_3COO)_8(\mathbf{L}^{1\text{-}4})_8(H_2O)_4]$ complexes. Full lines are the best fits to an Arrhenius law.

II.4.2 Magnetic measurements in dc mode

Magnetic measurements performed in dc mode were also characteristic of Mn_{12} derivatives and relevant of SMM behaviour. The χT versus T data are shown in the Figure II-15. The χT values at 280 K are in the range 17 – 19 $m^3 \cdot K \cdot mol^{-1}$, which is in a good agreement with the homo-substituted precursors and other Mn_{12} relatives.[1,11,15a,c,16,19,20] The χT product decrease progressively in lowering the temperature between 280 and 120 K, as consequence of the intramolecular antiferromagnetic coupling between the Mn^{IV} and Mn^{III} ions. As expected, the χT products increase significantly below 120 K, reaching maximum values of 35 – 48 $cm^3 \cdot K/mol$ around 12 – 13 K. At lower temperatures, the χT products decrease rapidly due to Zeeman and zero-field splitting (zfs) effects. Low temperature χT values for $[Mn_{12}O_{12}(CF_3COO)_8(\mathbf{L}^{2\text{-}4})_8(H_2O)_4]$ were smaller than for the $[Mn_{12}O_{12}(CF_3COO)_8(\mathbf{L}^1)_8(H_2O)_4]$ or parent $[Mn_{12}O_{12}(CF_3COO)_{16}(H_2O)_4]$ and Mn_{12}-OAc compounds supporting an $S_T = 9$ ground state, as suggested by the *ac* measurements.

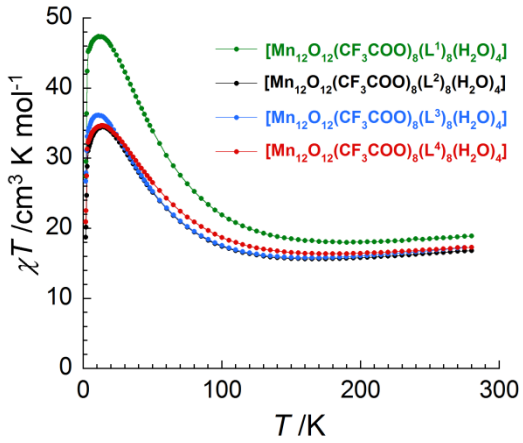

Figure II-15. χT versus T plots at 0.1 T for $[Mn_{12}O_{12}(CF_3COO)_8(\mathbf{L}^{i})_8(H_2O)_4]$ (***i*** = 1 – 4) complexes.

The opening of a hysteresis magnetization loop at low temperature is a characteristic feature of SMM behaviors. For all the samples, the field dependence of magnetization performed at 1.9 K with dc field varying between -7 to 7 T, reveals the presence of hysteresis loops (Figure II-16). The coercive field $\mu_0 H_C$ (ie, the magnetic field required to inverse the magnetization) is around 1.5 T for $[Mn_{12}O_{12}(CF_3COO)_8(\mathbf{L}^{i})_8(H_2O)_4]$ (i = 1, 2, 4) while it is found much lower for the mixed-carboxylate complex containing L^3 and for the homo-substituted complexes $[Mn_{12}O_{12}(\mathbf{L}^{i})_{16}(H_2O)_x]$ (x = 3-4; *i* = 1-4) (Table II-2). The significant decrease of the coercivity can be explained by the presence of the FR species.

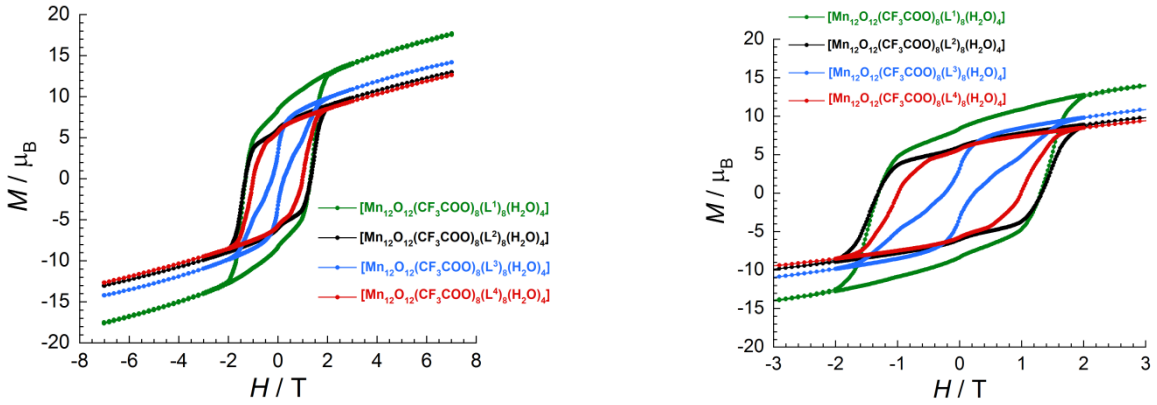

Figure II-16. Magnetization vs. applied at 1.9 K and at 0.035 T·min^{-1} sweep rate for all $[Mn_{12}O_{12}(F_3CCOO)_8(\mathbf{L}^{1\text{-}4})_8(H_2O)_4]$ complexes, the right figure is a zoom of the figure on the left side.

The shape of magnetization versus field curves and magnetization values (ca. 17 μ_B) at high fields show an absence of saturation (Figure S.II-8) which is consistent with magnetic anisotropy and high spin ground state (S_T > 8) in a randomly oriented polycrystalline samples. This is also confirmed by the *M* vs. HT^{-1} plots (Figures S.II-7) at different temperatures (from 1.9 to 10 K).

II.5. Thermal and self-organization properties

One of the main motivations of this work was to determine how the Mn_{12} functionalization might influence the thermal and self-organization properties in respect to the previous strategies. In particular we

sought to determine whether the regioselective functionalization might change the overall geometry of the molecule toward a discotic shape, allowing therefore the formation of columnar or nematic mesophases. Also, an important aspect, toward possible deposition on surface concerns the clearing temperature, which needs to be accessible at moderate temperature in order to avoid decomposition. These particular features were investigated by temperature-dependent measurements including themogravimetry (TGA), polarized optical microscopy (POM), differential scanning calorimetry (DSC) and small-angle X-ray scattering (SAXS).

As expected the complexes containing "short" ligands ($[Mn_{12}O_{12}(CF_3COO)_8(\mathbf{L^1})_8(H_2O)_4]$ and its precursors) do not show any mesomorphic properties and the discussion will be thereafter essentially focused on the characterization of the $[Mn_{12}O_{12}(CF_3COO)_8(\mathbf{L^{2\text{-}4}})_8(H_2O)_4]$ complexes and the comparison with their respective homo-substituted precursors. Phase transition temperatures, structural and thermodynamic parameters for $[Mn_{12}O_{12}(CF_3COO)_8(\mathbf{L^{2\text{-}4}})_8(H_2O)_4]$ and $[Mn_{12}O_{12}(\mathbf{L^{2\text{-}4}})_{16}(H_2O)_4]$ complexes are summarized in Table II-3.

Table II-3. Parameters describing the thermal and structural properties of $[Mn_{12}O_{12}(CF_3COO)_8(\mathbf{L^{2\text{-}4}})_8(H_2O)_4]$ and their precursors

Compound	**Transition**[a]	***T* / K**	**ΔH / kJ·mol^{-1}**
$[Mn_{12}O_{12}(CF_3COO)_8(\mathbf{L^2})_8(H_2O)_4]$	Cr - I[a]	454	243.3
$[Mn_{12}O_{12}(CF_3COO)_8(\mathbf{L^3})_8(H_2O)_4]$	Cr - Cub[b]	258	134.6
	Cub - I[c]	~ 448	--
$[Mn_{12}O_{12}(CF_3COO)_8(\mathbf{L^4})_8(H_2O)_4]$	Sm - I[b]	345	52.7
$[Mn_{12}O_{12}(\mathbf{L^2})_{16}(H_2O)_4]$*	Cr - g[a]	340	--
	g - I[a]	385	25.5
$[Mn_{12}O_{12}(\mathbf{L^3})_{16}(H_2O)_4]$*	Cr - Cub[b]	276	205.9
	Cub – dec[d]	423	--
$[Mn_{12}O_{12}(\mathbf{L^4})_{16}(H_2O)_4]$*	g - Sm[b]	295	--
	Sm - I[b]	347	73.3

*From ref. 16; [a] determined by DSC on 1st heating (irreversible behavior); [b] determined by DSC on 2nd heating; [c] estimated by SAXS on 4th heating; [d] estimated by TGA; Cr = crystal, I = isotropic liquid; Cub = cubic phase; g = glass; Sm = smectic phase; dec = decomposition.

The complexes are thermally stable up to ca. 410 K since only minor weight losses attributed to lattice solvent molecules (water) were detected by TGA. By analogy, the parent complex Mn_{12}-OAc starts to decompose at 320 K, confirming as previously reported, the benefit of benzoate functionalization to enhance the thermal stability of the Mn_{12} core.[15,16] Between ca. 410 – 480 K, a slight decrease, probably associated with the loss of water ligands, is observed while a major decomposition of the Mn_{12} core occurs above 480 K. Considering the low-kinetic for the loss of water ligands, temperature-dependent measurements can be performed up to 480 K without alteration the complexes, although reaching such extreme temperature was not necessary in most of the case.

II.5.1. $[Mn_{12}O_{12}(CF_3COO)_8(\mathbf{L^2})_8(H_2O)_4]$ (one C_{12} chain ligand)

The POM analysis for $[Mn_{12}O_{12}(CF_3COO)_8(\mathbf{L^2})_8(H_2O)_4]$ was not conclusive to determine the presence or absence of liquid crystalline features since no birefringent texture can be detected in all the temperature

range tested. Indeed, the absence of birefringent textures can be either due to a homotropic arrangement as typically observed in cubic phases or the absence of any organization (amorphous solid). By increasing temperature above 420 K, an increase of the fluidity is observed but it is difficult to determine accurately the temperature at which the compound reaches the isotropic liquid phase. The DSC thermogram on first heating (Figure II-17) displays only one transition at 454 K which is in agreement with the transition into the isotropic phase based on POM and confirmed by the SAXS investigations. The thermal behavior is not reversible and the DSC thermograms remain silent on cooling and further heating/cooling cycles. The transition into the isotropic liquid phase appears at much higher temperature for this complex than its $[Mn_{12}O_{12}(\mathbf{L}^{2})_{16}(H_2O)_4]$ precursor (385 K), which suggests stronger cohesion between the molecules in the material due probably to the decrease of aliphatic functions. It is worthwhile to note that the clearing temperature occurs above the temperature at which the compound starts to decompose. However, considering that the loss of the water ligands is very progressive and should not alter significantly the overall organization, the non-reversibility is more likely due to a very-slow dynamic of the thermal behavior than a decomposition process.

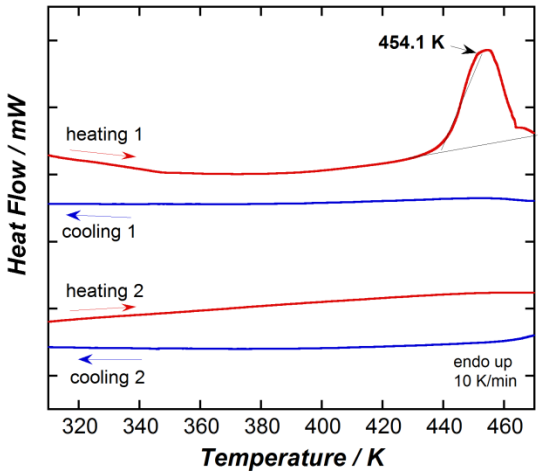

Figure II-17. DSC thermograms for $[Mn_{12}O_{12}(CF_3COO)_8(\mathbf{L}^{2})_8(H_2O)_4]$ (10 K/min).

SAXS investigations were performed between 298 and 473 K. During the first heating between room temperature and 430 K, the SAXS profiles were essentially the same and display numerous reflections in both small and wide-angle regions (Figure II-18), which indicates that the compound is crystalline. The absence of liquid crystalline behaviors is also supported by the absence of diffuse halo in wide-angle region which is typically observed in liquid crystalline materials and is attributed to the short-range ordering of the melted lateral alkyl chains. Hence, this confirms that the ratio between the rigid and flexible moieties is not favorable to promote mesomorphism as previously found for the $[Mn_{12}O_{12}(\mathbf{L}^{2})_{16}(H_2O)_4]$ precursor.[16] The SAXS profiles show also the presence of a small and broad signal in low-angle region (ca. 2.2 nm^{-1}), suggesting that the crystalline phase coexist with a glass phase. The intensity of this signal increases with the temperature, indicating that the material converges progressively toward an amorphous solid. The coexistence of phases is not unusual in macromolecular self-assemblies especially when samples have a virgin thermal history. At 458 K and above, the sharp reflections disappear and only a weak and broad signal

in low-angle region (ca. 2.1 nm^{-1}) is observed in agreement with the conversion into the isotropic liquid phase.

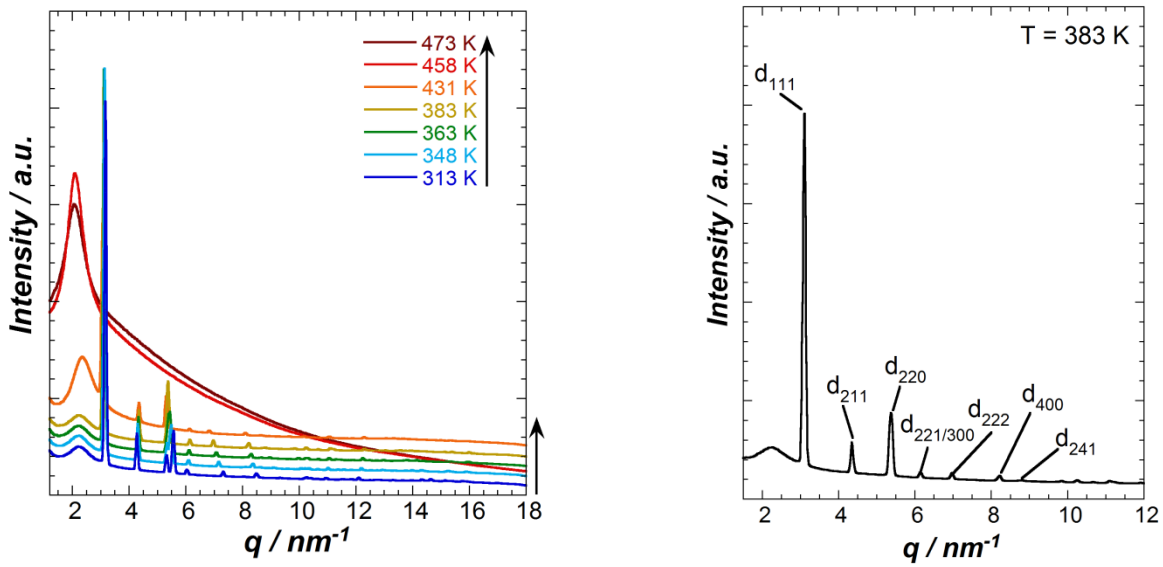

Figure II-18. (left) Small-angle X-ray scattering profiles for $[Mn_{12}O_{12}(CF_3COO)_8(L^2)_8(H_2O)_4]$ during the 1st heating from 313 K to 473 K; (right) Indexed SAXS diffraction profile at 383 K.

The crystalline profile is not recovered during the cooling and further thermal cycles (Figure S.II-9, right) confirming the irreversibility of the thermal behavior as shown by DSC experiments (Figure II-17).

The nature of the crystalline phase observed during the first heating was determined by the indexation of SAXS profiles between 313 and 431 K (Figure II-18, and Table S.II-3). The reflections are in the ratios ratios $\sqrt{3} : \sqrt{6} : \sqrt{8} : \sqrt{9} : \sqrt{12} : \sqrt{16} : \sqrt{21}$ suggesting a cubic lattice (Figure II-18, right). The reflections were then indexed with *hkl* Miller indices as (111), (211), (220), (221/300), (222), (400), (241) (using $\sqrt{h^2+k^2+l^2}$). The examination of general and systematic absences and fails to meet the reflection conditions allowed to eliminate the face-centered (*F*) cubic (reflection conditions *hkl: h + k = 2n, h + l = 2n, k + l = 2n*), body-centered (*I*) cubic (reflection conditions *hkl: h + k + l = 2n*), and some of the primitive (*P*) cubic (reflection conditions 0*kl*: *k + l = 2n, hhl: l = 2n, 00l: l = 2n*) space groups. The presence or absence of center of symmetry cannot be detected on the basis of these experiments (Friedel's law),[21] therefore all non-centrosymmetric groups (with Laue classes 23, 432 and $\bar{4}3m$) are unlikely. This leaves only $Pm\bar{3}$ and $Pm\bar{3}m$ space groups. The exact nature of the space group is still undetermined, but both of them a theoretically possible. However, $Pm\bar{3}m$ space group seems the most probable due to its higher symmetry. The lattice parameter *a* is related to the reciprocal spacing *q* by $a = 2\pi\sqrt{h^2 + k^2 + l^2} / q$. Extracted from the slope of 2π/q vs 1 / $\sqrt{h^2 + k^2 + l^2}$ plots (Figure S.II.10), the lattice parameter was found to be almost independent of the temperature, ca 35 Å. This value is comparable to the one found for its homo-substituted precursor (ca. 37.8 Å),[16] suggesting that the Mn_{12} molecules inside the cubic mesophase are arranged in both case is very similar fashion.

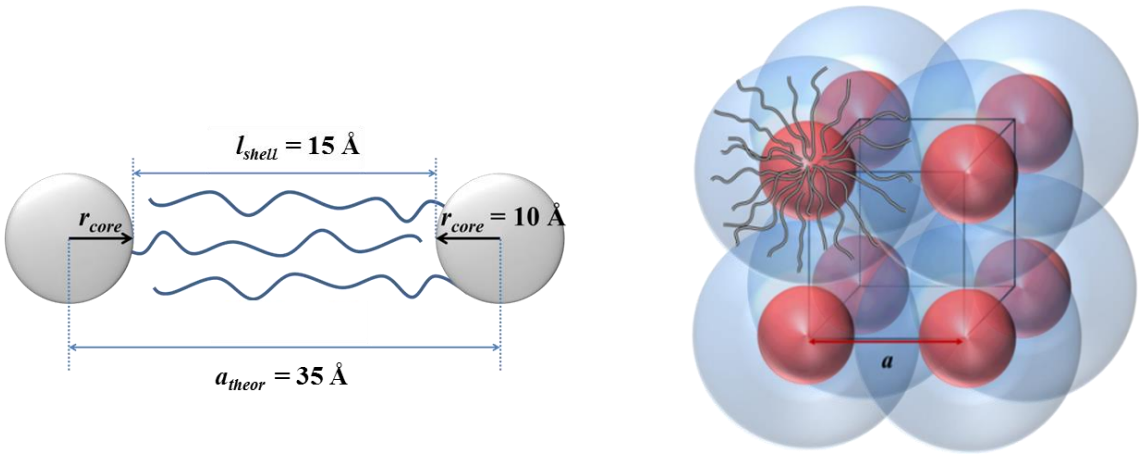

Figure II-19. Schematic representation of the primitive cubic crystalline lattice $Pm\bar{3}m$ symmetry, the spheres represent the preferred locations of rigid cores, the interstitial space is filled with aliphatic chains, a is the lattice parameter of the cubic cell update the caption.

This study shows that the overall geometry of the complex remains pseudo-spherical even though the mesogenic ligands are only on the equatorial sites of the molecules, presuming that the flexible chains are randomly spread all over the core. The size of the primitive cubic cell also indicates that the aliphatic chains are strongly interdigitated. Indeed, the complex can be idealized as spherulitic micelle in which the rigid nucleus, composed of the oxo-metallic core has a diameter of ca. 20 Å (based on the X-ray crystal structure), while the shell formed by the dodecyl chains has a thickness of ca. 15 Å. Therefore, after taking into account a maximal interdigitating of the aliphatic chains, the minimal lattice parameter a_{min} required for a primitive cubic cell can be estimated to 35 Å (using the relation $a_{min} = 2r_c + l_{ch}$ where r_c is the radius of the rigid core, and l_{ch} is the maximal thickness of the soft aliphatic shell, see Figure II-19).

II.5.2. $[Mn_{12}O_{12}(CF_3COO)_8(L^3)_8(H_2O)_4]$ (three C_{12} chains ligand)

Similarly to the previous complex, POM analyses for $[Mn_{12}O_{12}(CF_3COO)_8(\mathbf{L}^3)_8(H_2O)_4]$ did not reveals any birefringent texture over all the range of temperature tested, indicating that the material is either cubic or amorphous. The DSC thermogram shows only one reversible transition at 258 K, which corresponds to the melting of the aliphatic shell and transition into a mesophase (Figure II-20). Indeed, the enthalpy (ΔH) of phase transition is about 134.6 kJ/mol, i.e. 5.3 kJ/mol per dodecyl function, which is in the typical range for the melting of such substitutent.[22] Similarly to its precursor $[Mn_{12}O_{12}(\mathbf{L}^3)_{16}(H_2O)_4]$, the clearing point is above the thermal stability of the complex (> 410 K) and no peak was detected in DSC up to 473 K.

The exact nature of phase below 258 K could not be determined by means of SAXS investigations since this temperature cannot be reached with our experimental setup. The first thermal cycles performed up to 358 K (Figure S.II-11 and S.II-12, left), confirmed the presence of liquid crystalline features by the presence of a diffuse scattering halo around 14 nm^{-1}. However, the material is only weakly organized since only one broad and intense peak at 2.10 nm^{-1} was observed. This latter corresponds to a short-range organization between Mn_{12} molecules with a separating distance of 29.9 Å. When the sample is further heated above 363 K, the material becomes more fluid allowing an efficient reorganization of the molecules.

Thus, up to seven sharp reflections appears in the low-angle region (Figure II-21, left). This liquid crystalline organization, is then maintained on cooling in all the range of temperature tested (Figure II.21, right).

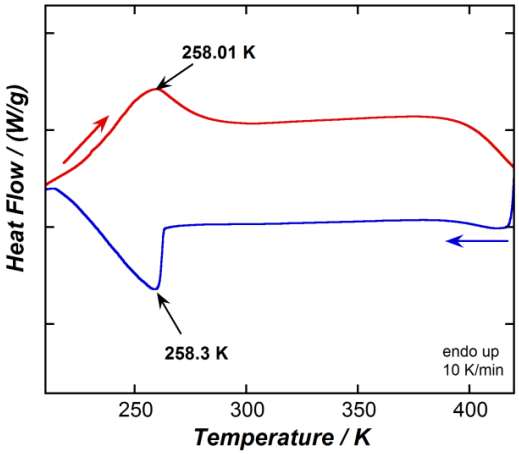

Figure II-20. DSC thermogram of $[Mn_{12}O_{12}(CF_3COO)_8(\mathbf{L}^3)_8(H_2O)_4]$ complex on 3rd cycle of heating and cooling between 200 and 420 K (10 K/min).

Measurements were also performed at higher temperatures in order to detect the conversion into the isotropic liquid phase (4th heating / cooling, Figure S.II-12, right). The SAXS diffractogram at 448 K shows a complete disappearance of the organization in agreement with isotropic liquid behavior.

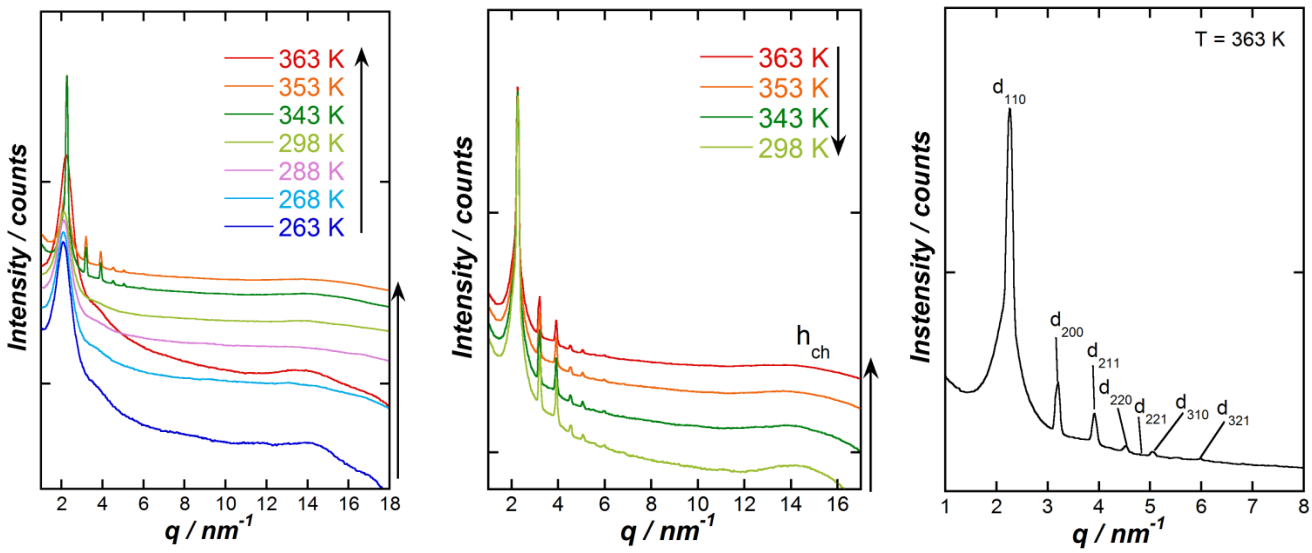

Figure II-21. Small angle X-Ray diffraction profiles in logarithmic scale for $[Mn_{12}O_{12}(CF_3COO)_8(\mathbf{L}^2)_8(H_2O)_4]$: (left) on 3rd heating between 263 and 363 K in high angle region; (center) on 3rd cooling between 363 and 298 K in high angle region; (right) indexed diffraction profile of $[Mn_{12}O_{12}(CF_3COO)_8(\mathbf{L}^2)_8(H_2O)_4]$ on 3rd cooling cycle at 363 K, only the small angle region is shown.

The exact temperature of the clearing point was not determined accurately since no signal was detected in this range of temperature by DSC, but it is located between 423 and 448 K according to the SAXS experiments. Also, we should emphasized, that the organization is not fully recovered on cooling and only the first sharp peak, $d_{110,}$ was observed while a broad signal in low-angle region is also present. This might be the result of a slow-dynamic thermal behavior as found for $[Mn_{12}O_{12}(CF_3COO)_8(\mathbf{L}^2)_8(H_2O)_4]$ or due to a partial decomposition of the molecular structure.

The reflections displayed in SAXS profiles between 298 and 423 K, are in the ratio of $\sqrt{2} : \sqrt{4} : \sqrt{6} : \sqrt{8} : \sqrt{9} : \sqrt{10} : \sqrt{14}$ and were thereafter indexed as (110), (200), (211), (220), (221/300), (310) and (321), which is once again well compatible with a primitive cubic lattice with $Pm\bar{3}m$ symmetry (Figure II-21 Table S.II-4). The unit cell parameter *a* is almost the same in all the range of temperature (298 - 423 K) and about 39 Å. (Figure S.II-13 and Table S.II-4). Therefore, the cubic mesophase can be viewed by the micellar model described above (Figure II-19), in which the lipophilic shell of Mn_{12} molecule is strongly interdigitated.

II.5.3. $[Mn_{12}O_{12}(CF_3COO)_8(\mathbf{L^4})_8(H_2O)_4]$ (two chains containing biphenyl moieties)

In contrast with previous compounds, the POM analyses of $[Mn_{12}O_{12}(CF_3COO)_8(\mathbf{L^4})_8(H_2O)_4]$ revealed the presence of fluid birefringent textures after the first thermal annealing at 348 K, suggesting a liquid crystalline behaviors (Figure II-22). The textures are homogeneous and stable from room temperature up to ~ 348 K, where the material become an isotropic liquid (black isotropic phase). No significant hysteretic behavior between the disappearance of textures on heating and their appearance on cooling was detected as expected for LC behavior. The exact nature of the mesophase is nonetheless difficult to determine since the textures are only composed of very small domains as for many macromolecular and/or metallomesogenic systems.

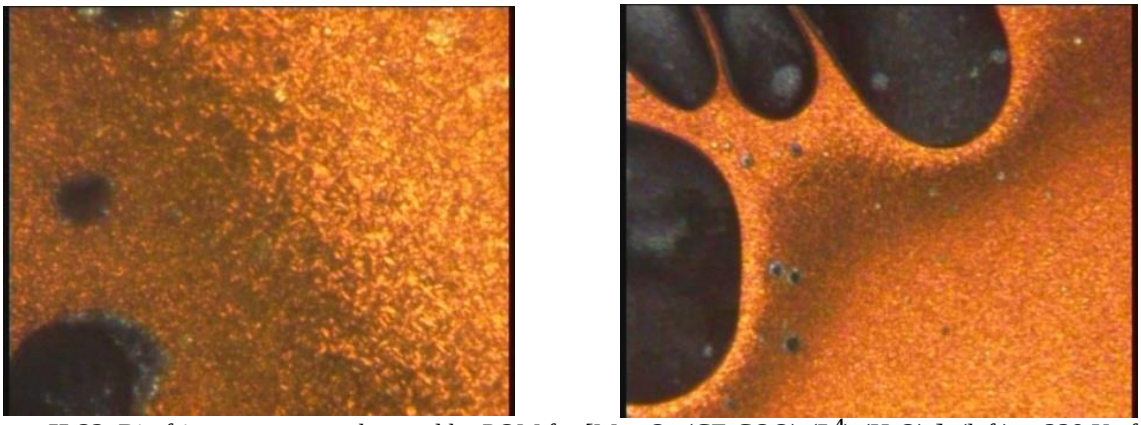

Figure II-22. Birefringent textures observed by POM for $[Mn_{12}O_{12}(CF_3COO)_8(\mathbf{L^4})_8(H_2O)_4]$: (left) at 338 K after cooling from isotropic liquid phase and (right) at 298 K.

DSC thermograms are in agreement with POM observations. The DSC thermograms show a reversible broad peak around 345 K, which corresponds to the conversion from a mesophase into the liquid isotropic phase (Figure II-23). Hence, the clearing point is much lower than the other complexes functionalized with lipophilic substituents and occurs well below the decomposition temperature, making of this compound the best candidate for a potential surface deposition so far. It is worth to note that the clearing point is almost identical to the one reported for the homoleptic $[Mn_{12}O_{12}(\mathbf{L^4})_{16}(H_2O)_4]$ precursor (ca. 347 K). Nonetheless, this is not very surprising since it has been previously described that the clearing temperature is related to the decorrelation on interactions between the pending pro-mesomorphic units rather than the interaction between the Mn_{12} cores.[15c] In other words, it depends essentially of the nature and not on the number of these units.

Hence these results confirms that the use of biphenyl pending units is a more judicious choice than cyanobiphenyl groups to obtain low-clearing materials.[16]

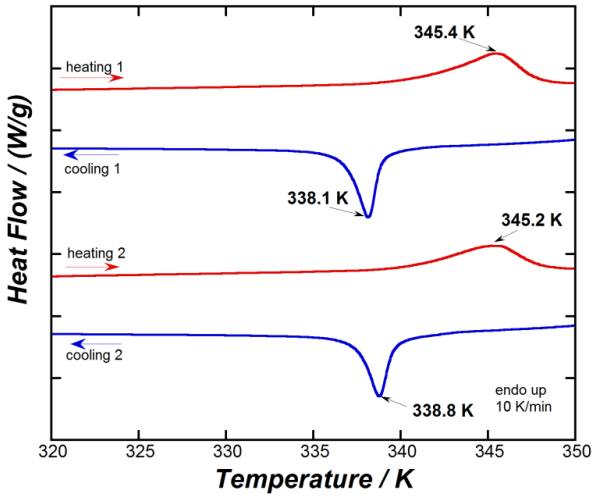

Figure II-23. DSC thermograms For $[Mn_{12}O_{12}(CF_3COO)_8(\mathbf{L^4})_8(H_2O)_4]$ complex between 280 and 420 (10 K/min).

SAXS investigations, performed between 303 and 353 K, confirm the liquid crystalline nature of the phase below 345 K (Figure II-24, S.II-14). Indeed, reflections were only found in low reciprocal spacing range while a diffuse halo, characteristic for the melted chains, is also detected around 14 nm^{-1}. The measurements confirm the reversibility of thermal behavior since no significant change was detected over several heating/cooling cycles.

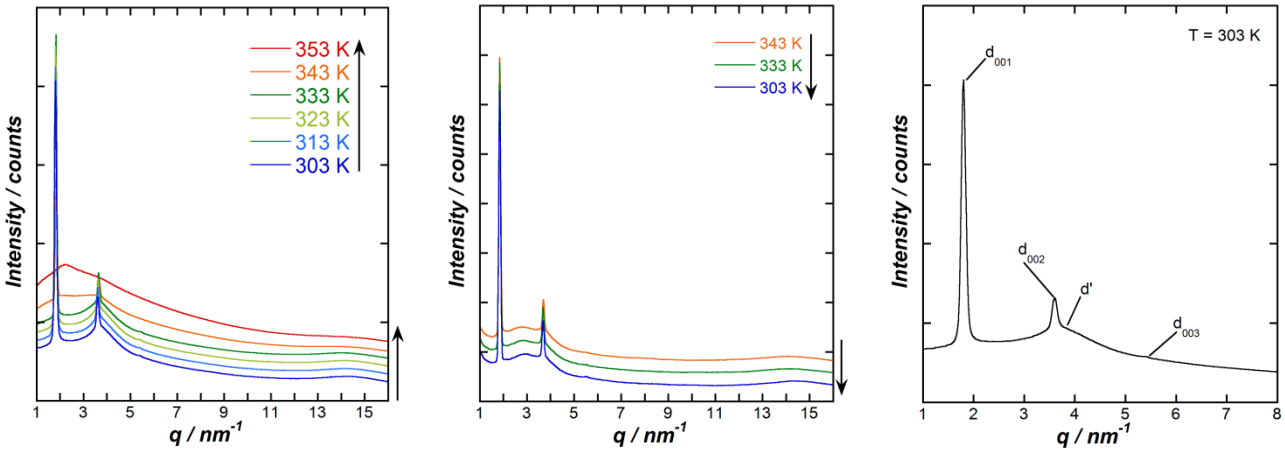

Figure II-24. SAXS diffraction profiles for $[Mn_{12}O_{12}(CF_3COO)_8(\mathbf{L^4})_8(H_2O)_4]$: (left) on 1st heating between 303 and 353 K; (center) on 2nd cooling between 343 and 303 K; (right) indexed SAXS diffraction profile on 1st heating cycle at 303 K.

The SAXS profiles are essentially the same between 303 and 333 K while the organization is progressively lost before reaching the isotropic liquid phase at 345 K (Figure II-24), in agreement with the broadness of peak observed in DSC. The SAXS pattern is composed of 3 equidistant sharp reflections (ratio 1:2:3), which were indexed as 001, 002 and 003 Miller indices (00*l*) (Figure II-24, right). Therefore, this indicates that the material self-organizes into a lamellar mesophase similarly to its homo-substituted precursor and other relatives.[15a,c,16] The interlamellar distance *d* is temperature-independent and calculated as 34.2 Å (using $d = \frac{1}{n}\sum_1^n l \cdot d_{00l}$, where *n* is the number of reflections and $d_{00l} = 2\pi/q$). The value is comparable

to the one found for $[Mn_{12}O_{12}(\mathbf{L^4})_{16}(H_2O)_4]$ (ca. d = 32.8 Å),[16] and lower than those found for analogue complexes containing cyanobiphenyl smectogens (ca. 40 Å),[15c,16] in agreement with the lower cohesion between biphenyl units and thus stronger interpenetration between layers.[16] Even though lamellar organizations are not incompatible with columnar phases (columnar lamellar Col_L), the formation of such mesophases is quite improbable in our case. Indeed, this would require a stacking of the cores along the main molecular axis while the flexible substituents in the molecular plane form the lamellar organization. Thus, considering that the eight equatorial ligands are equivalently distributed all over the Mn(III) crown, there is no reason to privilege one direction to form a layers and columnar with hexagonal or square symmetry would be more likely expected. Also, considering the diameter of the crown and the length of the chains and biphenyl units, a higher value for the interlayer distance should be expected. Finally, no evidence for a short-distance stacking between the cores was found in the wide-angle region. The mesomorphic organization can be more likely described by the previously reported bilayer model in which the mesogenic substituents are tilted in both side of the Mn_{12} core (along the main molecular axis) to form the lamellar organization (Figure II-25).

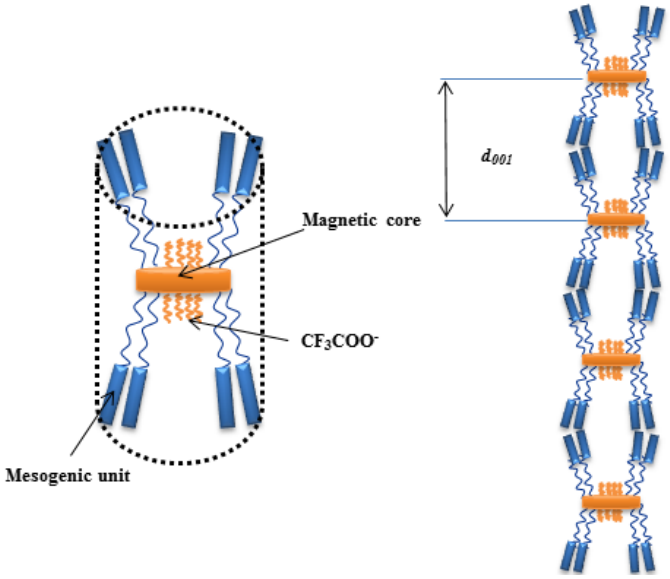

Figure II-25. Schematic representation of the lamellar organization of $[Mn_{12}O_{12}(\mathbf{L^4})_{16}(H_2O)_4]$ complex inside the smectic mesophase.

For the $[Mn_{12}O_{12}(\mathbf{L^4})_{16}(H_2O)_4]$ precursor, it have been previously shown that Mn_{12} cores in the sublayers display a long-range 2D order with an hexagonal symmetry.[16] In our case, no evidence of hexagonal pattern can be detected. In fact, the SAXS profiles display a very broad scattering which is overlapped with the intense reflection 002 and centered at 3.80 nm^{-1} (Figure II-24). This correspond to a distance d' = 17 Å, which is comparable to those found in the series of complexes reported by Terazzi et al.[15a,c] and might be attributed to a randomly and short-range 2D order of Mn_{12} cores. The exact nature of this organization remains uncertain as no computational modeling was performed; however, considering the structural similitude with the previously reported complexes, the distance is more compatible with a square symmetry. It is worthwhile to note that the broad scattering is slightly shifted to longer distance (20 Å) upon the first thermal annealing, presuming some substructure changes of the 2D arrangement.

II.6. Conclusions and perspectives

Mn_{12}-based SMMs containing two types of carboxylate ligands are extremely rare in the literature and the extension to mesomorphic systems was not reported before. By applying a regioselective methodology, it was possible to prepare successfully four new complexes $[Mn_{12}O_{12}(CF_3COO)_8^{ax}(\mathbf{L}^{1\text{-}4})_8^{eq}(H_2O)_4]$.

As expected, all the complexes preserve SMM properties, confirming the versatility of these molecular systems to undergo ligand substitutions without altering significantly the structure and properties of the magnetic core. However, substantial changes on some magnetic features were displayed in respect to their respective homoleptic precursors $[Mn_{12}O_{12}(\mathbf{L}^{1\text{-}4})_{16}(H_2O)_x]$ (x = 3, 4). More particularly, most of the complexes display only one relaxation mode of the magnetization process (SR mode) in contrast with their precursors that show systematically both SR and FR modes. This was explained by the presence of only one JT isomer in the sample (with all JT distortions nearly orthogonal to the molecular plane) as deduced from the crystallographic structure of $[Mn_{12}O_{12}(CF_3COO)_8(\mathbf{L}^{1})_8(H_2O)_4]$. As direct consequence, the magnetization hysteresis loops were found significantly larger than those found in $[Mn_{12}O_{12}(\mathbf{L}^{1\text{-}4})_8(H_2O)_x]$. An exception appears for the $[Mn_{12}O_{12}(CF_3COO)_8(\mathbf{L}^{3})_8(H_2O)_4]$ complexes, which does not follow the same trend and contains both JT isomers (where the FR specie is predominant), although it is difficult to understand the origin of this behavior and how to control the presence or not of the two JT isomers.

As mentioned early, the main motivation of this work was to determine how our functionalization strategy might influence the thermal and self-organization feature of the final materials in comparison to the homo-substitution method used before.

Similarly to their respective precursors, the two complexes containing dodecyl chains present high-temperature clearing points, in such way that the integrity of the complexes is not completely assured after annealing into the isotropic phase. Also, in contrast with our expectations, no columnar or nematic phase was obtained. Indeed, complexes self-organize either into crystal (with $\mathbf{L}^{1}$) or liquid crystalline (with $\mathbf{L}^{2}$) cubic phases, indicating that no improvement on the overall structural anisotropy was achieved. This result may reflect the tendency of the flexible moieties to reorganize themselves all around the Mn_{12} core leading therefore to a pseudo-spherical geometry of the complex.

Once again, no columnar mesophase was obtained for $[Mn_{12}O_{12}(CF_3COO)_8(\mathbf{L}^{4})_8(H_2O)_4]$, and the material self-organizes in the same fashion as its precursor (bilayer lamellar phase). Indeed, this can be explained by the presence of the pending biphenyl units, which tend to form layers. Considering the architecture of the molecule, the best way to achieve this result involves a tilt of the flexible spacers on either side of the Mn_{12} core (perpendicular to the molecular plane). This trend to form layers could have been overcome if Mn_{12} cores had a strong ability to stack and form columns; however, the presence of trifluoroacetate ligands in the axial positions is not an ideal situation to promote such strong stacking. Even though, our ligand design strategy did not allow us to promote new mesomorphic features, this material could be an interesting candidate for surface deposition. Indeed, similarly to its parent complex, the clearing point was found at a quite low temperature (345 K) and well below the decomposition temperature making them suitable for the preparation of homogeneous thin film or eventually monolayers. Additionally, the

presence of fluorine in axial positions might promote specific interactions with surfaces (eg. silicon surface) and thus help to control the orientation of molecules in one specific direction (easy axis perpendicular to the surface).

Many modifications on the structure of the ligands might be considered to improve the self-organization of the molecular systems and eventually promote new mesomorphs. In order to prevent from the reorganization of the flexible chains around the magnetic core as in our two first complexes, we should increase the separating distance between these two antagonist moieties. One idea would be to add a rigid spacer between the anchoring part of the ligand (carboxylate) and the mesogenic one. For instance, we could use for the equatorial positions, ligands containing diphenyl acetylene or terphenyl platforms instead of the benzoate one used so far (Scheme II-5).

To induce columnar phases, the ligands in the axial positions should be designed to promote efficient stacking via supramolecular interactions (eg. H-bonds or π-π stacking). For instance, we could add a phenyl ring while conserving fluoride groups in α-position of the carboxylate for keeping low pK_a.

Scheme II-5. Possible targets for the functionalization of equatorial and axial positions of the Mn_{12} core.

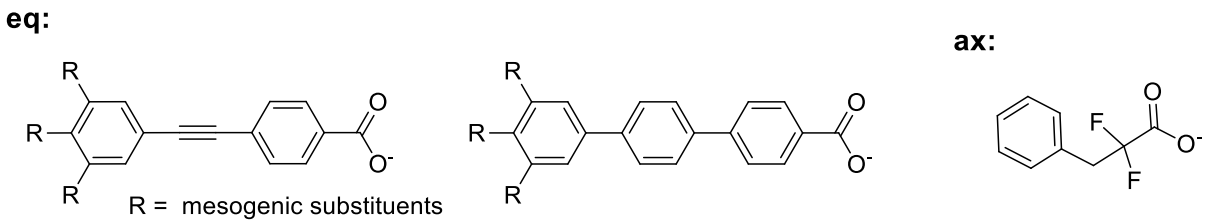

As mentioned before, we should also consider a second strategy consisting in the introduction of mesogenic ligands only in the axial positions of the core, which will promote the formation of lamellar phase. Thus, by playing on the design of the non-mesogenic ligands (in equatorial positions), we could promote specific interactions between molecules and improve the in-plane 2D organization.

II.7. Supporting materials

II.7.1. Experimental protocols

All the solvents and starting materials were purchased from Acros, Alfa Aesar or Aldrich, and used without further purification unless otherwise stated.

Preparation of 3,4,5-tris(dodecyloxy)benzoic acid (HL^3). To a solution of methyl 3,4,5-trihydroxybenzoate (4.00 g, 21.7 mmol) in 150 mL of butanone, was subsequently added anhydrous K_2CO_3 (26.95 g, 195.1 mmol), 1-bromododecane (19.20 g, 77.0 mmol) and a catalytic amount of KI (5 mol%). The reaction mixture was reflux under inert atmosphere for 4 days. After removal of the solvent, CH_2Cl_2 (200 mL) was added to the light brown solid and the organic layer was washed with H_2O (3x100 mL). The organic fraction was dried over anhydrous Na_2SO_4, filtered and the solvent removed under vacuum. After recrystallization from ethanol (200 mL), filtration, and drying under vacuum, **1** is obtained as white powder. The precursor **1** is dissolved in hot EtOH (150 mL) and a solution of KOH in water was added (20 wt%, 20 mL, 89.1 mmol) and the reaction mixture was refluxed for 12 hours. After cooling to room temperature, the solution was diluted with H_2O (100 mL) and a HCl (37 wt%) was dropwise added until reaching pH = 1. The solution is concentrated under reduced pressure, and extracted several times with CH_2Cl_2 (3x100 mL). The combined organic layer was dried over anhydrous Na_2SO_4 and filtered. After removal of the solvent, **HL^3** was obtained as white powder: Yield 9.80 g, 66 %. ^{1}H NMR (400 MHz) in $CDCl_3$ (δ, ppm): 7.30 (s, 2H), 4.06 – 3.80 (m, 6H), 1.85 – 1.70 (m, 6H), 1.51 – 1.41 (m, 6H), 1.38 – 1.21 (m, 48H), 0.86 (t, *J* = 6.8 Hz, 9H). Elemental analysis – Calc. (Found) for $C_{43}H_{78}O_5$: C, 76.50 (76.39); H, 11.65 (11.80). Selected FT-IR data (ATR, cm^{-1}): 2952 (m), 2916 (vs), 2847 (s), 1680 (vs), 1585 (s), 1504 (m), 1466 (m), 1429 (s), 1332 (s), 1225 (s), 1119 (vs), 968 (m), 863 (m), 720 (s).

Preparation of 4-((10-bromodecyl)oxy)-1,1'-biphenyl (2). A mixture of 4-hydroxybiphenyl (2 g, 11.8 mmol), 1,10-dibromodecane (17.62 g, 58.7 mmol), and anhydrous K_2CO_3 (3.24 g, 23.5 mmol) in 50 mL butanone was refluxed for 24 hours under inert atmosphere (Ar). The reaction mixture was filtered and the solid washed with several time with CH_2Cl_2. The filtrate was evaporated and the resulting light brown residue was purified by column chromatography on silica gel using pentane as eluent until complete removal of the starting material and then a mixture pentane/dichloromethane (9:1). After evaporation, **2** was isolated as white-off powder: Yield 6.24 g, 65%. ^{1}H NMR (400 MHz) in $CDCl_3$ (δ, ppm): 7.52 (dd, *J* = 13.8, 8.0 Hz, 4H), 7.39 (t, *J* = 7.6 Hz, 2H), 7.28 (t, *J* = 7.3 Hz, 1H), 6.96 (d, *J* = 8.6 Hz, 2H), 3.98 (t, *J* = 6.6 Hz, 2H), 3.39 (t, *J* = 6.9 Hz, 2H), 1.89 – 1.74 (m, 4H), 1.50 – 1.37 (m, 4H), 1.36 – 1.22 (m, 8H). Elemental analysis – Calc. (Found) for $C_{22}H_{29}BrO$: C, 67.86 (67.67); H, 7.51 (7.61).

Preparation of methyl 3,5-bis((10-(biphenyl-4-yloxy)decyl)oxy)benzoate (3). A mixture of methyl 3,5-dihydroxybenzoate (0.988 g, 5.88 mmol), **2** (4.7 g, 12.09 mmol) and anhydrous K_2CO_3 (4.27 g, 4.26 mmol) in 150 mL butanone was refluxed for 4 days. After cooling to room temperature, the mixture was diluted

with H_2O (300 mL) and extracted several times with CH_2Cl_2 (3x100mL). The organic fraction was dried over anhydrous Na_2SO_4, filtered and the solvent was removed under reduced pressure. The obtained solid was purified by column chromatography on silica gel using pentane/dichloromethane (7:3) as eluent. After evaporation, **3** was obtained as white microcrystalline powder: Yield 4.15 g, 89%. ^{1}H NMR (400 MHz) in $CDCl_3$ (δ, ppm): 7.58 – 7.45 (m, 8H), 7.40 (t, *J* = 7.7 Hz, 4H), 7.30 – 7.26 (m, 2H), 7.15 (d, *J* = 2.3 Hz, 2H), 6.96 (d, *J* = 8.6 Hz, 4H), 6.63 (t, *J* = 2.3 Hz, 1H), 4.01 – 3.93 (m, 8H), 3.87 (s, 3H), 1.88 – 1.70 (m, 8H), 1.51 – 1.38 (m, 8H), 1.33 (s, 16H). Elemental analysis – Calc. (Found) for $C_{52}H_{64}O_6$: C, 79.56 (79.46); H, 8.22 (8.31).

Preparation of 3,5-bis((10-(biphenyl-4-yloxy)decyl)oxy)benzoic acid (HL^4). To a solution of **3** (4.00 g, 5.086 mmol) in hot ethanol/THF (1:1; 100 mL) was added KOH (0.96 g, 17.08 mmol) dissolved in a minimum amount of water. The mixture was stirred under reflux for 12 hours. After cooling to room temperature, the solution was diluted with H_2O (100 mL) and HCl (37 wt%) was dropwise added until reaching pH = 1. The solution is concentrated under reduced pressure, and extracted several times with CH_2Cl_2 (3x300 mL). The organic layers were combined and dried over anhydrous Na_2SO_4, filtered and evaporated. The product **HL^4** was isolated as white powder: Yield 1.85 g, 47 %. ^{1}H NMR (400 MHz) in $CDCl_3$ (δ, ppm): ^{1}H NMR (400 MHz,) δ 7.56 – 7.46 (m, 8H), 7.39 (t, *J* = 6.7 Hz, 4H), 7.27 (t, *J* = 6.4 Hz, 2H), 6.94 (dd, *J* = 8.7, 2.1 Hz, 4H), 6.67 (d, *J* = 2.1 Hz, 1H), 4.01 – 3.92 (m, 8H), 1.84 – 1.72 (m, 8H), 1.44 (d, *J* = 6.1 Hz, 8H), 1.33 (s, 16H). Elemental analysis – Calc. (Found) for $C_{51}H_{62}O_6$: C, 79.44 (79.51); H, 8.10 (8.20). Selected FT-IR data (ATR, cm^{-1}): 2918 (vs), 2849 (s), 2224 (s), 1676 (vs), 1602 (vs), 1488 (s), 1271 (s), 1171 (s).

Preparation of [Mn$_{12}$O$_{12}$(CH$_3$COO)$_{16}$(H$_2$O)$_4$]. $Mn(CH_3COO)_2{\cdot}4H_2O$ (4.00 g, 16.32 mmol) was dissolved in 40 mL of 60 % CH_3COOH at room temperature. After cooling down the solution to 0°C, $KMnO_4$ (1.00 g, 6.33 mmol) was slowly added. The mixture was then warmed up to room temperature while stirring during 30 minutes (until the $KMnO_4$ was totally dissolved). The solution was filtered and the filtrate was allowed to stand at room temperature for few days. The resulting black crystals were filtered and washed with acetone (100 mL) and tetrahydrofuran (100 mL): Yield 2.10 g, 55 %. Selected FT-IR data (ATR, cm^{-1}): 2934 (w), 1752 (w) 1704 (m), 1554 (s), 1381 (s), 1021 (m), 706 (m), 666 (s).

Preparation of [Mn$_{12}$O$_{12}$(CF$_3$COO)$_{16}$(H$_2$O)$_4$]. A suspension of $[Mn_{12}O_{12}(CH_3COO)_{16}(H_2O)_4]$ (1.868 g, 1.0 mmol) in CH_2Cl_2 (50.5 ml) and CF_3COOH (10 ml) was stirred for 24 hours at room temperature. The solution was then filtered, transferred into in thin tube and layered with hexanes. After a week, black crystals were filtered and washed with Et_2O and hexane: Yield 0.66 g, 30%. Selected FT-IR data (ATR, cm^{-1}): 1673 (s), 1635 (s), 1597 (s), 1426 (s), 1599 (s), 1154 (s). Elemental analysis – Calc. (Found) for $C_{32}H_8F_{48}Mn_{12}O_{48}$: C, 14.07 (14.40); H, 0.30 (0.90).

Preparation of $[Mn_{12}O_{12}(L^1)_{16}(H_2O)_3]$. To a suspension of $[Mn_{12}O_{12}(CH_3COO)_{16}(H_2O)_4]$ (0.573 g, 0.3 mmol) in 20 mL of CH_2Cl_2/toluene (1:1), 4-methoxybenzoic acid (**HL^1**) (1.27 g, 8.4 mmol, 28 eq.) was added. The reaction mixture was stirred at 45°C for 24 hours during which the solution color turned from brown to brownish black. After cooling to room temperature, the mixture was filtered and the solvent was removed. Toluene (40 mL) was added to the residue, stirred for 3 hours, and then evaporated to dryness. This procedure aiming to remove the produced acetic acid as an azeotropic mixture with toluene was repeated three more times. The brownish-black residue was dissolved in CH_2Cl_2 (8 mL) and crystallized by slow diffusion of Et_2O vapor at 4°C. After 2 days, the resulting crystals were collected by filtration and washed with Et_2O: Yield 0.53 g, 71.6%. Elemental analysis – Calc. (Found) for $C_{128}H_{120}Mn_{12}O_{64}$ ($[Mn_{12}O_{12}(\mathbf{L^1})_{16}(H_2O)_3]\cdot H_2O$): C, 31.64 (30.11); H, 2.12 (2.07). Selected FT-IR data (ATR, cm^{-1}): 2928 (w), 2837 (w), 1601 (s), 1382 (vs), 1248 (s), 1168 (s), 1024 (m), 847 (w), 776 (m).

Preparation of $[Mn_{12}O_{12}(L^i)_{16}(H_2O)_4]$ (i = 2-4). To a suspension of $[Mn_{12}O_{12}(CH_3COO)_{16}(H_2O)_4]$ (0.10 g, $5.25\cdot10^{-2}$ mmol) in 20 mL of CH_2Cl_2/toluene 1:1, **HL^i** (0.45 g (**HL^2**) and 0.98 g (**HL^3**), 1.13 g (**HL^4**) 1.46 mmol, 28 eq.) was added. The mixture was stirred at 45°C (or 55°C for **HL^4**) for 24 hours during which the solution color changed from brown to brownish black. The solution was filtered and the solvent was then evaporated. Toluene (20 mL) was added to the residue, stirred for 3 hours, and then evaporated to dryness. This procedure was repeated three times more. The resulting residue was re-dissolved in CH_2Cl_2 (1-2 mL) affording a viscous mixture, which was purified by two successive gel permeation chromatography with Biorad S-X3 beads eluted with CH_2Cl_2. The compounds $[Mn_{12}O_{12}(\mathbf{L^i})_{16}(H_2O)_4]$, were isolated as brownish black powder or glassy solids. The yields were 70 % (i = 2), 61 % (i = 3) and 42 % (i = 3). Elemental analysis – Calc. (Found) for $C_{304}H_{476}Mn_{12}O_{66}$ ($[Mn_{12}O_{12}(\mathbf{L^2})_{16}(H_2O)_4]\cdot 2H_2O$): C, 62.28 (62.32); H, 8.21 (8.17). Selected FT-IR data (ATR, cm^{-1}): 2922 (m), 2853 (m), 1604 (s), 1380 (vs), 1250 (s), 1173 (m), 848 (w), 779 (w). Elemental analysis – Calc. (Found) for $C_{496}H_{868}Mn_{12}O_{86}$ ($[Mn_{12}O_{12}(\mathbf{L^3})_{16}(H_2O)_4]\cdot 6H_2O$): C, 67.18 (67.30); H, 9.87 (9.72). Selected FT-IR data (ATR, cm^{-1}): 2924 (s), 2852 (s), 1561(s), 1412 (vs), 1248 (m), 1114 (m), 762 (w). Elemental analysis – Calc. (Found) for $C_{688}H_{1246}Mn_{12}O_{99}$ ($[Mn_{12}O_{12}(\mathbf{L^4})_{16}(H_2O)_4]\cdot H_2O$): C, 70.25 (69.85); H, 10.68 (10.79). Selected FT-IR data (ATR, cm^{-1}): 2920 (s), 2852 (s), 1567 (s), 1409 (vs), 1227 (s), 1112 (m), 868 (w), 777 (w).

Preparation of $[Mn_{12}O_{12}(CF_3COO)_8(L^1)_8(H_2O)_4]$. A solution of complex $[Mn_{12}O_{12}(\mathbf{L^1})_{16}(H_2O)_4]$ (0.125 g, 0.043 mmol) in CH_2Cl_2 (4 mL) was treated with a solution of complex $[Mn_{12}O_{12}(CF_3COO)_{16}(H_2O)_4]$ (0.153 g, 0.043 mmol) in THF (4 mL). After 24 hours, the solution was filtered and the filtrate was allowed to stand for slow evaporation. The resulting brownish black crystals were collected by filtration, and washed with small fraction of Et_2O and THF: Yield 68 mg, 50 %. Elemental analysis – Calc. (Found) for $C_{80}H_{74}Mn_{12}O_{61}$: C, 30.73 (30.11); H, 2.39 (2.07). Selected FT-IR data (ATR, cm^{-1}): 2968 (w), 1660 (s), 1603 (s), 1393 (vs), 1257 (s), 1177 (vs), 1146 (vs), 847 (s), 776 (s).

Preparation of $[Mn_{12}O_{12}(CF_3COO)_8(L^i)_8(H_2O)_4]$ (i = 2-4). To a suspension of complex $[Mn_{12}O_{12}(CF_3COO)_{16}(H_2O)_4]$ (0.164 g, 0.0602 mmol) in dry CH_2Cl_2 (2 mL) was added a solution of $[Mn_{12}O_{12}(\mathbf{L^i})_{16}(H_2O)_4]$ (0.35 g (i=2), 0.704 g (i=3), 0.80 g (i=4); 0.0602 mmol) in dry CH_2Cl_2 (2 mL). After 24 hours, the solution was filtered and the solvent was evaporated to dryness. The product was dried in vacuum at 40°C overnight. The yields were 53 % for $[Mn_{12}O_{12}(CF_3COO)_8(\mathbf{L^2})_8(H_2O)_4]$, 48% for $[Mn_{12}O_{12}(CF_3COO)_8(\mathbf{L^3})_8(H_2O)_4]$ and 52% for $[Mn_{12}O_{12}(CF_3COO)_8(\mathbf{L^4})_8(H_2O)_4]$. Elemental analysis – Calc. (Found) for $C_{80}H_{64}F_{24}Mn_{12}O_{56}$ ($[Mn_{12}O_{12}(CF_3COO)_8(\mathbf{L^2})_8(H_2O)_4]$): C, 46.17 (46.75); H, 5.79 (5.92). Selected FT-IR data (ATR, cm^{-1}): 2924 (s), 2849 (s), 1603 (s), 1601 (s), 1493 (s), 1409 (vs), 1255 (s), 1175 (vs), 817 (s), 775 (s). Elemental analysis – Calc. (Found) for $C_{360}H_{624}F_{24}Mn_{12}O_{72}$ ($[Mn_{12}O_{12}(CF_3COO)_8(\mathbf{L^3})_8(H_2O)_4]$): C, 59.46 (58.62); H, 8.93 (8.94). Selected FT-IR data (ATR, cm^{-1}): 2920 (s), 2850 (s), 1710 (s), 1672 (s), 1409 (vs), 1376 (vs), 1491 (s), 1409 (vs), 1201 (vs), 1146 (s), 1063 (s), 905 (m), 848 (m), 823 (s), 776 (m), 716 (s), 696 (s). Elemental analysis – Calc. (Found) for $C_{424}H_{496}F_{24}Mn_{12}O_{80}$ ($[Mn_{12}O_{12}(CF_3COO)_8(\mathbf{L^4})_8(H_2O)_4]$): C, 63.04 (62.86); H, 6.31 (6.67). Selected FT-IR data (ATR, cm^{-1}): 2922 (s), 2850 (s), 1664 (s), 1605 (s), 1518 (s), 1484 (s), 1463 (s), 1410 (vs), 1380 (s), 1246 (s), 1155 (vs), 1110 (s), 1046 (s), 829 (s), 762 (vs), 691 (s).

II.7.2. Analytical characterizations

II.7.2.1. Crystallographic data for $[Mn_{12}O_{12}(CF_3COO)_8(L^1)_8(H_2O)_4]$

Table S.II-1. Crystal data and structure refinement for $[Mn_{12}O_{12}(CF_3COO)_8(\mathbf{L^1})_8(H_2O)_4]$ at 120K.

Empirical formula	$C_{80}H_{56}F_{24}Mn_{12}O_{56}$	$C_{84}H_{66}Mn_{12}O_{57}F_{24}$
Formula weight	3028.52	3102.61
Crystal system	Orthorhombic	Tetragonal
Space group	C222	$I4_1/a$
Wavelength, Å	0.71073	0.71073
a (Å)	17.7568(16)	34.586(4)
b (Å)	28.5324(18)	34.586(4)
c (Å)	32.136(2)	12.6043(11)
α = β = γ (°)	90	90
V ($Å^3$)	16282(2)	15077(4)
Z	2	4
ρ_{calcd} (g/cm^3)	0.618	1.465
μ (mm^{-1})	0.494	1.077
Reflections collected	105640	4949
Independent reflections	5372	2649
R_1[a]	0.0786	0.1135
wR_2[a]	0.2220	0.4404
GoF[a]	1.032	1.132

[a] $I > 2\sigma(I)$, $R_1 = \Sigma(||F_o| - |F_c||)/\Sigma|F_o|$; $wR_2 = \{\Sigma[w(F_o^2 - F_c^2)^2]/\Sigma[w(F_o^2)^2]\}^{1/2}$. GoF (goodness of fit on F^2) = $\{\Sigma[w(F_o^2 - F_c^2)^2]/ (n-p)\}^{1/2}$, where n is the number of reflections and p is the total number of refined parameters.

Table S.II-2. Selected bond length distances for $[Mn_{12}O_{12}(CF_3COO)_8(\mathbf{L^1})_8(H_2O)_4]$ and $[Mn_{12}O_{12}(CF_3COO)_8(\mathbf{L^1})_8(H_2O)_4]\cdot Et_2O$

Bond Type	$[Mn_{12}O_{12}(CF_3COO)_8(\mathbf{L^1})_8(H_2O)_4]$		$[Mn_{12}O_{12}(CF_3COO)_8(\mathbf{L^1})_8(H_2O)_4]\cdot Et_2O$	
	Mn-O	**Length / Å**	**Mn-O**	**Length / Å**
Mn^{IV}-$O_{(cub)}$	Mn(1)-O(1)	1.917(9)	Mn(3)-O(4)	1.957(7)
	Mn(1)-O(1)'	1.922(8)	Mn(3)-O(4)'	1.872(10)
	Mn(1)-O(1)''	1.914(7)	Mn(3)-O(4)''	1.941(10)
Mn^{IV}-$O_{(\mu3\text{-}O)}$ (eq)	Mn(1)-O(2)	1.881(9)	Mn(3)-O(1)	1.857(10)
	Mn(1)-O(4)	1.832(7)	Mn(3)-O(3)	1.867(10)
Mn^{IV}-$O_{(TFA)}$ (ax)	Mn(1)-O(3)	1.914(10)	Mn(3)-O(12)	1.948(10)
Mn^{III}-$O_{(\mu3\text{-}O)}$ (eq)	Mn(2)-O(4)	1.947(8)	Mn(1)-O(1)	1.880(10)
	Mn(3)-O(2)	1.882(7)	Mn(1)-O(3)	1.878(10)
	Mn(3)-O(4)	1.878(9)	Mn(2)-O(1)	1.909(10)
	Mn(4)-O(2)	1.926(8)	Mn(2)-O(3)	1.896(10)
Mn^{III}-$O_{(L^1)}$ (eq)	Mn(2)-O(12)	1.913(10)	Mn(1)-O(6)	1.925(10)
	Mn(3)-O(10)	1.913(10)	Mn(1)-O(8)	1.920(10)
	Mn(3)-O(11)	1.843(9)	Mn(2)-O(5)	1.931(10)
	Mn(4)-O(9)	1.879(8)	Mn(2)-O(9)	1.975(10)
Mn^{III}-$O_{(TFA)}$ (ax)	Mn(3)-O(5)	2.224(10)	Mn(1)-O(11)	2.194(10)
	Mn(3)-O(7)	2.300(10)	Mn(1)-O(13)	2.192(10)
	Mn(4)-O(9)	2.177(8)	Mn(2)-O(14)	2.143(10)
Mn^{III}-$O_{(w)}$ (ax)	Mn(2)-O(6)	2.142(10)	Mn(2)-O(2)	2.183(10)

cub = cubane; TFA = trifluoroacetate ligand ; w = water ligand

II.7.2.2. FTIR spectroscopic analyses

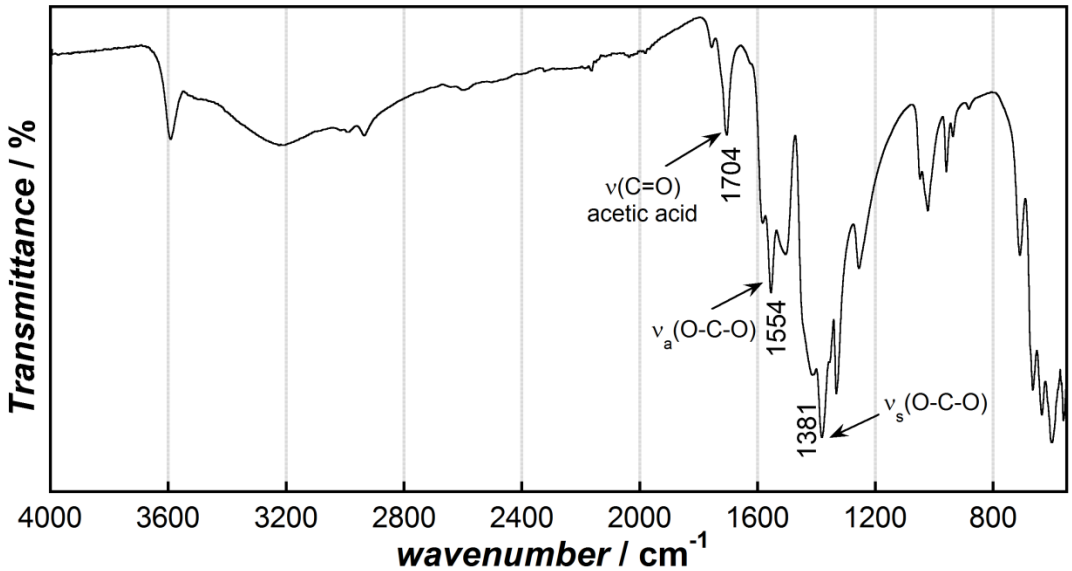

Figure S.II-1. FTIR spectrum of $[Mn_{12}O_{12}(CH_3COO)_{16}(H_2O)_4]$.

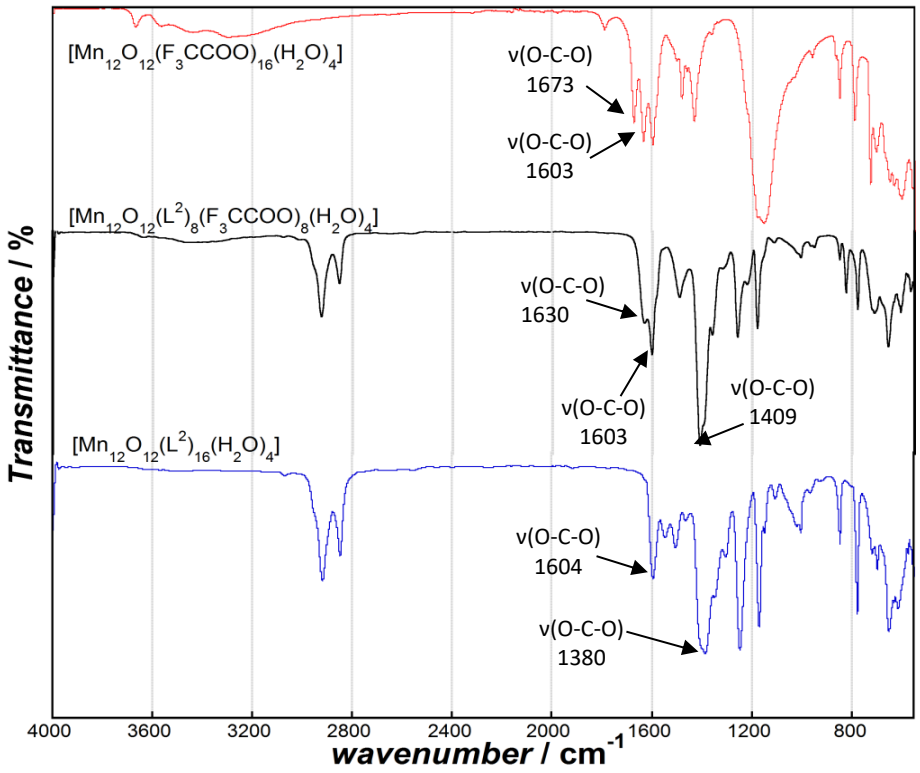

Figure S.II-2. FTIR spectrum of $[Mn_{12}O_{12}(CF_3COO)_8(\mathbf{L}^2)_8(H_2O)_4]$ and its precursors.

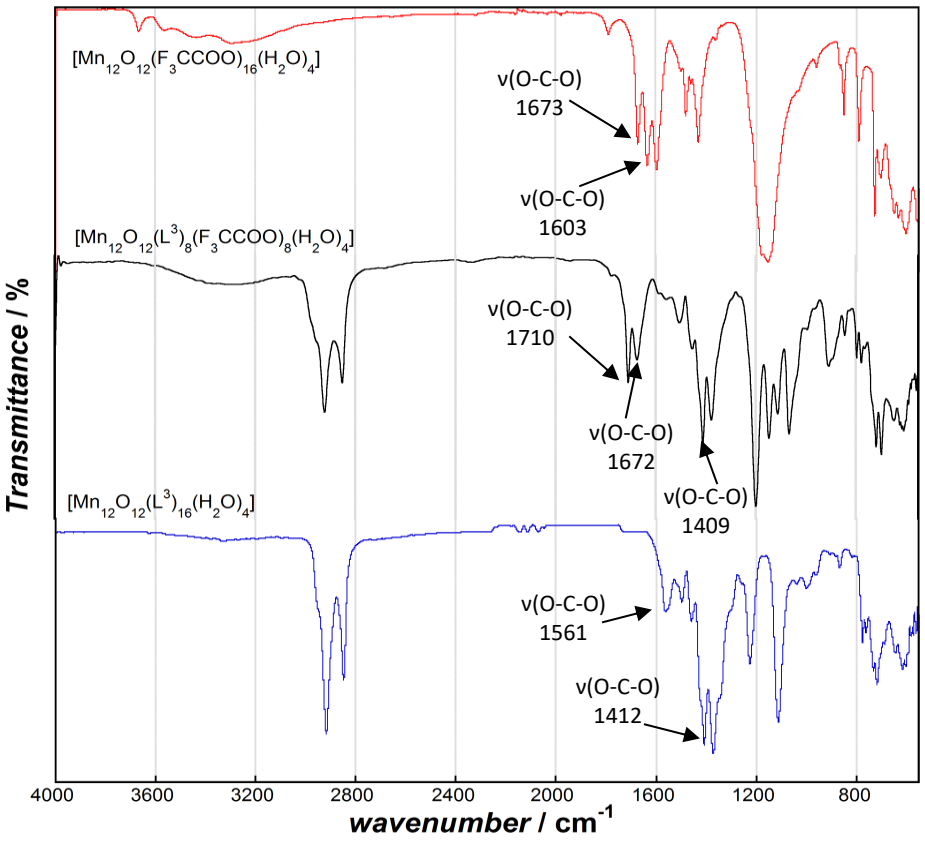

Figure S.II-3. FTIR spectrum of $[Mn_{12}O_{12}(CF_3COO)_8(\mathbf{L}^3)_8(H_2O)_4]$ and its precursors.

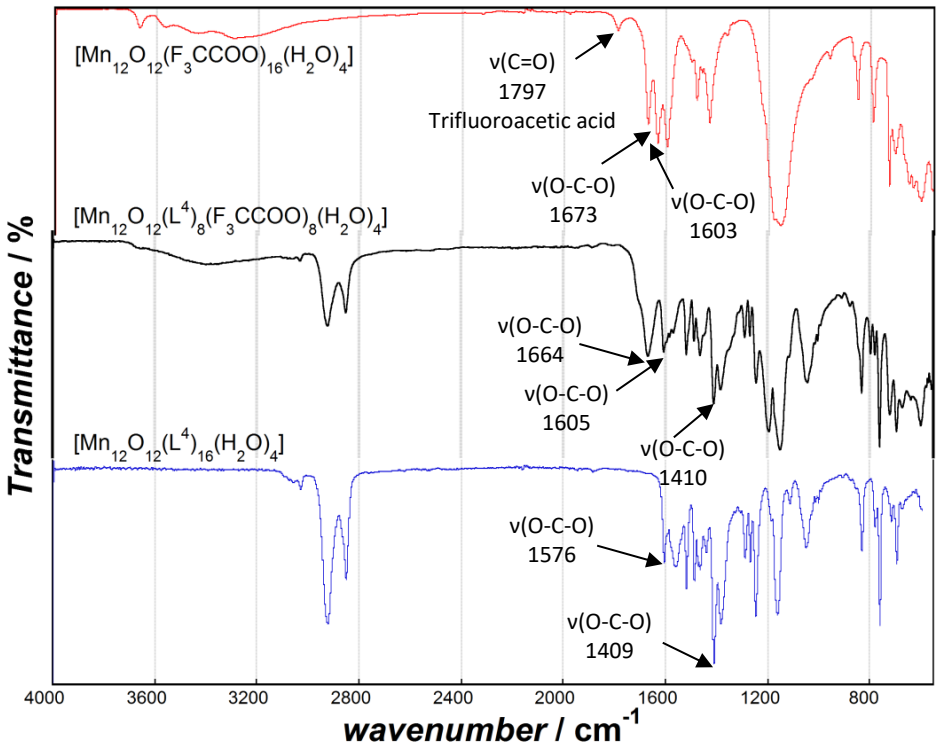

Figure S.II-4. FTIR spectrum of $[Mn_{12}O_{12}(CF_3COO)_8(\mathbf{L^4})_8(H_2O)_4]$ and its precursors.

II.7.2.3. ^{1}H NMR spectroscopic analyses

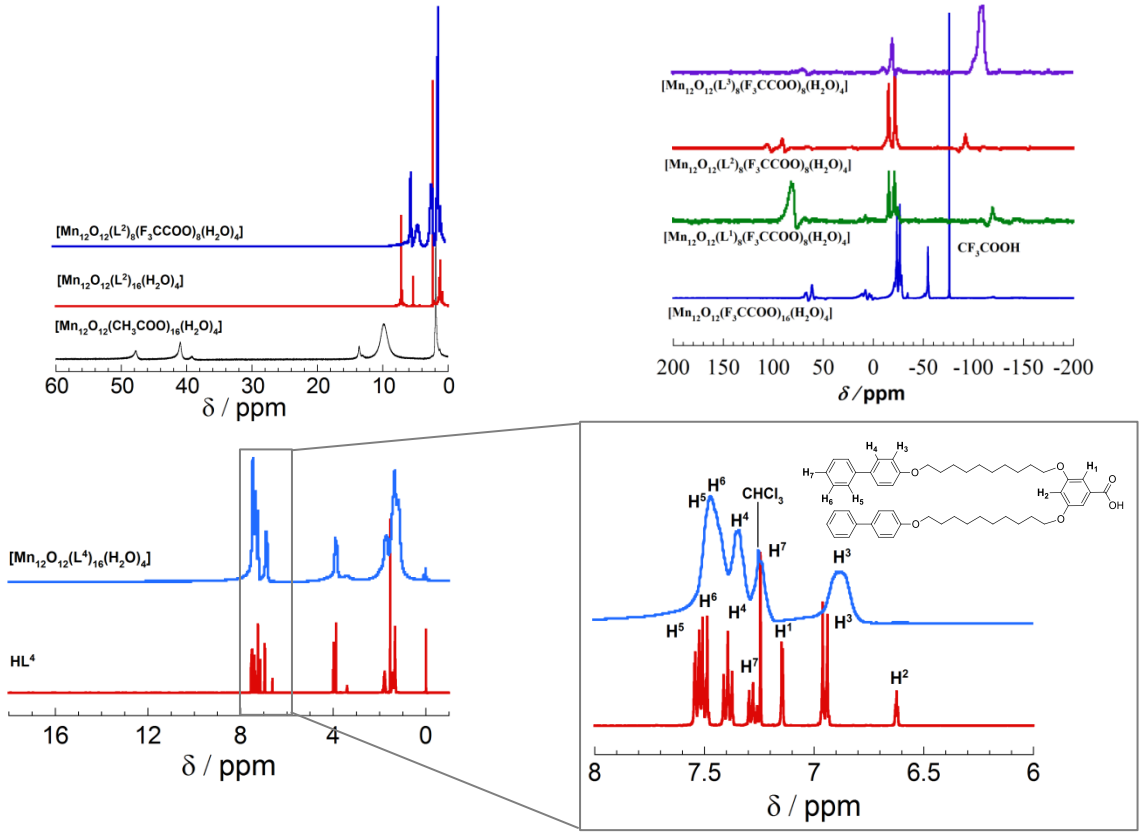

Figure S.II-5. (top, left) ^{1}H NMR spectra of Mn_{12}-OAc (black), $[Mn_{12}O_{12}(\mathbf{L^2})_{16}(H_2O)_4]$ (red) and $[Mn_{12}O_{12}(\mathbf{L^2})_{16}(CF_3COO)_{16}(H_2O)_4]$ (blue) complexes; (top, right) ^{19}F NMR spectra of mixed-carboxylate Mn_{12} complexes; (bottom) Aromatic region of ^{1}H NMR spectra for (red) $\mathbf{HL^4}$ and (blue) $[Mn_{12}O_{12}(\mathbf{L^4})_{16}(H_2O)_4]$.

II.7.2.4. Thermogravimetric analyses

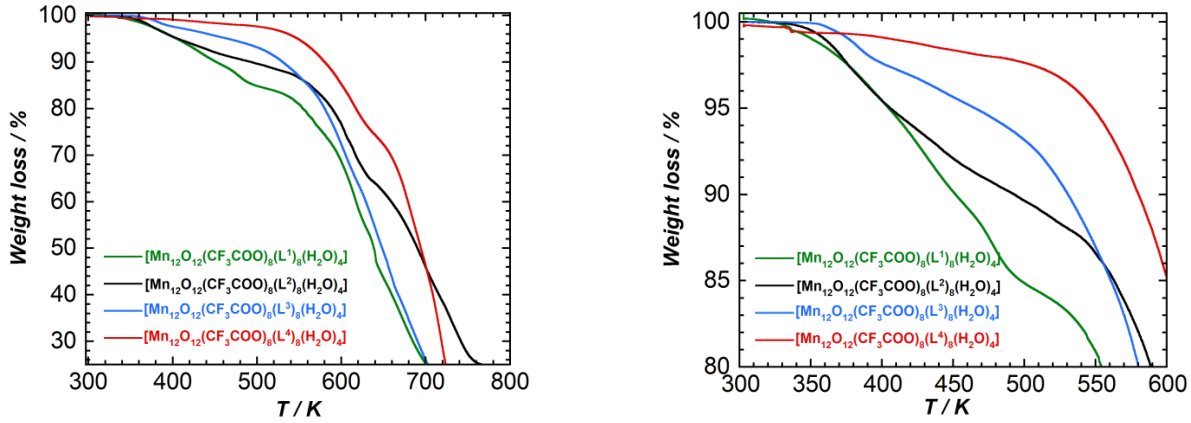

Figure S.II-6. (left) TGA thermogram for $[Mn_{12}O_{12}(CF_3COO)_8(\mathbf{L}^{1\text{-}4})_8(H_2O)_4]$ complexes; (right) zoom of TGA.

II.7.3. Magnetic measurements

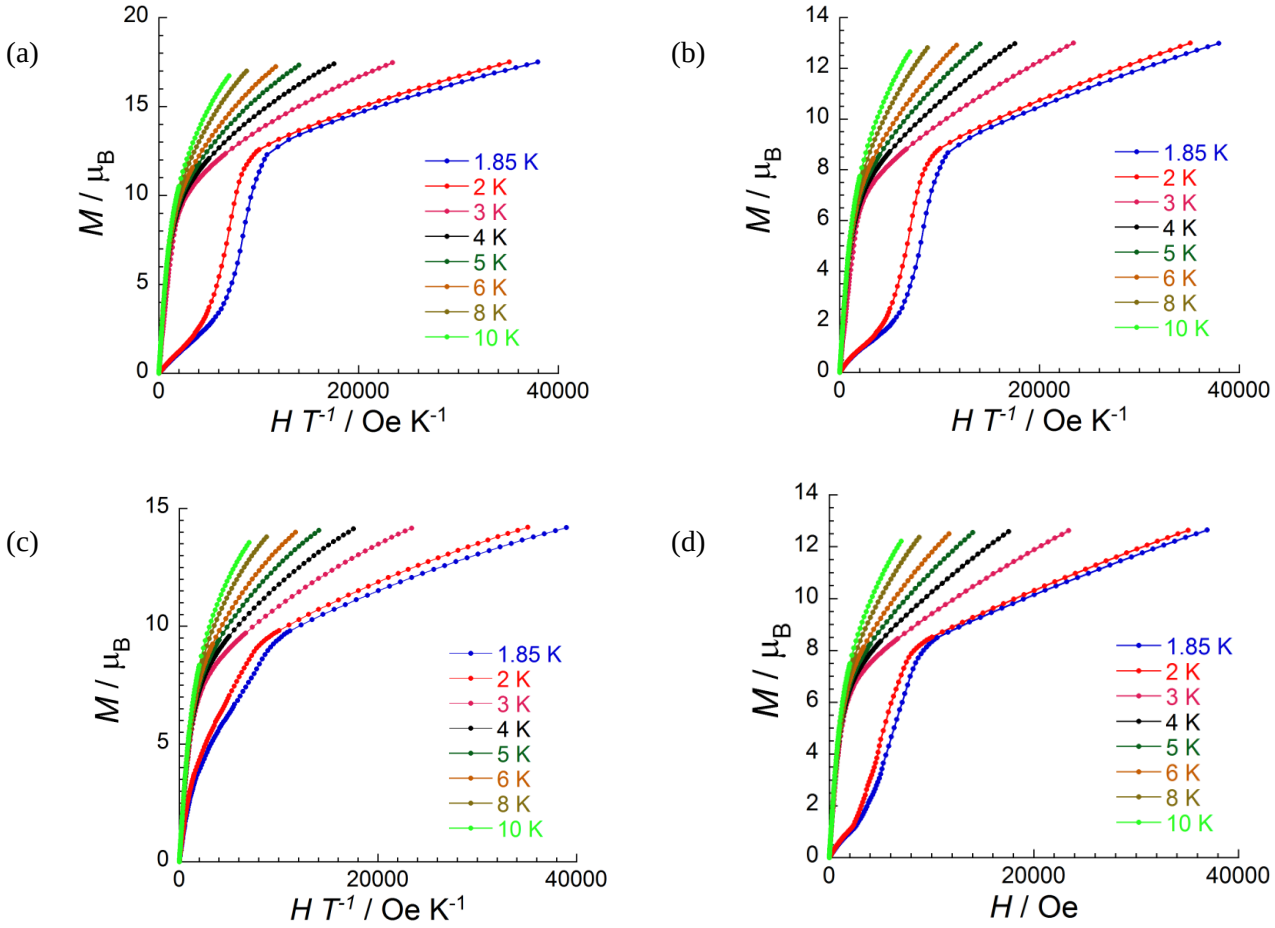

Figure S.II-7. *M* vs HT^{-1} plots at different temperatures: (a) $[Mn_{12}O_{12}(CF_3COO)_8(\mathbf{L}^{1})_8(H_2O)_4]$; (b) $[Mn_{12}O_{12}(CF_3COO)_8(\mathbf{L}^{2})_8(H_2O)_4]$; (c) $[Mn_{12}O_{12}(CF_3COO)_8(\mathbf{L}^{3})_8(H_2O)_4]$; (d) $[Mn_{12}O_{12}(CF_3COO)_8(\mathbf{L}^{4})_8(H_2O)_4]$.

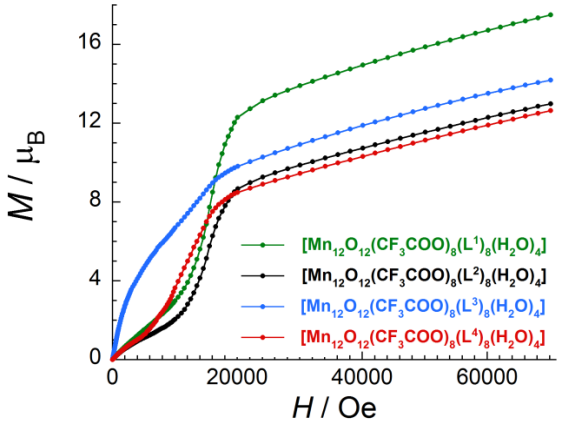

Figure S.II-8. *M* vs *H/T* plots at 1.9 K for $[Mn_{12}O_{12}(CF_3COO)_8(\mathbf{L}^{1\text{-}4})_8(H_2O)_4$. The solid lines guides for the eyes.

II.7.4. Small-angle X-ray scattering

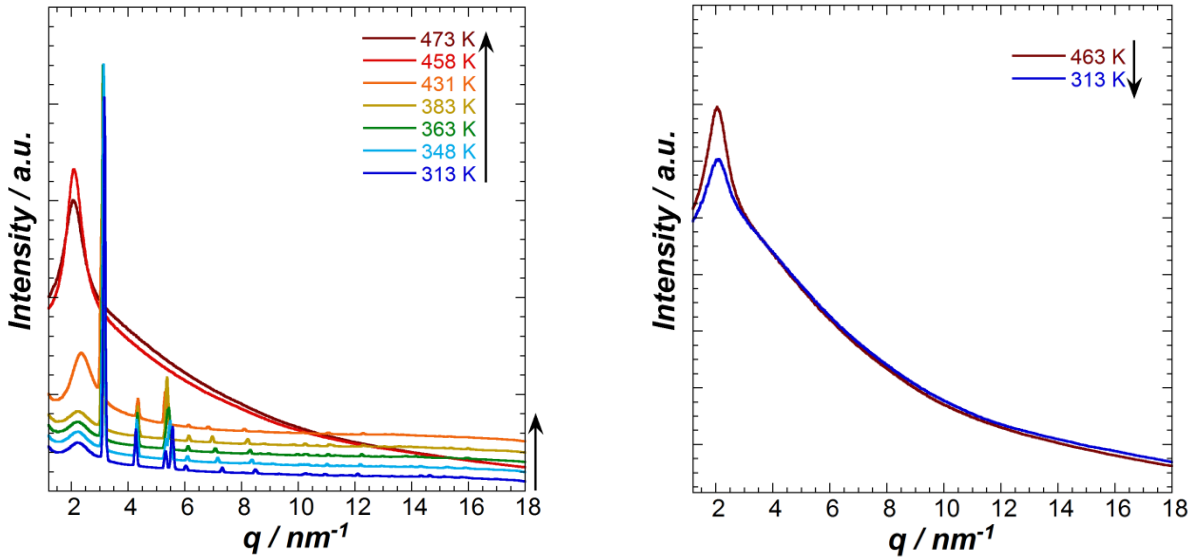

Figure S.II-9. SAXS diffractograms for $[Mn_{12}O_{12}(CF_3COO)_8(\mathbf{L}^2)_8(H_2O)_4]$ at different temperatures: (left) on the 1st heating; (right) on 1st cooling.

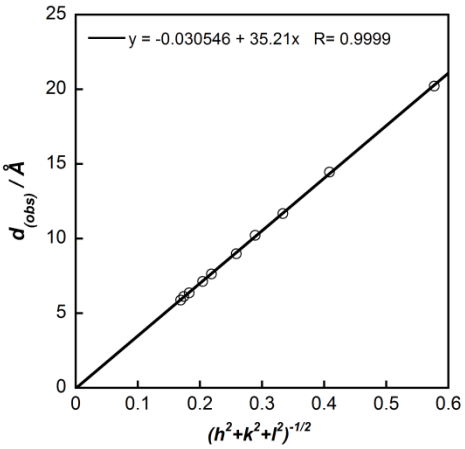

Figure S.II-10. $d_{(obs)}$ vs $1/\sqrt{h^2+k^2+l^2}$ plot for $[Mn_{12}O_{12}(CF_3COO)_8(\mathbf{L}^2)_8(H_2O)_4]$ at 383 K. The black line corresponds to the best linear fit. The lattice parameter a = 35.21 Å corresponds to the slope of the linear fit.

Table S.II-3. Indexation of observed reflections on 1st heating for $[Mn_{12}O_{12}(F_3CCOO)_8(\mathbf{L^2})_8(H_2O)_4]$

T / K	Peak number	$q_{(obs)}$ / nm^{-1}	$d_{(obs)}$ / Å	hkl	$h^2+k^2+l^2$	$d_{(calc)}$ / Å	Calculated cell parameters
	1	3.16	19.90	111	3	20.06	
313 K	2	4.30	14.61	211	6	14.18	
	3	5.34	11.76	220	8	11.76	
	4	5.57	11.28	300/221	9	11.58	**a = 34.75 Å**
	5	6.04	10.41	311	11	10.47	**V = 41.9·10^3 Å**
	6	7.33	8.57	400	16	8.68	**$Z \approx 6$**
	7	849	7.40	332	22	7.41	
	8	9.32	6.74	510/431	26	6.81	
	9	10.27	6.12	-	31	6.24	
	10	10.41	6.03	440	32	6.14	
	1	3.13	20.06	111	3	20.21	
348 K	2	4.31	14.60	211	6	14.29	
	3	5.34	11.75	220	8	12.37	
	4	5.49	11.44	221/300	9	11.67	**a = 35.01Å**
	5	6.09	10.31	311	11	10.55	**V = 42.9·10^3 Å**
	6	7.16	8.76	400	16	8.75	**$Z \approx 6$**
	7	8.37	7.51	241	21	7.63	
	8	8.63	7.27	-	23	7.30	
	9	10.07	6.23	-	31	6.28	
	10	10.21	6.15	440	32	6.18	
	1	3.11	20.18	111	3	20.27	
363 K	2	4.32	14.53	211	6	14.33	
	3	5.39	11.66	220	8	11.70	
	4	5.44	11.54	221/300	9	11.70	**a = 35.12 Å**
	5	6.11	10.28	222	12	10.13	**V = 43.3·10^3 Å^3**
	6	7.01	8.86	400	16	8.78	**$Z \approx 6$**
	7	8.31	7.56	241	21	7.66	
	8	8.68	7.23	-	23	7.32	
	9	8.96	7.00	500	25	7.02	
	10	9.98	6.29	-	31	6.30	
	1	3.10	20.22	111	3	20.32	
383 K	2	4.34	14.46	211	6	14.37	**a = 35.21 Å**
	3	5.37	11.69	221/300	9	11.73	**V = 43.6·10^3 Å^3**
	4	6.14	10.23	222	12	10.16	**$Z \approx 6$**
	5	6.98	9.00	400	16	9.09	
	6	8.22	7.63	241	21	7.68	
	7	8.81	7.13	224	24	7.18	
	8	9.85	6.38	-	30	6.42	
	9	10.25	6.13	-	33	6.13	
	10	10.68	5.88	-	35	5.95	
	1	3.06	20.53	110	3	20.51	
	2	4.35	14.44	211	6	14.51	
431 K	3	5.31	11.81	221/300	9	11.84	
	4	6.13	10.25	222	12	10.25	
	5	6.83	9.19	-	15	9.17	**a = 35.53Å**
	6	8.11	7.74	241	21	7.75	**V = 44.8·10^3 Å^3**
	7	8.36	7.51	332	22	7.57	**$Z \approx 6$**
	8	8.63	7.27	224	24	7.25	
	9	9.67	6.49	-	30	6.48	
	10	10.17	6.17	-	33	6.18	

$q_{(obs)}$ is the observed reciprocal spacing, $q = 4\pi \cdot sin\theta/\lambda$, where λ is the wavelength (1.5418 Å), 2θ is the diffraction angle, $d_{(obs)}$ and $d_{(calc)}$ are observed and calculated diffraction spacing distances: $d_{(obs)} = 2\pi/q_{(obs)}$, $d_{(calc)} = a/\sqrt{h^2+k^2+l^2}$, a is the lattice parameter of the cubic phase, V is the volume of the cubic cell unit ($V = a^3$), Z is the number of complexes per cubic cell, $Z = (\rho \cdot V \cdot N_A)/Mw$, where ρ is the density ≈ 1 g/cm^3, N_A is the Avogadro constant $6.0225 \cdot 10^{23}$ (note: 1 Å^3 = $1.0 \cdot 10^{-24}$ cm^3).

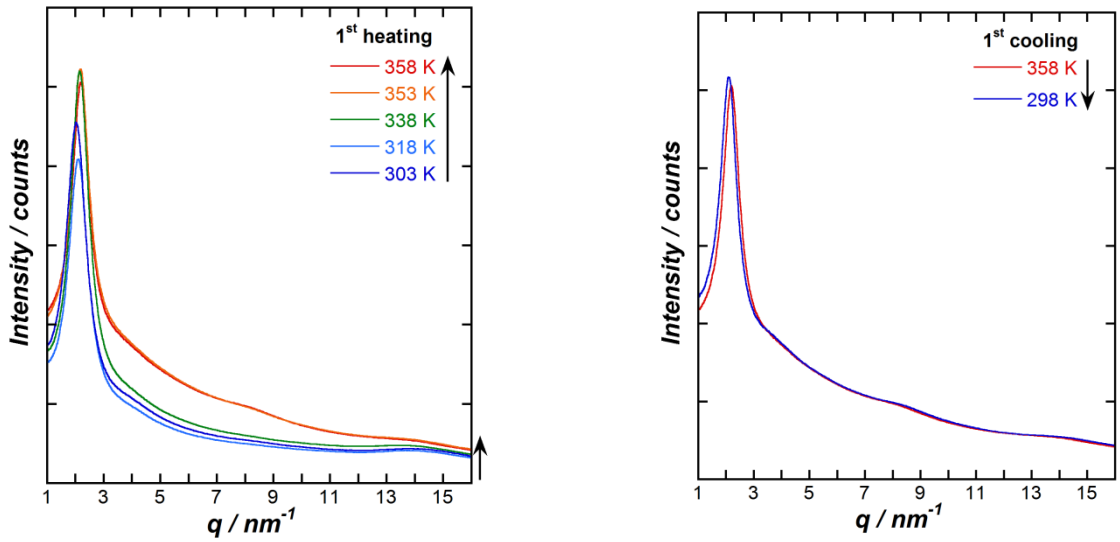

Figure S.II-11. SAXS diffractograms for $[Mn_{12}O_{12}(CF_3COO)_8(\mathbf{L}^3)_8(H_2O)_4]$: (left) on first heating between 303 and 358 K; (right) on first cooling between 358 and 298 K

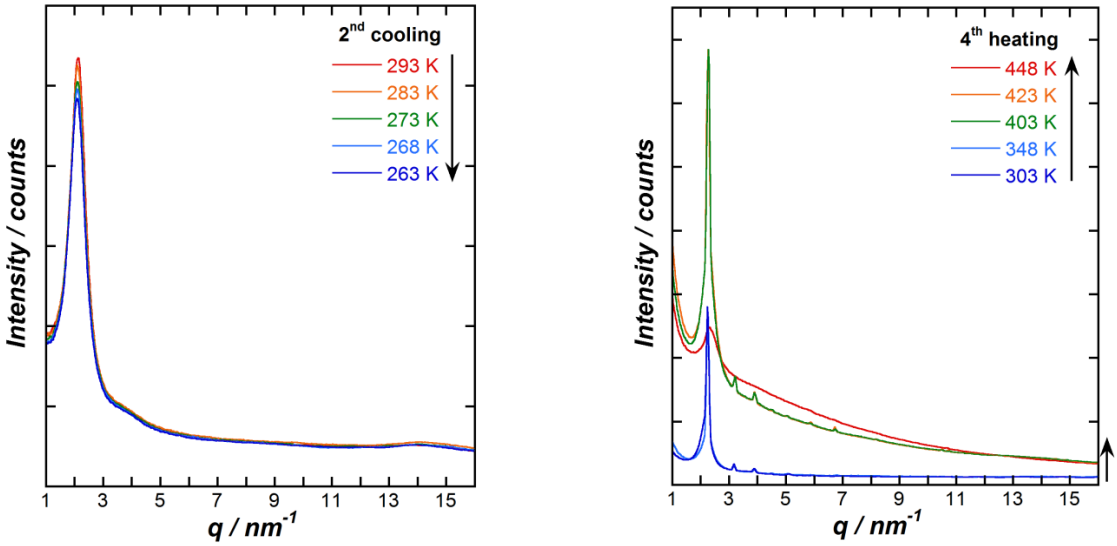

Figure S.II-12. SAXS diffractograms for $[Mn_{12}O_{12}(CF_3COO)_8(\mathbf{L}^3)_8(H_2O)_4]$: (left) on second cooling between 293 and 263 K; (right) on fourth heating between 303 and 448 K.

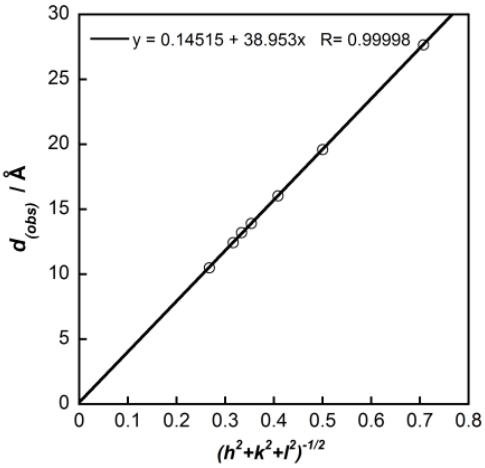

Figure S.II-13. $d_{(obs)}$ vs $1/\sqrt{h^2+k^2+l^2}$ plot for $[Mn_{12}O_{12}(CF_3COO)_8(\mathbf{L}^3)_8(H_2O)_4]$ at 343 K. The black line corresponds to the best linear fit. The lattice parameter a = 38.95 Å corresponds to the slope of the linear fit.

Table S.II-4. Indexation of observed reflections on 3rd cooling and 4th heating for $[Mn_{12}O_{12}(F_3CCOO)_8(L^3)_8(H_2O)_4]$.

T / K	Peak number	$q_{(obs)}$ / nm^{-1}	$d_{(obs)}$ /Å	hkl	$h^2+k^2+l^2$	$d_{(calc)}$ /Å	Calculated cell parameters
298 K[a]	1	2.27	27.66	110	2	27.51	**a = 38.90 Å** **V = 58.8·10^3 Å^3** **$Z \approx 5$**
	2	3.22	19.50	200	4	19.45	
	3	3.91	16.04	211	6	15.88	
	4	4.53	13.84	220	8	13.75	
	5	4.75	13.20	221/300	9	12.96	
	6	5.05	12.43	310	10	12.30	
	7	5.98	10.49	231	14	10.39	
343 K[a]	1	2.27	27.68	110	2	27.54	**a = 38.95 Å** **V = 59.1·10^3 Å^3** **$Z \approx 5$**
	2	3.20	19.61	200	4	19.47	
	3	3.91	16.04	211	6	15.90	
	4	4.51	13.92	220	8	13.77	
	5	4.75	13.20	221/300	9	12.98	
	6	5.05	12.43	310	10	12.31	
	7	5.97	10.51	231	14	10.41	
353 K[a]	1	2.25	27.89	110	2	27.90	**a = 38.95 Å** **V = 59.1·10^3 Å^3** **$Z \approx 5$**
	2	3.20	19.60	200	4	19.73	
	3	3.91	16.03	211	6	16.11	
	4	4.52	13.89	220	8	13.95	
	5	4.9	13.10	221/300	9	13.15	
	6	5.05	12.43	310	10	12.47	
	7	5.96	10.52	231	14	10.54	
363 K[a]	1	2.25	27.91	110	2	27.94	**a = 39.52 Å** **V = 61.7·10^3 Å^3** **$Z \approx 5$**
	2	3.20	19.62	200	4	19.76	
	3	3.92	16.04	211	6	16.13	
	4	4.52	13.90	220	8	13.97	
	5	4.79	13.11	221/300	9	13.17	
	6	5.05	12.44	310	10	12.49	
	7	5.98	10.50	231	14	10.56	
303 K[b]	1	2.23	28.11	110	2	28.49	**a = 40.3 Å** **V = 65.4·10^3 Å^3** **$Z \approx 5$**
	2	3.17	19.81	200	4	20.15	
	3	3.88	16.18	211	6	16.45	
	4	4.46	14.06	220	8	14.24	
	5	4.86	12.90	221/300	9	13.43	
	6	5.10	12.31	310	10	12.74	
348 K[b]	1	2.25	27.89	110	2	27.93	**a = 39.51 Å** **V = 61.6·10^3 Å^3** **$Z \approx 5$**
	2	3.18	19.70	200	4	19.75	
	3	3.89	16.14	211	6	16.12	
	4	4.48	14.00	220	8	13.96	
	5	4.77	13.14	221/300	9	13.17	
	6	5.08	12.35	310	10	12.49	
403 K[b]	1	2.27	27.67	110	2	27.40	**a = 38.75 Å** **V = 58.2·10^3 Å^3** **$Z \approx 5$**
	2	3.21	19.58	200	4	19.38	
	3	3.89	16.14	211	6	15.82	
	4	4.49	13.97	220	8	13.70	
	5	5.03	12.49	310	10	12.25	

[a] – 3rd cooling; [b] – 4th heating; $q_{(obs)}$ is the observed reciprocal spacing, $q = 4\pi \cdot sin\theta/\lambda$,where λ is the wavelength (1.5418 Å), 2θ is the diffraction angle, $d_{(obs)}$ and $d_{(calc)}$ are observed and calculated diffraction spacing distances: $d_{(obs)} = 2\pi/q_{(obs)}$, $d_{(calc)} = a/\sqrt{h^2 + k^2 + l^2}$, a is the lattice parameter of the cubic phase, V is the volume of the cubic cell unit ($V = a^3$), Z is the number of complexes per cubic cell, $Z = (\rho \cdot V \cdot N_A)/Mw$, where ρ is the density ≈ 1 g/cm^3, N_A is the Avogadro constant 6.0225 · 10^{23} (note: 1 Å^3 = 1.0 · 10^{-24} cm^3).

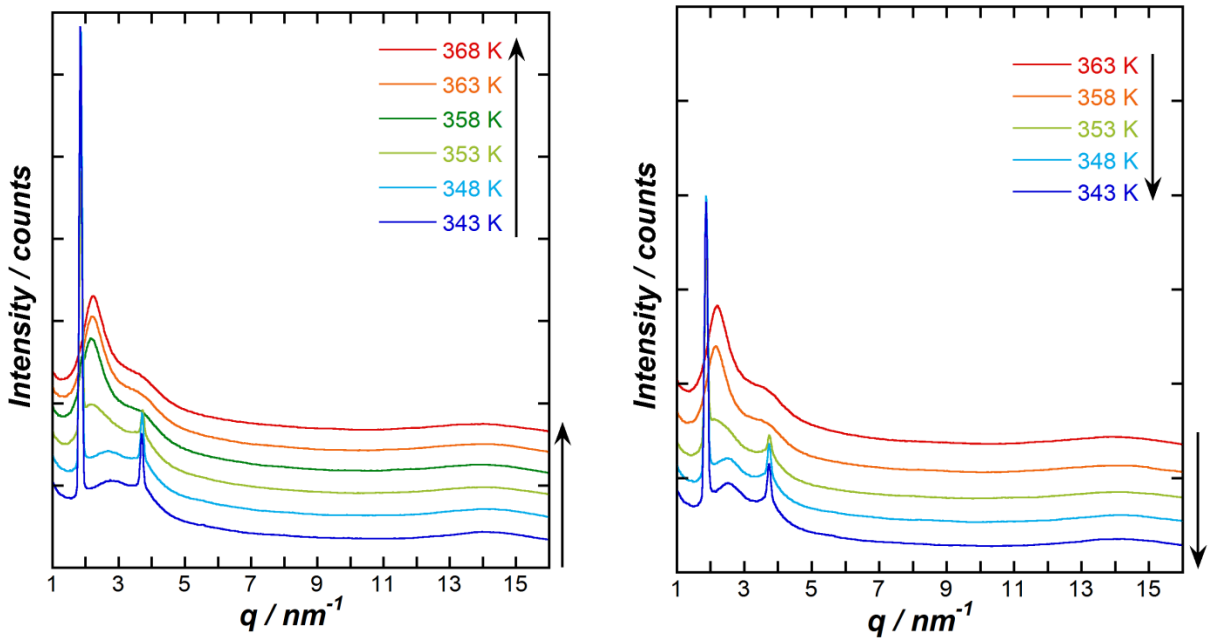

Figure S.II-14. SAXS diffractograms for $[Mn_{12}O_{12}(CF_3COO)_8(\mathbf{L^4})_8(H_2O)_4]$: (left) on 3rd heating from 343 to 368 K and (right) on 3rd cooling from 363 to 343 K.

Table S.II-5. Indexation of observed reflections on first cooling for $[Mn_{12}O_{12}(CF_3COO)_8(L^4)_8(H_2O)_4]$.

***T* / K**	**Peak number**	**$q_{(obs)}$ / nm^{-1}**	**$d_{(obs)}$ /Å**	**hkl**	**Calculated cell parameters**
343 K cooling	1	1.84	34.17	001	d = 34.10
	2	3.68	17.08	002	
	3	3.82	16.44	*d'*	
	4	5.55	11.32	003	
323 K cooling	1	1.84	34.18	001	d = 34.16
	2	3.68	17.07	002	
	3	3.80	16.52	*d'*	
	4	5.52	11.39	003	
303 K cooling	1	1.84	34.17	001	d = 34.18
	2	3.68	17.08	002	
	3	3.80	16.52	*d'*	
	4	5.51	11.40	003	

$q_{(obs)}$ is the observed reciprocal spacing, $q = 4\pi \cdot sin\theta/\lambda$, where λ is the wavelength, 2θ is the diffraction angle, $d_{(obs)}$ observed diffraction spacing: $d_{(obs)} = 2\pi/q_{(obs)}$, d is average of lamellar periodicity: $d = \frac{1}{n}\sum_{i=1}^{n} i \cdot d_{00i}$; *d'* corresponds to the distance of the short-range 2D organization

II.8. References

1. (a) Lis, T. *Acta. Cryst. B* **1980**, *36*, 2042-2046. (b) Caneschi, A.; Gatteschi, D.; Sessoli, R.; Barra, A. L.; Brunel, L. C.; Guillot, M. *J. Am. Chem. Soc.* **1991**, *113*, 5873-5874. (c) Sessoli, R.; Tsai, H. L.; Schake, A. R.; Wang, S. Y.; Vincent, J. B.; Folting, K.; Gatteschi, D.; Christou, G.; Hendrickson, D. N.; *J. Am. Chem. Soc.* **1993**, *115*, 1804-1816. (d) Sessoli, R.; Gatteschi, D.; Caneschi, A.; Novak, M. A. *Nature* **1993**, *365*, 141-143. (e) Thomas, L.; Lionti, F.; Balou, R.; Gatteschi, D.; Sessoli, R.; Barbara, B. *Nature* **1996**, *383*, 145-157. (f) Schake, R.; Tsai, H.-L.; De Vries, N.; Webb, J.; Folting, K.; Hendrickson, D.N.; Christou, G. *J. Chem. Soc., Chem. Comm.*, **1992**, 181-183. (g) Christou, G. *Acc. Chem. Res*. **1989**, 328-335.

2. Chakov, N. E.; Lee, S.-C.; Harter, A. G.; Kuhns, P. L.; Reyes, A. P.; Hill, S. O.; Dalal, N. S.; Wernsdorfer, W.; Abboud, K.; Christou, G. *J. Am. Chem. Soc.* **2006**, *128*, 6975-6989.

3. (a) Rogez, G.; Donnio, B.; Terazzi, E.; Gallani, J.-L.; Kappler, J.-P.; Bucher, J.-P.; Drillon, M.; *Adv. Mater.* **2009**, *21*, 4323-4333. (b) Henthorn, J. D.; Mishra, N.; Haun, C.D.; Castro, A. L.; Douglas, H. G.; Pegram, M.; Stadelmaier, B.; Huebner, J. S.; Lampropoulos, C. *Polyhedron* **2013**, *66*, 294-298.

4. (a) Bogani, L.; Wernsdorfer W. *Nature Materials* **2008**, *7*, 179-186. (b) Yan, Y.; Lee, J. S.; Ruddy, D. A. *Inorg. Chem.* **2015**, *54*, 4550-4555.

5. (a) Cornia, A.; Fabretti, A. C.; Pacchioni, M.; Bonacchi, D.; Caneschi, A.; Gatteschi, D.; Biagi, R.; Del Penino, U.; De Renzi, V.; Gurevich, L.; Van der Zant, H. S. J. *Angew. Chem. Int. Ed.* **2003**, *42*, 1645-1648. (b) Condorelli, G. G.; Motta, A.; Fragala, I. L.; Giannazzo, F.; Raineri, V.; Caneschi, A.; Gatteschi, D. *Angew. Chem. Int. Ed.* **2004**, *43*, 4081-4084. (c) Naitabdi, A.; Bucher, J.-P.; Gerbier, P.; Rabu, P.; Drillon, M. *Adv. Mater.* **2005**, *17*, 1612-1616. (d) Mannini, M.; Pineider F.; Sainctavit, P.; Danieli, C.; Otero, E.; Sciancalepore, C.; Talarico, A. M.; Arrio, M.-A.; Cornia, A.; Gatteschi, D.; Sessoli, R. *Nature Materials* **2009**, *8*, 194-197. (e) Ababei, R.; Li, Y.-G.; Roubeau, O.; Kalisz, M.; Bréfuel, N.; Coulon, C.; Harté, E.; Liu, X.; Mathonière, C.; Clérac, R. *New J. Chem.* **2009**, *33*, 1237-1248. (f) Jeon; I.-R.; Ababei, R.; Lecren, L.; Li, Y.-G.; Wernsdorfer, W.; Roubeau, O.; Mathonière, C.; Clérac, R. *Dalton Trans.*, **2010**, *39*, 4744-4746.

6. (a) Gonidec, M.; Luis, F.; Vilchez, A.; Esquena, J. ; Ambilino, D. B. ; Veciana, B. *Angew. Chem., Int. Ed.* **2010**, *49*, 1623-1626. (b) Donnio, B. *Inorg. Chim. Acta* **2014**, *409*, 53-67. (c) Tamura, R.; Uchida, Y.; Suzuki, K. *Handbook of Liquid Crystals*, 2nd ed., Oxford University Press: Wiley-VCH, 2014.

7. Bagai, K.; Christou, G. *Chem. Soc. Rev*. **2009**, 38, 1011-1026.

8. Zhao, H. H.; Berlinguette, C. P.; Bacsa, J.; Prosvirin, A. V.; Bera J. K.; Tichy, S. E.; Schelter, E. J. ; Dunbar K. R. *Inorg. Chem*., **2004**, *43*, 1359-1369.

9. Soler, M.; Artus, P.; Folting, K.; Huffman, J. C.; Hendrickson, D. N.; Christou, G. *Inorg. Chem.* **2001**, *40*, 4902-4912.

10. Aubin, S. M., Sun, Z.; Eppley, H. J.; Rumberger, E. M.; Guzei, i. A.; Folting, K.; Gantzel, P. K.; Rheingold, A. I.; Christou, G.; Hendrickson, D. N. *Inorg. Chem.* **2001**, *40*, 2127-2146.

11. (a) Halcrow, M. A. *Chem. Soc. Rev.* **2013**, *42*, 1784-1795. (b) Winter, M. J. *d-Block Chemistry*, Oxford University Press: Oxford, **1994**, 83-86.

12. (a) Soler, M.; Wernsdorfer, W.; Sun, Z. M.; Huffman, J. C.; Hendrickson, D. N.; Christou, G. *Chem. Commun.* **2003**, 2672-2673. (b) Cornia, A.; Sessoli, R.; Sorace, L.; Gatteschi, D.; Barra, A. L.; Daiguebonne, C. *Phys. Rev. Lett.* **2002**, *89*, 257201.

13. (a) Eppley, H. J.; Tsai, H.; Vries, N.; Folting, K.; Christou, G.; Hendrickson, D. N. *J. Am. Chem. Soc.* **1995,** *117*, 301-317. (b) Chakov, N. E.; Soler, M.; Wernsdorfer, W.; Abboud, K. A.; Christou, G. *Inorg. Chem*., **2005**, *44*, 5304-5321.

14. (a) Chakov, N. E.; Wernsdorfer, W.; Abboud, K.A.; Hendrikson, D. N.; Christou, G. *Dalton Trans*., **2003**, 2243-2248. (b) Boskovic, C; Pink, M; Huffman, J. C.; Hendrikson, D. N.; Christou, G. *J. Am. Chem. Soc*., **2001**, *123*, 9914-9915. (c) Kuroda-Sowa, T.; Fukuda, S.; Miyoshi, S.; Maekawa, M.; Munakata, M.; Miyasaka, H.; Yamashita, M. *Chem. Lett*. **2002**, 682.

15. (a) Terazzi, E.; Bourgogne, C.; Welter, R.; Gallani, J.-L.; Guillon, D.; Rogez, G.; Donnio, B. *Angew. Chem., Int. Ed*. **2008**, *47*, 490-495. (b) Terazzi, E.; Jensen, T. B.; Donnio, B.; Buchwalder, K.; Bourgogne, C.; Rogez, G.; Heinrich, B.; Gallani, J.-L.; Piguet, C. *Dalton Trans.*, **2011**, *40*, 12028-12032. (c) Terazzi, E.; Rogez, G.; Gallani, J.-L.; Donnio, B. *J. Am. Chem. Soc.*, **2013**, *135*, 2708-2722.

16. Mitcov, D. *PhD Thesis*, Univ. of Bordeaux, **2014.**

17. Saez, I. M.; Goodby J. W. *Struct. Bond*. **2008**, *128*, 1-62.

18. Siretanu, D. *PhD Thesis*, Univ. of Bordeaux 1, **2011**.

19. (a) Gerbier, P.; Ruiz-Molina, D.; Domingo, N.; Amabilino, D. B.; Vidal-Gancedo, J.; Tejada, J.; Hendrickson, D. N.; Veciana, J. *Monatsh. Chem.* **2003**, *134*, 265-276. (b) Coronado, E.; Forment-Aliaga, A.; Gaita-Ariño, A.; Giminéz-Saiz, C.; Romero, F. M.; Wernsdorfer, W. *Angew. Chem., Int. Ed.* **2004**, *43*, 6152-6156. (c) Park, C.-D.; Jung, D.-Y. *Bull. Korean Chem. Soc*. **2001**, *22*, 611-615. (d) Sun, H.; Li, W.; Wollenberg, L.; Li, B.; Wu, L.; Li, F.; Xu, L. *J. Phys. Chem. B* **2009**, *113*, 14674-14680. (e) Li, W.; Li, B.; Wang, Y.; Zhang, J.; Wang, S.; Wu, L. *Chem. Commun*. **2010**, *46*, 6548–6550. (f) Wang, Y.; Li, W.; Zhou, S.; Kong, D.; Yang, H.; Wu, L. *Chem. Commun.* 2011, 47, 3541-3543. (g) Heersche, H. B.; De Groot, Z.; Folk, J. A.; van der Zant, H. S. J.; Romeike, C.; Wegewijs, M. R.; Zobbi, L.; Barreca, D.; Tondello, E.; Cornia, A. *Phys. Rev. Lett.* **2006**, 96, 206801. (h) Bian, G. Q.; Kuroda-Sowa, T.; Nogami, T.; Sugimoto, K.; Maekawa, M.; Munakata, M.; Miyasaka, H.; Yamashita, M. *Bull. Chem. Soc. Jpn.* **2005**, *78*, 103210-39. (i) Willemin, S.; Donnadieu, B.; Lecren, L.; Henner, B.; Clérac, R.; Guérin, C.; Meyer, A.; Pokrovskii A. V.; Larionova, J. *New J. Chem.* **2004**, *28*, 919-928. (j) Burgert, M.; Voss, S.; Herr, S.; Fonin, M.; Groth, U.; Ruediger, U. *J. Am. Chem. Soc.* **2007**, *129*, 14362-14366. (k) Cornia, A.; Fabretti, A. C.; Pacchioni, M.; Zobbi, L.; Bonacchi, D.; Caneschi, A.; Gatteschi, D.; Biagi, R.; Del Pennino, U.; De Renzi, V.; Gurevich, L.; Van der Zant, H. S. J. *Angew. Chem., Int. Ed.* **2003**, *42*, 1645-1648. (l) Pacchioni, M.; Cornia, A.; Fabretti, A. C.; Zobbi, L.; Bonacchi, D.; Caneschi, A.; Chastanet, G.; Gatteschi, D.; Sessoli, R. *Chem. Commun.* **2004**, 2604-2605.

20. (a) Ruiz-Molina, D.; Gerbier, P.; Rumberger, E.; Amabilino, D. B.; Guzei, I. A.; Folting, K.; Huffman, J. C.; Rheingold, A.; Christou, G.; Veciana J.; Hendrickson D. N. *J. Mater. Chem.*, **2002**, *12*, 1152–1161. (b) Kushch, L. A.; Sasnovskayaa, V. D.; Dmitriev, A. I.; Yagubskii, E. B.; Koplak, O. V.; Zorina, L. V.; Boukhvalov D. W. *Dalton Trans.* **2012**, *41*, 13747-13754.

21. Hammond, C. *The Basics of Crystallography and Diffraction*, 2nd ed., Oxford University Press: New York, **2001**.

22. (a) Nakanishi, T.; Morita, M.; Murakami, H.; Sagara, T.; Nakashima, N. *Chem. Eur. J.* **2002**, *8*, 1641-1648. (b) Zhang, T.; Liu, S.; Kurth, D. G.; Faul, C. F. J. *Adv. Funct. Mater.* **2009**, *19*, 642–652.

Chapter III

Mononuclear Fe^{II} Spin-Crossover Complexes: From Crystalline Toward Soft Materials

Table of Contents for Chapter III:

III.1. Introduction

During the recent decades, an important research activity has been dedicated on the development of molecular materials that display critical changes of their physical properties as function of an external stimuli such as temperature, pressure, light irradiation and magnetic or electric fields. In this scope, spin-crossover (SCO) compounds are among the most studied.[1] The SCO phenomenon is encountered in certain transition metal complexes and involves a change of the spin configuration of the metal ion center.[1] It is accompanied by important changes in magnetic and optical properties as well as structural features. For instance, in Fe(II) complexes, the SCO is associated with paramagnetic-to-diamagnetic switching. The particular features displayed in these compounds may have interest for numerous practical applications such as sensors, molecular switches, data storage and display devices. Although these potential applications are often highlighted in numerous fundamental studies, to date none of these magnetic components have been utilized industrially for any commercial devices. One of the main issues involves the fabrication of technologically sustainable materials. Indeed, these compounds are generally produced as powders or crystalline solids which are not the best candidates for technological devices. Thus, important research efforts have been devoted to the processing of SCO compounds by depositing them on surfaces,[2] inserting them into polymer matrices,[3] forming nanoparticles,[4] or gels.[5] More recently, another interesting approach has been proposed and consists in the preparation of spin crossover hybrids displaying liquid crystalline (LC) properties.[6] This approach received much consideration because the SCO phenomenon can be tuned around room temperature and this could be used for the development of advanced multifunctional materials with advantages in both molecular magnetism (processing/shaping, tuning of magnetic and optical features) and LC (introduction of paramagnetic, photo- or thermochromic properties) fields. The first complex combining LC and SCO properties was reported in 2001 by Galyametdinov and co-workers on a Fe(III) complex.[7] In this study, a Schiff base ligand (salicylidenyl-N'-ethyl-N-ethylenediamine) was functionalized with a dodecyl tail, providing a calamitic geometry to the resulting complex. The material self-organizes into a lamellar mesophase (smectic A) above 388 K and displays a gradual SCO with a $T_{1/2}$ = 125 K. The first metallomesogen system based on a Fe(II) SCO complex, namely $[Fe(L)_2(NCS)_2]$ (with L = 3,4,5-tris(hexadecyloxy)-N-(pyridin-2-ylmethylene)aniline), was reported shortly later by Hayami and co-workers.[8] Once again, the compound exhibits LC properties above room temperature, while the SCO was found at much lower temperature ($T_{1/2}$ = 217 K). Subsequently, several groups proposed to develop molecular systems that display SCO at higher temperature in order to promote a synergetic effect between SCO and LC properties.[9,10] Such realization was demonstrated for the first time in 2002 by Fujigaya and co-workers, which reported a series of $[Fe(RTrz)_3](ClO_4)_2$ complexes (with RTrz = 5-bis(alkoxyloxy)-*N*-(4*H*-1,2,4-triazol-4-yl)benzamide) in which the SCO is triggered by a crystal-to-mesophase transition.[9] Despite these promising examples, the number of SCO systems within metallomesogens remains very limited and most of the time materials display gradual and/or incomplete SCO.[6-10] Additionally, the behavior is often irreversible after clearing due to decomposition and/or oxidation and/or lattice solvent loss processes.

During this PhD work, we proposed to develop new metallomesogens based on a mononuclear Fe(II) complex containing Schiff base ligands belonging to the family of pyridylaroylhydrazones (Scheme III.1).

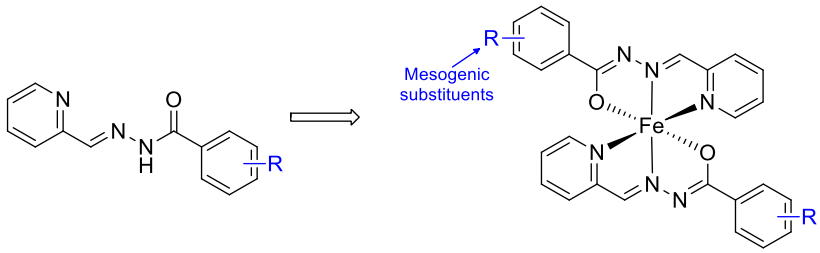

Scheme III-1. General structure of functionalized $[Fe^{II}(L)_2]$ complexes based on pyridylaroylhydrazone ligands.

These monoacid ligands exhibit keno-enol tautomerism, giving rise to versatile coordination chemistry where dicationic, monocationic and neutral forms of divalent metal ion complexes can be isolated.[11-16] The coordination chemistry of these ligands with various *3d-5d*[11-15] and *4f*[16] divalent and trivalent ions have been widely studied since more than 30 years. Among them, much attention has been devoted to Fe(II) systems. Indeed, these ligands are able to bind efficiently and selectively Fe(II), forming robust complexes and have been intensively examined as potential chelators for clinical treatments of iron overload diseases and tumor growth inhibitors.[12] In other hand, the interest for their magnetism is very recent and only few studies have been reported so far.[13-15] To the best of our knowledge, only one example of Fe(II) dicationic complex have been magnetically characterized and found to exhibit a Curie-Weiss paramagnetic behavior,[14] while no data is available for the monocationic form. More interestingly, few examples of neutral complexes were found to display photo- and/or thermo-induced SCO according to the functionalization.[13-15]

Figure III-1. Spin transition induced by a crystal-to-liquid phase transition. Reprinted and adapted from ref. 15.

Although no examples with LC properties have been reported, the architecture and features of these complexes make them prime candidates for the development of metallomesogens systems. Indeed, they have a bent geometry which might favor, after an appropriate functionalization, the formation of lamellar or eventually banana-like (BN) mesophases. Additionally, they are quite stable in temperature and against oxidation, which is a *sine qua non* condition for eventual surface deposition (upon reaching the isotropic liquid phase). The absence of counter-anions is also a clear advantage since their role on the self-organization (and magnetic behavior) remains somewhat unclear. Finally, the spin crossover can be tuned above room temperature, giving the opportunity to promote an interplay between the LC and SCO properties. Indeed, Real and co-workers reported very recently a series of long chain-functionalized analogue

complexes displaying spin transition with large hysteresis induced by the melting/crystallization transitions (Figure III-1),[15] and this could be potentially transposed in metallomesogenic systems.

In the first part of the chapter, we discuss on the synthesis and characterization of model complexes containing non-mesogenic ligands. Indeed, only few examples of SCO systems based on aroylhydrazone ligands have been described. In the second part of the chapter, we describe our attempts to promote liquid crystalline features on this molecular system by using strongly lipophilic ligands. Several sites are available for the grafting of mesogenic substituents and we mainly focused on the functionalization of the aryl scaffold (Scheme III-1). Although these attempts were unsuccessful, the interesting effects of these functional groups on thermo-structural and thermo-magnetic properties on the resulting materials are discussed in detail.

III.2. SCO complexes with non-mesogenic ligands

In this section, we describe the synthesis, structural and magnetic characterizations of a serie of Fe^{II} complexes containing non-mesogenic ligands (Scheme III-2). The initial goal was to test whether the introduction of methoxy functions on the aryl ring is appropriate for the preservation of SCO features, before going further on the functionalization with alkoxy mesogenic substituents. Indeed, no example of complexes functionalized with such functional groups was available during the maturation of the project (a series of complexes containing alkyloxy chains have been described since then[15]). Thus, three new ligands containing one to three methoxy groups and corresponding complexes were synthetized and characterized.

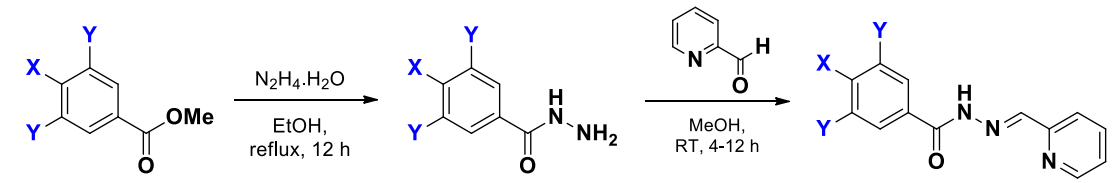

1a: X = OMe; Y = H
1b: X = H; Y = OMe
1c: X = Y = OMe

2a: X = OMe; Y = H
2b: X = H; Y = OMe
2c: X = Y = OMe

HL^1: X = OMe; Y = H
HL^2: X = H; Y = OMe
HL^3: X = Y = OMe

Scheme III-2. General pathway for the synthesis of N'-(pyridin-2-ylmethylene)benzohydrazide ligands.

All the ligands were prepared in good yields by a two-step synthesis according to general procedures described in the literature (Scheme III-2).[12,13] In short, benzohydrazide precursors **2a-c** were obtained after treatment of the methyl benzoate derivatives with excess of hydrazine. Then, the **HL^{1-3}** ligands were synthetized by an equimolar condensation of **2a-c** with 2-pyridinecarboxaldehyde.

III.2.1 Mononuclear Fe(II) complexes based on HL^1 ligand

III.2.1.1. Synthesis of $[Fe(L^1)_2]$ and general comments

$[Fe(\mathbf{L^1})_2]$ can be prepared according to the literature,[12-14] by reacting a stoichiometric amount of **HL^1** and $Fe(ClO_4)_2 \cdot 6H_2O$ (ratio 2:1) in presence of excess of triethylamine (Scheme III-3). This latter is required to deprotonate the ligand and promote the formation of desired neutral complex (enolate form). Indeed, in

absence of base, the cationic forms, $[Fe(\mathbf{HL^1})(\mathbf{L^1})]^+$ and $[Fe(\mathbf{HL^1})_2]^{2+}$, can be selectively isolated depending on the synthetic conditions. The synthesis, structural descriptions and magnetic properties of these cationic complexes are briefly discussed in section III.2.1.4.

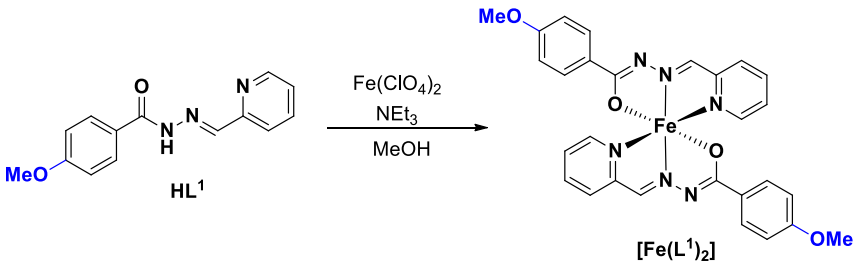

Scheme III-3. Synthetic pathway for the formation of $[Fe(\mathbf{L^1})_2]$

Interestingly, $[Fe(\mathbf{L^1})_2]$ can be isolated as different polymorphs and solvatomorphs according to the reaction conditions. When the reagents are combined in methanol and the reaction mixture is stirred at RT, a dark green precipitate, whose composition was found as $[Fe(\mathbf{L^1})_2]\cdot$MeOH and thereafter referred as α-phase, appears quickly in less than one hour. However, if the reaction mixture is warmed to 50 °C, the dark green microcrystalline powder turns rapidly and irreversibly to olive green. This latter has the exact same chemical composition (not a solvatomorph), and is then referred as β-polymorph. The exact mechanism for the transformation from the α to β-phase remains not completely elucidated and understood since the existence of polymorphism in this system was fortuitously discovered only very recently. However, this result strongly suggests that α-{$[Fe(\mathbf{L^1})_2]\cdot$MeOH} complex is actually a kinetic product that undergo transformation into the thermodynamic one, β-{$[Fe(\mathbf{L^1})_2]\cdot$MeOH}, upon thermal activation. Single-crystals of each polymorphic form were isolated as dark green thin needles, which are undistinguishable from each other by eyes. Typically, α-{$[Fe(\mathbf{L^1})_2]\cdot$MeOH} single crystals were obtained after mixing the different reagents in methanol and allowing the solution to stand at RT for one day. Same result can be obtained using slow diffusion technique, by layering two methanol solutions containing in one side $\mathbf{HL^1}$ and triethylamine and in the other side $Fe(ClO_4)_2\cdot 6H_2O$ (crystals are obtained within 24 hours). For the β-form, crystals were obtained using the first procedure at 50 °C. By analogy with our previous observations in powder samples, when a solution containing α-{$[Fe(\mathbf{L^1})_2]\cdot$MeOH} crystals is warmed to 50 °C, a complete conversion into the β-phase is observed within 24 hours. From this experiment, it is nonetheless not possible to determine if this phase conversion is due to a crystal-to-crystal transition or if it is due to a progressive dissolution of α-{$[Fe(\mathbf{L^1})_2]\cdot$MeOH} complex in the hot solution, which recrystallizes thereafter directly in the β-phase. However, when the reagents are directly dissolved in hot methanol (50 °C), the analysis of the first crystals formed revealed essentially the α-phase, supporting the hypothesis of a crystal-to-crystal transformation from kinetic into thermodynamic phase. When separated from the mother liquor, α-{$[Fe(\mathbf{L^1})_2]\cdot$MeOH} complex does not undergo transformation into β-phase. Instead, the complex loses rapidly its methanol molecule, leading to the solvent-free α-$[Fe(\mathbf{L^1})_2]$ complex. Although the process is much slower, a complete desolvation of β-{$[Fe(\mathbf{L^1})_2]\cdot$MeOH} is also occurring by natural evaporation, giving rise to β-$[Fe(\mathbf{L^1})_2]$ form. Both $[Fe(\mathbf{L^1})_2]$ polymorphs are thermodynamically stable since no interconversion between the two phases was detected over time or thermal treatments (from 1.8 K to 470 K).

Due to loss of solvent, a complete characterization of the two [Fe($\mathbf{L^1}$)$_2$]·MeOH products was not possible but their polymorphism was nonetheless evidenced by single-crystal X-ray diffraction analysis (*vide infra*). The chemical and phase purity of the two samples were mainly deduced from the characterization on the dried compounds (including EA, mass spectroscopy (ESI-MS), FTIR, single-crystal or powder X-ray diffraction and DSC) combined with the analysis of the desolvation process by TGA. FTIR was found to be a very convenient technique to routinely identify the nature of different phases in bulk samples, which was systematically confirmed by X-ray diffraction, calorimetric and/or magnetic measurements (*vide infra*). The FTIR spectra of desolvated complexes and the ligand are compared in Figure III-2.

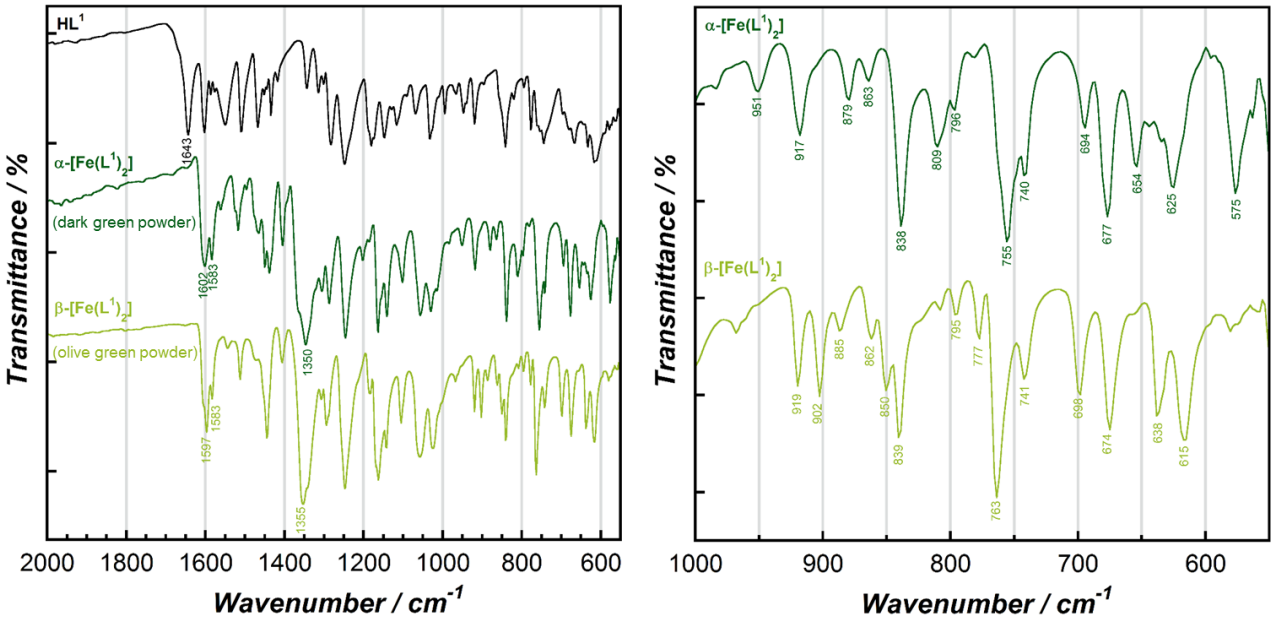

Figure III-2. (left) FTIR spectra for **HL^1** (black), α-[Fe($\mathbf{L^1}$)$_2$] (dark green) and β-[Fe($\mathbf{L^1}$)$_2$] (olive green). (right) zoom of the region 1000 - 550 cm^{-1} emphasizing the difference between the polymorphs.

The strong absorption band at 1643 cm^{-1} ascribed to $\nu_{(C=O)}$ stretching vibration in the free ligand is missing in FTIR spectra of isolated complexes confirming its absence in the bulk samples (Figure III-2). The spectra display intense double bands in the region 1602 - 1583 cm^{-1} and strong peaks at 1350 cm^{-1} (α-phase) and 1355 cm^{-1} (β-phase), which are assigned to $\nu_{(C=N-N=C)}$ and $\nu_{(C-O)}$, respectively, confirming the presence of chelating ligands in the enolate form.[13a,b,14] The formation of the expected neutral complexes is also supported by the absence of the strong band around 1050 - 1100 cm^{-1} expected for perchlorate-containing samples. The two spectra are not completely superimposable and strong differences are especially found in the far-infrared region. This reflects the difference in the bending vibration modes of aromatic C-H as consequence of distinct crystal packing in α- and β-phase.

Powder samples of the dried complexes have the same color as their respective solvated forms, ie. dark green and olive green for α- and β-phase, respectively. Based upon previous descriptions on closely related complexes,[15] these colors suggest that α-[Fe($\mathbf{L^1}$)$_2$] and β-[Fe($\mathbf{L^1}$)$_2$] are in the low-spin (LS) and high-spin (HS) configuration, respectively. The two dried compounds exhibit thermochromism (dark green ↔ olive green) upon heating at 380 K (α-phase) or cooling in liquid nitrogen (β-phase), suggesting that both

polymorphs experience thermally-induced SCO. We should notice that the solvated β-[Fe($\mathbf{L^1}$)$_2$] complex does not show color change during cooling to low temperature, suggesting it remains paramagnetic.

Hence, with our experimental conditions, it was possible to selectively isolate [Fe($\mathbf{L^1}$)$_2$] in four different crystalline forms (polymorphs or solvatomorphs from each other) that are accessible through the pathways proposed in Scheme III-4 and the two solvent-free complexes are suggested to exhibit SCO at very different temperatures.

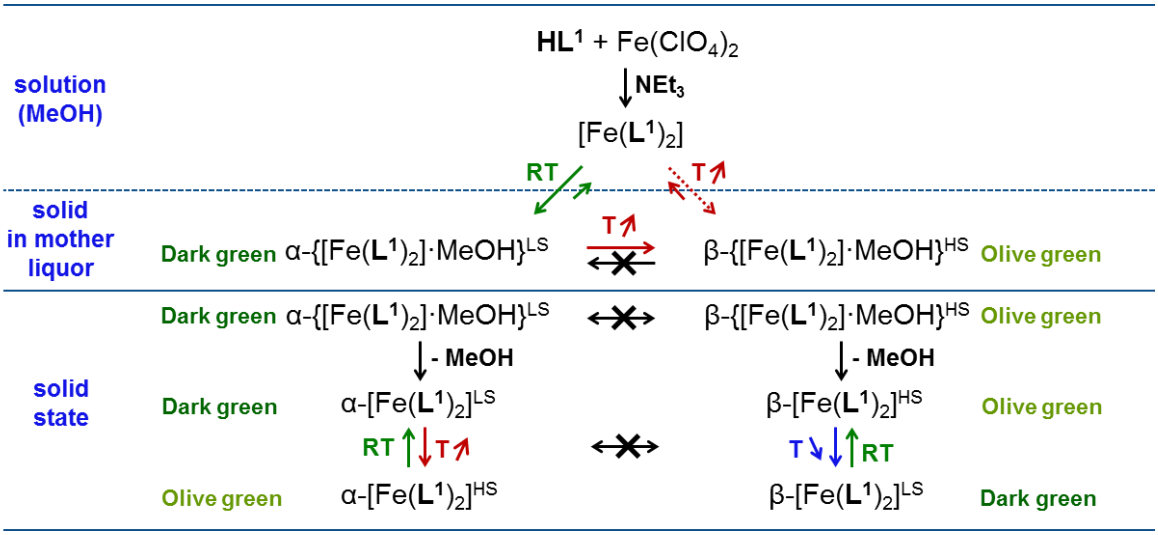

Scheme III-4. Proposed pathway for the production of polymorphs and solvatomorphs of [Fe($\mathbf{L^1}$)$_2$] and spin configuration of the different phases.

III.2.1.2. Analytical characterizations

III.2.1.2.1. Structural description of the [Fe(L^1)$_2$]·MeOH polymorphs

The fundamental differences existing within [Fe($\mathbf{L^1}$)$_2$]·MeOH polymorphs were evidenced by single-crystal X-ray diffraction analysis. The measurements were performed at 120 K on freshly filtered crystals, which were rapidly coated in paraffin oil to prevent from solvent loss. Views of the structures are shown in Figure III-3 and selected crystallographic data are gathered in Table III-1 (detailed crystal data, refinement parameters, bond lengths and angles can be found in Table S.III-1 in supporting information section).

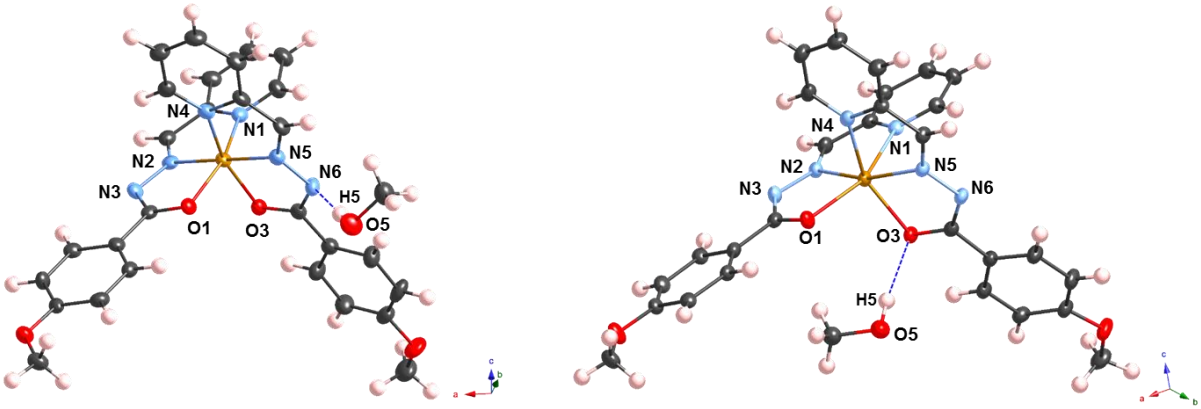

Figure III-3. ORTEP views of α-{[Fe($\mathbf{L^1}$)$_2$]·MeOH} (left) and of β-{[Fe($\mathbf{L^1}$)$_2$]·MeOH} (right) at 120 K. Thermal ellipsoids are depicted at 50 % probability. The blue dashed lines correspond to hydrogen bonds. Color Figure: Fe orange, O red, C grey, N blue, H light pink.

α- and β-polymorph crystallize in the monoclinic $P2_1/c$ and triclinic *P-1* space groups, respectively. In both cases, the asymmetric unit consists in one {[Fe($\mathbf{L^1}$)$_2$]·MeOH} adduct that is repeated 4 and 2 times in the unit cells of α- and β-form, respectively, providing a volume cell twice bigger for α-phase in comparison to the β-one. No counter anion was detected in the lattice, confirming the deprotonated form of the ligands to satisfy charge neutrality. In both cases, the iron(II) ion is chelated by 2 oxygen and 4 nitrogen donors provided by two tridentate Schiff base ligands. The ligands are nearly planar, leading therefore to a *mer* coordination environment in which the central nitrogen donor of both Schiff base ligands are in *trans* configuration; The N2-Fe1-N5 bond angles are 178.8° (α-phase) and 161.9° (β-phase) reflecting a stronger distortion of the meridional environment in the second case. Due to the asymmetry of pyridylbenzohydrazone ligands, it should be noticed that the resulting hexa-coordinated complexes are chiral molecules. However, the compounds crystallize in a racemic way and the two enantiomers (Δ and Λ) are crystallographically equivalent due to the symmetry (achiral space group) provided by an inversion center (See Figure S.III-3).

Table III-1. Crystallographic data for [Fe($\mathbf{L^1}$)$_2$]·MeOH polymorphs at 120 K.

Compound	**α-{[Fe($\mathbf{L^1}$)$_2$]·MeOH}**	**β-{[Fe($\mathbf{L^1}$)$_2$]·MeOH}**
Temperature, K	120	120
Crystal system	Monoclinic	Triclinic
Space group	$P2_1/c$	*P-1*
a, Å	24.1677(6)	8.7893(4)
b, Å	13.2155(4)	11.1963(5)
c, Å	8.7284(2)	14.8884(7)
α, °	90	111.717(2)
β, °	99.860(1)	91.037(2)
γ, °	90	97.507(2)
V, Å^3	2746.6(1)	1345.96
Z	4	2
<Fe-N$_{(py)}$>, Å	1.953	2.233
<Fe-N$_{(im)}$>, Å	1.865	2.114
<Fe-O>, Å	1.976	2.101
V$_{FeN4O2}$, Å^3	9.34	11.84
Σ(X-Fe-X),[a] °	81.1	157.6

[a] $\sum = \sum_{i=1}^{12}|90 - \varphi_i|$, where φ_i are cis X-Fe-X bond angles with X = O or N

In both cases, the FeN_4O_2 coordination sphere departs strongly from an ideal octahedral symmetry as shown from the $\Sigma_{(X\text{-}Fe\text{-}X)}$ parameter (with X = O or N), which sums the deviations from 90° of the 12 *cis* angles in the coordination sphere of Fe(II) ion.[17] A $\Sigma_{(X\text{-}Fe\text{-}X)}$ parameter of 81.1° was found for α-complex, while the distortion in β-{[Fe($\mathbf{L^1}$)$_2$]·MeOH} structure (157.6°) is much more pronounced (Tables III-1 and S.III-1). These values are comparable to those reported for closely related analogues in LS and HS configurations, respectively.[13] The average Fe-N$_{(py)}$, Fe-N$_{(im)}$ and Fe-O bond lengths in α-{[Fe($\mathbf{L^1}$)$_2$]·MeOH} are 1.953, 1.865 and 1.976 Å, respectively, confirming unambiguously that the compound is in LS state at 120 K. The coordination bond lengths in the β-polymorph are much longer, $\Delta_{Fe\text{-}X}$ of ca. 0.2 Å, and the

volume of the FeN_4O_2 pseudo-octahedron is about 27 % bigger than the previous one, pointing clearly the HS configuration (Tables III-1 and S.III-1).

These results nicely illustrate how the coordination sphere of a complex having the same chemical composition can be affected and stabilized in different spin configuration depending on effects arising purely from the crystal packing. From the multiples weak interactions that characterize the two distinct polymorphs, we should highlight the different manner that have the complexes for interacting with the methanol molecules through hydrogen bonds and with neighboring complexes through π-π contacts (Figure III-4).

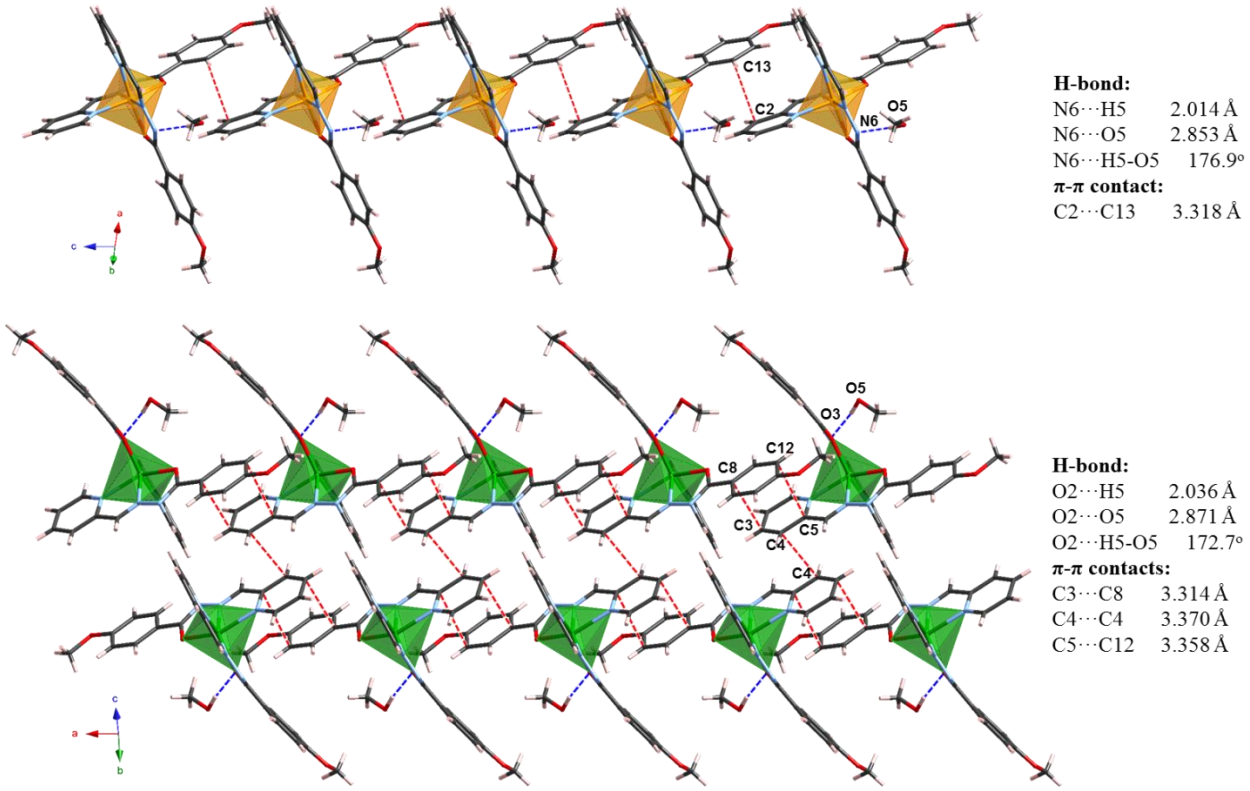

Figure III-4. Crystal packing showing the π-π interactions (red dashed lines) and hydrogen bonds (blue dashed lines) in α-{[Fe($\mathbf{L}^1$)$_2$]·MeOH} (top) and β-{[Fe($\mathbf{L}^1$)$_2$]·MeOH} (bottom). Other weak interactions are omitted for clarity. Color Figure: Fe^{II}_{LS} orange, Fe^{II}_{HS} green,O red, C grey, N blue, H light pink.

In α-phase, the methanol molecule is hydrogen bonded with one hydrazone ligand *via* a nitrogen atom (N6···O5, ca. 2.85 Å), while the second ligand establishes π-π interactions (C2···C13, ca. 3.32 Å) with two neighboring complexes, creating a 1D supramolecular chain along *c*-axis (see top of Figure III-4). The presence of these π-π interactions might be responsible for the slight dissymmetry on the coordination bond lengths that were found systematically longer when provided by the ligand featuring this type contact. In β-polymorph, a hydrogen bond is also formed between the methanol molecule and the complex (see Figures III-3 and III-4 bottom), but this time through an oxygen donor (O3···O5, ca. 2.87 Å) instead of a nitrogen, causing a dissymmetry on the Fe-O bonds (Fe1-O3 is ca. 0.03 Å shorter than Fe1-O1). It is reasonable to assume that this latter will affect more efficiently the ligand field strength of the complex since O3 is directly involved in the Fe(II) coordination sphere and it should be noticed that the complex, which is paramagnetic at 120 K, become diamagnetic after removal of the methanol molecule (*vide infra*). However, the real role of the methanol molecule in the stabilization of the paramagnetic phase remains uncertain. Indeed, no

crystallographic structure could be successfully obtained for the desolvated complex and it is thus difficult to estimate how the removal of methanol molecule might affect the overall crystal packing. Doubts about its contribution were also raised after the isolation of another [Fe($\mathbf{L^3}$)$_2$]·MeOH relater complex featuring the opposite behavior. This complex, which will be discussed more in detail in section III.2.3, displays a similar H-bond with an oxygen donor and was found diamagnetic until it loses the MeOH above 400 K. The complex is then stabilized in the HS configuration for a large range of temperature on cooling (gradual SCO with $T_{1/2}$ of ca. 340 K). The stabilization of [Fe($\mathbf{L^1}$)$_2$]·MeOH in the paramagnetic β-phase was tentatively attributed to the multiple π-π interactions. Each complex interacts with two neighboring complexes through a double π-π contact (C3···C8, ca. 3.31 Å, and C5···C12, ca. 3.36 Å), generating a supramolecular chain along *a*-axis (Figure III-4, bottom). The π-chains dimerize through an additional π-π contact involving C4 atoms from an adjacent chain (C4···C4, ca. 3.37 Å). π-π contacts play a critical role on the cooperativity of SCO through elastic interactions, however, it is reasonable to assume that the proliferation of such interactions in β-{[Fe($\mathbf{L^1}$)$_2$]·MeOH} packing might create a certain frustration on the Fe(II) coordination sphere, which needs to expand or contract to undergo spin configuration change and ultimately prevent from SCO. This hypothesis would need nonetheless to be confirmed by the analysis of the crystal packing of the desolvated complex that exhibit spin transition at low temperature and important efforts are in progress in order to obtain the crystal structure of this material. The stabilization of the HS configuration might also arises from other supramolecular effects that did not appear clear in our eyes, which include multiple weak C-H···X interactions (with X = N, O, π).

Powder X-ray diffraction measurements were performed in order to determine whether the collected single-crystals were representative of bulk samples. The measurements were carried at RT using wet ground crystals (β-phase) or directly in the mother liquor (α-phase). The diffractograms are shown in Figure III-5 and compared with simulations provided by the crystal structure determinations at 120 K.

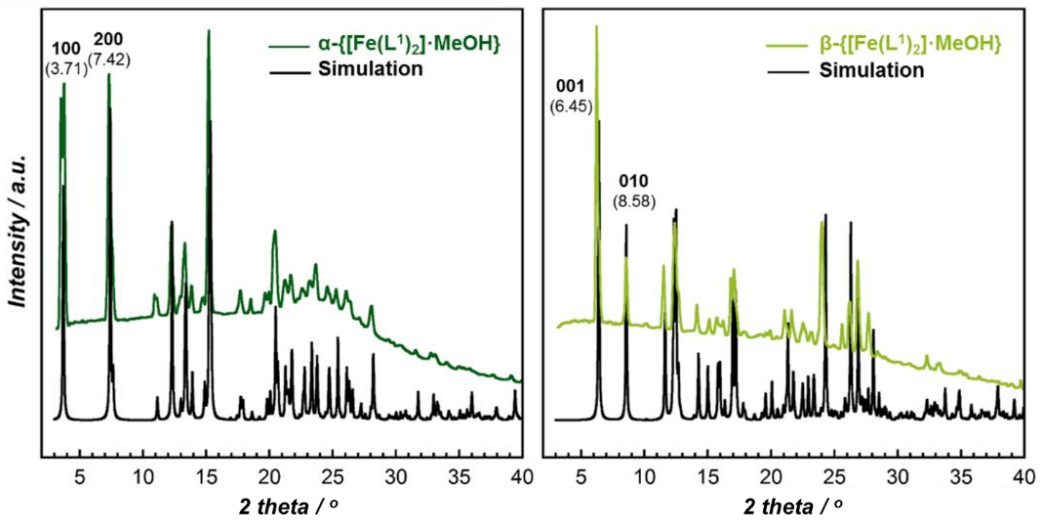

Figure III-5. Experimental (298 K) and simulated (120 K) powder diffraction patterns for α-{[Fe($\mathbf{L^1}$)$_2$]·MeOH} (left) and β-{[Fe($\mathbf{L^1}$)$_2$]·MeOH} (right). Note: for convenience reasons, measurements were performed on a SAXS setup that is not appropriate for high resolution determination when used for wide windows of angles.

In both cases, diffractograms patterns fits well with the simulated ones even though some variations can be detected due to the difference in temperature between the experimental and simulated diffraction

patterns and the resolution of the used technique. In each sample, no peak associated to the second polymorph could be found within the detection limit, approving our synthetic procedures for isolating pure fractions of each phase.

III.2.1.2.2. Desolvation process

As mentioned before, both [Fe($\mathbf{L^1}$)$_2$]·MeOH products are subject to complete desolvation, leading therefore to two distinct solvent-free polymorphs. This was verified by TGA measurements on freshly filtered samples that show a weight loss of 5.4 - 5.5 %, corresponding perfectly to the expected value, 5.37 %, for the loss of one methanol molecule (Figure III-6). For α-{[Fe($\mathbf{L^1}$)$_2$]·MeOH}, the desolvation process is very fast, even at room temperature. The TGA experiment showed that the methanol loss is actually completed during the initial isothermal equilibrium at 304 K (see the inset on left Figure III-6). From the weight loss *vs.* time plot, a half-time decay $t_{1/2}$ of about 6 minutes can be estimated while only traces of methanol remain after 1 hour.

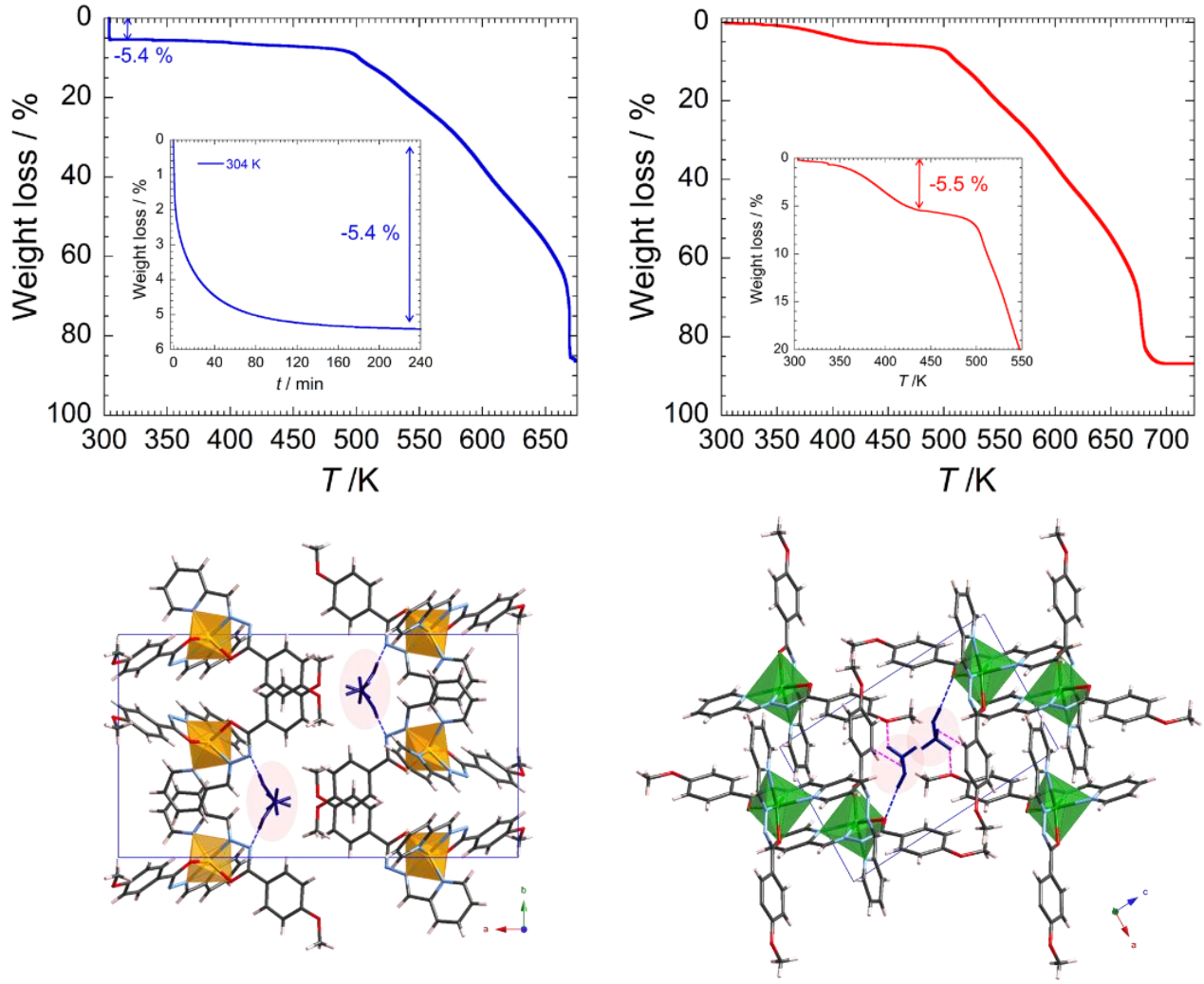

Figure III-6. (top left) TGA thermogram for α-{[Fe($\mathbf{L^1}$)$_2$]·MeOH} (inset) time dependence of the weight loss at 304 K. (top right) TGA thermogram for β-{[Fe($\mathbf{L^1}$)$_2$]·MeOH}.(inset) zoom highlighting the MeOH loss. (bottom) packing emphasizing the environment of MeOH molecules in α phase (left) and β phase (right). MeOH is shown in blue, O-H···X (X = N or O) in dashed blue lines and C-H···X (X = O, π) in dashed pink lines.

The relative facility of the methanol molecules to leave is tentatively explained by the crystal packing that shows their presence in relatively "open" channels along *c*-axis (Figure III-6, bottom left). β-{[Fe($\mathbf{L^1}$)$_2$]·MeOH} is also subject to methanol loss at RT, however the process is much slower due to either stronger hydrogen binding or packing constraints (Figure III-6, bottom right). Thus, a desolvation is completed after few days for microcrystalline powder samples, while months are necessary on single-crystal samples.

III.2.1.2.3. Structural descriptions of [Fe($\mathbf{L^1}$)$_2$]

The desolvation of α-polymorph does not involve loss of crystallinity and a crystal-to-crystal transformation occurs without change of the general symmetry (same space group). Selected crystallographic data for solvated and desolvated complexes are compared in Table III-2 and views of the structures and crystal packings are shown in Figure III-7.

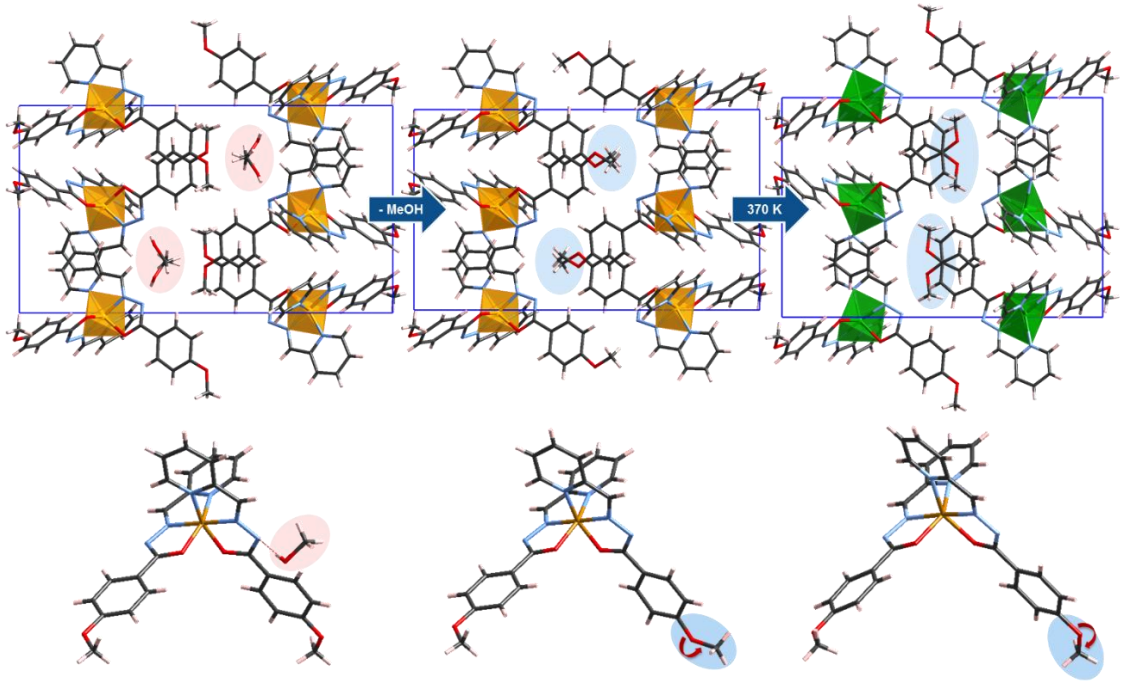

Figure III-7. Projection of the crystal packing along *c*-axis and structure for α-{[Fe($\mathbf{L^1}$)$_2$]·MeOH} at 120 K (left) and α-[Fe($\mathbf{L^1}$)$_2$] at 120 K (middle) and 370 K (right). The FeN_4O_2 coordination spheres are represented in orange and green pseudo-octahedrons for the LS and HS configurations, respectively.

To compensate the void space left by the methanol molecule, an important contraction of the unit cell, mainly along *a*-axis, is observed in the structure at 120 K, resulting in a volume decrease of about 7 %. At the molecular level, some changes are also revealed, especially for the methoxy group of one of the ligands that features a change of rotational conformation, filling up the former methanol channels (Figure III-7, middle). The loss of MeOH molecule seems not affecting significantly the Fe(II) coordination sphere at this temperature. The Fe-X bond lengths and $\Sigma_{(X\text{-}Fe\text{-}X)}$ parameter are readily identical to the previous case, confirming the preservation of the diamagnetic configuration (Tables III-2 and S.III-2).

Table III-2. Crystallographic data for α-{[Fe($\mathbf{L^1}$)$_2$]·MeOH} and α-[Fe($\mathbf{L^1}$)$_2$]

Compound	**α-{[Fe($\mathbf{L^1}$)$_2$]·MeOH}**	**α-[Fe($\mathbf{L^1}$)$_2$]**			
Temperature, K	**120**	**120**	**260**	**350**[a]	**370**
Crystal system	Monoclinic	Monoclinic	Monoclinic	Monoclinic	Monoclinic
Space group	*P2$_1$/c*	*P2$_1$/c*	*P2$_1$/c*	*P2$_1$/c*	*P2$_1$/c*
a, Å	24.1677(6)	22.7027(14)	22.806(6)	22.88	21.451(3)
b, Å	13.2155(4)	12.9995(8)	13.1051(14)	13.22	14.565(3)
c, Å	8.7284(2)	8.7405(6)	8.7743(9)	8.80	8.6226(8)
β, °	99.860(1)	98.705(3)	98.307(4)	98.32	96.467(6)
V, Å^3	2746.6(1)	2549.8(3)	2595.1(3)	2634.2	2676.9(8)
Z	4	4	4	--	4
<Fe-N$_{(py)}$>, Å	1.953	1.960	1.958	--	2.203
<Fe-N$_{(im)}$>, Å	1.865	1.865	1.862	--	2.060
<Fe-O>, Å	1.976	1.970	1.967	--	2.079
Σ(X-Fe-X),[b] °	81.1	80.3	80.4	--	144.0
C8···C13, Å	3.318	3.311	3.362	--	3.341

[a] Only the unit cell was checked at 350 K. [b] $\Sigma = \sum_{i=1}^{12}|90 - \varphi_i|$, where φ_i are X-Fe-X bond angles with X = O or N

Measurements were performed at higher temperature to detect eventual structural changes that are often indicative of SCO behavior. The unit cell parameters of [Fe($\mathbf{L^1}$)$_2$] remain unchanged up to 350 K, while important modifications were found at 370 K, which corresponds well to the temperature at which thermochromism (dark green to olive green) is featured in the powder sample. A contraction and increase of *a* and *b* parameters, respectively, and an expansion of about 5% of the unit cell are observed, while no crystallographic space group change is featured, remaining the monoclinic *P2$_1$/c* space group (Tables III-2 and S.III-2). Similarly to solvent loss situation, a modification of the conformation of one of the methoxy groups is occurring upon heating to 370 K (Figure III-7). These structural changes can be unambiguously ascribed to spin switching phenomenon by the examination of the Fe(II) coordination sphere. Indeed, the volume of the FeN_4O_2 speudo-octahedron increase from 9.3 to 11.5 Å^3 consequently to the elongation of the Fe-N and Fe-O bond lengths. The octahedral symmetry is also more distorted than in the previous structure at 120 K (with a $\Sigma_{(X\text{-}Fe\text{-}X)}$ parameter of 144.0°), as expected for structures in HS configuration. It is worthwhile to mention that the average bond length values, Fe-N$_{(py)}$ 2.203 Å, Fe-N$_{(im)}$ 2.060 Å, and Fe-O 2.079 Å, are slightly shorter than expected in fully paramagnetic analogues (if compared for example with β-{[Fe($\mathbf{L^1}$)$_2$]·MeOH}), suggesting the presence of a residual diamagnetic species at 370 K. Attempts to measure crystals at higher temperature to reveal the pure paramagnetic phase were unfortunately unsuccessful due to degradation of the single crystal. In both LS and HS phases, the structural changes appear mainly in the *b*- and/or *a*-direction (*c*-parameter is almost unchanged for all the structures) and this can be explained by the conservation of the supramolecular π-chains along the *c*-axis. The distance C2···C13 remains the same upon desolvation and SCO processes (Table III-2). Once again, the measured crystal was representative of the bulk sample as verified by the powder X-ray diffractogram, which is virtually identical to the simulation provided by the structure at 120 K (Figure III-8, left).

Complex β-[Fe($\mathbf{L^1}$)$_2$] remains crystalline upon methanol loss. However, the desolvation process create multiple microfractures in such manner that crystals fall apart into tiny crystallites (microcrystalline powder and needles) that were unfortunately not suitable for single-crystal X-ray analysis. Additional attempts to remove the methanol in a soften fashion, using exfoliation techniques (after soaking the crystals in Et_2O or

hexane) were performed, but it remains unsuccessful so far. Nonetheless, powder X-ray diffraction experiments confirmed that the compound is structurally different from α-[Fe($\mathbf{L^1}$)$_2$] complex, reflecting their polymorphism (Figure III-8, right).

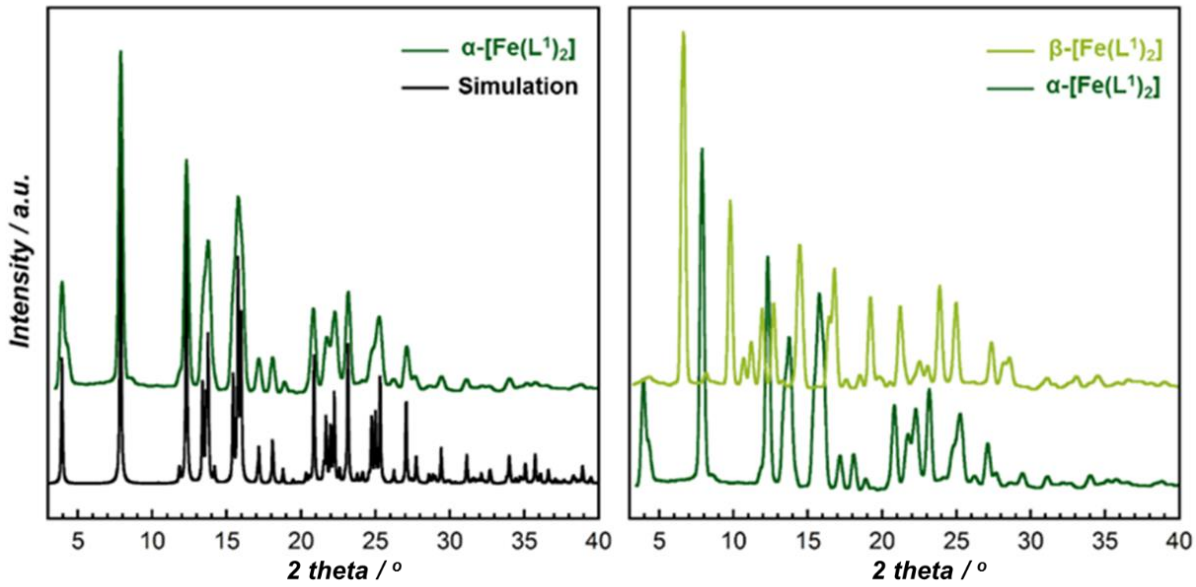

Figure III-8. (left) Experimental (298 K) and simulated (120 K) powder diffraction patterns for α-[Fe($\mathbf{L^1}$)$_2$]. (right) Comparison between powder diffraction patterns of α-[Fe($\mathbf{L^1}$)$_2$] and β-[Fe($\mathbf{L^1}$)$_2$] (298 K). Note: For convenience reasons, measurements were performed on SAXS setup that is not appropriate for high-resolution determination when used for wide windows of angles.

III.2.1.3. Spin crossover properties

III.2.1.3.1. Thermally-induced spin crossover properties

Temperature-dependent magnetic and DSC measurements were performed to further probe SCO features in these complexes. As mentioned above, α-{[Fe($\mathbf{L^1}$)$_2$]·MeOH} is not suitable for such experiments since it is diamagnetic at room temperature and does not survive upon heating (desolvation). The thermal dependence of the χT product (where χ is the molar magnetic susceptibility) for the solvent-free α-[Fe($\mathbf{L^1}$)$_2$] analogue, is shown in Figure III-9 and selected magnetic and thermodynamic parameters are summarized in Table III-3.

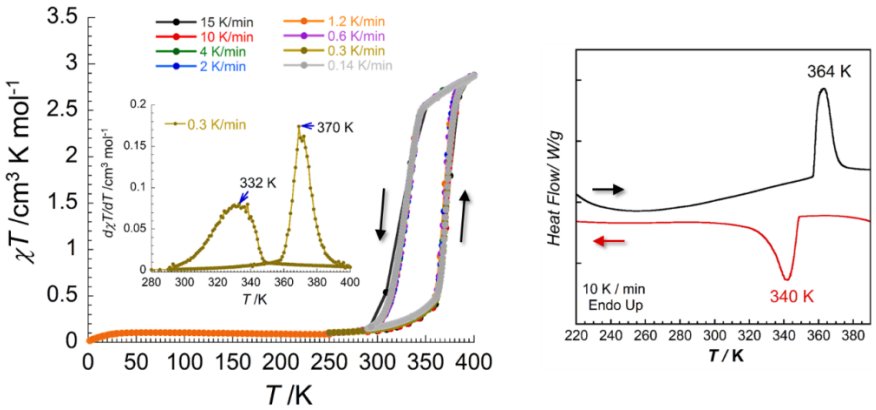

Figure III-9. (left) Temperature dependence of the χT product for α-[Fe($\mathbf{L^1}$)$_2$] with an applied *dc* field of 1 T (scan rate: 0.14 to 15 K/min). (inset) dχT/dT vs. T plots at 0.3 to 15 K/min. (right) DSC data for α-[Fe($\mathbf{L^1}$)$_2$] between 220 and 390 K.

Table III-3. Selected SCO parameters for [Fe($\mathbf{L^1}$)$_2$] polymorphs

Compound	α-[Fe($\mathbf{L^1}$)$_2$]	β-[Fe($\mathbf{L^1}$)$_2$]
$T_{1/2\uparrow}$,[a] K	370	262
$T_{1/2\downarrow}$,[a] K	332	235
$\Delta T_{1/2}$,[a] K	38	27
$\Delta H\uparrow / \Delta H\downarrow$,[b] kJ·mol^{-1}	18.4 / 18.0	12.7 / 10.9
$\Delta S\uparrow / \Delta S\downarrow$,[b] J·mol^{-1}·K^{-1}	50 / 52	48 / 46

[a] determined by magnetic measurements at 0.3 K/min, [b] determined by DSC measurements at 10 K/min.

On heating up to 320 K, the χT value is constant and worth ca. 0.09 cm^3·K·mol^{-1}, indicating that the sample is almost purely diamagnetic (Fe(II) LS (S = 0)), in agreement with X-ray diffraction data. When heated further, the χT product rises slightly and gradually up to 0.43 cm^3·K·mol^{-1} at 360 K, indicating a statistic conversion of about 10 % of species into the HS state. Above this temperature, the χT product sharply increases, suggesting a first-order spin transition. This indicates that above 360 K, the system is not anymore able to support local structural changes (expansion of the coordination sphere) and a deeper and propagative transformation of the material, involving notably the change of the conformation of one methoxy group, is occurring. At 400 K, the material is not fully paramagnetic as shown by χT value of 2.92 cm^3·K·mol^{-1}, which is lower than expected for Fe^{II}_{HS} (S = 2 with g ~ 2). Nevertheless, the shape of the curve suggests that the pure HS phase could be reached at higher temperature. The interconversion between the paramagnetic and diamagnetic phases is perfectly reversible. However, the transition appears at much lower temperature ($T_{1/2\downarrow}$ = 332 K) on cooling mode, revealing a thermal hysteresis of about 38 K (for a sweeping rate of 0.3 K/min). The presence of this hysteresis clearly confirms the first-order spin transition and indicates a strong cooperativity within the crystal packing. The width of the hysteresis loop is almost independent of the sweeping rate (measured between 15 and 0.14 K/min), presuming that the metastable phases have a long life-time.[1,18] The SCO was confirmed by DSC experiments that revealed only a single transition in both heating and cooling modes (Figure III-9, right), while the hysteresis loop width is also found independent of the scan rate (See Figure S.III-5).

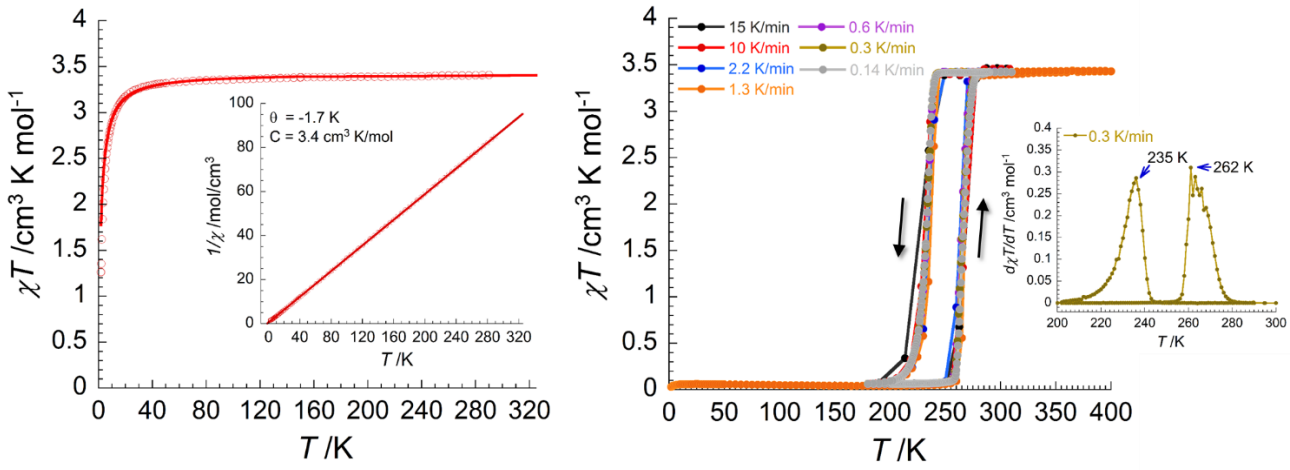

Figure III-10. (left) Temperature dependence of the χT product for β{-[Fe($\mathbf{L^1}$)$_2$]·MeOH} with an applied *dc* field of 1000 Oe, (inset) $1/\chi$ *vs.* *T* plot. Solid red lines are the best fits to Curie-Weiss law. (Right) Temperature dependence of the χT product for β-[Fe($\mathbf{L^1}$)$_2$] with an applied *dc* field of 10000 Oe. (inset) d$\chi T/dT$ vs. *T* plots at 0.3 K/min.

Magnetic measurements were performed in both solvated and solvent-free β-[Fe($\mathbf{L^1}$)$_2$] complexes. As expected from X-ray diffraction analysis and absence of thermochromism, β-{[Fe($\mathbf{L^1}$)$_2$]·MeOH} does not exhibit thermally-induced SCO behavior (Figure III-10, left).

Above 40 K, the χT product is ca. 3.4 cm^3·K·mol^{-1}, which is typical for Fe(II) in HS configuration with g ~ 2. At low temperature, the χT value decrease slightly, owing to weak antiferromagnetic interactions or magnetic anisotropy on the Fe(II) site. Accordingly, the DSC of the solvated compound did not revealed any transition upon the first cooling from 290 K to 200 K, while a broad signal around 350 K, corresponding to the methanol loss, is observed during the first heating (Figure S.III-5). On subsequent cooling/heating cycles, the material displays a reversible transition around 230 and 260 K, on cooling and heating modes, respectively. The temperature-dependent magnetic measurements performed on the desolvated sample (after DSC) confirmed unambiguously that the transitions observed in DSC reflects a hysteretic spin transition behavior (Figure III-10, right). Similarly to α-[Fe($\mathbf{L^1}$)$_2$], the χT versus T plots reveal only one reversible transition, confirming the absence of the second polymorph in the bulk sample. The χT values at low and high-temperature plateaus are 0.04 and 3.4 cm^3 K mol^{-1}, which is consistent with a complete transition from the LS to HS configuration. The $T_{1/2\uparrow}$ and $T_{1/2\downarrow}$ can be estimated to 262 and 235 K, respectively, giving rise to a hysteresis loop of about 27 K for a sweeping rate of 0.3 K/min (Table III-3). These values are about 100 K lower than those obtained for α-[Fe($\mathbf{L^1}$)$_2$], illustrating the huge impact of crystal packing on the critical temperature of the SCO phenomenon. Once again, the hysteresis width is almost independent of the scan rate as shown by the magnetic measurements performed at 15 to 0.14 K/min and DSC experiments (see Figure S.III-5). It is worthwhile to mention that the transitions in β-[Fe($\mathbf{L^1}$)$_2$] are sharper than the previous case, which might indicate a stronger cooperativity in the system, even though this is not reflected by a wider hysteresis loop. The enthalpy ΔH and entropy ΔS parameters, determined by DSC, were comparable for both complexes and are in the range of values reported for mononuclear Fe(II) SCO complexes (Table III-3).[19]

III.2.1.3.2. Photo-induced spin crossover properties

Preliminary temperature-dependent reflectivity measurements were also performed in order to confirm the thermally-induced SCO behavior and determine whether this latter can triggered by means of light.

The spectra of both samples are barely identical and display a maximal absorption around 700 nm (Figure III-11, top). The optical features of the thermally-induced paramagnetic phase of α-[Fe($\mathbf{L^1}$)$_2$] could not be characterized since this latter is well above the temperature window of our experimental setup. Thus, no significant change of the spectrum was detected between 285 and 10 K (Figure III-11, top left). For β-[Fe($\mathbf{L^1}$)$_2$] polymorph, the differences between high and low-temperature spectra are more relevant, especially in the region 530-720 nm, for which an increase of the absorption is observed upon cooling (Figure III-11, top center), in agreement with a spin transition from the paramagnetic into diamagnetic phase. The temperature dependence of the absolute reflectivity at 600 nm (noted R_{600}) in cooling and heating modes is shown in Figure III-11 (bottom right) and reflects quite well the hysteretic spin transition behavior revealed by magnetic measurements, even though slight shifts on the temperature transitions are observed (probably associated with the reflectivity *versus* magnetism techniques, which are respectively probing the surface and

buck of the compound). It is worth noting that a slight increase of the R_{600} value is observed below 80 K, due to a weak photo-conversion induced by the light required during the reflectivity acquisition.

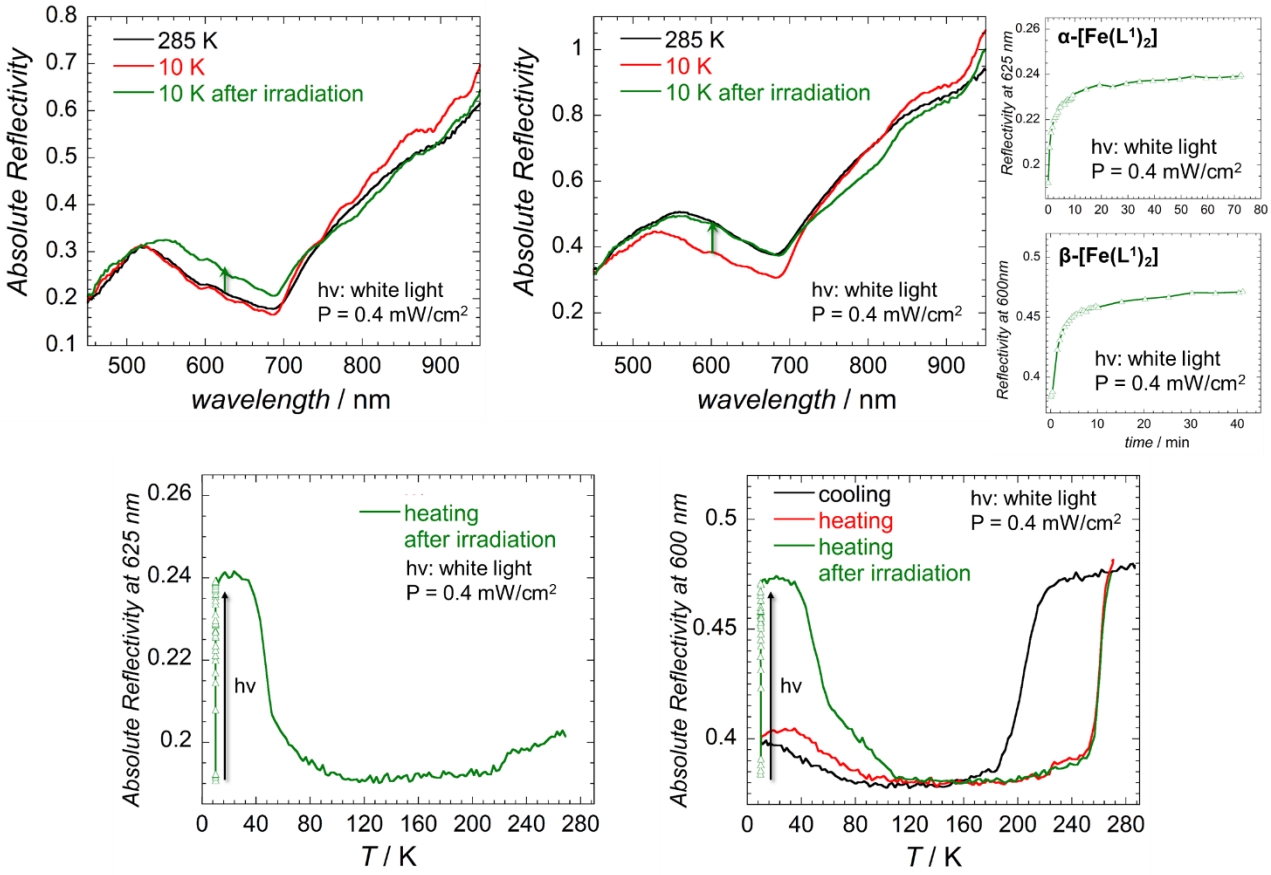

Figure III-11. (top) Optical reflectivity spectra at 285 K, 10 K and 10 K after irradiation with white light for α-[Fe($\mathbf{L}^1$)$_2$] (left) and β-[Fe($\mathbf{L}^1$)$_2$] (middle).(top right) Time dependence of the reflectivity during the photo-excitation. (bottom) temperature dependence of the R_{625} and R_{600} for α-[Fe($\mathbf{L}^1$)$_2$] (left) and β-[Fe($\mathbf{L}^1$)$_2$] (right). All temperature-dependent measurements were performed at 4 K/min.

The samples were cooled from 285 to 10 K in the dark, and then irradiated with white light (0.4 mW/cm^2) for 40 to 70 min. The evolution of the reflectivity with time was monitored at R_{625} and R_{600} for α and β polymorphs, respectively (Figure III-11, top right) and revealed in both cases a rapid increase of the reflectivity intensity, while the saturation was reached after about 20 minutes. The spectrum of β-[Fe($\mathbf{L}^1$)$_2$] complex after irradiation is almost perfectly superimposed (in the region 530-720 nm) with the one collected at high temperature, suggesting a full conversion into the metastable paramagnetic phase. For α-[Fe($\mathbf{L}^1$)$_2$] polymorph, an increase of the reflectivity is also observed in this region, however, it is not possible to estimate the photo-conversion since no spectrum is available for the thermally-induced paramagnetic phase. Then, the temperature was raised in order to probe the thermal relaxation of the photo-excited phase (Figure III-11, bottom). In both samples, the reflectivity intensity is stable up to ca. 40 K, while it drops rapidly above, reaching the thermodynamic diamagnetic phase around 90 K (α-phase) and 110 K (β-phase). It should be noticed that the relaxation temperatures are probably over estimated since, in this range of temperature, the thermal relaxation process competes with the photo-conversion induced by the spectroscopic light source used during the spectra acquisition. Additional experiments using different light sources of specific

wavelengths (ranging from 1050 to 365 nm) were performed to determine the optimal conditions for the photo-excitation. Using the same experimental protocol, it was found that the red light (630 nm) is the most efficient for the photo-conversion of both polymorphs and was selected for studies of the photomagnetism.

Photomagnetic measurements were only performed for β-[Fe($\mathbf{L^1}$)$_2$] complex to date. The sample was cooled down to 10 K, irradiated with red light and the photo-conversion with time was monitored by measuring the magnetic susceptibility. Despite very long exposure (ca. 13 h), the χT value did not worth much than 0.56 cm^3 K mol^{-1}, meaning that less than 15 % of species were converted into the metastable paramagnetic phase (Figure III-12). This result might be explained by the low efficiency of the light to penetrate the dark green sample, in such a way that only the material in surface can be activated. After irradiation, the sample was cooled down to 2 K in the dark and the evolution of the photo-induced paramagnetic phase with temperature was followed. Between 2 and 10 K, the χT product increases from 0.09 to 0.57 cm^3·K·mol^{-1}, indicating the presence antiferromagnetic interactions within the packing. Then, the χT value decrease progressively to reach the thermodynamic diamagnetic phase at 65 K.

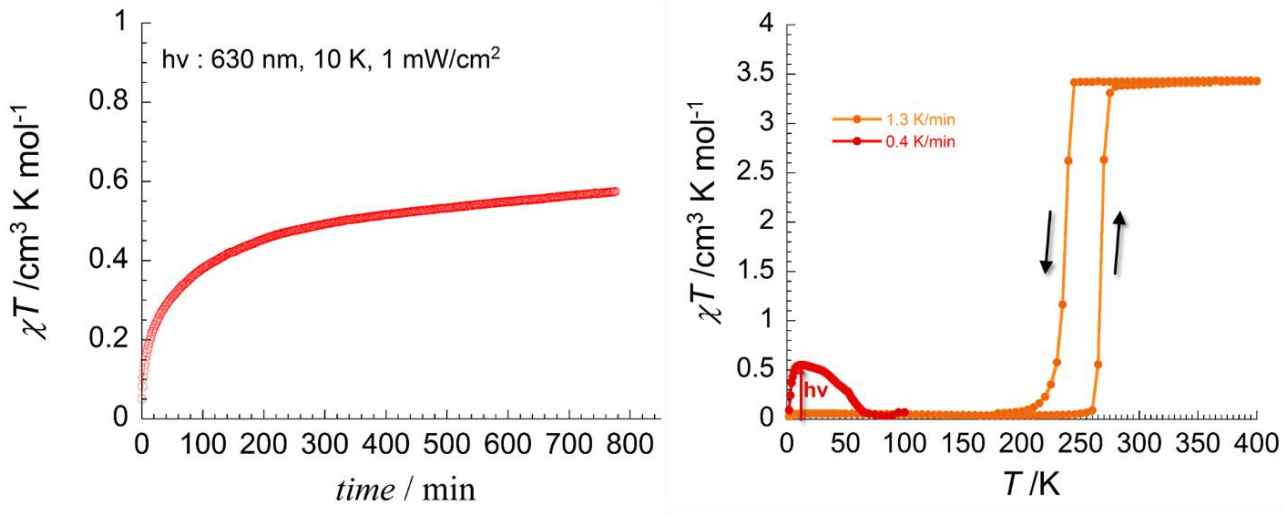

Figure III-12. (left) Time dependence of χT product during the photo-excitation for β-[Fe($\mathbf{L^1}$)$_2$]. (right) temperature dependence of the χT for β-[Fe($\mathbf{L^1}$)$_2$]

Hence, these studies confirmed that both polymorphs display thermally and photo-induced SCO properties. However, the light irradiation was not found to be very efficient to promote spin switching, probably due to the darkness of the sample, and only a very partial photo-conversion could be detected as in all other Fe(II) analogues reported so far in the litterature.[13]

III.2.1.4. Synthesis and properties of cationic complexes

As mentioned earlier, pyridyl benzohydrazone ligands exhibit keto-enol tautomerism allowing the isolation of cationic and neutral forms of complexes according to the experimental conditions (Scheme III-5).[11,12,14] With Fe(II) ion, numerous examples of neutral and dicationic pyridylbenzohydrazone-based complexes have been described,[11-15] while no example of mono-charged complex has been reported. During this work, we were able to isolate both dicationic [Fe($\mathbf{HL^1}$)$_2$]$^{2+}$ and mono-cationic [Fe($\mathbf{HL^1}$)($\mathbf{L^1}$)]$^+$ complexes.

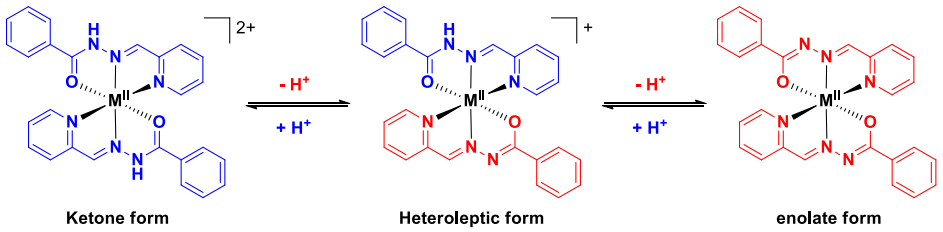

Scheme III-5. Keto-enol tautomerism in pyridylbenzohydrazone-based complexes

The dicationic form can be obtained according to literature,[14] by reacting **HL^1** with an excess of $Fe(ClO_4)_2$ (ligand:metal ratio 1:1) in MeOH at room temperature. The complex was isolated as red-purple single-crystals after slow evaporation of the reaction mixture. Interestingly, when the reaction is performed in stoichiometric conditions (ligand:metal ratio 2:1), both mono-cationic and dicationic complexes are concomitantly formed. Indeed, upon addition of the iron salt into a MeOH solution of ligand, the reaction mixture turns instantly to red-purple as expected for the formation of $[Fe(\mathbf{HL^1})_2]^{2+}$ complex, but a shiny gray precipitate corresponding to $[Fe(\mathbf{HL^1})(\mathbf{L^1})]^{+}$ complex appears after a while. Thus, by using slow diffusion technique, it was possible to isolate single-crystalline dark grey needles of this material, while the dicationic form, much soluble, remains in solution. We should notice that the slow evaporation of the remaining filtrate allowed us to confirm the presence of $[Fe(\mathbf{HL^1})_2]^{2+}$ complex but this synthetic method was not suitable to isolate the dicationic form as pure (mixture with mono-cationic complex and free ligand).

XRD analysis revealed that the dicationic complex crystallizes in the monoclinic $P2_1/c$ space group. A view of the structure at 120 K is shown in Figure III-13 (left) and selected crystallographic data are gathered in Table III-3 (detailed crystal data, refinement parameters, bond lengths and angles are summarized in Table S3).

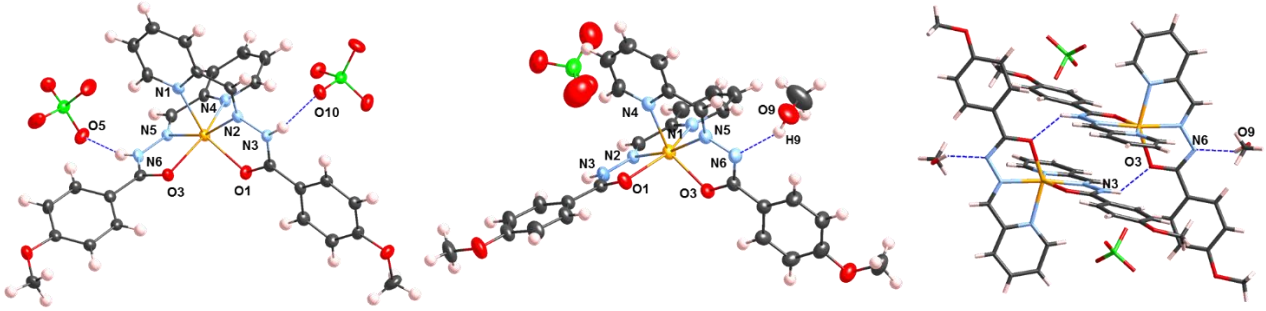

Figure III-13. ORTEP views of $[Fe(\mathbf{HL^1})_2](ClO_4)_2$ (left) and $[Fe(\mathbf{HL^1})(\mathbf{L^1})](ClO_4)\cdot MeOH$ (center) at 120 K. Thermal ellipsoids are depicted at 50 % probability. (right) Supramolecular dimer formed by $[Fe(\mathbf{HL^1})(\mathbf{L^1})]^{+}$ complexes. The dashed blue lines correspond to hydrogen bonds. Color Figure: Fe orange, O red, C grey, N blue, H light pink.

The asymmetric unit is composed of one hexa-coordinated Fe(II) complex and two perchlorate counter-anions, which are hydrogen bonded with the complex *via* the NH functions (N···O ~ 2.86 Å). In addition to the two perchlorate counter-anions that confirm the dicationic nature of the complex, the presence of ligands in the ketone form is also supported by the C-O bond lengths, ca.1.25 Å, which are shorter than those found in the neutral $[Fe(\mathbf{L^1})_2]$ polymorphs, ca. 1.29 Å, while the C-N(H) distances, ca. 1.37 Å, are longer in comparison to the corresponding enolate form, ca 1.34 Å. The Fe-O and Fe-N bond distances,

ranging from 2.107 to 2.218 Å, and strong distortion of the coordination sphere, $\Sigma_{(X\text{-}Fe\text{-}X)}$ = 165°, clearly indicate that the complex is in the HS configuration at 120 K.

Table III-3. Crystallographic data for $[Fe(\mathbf{HL^1})_2]^{2+}$ and $[Fe(\mathbf{HL^1})(\mathbf{L^1})]^{+}$ compounds at 120 K.

Compound	$[Fe(HL^1)_2](ClO_4)_2$	$[Fe(HL^1)(L^1)](ClO_4)\cdot MeOH$
Temperature, K	120	120
Crystal system	Monoclinic	Triclinic
Space group	$P2_1/c$	*P-1*
a, Å	11.320(1)	10.876(1)
b, Å	12.611(1)	11.557(1)
c, Å	21.564(2)	13.444(1)
α, °	90	72.307(2)
β, °	90.458(2)	79.470(2)
γ, °	90	79.920(2)
V, Å^3	3078.4(1)	1569.9(1)
Z	4	2
Σ(X-Fe-X),[a] °	165.5	125.3
<Fe-$N_{(py)}$>, Å	2.199	2.225
<Fe-$N_{(im)}$>, Å	2.121	2.107
<Fe-O>, Å	2.122	2.153
C=O, Å	1.251 (av)	1.233
C-O, Å	--	1.289
(O)C=N, Å	--	1.336
(O)C-N(H), Å	1.366 (av)	1.364

[a] $\sum = \sum_{i=1}^{12}|90 - \varphi_i|$, where φ_i are cis X-Fe-X bond angles with X = O or N

In the other hand, the monocationic complex was found to crystallize into the triclinic *P-1* space group (Figure III-13 and Tables III-3 and S.III-3). The unit cell consists of a heteroleptic complex, a disordered perchlorate ion and a methanol molecule, which interacts with the complex through O9-H9···N6 hydrogen bond (O9···N6, 2.84 Å). The two types of ligand (enolate and ketone forms) can be unambiguously distinguished by the C-O and C-N bond lengths, which are either comparable to those observed in the neutral or dicationic complexes (Table III-3). In contrast with the previous example, no hydrogen bond is established between the perchlorate anion and the NH function. Instead, this latter establishes a hydrogen bond (N3-H3A···O3, 2.79 Å) with a neighboring complex, forming a supramolecular dimer (Figure III-13, right). Similarly to the dicationic complex, the Fe-N and Fe-O bond distances and distortion of the coordination, clearly point the HS configuration at 120 K. Attempts were also made to determine whether the spin configuration can change after removal of the methanol molecule. However, no desolvation occurs even after a thermal treatment at 420 K for 24 hours under vacuum. Solvent-free crystals were obtained in low yield (~ 5 %), by diffusion of diethyl ether vapor into a solution of complex in dichloromethane. Although the quality of the structure was poor, the analysis of the coordination sphere was once again in fair agreement with the paramagnetic state down to 120 K (Figure S.III-4 and Table S.III-3).

As suspected by the X-ray diffraction analyses at 120 K, magnetic susceptibility measurements for both dicationic and monocationic complexes did not show any sign of thermally-induced SCO (Figure III-14). Above 30 K, the χT products remain nearly constant and worth 3.3 to 3.5 $cm^3\cdot K\cdot mol^{-1}$, in good

agreement with the expected value for Fe^{II}_{HS} (S = 2, with $g \approx 2$). The χT products decrease slightly at low temperature as a result of weak intermolecular antiferromagnetic interactions or magnetic anisotropy on Fe(II) centrer. These results suggest that the presence of one or two ligands in the ketone form strongly weakened the ligand field splitting, stabilizing systematically the paramagnetic phase. Potentially we might take advantage of this feature and use protonation/deprotonation as chemical stimuli to promote spin switching between the diamagnetic neutral complex and the paramagnetic cationic forms.

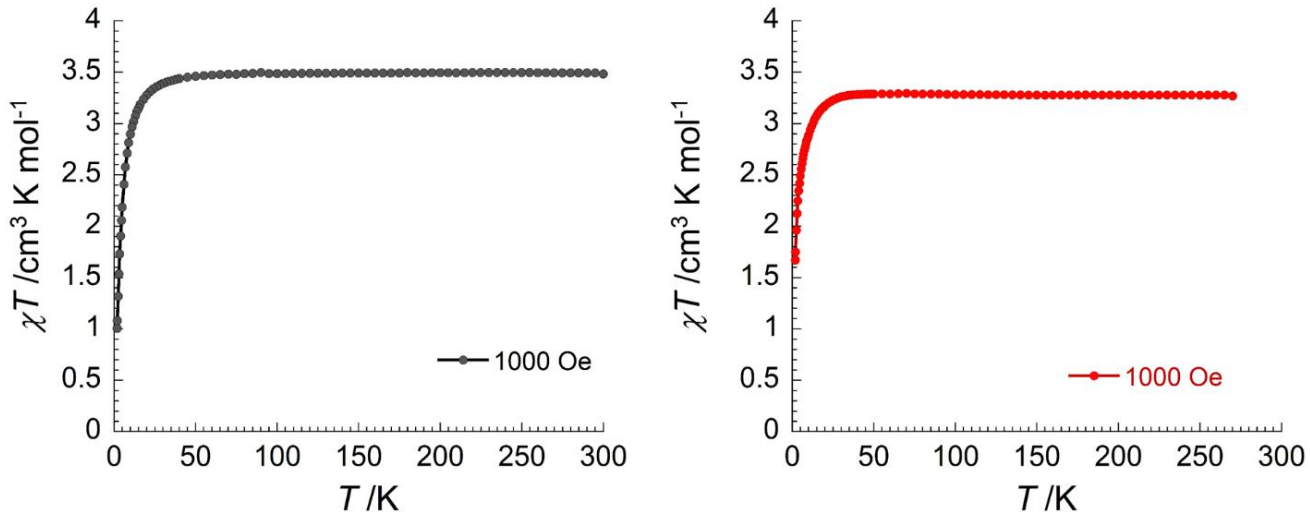

Figure III-14. Temperature dependence of the χT product for [Fe($\mathbf{HL^1}$)$_2$](ClO$_4$)$_2$ (left) and [Fe($\mathbf{HL^1}$)($\mathbf{L^1}$)](ClO$_4$)·MeOH (right) with an applied *dc* field of 1000 Oe. Sweep rate: 1.3 K/min.

III.2.2. Synthesis and properties of [Fe($\mathbf{L^2}$)$_2$] complexes

III.2.2.1. Synthetic approach and general comments

Similarly to [Fe($\mathbf{L^1}$)$_2$] complex, [Fe($\mathbf{L^2}$)$_2$] was found to exhibit polymorphism. When $\mathbf{HL^2}$ and Fe(ClO$_4$)$_2$·6H$_2$O (ratio 2:1) are combined in MeOH in presence of excess of triethylamine, and the resulting dark-green solution is allowed to stand at room temperature, dark green needles corresponding to solvent-free [Fe($\mathbf{L^2}$)$_2$] complex are obtained in good yield within one hour. The complex, which will be thereafter referred as α-phase, crystallizes in the monoclinic *C2/c* space group. The isolated sample was analytically pure as shown by the powder X-ray diffractogram that is identical to the simulation provided by the crystal structure at 120 K (Figure III-15, left). When the rate of the reaction is artificially increased by applying stirring, a second polymorph, corresponding to the thermodynamic product and called thereafter β-polymorph, is progressively formed as shown by the appearance of additional diffraction peaks on the powder diffractogram (Figure III-15, center). This second polymorph was isolated in good yield as large and irregular prismatic crystals by diffusion of methanol into a dichloromethane solution of [Fe($\mathbf{L^2}$)$_2$] complex and found to crystallize in the triclinic *P-1* space group. It is worth noting that a very small fraction of α-[Fe($\mathbf{L^2}$)$_2$] (needles) was systematically obtained after the recrystallization and was separated mechanically from β-[Fe($\mathbf{L^2}$)$_2$] crystals. Following this workup, an analytically pure sample of the β-phase was isolated as

shown by the powder X-ray diffraction, which did not reveal any traces of α-[Fe($\mathbf{L}^2$)$_2$] complex and was found to be in good agreement with the simulated powder pattern (Figure III-15, right).

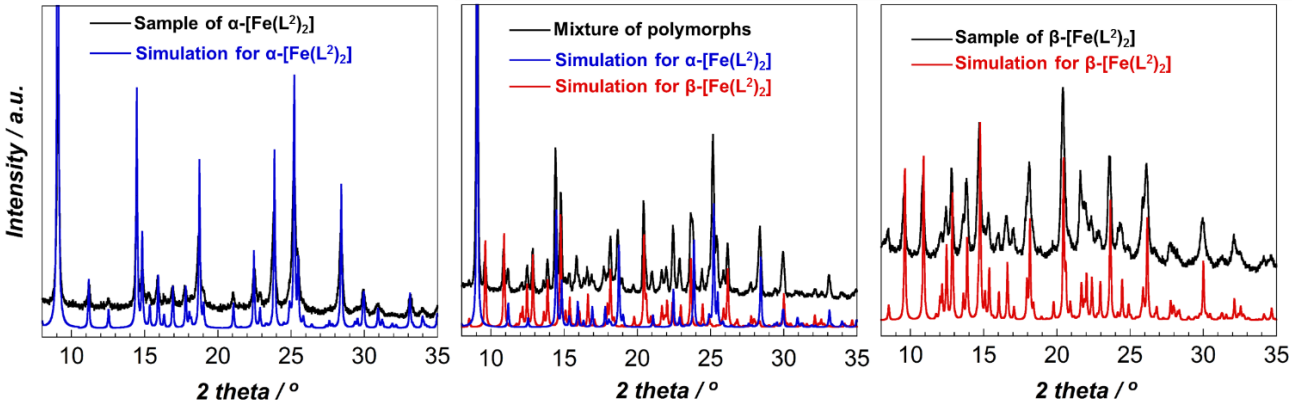

Figure III-15. Experimental and simulated powder diffraction patterns for α-[Fe($\mathbf{L}^2$)$_2$] (left), mixture of α and β polymorphs (center) and β-[Fe($\mathbf{L}^2$)$_2$] (right).

Similarly to [Fe($\mathbf{L}^1$)$_2$] complexes, both polymorphs can be clearly distinguished by FTIR spectroscopy, which reveals differences in the 1800 - 550 cm^{-1} window, while the characteristic absorption bands in the region 1600 - 1580 cm^{-1} and 1350 cm^{-1} ascribed to $\nu_{(C=N-N=C)}$ and $\nu_{(C-O)}$, respectively, are displayed confirming the presence of chelating enolate ligands (Figure S.III-1).

Powdered samples of the polymorphs are olive green and dark green, respectively for α-[Fe($\mathbf{L}^2$)$_2$] and β-[Fe($\mathbf{L}^2$)$_2$], as expected for this type of complexes in the HS and LS configurations, respectively, suggesting once again the strong impact of polymorphism on the Fe(II) coordination sphere and resulting magnetic properties. However, in contrast with previous system, no change of color could be clearly detected upon cooling down to liquid nitrogen temperature (α-phase) or heating up to 400 K (β-phase), presuming the absence of SCO feature in this range of temperatures.

III.2.2.2. Structural description of [Fe($\mathbf{L}^2$)$_2$] polymorphs

Single-crystal X-ray diffraction analyses were performed in order to reveal the differences between the two polymorphs. Views of the complexes collected at 120 K are displayed in Figure III-16 and selected crystallographic data are summarized in Tables III-4, S.III-4 and S.III-5.

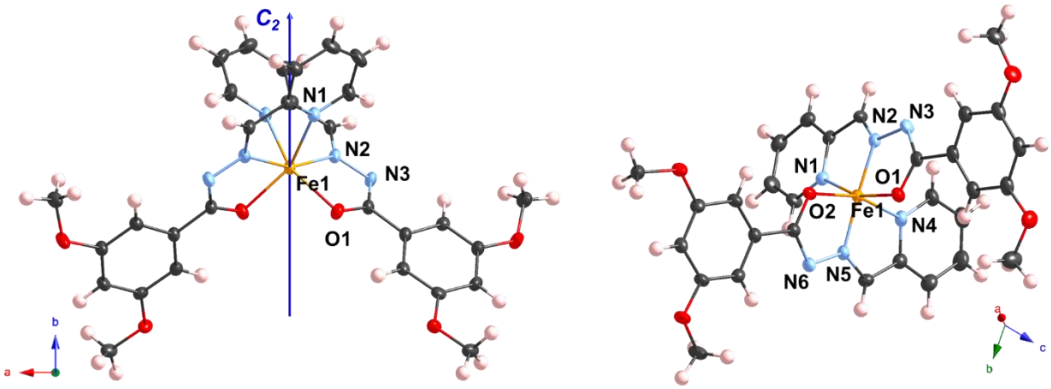

Figure III-16. ORTEP views of α-[Fe($\mathbf{L}^2$)$_2$] (left) and of β-[Fe($\mathbf{L}^2$)$_2$] (right) at 120 K. Thermal ellipsoids are depicted at 50 % probability. Fe orange, O red, C grey, N blue, H light pink.

Table III-4. Crystallographic data for [Fe($\mathbf{L^2}$)$_2$] polymorphs at 120 K.

Compound	**α-[Fe($\mathbf{L^2}$)$_2$]**	**β-[Fe($\mathbf{L^2}$)$_2$]**
Temperature, K	120	120
Crystal system	Monoclinic	Triclinic
Space group	*C2/c*	*P-1*
a, Å	23.0807(7)	9.2954(4)
b, Å	10.8025(3)	12.2093(5)
c, Å	11.8221(2)	13.4330(6)
α, °	90	70.760(2)
β, °	105.654(1)	79.229(2)
γ, °	90	85.841(2)
V, Å^3	2838.3	1413.8
Z	4	2
<Fe-N$_{(py)}$>, Å	2.261	1.954
<Fe-N$_{(im)}$>, Å	2.111	1.866
<Fe-O>, Å	2.112	1.978
Σ(X-Fe-X),[a] °	166.6	83.0

[a] $\sum = \sum_{i=1}^{12} |90 - \varphi_i|$, where φ_i are cis X-Fe-X bond angles with X = O or N

As mentioned above, [Fe($\mathbf{L^2}$)$_2$] polymorphs crystallize in two distinct space groups (*C2/c* and *P-1* for α-and β-phase, respectively). In the same fashion as previous [Fe($\mathbf{L^1}$)$_2$] system, both polymorphs reside in a hexa-coordinated Fe(II) complex surrounding by two anionic ligands in *mer* configuration. Beside this general feature, strong differences between the two polymorphs are displayed at both molecular and packing scale. In the α-polymorph, the two chelating ligands are crystallographically equivalents and related by a 2-fold symmetry axis, which crosses the Fe(II) site along *b*-axis (asymmetric unit composed of a half molecule), while no symmetry is found in the β-form. We should also notice the differences in the rotamer conformations featured by the methoxy groups, which adopt a syn/anti configuration (in respect with the position 4 of the 3,5 dimethoxyaryl moiety) in the case of the α-[Fe($\mathbf{L^2}$)$_2$] complex, while the conformations syn/anti and anti/anti are found in the two non-equivalent ligands of β-[Fe($\mathbf{L^2}$)$_2$] (Figure III-16). Beside these structural aspects, the most fundamental differences occurring at the molecular level, arise from the coordination sphere. Indeed, the Fe-O (2.112 Å), Fe-N$_{(py)}$ (2.261 Å) and Fe-N$_{(im)}$ (2.111 Å) bond lengths featured in α-[Fe($\mathbf{L^2}$)$_2$] complex, clearly indicate that the Fe(II) center is in HS configuration, whereas the average bond distances in the β form were found much shorted (ranging from 1.954 to 1.978 Å) and in fair agreement with the LS configuration. The $\Sigma_{(X\text{-}Fe\text{-}X)}$ distortion parameters for the HS and LS complexes have a value of 166.6° and 83.0°, respectively, and are comparable to those measured in [Fe($\mathbf{L^1}$)$_2$] in the same respective spin configurations. Since the two compounds have the exact same chemical composition, the differences in their magnetic properties displayed by these materials, are necessarily arising from crystal packing effects. However, determining the factors responsible for the stabilization of either diamagnetic or paramagnetic phase is not an easy task. From the multiple and distinct supramolecular interactions present in the crystal lattices, those which are expected to have the strongest effects are described below. In the crystal packing of α-[Fe($\mathbf{L^2}$)$_2$] polymorph, each complex interacts with neighboring molecules *via* multiple π-π interactions, giving rise to a complicate 3D supramolecular network as shown in Figure III-17. Indeed, each

dimethoxyaryl moiety establishes relatively strong π-π interactions with two adjacent molecules through C10···C12 contacts (3.39 Å), forming a zig-zag chain along *a*-axis (see bottom left of Figure III-17). Short π-π contacts of 3.37 Å between C5 and C6 centers are present along *c*-axis, allowing the formation of the 3D assembly (another view emphasizing the formation of a chain along *c*-axis is shown in the bottom right of Figure III-17). Thus, for each molecule eight carbon atoms are involved in π-π overlapping with four neighboring analogues. The FeN_4O_2 coordination sphere is also directly implicated in the supramolecular assembly through weak C-H···O bonds. Each O1 donor atom interacts with H4 and H6 from a neighboring molecule (C4···O1: 3.28 Å; C6···O1: 3.35 Å), participating to the extension of the network along *c*-axis (dashed green lines in Figure III-17).

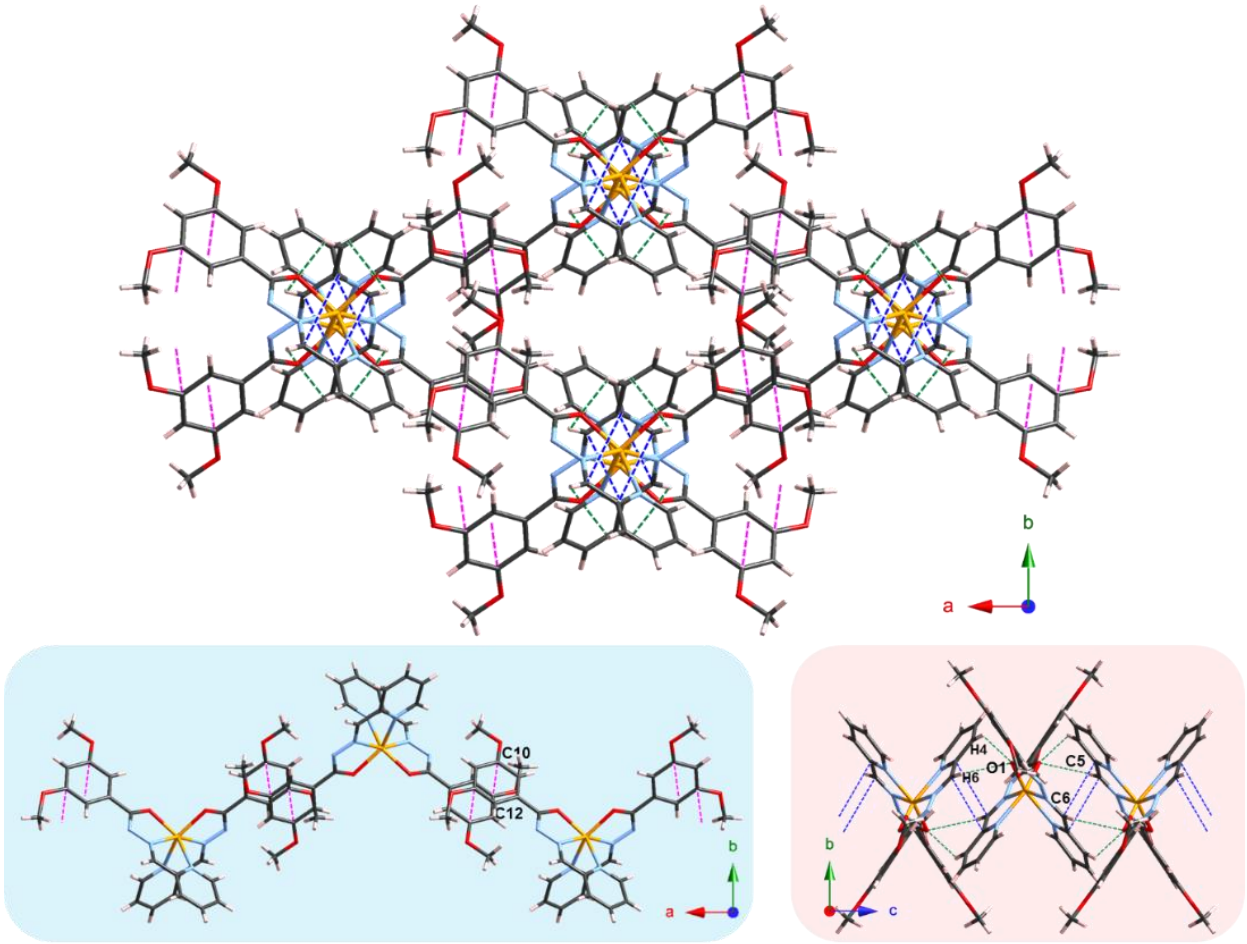

Figure III-17. Crystal packing of α-[Fe($\mathbf{L}^2$)$_2$] emphasizing the 3D supramolecular network formed by π-π and C-H···O(Fe) contacts. C10···C12 contacts are shown in dashed pink lines, C5···C6 contacts in dashed blue lines and C-H···O in dashed green lines. Other weaker interactions are omitted for clarity. Color Figure: Fe orange, O red, C grey, N blue. H, light pink.

In the second polymorph (β), the crystal packing implicates less π-π contacts. Indeed, only the carbon atoms C4 and C10 from each molecule are involved in short contacts with an adjacent complex (C4···C10: 3.22 Å), forming a supramolecular dimer (Figure III-18, left). Each oxygen donor from the coordination sphere forms only one weak C-H···O contact (C21···O1: 3,26 Å; C30···O2: 3.32 Å; Figure III-18, right). The stronger contribution in both π-π and C-H···O(Fe) interactions found in α-polymorph in comparison to

β-form might be responsible for the stabilization of the paramagnetic state even at low temperature, although other short contacts might contribute and explain the differences in behavior between the two complexes.

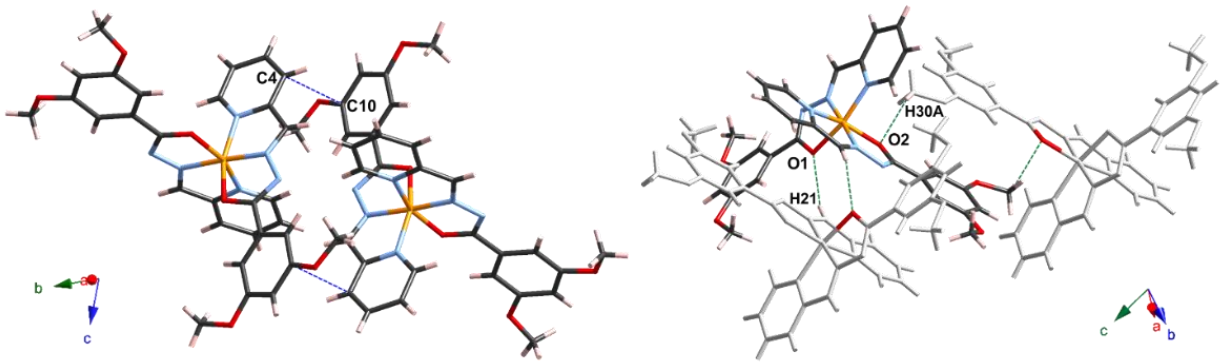

Figure III-18. Crystal packing of β-[Fe($\mathbf{L}^2$)$_2$] emphasizing the supramolecular dimer formed by the π-π contacts (left) and 3D supramolecular network formed by the C-H···O(Fe) interactions (right). Other weaker interactions are omitted for clarity. Color Figure: Fe orange, O red, C grey, N blue.

Single-crystal X-ray diffraction analyses were performed at higher temperature in order to reveal eventual SCO features in β-[Fe($\mathbf{L}^2$)$_2$] polymorph. Selected crystallographic data are gathered in Table III-5 and S.III-5 and their evolution with temperature are plotted in Figure III-19.

Table III-5. Crystallographic data for β-[Fe($\mathbf{L}^2$)$_2$] between 120 and 450 K

Temperature	**120 K**	**300 K**	**390 K**	**400 K**	**450 K**
Crystal system	Triclinic	Triclinic	Triclinic	Triclinic	Triclinic
Space group	*P-1*	*P-1*	*P-1*	*P-1*	*P-1*
a, Å	9.2954(4)	9.3765(3)	9.402(2)	9.3875(6)	9.611(2)
b, Å	12.2093(5)	12.2641(3)	12.415(2)	12.4485(8)	12.544(2)
c, Å	13.4330(6)	13.5941(4)	13.709(2)	13.7215(9)	13.543(9)
α, °	70.760(2)	70.018(1)	69.595(5)	69.609(3)	72.868(7)
β, °	79.229(2)	78.963(1)	78.414(6)	78.233(3)	74.071(7)
α, °	85.641(2)	84.903(1)	83.639(5)	83.296(3)	75.934(7)
V, Å^3	1413.8	1441.5	1467.7	1469.6	1478.0
Z	2	2	2	2	2
<Fe-N$_{(py)}$>, Å	1.954	1.957	2.010	2.035	2.212
<Fe-N$_{(im)}$>, Å	1.866	1.867	1.916	1.938	2.090
<Fe-O>, Å	1.978	1.981	2.001	2.005	2.067
Σ(X-Fe-X),[a] °	83.0	83.9	96.8	102.5	144.9

[a] $\Sigma = \sum_{i=1}^{12}|90 - \varphi_i|$, where φ_i are X-Fe-X bond angles with X = O or N.

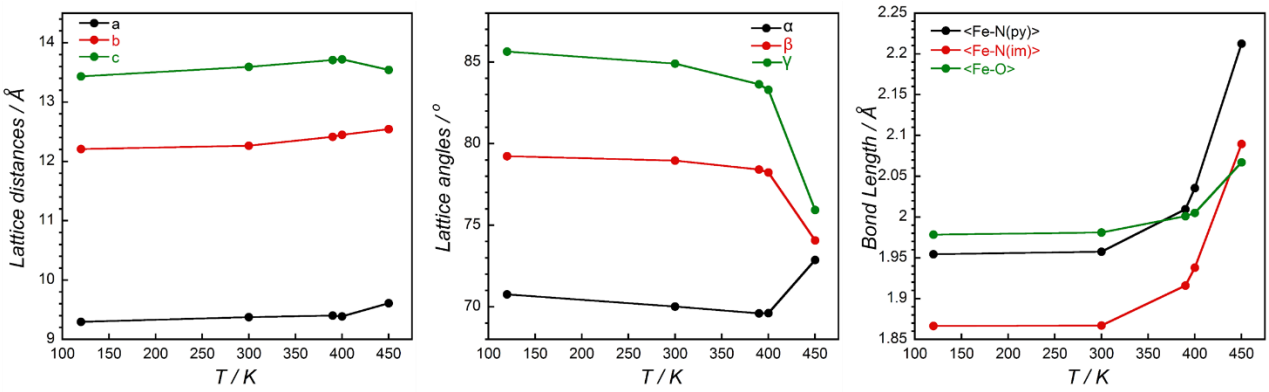

Figure III-19. Evolution of selected crystallographic parameters and coordination bond distances with temperature for β-[Fe($\mathbf{L}^2$)$_2$] complex.

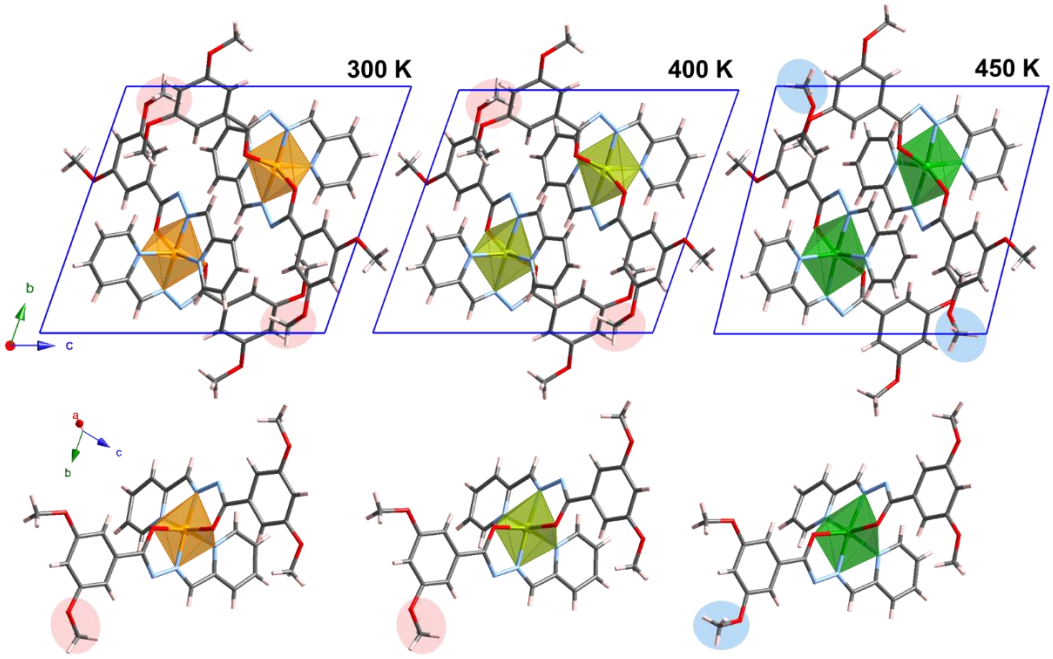

Figure III-20. Crystal packing along the *a*-axis and molecular structure for β-[Fe($\mathbf{L}^2$)$_2$] emphasizing the distortion of the lattice and change of rotamer conformation with temperature: 300 K (left), 400 K (middle) and 450 K (right).

The measurements performed up to 450 K, did not reveal any change of crystallographic space group in the material, which remains in the triclinic *P-1* space group. Similarly, almost no evolution of the *a*, *b* and *c* parameters was detected with temperature, while a moderate increase of the lattice volume (less than 5 %) was found upon heating to 450 K. However, clear changes of the lattice distortion were observed and a substantial increase of α angle was found above 400 K, while the β and γ angle decrease significantly. The distortion of the lattice is unambiguously associated to a SCO phenomenon as shown by the important increase of the Fe-X bond lengths and $\Sigma_{(X\text{-}Fe\text{-}X)}$ parameter. At 450 K, the coordination bond distances are nonetheless shorter than expected in purely paramagnetic materials especially if compared with α-polymorph (*vide supra*). The fully paramagnetic phase could not be reached for this compound since the decomposition was estimated to occur around 480 K by TGA. Similarly to α-[Fe($\mathbf{L}^1$)$_2$] complex, one methoxy group in one of the two ligands changes its conformation during the SCO process from the antiperiplanar configuration to the synperiplanar one (Figure III-20). We should also notice that due to the increase of the coordination sphere and distortion of the lattice, less supramolecular interactions were found in the crystal packing at 450 K. Especially, the distance between C4 and C10 atoms increases from 3.22 to 3.41 Å. Similarly, C30-H30···O2 interaction was found weaker (C30···O2: 3.41 Å), while C21-H21···O1 contact found previously cannot be deduced in the present case.

III.2.2.3. Magnetic properties

Temperature-dependent magnetic susceptibility measurements were performed to confirm the behavior of the two polymorphs (Figure III-21).

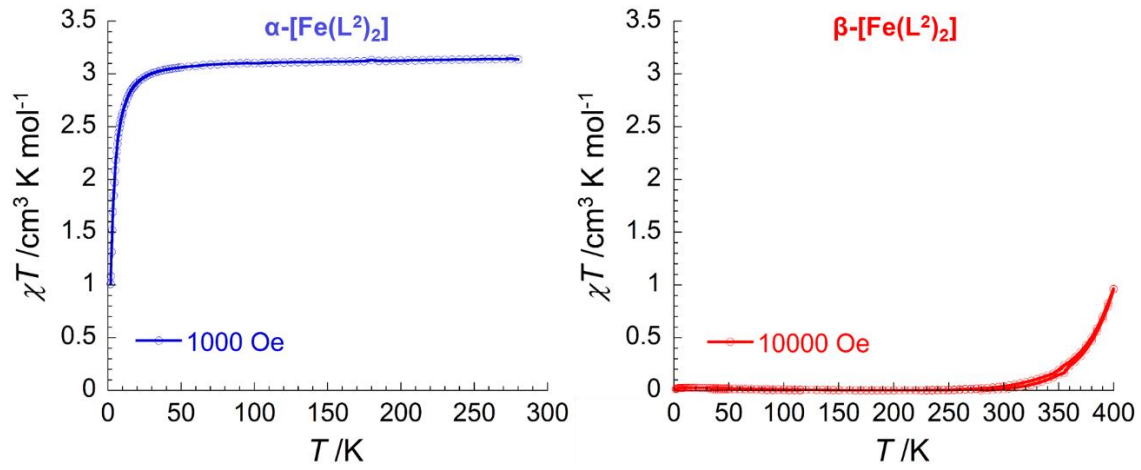

Figure III-21. Temperature dependence of the χT product for α-[Fe($\mathbf{L}^2$)$_2$] (left) and β-[Fe($\mathbf{L}^2$)$_2$] (right). Sweep rate: 1.3 K/min.

In agreement with X-ray crystal structure, no SCO feature was detected for α-[Fe($\mathbf{L}^2$)$_2$] complex, which exhibits a typical Curie-Weiss paramagnetic behavior. The χT product is ca. 3.15 cm^3 K mol^{-1} down to about 30 K, where it drop to 1.0 cm^3 K mol^{-1} due to antiferromagnetic interactions within the crystal packing or magnetic anisotropy on the Fe(II) site. It is worthwhile to mention that no transition was detected by magnetic and calorimetric measurements at higher temperatures (up to 400 K for squid measurements and 473 for DSC measurements), indicating that the complex is thermodynamically stable (no conversion toward the β-form is possible). The sample of β-[Fe($\mathbf{L}^2$)$_2$] polymorph was found to be purely diamagnetic up to about 300 K as shown by the χT product of ca. 0.02 $cm^3 \cdot$ K$\cdot mol^{-1}$ (Figure III-22, left). This value confirms that the α-polymorph formed as an impurity during the recrystallization in CH_2Cl_2/MeOH, was efficiently removed (*vide supra*). Above 300 K, the χT product increases gradually to reach 1.1 $cm^3 \cdot K \cdot mol^{-1}$, revealing the onset of SCO behavior in agreement with XRD analysis at 400 K. Preliminary investigations were performed at higher temperatures using vibrating sample magnetometer (VSM). The measurements revealed that the thermally-induced SCO behavior is actually more complex than we expected and remains not clearly understood. On the first heating from 300 K to 450 K, an incomplete two-step SCO is observed as shown by the presence of two peaks at 397 and 421 K on the plot of χT product derivative (Figure III-22, inset). The high-temperature plateau, reached at ca. 433 K, has a value of ca. 2.62 $cm^3 \cdot K \cdot mol^{-1}$, which is quite far from expected value for a purely paramagnetic phase, confirming the relatively short coordination bond distances (for an Fe(II) HS site) found at 450 K. In fact, assuming that the χT product and bond lengths for pure HS phase should be close to those recorded in the α-form and taking this as reference, a good correlation between the magnetic and crystallographic data can be found in β-[Fe($\mathbf{L}^2$)$_2$]. The correlation between the temperature-dependent χT and <Fe-$N_{(py)}$> is shown as an example in Figure III-22 (right). Therefore, we can estimate that about 20 % of the species remain in the LS configuration at 450 K.

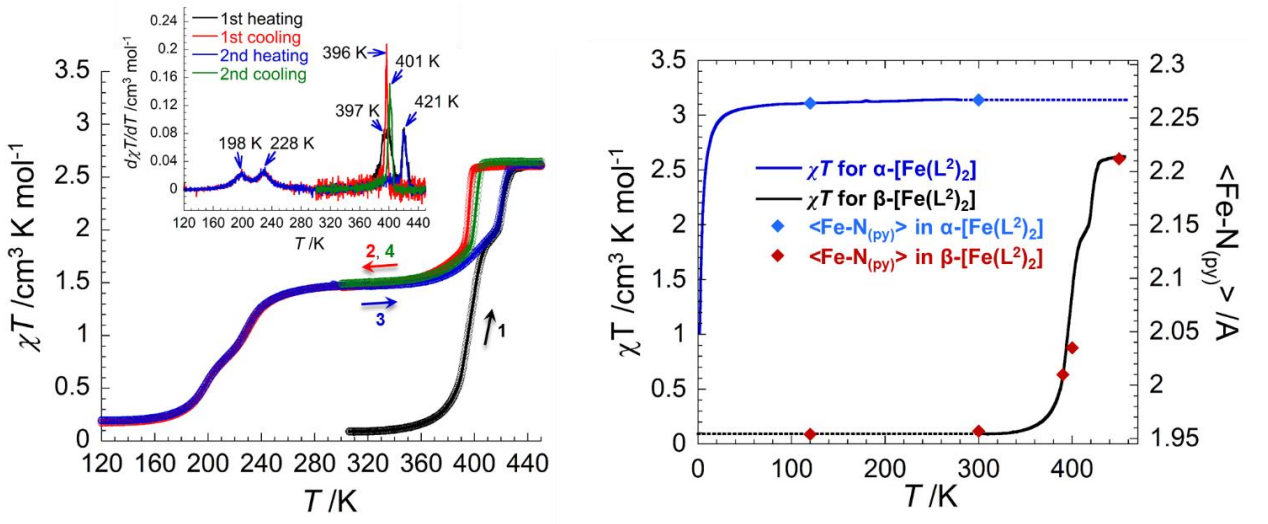

Figure III-22. (left). Temperature dependence of the χT product for β-[Fe($\mathbf{L}^2$)$_2$] at 10000 Oe (sweep rate: 10 K/min). inset: derivative of χT product as function of the temperature. (right) Temperature dependence of χT product and average Fe-$N_{(Py)}$ bond distances for α-[Fe($\mathbf{L}^2$)$_2$] and β-[Fe($\mathbf{L}^2$)$_2$] polymorphs.

Upon the first heating, the behavior is not reversible. On cooling, a sharp transition is observed at 396 K, giving rise to a thermal hysteresis of about 24 K. However, the material does not return into the diamagnetic phase and reaches instead a plateau at ca. 390 K, which corresponds to a new phase containing both HS and LS species in approximatively equal proportion (χT = 1.48 cm^3 K mol^{-1}). Below ca. 240K, a gradual and stepwise conversion into an almost pure diamagnetic phase is observed. On second thermal cycle, the behavior is found perfectly reversible, confirming a three-step SCO process, which includes one hysteretic spin transition in high-temperature range. Nonetheless, this result should be taken with care. Indeed, one attempt to probe the thermal behavior by Mössbauer spectroscopy was performed and did not reflect perfectly the previous magnetic measurements. The Mössbauer spectrum performed at 298 K after a thermal treatment at 450 K (for 30 min), confirmed that the material does not return in the diamagnetic phase, but the HS/LS ratio was 4/1 instead of 1/1 as expected (Figure III-23). Further investigations including temperature dependent single-crystal and powder X-ray diffraction measurements need to be performed on the complex to confirm and better understand the behavior.

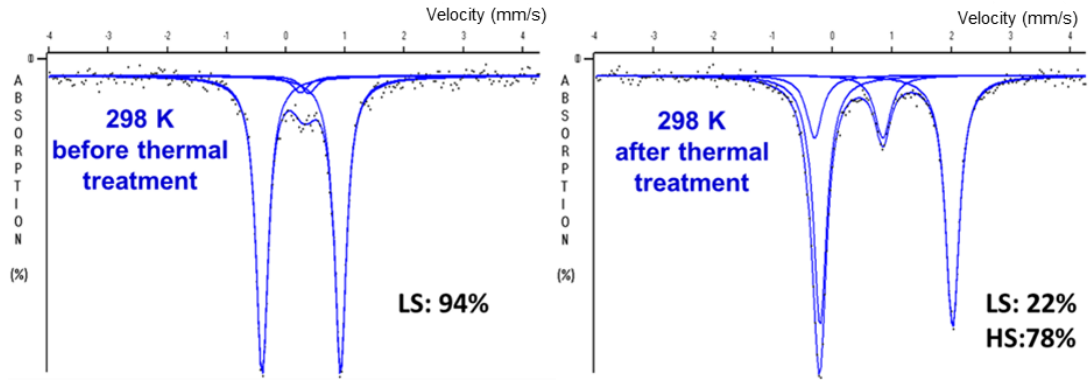

Figure III-23. Mössbauer spectra for β-[Fe($\mathbf{L}^2$)$_2$] at 298 K (left) and 298 K after thermal treatment at 450 K.

III.2.3. Synthesis and properties of [Fe(L^3)$_2$]

III.2.3.1. Synthesis and structural description

Complex [Fe(L^3)$_2$] can be obtained in the similar fashion as previous samples described in the chapter, using a slightly modified crystallization procedure. Indeed, no single-crystal could be isolated by direct crystallization in methanol, and the material was recovered as a microcrystalline powder. Thus, a recrystallization was performed by methanol diffusion into a solution of complex in dichloromethane and the compound was obtained in good yield as dark green plate-like crystals. The complex was found to crystallize in the monoclinic *P2$_1$/n* space group, in which the assymetric unit is composed of one hexa-coordinated [Fe(L^3)$_2$] complex co-crystallized with one molecule of methanol. A view of the structure is given in Figure III-24 (left) and selected crystallographic data are summarized in Table III-6 (detailed data can be found in Table S.III-6 as supporting material).

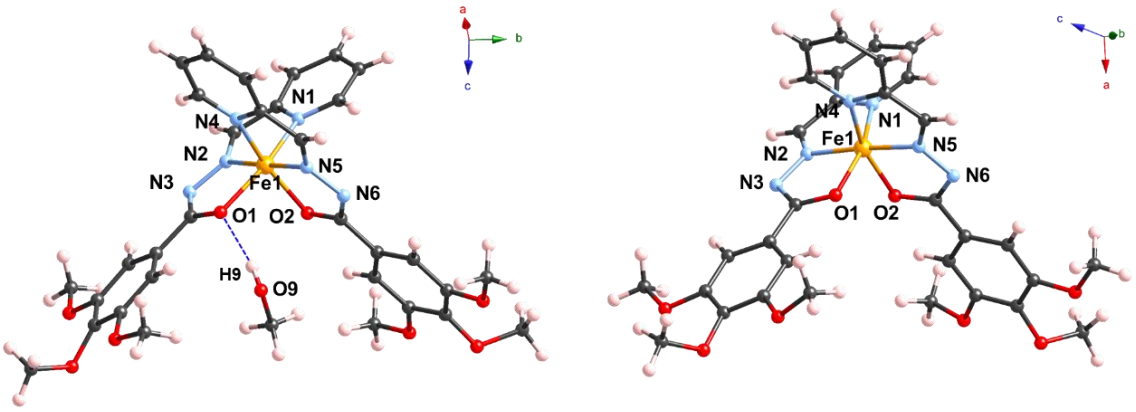

Figure III-24. Crystal structure of [Fe(L^3)$_2$]·MeOH complex (left) and solvent-free [Fe(L^3)$_2$] complex (right) at 120 K. Color Figure: Fe orange, O red, C grey, N blue, H light pink.

Table III-6. Crystallographic data for [Fe(L^3)$_2$]·MeOH and [Fe(L^3)$_2$] complexes at 120 K.

Compound	**[Fe(L^3)$_2$]·MeOH**	**[Fe(L^3)$_2$]**
Temperature, K	120	120
Crystal system	Monoclinic	Triclinic
Space group	*P2$_1$/n*	*P-1*
a, Å	9.1200(4)	10.720(2)
b, Å	25.3030(10)	12.981(3)
c, Å	15.1708(6)	13.188(2)
α, °	90	102.214(9)
β, °	102.552(2)	113.967(8)
γ, °	90	90.034(9)
V, Å^3	3417.2	1631.3
Z	4	2
<Fe-N$_{(py)}$>, Å	1.955	1.934
<Fe-N$_{(im)}$>, Å	1.866	1.854
<Fe-O>, Å	1.972	1.969
Σ(X-Fe-X),[a] °	81.0	78.4

[a] $\Sigma = \sum_{i=1}^{12}|90 - \varphi_i|$, where φ_i are cis X-Fe-X bond angles with X = O or N

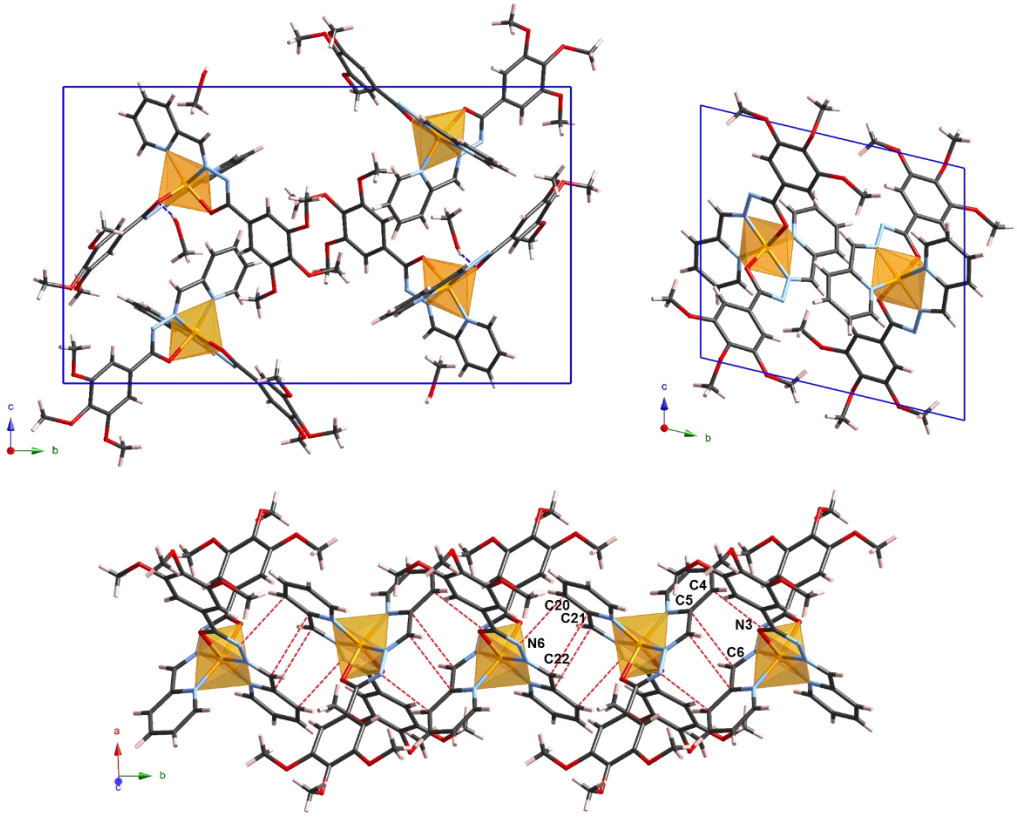

Figure III-25. (top) Projection of the crystal packing viewed along *a*-axis for [Fe($\mathbf{L}^3$)$_2$]·MeOH complex (left) and solvent-free [Fe($\mathbf{L}^3$)$_2$] complex (right). (Bottom) Projection of crystal packing of [Fe($\mathbf{L}^3$)$_2$] emphasizing the π-π interactions along *b*-axis.

The methanol molecule establishes a hydrogen bond with the complex *via* one of oxygen atom from the coordination sphere (O1···O9 = 2.83 Å), as found previously in β-{[Fe($\mathbf{L}^1$)$_2$]·MeOH} (Figure III-3). At 120 K, the compound is diamagnetic as shown by the Fe-X bond distances ranging from 1.860 to 1.979 Å, and $\Sigma_{(X\text{-}Fe\text{-}X)}$ distortion parameter, 81.0°, which are comparable to previous analogues in same spin configuration. The unit cell was checked at 400 K, and was exactly the same as at low temperature, showing that no SCO process is occurring and also that the methanol molecule is preserved in the structure. Unfortunately, no measurement could be achieved at higher temperature, due to the desolvation process which affect dramatically the quality of the crystal. Additional attempts to remove the methanol molecule in a soften fashion, were performed using lower temperature with reduced pressure conditions but in all cases no crystal of enough quality could be obtained. A solvent-free version of the complex was obtained by recrystallization, using diethyl ether diffusion into a dichloromethane solution of complex. The compound was isolated in low-yield as tiny dark green plates and found to crystallize in the triclinic *P-1* space group (Figure III-24 right, Tables III-6 and SIII-6). The molecules inside the crystal packing are arranged in a complete different manner comparing to the solvated form as shown in Figure III-25. Especially, while no π-π contact is present in the [Fe($\mathbf{L}^3$)$_2$]·MeOH, a strong π-π stacking is displayed in the solvent-free structure. Thus, each molecule interacts with two adjacent complexes by C···C and C···N contacts of 3.22 to 3.35 Å, giving rise to a supramolecular chain along *b*-axis. Nevertheless, despite these strong differences of the packing, no significant change is observed in the coordination sphere, which is once again consistent with LS

configuration at 120 K and no evolution of the unit was detected up to 400 K, suggesting no SCO feature in this material.

III.2.3.2. Thermal and magnetic behavior

As seen earlier in the structure of [Fe($\mathbf{L}^3$)$_2$]·MeOH, the methanol molecule interacts strongly with the lattice *via* the hydrogen bond and additional weak C-H···X (O, π) short contacts, in such a way that no desolvation was observed by X-ray diffraction analysis up to 400 K. Thermogravimetric measurements were performed to confirm the stability of the compound and determine at which temperature the loss of methanol molecule occurs. The thermogram shown in Figure III-26 (left), reveals only minor weight loss up to ca. 420 K, while an abrupt decrease corresponding to 5.5 % is observed between 420 and 430 K, in good agreement with the removal of one methanol molecule. The desolvated complex remains stable at this range of temperature (decomposition occurring at about 500 K), giving then the opportunity to probe eventual SCO features in this desolvated material.

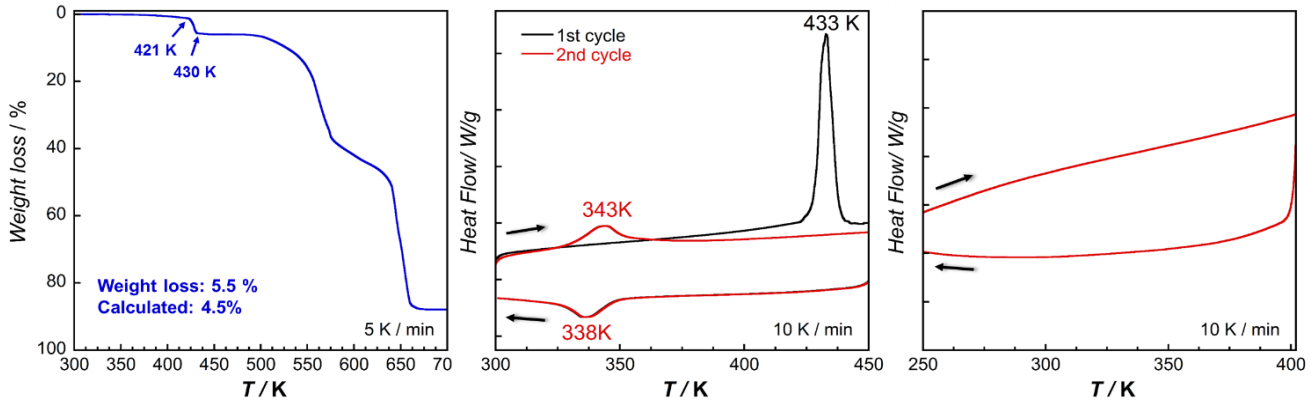

Figure III-26. (left) TGA data for [Fe($\mathbf{L}^3$)$_2$]·MeOH complex. (center) DSC thermogram for [Fe($\mathbf{L}^3$)$_2$]·MeOH complex. (right) DSC thermogram for solvent-free [Fe($\mathbf{L}^3$)$_2$] complex obtained by crystallization (Et_2O diffusion).

DSC measurement performed on [Fe($\mathbf{L}^3$)$_2$]·MeOH complex revealed an highly energetic endothermic peak (ΔH = 36 kJ/mol) at 433 K, which is compatible with a phase transition induced by the loss of the methanol molecule based upon TGA analysis (Figure III-26, center). After desolvation, the material displayed a reversible broad signal around 340 K, suggesting the occurrence of a spin crossover. This is supported by the ΔS value of ca. 20.7 J/mol·K, which is in the range of values found in the compounds reported earlier in the chapter. Interestingly, this reversible process could not be deduced in the DSC of the solvent-free complex obtained by recrystallization (using diethyl ether diffusion, *vide supra*), which remains silent up to 400 K (Figure III-26, right), confirming the absence of SCO feature predicted by XRD. This result indicates that the samples produced by the two different methods (crystallization *vs.* desolvation), are structurally distinct and therefore polymorphs from each other. This might explain the strong differences found between the X-ray structures of solvated and solvent-free complexes. Some minor differences between the two solvent-free samples were revealed by FTIR (see Figure S.III-2), although additional measurements including powder X-ray diffraction analysis must be performed to confirm unambiguously polymorphism in these materials.

The scenario suggested by DSC experiments, was confirmed by magnetic susceptibility measurements. The χT product for [Fe($\mathbf{L}^3$)$_2$]·MeOH as function of the temperature, recorded between 1.8 and 450 K with an applied *dc* field of 10000 Oe, is shown in Figure III-27. During the first heating, an abrupt and complete spin transition from the diamagnetic phase (χT = 0.01 cm^3·K·mol^{-1}) to the paramagnetic one (χT = 3.26 cm^3·K·mol^{-1}) is observed around 407 K at which the desolvation process happens. This indicates that the structural changes induced by the methanol loss affect significantly the Fe(II) coordination sphere stabilizing therefore the HS configuration. As expected from DSC data, the desolvated material exhibits a complete SCO for which the $T_{1/2}$ can be estimated at 344 K from the derivative of the χT *versus* temperature plot (Figure III-28). Thus, this result highlights once again the strong influence of the crystal packing on the magnetic properties of the complex.

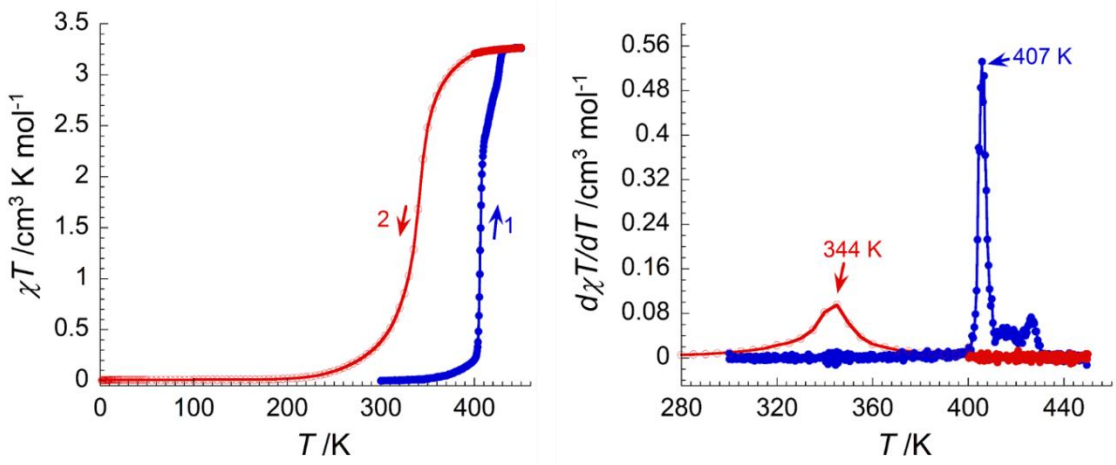

Figure III-27. (left) Temperature dependence of the χT product for [Fe($\mathbf{L}^3$)$_2$]·MeOH with an applied *dc* field of 10000 Oe. (right) dχT/dT *vs.* T plots. Full symbols: data measured on VSM magnetometer at 5 K/min. Empty symbols: data measured on SQUID magnetometer at 1.3 K/min.

The magnetism of the solvent-free complex obtained directly by crystallization could not been studied so far, as we did not obtained a sufficient amount of the material to perform all the measurements and its preparation was found not very easy to reproduce (most of the time only precipitate was formed). However, taking into account the DSC performed up to 450 K, the single-crystal X-ray diffraction checked up to 400 K and the absence of color change, we are quite confident that the material does not display any SCO feature up to decomposition.

III.2.4. Summary and concluding remarks

In the first part of the chapter, we described the synthesis, structural and magnetic characterizations of a series of mononuclear Fe(II) complexes based on pyridylbenzohydrazone ligands functionalized with one to three methoxy groups. Our initial concern was to verify if the addition of these donating groups would fulfill the electronic requirements for SCO, before going further on the functionalization with long alkyloxy chains (assuming that the donating character of these functionalized ligands is about the same as a methoxy). From our study, we can conclude that the presence of methoxy functions on the benzohydrazide scaffold is not incompatible with SCO, since such features were displayed for complexes based on the three ligands.

However, the SCO characteristics are strongly dependent on the way the molecules are organized in solid-state and on the solvation and therefore SCO phenomenon was not systematically observed.

The main interesting achievement of this work has been the discovery of polymorphism in these molecular systems. Indeed, polymorphism in SCO materials has received much interest over the recent years since they give the opportunity to better understand (or at least to emphasize) the role of crystal packing and supramolecular interactions on SCO phenomenon, which includes effects on the SCO temperature and cooperativity. The first example of polymorphic SCO was reported by Köning and co-workers on the very well-known $[Fe(phen)_2(NCS)_2]$ complex (phen = phenanthroline).[20] Despite thousands of new SCO materials developed since then, only relatively few of them have shown the ability to exist in two or more crystalline forms.[21] Also, most of the time, polymorphs are obtained as mixtures, in such a way that it is not always possible to separate them efficiently and then to perform a full investigation of their respective properties.[22] Except for the raw sample of β-$[Fe(\mathbf{L^2})_2]$ complex that contained small fraction of the β-form and needed mechanical separation, we developed synthetic procedures to isolated all the other polymorphs as pure samples. We should emphasize that the isolation of pure fractions of each $[Fe(\mathbf{L^1})_2]$·MeOH polymorph by applying different synthetic procedures, was essential since the crystals of the two polymorphic forms have the same morphology and color (at least by eyes) and it would be not possible to separate them in case of a mixture. For this complex, we have seen that a transformation from the kinetic to the thermodynamic phase can occur in the mother liquor upon a thermal activation. To the best of our knowledge, the observation of such transformation has been reported only in one other system, namely $[Fe(tpa)(NCS)_2]$ (with tpa = *tris*-(pyridylmethyl)amine), which is converted successively into two polymorphs when soaked in DMF/water mixture for a long time (one month).[23] An evolution of the α-phase into β-phase with time was evidenced in $[Fe(\mathbf{L^2})_2]$, but we found that the change of crystallization solvents was a better option to isolate the two different polymorphs. $[Fe(\mathbf{L^3})_2]$ polymorphs were obtained fortuitously using a different approach involving in one hand the formation of a the solvent-free complex by crystallization and in the other hand by desolvation of $[Fe(\mathbf{L^3})_2]$. This strategy have been already successfully employed to produce polymorphs of different SCO systems such as recently reported by Aromí and co-workers on $[Fe(1,3\text{-bpp})_2](ClO_4)_2$ complex (1,3-bpp = 2-(pyrazol-1-yl)-6-(pyrazol-3-yl)-pyridine).[24] It should be mentioned that one other example of pyridylbenzohydrazide-based $[Fe(L)_2]$ complex (L = (E)-2-hydroxy-N'-(1-(pyridin-2-yl)propylidene)benzohydrazide) is known.[25,26] Unfortunately, no synthetic, crystallographic or magnetic data for these materials are available (published on a PhD thesis[25]) and only computational calculations predicting the critical temperatures of the two polymorphs were published.[26]

As in many other systems,[27] only one of the polymorphs exhibits SCO feature in the case of $[Fe(\mathbf{L^2})_2]$ and $[Fe(\mathbf{L^3})_2]$, highlighting the strong impact of the supramolecular organization (in solid-state) on the SCO phenomenon. Most spectacular properties were found in the desolvated $[Fe(\mathbf{L^1})_2]$ polymorphs that both showed spin transition at very different temperatures (ΔT ~ 100 K) and with wide hysteresis of 38 K (α-form) and 27 K (β-form) at 0.3 K/min. To the best of our knowledge only one other example, namely $[Fe(L^{Me})(NCS)_2]$ (L^{Me} = *N,N'*-bis[(1-methyl-1,2,3-triazol-4-yl)methylene]propane-1,3-diamine), was reported to exhibit hysteretic spin transition for both isolated polymorphs and the hysteresis width did not

exceed 7 K for high sweeping rates.[28] When possible, we have shown the critical differences that are displayed on the crystals packing and we have attempted to identify the main factors responsive to their magnetic behaviors. Remarkably the three structures that feature the highest number of π-π contacts (β-{[Fe($\mathbf{L^1}$)$_2$]·MeOH}, α-[Fe($\mathbf{L^2}$)$_2$] and solvent-free [Fe($\mathbf{L^2}$)$_2$] complexes) do not exhibit SCO feature suggesting that the proliferation of such interactions in the packing might create a certain stress to the molecules that need to expand or contract during the SCO process. However, taking into account the multiple and complex intermolecular interactions existing in these molecular materials, the discussion remain only qualitative and should be supported by deeper investigations including computational calculations.

III.3. Functionalization of FeN_4O_2 complexes with alkyl chains

As described in the first part of the chapter, the strong impact of the crystal packing on SCO phenomenon reinforced our conviction that these molecular systems are interesting candidates for the development of metallomesogens or at least soft systems with low-melting temperature. Indeed, we can expect that a crystal-to-mesophase phase transition and resulting changes on the self-organization might affect significantly Fe(II) coordination sphere and eventually provoke spin switching. Interplays between the SCO phenomenon and a matter phase transition has been actually shown very recently by Real and co-workers on a series of pyridylbenzohydrazide-based complexes functionalized with strongly lipophilic groups.[15] Although non-mesogenic, these materials melt at low temperature and a change of the spin configuration was systematically observed during the transition into the liquid phase. The natural thermal hysteresis existing between the melting and crystallization (first order phase transition) was reflected on the spin crossover phenomenon, which was then revealed as a hysteretic process, which is strongly dependent of the scan rate. It is worth to recall that interplays between the SCO process and crystal-to-mesophase transitions have been previously described, notably on [Fe(RTrz)$_3$](X)$_2$ systems (RTrz = 4-substituent-1,2,4-trizole; X = nonovalent anions).[9,10] Furthermore, the introduction of flexible alkyl chains might also give rise to unconventional magnetic behaviors such as thermally-induced reverse-SCO (ie. conversion from HS into LS by increasing the temperature) as shown by Hayami and co-workers on [Co(C*n*-terpy)$_2$](BF$_4$)$_2$ (C*n*-terpy = 4'-alkyloxy-2,2':6',2''-terpyridine, *n* = 14, 16).[29]

During this work, our attempts to produce metallomesogens mainly relied on the functionalization of the benzohydrazyde moiety by one to three long alkyl chains. This strategy was unfortunately unsuccessful to promote the desired liquid crystalline features but the interesting effects of the functionalization on thermo-structural and thermo-magnetic behaviors are discussed in this part of the chapter.

III.3.1. Synthesis of ligands and [Fe($\mathbf{L^{4-8}}$)$_2$] complexes

Five ligands containing one to three dodecyl or octadecyl chains were targeted during this work and were prepared by a three-step synthesis (Scheme III-6). The non-commercial **1d-g** precursors were obtained accordingly to procedures described in Chapter II, by a Williamson coupling with the corresponding alkyl bromide. Then, the same sequential steps and reaction conditions used for the preparation of analogues with

methoxy functions were employed for the synthesis of the five **HL$^{4-8}$** ligands. Their respective complexes were obtained in same fashion as previously described with only slight modifications of the synthetic procedure. Indeed, when reactions were performed at room temperature, the raw samples systematically contained unreacted free-ligand, which could not be separated efficiently from desired compounds. Reactions were thereafter carried out in methanol at 60 °C for 2 hours and products were recovered as green powders after cooling to room temperature.

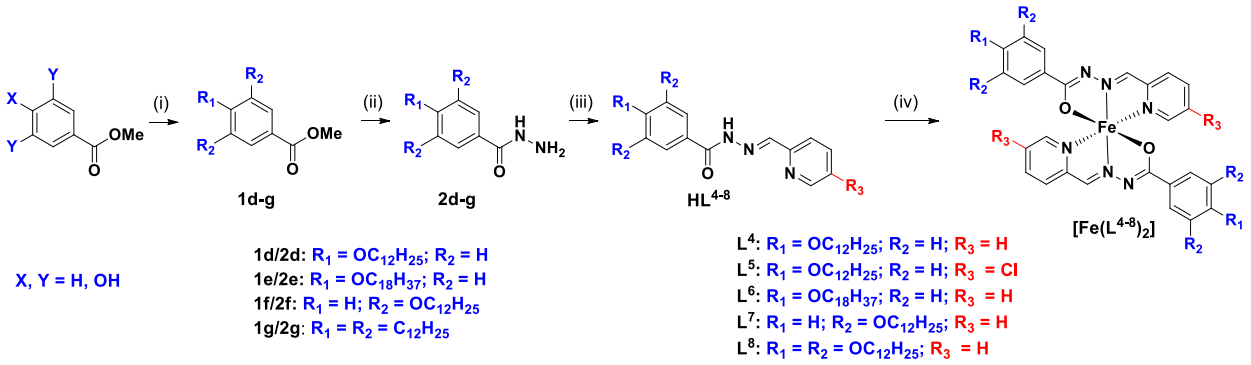

Scheme III-6. General pathway for the synthesis of N'-(pyridin-2-ylmethylene)benzohydrazide ligands and complexes. Conditions: (i) $C_nH_{2n+1}Br$, K_2CO_3, butanone, reflux, 16h. (ii) $N_2H_4{\cdot}H_2O$, EtOH, reflux, 16h. (iii) 2-pyridinecarboxaldehyde or 5-chloropicolinaldehyde, RT, MeOH, 16h. (iv) $Fe(ClO_4)_2{\cdot}6H_2O$, NEt_3, MeOH, 60°C, 2h.

The purity of the samples was verified by elemental analysis and FTIR, which show the characteristic signatures for chelating enolate ligands around 1600-1580 cm^{-1} ($\nu_{(C=N-N=C)}$) and 1360 cm^{-1} ($\nu_{(C-O)}$) and did not reveal any sign of free-ligand ($\nu_{(C=O)}$ expected around 1640 cm^{-1}). As seen in Chapter II, the presence of dodecyl chains can be also clearly identified by the strong double band around 2900 cm^{-1} attributed to C-H stretching vibrations. Confirmation of the structure by single-crystal X-ray diffraction analysis was also possible in the cases of [Fe(**L^4**)$_2$] and [Fe(**L^5**)$_2$] complexes and their structural descriptions are discussed later in the chapter.

III.3.2. Properties of [Fe(L^4)$_2$] complex

III.3.2.1. Thermo-structural features

As we first thought that it would be not possible to isolate crystals of [Fe(**L^4**)$_2$] complex due to flexible dodecyl chains, we mainly focused our investigations on microcrystalline powder samples. The thermal behavior was thereafter confirmed by X-ray diffraction studies on single-crystals. The compound was first checked for liquid crystalline properties by POM, DSC and SAXS measurements. The absence of liquid crystalline feature in this material was rapidly evidenced by POM analysis. The melting was detected around 475 K, as illustrated by the formation of black isotropic phase observed in crossed polarizers mode (Figure III-28).

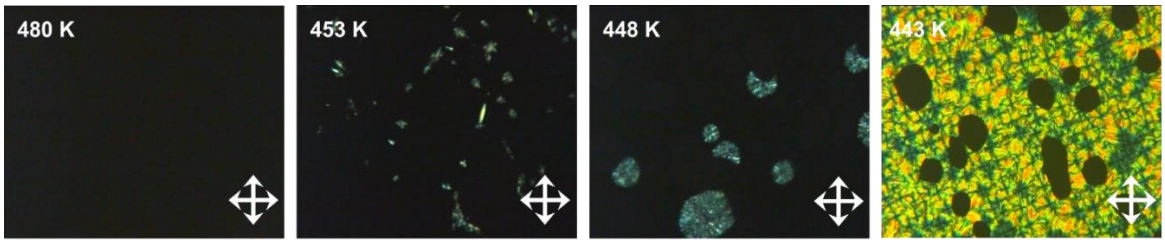

Figure III-28. Optical micrographs for [Fe($\mathbf{L^4}$)$_2$] (in crossed polarizers mode), showing the growth of crystalline birefringent textures during the cooling from isotropic liquid phase.

During the cooling, the reappearance of birefringence was detected around 450 K. The growth from limited focal points (defects) and aspect of birefringent textures was clearly indicative of crystalline materials. This is also supported by the large thermal hysteresis observed between the melting and crystallization. Upon cooling down to room temperature, no significant change of the texture could be perceived and the material remains as a homogeneous thin film.

DSC measurements were performed in order detect an eventual transition associated to a SCO process. Unexpectedly, in addition to the melting point found at 474 K, two phase transitions at 337 and 432 K were observed during the first heating, indicating that the material exists successively in three crystalline forms (noted Cr1, Cr2 and Cr3 in Figures III-29).

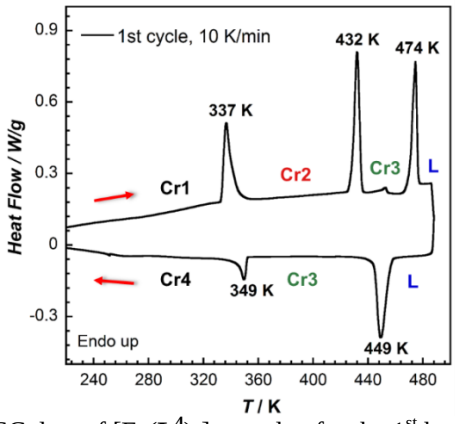

Figure III-29. DSC data of [Fe($\mathbf{L^4}$)$_2$] complex for the 1st heating/cooling cycle.

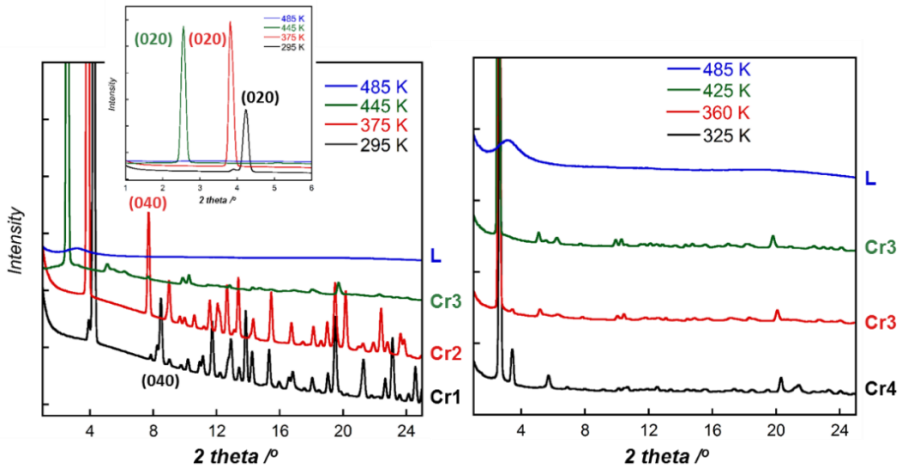

Figure III-30. SAXS profiles for [Fe($\mathbf{L^4}$)$_2$] on 1st heating (left) and 1st cooling (right).

The SAXS profiles corresponding to the different phases are shown in Figure III-30 (left). The first two phases were found to be highly crystalline. A lamellar order corresponding to the separation distance

imposed by the dodecyl chains between the layers of metal centers can be clearly identified and was indexed with *0k0* Miller indices based upon crystal structure (*vide infra*). Thus, an increase of the interlayer distance *d* from 20.9 to 23.1 Å is displayed after transition into Cr2 phase. The second phase transition involves deeper changes of the organization. The material become poorly crystalline and the interlayer distance increase significantly to 34.5 Å (see Cr3 on Figure III-30 left). This result can be either explained by a lower interdigitating of the aliphatic chains or change of bent geometry of the complex (*vide infra*). Upon the first heating, the behavior is not reversible as shown by the presence of only two transitions on the cooling. The transition observed at 449 K corresponds to the crystallization into Cr3 phase based on SAXS diffractograms. However, the material does not return into Cr2 phase but undergoes into a new crystalline phase at 349 K (noted Cr4 in Figure III-30, right). The SAXS profile of this latter is almost the same as Cr3 phase, indicating that only minor sub-structural changes occurs, which seems reasonable considering the low-enthalpy value recorder during the transition (ΔH = 5.5 kJ/mol). It is important to mention that the irreversible behavior is not consecutive to a decomposition process as often observed in mesogenic SCO systems.[6] Indeed, the material remains homogeneous in aspect and color upon heating up to 485 K, while TGA measurements did not revealed significant weight loss below 520 K (Figure S.III-6). In addition, the FTIR spectrum after the thermal treatment displays the same characteristic signatures for chelating ligands, even though minor differences could be detected in the overall spectrum due to important changes in the packing organization. Finally, DSC performed on additional cycles did not revealed any evolution in term of temperature and enthalpy values for the reversible interconversion between the two crystalline phases (Cr3 and Cr4) and melting/crystallization transitions (Figure S.III-7). In fact, these results suggests that the Cr1 and Cr2 phases are related to a kinetic product inherent to the synthetic conditions employed, which is then converted at 432 K into a thermodynamic one, as found before in other SCO systems.[30] Assuming that, we suggested that the thermal behavior might be reversible if the temperature is maintained below the second transition. To verify this hypothesis a new set of DSC and SAXS measurements were performed up to 375 K (Figure III-31). In these conditions, DSC revealed only one endothermic transition at ca. 340 K in heating and the corresponding exothermic transition around 320 K on cooling mode (Figure III-31, left).

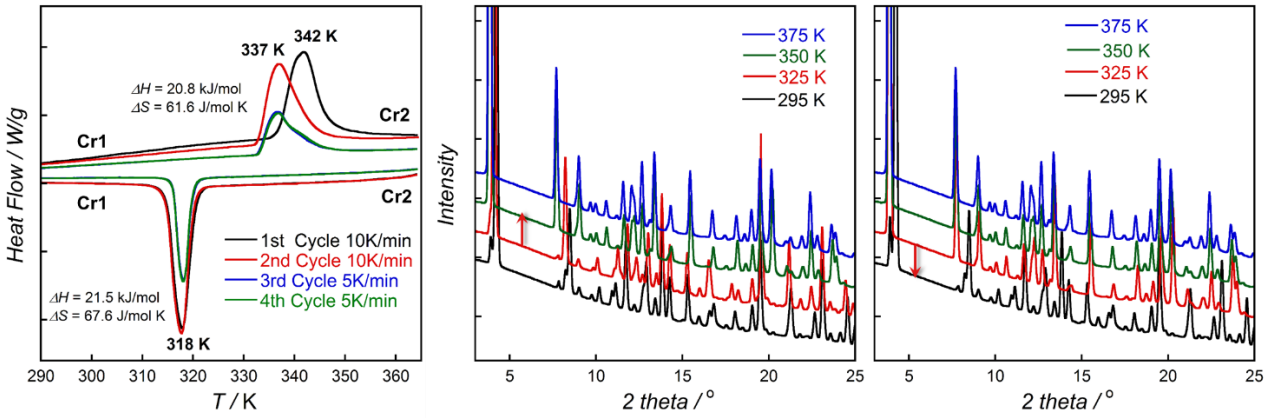

Figure III-31. (left) DSC thermogram for [Fe($\mathbf{L}^4$)$_2$] between 290 and 365 K. (center) SAXS profile for [Fe($\mathbf{L}^4$)$_2$] on heating from 295 to 375 K (2nd heating). (right) SAXS profile for [Fe($\mathbf{L}^4$)$_2$] on cooling from 375 to 295 K (2nd cooling).

SAXS measurements confirmed that the transition at ca. 320 K observed during the cooling corresponds to the return into Cr1 phase (Figure III-31, center and right). It is worth to note that the organization in Cr1 phase is slightly temperature-dependent, showing notably an increase of interlayer distance, while no change with temperature could be perceived within Cr2 phase. No significant evolution of the thermograms could be detected over cycling (same enthalpy values) confirming the stability of the material and reversibility of its thermal behavior in the range of temperature tested. We should nonetheless mention that a slight shift of the transition temperature is observed between the 1st and 2nd cycles, which can be explained by minor structural rearrangement as classically found during first annealing.

From these prior investigations, it was not possible to determine unambiguously the nature of the Cr1→Cr2 transition. It seems legit to attribute this feature to a SCO induced phase transition since a similar process could not be detected in this range of temperature in the DSC of purely diamagnetic [Zn($\mathbf{L}^4$)$_2$] analogue, which remarkably display a transition around 430 K corresponding to the irreversible transformation in [Fe($\mathbf{L}^4$)$_2$] complex (Figure S.III-8). However, some doubts remained since no significant change of color could be perceived upon the transition into Cr2 phase and the material appears as a dark green powder, which is the usual color for the LS configuration (Figure III-32). A change of color to olive green is actually observed, but upon the transition into Cr3 phase, suggesting a conversion into the paramagnetic phase. It is worth to note that the material remains thereafter olive green upon cooling from the liquid phase down to room temperature, suggesting the absence of SCO during the Cr3→Cr4 transition.

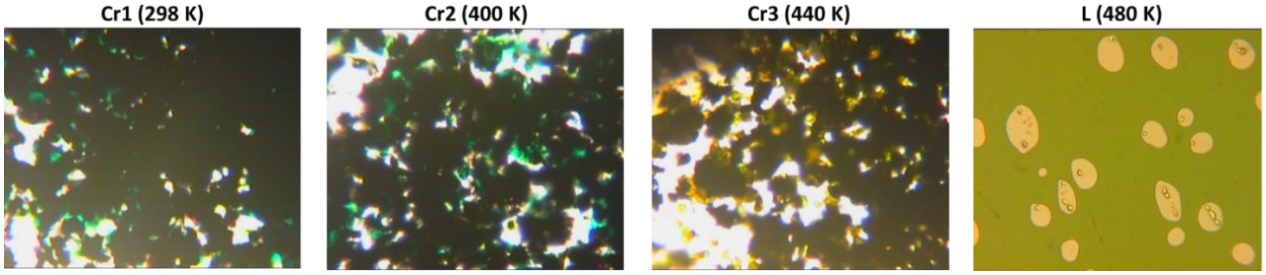

Figure III-32. Optical micrographs for [Fe($\mathbf{L}^4$)$_2$] recorded during the first heating (under parallel polarizers). From left to right: Cr1, Cr2, Cr3 and liquid phases.

In order to understand the origin of the Cr1→Cr2 transition, further investigations including, magnetic measurements and X-ray diffraction studies on single-crystals were performed.

III.3.2.2. Magnetic measurements and single-crystal X-ray diffraction analysis

Direct current magnetic susceptibility measurements were first performed up to 400 K, in order to prevent from the irreversible transformation occurring around 430 K. The temperature dependence of the χT product is shown in Figure III-33 (top). At low temperature, the χT value is 0.05 $cm^3 \cdot K \cdot mol^{-1}$ and remains nearly constant up to 335 K, confirming the diamagnetic state predicted by the dark green color of the material. Above this temperature, a first-order spin transition is displayed around 340 K, which corresponds well to the first transition, Cr1 to Cr2, recorded in DSC. In cooling, the reverse transition appears at ca. 321 K, giving rise to a thermal hysteresis of about 19 K (for a sweeping rate of 0.6 K/min). The SCO is completely reversible, even though a slight shift in temperature is observed between the first and second

heating as seen before by DSC and SAXS investigations. Remarkably, the χT product in the plateau is 1.65 $cm^3 \cdot K \cdot mol^{-1}$, which corresponds to about half of expected value for a full conversion into the HS state. This result suggests therefore the formation of a mixed {LS·HS} phase, which also explain the absence of significant change of color.

When the temperature is further raised, a second sharp transition generating a fully paramagnetic phase (χT =3.25 $cm^3 \cdot K \cdot mol^{-1}$) occurs around 424 K in agreement with the change of color observed above the second transition (Figure III-33, bottom). As mentioned above, the existence of a structural phase transition at about the same temperature in the diamagnetic [Zn($\mathbf{L}^4$)$_2$] analogue, makes us think that the SCO is not the driving force behind this latter transition but is most likely a fortuitous consequence of the reorganization of the packing that stabilizes the HS configuration.

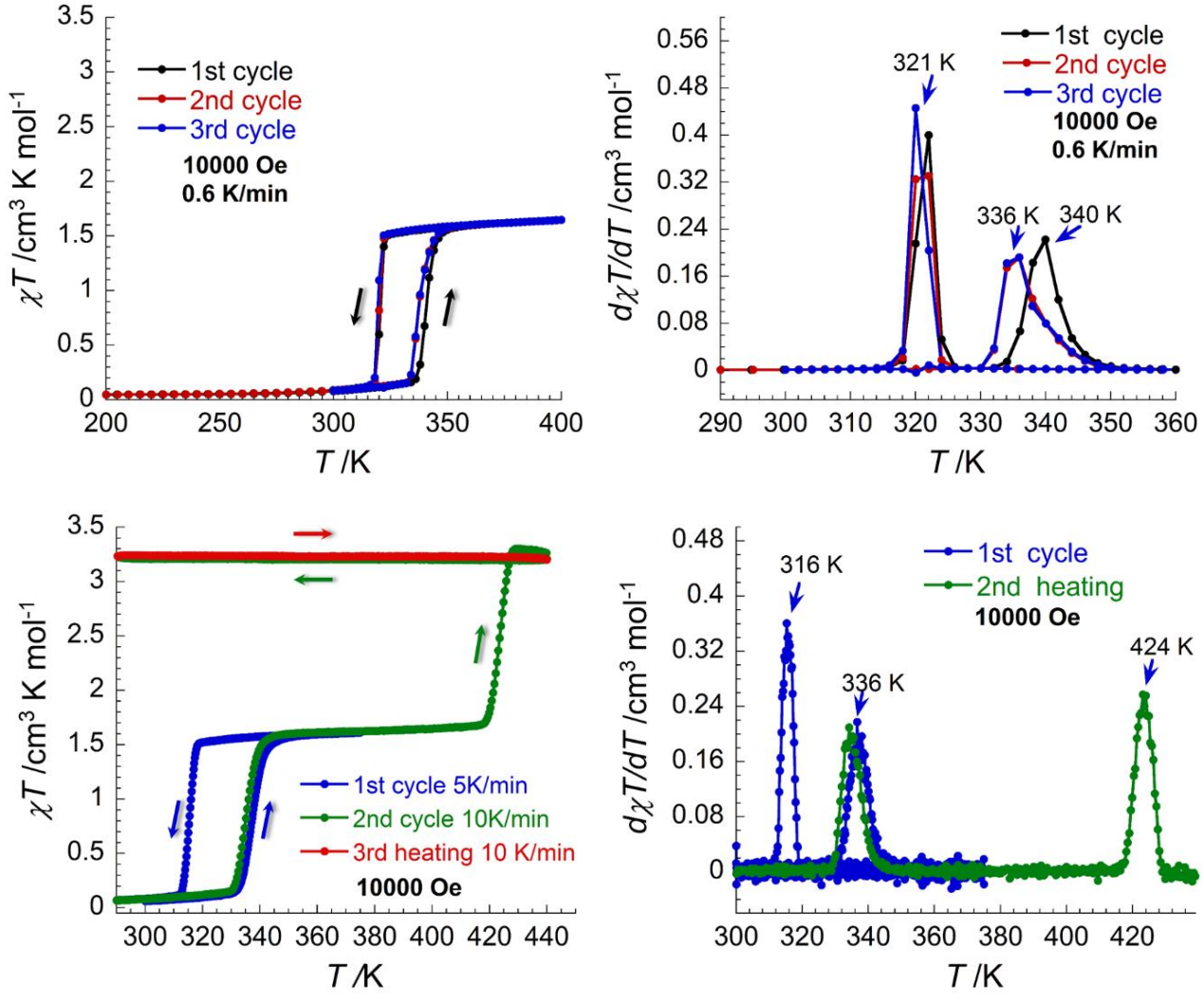

Figure III-33. (top left) Temperature dependence of the χT product for [Fe($\mathbf{L}^4$)$_2$] between 200 and 400 K. (top right) d$\chi T/dT$ vs. T plots. (bottom left) Temperature dependence of the χT product for [Fe($\mathbf{L}^4$)$_2$] between 300 and 440 K. (bottom right) d$\chi T/dT$ vs. T plots.

In other words, the SCO is induced by the formation of a new polymorphic form and not the reverse as classically observed. It should be recalled that the analogic situation was found for [Fe($\mathbf{L}^1$)$_2$]·MeOH during the transformation in mother liquor from the kinetic (diamagnetic) α-polymorph into the thermodynamic

(paramagnetic) β-phase. Afterward, the behavior becomes irreversible and the material remains in the HS configuration down to 300 K, showing that the Cr3-to-Cr4 transition is not associated to SCO process. Magnetic measurements after this thermal treatment must be performed below 300 K to check whether a return into the diamagnetic phase is possible (only DSC down to 200 K were performed and did not reveal any evidence for SCO).

The formation of the intermediate mixed {LS·HS} phase around 340 K retained our attention since the process is perfectly reversible (below 400 K) and such behavior is not so usual in SCO systems. Two scenarios can be considered to explain this particular phenomenon: (i) the compound crystallize in such a way that two (or more) crystallographically unique complexes are present in the packing and due to their distinct environment, only one or half species experience SCO with temperature, or (ii) all the Fe(II) sites are equivalent at low temperature and the SCO involves a crystallographic symmetry breaking (CSB) generating two (or more) crystallographically and magnetically non-equivalent species.[31] In order to investigate the structural-properties relationship and have a better overview on this compound, important efforts were made to isolate it as single-crystals and solve the structures of both diamagnetic and mixed {LS·HS} phases. Dark green sheet-like single-crystals were obtained in moderate yield by recrystallizing of the microcrystalline powder after dissolution in dichloromethane and layering with hexane. The single-crystal X-ray diffraction measurements were performed below (250 K) and above (360 K) the transition. For the pertinence of the following structural analysis, we should first mention that the isolated single-crystals are structurally identical to the microcrystalline sample used for previous measurements. This can be shown by comparing the SAXS diffractograms to the simulated powder patterns provided by X-ray diffraction on a single-crystal (Figure III-34).

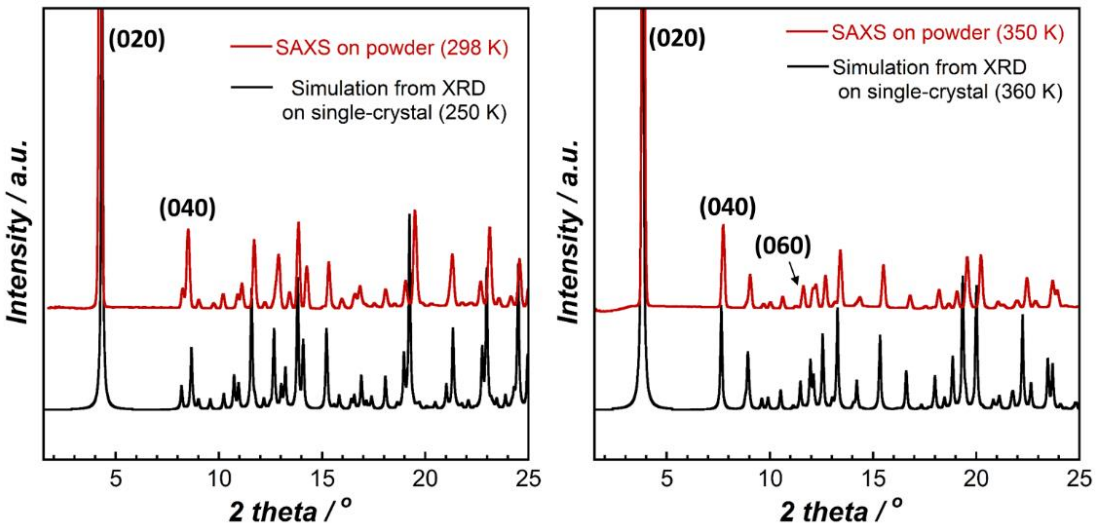

Figure III-34. SAXS and simulated powder diffraction patterns for [Fe($\mathbf{L}^4$)$_2$] in the LS phase (left) and in the mixed {LS·HS} phase (right).

Table III-7. Crystallographic data for [Fe($\mathbf{L^4}$)$_2$] at 250 and 360 K .

Temperature / K	250	360	
Crystal system	Monoclinic	Orthorhombic	
Space group	$P2_1/c$	$P2_12_12$	
***a* / Å**	10.4722(14)	10.036(2)	
***b* / Å**	40.801(5)	46.263(10)	
***c* / Å**	14.2308(16)	10.951(2)	
***β* / °**	128.100(7)	90	
***V* / Å^3**	4787.9(11)	5084.5(18)	
Z	4	4	
Flack parameter	--	0.49	
Bond Lengths	**Site 1**	**Site 1** (Fe1)	**Site 2** (Fe2)
<Fe-N$_{py}$>, Å	1.938	1.917	2.203
<Fe-N$_{im}$>, Å	1.867	1.854	2.092
<Fe-O>, Å	1.966	1.972	2.073
Σ(X-Fe-X),[a] °	85.7	81.8	158.8

[a] $\sum = \sum_{i=1}^{12}|90 - \varphi_i|$, where φ_i are cis X-Fe-X bond angles with X = O or N

The compound crystallizes in the monoclinic $P2_1/c$ space group as shown by the structure collected at 250 K (Figure III-35 left, Tables III-7 and S.III-7). The asymmetric unit is composed of only one [Fe($\mathbf{L^4}$)$_2$] molecule, discarding therefore the hypothesis of multiple non-equivalent sites in the low-temperature phase. The analysis of the Fe(II) coordination sphere confirmed the LS configuration and the average Fe-X bond lengths, ranging from 1.867 to 1.966 Å, and $\Sigma_{(X\text{-}Fe\text{-}X)}$ parameter, 85.7°, are favorably comparable to other examples with LS configuration described earlier.

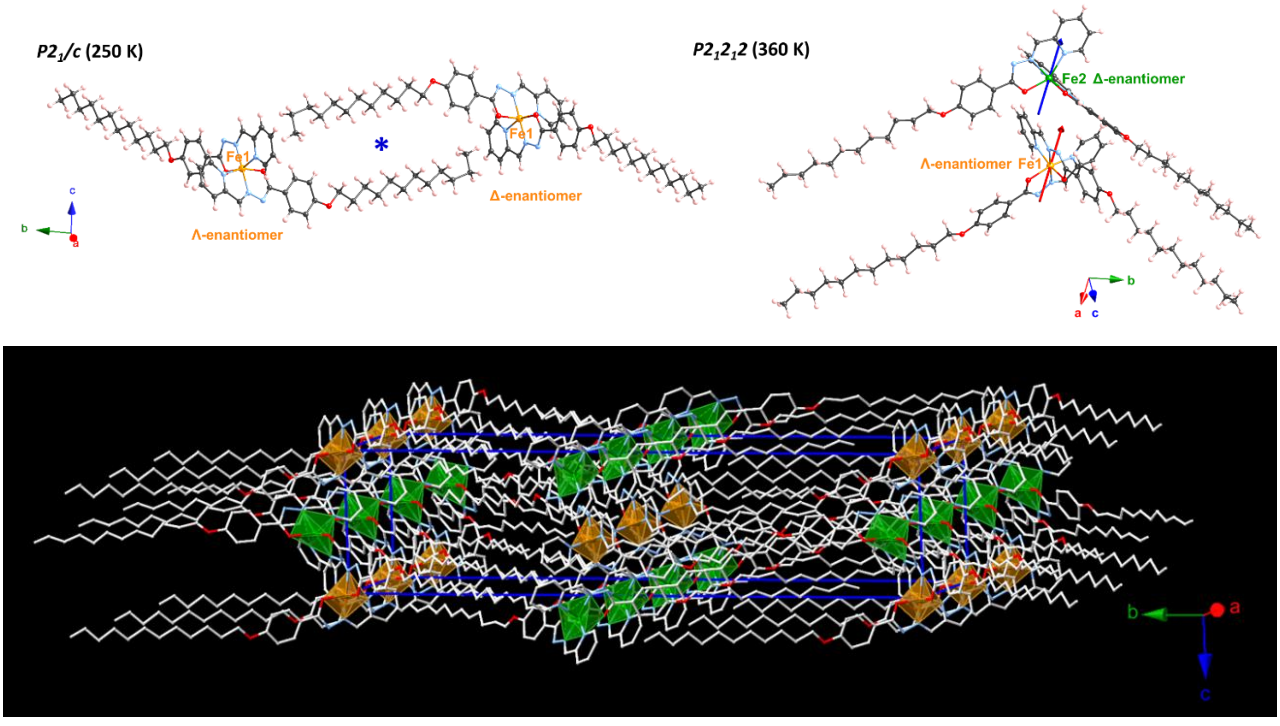

Figure III-35. (Top) Views of the two [Fe($\mathbf{L^4}$)$_2$] enantiomers at 250 K (left) and 360 K (right). The blue star represent the inversion center of symmetry relating the two crystallographically equivalent enantiomers in the $P2_1/c$ space group. The blue and red vectors represent the 2-fold symmetry axes crossing the two non-equivalent isomers in the $P2_12_12$ space group. (bottom) projection of the packing at 360 K, emphasizing the distribution of LS (orange) and HS (green) species in the space. H-atoms are omitted for clarity.

Thus, the only reasonable ways to explain the magnetic behaviors involve a CSB during the SCO process. This was, indeed, confirmed at 360K, at which a transformation from monoclinic $P2_1/c$ space group into orthorhombic $P2_12_12$ was observed. Therefore, the centrosymmetry is lost, giving rise to two

crystallographically unique complexes (Figure III-35, right). Each of them is located on a 2-fold rotation axis that crosses the metal center along *a*-axis and each complex can be then described by two equivalent halves of molecule.

As mentioned earlier in the chapter, pyridylaroylhydrazone-based $[Fe(L)_2]$ complexes are chiral molecules due to the asymmetry of the Schiff base ligand. However, in all previous cases (including $[Fe(\mathbf{L}^4)_2]$ at 250 K) the Δ and Λ enantiomers were related by a symmetry inversion center. In the present case, no symmetry operation can rely the two enantiomers and the asymmetric unit is then composed of the racemic pair. The analysis of the coordination sphere confirmed that the spin configuration is not the same in the two distinct sites; The Δ-form having a Fe(II) in HS state, while Λ-form display the LS configuration (Table III-7). Actually, the reverse situation can be find in the crystal, which has been refined as an inverse-twin and characterized by a flack parameter of 0.49. A view emphasizing the repartition of the LS and HS species in the packing is provided in Figure III-35 (bottom) and shows the formation of HS and LS channels along *a*-axis, which are alternated in *b*- and *c*-directions.

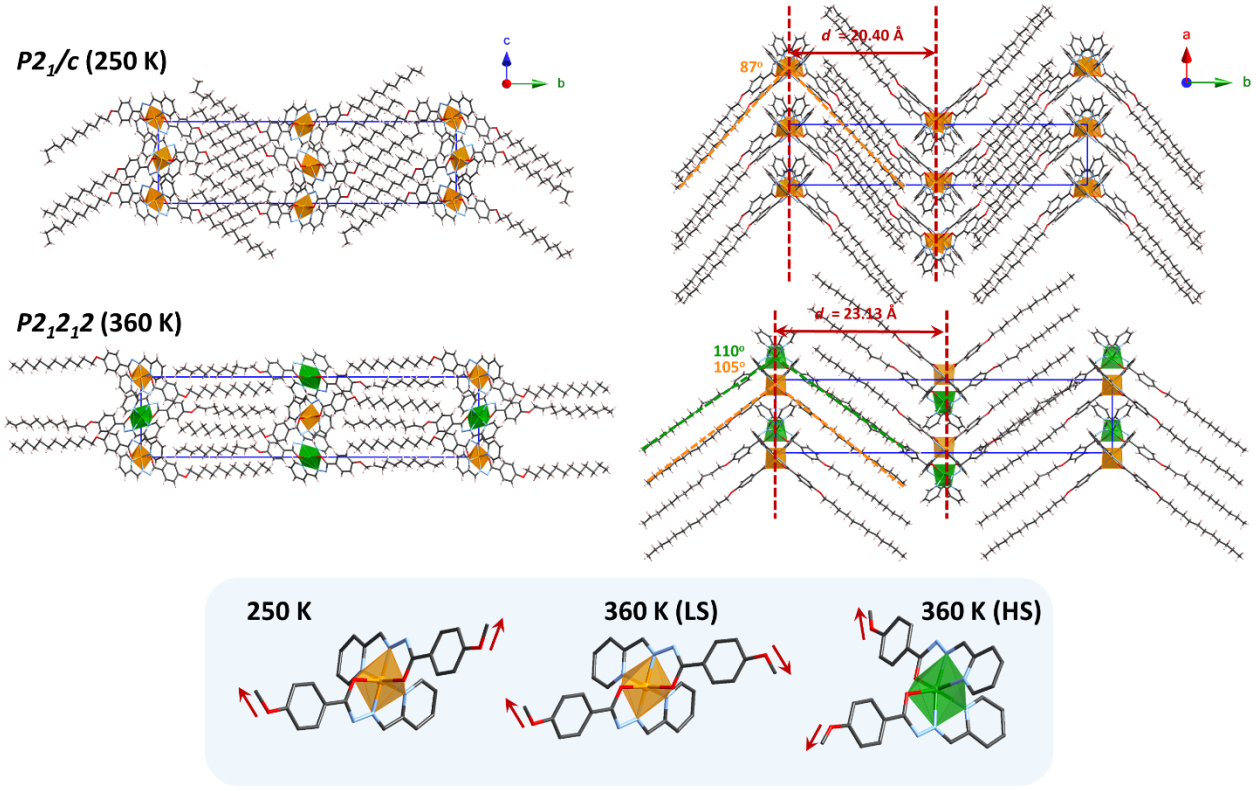

Figure III-36. Projection of the packing viewed along *a* and *c* directions for $[Fe(\mathbf{L}^4)_2]$ at 250 K (top) and 360 K (bottom). (inset) Fragment of $[Fe(\mathbf{L}^4)_2]$ structures emphasizing the change of the conformation of alkoxy functions. For clarity, only the ether of the dodexyloxy function is displayed. FeN_4O_2 coordination sphere are shown in orange and green octahedrons for LS and HS species, respectively.

The packing can be described by nearly planar Fe(II) layers parallel to the *ac* plan and separated from each other by a distance $d = b/2$ (Figures III-35 to III-37). The cohesion between layers is mainly assured through van der Waals interactions between the dodecyl chains, which were found almost perfectly interdigitated. As seen before, the interlayer distance increases substantially between the low and high-temperature phases (from 20.40 to 23.13 Å) and this can be explained by an increase of the bent angle formed by the almost linear chains and the metal-complex core (see Figure III-36, right). At 250 K, this

angle can be estimated to ca. 87°, which is close to the expected value for octahedral symmetry with *mer* configuration, while the value increase at 360 K to about 105° and 110°for the LS and HS species, respectively. This changes are probably driven by the increase of the distortion of octahedral symmetry ($\Sigma_{(X\text{-}Fe\text{-}X)}$ = 158.8°) in the HS specie and provokes deep changes of the aliphatic organization in both species. Especially, this includes a change of the rotamer conformation of alkyloxy functions in order to minimize torsions and maintain an optimal interdigitating (see inset Figure III-36).

Beside the change of the bent geometry impacting the interlayer distance along *b*-direction, important modifications of the metal center organization within the layers are also observed. As mentioned earlier, the metal center layers are nearly planar (especially true at 360 K, see Figure III-36), but important displacements of the molecules and modest change of their orientation is occurring within the *ac* plan (Figure III-37). More particularly, the important contraction of the *c* lattice parameter, from 14.23 Å at 250 K to 10.95 Å at 360 K, is accompanied by the loss of the metal center alignment in this direction. A modest contraction of *a* lattice parameter is also found, giving rise to a general contraction of the *ac* surface area from 117.3 $Å^2$ to 109.9 $Å^2$. Taking into account this contraction and considering that the SCO process requires an expansion of the coordination sphere, this might explain that only half of the Fe(II) species are converted into the HS configuration. Relatively few supramolecular interactions insure the cohesion within the metal center layers. Indeed, the orientation of the molecules is not favorable for establishing π-π contacts and only weak C-H···X (with X = N, O, π) interactions are present. The sets of interactions are displayed in Figure III-37. In the low-temperature phase, interactions mainly arises from C-H···π contacts between pyridyl and benzohydrazide rings, while only one interaction involving directly the coordination sphere (C-H···O = 2.30 Å), is present. At high temperature, all the oxygen donors are involved in C-H···O contacts, although these interactions are found weaker (2.41 and 2.70 Å) than at 250 K.

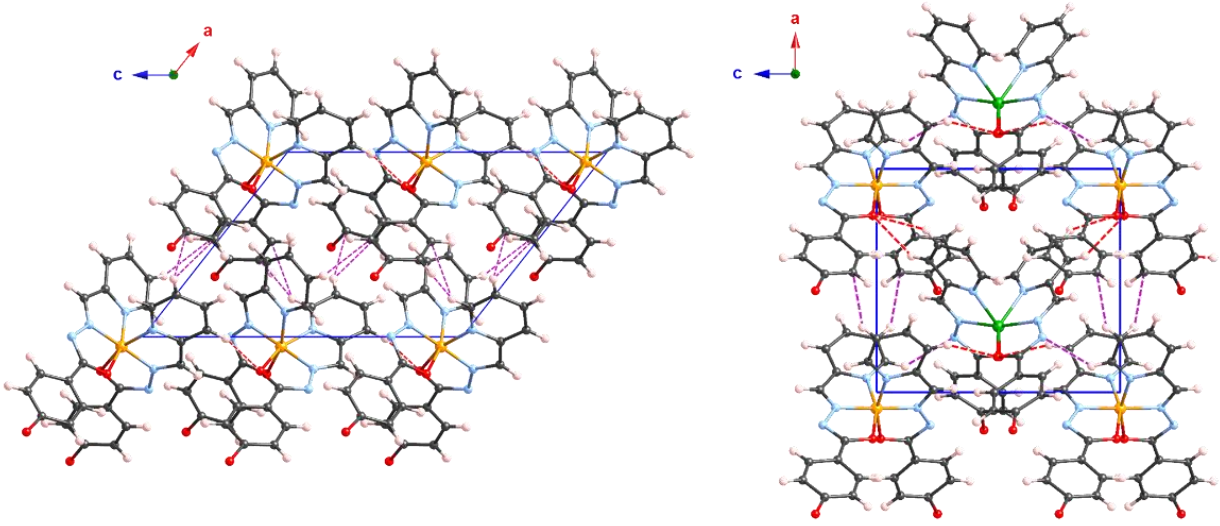

Figure III-37. Projection of the packing viewed along *b*-axis for [Fe($\mathbf{L}^4$)$_2$] at 250 K (left) and 360 K (right) emphasizing the weak C-H···X interactions (X = O, N, π). Weak interactions involving the coordination sphere are displayed in red dashed lines and the other short contacts are shown in violet dashed lines. Dodecyl chains are omitted for clarity.

In the above section, we described the dramatic structural changes arising from the CSB that accompanies the SCO process and after this analysis we should attempt to answer to the question: what is the driving force behind this behavior?

Obviously, the occurrence of CSB rely on the strong cooperativity resulting from elastic interactions in the packing and the manifestation of that have been experimentally evidenced by the magnetic measurements that revealed an abrupt and hysteretic spin transition. Although the origin of CSB cannot be determined with certitude, some intriguing points make us think that the presence of alkyl chains is not innocent and possibly be the main driving force behind this particular behavior. The first evidence, is the suspicious contraction of the metal center layers (*ac* plan), while an expansion is more likely expected considering the natural expansion of the coordination sphere after conversion into the HS state. Of course, a contraction of one of the lattice faces is not unusual but should be motivated by certain criteria, which include: the displacement of certain molecules in the third direction and/or a reorientation of the molecules in such a way that their specific area in the considered plane is minimized and/or the creation of favorable interactions. As seen before, the metal centers remain perfectly in plane in the high-temperature phase, while the moderate reorientation of the molecules is mainly resulting from the change of the β angle from 128 to 90° and does not contribute to minimize their specific surface in the *ac* plane. Moreover, the relatively few number and nature of the supramolecular interactions within the layers are not very convicting to describe a strongly cooperative system. In fact, we suggest that the contraction of the *ac* plane, which prevent from full conversion of the Fe(II) sites, is dictated by the cooperative effects between alkyl chains, which maintain strong interdigitating whatever the phase. Indeed, taking into account the natural increase of the bent geometry induced the increase of the coordination sphere distortion, the conservation of an almost perfect interdigitating requires mechanically a contraction of the *ac* plane.

III.3.3. Extension to other complexes with mono-alkylated ligands

In order to reinforce our hypothesis about the key role played by the alkyl chains on crystallographic symmetry breaking and check whether it is possible to improve the behavior by obtaining this time a reversible two-step SCO, we proposed to design new closely related complexes such as [Fe($\mathbf{L}^5$)$_2$] and [Fe($\mathbf{L}^6$)$_2$] (Scheme III-7).

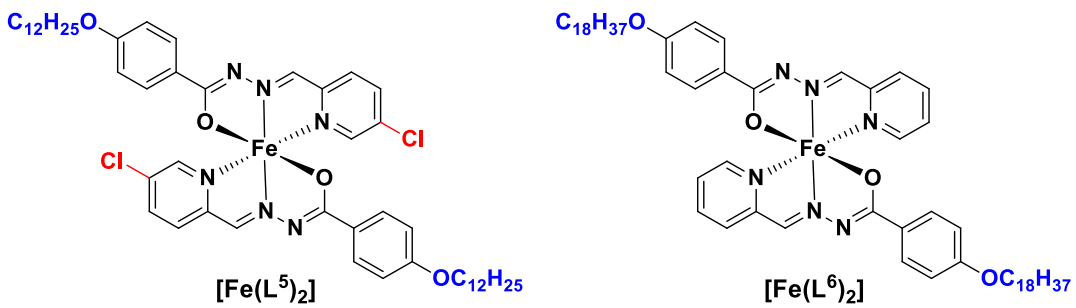

Scheme III-7. Chemical structure of [Fe($\mathbf{L}^5$)$_2$] and [Fe($\mathbf{L}^6$)$_2$] complexes

III.3.3.1. Structural and magnetic properties of [Fe(L^5)$_2$] complex

Our first strategy was to slightly modify [Fe($\mathbf{L^4}$)$_2$] complex by adding a chloride function onto the pyridyl ring, assuming that this minor modification would not affect significantly the overall organization and would therefore allow CSB in the resulting [Fe($\mathbf{L^5}$)$_2$] material. Furthermore, the idea behind the introduction of a chloride function was to promote SCO at lower temperature in such a way that the second SCO step could eventually occurs before the irreversible transformation found previously. However, this ligand design strategy did not fulfill our expectations, and the tiny change of the ligand completely changed both structural and magnetic features.

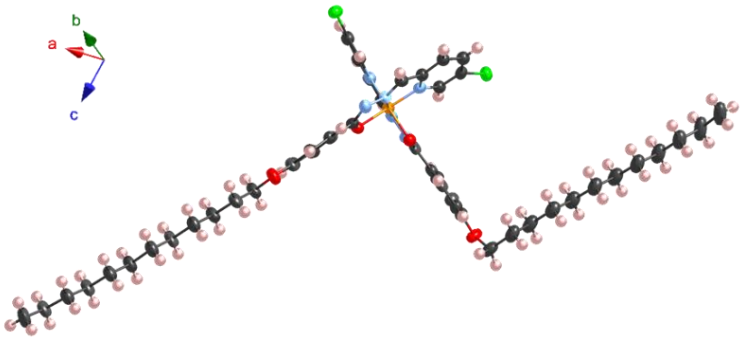

Figure III-38. ORTEP views of [Fe($\mathbf{L^5}$)$_2$] at 120 K. Thermal ellipsoids are depicted at 50 % probability.

Table III-8. Crystal data for [Fe($\mathbf{L^5}$)$_2$]

Temperature / K	120
Crystal system	Monoclinic
Space group	$P2_1/c$
***a* / Å**	22.8322(13)
***b* / Å**	12.6464(8)
***c* / Å**	17.092(11)
***β* / °**	94.39(3)
***V* / Å^3**	4940.2
Z	4
<Fe-N_{py}>, Å	1.967
<Fe-N_{im}>, Å	1.867
<Fe-O>, Å	2.003
Σ(X-Fe-X), °	83.6

The compound was isolated as sheet-like single-crystals by slow diffusion of methanol into a solution of the complex in dichloromethane. Single-crystal X-ray diffraction analysis performed at 120 K revealed that the complex crystallizes in the monoclinic $P2_1/c$ space group in which the asymmetric unit is composed of one hexa-coordinated complex. A view of the complex is shown in Figure III-38 and selected crystallographic parameter are summarized in Table III-8 (see also Table S.III-8). The LS configuration was confirmed by the analysis of the coordination sphere, for which the averages Fe-X (1.867 – 2.003 Å) and $\Sigma_{(X\text{-}Fe\text{-}X)}$ parameter (83.6°) are in the same range of values found for analogues in LS configuration (Table III-8).

The architecture of [Fe($\mathbf{L^5}$)$_2$] and crystal packing is significantly different from the non-chlorinated [Fe($\mathbf{L^4}$)$_2$] analogue. The metal centers inside the packing arrange themselves in nearly planar layers parallel to *bc* plan and separated from each other through the interdigitated dodecyl chains (Figure III-39). In contrast with [Fe($\mathbf{L^4}$)$_2$] complex, the bent geometry cannot be observed, and the two alkyl chains are oriented in anti-parallel fashion (Figures III-38 and III-39, left). These are nearly orthogonal to *b*-axis and tilted from the *c*-axis with an angle of about 45°. The cohesion between the layers is mainly maintained through electrostatic van der Waals inter-chain interactions and weak C-H···Cl (2.86 Å) contacts involving the terminal methyl position of one chain and one chlorine atom from the neighboring layer. The unexpected arrangement of the alkyl chains can be explained by the very different organization of the molecules in the *bc* plane. Indeed, in contrast with the previous example, numerous weak interactions are established between the pyridylbenzohydrazone ligands to generate supramolecular layers. Especially, this includes multiple C···C

and C···N π-π contacts with distances ranging from 3.18 to 3.39 Å (blue dashed lines in Figure III-39, right), as well as Cl···π contacts of 3.21 Å (green dashed lines).

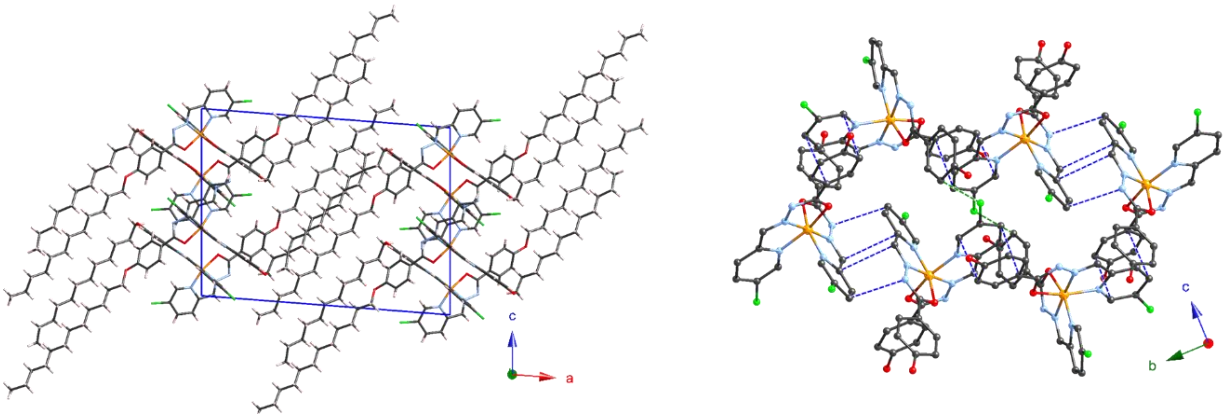

Figure III-39. Projection of the packing for [Fe($\mathbf{L}^5$)$_2$] at 120 K viewed along *b*-axis (left) and *a*-axis (right). The π-π and Cl···π interactions are shown as blue and green dashed lines, respectively. In the right figure, dodecyl chains, hydrogen atoms and other C···X interactions (X = O, N, π) are omitted for clarity.

Attempts to determine the structure at higher temperature were unsuccessful. The unit cell was checked at 320 K, and revealed important changes of the lattice, suggesting the occurrence of SCO in this range of temperature. The Bravais lattice was not anymore compatible with monoclinic P but more likely with triclinic P-1 (α = 79.93°, β = 87.94°, γ = 87.72°), suggesting once again the occurrence of CSB with temperature. The lattice distances were found slightly longer while the cell volume increased of about 7%. Unfortunately, the crystal did not survive very long time at this temperature, and the data set collection was not sufficient to attain an acceptable refinement of the structure. It should be nonetheless mentioned that the preliminary solution suggested that at least two crystallographically independent Fe(II) sites are present.

Magnetic susceptibility measurements were performed to confirm the occurrence of SCO. The temperature dependence of the χT product is displayed in Figure III-40. The first runs were performed between 1.8 and 300 K, and revealed a gradual and incomplete SCO that is reversible on cooling. The χT product tends to reach a plateau with a value of about 1.1 $cm^3 \cdot K \cdot mol^{-1}$, which indicates that about one third of Fe(II) species were converted into the HS state. The incomplete SCO occurs in a stepwise fashion as suggested by the plots of derivative of the χT product that show a maximum at 175 K and a weak and broad deformation centered at 240 K. When the temperature is further raised, the product χT product increases sharply around 350 K, reaching thereafter a plateau of 3.1 $cm^3 \cdot K \cdot mol^{-1}$ corresponding to a full conversion into the paramagnetic phase. During the cooling, the reverse process is not observed, indicating that the material was irreversibly converted into another crystalline phase. Thereafter, the material exhibits a SCO between 340 and 220 K (with $T_{1/2}$ = 280 K), which is found perfectly reversible on additional heating and cooling cycles. The χT value in the low-temperature plateau is ca. 1.6 $cm^3 \cdot K \cdot mol^{-1}$ indicating that the SCO occurs between a mixed {LS·HS} phase and a fully paramagnetic phase.

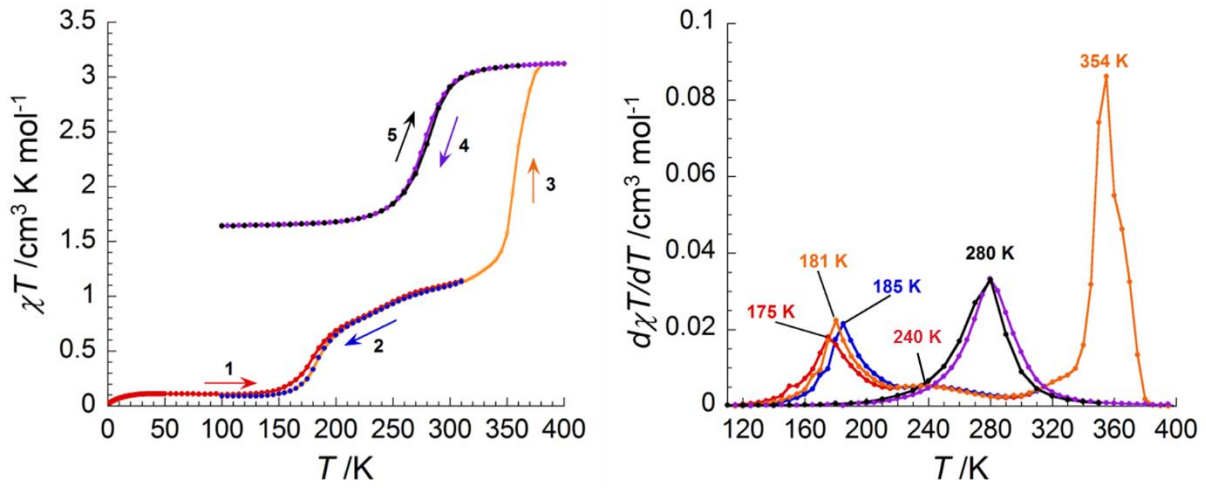

Figure III-40. Temperature dependence of the χT product (left) and derivative of χT product as function of the temperature for single-crystal of [Fe($\mathbf{L}^5$)$_2$]. Applied *dc* field of 10000 Oe; Sweeping rate: 1.4 K/min.

Magnetic measurements were also performed on the microcrystalline sample obtained before the recrystallization and revealed a quite different magnetic behavior (Figure III-41). Indeed, the thermally virgin sample is found to be already in a {LS·HS} phase as shown by the χT value of 1.67 cm^3·K·mol^{-1} in the low-temperature plateau. As the temperature increase, a conversion from the {LS·HS} into the HS phase (3.26 cm^3·K·mol^{-1}) appears at slightly higher temperature ($T_{1/2}$ = 295 K) and steeper fashion than observed for the previous sample. On cooling the reverse conversion take places in a stepwise fashion, giving rise to a weak thermal hysteresis. These results clearly indicate that the two samples are not in the same polymorphic form. Evidences of their polymorphism were deduced from the FTIR spectra that show slight differences in the overall spectral window, although additional measurements (powder X-ray diffraction) need to be performed to unambiguously confirm that.

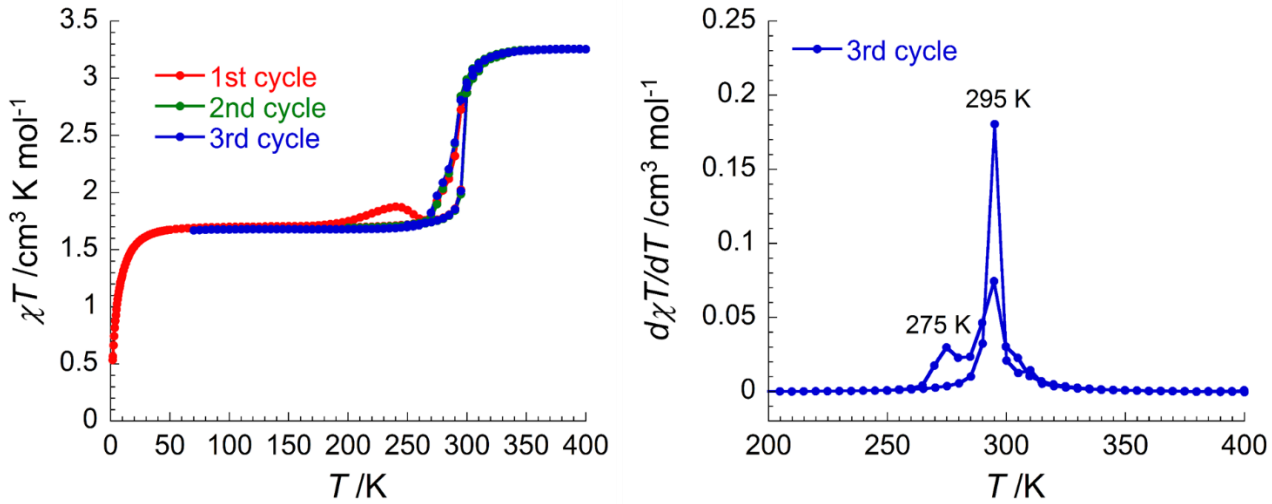

Figure III-41. Temperature dependence of the χT product (left) and derivative of χT product as function of the temperature for microcrystalline powder of [Fe($\mathbf{L}^5$)$_2$] (sample before recrystallization). Applied *dc* field of 10000 Oe; Sweeping rate: 1.4 K/min.

III.3.3.2. Thermo-structural and magnetic properties of [Fe($\mathbf{L}^6$)$_2$] complex

Preliminary investigations were performed on [Fe($\mathbf{L}^6$)$_2$] complex, which differs only from [Fe($\mathbf{L}^4$)$_2$] by the length of the alkyl chain (octadecyl). Unfortunately, due to the elongation of chain length, it was not

possible to isolate single-crystals of enough good quality for X-ray diffraction analysis (only tiny pellets could be obtained). Thus, the compound was mainly characterized by DSC, SAXS and magnetic susceptibility measurements on microcrystalline powder samples.

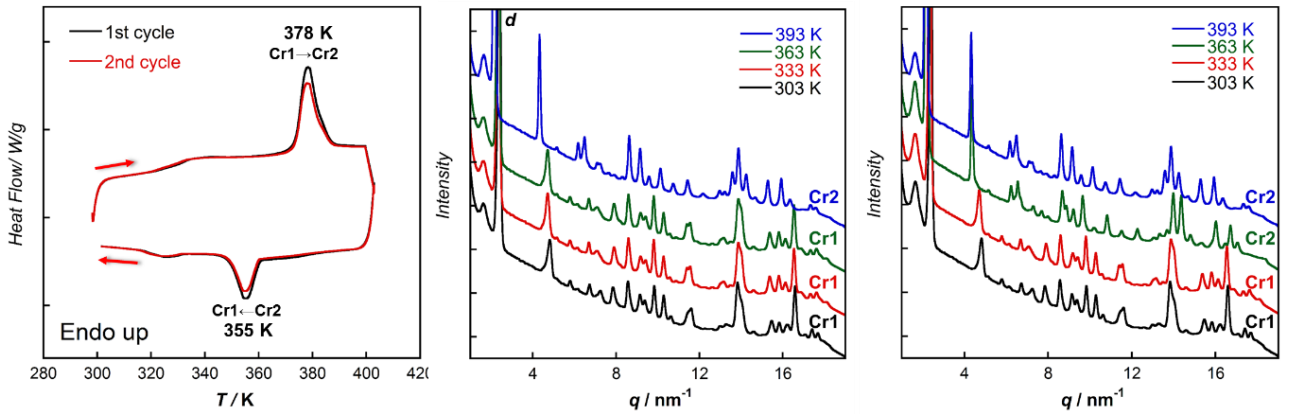

Figure III-42. (left) DSC thermograms for [Fe($\mathbf{L}^6$)$_2$] between 300 and 400 K at 10 K/min. (center) SAXS profiles of [Fe($\mathbf{L}^4$)$_2$] during the 2nd heating. (right) SAXS profiles of [Fe($\mathbf{L}^4$)$_2$] during the 2nd cooling.

The DSC and SAXS measurements revealed that [Fe($\mathbf{L}^6$)$_2$] complex has a complicate thermal behavior, which is nonetheless relatively similar to its analogue with dodexyloxy functions. The DSC between 300 and 400 K (Figure III-42, left), displays a reversible transition around 380 K (heating) and 355 K (cooling), that was thereafter ascribed to a spin transition process based upon magnetic measurements. Both phases were found to be well crystalline as shown by the SAXS diffractograms (Figure III-42, center and right). By analogy with [Fe($\mathbf{L}^4$)$_2$] complex, the first intense reflection found at 2.40 and 2.16 nm^{-1} at 303 K and 393 K, respectively, was attributed to the separating distance between two adjacent metal center layers. The interlamellar distances, 26.2 Å at 303 K and 29.0 Å at 393 K, are larger than those found for [Fe($\mathbf{L}^4$)$_2$] in their respective crystalline phases as a direct result of the increase of alkyl chain length.

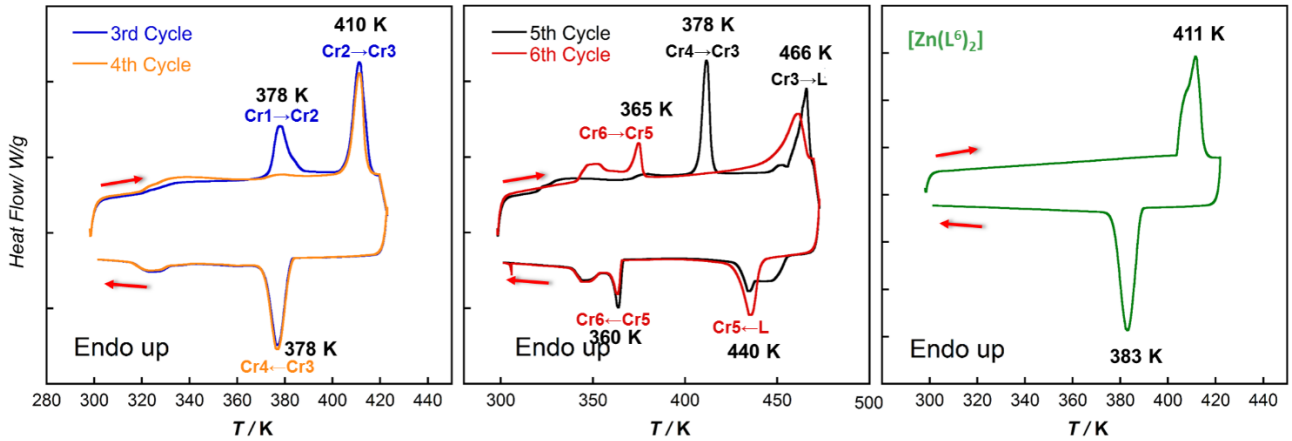

Figure III-43. DSC thermograms for [Fe($\mathbf{L}^6$)$_2$] on 3rd and 4th heating/cooling cycle between 300 and 420 K (left), on 5rd and 6th heating/cooling cycle between 300 and 470 K (center) and for [Zn($\mathbf{L}^6$)$_2$] on 1st heating between 300 and 420 K (right). Sweeping rate: 10K/min

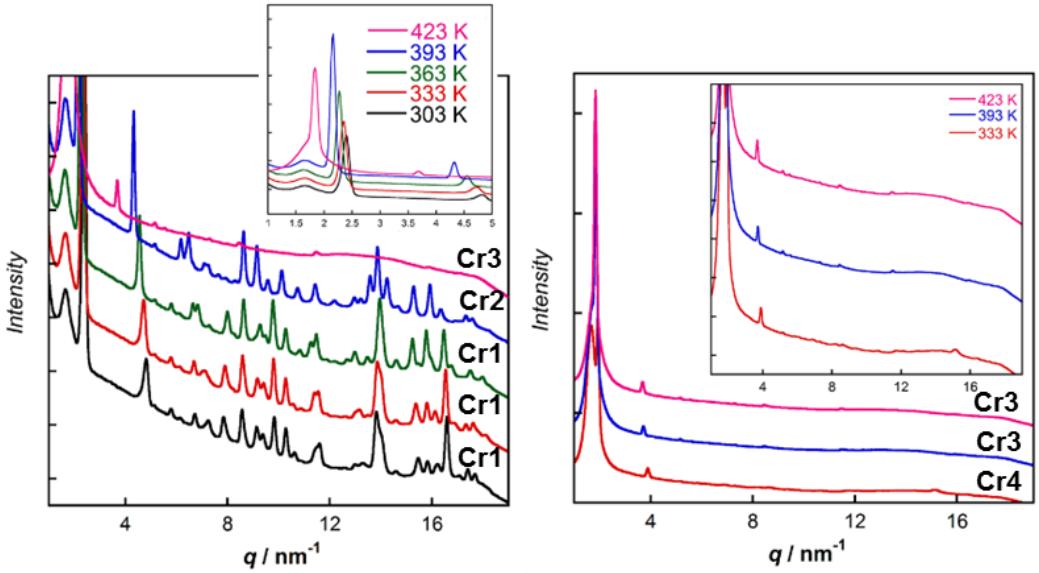

Figure III-44. SAXS profiles for [Fe($\mathbf{L}^4$)$_2$] on heating from 303 to 423 K (left) and on cooling from 423 to 333 K (right).

Similarly to [Fe($\mathbf{L}^4$)$_2$], when the temperature is further raised, the material is converted to a poorly crystalline phase (Cr3) at 410 K (Figures III-43, left and III-44, left). On cooling the DSC indicates the formation of another crystalline phase (Cr4) at 378 K, while no significant changes could be detected on SAXS profiles (Figure III-44, right). As seen before, these transitions are not directly related to the SCO, since the same reversible process is displayed on the purely diamagnetic [Zn($\mathbf{L}^6$)$_2$] analogue (Figure III-43, right). After reaching the liquid phase at 466 K, the DSC on cooling did not revealed any signal at 378 K as expected for the transition from Cr3 into Cr4 phase (Figure III-43, center). This suggests that the compound crystallizes into another phase (Cr5) at 440 K which undergoes transformation into Cr6 phase around 360 K. Attempts to characterize these transformations by SAXS investigations were unsuccessful since the material does not survive very long time in the liquid phase.

Susceptibility magnetic measurements were performed to confirms the presence of SCO in [Fe($\mathbf{L}^6$)$_2$]. The temperature dependence of product χT is displayed in Figure III-45. At low temperature, the complex is diamagnetic, which is consistent with dark green color of the microcrystalline sample. The χT value is 0.11 $cm^3 \cdot K \cdot mol^{-1}$ and remains constant up to ca. 200 K at which a slight and very gradual increase of the χT value up to 0.49 $cm^3 \cdot K \cdot mol^{-1}$ at 360 K is detected. Above this temperature, a sharp transition centered at 380 K is displayed in agreement with DSC experiments. The χT product in the high-temperature plateau is 1.66 $cm^3 \cdot K \cdot mol^{-1}$, which is the half of expected value for Fe^{II}_{HS}, showing once again the coexistence of both LS and HS species in this crystalline phase. On cooling the reverse transition is observed at 357 K, revealing a thermal hysteresis of 23 K. No magnetic measurement were performed so far above 400 K, nevertheless the DSC and SAXS experiments strongly suggest that the compound will behave in the same manner as [Fe($\mathbf{L}^4$)$_2$], leading irreversibly to the fully paramagnetic phase after the thermal treatment above 410 K.

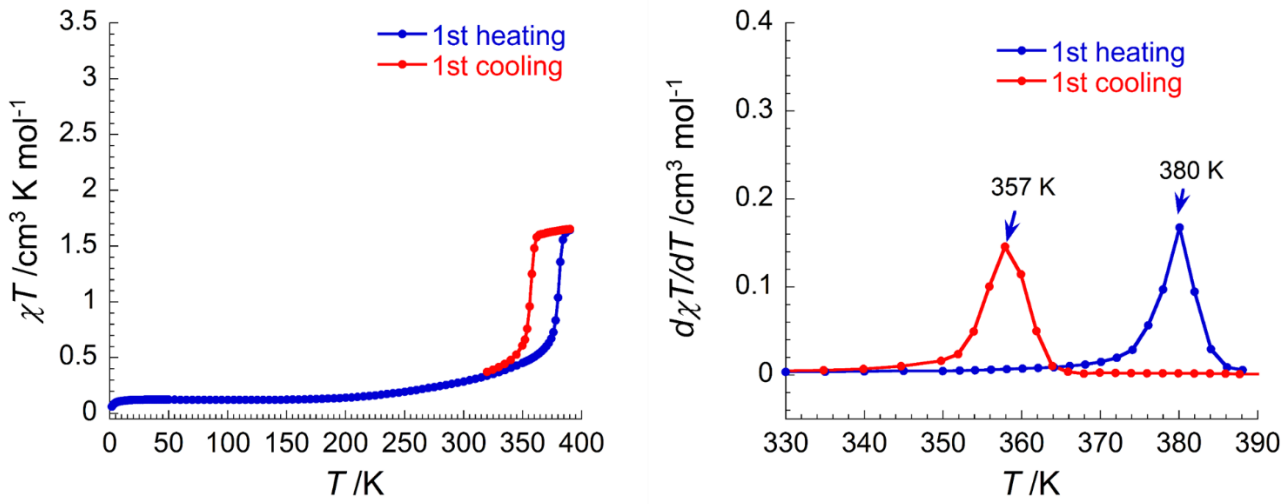

Figure III-45. Temperature dependence of the χT product (left) and derivative of χT product as function of the temperature for [Fe($\mathbf{L}^6$)$_2$]. Applied *dc* field of 10000 Oe; Sweeping rate: 1.3 K/min.

Additional analogue ligands functionalized with one alkyl chain were recently prepared in the team, and the preliminary investigations of resulting Fe(II) complexes revealed systematically the coexistence of LS and HS species in an intermediate phase confirming the important role of alkyl chains in the CSB process.

III.3.4. Functionalization with multiple dodecyl chains

As seen in the previous section, the functionalization of pyridylbenzohydrazone ligands lead to interesting magnetic properties on resulting complexes, systematically showing the formation of an intermediate {LS·HS} phase. However, no liquid crystalline features could be observed in these materials. Although their melting is accessible at relatively low temperature, giving the possibility to form homogeneous thin films, the resulting materials lose irremediably their SCO ability upon such thermal treatment. With the aim to promote reversible behavior with liquid crystalline features, we applied a classical strategy, which consist to introduce additional greasy substituents onto the ligand scaffold. Therefore two new ligands bearing two ($\mathbf{L}^7$) and three ($\mathbf{L}^8$) dodecyloxy chains were considered for the preparation of Fe(II) SCO complexes (Scheme III-8).

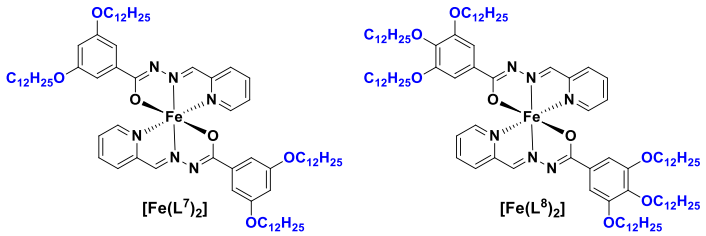

Scheme III-8. Chemical structure of [Fe($\mathbf{L}^7$)$_2$] and [Fe($\mathbf{L}^8$)$_2$] complexes

III.3.4.1. Thermo-structural properties

The two complexes were prepared as previously described by mixing the chosen ligand, iron(II) salt and trimethylamine in methanol at 60 °C. In contrast with previous examples, no shinny microcrystalline

powder precipitate during the cooling. Instead, the dark green powder samples flocculate, forming weakly sticky aggregates, which is an indication for either amorphous, poorly crystalline or liquid crystalline materials. The materials melts into the isotropic liquid phase at much lower temperature than [Fe($\mathbf{L}^4$)$_2$] analogue (474 K). The melting points were estimated based upon POM and DSC analyses to ca. 380 and 350 K for [Fe($\mathbf{L}^7$)$_2$] and [Fe($\mathbf{L}^8$)$_2$], respectively. By cooling from the isotropic liquid phase down to room temperature (with a sweep rate of ca. 5 K/min), no birefringence was detected and the material solidify as thin homogeneous film that appears black under polarized light, excluding the hypothesis of liquid crystalline features in these materials.

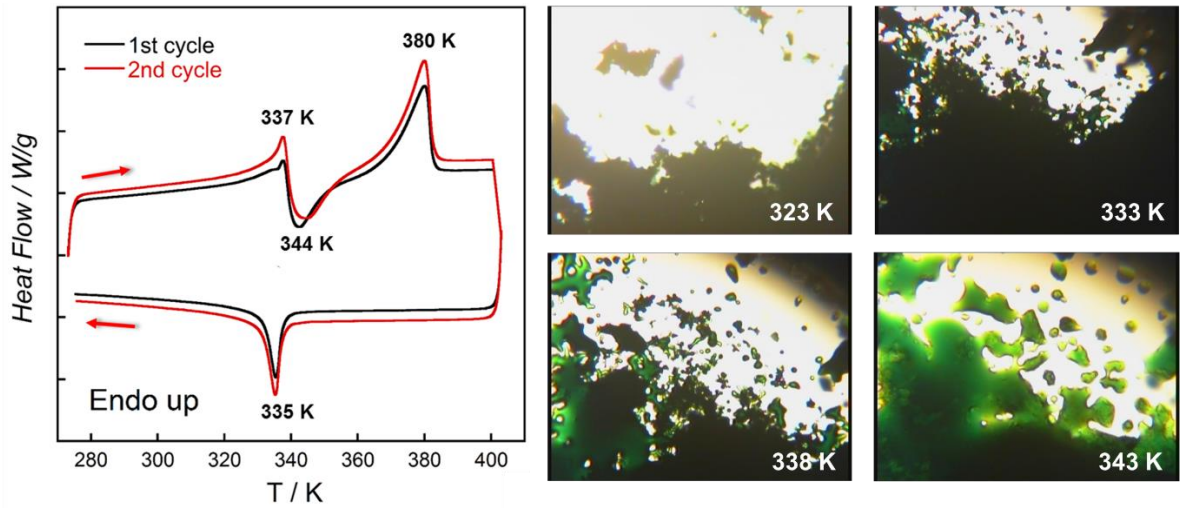

Figure III-46. (left) DSC thermograms for [Fe($\mathbf{L}^7$)$_2$] between 280 and 400 K at 10 K/min. (right) Optical micrographs of [Fe($\mathbf{L}^7$)$_2$] recorded during the 1st heating emphasizing the formation of metastable liquid-like phase (starting at 333 K) and beginning of solidification at 343 K (parallel polarizers mode).

The DSC of [Fe($\mathbf{L}^7$)$_2$] complex revealed a monotropic thermal behavior (Figure III-46, left). Indeed, in addition to the melting transition found around 380 K, the material displays a weak endothermic peak at 337 K followed by an exothermic signal around 344 K, while only one exothermic peak, corresponding to the solidification of material is observed in cooling mode. The presence of this endothermic/exothermic process on heating mode was attributed to the formation of a metastable liquid-like phase around 334 K and reentrance into solid state at 344 K as illustrated by the optical micrographs recorded during the first heating that show the onset of melting at 333 K and solidification at 343 K (Figure III-46, right). It should be noticed that no birefringent texture was observed for this fluid phase which discards the possibility of metastable liquid-crystalline phase.

The phenomenon of reentrance or "inverse melting" is not rare especially in polymer, colloid and liquid-crystal materials,[32] and has been notably observed on the [$Mn_{12}O_{12}(L)_{16}(H_2O)_4$] (with L = 3,4,5-tris(dodecyloxybenzoate)) metallomesogen used as precursor in Chapter II.[33] This behavior is often explained by the existence of a low-ordered phase which tends to reorganize itself with increasing temperature thanks to the increase of fluidity (or decrease of viscosity) and it involves and equilibrium between a fluid and solid phases. The presence of such low-ordered phase was confirmed by the SAXS experiments (Figure III-47).

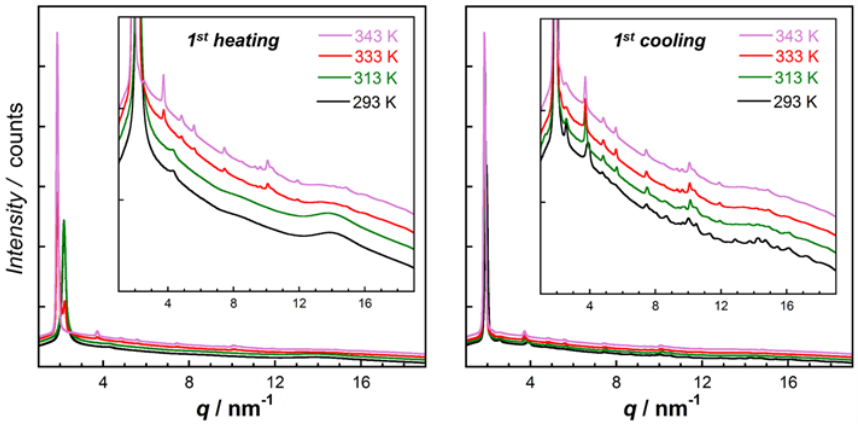

Figure III-47. SAXS profiles for [Fe($\mathbf{L}^7$)$_2$] recorded between 293 and 343 K on heating (left) and cooling (right) modes.

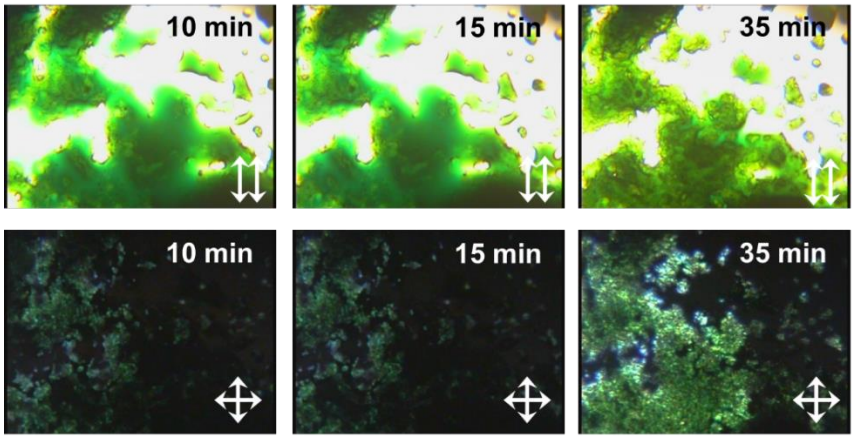

Figure III-48. Optical micrographs for [Fe($\mathbf{L}^7$)$_2$] at 343 K in parallel polarizers mode (top) and crossed polarizers mode (bottom) emphasizing the crystal growth from the metastable liquid phase. Performed during the first heating.

At room temperature, the SAXS profile exhibits only two weak and broad equidistant reflections at 2.16 and 4.33 nm^{-1} that correspond to random lamellar ordering with separating distance of ca. 29.1 Å as well as a broad and diffuse halo in the wide-angle region (centered at 14 nm^{-1}) attributed to short-range lateral order between dodecyl chains. When the temperature is increased, a reorganization occurs, giving rise to a poorly crystalline phase resembling to those observed for mono-alkylated analogues at high temperature. The crystalline phase remains predominantly lamellar as shown by the intense peak at 1.86 nm^{-1} for which a periodicity up to the fifth order was found at 343 K. This value corresponds to an interlamellar distance of about 33.7 Å, which is comparable to the one found for [Fe($\mathbf{L}^4$)$_2$] in the high-temperature phase (Cr3 : 34.5 Å). It should be noticed that the crystallization is a relatively slow-dynamic process and its observation was only possible due to the slow sweeping rate (1 K/min) and pre-acquisition isothermal equilibrium (typically 30 min) applied. The time evolution of the crystallization from the metastable liquid-like phase measured at 343 K is provided in Figure III-48 and reveals that at least 35 minutes are required for a complete solidification of the material.

Additional SAXS were performed to probe the behavior up to the melting temperature and revealed a reorganization of the material around 373 K into another poorly crystalline phase, while the conversion into the isotropic liquid phase was confirmed at 393 K (Figure III-49, left). Even though the experimental conditions were the same, almost no crystallization was detected during the cooling down to room

temperature and the material remains likely as a glass, confirming the monotrope thermal behavior predicted by DSC. This can be shown by the low intensity of reflection peaks in comparison to those recorded during the heating (see for example diffractogram at 343 K, Figure III-49, right). This was also confirmed by POM analysis, which revealed a lower kinetic for the formation of birefringent textures (several hours) during the cooling from the liquid phase than the first heating from the metastable liquid-like phase (see inset Figure III-49). It is worthwhile to mention that solidification/crystallization was detected at higher temperature during SAXS and POM than DSC analyses, and this can be explained by the slow dynamic of the thermal behaviors and differences of sweeping rates between the experiments.

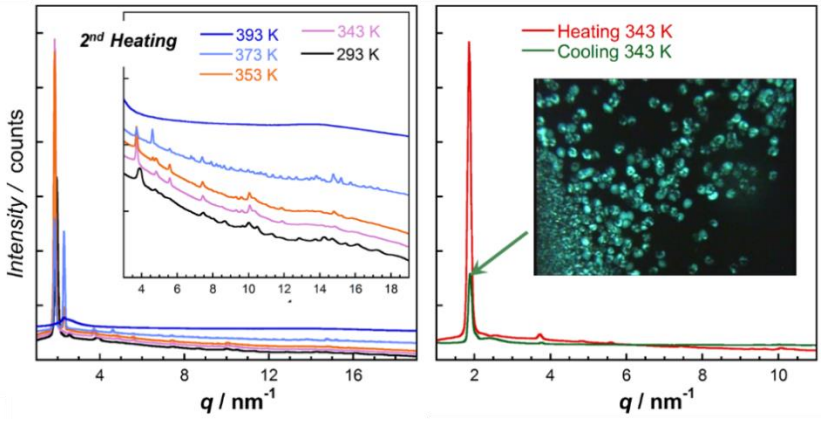

Figure III-49. (left) SAXS profiles for [Fe($\mathbf{L}^7$)$_2$] recorded between 293 and 393 K during the 2nd heating. (right) Comparison of SAXS profiles at 343 K on heating from 293 K and cooling from 393 K. (Inset) Polarized optical micrograph after slow cooling (1K/min) from the isotropic liquid phase down to 343 K, isothermal at 343 K for 12 hours, and cooling down to room temperature.

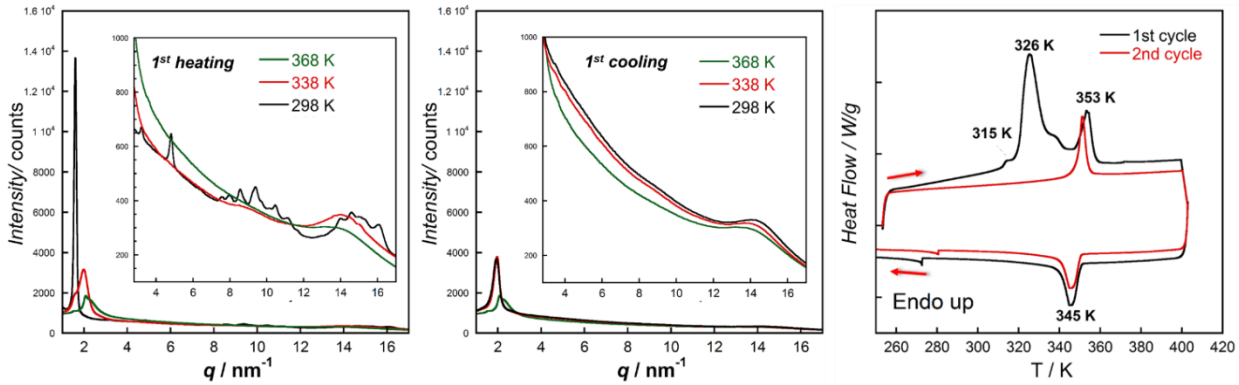

Figure III-50. (left) SAXS profiles for [Fe($\mathbf{L}^8$)$_2$] recorded during the 1st heating from 298 up to 368 K. (center) SAXS profiles for [Fe($\mathbf{L}^8$)$_2$] recorded during the cooling from between 368 down to 298 K.(right) DSC thermogram of [Fe($\mathbf{L}^8$)$_2$] for the 1st and 2nd heating/cooling cycles between 260 and 400 K. DSC sweeping rate: 10 K/min

DSC and SAXS measurements for [Fe($\mathbf{L}^8$)$_2$] revealed a quite different and simpler thermal behavior than previous example. At room temperature, the SAXS profile exhibits one sharp and intense reflection at 1.59 nm^{-1} as well as weak and broad signals in the low and wide-angle regions, suggesting a poorly crystalline or plastic crystal behavior (Figure III-50, left). By analogy with previous examples, the intense peak at 1.59 nm^{-1} was attributed to the lamellar organization and the interlamellar distance was calculated as 39.5 Å, which is favorably comparable to the distance, 42.1 Å, reported by Real and co-workers on a very similar analogue (which differs from $\mathbf{L}^8$ ligand only by an additional methyl group on the Schiff base function).[15] Upon heating to 338 K, the crystalline organization is lost a the material become amorphous.

This transition into a glass phase was observed in DSC, which shows an intense endothermic signal at 326 K (Figure III-50, right). The shape of the signal and enthalpy value (56.6 kJ/mol), is quite unsual for a glass transition and suggests that the transformation is associated or provoked by a SCO. This was confirmed thereafter by the magnetic measurements. On cooling from the liquid phase, the material does not crystallize again and solidify as a glass even when very slow sweeping rates are applied (no birefringent texture was observed).

III.3.4.2. Magnetic measurements

Preliminary magnetic susceptibility measurements on [Fe($\mathbf{L}^7$)$_2$] and [Fe($\mathbf{L}^8$)$_2$] were performed between 1.8 and 400 K with an applied field of 1 T. The χT *versus* temperature plot for [Fe($\mathbf{L}^7$)$_2$] is displayed in Figure III-51. Below 200 K, the χT product is ca. 0.23 $cm^3 \cdot K \cdot mol^{-1}$, in agreement with an almost pure diamagnetic phase. As the temperature increases from 200 to 283 K, a progressive increase of the χT product up to 2.94 $cm^3 \cdot K \cdot mol^{-1}$ is observed, confirming the occurrence of a gradual SCO. The derivative of the χT plot indicates that the conversion occurs in a two-step fashion, which can be explained by the slow crystallization of the material after the formation of the metastable liquid-like phase around 340 K (*vide supra*). At 283 K, the material starts to melt into the thermodynamic liquid phase and the χT value drops steeply to 2.42 $cm^3 \cdot K \cdot mol^{-1}$, while the onset of a gradual SCO happening in the liquid phase can be deduced above 395 K.

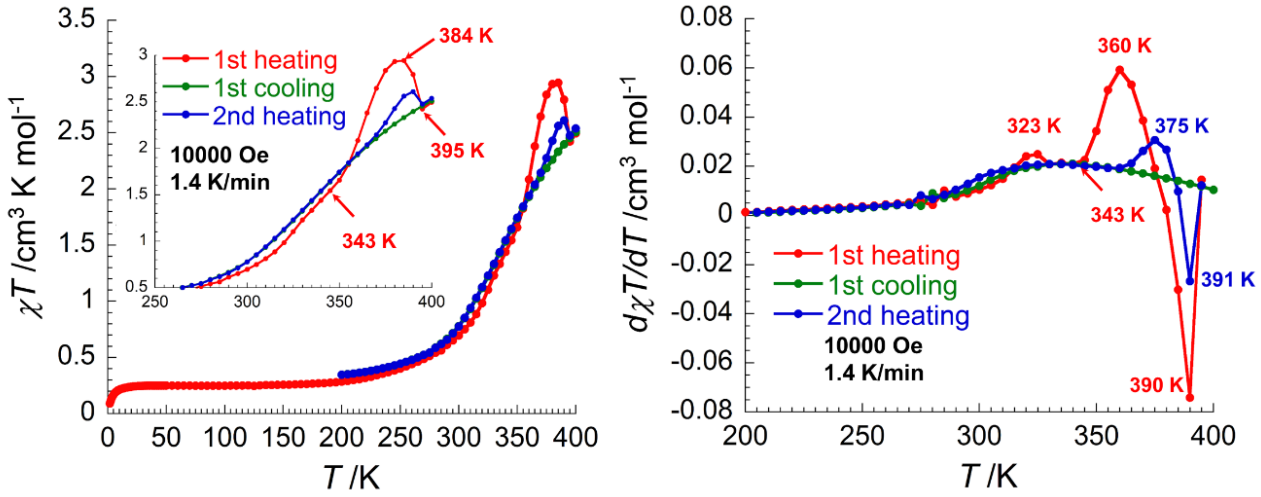

Figure III-51. Temperature dependence of the χT product (left) and derivative of χT product as function of the temperature for [Fe($\mathbf{L}^7$)$_2$]. Applied *dc* field of 10000 Oe; Sweeping rate: 1.4 K/min.

This particular behavior was confirmed on a second heating run, even though the stepwise and reverse-SCO effects are less pronounced, confirming the slow dynamic of the crystallization after the first thermal annealing (*vide supra*). Looking more closely these data, the crossover in the liquid and glass phases follow barely the same pathway, while the "bump" in χT is essentially associated to the partial crystallization occurring above 343 K, which suggests therefore that the crystalline phase is paramagnetic. Assuming that, we might eventually promote a fully paramagnetic phase by playing on the dynamic of the experiment.

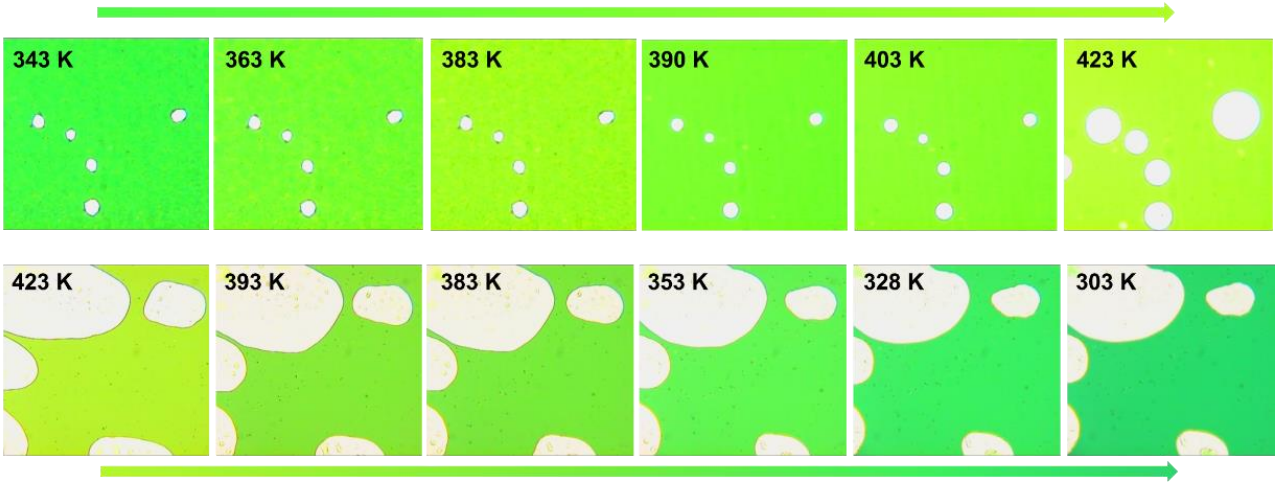

Figure III-52. (Top) Optical micrographs of [Fe($\mathbf{L}^7$)$_2$] recorded during the first heating from 343 K up to 423 K emphasizing the reverse-SCO between 383 and 390 K. (bottom) Optical micrographs of [Fe($\mathbf{L}^7$)$_2$] recorded during the cooling from the isotropic liquid phase (423 K) down to 303 K emphasizing the gradual conversion from the HS (olive green) liquid phase into the LS (dark green) solid phase.

The reverse SCO effect was also visualized by the change of color as illustrated in the optical micrographs shown in top of Figure III-52. For that, the material was heat up to the metastable liquid-like phase (338 K) in order to form a homogeneous thin film and allowed to stand at 343 K for 40 minutes during which the material crystallizes progressively (the evolution of crystallization was checked under polarized light). As the temperature increase up to 383 K, the green material turns progressively toward olive green as a result of the gradual SCO, while a darkening of the color can be perceived around 390 K (at which the compound reach the liquid phase). Then, a gradual lightening of the color is again observed by increasing the temperature. On cooling, only a gradual change from olive green into dark green is shown, confirming the monotrope character of the material (Figure III-52 bottom).

The temperature dependence of χT product for [Fe($\mathbf{L}^8$)$_2$] is shown in Figure III-53. As the temperature increase an abrupt increase of the χT value is observed between 315 K and 343 K at which the value was 2.52 $cm^3 \cdot K \cdot mol^{-1}$, indicating and incomplete SCO transition. This latter correspond well to the transition from the poorly crystalline into glass phase deduced from DSC and SAXS experiment. Interestingly, such crystal-to-glass transition was not observed in the purely diamagnetic [Zn($\mathbf{L}^8$)$_2$] analogue, which remains crystalline up to the melting around 360 K, suggesting therefore that the loss of crystallinity is induced by the SCO transition (see Figure S.III-8). Similarly to [Fe($\mathbf{L}^7$)$_2$], a steep drop of the χT value to 1.92 $cm^3 \cdot K \cdot mol^{-1}$, is detected when the material starts to melt above 343 K, while the onset of a crossover is exhibited in the liquid phase (above 354 K). On cooling down to 343 K, the curve follows almost the same pathway as in heating and the χT value jumps again to 1.92 $cm^3 \cdot K \cdot mol^{-1}$ as the result of the transition into glass phase. Below this temperature, the material does not return into the diamagnetic phase but exhibits a very gradual and incomplete crossover to reach a value of about 1.55 $cm^3 \cdot K \cdot mol^{-1}$ at 50 K. This behavior was found perfectly reversible over cycling and found independent of the sweeping rate or applied magnetic field (up to 7 T), showing no orientation with field as previously described for SCO-based soft materials.[7]

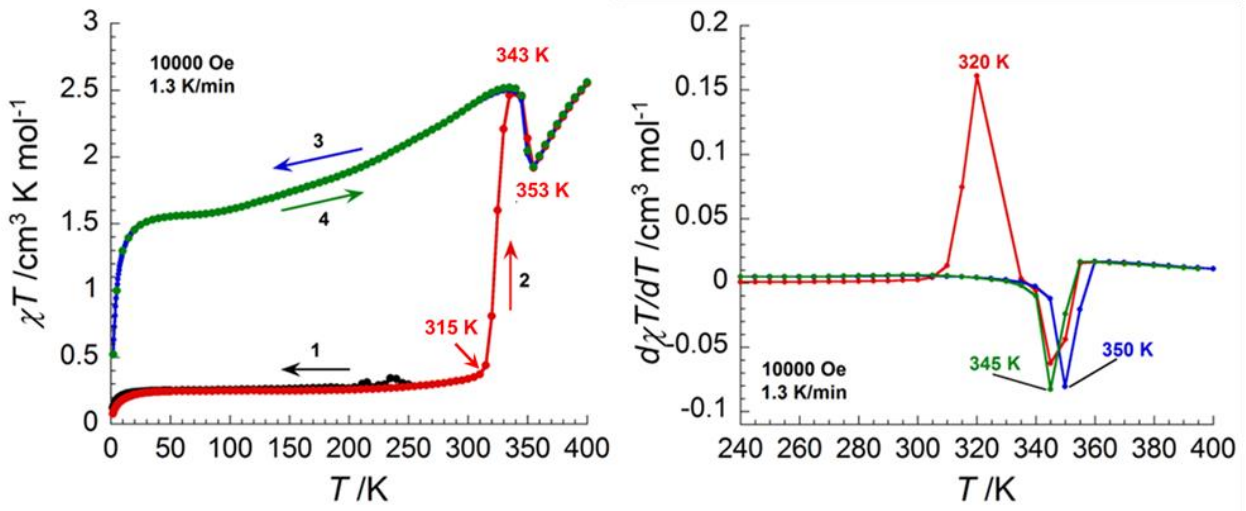

Figure III-53. Temperature dependence of the χT product (left) and derivative of χT product as function of the temperature for [Fe($\mathbf{L}^{8}$)$_2$]. Applied *dc* field of 10000 Oe; Sweeping rate: 1.3 K/min.

Although the introduction of additional dodecyl chains onto the ligand scaffold was unsuccessful to promote liquid crystalline properties, this strategy allowed us to reveal interesting effects of the functionalization. The two compounds melt at quite low temperature and can then be used to form homogeneous thin films. This is particularly interesting for [Fe($\mathbf{L}^{7}$)$_2$] that shows a reversible spin crossover behavior. Although incomplete, we revealed the existence of reverse-SCO phenomenon, which is very unusual and has been only observed on few examples of Co(II) SCO.[29] This latter is induced by a phase transition, which is to the best of our knowledge unprecedented.

III. 4. Conclusions and perspectives

In this chapter, we have been focused on the synthesis and study of pyridylbenzohydrazone-based SCO with ambition to induce liquid crystalline properties to these materials. The discovery of SCO features in this family of FeN_4O_2 complexes is relatively recent and only a few examples are reported.[13-15] Therefore, we dedicated an important part of the project on the study of model complexes in order to learn more on the coordination chemistry and properties of these molecular systems. The main achievements of this work have been already summarized in section III.2.4 and we recall here the main conclusions to emphasize the motivations of our current and future work. Through the isolation of polymorphic forms of [Fe($\mathbf{L}^{1\text{-}3}$)$_2$] complexes, we have highlighted the strong impact of crystal packing effects on the magnetic properties. We have seen that no SCO is featured when the crystal packing involves a multitude of π-π interactions. However, it remains adventurous to conclude on the basis of these few examples considering the complexity and diversity of supramolecular interactions found in these materials. New analogues, which include derivatives of $\mathbf{HL}^{1}$ functionalized by various substituents (electro- donating or withdrawing functions and extended π-systems) in various positions of the ligand scaffold, are currently under investigation to have a better overview on the correlation structure-properties of these interesting molecular systems. Active researches are still in progress on the three molecular systems described in the manuscript, especially for [Fe($\mathbf{L}^{1}$)$_2$] that exhibits hysteretic spin transition processes in both polymorphic forms and for which a

transformation from the α-polymorph into the β-one have been observed for the solvated forms in the mother liquor (in methanol). One of our great motivation is to learn more about the mechanism of this transformation. In our recent work, we have demonstrated that a thermal activation is necessary since no conversion is occurring at room temperature even after a long stay in the mother liquor (2 months). Experiments to probe the kinetic of the transformation at different temperatures are currently in progress by DSC and powder X-ray diffraction investigations. From our preliminary results, no evidence for the formation of intermediate polymorphic forms was revealed (in contrast with $[Fe(tpa)(NCS)_2]$ previously reported showing the generation of two successive polymorphs[23]), suggesting that the transformation involves a direct pathway. However, the chemistry of this complex is more surprising and rich than we thought. Indeed, an evolution with time from the solvent-free α-$[Fe(\mathbf{L^1})_2]$ into a new γ-$[Fe(\mathbf{L^1})_2]$ polymorphic form have been very recently found when the reaction is performed in acetonitrile instead of methanol (at room temperature). This latter have been structurally and magnetically characterized and found to exhibit an abrupt spin transition at 326 K without significant thermal hysteresis (selected crystallographic, calorimetric and magnetic data are shown for information in section III.5.5). Moreover, a transformation from α-$[Fe(\mathbf{L^1})_2]$ toward another polymorphic form that have been yet clearly identified is occurring in acetonitrile upon thermal activation at 50 °C. In all the cases, polymorphs were obtained in a serendipitous fashion but this promising results should motivate us to systematically dedicate more energy on synthetic aspects for this family of complexes and more generally for SCO systems.

In the second part of this work, we were focused on the functionalization of the complexes with strongly lipophilic substituents with objective to promote mesomorphic features on the resulting materials. Although, the strategy employed was inefficient to reach our initial goal, interesting features originating from the functionalization were highlighted during the work. Especially, we reported the formation of intermediate phase in which both LS and HS species coexist when a mono-alkylation (with dodecyl or octadecyl chains) is applied. This behavior observed in the three $[Fe(\mathbf{L^{4\text{-}6}})_2]$ complexes, was attributed to a crystallographic symmetry breaking (CSB) occurring during the SCO process and have been unambiguously evidenced in one case, $[Fe(\mathbf{L^4})_2]$, by single-crystal X-ray diffraction. Three additional examples, including one with shorter substituent (hexyl) and two analogues of $[Fe(\mathbf{L^4})_2]$ and $[Fe(\mathbf{L^6})_2]$ with additional substituents in the Schiff base function, have been recently developed in the group and the preliminary results seems to confirm similar behaviors supporting the key-role played by the alkyl chains on CSB process that accompanies the SCO process. In all the cases, irreversible transformations into new polymorphic phases were found upon thermal treatment at more or less high temperature. In the case of $[Fe(\mathbf{L^4})_2]$ (and probably also $[Fe(\mathbf{L^6})_2]$), the material is converted into an poorly crystalline phase that has no SCO ability (paramagnetic), while $[Fe(\mathbf{L^5})_2]$ undergoes transformation into a thermodynamic product, which displays a reversible SCO from a pure HS phase into mixed {LS·HS} phase. In the other side, we have seen that the introduction of multiple dodecyl chains gives access to soft materials with low-melting points. The transition into the liquid phase has a direct impact on the Fe(II) coordination sphere and a partial SCO is occurring as previously described by Real and co-workers on a series of analogue complexes.[15] However, our situation was different and the melting was accompanied by an unexpected reverse-SCO, which is to the best of our

knowledge unprecedented. Numerous studies might be realized in continuation to this work. Especially, one of our future directions could be the preparation of solid solutions of $[Fe_xZn_{(1-x)}(\mathbf{L})_2]$. For complexes with mono-alkylated ligands, it would be indeed interesting to study the impact of these SCO-inactive spectator ions on the CSB process. In the case of $[Fe(\mathbf{L^8})_2]$, which loses crystallinity upon SCO, the dilution in Zn(II) complex might help in this case to maintain it (since the $[Zn(\mathbf{L^8})_2]$ was found crystalline up to melting) and thus obtain reversible SCO.

Of course, the elaboration of metallomesogens remains one of our main priority and several strategies to reach this goal are considered. First, we can introduce calamitic smectogen units (biphenyl or cyanobiphenyl), which have been successful to promote bilayer lamellar mesophase in the case of Mn_{12} SMM (see Chapter II).[33] One other approach is to induce more geometrical constrains to the complex, especially by elaborating [2 x 2] grids in which the mesogenic substituents would be oriented perpendicular to the $[Fe_4L_4]$ core (Figure III-54). Although several grids based on pyrylaroylbenzohydrazide ditopic ligands have been recently reported with different *3d* and *4f* metal ions,[34] no example are known with Fe(II) ion. We have recently prepared one model Fe(II)-complex in collaboration with Kruger's group (University Canterbury, New Zealand) and studies are in progress to determine if this latter displays SCO features.

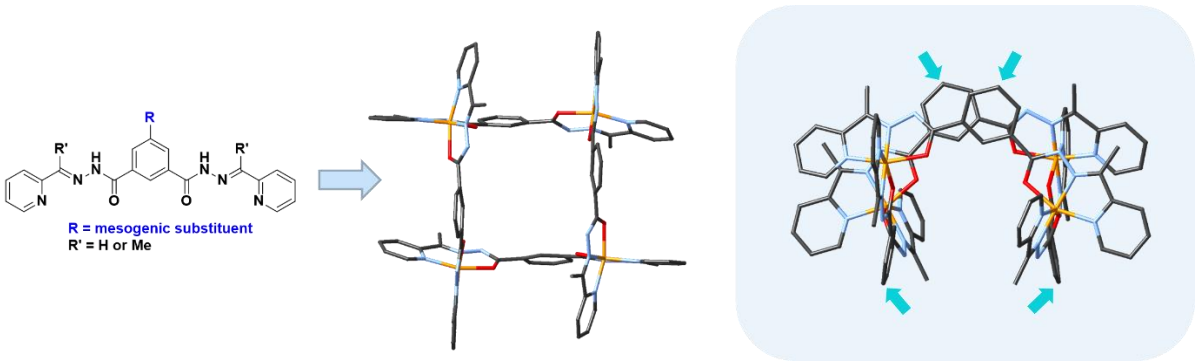

Figure III-54. Strategy proposed to elaborate $[Fe_4L_4]$ grids with mesomorphic properties (the functionalization is represented as turquoise arrows). Note: structure of $[Fe_4L_4]\cdot NEt_3$ (R = H; R' = Me) at 120 K.[35] Hydrogen atoms and solvent lattice are omitted for clarity.

III.5. Supporting materials

III.5.1. Experimental protocols

All the solvents and starting materials were purchased from Acros, Alfa Aesar or Aldrich, and used without further purification unless otherwise stated. All the Fe(II) complexes were prepared under inert atmosphere using Schlenk line technique or in gloves box. ***Caution!*** Perchlorate salts are potentially explosive and must be handled with care and in small quantities.

III.5.1.1. Synthesis and characterization of HL^{1-8} Ligands

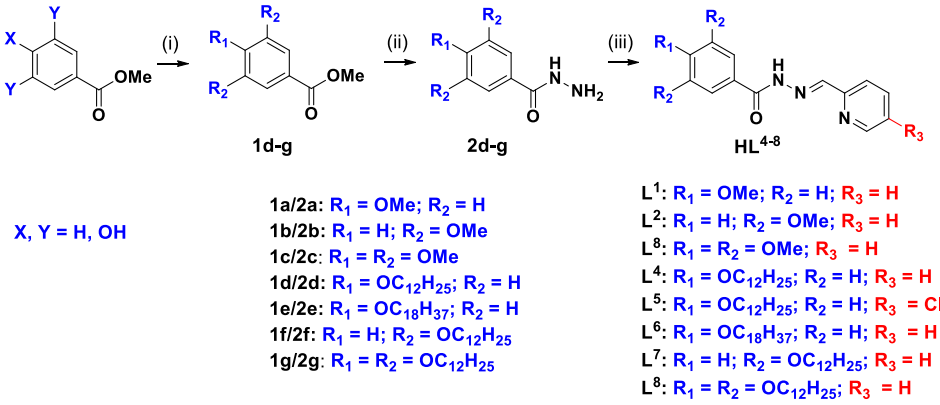

Scheme III-6. General pathway for the synthesis of N'-(pyridin-2-ylmethylene)benzohydrazide ligands and complexes. Conditions: (i) $C_nH_{2n+1}Br$, K_2CO_3, butanone, reflux, 16h. (ii) $N_2H_4{\cdot}H_2O$, EtOH, reflux, 16h. (iii) 2-pyridinecarboxaldehyde or 5-chloropicolinaldehyde, RT, MeOH, 16h.

The non-commercial **1d-g** precursors were prepared according to procedures described in Chapter II. All the ligands were prepared in the same fashion and the general procedure is given for $\mathbf{HL^1}$. To a solution of methyl 4-methoxybenzoate (10.0 g, 60.2 mmol, 1 eq) in hot ethanol (25 mL) was added hydrazine monhydrate (14.8 mL, 300.9 mmol, 5 eq) and the reaction mixture was refluxed for 16 h. After cooling down to room temperature, the resulting precipitate was collected by filtration, washed several times with water (3 x 25 mL), cold ethanol (3 x 10 mL) and dried several hours under vacuum. The precursor **2a** was obtained as white powder (Yield 7.2 g, 72 %). To a sample of **2a** (5 g, 30.0 mmol, 1 eq) in methanol (20 mL) was added 2-pyridinecarboxaldehyde (3.42 mL, 36.0 mmol, 1.2 eq) and the mixture was stirred at RT for 12 h. The white precipitate formed was collected by filtration. After washing with cold MeOH (3 x 5 mL) and Et_2O (2 x 10 mL), $\mathbf{HL^1}$ was obtained as white powder

(E)-4-methoxy-N'-(pyridin-2-ylmethylene)benzohydrazide (HL^1). Yield 74 %. ^{1}H NMR (400 MHz, d_4-MeOH): δ 8.57 (d, J = 4.8 Hz, 1H, CH_{py}), 8.38 (s, 1H, CH_{im}), 8.32 (d, J = 7.5 Hz, 1H, CH_{py}), 7.96 (d, J = 9.0 Hz, 2H, CH_{ar}), 7.90 (t, J = 7.9 Hz, 1H, CH_{py}), 7.43 (t, J = 6.1 Hz, 1H, CH_{py}), 7.06 (d, J = 9.2 Hz, 2H, CH_{ar}), 3.85 (s, 3H, CH_3O). $^{13}C\{^1H\}$ NMR (100 MHz, d_4-MeOH): δ 166.7, 164.6, 154.6, 150.1, 148.7, 138.6, 130.9, 125.9, 125.7, 122.2, 115.0, 56.0. Selected FT-IR data (ATR, cm^{-1}): 1643 (vs, C=O), 1603, 1586, 1550, 1509, 1467, 1434, 1343, 1283, 1248, 1180, 1148, 947, 920, 841, 776, 744, 667, 633, 616. Elemental analysis – Calc. (Found) for $C_{14}H_{13}N_3O_2$: C, 65.87 (66.02); N, 16.46 (16.43); H, 5.13 (5.09).

(E)-3,5-dimethoxy-N'-(pyridin-2-ylmethylene)benzohydrazide (HL^2). Yield 92 %. ^{1}H NMR (400 MHz, *d*$_4$-MeOH): δ 8.57 (d, *J* = 5.0 Hz, 1H, *CH*$_{py}$), 8.39 (s, 1H, *CH*$_{im}$), 8.28 (d, *J* = 8.0 Hz, 1H, *CH*$_{py}$), 7.88 (t, *J* = 8.0 Hz, 1H, *CH*$_{py}$), 7.42 (t, *J* = 6.2 Hz, 1H, C*H*$_{py}$), 7.11 (s, 2H, *CH*$_{ar}$), 6.69 (s, 1H, *CH*$_{ar}$), 3.84 (s, 6H, *CH*$_3$O). ^{13}C{^{1}H} NMR (100 MHz, *d*$_4$-MeOH): δ 166.9, 162.5, 154.5, 150.1, 149.5, 138.6, 135.6, 126.0, 122.3, 106.7, 105.4, 56.1. Selected FT-IR data (ATR, cm^{-1}): 1662 (ν$_{C=O}$), 1586, 1436, 1346, 1260, 1230, 1179, 1168, 951, 912, 825, 744, 621. Elemental analysis – Calc. (Found) for $C_{15}H_{15}N_3O_3$: C, 63.15 (63.43); N, 14.73 (14.31); H, 5.30 (5.19).

(E)-3,4,5-trimethoxy-N'-(pyridin-2-ylmethylene)benzohydrazide (HL^3). Yield 85 %. ^{1}H NMR (400 MHz, $CDCl_3$): δ 8.46 (m, 2H, *CH*$_{py}$ + *CH*$_{im}$), 8.00 (m, 1H, *CH*$_{py}$), 7.67 (t, *J* = 8.0 Hz, 1H, *CH*$_{py}$), 7.22 (t, *J* = 6.2 Hz, 1H, C*H*$_{py}$), 7.18 (s, 2H, *CH*$_{ar}$), 3.86 (s, 6H, *CH*$_3$O), 3.81 (s, 3H, *CH*$_3$O). ^{13}C{^{1}H} NMR (100 MHz, $CDCl_3$): δ 164.3, 153.2, 148.9, 148.2, 141.5, 136.9, 127.7, 124.4, 121.4, 104.9, 61.0, 56.3. Selected FT-IR data (ATR, cm^{-1}): 1679 (ν$_{C=O}$), 1583, 1552, 1501, 1472, 1461, 1344, 1267, 1237, 1187, 1168, 1124, 1075, 1048, 998, 931, 897, 864, 833, 807, 780, 770, 747, 621.

(E)-4-(dodecyloxy)-N'-(pyridin-2-ylmethylene)benzohydrazide (HL^4). Yield 98 %. ^{1}H NMR (400 MHz, $CDCl_3$): δ 8.46 (m, 2H, *CH*$_{py}$ + *CH*$_{im}$), 8.01 (m, 1H, *CH*$_{py}$), 7.90 (m, 2H, *CH*$_{ar}$), 7.59 (t, 1H, C*H*$_{py}$), 7.16 (t, 1H, C*H*$_{py}$), 6.81 (m, 2H, *CH*$_{ar}$), 3.90 (t, 2H, *CH*$_2$O), 1.74 (m, 2H, *CH*$_2$CH$_2$O), 1.41-1.26 (m, 18 H, CH$_2$), 0.87 (t, 3H, *CH*$_3$). ^{13}C{^{1}H} NMR (100 MHz, $CDCl_3$): δ 164.6, 162.3, 153.4, 149.0, 148.0, 136.6, 129.9, 124.7, 124.1, 121.1, 114.2, 68.3, 32.0, 29.7, 29.7, 29.6, 29.5, 29.4, 29.2, 26.1, 22.8, 14.2. Selected FT-IR data (ATR, cm^{-1}): 2920 (ν$_{C-H}$), 2851(ν$_{C-H}$), 1633 (ν$_{C=O}$), 1612, 1551, 1508, 1461, 1344, 1279, 1253, 1189, 1072, 1020, 839, 761. Elemental analysis – Calc. (Found) for $C_{25}H_{35}N_3O_2$: C, 73.31 (72.67); N, 10.25 (10.08); H, 8.61 (8.59).

(E)-N'-((5-chloropyridin-2-yl)methylene)-4-(dodecyloxy)benzohydrazide (HL^5). Yield 86 %. ^{1}H NMR (400 MHz, $CDCl_3$): δ 8.57 (s, 1H, *CH*$_{py}$), 8.57 (s, 1H, *CH*$_{im}$), 8.28 (d, *J* = 8.4 Hz, 1H, *CH*$_{py}$), 7.96-7.89 (m, 3H, *CH*$_{ar}$ + *CH*$_{py}$), 7.05 (d, *J* = 8.8 Hz, 2H, *CH*$_{ar}$), 3.92 (t, 2H, *CH*$_2$O), 1.72 (m, 2H, *CH*$_2$CH$_2$O), 1.38-1.25 (m, 18 H, CH$_2$), 0.90 (t, 3H, *CH*$_3$). Selected FT-IR data (ATR, cm^{-1}): 2918 (ν$_{C-H}$), 2848 (ν$_{C-H}$), 1656 (ν$_{C=O}$), 1604, 1542, 1505, 1461, 1243, 1144, 1224, 1009, 843, 634. Elemental analysis – Calc. (Found) for $C_{25}H_{34}ClN_3O_2$: C, 67.63 (67.47); N, 9.46 (9.17); H, 7.72 (7.96).

(E)-N'-((5-chloropyridin-2-yl)methylene)-4-(dodecyloxy)benzohydrazide (HL^6). Yield 58 %. ^{1}H NMR (400 MHz, CD_2Cl_2): δ 8.56 (s, *J* = 4.1 Hz, 1H, *CH*$_{py}$), 8.18-8.05 (m, 2H, *CH*$_{im}$ + *CH*$_{py}$), 7. 81 (m, 2H, *CH*$_{ar}$), 7. 72 (t, 1H, *J* = 7.6 Hz, *CH*$_{py}$), 7. 27 (d, 1H, *J* = 7.5 Hz, *CH*$_{py}$), 6.94 (d, *J* = 8.8 Hz, 2H, *CH*$_{ar}$), 3.92 (t, *J* = 6.6 Hz, 2H, *CH*$_2$O), 1.79 (m, 2H, *CH*$_2$CH$_2$O), 1.45-1.23 (m, 30 H, CH$_2$), 0.84 (t, *J* = 6.4 Hz, 3H, *CH*$_3$). Selected FT-IR data (ATR, cm^{-1}): 2919 (ν$_{C-H}$), 2849 (ν$_{C-H}$), 1639(ν$_{C=O}$), 1608, 1551, 1510, 1464, 1395, 1254, 1183, 1144, 650.

(E)-3,5-bis(dodecyloxy)-N'-(pyridin-2-ylmethylene)benzohydrazide (HL^7). Yield 93 %. ^{1}H NMR (400 MHz, $CDCl_3$): δ 8.48 (d, *J* = 4.8 Hz, 1H, *CH*$_{py}$), 8.41 (s, 1H, *CH*$_{im}$), 8.05 (d, *J* = 7.2 Hz, 1H, *CH*$_{py}$), 7.64 (t, *J*

= 5.8 Hz, 1H, CH_{py}), 7.00 (s, 2H, CH_{ar}), 6.54 (s, 1H, CH_{ar}), 3.84 (t, 4H, CH_2O), 1.87 (m, 4H, CH_2CH_2O), 1.45-1.23 (m, 36 H, CH_2), 0.88 (t, J = 5.9 Hz, 6H, CH_3). Selected FT-IR data (ATR, cm^{-1}: 2920 (ν_{C-H}), 2851 (ν_{C-H}), 1645 ($\nu_{C=O}$), 1590, 1554, 1464, 1349, 1301, 1269, 1246, 1150, 1071, 1096, 776. Elemental analysis – Calc. (Found) for $C_{37}H_{59}N_3O_3$: C, 74.83 (74.42); N, 7.08 (7.11); H, 10.01 (10.89).

(E)-3,4,5-tris(dodecyloxy)-N'-(pyridin-2-ylmethylene)benzohydrazide (HL^8). Yield 95 %. ^{1}H NMR (400 MHz, $CDCl_3$): δ 8.49 (m, 1H, CH_{py}), 8.39 (s, 1H, CH_{im}), 8.05 (m, 1H, CH_{py}), 7.60 (t, 1H, CH_{py}), 7.21-7.04 (m, 3H, CH_{py} + CH_{ar}), 3.89 (m, 6H, CH_2O), 1.94-1.87 (m, 6H, CH_2CH_2O), 1.5-1.0 (m, 54 H, CH_2), 0.88 (m, 9H, CH_3). Selected FT-IR data (ATR, cm^{-1}): 2920 (ν_{C-H}), 2851 (ν_{C-H}), 1639 ($\nu_{C=O}$), 1580, 1552, 1465, 1329, 1232, 1145, 992, 776, 756, 617. Elemental analysis – Calc. (Found) for $C_{49}H_{83}N_3O_4$: C, 75.63 (76.47); N, 5.40 (5.47); H, 10.75 (10.72).

III.5.1.2. Synthesis and characterization of Fe(II) complexes

Preparation of α-[Fe(L^1)$_2$] polymorph. To a solution of **HL^1** (100 mg, $3.92\cdot10^{-4}$ mol, 1 eq.) and trimethylamine (100 µL, $7.88\cdot10^{-4}$ mol, 2 eq.) in methanol (4 mL), was added a solution of $Fe(ClO_4)_2\cdot6H_2O$ (71.1 mg, $1.96\cdot10^{-4}$ mol, 0.5 eq.). The dark green solution was homogenized and then allowed to stand at room temperature for 24 hours. The resulting dark green needles of **α-[Fe(L^1)$_2$]·MeOH** were collected by filtration. The **α-[Fe(L^1)$_2$]** complex is obtained by natural desolvation of the complex in air : Yield 75 mg, 68 %. Elemental analysis – Calc. (Found) for $C_{28}H_{24}FeN_6O_4$: C, 59.59 (59.32); N, 14.89 (14.66); H, 4.29 (4.40). Selected FT-IR data (ATR, cm^{-1}): 1602 ($\nu_{C=N-N=C}$), 1583 ($\nu_{C=N-N=C}$), 1516, 1466, 1450, 1437, 1404, 1350 (ν_{C-O}), 1287, 1246, 1162, 1141, 1102, 1057, 1028, 917, 879, 838, 809, 755, 740, 694, 677, 625.

Preparation of β-[Fe(L^1)$_2$] polymorph. $Fe(ClO_4)_2\cdot6H_2O$ (71.1 mg, $1.96\cdot10^{-4}$ mol, 0.5 eq.) was added into a solution of **HL^1** (100 mg, $3.92\cdot10^{-4}$ mol, 1 eq.) and trimethylamine (100 µL, $7.88\cdot10^{-4}$ mol, 2 eq.) in methanol (8 mL) preheated to 50°C. After homogenization of the dark green solution, the mixture was allowed to stand at room temperature for 20 hours. The resulting dark green needles of **β-[Fe(L^1)$_2$]·MeOH** were collected by filtration. The needle sample was dried under vacuum at 40 °C for 12 hours to obtain the solvent-free **β-[Fe(L^1)$_2$]**·complex: Yield 79 mg, 72 %. Elemental analysis – Calc. (Found) for $C_{28}H_{24}FeN_6O_4$: C, 59.59 (58.89); N, 14.89 (14.70); H, 4.29 (4.57). Selected FT-IR data (ATR, cm^{-1}): 1597 ($\nu_{C=N-N=C}$), 1583 ($\nu_{C=N-N=C}$), 1511, 1444, 1355 (ν_{C-O}), 1296, 1248, 1162, 1143, 1105, 1057, 1023, 919, 902, 850, 838, 763, 698, 674, 638, 615.

Preparation of [Fe(HL^1)$_2$](ClO$_4$)$_2$. **HL^1** (100 mg, $3.92\cdot10^{-4}$ mol, 1 eq.) and $Fe(ClO_4)_2\cdot6H_2O$ (143 mg, $3.94\cdot10^{-4}$ mol, 1 eq.) were combined in methanol (5 mL) and the mixture was stirred at room temperature for 2 hours. The clear red-purple solution is then allowed to stand for slow evaporation. Red-purple plate-like crystal were collected after about 3 weeks: Yield 67 mg, 45 %. Elemental analysis – Calc. (Found) for $C_{28}H_{26}Cl_2FeN_6O_{12}$: C, 43.94 (43.36); N, 10.98 (11.00); H, 3.42 (3.71).Selected FT-IR data (ATR, cm^{-1}): 1588, 1562, 1503, 1468, 1357, 1314, 1303, 1262, 1175, 1096 (ClO_4), 1041, 1018, 909, 846, 773, 761, 742, 617.

Preparation of [Fe(HL^1)(L^1)](ClO$_4$)·MeOH. A solution of **HL^1** (100 mg, $3.92\cdot10^{-4}$ mol, 1 eq) in methanol (4 mL) was added layered with a solution of $Fe(ClO_4)_2\cdot6H_2O$ (71.1 mg, $1.96\cdot10^{-4}$ mol, 0.5 eq.) in methanol (4 mL). The resulting greenish gray needles formed at the interface were collected after 24 hours and washed with cold methanol: Yield 17 mg, 12 %. 1602, 1560, 1508, 1444, 1424, 1402, 1370, 1330, 1297, 1254, 1176, 1084 (ClO_4), 1022, 934, 914, 844, 777, 759, 692, 676, 617.

Preparation of α-[Fe(L^2)$_2$] polymorph. To a solution of **HL^2** (100 mg, $3.50\cdot10^{-4}$ mol, 1 eq.) and trimethylamine (100 µL, $7.88\cdot10^{-4}$ mol, 2.2 eq.) in methanol (6 mL), was added a solution of $Fe(ClO_4)_2\cdot6H_2O$ (63.6 mg, $1.75\cdot10^{-4}$ mol, 0.5 eq.). The dark green solution was homogenized for few second and then allowed to stand at room temperature. Dark green needles of **α-[Fe(L^2)$_2$]** were formed within 1 hour and collected by filtration: Yield 90 mg, 82 %. Elemental analysis – Calc. (Found) for $C_{30}H_{28}FeN_6O_6$: C, 57.70 (56.96); N, 13.46 (13.16); H, 4.52 (4.77). Selected FT-IR data (ATR, cm^{-1}): 1593 ($\nu_{C=N-N=C}$), 1485, 1460, 1438, 1411, 1355 (ν_{C-O}), 1342, 1325, 1303, 1246, 1201, 1147, 1111, 1058, 1041, 962, 915, 843, 801, 759, 746, 674.

Preparation of β-[Fe(L^2)$_2$] polymorph. **HL^2** (200 mg, $7.01\cdot10^{-4}$ mol, 1 eq.), trimethylamine (200 µL, $15.8\cdot10^{-4}$ mol, 2.2 eq.) and $Fe(ClO_4)_2\cdot6H_2O$ (127.2 mg, $3.50\cdot10^{-4}$ mol, 0.5 eq.) were combined in methanol and the mixture was stirred at room temperature for 1 hour. The resulting microcrystalline powder was collected by filtration and allowed to dry for few hours. The powder sample was fractioned in four and each fraction was dissolved in 1.5 mL of dichloromethane. The solutions were layered with methanol (6 mL) in capped glass tubes. The resulting dark green block-like crystals of **β-[Fe(L^2)$_2$]** were collected after 36 hours. The crude sample contained a small amount of needles (α-polymorph), which were discarded by hand: Yield 149 mg, 68 %. Elemental analysis – Calc. (Found) for $C_{30}H_{28}FeN_6O_6$: C, 57.70 (56.99); N, 13.46 (12.75); H, 4.52 (4.88). Selected FT-IR data (ATR, cm^{-1}): 1593 ($\nu_{C=N-N=C}$), 1561, 1477, 1457, 1434, 1363, 1326, 1288, 1249, 1204, 1192, 1147, 1116, 1056, 874, 844, 813, 755, 676, 580.

Preparation of [Fe(L^3)$_2$]·MeOH and [Fe(L^3)$_2$] complexes. **HL^3** (100 mg, $3.17\cdot10^{-4}$ mol, 1 eq.), trimethylamine (90 µL, $6.5\cdot10^{-4}$ mol, 2 eq.) and $Fe(ClO_4)_2\cdot6H_2O$ (57.5 mg, $1.59\cdot10^{-4}$ mol, 0.5 eq.) were combined in methanol and the mixture was stirred at room temperature for 1 hour. The resulting microcrystalline powder was collected by filtration and allowed to dry for few hours. Plate-like crystals of **[Fe(L^3)$_2$]·MeOH** were obtained after dissolving the powder in 1.5 mL of dichloromethane and layering with MeOH (6 mL): Yield 95 mg, 83 %. Calc. (Found) for $C_{33}H_{36}FeN_6O_9$: C, 55.32 (54.89); N, 11.73 (11.59); H, 5.06 (5.02). Selected FT-IR data (ATR, cm^{-1}): 3385, 1596 ($\nu_{C=N-N=C}$), 1587 ($\nu_{C=N-N=C}$), 1501, 1475, 1450, 1432, 1364 (ν_{C-O}), 1289, 1235, 1222, 1179, 1120, 1061, 1001, 860, 835, 827, 768, 753, 688, 580.
Single-crystals of solvent-free **[Fe(L^3)$_2$]** complex were obtained by diethyl ether vapor diffusion into a solution of the raw sample in dichloromethane (2 mL). The tiny plate-like crystals were collected after 24 h: Yield 38 mg, 35 %. Selected FT-IR data (ATR, cm^{-1}): 1595 ($\nu_{C=N-N=C}$), 1587($\nu_{C=N-N=C}$), 1499, 1478, 1457, 1430, 1363 (ν_{C-O}), 1289, 1231, 1218, 1185, 1121, 1054, 1039, 997, 862, 828, 767, 751, 733, 685, 580.

General procedure for the preparation of [Fe(L^{4-8})$_2$] complexes. A solution of **HL^{4-8}** (100 mg, 1 eq.) and trimethylamine (2 eq.) in 15 mL of MeOH was heated to 60 °C and $Fe(ClO_4)_2 \cdot 6H_2O$ (0.5 eq.) was added. The reaction mixture was stirred at 60°C for 2-3 hours. Then, the reaction was slowly cooled to room temperature over 2 hours, during which microcrystalline powder (with **L^{4-6}**) or aggregates (with **$L^{7,8}$**) precipitated. The dark green precipitates were collected by filtration and leave to dry for few hour in air. The powder samples were obtained with 74 to 87 % yields. Single-crystals of [Fe(**L^4**)$_2$] were obtaining after dissolution of the microcrystalline powder in dichloromethane (2 mL) and layering with hexane. The sheet-like crystals were isolated after about one week (yield 42 %). Single-crystals of [Fe(**L^5**)$_2$] were prepared in the same fashion using methanol instead of hexane and isolated in 54 % yield.

[Fe(L^4)$_2$]: Yield 87 % (42 % for single-crystals). Elemental analysis – Calc. (Found) for $C_{50}H_{68}FeN_6O_4$: C, 68.79 (68.49); N, 9.63 (9.27); H, 7.85 (8.36). Selected FT-IR data (ATR, cm^{-1}): 2916 (ν_{C-H}), 2848 (ν_{C-H}) 1606 ($\nu_{C=N-N=C}$), 1583 ($\nu_{C=N-N=C}$), 1521, 1469, 1440, 1366 (ν_{C-O}), 1335, 1298, 1243, 1167, 1152, 1052, 840, 683.

[Fe(L^5)$_2$]: Yield 82% (54 % for single-crystals). Elemental analysis – Calc. (Found) for $C_{50}H_{66}Cl_2FeN_6O_4$: C, 63.76 (63.61); N, 8.92 (8.01); H, 7.06 (7.25). Selected FT-IR data (ATR, cm^{-1}): 2919 (ν_{C-H}), 2850 (ν_{C-H}) 1604 ($\nu_{C=N-N=C}$), 1581($\nu_{C=N-N=C}$), 1551, 1518, 1466, 1439 1354 (ν_{C-O}), 1245, 1163, 1145, 1066, 1024, 841, 761, 663.

[Fe(L^6)$_2$]: Yield 78 %. Elemental analysis – Calc. (Found) for $C_{62}H_{92}FeN_6O_4$: C, 71.51 (69.74); N, 8.07 (7.87); H, 8.91 (9.31). Selected FT-IR data (ATR, cm^{-1}): 2917 (ν_{C-H}), 2849 (ν_{C-H}), 1606 ($\nu_{C=N-N=C}$), 1579 ($\nu_{C=N-N=C}$), 1440, 1369 (ν_{C-O}), 1299, 1243, 1168, 1143, 1052, 841, 757.

[Fe(L^7)$_2$]: Yield 74 %. Elemental analysis – Calc. (Found) for $C_{74}H_{116}FeN_6O_6$: C, 71.58 (71.46); N, 6.77 (6.66); H, 9.42 (10.30).Selected FT-IR data (ATR, cm^{-1}): 2919 (ν_{C-H}), 2851 (ν_{C-H}), 1593 ($\nu_{C=N-N=C}$), 1485, 1450, 1451, 1357 (ν_{C-O}), 1155, 1057, 829, 754, 677.

[Fe(L^8)$_2$]: Yield 77 %. Elemental analysis – Calc. (Found) for $C_{98}H_{164}FeN_6O_8$: C, 73.10 (72.25); N, 5.22 (5.11); H, 10.27 (10.93). Selected FT-IR data (ATR, cm^{-1}): 2918 (ν_{C-H}), 2849 (ν_{C-H}), 1585 ($\nu_{C=N-N=C}$), 1468, 1444, 1399, 1361 (ν_{C-O}), 1289, 1222, 1108, 1063, 1051, 755, 719, 686, 652.

II.5.2. Selected FTIR spectra

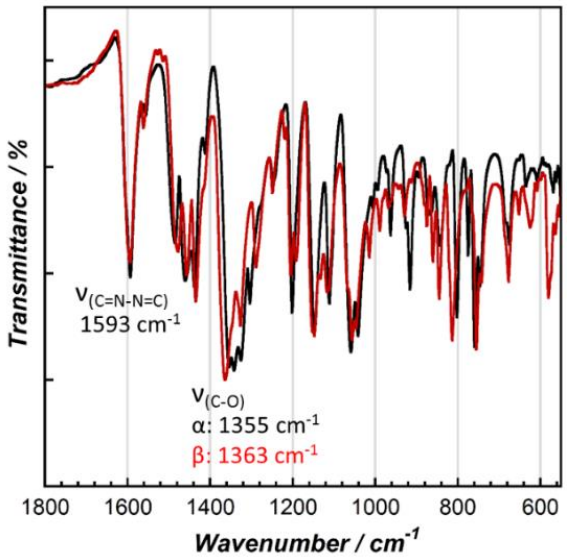

Figure S.III-1. FTIR spectra for α-[Fe($\mathbf{L}^2$)$_2$] (black) and β-[Fe($\mathbf{L}^2$)$_2$] (red)

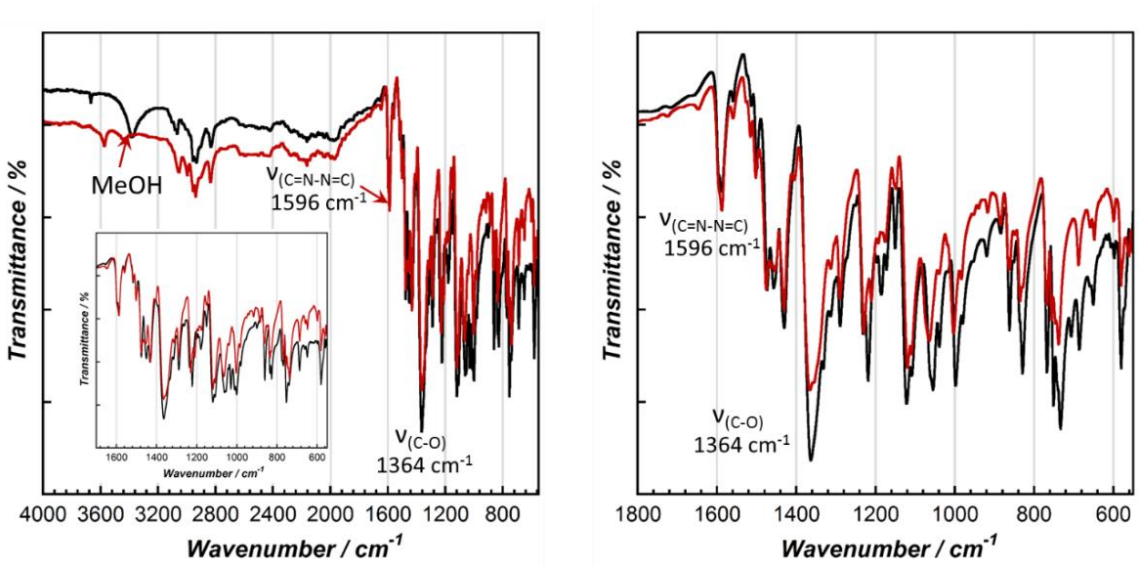

Figure S.III-2. (left) FTIR spectra for [Fe($\mathbf{L}^3$)$_2$]·MeOH (black) and solvent-free [Fe($\mathbf{L}^3$)$_2$] (red) obtained after desolvation in DSC. (left) FTIR spectra for solvent-free [Fe($\mathbf{L}^3$)$_2$] complexes obtained by crystallization (black) and desolvation of [Fe($\mathbf{L}^3$)$_2$]·MeOH.

III.5.3. Crystallographic data

Table S.III-1. Crystallographic data for $[Fe(\mathbf{L^1})_2]\cdot MeOH$ polymorphs

Compound	α-{$[Fe(\mathbf{L^1})_2]\cdot MeOH$}		β-{$[Fe(\mathbf{L^1})_2]\cdot MeOH$}	
Temperature, K	120	260	120	290
Crystal description	Dark green needle	Dark green needle	Green needle	Green needle
Moiety formula	$C_{28}H_{24}FeN_6O_4$, CH_4O	$C_{28}H_{24}FeN_6O_4$, CH_4O	$C_{28}H_{24}FeN_6O_4$, CH_4O	$C_{28}H_{24}FeN_6O_4$, CH_4O
Empirical formula	$C_{29}H_{28}FeN_6O_5$	$C_{29}H_{28}FeN_6O_5$	$C_{29}H_{28}FeN_6O_5$	$C_{29}H_{28}FeN_6O_5$
Formula weight	596.42	596.42	596.42	596.42
Crystal system	Monoclinic	Monoclinic	Triclinic	Triclinic
Space group	*$P2_1/c$*	*$P2_1/c$*	*P-1*	*P-1*
Wavelength, Å	0.71073	0.71073	0.71073	0.71073
a, Å	24.1677(6)	22.808(2)	8.7893(4)	8.883(13)
b, Å	13.2155(4)	13.1051(14)	11.1963(5)	11.170(17)
c, Å	8.7284(2)	8.7743(9)	14.8884(7)	15.09(3)
α, °	90	90	111.717(2)	111.71(5)
β, °	99.860(1)	98.307(4)	91.037(2)	91.93(7)
γ, °	90	90	97.507(2)	96.71(5)
V, $Å^3$	2746.6(1)	2595.1(4)	1345.96(11)	1377(4)
Z	4	4	2	2
ρ_{calcd}, g/cm^3	1.408	1.439	1.472	1.584
$\mu_{MoK\alpha}$, 1/mm	0.600	0.628	0.612	0.617
R_1[a]	0.0406	0.1174	0.0332	0.0974
wR_2[b]	0.0895	0.2881	0.0941	0.2399
GoF[c]	1.055	1.115	1.101	0.993
		Selected bond distances		
Fe(1)-N(1)	1.961(3)	1.965(7)	2.2618(13)	2.246(12)
Fe(1)-N(2)	1.871(2)	1.868(7)	2.1175(12)	2.100(13)
Fe(1)-N(4)	1.947(2)	1.951(7)	2.2037(12)	2.269(10)
Fe(1)-N(5)	1.869(2)	1.855(8)	2.1090(12)	2.104(12)
Fe(1)-O(1)	1.980(2)	1.981(5)	2.0866(11)	2.093(10)
Fe(1)-O(3)	1.972(2)	1.954(7)	2.1160(10)	2.107(10)
		Selected bond angles		
N(1)-Fe(1)-N(2)	81.18(1)	81.6(3)	73.09(5)	74.1(5)
N(1)-Fe(1)-N(4)	91.35(1)	91.4(3)	87.36(4)	88.8(3)
N(1)-Fe(1)-N(5)	98.40(1)	97.7(3)	89.25(5)	89.0(4)
N(1)-Fe(1)-O(3)	90.96(9)	91.2(3)	97.65(4)	96.0(4)
N(1)-Fe(1)-O(1)	160.76(1)	160.7(3)	146.54(4)	146.8(5)
N(2)-Fe(1)-N(4)	99.97(1)	98.8(3)	100.25(5)	101.5(5)
N(2)-Fe(1)-N(5)	178.6(1)	179.2(3)	161.88(5)	162.5(4)
N(2)-Fe(1)-O(1)	79.58(9)	79.0(2)	73.04(4)	73.4(5)
N(2)-Fe(1)-O(3)	98.61(1)	99.1(3)	112.58(4)	111.6(4)
N(4)-Fe(1)-N(5)	81.33(1)	81.6(4)	74.31(5)	73.9(4)
N(4)-Fe(1)-O(1)	92.33(9)	92.0(2)	97.45(4)	97.1(4)
N(4)-Fe(1)-O(3)	161.41(9)	162.0(3)	146.87(4)	147.3(5)
N(5)-Fe(1)-O(1)	100.80(1)	101.7(3)	123.99(4)	123.5(4)
N(5)-Fe(1)-O(3)	80.10(1)	80.5(4)	73.47(4)	73.5(4)
O(1)-Fe(1)-O(3)	91.54(8)	91.3(2)	96.06(4)	96.4(4)

[a] $I > 2\sigma(I)$, $R_1 = \Sigma(||F_o| - |F_c||)/\Sigma|F_o|$. [b] $wR_2 = \{\Sigma[w(F_o^2 - F_c^2)^2]/\Sigma[w(F_o^2)^2]\}^{1/2}$. [c] GoF (goodness of fit on F^2) $= \{\Sigma[w(F_o^2 - F_c^2)^2]/(n-p)\}^{1/2}$, where n is the number of reflections and p is the total number of refined parameters.

Table S.III-2. Crystallographic data for α-[Fe($\mathbf{L^1}$)$_2$]

Temperature, K	120	260	370
Crystal description	Dark green needle	Dark green needle	Green needle
Moiety formula	$C_{28}H_{24}FeN_6O_4$	$C_{28}H_{24}FeN_6O_4$	$C_{28}H_{24}FeN_6O_4$
Empirical formula	$C_{28}H_{24}FeN_6O_4$	$C_{28}H_{24}FeN_6O_4$	$C_{28}H_{24}FeN_6O_4$
Formula weight	564.38	564.38	564.38
Crystal system	Monoclinic	Monoclinic	Monoclinic
Space group	$P2_1/c$	$P2_1/c$	$P2_1/c$
Wavelength, Å	0.71073	0.71073	0.71073
a, Å	22.7027(14)	22.808(2)	21.451(3)
b, Å	12.9995(8)	13.1051(14)	14.565(3)
c, Å	8.7405(6)	8.7743(9)	8.6226(15)
β, °	98.705(3)	98.307(4)	96.467(6)
V, Å^3	2549.8(3)	2595.1(4)	2676.9(8)
Z	4	4	4
ρ_{calcd}, g/cm^3	1.470	1.439	1.400
$\mu_{MoK\alpha}$, 1/mm	0.639	0.628	0.609
R_1[a]	0.0879	0.1174	0.0815
wR_2[b]	0.1872	0.2881	0.1792
GoF[c]	1.226	1.115	1.090
	Selected bond distances		
Fe(1)-N(1)	1.955(5)	1.965(7)	2.194(6)
Fe(1)-N(2)	1.858(6)	1.868(7)	2.061(8)
Fe(1)-N(4)	1.965(4)	1.951(7)	2.213(8)
Fe(1)-N(5)	1.869(5)	1.855(8)	2.059(8)
Fe(1)-O(1)	1.959(5)	1.981(5)	2.077(5)
Fe(1)-O(3)	1.980(3)	1.954(7)	2.079(6)
	Selected bond angles		
N(1)-Fe(1)-N(2)	81.3(2)	81.6(3)	75.0(3)
N(1)-Fe(1)-N(4)	91.32(19)	91.4(3)	89.8(2)
N(1)-Fe(1)-N(5)	98.28(19)	97.7(3)	102.8(3)
N(1)-Fe(1)-O(3)	92.30(16)	91.2(3)	92.3(2)
N(1)-Fe(1)-O(1)	162.1(2)	160.7(3)	147.6(3)
N(2)-Fe(1)-N(4)	97.5(2)	98.8(3)	115.2(4)
N(2)-Fe(1)-N(5)	178.78(19)	179.2(3)	170.5(3)
N(2)-Fe(1)-O(1)	80.8(2)	79.0(2)	73.8(2)
N(2)-Fe(1)-O(3)	101.78(17)	99.1(3)	96.2(3)
N(4)-Fe(1)-N(5)	81.32(19)	81.6(4)	73.8(4)
N(4)-Fe(1)-O(1)	91.52(19)	92.0(2)	95.5(2)
N(4)-Fe(1)-O(3)	160.68(19)	162.0(3)	147.9(4)
N(5)-Fe(1)-O(1)	99.6(2)	101.7(3)	109.3(2)
N(5)-Fe(1)-O(3)	79.37(17)	80.5(4)	74.5(3)
O(1)-Fe(1)-O(3)	90.85(16)	91.3(2)	99.6(2)

[a] $I > 2\sigma(I)$, $R_1 = \Sigma||F_o| - |F_c||/\Sigma|F_o|$. [b] $wR_2 = \{\Sigma[w(F_o^2 - F_c^2)^2]/\Sigma[w(F_o^2)^2]\}^{1/2}$. [c] GoF (goodness of fit on F^2) = $\{\Sigma[w(F_o^2 - F_c^2)^2]/(n\text{-}p)\}^{1/2}$, where n is the number of reflections and p is the total number of refined parameters.

Table S.III-3. Crystallographic data for $[Fe(\mathbf{HL^1})_2]^{2+}$ and $[Fe(\mathbf{HL^1})(\mathbf{L^1})]^{+}$ complexes

Compound	$[Fe(\mathbf{HL^1})_2](ClO_4)_2$	$[Fe(\mathbf{HL^1})(\mathbf{L^1})](ClO_4)\cdot MeOH$	$[Fe(\mathbf{HL^1})(\mathbf{L^1})](ClO_4)$
Temperature, K	120	120	120
Crystal description	Purple plate	Greenish gray needle	Greenish gray block
Moiety formula	$C_{28}H_{26}FeN_6O_4,2ClO_4$	$C_{28}H_{25}FeN_6O_4,ClO_4,CH_4O$	$C_{28}H_{25}FeN_6O_4,ClO_4$
Empirical formula	$C_{28}H_{26}FeCl_2N_6O_{12}$	$C_{29}H_{29}FeClN_6O_9$	$C_{28}H_{25}FeClN_6O_8$
Formula weight	764.03	694.10	664.83
Crystal system	Monoclinic	Triclinic	Orthorhombic
Space group	*$P2_1/c$*	*P-1*	*Pnna*
Wavelength, Å	0.71073	0.71073	0.71073
a, Å	11.3202(9)	10.8762(4)	14.9875(12)
b, Å	12.6110(13)	11.5572(5)	25.0245(18)
c, Å	21.564(2)	13.4441(6)	14.8207(14)
α, °	90	72.307(2)	90
β, °	90.458(2)	79.470(2)	90
γ, °	90	79.920(2)	90
V, Å^3	3078.4(5)	1569.92(12)	5558.6(8)
Z	4	2	8
ρ_{calcd}, g/cm^3	1.351	1.474	1.510
$\mu_{MoK\omega}$, 1/mm	0.623	0.628	0.686
R_1[a]	0.0462	0.0641	0.0783
wR_2[b]	0.1299	0.2002	0.2621
GoF[c]	1.068	1.049	0.896
	Selected bond distances		
Fe(1)-N(1)	2.217(3)	2.237(3)	2.131(6)
Fe(1)-N(2)	2.121(3)	2.126(3)	2.099(5)
Fe(1)-N(4)	2.179(3)	2.213(3)	2.160(6)
Fe(1)-N(5)	2.131(3)	2.088(3)	2.106(5)
Fe(1)-O(1)	2.135(2)	2.184(3)	1.974(5)
Fe(1)-O(3)	2.107(2)	2.122(3)	1.952(5)
	Selected bond angles		
N(1)-Fe(1)-N(2)	73.27(10)	73.23(12)	74.6(2)
N(1)-Fe(1)-N(4)	87.28(10)	93.62(12)	98.0(2)
N(1)-Fe(1)-N(5)	89.14(10)	97.55(12)	100.0(2)
N(1)-Fe(1)-O(3)	101.24(9)	94.28(12)	91.5(2)
N(1)-Fe(1)-O(1)	145.41(10)	145.07(12)	147.9(2)
N(2)-Fe(1)-N(4)	95.64(10)	97.89(12)	93.4(2)
N(2)-Fe(1)-N(5)	159.96(11)	167.92(13)	165.6(2)
N(2)-Fe(1)-O(1)	72.78(10)	71.84(11)	74.7(2)
N(2)-Fe(1)-O(3)	119.27(9)	114.54(11)	118.5(2)
N(4)-Fe(1)-N(5)	73.54(10)	74.52(13)	73.9(2)
N(4)-Fe(1)-O(1)	102.42(10)	90.60(12)	92.9(2)
N(4)-Fe(1)-O(3)	145.08(10)	147.54(12)	148.0(2)
N(5)-Fe(1)-O(1)	125.44(10)	116.94(12)	112.0(2)
N(5)-Fe(1)-O(3)	72.80(9)	73.25(12)	74.5(2)
O(1)-Fe(1)-O(3)	89.63(9)	100.51(11)	94.9(2)

[a] $I > 2\sigma(I)$, $R_1 = \Sigma(||F_o| - |F_c||)/\Sigma|F_o|$. [b] $wR_2 = \{\Sigma[w(F_o^2 - F_c^2)^2]/\Sigma[w(F_o^2)^2]\}^{1/2}$. [c] GoF (goodness of fit on F^2) = $\{\Sigma[w(F_o^2 - F_c^2)^2]/(n-p)\}^{1/2}$, where n is the number of reflections and p is the total number of refined parameters.

Table S.III-4. Crystallographic data for α-[Fe($\mathbf{L^2}$)$_2$] complex

Temperature, K	120	300
Crystal description	Green needle	Green needle
Moiety formula	$C_{30}H_{28}FeN_6O_6$	$C_{30}H_{28}FeN_6O_6$
Empirical formula	$C_{30}H_{28}FeN_6O_6$	$C_{30}H_{28}FeN_6O_6$
Formula weight	624.42	624.42
Crystal system	Monoclinic	Monoclinic
Space group	*C2/c*	*C2/c*
Wavelength, Å	0.71073	0.71073
a, Å	23.0807(7)	23.0694(19)
b, Å	10.8025(3)	10.8626(7)
c, Å	11.8221(2)	11.9644(11)
β, °	105.6540(10)	105.223(4)
V, Å^3	2838.26(13)	2893.0(4)
Z	4	4
ρ_{calcd}, g/cm^3	1.611	1.566
$\mu_{MoK\alpha}$, 1/mm	0.595	0.607
R_1[a]	0.0356	0.0762
wR_2[b]	0.1246	0.1933
GoF[c]	0.974	1.246
	Selected bond distances	
Fe(1)-N(1)	2.2611(17)	2.267(3)
Fe(1)-N(2)	2.1106(16)	2.113(3)
Fe(1)-O(1)	2.1121(14)	2.113(2)
	Selected bond angles	
N(1)-Fe(1)-N(1)'	82.50(9)	83.17(14)
N(1)-Fe(1)-N(2)	73.30(6)	72.75(10)
N(1)-Fe(1)-N(2)'	91.23(6)	91.71(10)
N(1)-Fe(1)-O(1)	146.43(6)	145.90(9)
N(1)-Fe(1)-O(1)'	100.19(6)	99.66(9)
O(1)-Fe(1)-O1'	95.60(8)	96.53(12)
N(2)-Fe(1)-N(2)'	159.62(9)	159.46(14)
N(2)-Fe(1)-O(1)	73.19(6)	73.20(9)
N(2)-Fe(1)-O(1)'	121.79(6)	121.76(9)

[a] $I > 2\sigma(I)$, $R_1 = \Sigma(||F_o| - |F_c||)/\Sigma|F_o|$. [b] $wR_2 = \{\Sigma[w(F_o^2 - F_c^2)^2]/\Sigma[w(F_o^2)^2]\}^{1/2}$. [c] GoF (goodness of fit on F^2) = $\{\Sigma[w(F_o^2 - F_c^2)^2]/(n-p)\}^{1/2}$, where n is the number of reflections and p is the total number of

Table S.III-5. Crystallographic data for β-[Fe($\mathbf{L}^2$)$_2$] complex

Temperature, K	120	300	390	400	450
Crystal description			Dark green block		
Moiety formula			$C_{30}H_{28}FeN_6O_6$		
Empirical formula			$C_{30}H_{28}FeN_6O_6$		
Formula weight			624.42		
Crystal system			Triclinic		
Space group			*P-1*		
Wavelength, Å			0.71073		
a, Å	9.2954(4)	9.3765(3)	9.4017(15)	9.3875(6)	9.285(3)
b, Å	12.2093(5)	12.2641(3)	12.4153(19)	12.4485(8)	12.217(4)
c, Å	13.4330(6)	13.5941(4)	13.709(2)	13.7215(9)	13.445(4)
α, °	70.760(2)	70.0180(10)	69.595(5)	69.609(3)	70.591(15)
β, °	79.229(2)	78.9630(10)	78.414(6)	78.233(3)	78.987(15)
γ, °	85.641(2)	84.9030(10)	83.629(5)	83.296(3)	85.177(14)
V, Å^3	1413.84(11)	1441.50(7)	1467.8(4)	1469.61(16)	1411.6(7)
Z	2	2	2	2	2
ρ_{calcd}, g/cm^3	1.266	1.242	1.599	1.078	1.116
$\mu_{MoK\alpha}$, 1/mm	0.334	0.328	0.580	0.311	0.321
R_1[a]	0.0311	0.0384	0.0483	0.0452	0.0767
wR_2[b]	0.0974	0.1251	0.1584	0.1318	0.1956
GoF[c]	0.540	0.985	0.968	0.952	0.989
			Selected bond distances		
Fe(1)-N(1)	1.9555(17)	1.959(2)	2.009(3)	2.034(3)	1.953(6)
Fe(1)-N(2)	1.8653(17)	1.864(2)	1.910(2)	1.936(3)	1.844(6)
Fe(1)-N(4)	1.9534(17)	1.956(2)	2.008(3)	2.037(3)	1.968(6)
Fe(1)-N(5)	1.8679(17)	1.870(2)	1.923(3)	1.940(3)	1.853(6)
Fe(1)-O(1)	1.9686(14)	1.9717(18)	1.990(2)	1.997(2)	1.975(5)
Fe(1)-O(2)	1.9880(14)	1.9901(17)	2.013(2)	2.013(2)	1.985(5)
			Selected bond angles		
N(1)-Fe(1)-N(2)	81.49(7)	81.38(9)	79.52(10)	78.99(11)	81.5(3)
N(1)-Fe(1)-N(4)	93.57(7)	93.44(9)	92.55(11)	92.43(11)	94.0(2)
N(1)-Fe(1)-N(5)	100.03(7)	100.60(9)	101.89(10)	102.21(11)	100.0(3)
N(1)-Fe(1)-O(2)	91.57(6)	91.47(8)	92.35(10)	92.34(10)	91.4(2)
N(1)-Fe(1)-O(1)	161.61(7)	161.27(8)	157.93(10)	156.68(11)	161.7(2)
N(2)-Fe(1)-N(4)	95.94(7)	96.23(9)	96.43(11)	96.61(11)	95.9(3)
N(2)-Fe(1)-N(5)	176.74(7)	176.70(9)	175.78(11)	175.37(11)	176.9(3)
N(2)-Fe(1)-O(1)	80.14(7)	79.89(8)	78.41(9)	77.68(10)	80.2(2)
N(2)-Fe(1)-O(2)	103.08(6)	102.98(8)	105.63(10)	106.69(10)	102.8(2)
N(4)-Fe(1)-N(5)	81.11(7)	81.06(9)	79.58(11)	78.91(12)	81.3(3)
N(4)-Fe(1)-O(1)	88.95(7)	89.16(8)	89.88(10)	89.93(10)	88.5(2)
N(4)-Fe(1)-O(2)	160.83(7)	160.68(8)	157.92(11)	156.70(11)	161.0(2)
N(5)-Fe(1)-O(1)	98.36(7)	98.13(8)	100.12(10)	101.02(10)	98.3(2)
N(5)-Fe(1)-O(2)	79.82(6)	79.67(8)	78.35(10)	77.79(10)	79.9(2)
O(1)-Fe(1)-O(2)	91.97(6)	92.16(7)	93.58(9	94.62(10)	92.1(2)

[a] $I > 2\sigma(I)$, $R_1 = \Sigma(|F_o| - |F_c|)|/\Sigma|F_o|$. [b] $wR_2 = \{\Sigma[w(F_o^2 - F_c^2)^2]/\Sigma[w(F_o^2)^2]\}^{1/2}$. [c] GoF (goodness of fit on F^2) = $\{\Sigma[w(F_o^2 - F_c^2)^2]/(n-p)\}^{1/2}$, where n is the number of reflections and p is the total number of refined.

Table S.III-6. Crystallographic data for [Fe($\mathbf{L^3}$)$_2$] and [Fe($\mathbf{L^3}$)]·MeOH complexes

Compound	[Fe($\mathbf{L^3}$)$_2$]	[Fe($\mathbf{L^3}$)$_2$]·MeOH
Temperature, K	120	120
Crystal description	Dark green plate	Dark green plate
Moiety formula	$C_{32}H_{32}FeN_6O_8$	$C_{32}H_{32}FeN_6O_8,CH_4O$
Empirical formula	$C_{32}H_{32}FeN_6O_8$	$C_{33}H_{36}FeN_6O_9$
Formula weight	684.48	716.52
Crystal system	Triclinic	Monoclinic
Space group	*P-1*	*P2$_1$/n*
Wavelength, Å	0.71073	0.71073
a, Å	10.720(2)	9.1200(4)
b, Å	12.981(3)	25.3030(10)
c, Å	13.188(2)	15.1708(6)
α, °	102.214(9)	90
β, °	113.967(8)	102.552(2)
γ, °	90.034(10)	90
V, Å^3	1631.3(5)	3417.2(2)
Z	2	4
ρ_{calcd}, g/cm^3	1.347	1.673
$\mu_{MoK\alpha}$, 1/mm	0.515	0.906
R_1[a]	0.0694	0.1007
wR_2[b]	0.1971	0.2294
GoF[c]	0.970	1.131
	Selected bond distances	
Fe(1)-N(1)	1.936(5)	1.956(6)
Fe(1)-N(2)	1.855(5)	1.872(5)
Fe(1)-N(4)	1.934(4)	1.954(5)
Fe(1)-N(5)	1.849(5)	1.860(5)
Fe(1)-O(1)	1.964(4)	1.979(4)
Fe(1)-O(2)	1.976(3)	1.965(4)
	Selected bond angles	
N(1)-Fe(1)-N(2)	81.8(2)	81.3(2)
N(1)-Fe(1)-N(4)	92.50(17)	92.8(2)
N(1)-Fe(1)-N(5)	101.02(19)	96.5(2)
N(1)-Fe(1)-O(2)	91.54(16)	91.1(2)
N(1)-Fe(1)-O(1)	161.83(18)	161.2(2)
N(2)-Fe(1)-N(4)	100.90(19)	98.4(2)
N(2)-Fe(1)-N(5)	176.11(19)	177.7(2)
N(2)-Fe(1)-O(1)	80.02(18)	80.1(2)
N(2)-Fe(1)-O(2)	97.06(17)	100.2(2)
N(4)-Fe(1)-N(5)	81.69(19)	82.2(2)
N(4)-Fe(1)-O(1)	91.90(16)	92.3(2)
N(4)-Fe(1)-O(2)	161.97(18)	161.4(2)
N(5)-Fe(1)-O(1)	97.05(17)	102.1(2)
N(5)-Fe(1)-O(2)	80.29(17)	79.3(2)
O(1)-Fe(1)-O(2)	89.70(14)	89.73(19)

[a] $I > 2\sigma(I)$, $R_1 = \Sigma||F_o| - |F_c||/\Sigma|F_o|$. [b] $wR_2 = \{\Sigma[w(F_o^2 - F_c^2)^2]/\Sigma[w(F_o^2)^2]\}^{1/2}$. [c] GoF (goodness of fit on F^2) = $\{\Sigma[w(F_o^2 - F_c^2)^2]/(n\text{-}p)\}^{1/2}$, where n is the number of reflections and p is the total number of refined.

Table S.III-7. Crystallographic data for $[Fe(\mathbf{L^4})_2]$ complex.

Temperature / K	250	360
Crystal description	Dark green sheet	Green sheet
Moiety formula	$C_{50}H_{68}FeN_6O_4$	$C_{50}H_{68}FeN_6O_4$
Empirical formula	$C_{50}H_{68}FeN_6O_4$	$C_{50}H_{68}FeN_6O_4$
Formula weight	931.03	931.03
Crystal system	Monoclinic	Orthorhombic
Space group	$P2_1/c$	$P2_12_12$
Wavelength, Å	0.71073	0.71073
a / Å	10.4722(14)	10.036(2)
b / Å	40.801(5)	46.263(10)
c / Å	14.2308(16)	10.951(2)
β / °	128.100(7)	90
V / $Å^3$	4787.9(11)	5084.5(18)
Z	4	4
Flack parameter	--	0.49
μ, 1/mm	0.364	0.343
R_1[a]	0.0633	0.0748
wR_2[a]	0.1872	0.2254
GoF[a]	0.952	0.938

Site 1 (LS)		**Site 1(LS)**		**Site 2 (HS)**	
Fe1-N1	1.935(4)	Fe1-N1	1.917(1)	Fe2-N4	2.203(2)
Fe1-N2	1.868(2)	Fe1-N2	1.854(1)	Fe2-N5	2.092(1)
Fe1-N4	1.941(3)	Fe1-O1	1.972(1)	Fe2-O3	2.073(1)
Fe1-N5	1.866(2)				
Fe1-O1	1.966(3)				
Fe1-O3	1.966(3)				

Site 1 (LS)		**Site 1(LS)**		**Site 2 (HS)**	
N1-Fe1-N2	81.7(1)	N1-Fe1-N1’	89.70(1)	N4-Fe2-N4’	87.36(1)
N1-Fe1-N4	87.7(1)	N1-Fe1-N2	80.87(1)	N4-Fe2-N5	73.64(1)
N1-Fe(1)-N5	98.8(1)	N1-Fe1-N2’	97.8(1)	N4-Fe2-N5’	96.25(1)
N1-Fe1-O3	94.4(1)	N1-Fe1-O1	161.23(1)	N4-Fe2-O3	146.29(1)
N1-Fe1-O1	161.6(1)	N1-Fe1-O1’	92.26(1)	N4-Fe2-O3’	96.79(1)
N2-Fe1-N4	98.7(1)	N2-Fe1-N2’	178.1(1)	N5-Fe2-N5’	166.27(1)
N2-Fe1-N5	179.4(1)	N2-Fe1-O1	80.37(1)	N5-Fe2-O3	72,66(1)
N2-Fe1-O1	80.0(1)	N2-Fe1-O1’	100.95(1)	N5-Fe2-O3’	117.07(1)
N2-Fe1-O3	99.9(1)	O1-Fe1-O1’	91.85(1)	O3-Fe2-O3’	97.88(1)
N4-Fe1-N5	81.6(1)				
N4-Fe1-O1	94.5(1)				
N4-Fe1-O3	161.3(1)				
N5-Fe1-O1	99.6(1)				
N5-Fe1-O3	79.7(1)				
O1-Fe1-O3	89.3(1)				

[a] $I > 2\sigma(I)$, $R_1 = \Sigma(||F_o| - |F_c||)/\Sigma|F_o|$. [b] $wR_2 = \{\Sigma[w(F_o^2 - F_c^2)^2]/\Sigma[w(F_o^2)^2]\}^{1/2}$. [c] GoF (goodness of fit on F^2) $= \{\Sigma[w(F_o^2 - F_c^2)^2]/(n-p)\}^{1/2}$, where n is the number of reflections and p is the total number of refined.

Table S.III-8. Crystallographic data for [Fe($\mathbf{L^3}$)$_2$] and [Fe($\mathbf{L^3}$)]·MeOH complexes

Compound	[Fe($\mathbf{L^3}$)$_2$]
Temperature, K	120
Crystal description	Dark green sheet
Moiety formula	$C_{50}H_{66}Cl_2FeN_6O_4$
Empirical formula	$C_{50}H_{66}Cl_2FeN_6O_4$
Formula weight	941.84
Crystal system	Monoclinic
Space group	$P2_1/c$
Wavelength, Å	0.71073
a, Å	22.8322(13)
b, Å	12.6464(8)
c, Å	17.0912(11)
β, °	94.392(3)
V, Å^3	4920.2(5)
Z	4
ρ_{calcd}, g/cm^3	1.271
$\mu_{MoK\omega}$, 1/mm	0.464
R_1[a]	0.0581
wR_2[b]	0.1793
GoF[c]	0.773
Selected bond distances	
Fe(1)-N(1)	1.947(3)
Fe(1)-N(2)	1.863(3)
Fe(1)-N(4)	1.871(4)
Fe(1)-N(5)	1.986(4)
Fe(1)-O(1)	2.010(3)
Fe(1)-O(3)	1.997(3)
Selected bond angles	
N(1)-Fe(1)-N(2)	81.0(1)
N(1)-Fe(1)-N(4)	92.8(1)
N(1)-Fe(1)-N(5)	97.9(1)
N(1)-Fe(1)-O(2)	87.7(1)
N(1)-Fe(1)-O(1)	160.1(1)
N(2)-Fe(1)-N(4)	96.8(1)
N(2)-Fe(1)-N(5)	176.8(1)
N(2)-Fe(1)-O(1)	80.1(1)
N(2)-Fe(1)-O(2)	103.1(1)
N(4)-Fe(1)-N(5)	80.3(1)
N(4)-Fe(1)-O(1)	95.5(1)
N(4)-Fe(1)-O(3)	159.9(1)
N(5)-Fe(1)-O(1)	101.4(1)
N(5)-Fe(1)-O(2)	79.8(1)
O(1)-Fe(1)-O(2)	90.6(1)

[a] $I > 2\sigma(I)$, $R_1 = \Sigma||F_o| - |F_c||/\Sigma|F_o|$. [b] $wR_2 = \{\Sigma[w(F_o^2 - F_c^2)^2]/\Sigma[w(F_o^2)^2]\}^{1/2}$. [c] GoF (goodness of fit on F^2) = $\{\Sigma[w(F_o^2 - F_c^2)^2]/(n\text{-}p)\}^{1/2}$, where n is the number of reflections and p is the total number of refined.

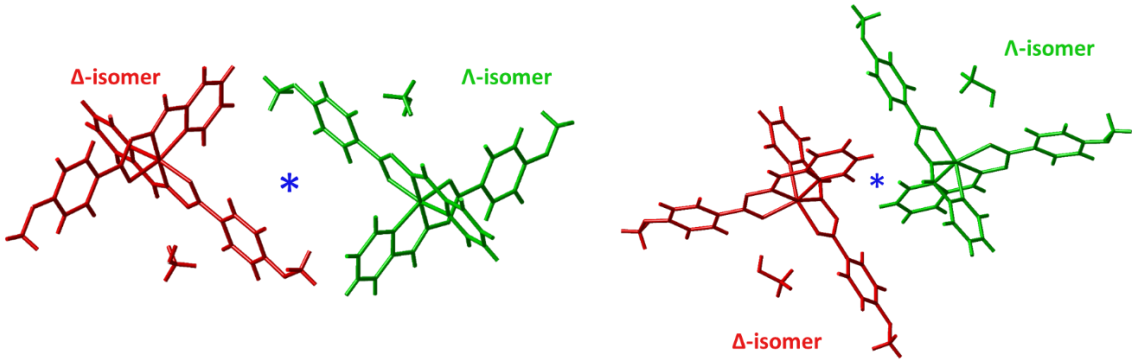

Figure S.III-3. Projection of the packing of α-{[Fe($\mathbf{L^1}$)$_2$]·MeOH} (left) and β-{[Fe($\mathbf{L^1}$)$_2$]·MeOH} (right) emphasizing the two enantiomers that are related by an inversion center of symmetry (blue star).

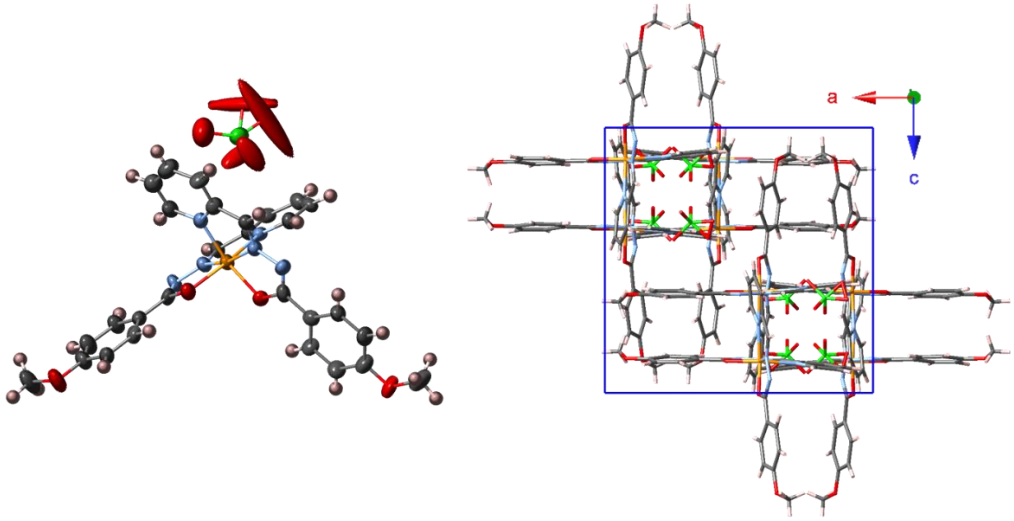

Figure S.III-4. Structure and packing for the solvent-free [Fe($\mathbf{HL^1}$)($\mathbf{L^1}$)](ClO$_4$).

III.5.4. Thermal data

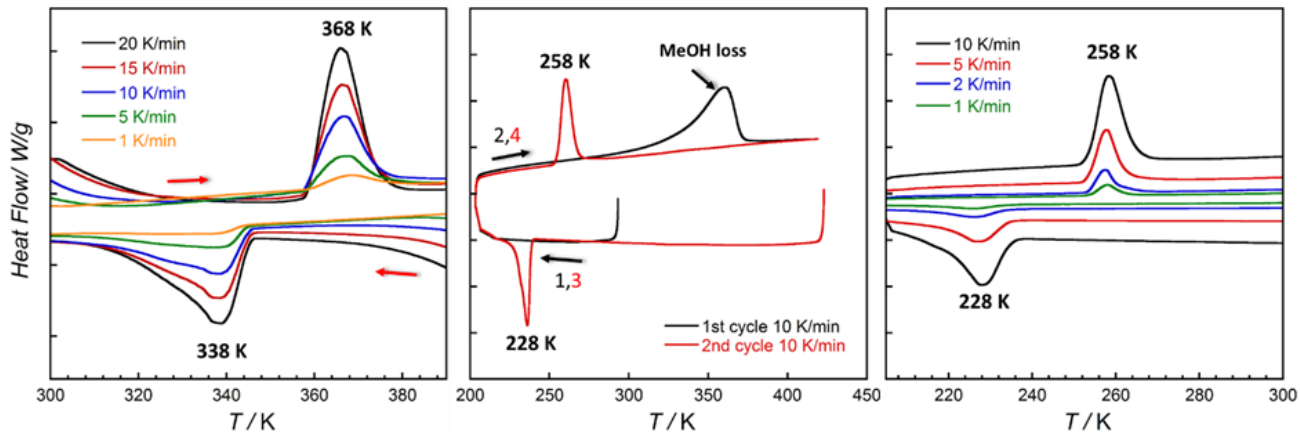

Figure S.III-5. (left) DSC thermograms for α-[Fe($\mathbf{L^1}$)$_2$] at different sweeping rate. (Center) DSC thermograms showing the desolvation of β-{[Fe($\mathbf{L^1}$)$_2$]·MeOH} during the 1st cycle and spin crossover of β-[Fe($\mathbf{L^1}$)$_2$] in the 2nd cycle. (right) DSC thermograms for β-[Fe($\mathbf{L^1}$)$_2$] at different sweeping rate.

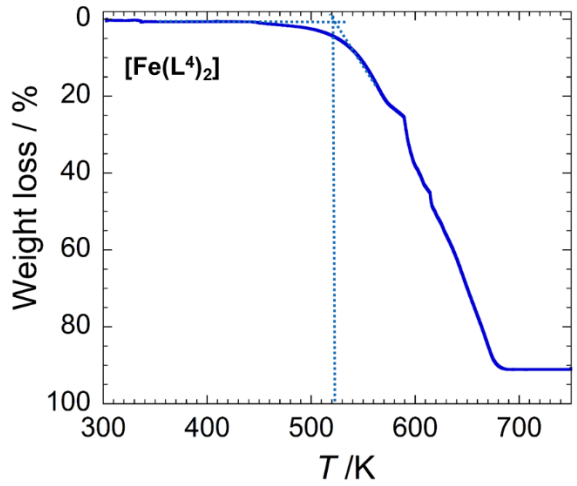

Figure S.III-6. Thermogravimetric data for [Fe($\mathbf{L}^4$)$_2$]. Sweeping rate: 5 K/min

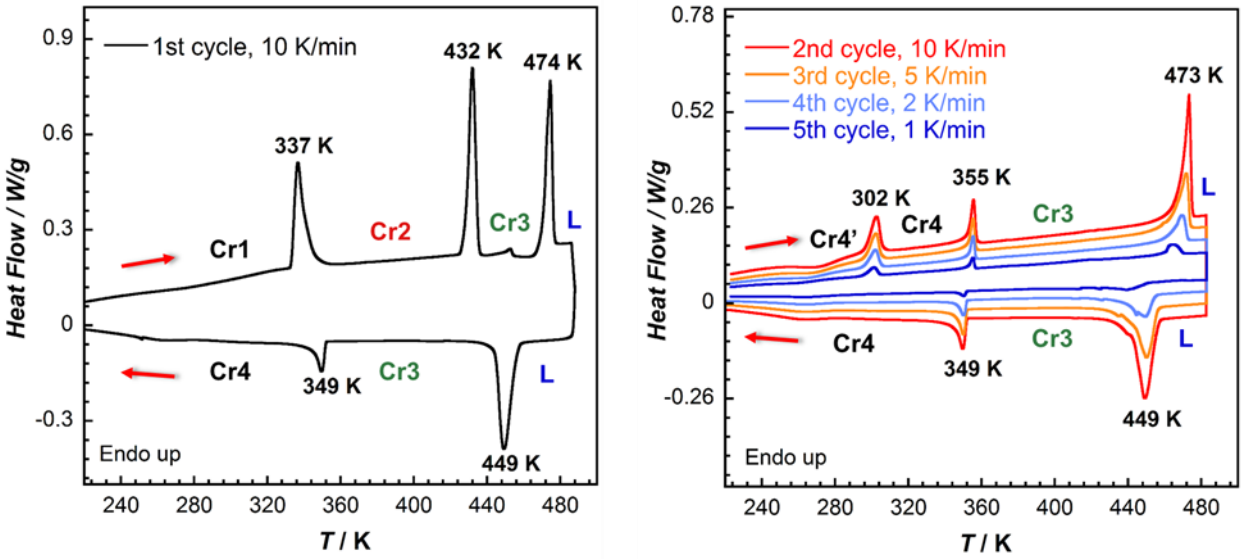

Figure S.III-7. DSC thermograms for [Fe($\mathbf{L}^4$)$_2$] on 1st heating/cooling cycle (left) and 2nd to 5th heating/cooling cycle (right).

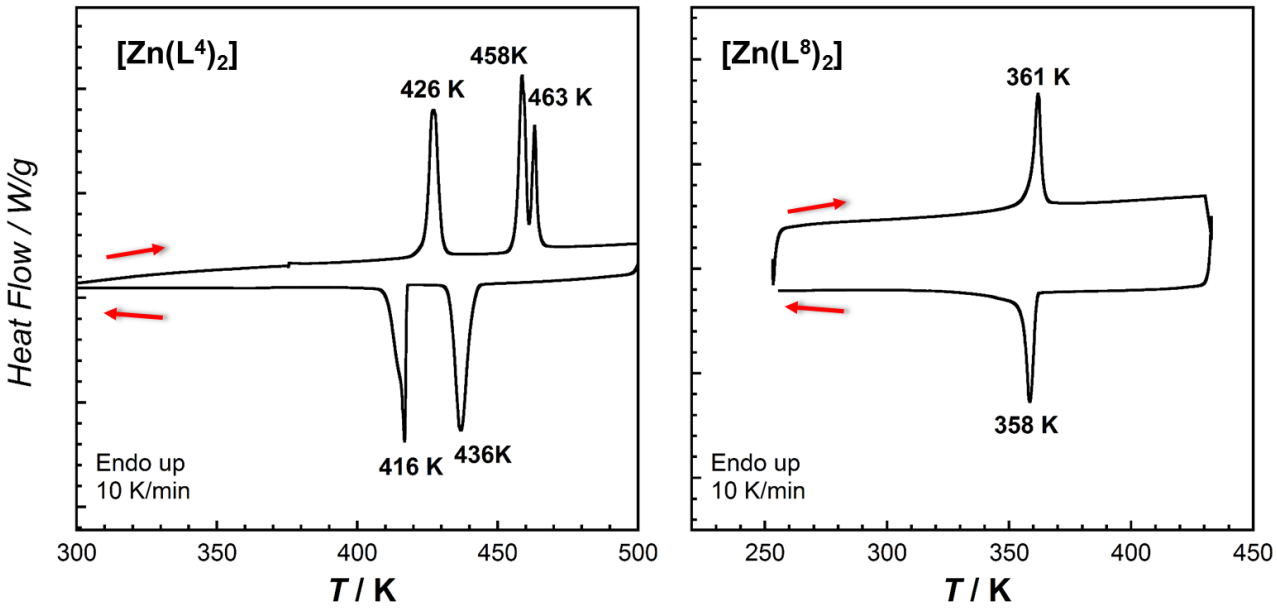

Figure S.III-8. DSC thermograms for [Zn($\mathbf{L}^4$)$_2$] (left) and [Zn($\mathbf{L}^8$)$_2$] (right).

III.5.5. Structural, thermal and magnetic properties of γ-[Fe(L^1)$_2$] complex

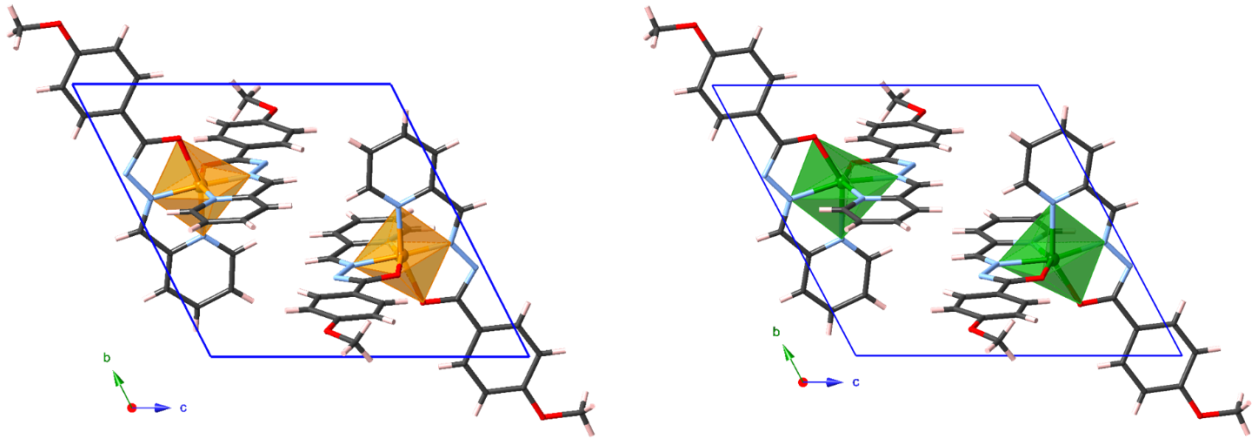

Figure S.III-9. Projection of the crystal packing viewed along *a*-axis for γ-[Fe($\mathbf{L^1}$)$_2$] in (at 120 K, left) and HS configuration (340 K, right).

Table S.III-9. Crystallographic data for γ-[Fe($\mathbf{L^1}$)$_2$] complex

Temperature, K	**120**	**340**
Crystal description	Dark green block	Dark green block
Moiety formula	$C_{28}H_{24}FeN_6O_4$	$C_{28}H_{24}FeN_6O_4$
Empirical formula	$C_{28}H_{24}FeN_6O_4$	$C_{28}H_{24}FeN_6O_4$
Formula weight	564.38	564.38
Crystal system	Triclinic	Triclinic
Space group	*P-1*	*P-1*
Wavelength, Å	0.71073	0.71073
a, Å	10.6982(19)	10.6225(14)
b, Å	11.190(2)	11.3450(15)
c, Å	12.531(2)	12.8603(17)
α, °	114.058	116.17
β, °	111.426	109.99
γ, °	92.199	90.00
V, Å^3	1243.7(4)	1286.1(3)
Z	2	2
ρ_{calcd}, g/cm^3	1.502	1.328
$\mu_{MoK\alpha}$, 1/mm	0.655	0.626
R_1[a]	0.0295	0.0380
wR_2[b]	0.1400	0.1463
GoF[c]	1.274	1.274
<Fe-$N_{(py)}$>, Å	1.960	2.199
<Fe-$N_{(im)}$>, Å	1.870	2.070
<Fe-O>, Å	1.997	2.076
Σ(X-Fe-X),[d] °	86.3	142.7

[a] $I > 2\sigma(I)$, $R_1 = \Sigma||F_o| - |F_c||/\Sigma|F_o|$. [b] $wR_2 = \{\Sigma[w(F_o^2 - F_c^2)^2]/\Sigma[w(F_o^2)^2]\}^{1/2}$. [c] GoF (goodness of fit on F^2) = $\{\Sigma[w(F_o^2 - F_c^2)^2]/(n\text{-}p)\}^{1/2}$, where n is the number of reflections and p is the total number of refined. [d] $\sum = \sum_{i=1}^{12}|90 - \varphi_i|$, where φ_i are cis X-Fe-X bond angles with X = O or N.

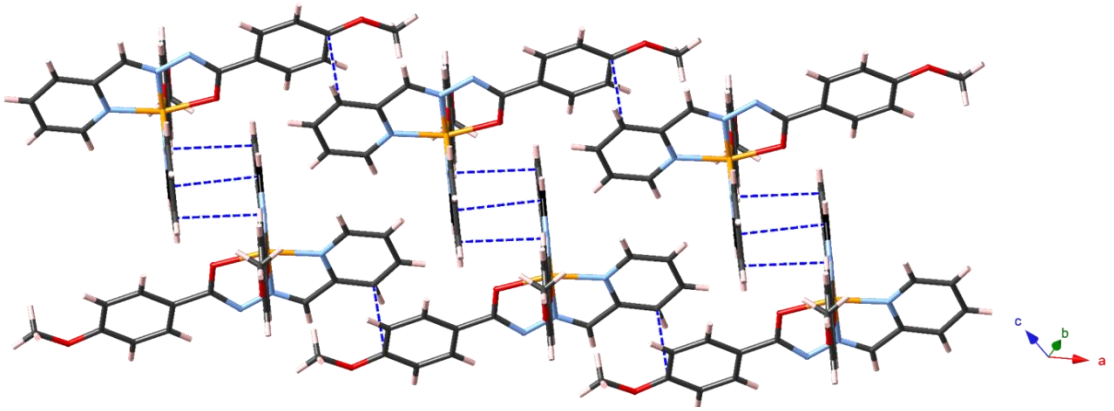

Figure S.III-10. Projection of the crystal packing for γ-[Fe($\mathbf{L^1}$)$_2$] at 120 K emphasizing the intermolecular π-π interactions.

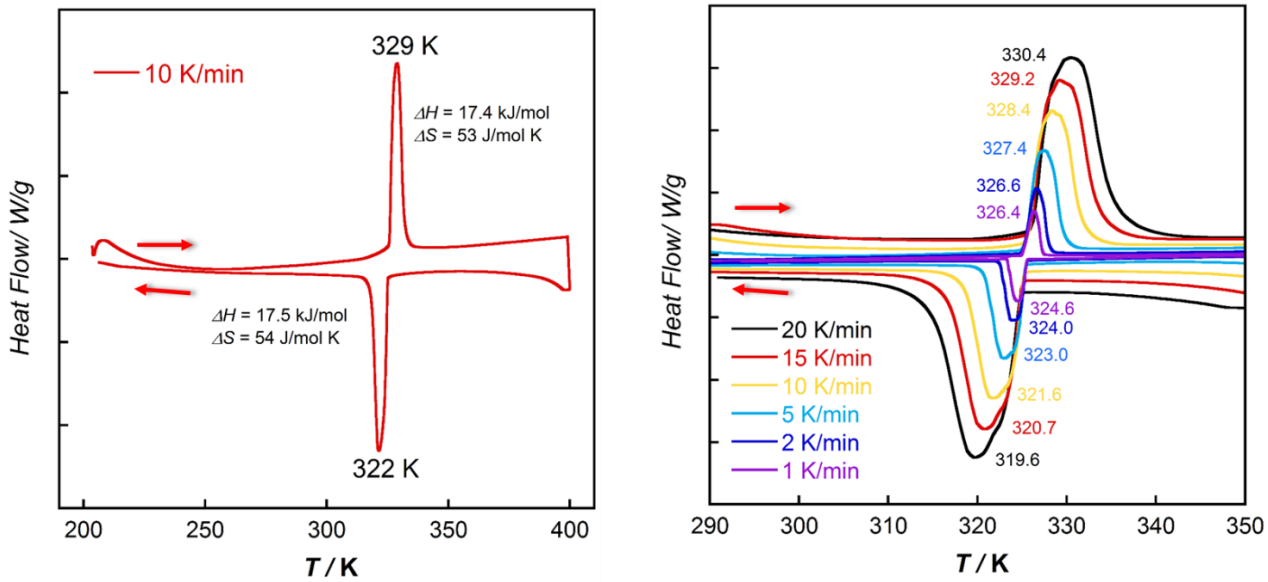

Figure S.III-11. (left) DSC data for γ-[Fe($\mathbf{L^1}$)$_2$] between 220 and 400 K at 10 K/min. (right) DSC data for γ-[Fe($\mathbf{L^1}$)$_2$] at different sweeping rates.

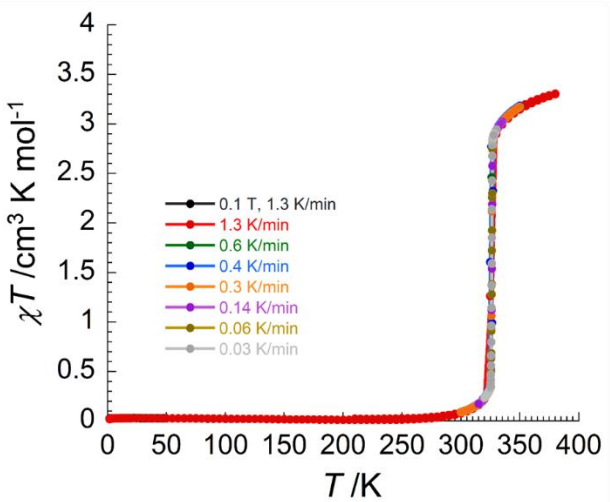

Figure S.III-12. Temperature dependence of the χT product for γ-[Fe($\mathbf{L^1}$)$_2$] at 0.1-1 T (sweep rate: 1.3 to 0.03 K/min).

III. 6. References

1. (a) Gütlich, P.; Goodwin, H. A. *Spin Crossover in Transition Metal Compounds*, Topics in Current Chemistry, Springer, Wien New York, vol. 233-235, **2004**. (b) Halcrow, M. A. *Spin-Crossover Materials: Properties and Applications*, John Wiley & Sons, Ltd., Chichester, **2013**.

2. Roubeau, O.; Agricole, B.; Clérac, R.; Ravaine, S. *J. Phys. Chem. B* **2004**, *108*, 15110.

3. Ruiz-Molina, D.; Mas-Torrent, M.; Gómez, J.; Balana, A. I.; Domingo, N.; Tejada, J.; Martínez, M. T.; Rovira, C.; Veciana, J. *Adv. Mater.* **2003**, *15*, 42.

4. Forestier, T.; Mornet, S.; Daro, N.; Nishihara, T.; Mouri, S.-I.; Tanaka, K.; Fouché, O.; Freysz, E.; Létard, J.-F.; *Chem. Commun.* **2008**, 4327.

5. Roubeau, O.; Colin, A.; Schmitt, V.; Clérac, R. *Angew. Chem. Int. Ed.* **2004**, *43*, 3283.

6. (a) Gaspar, A. B.; Seredyuk, M.; Gütlich, P. *Coord. Chem. Rev*. **2009**, *253*, 2399. (b) Gaspar, A. B.; Seredyuk, M.; Gütlich, *J. Mol. Struct*. **2009**, *924-926*, 9. (c) Roubeau, O. *Chem. Eur. J.* **2012**, *18*, 15230. (d) Gaspar, A. B.; Seredyuk, M. *Coord. Chem. Rev.* **2014**, *268*, 41.

7. Galyametdinov, Y.; Ksenofontov, V.; Prosvirin, A.; Ovchinnikov, I.; Ivanova, G.; Gütlich, P.; Haase, W. *Angew. Chem. Int. Ed*. **2001**, *40*, 4269.

8. (a) Hayami, S.; Danjobara, K.; Inoue, K.; Ogawa, Y.; Matsumoto, N.; Maeda, Y. *Adv. Mater*. **2004**, *16*, 869-872. (b) Hayami, S.; Motokawa, N.; Shuto, A.; Masuhara, N; Someya, T.; Ogawa, Y.; Inoue, K.; Maeda, Y. *Inorg. Chem.* **2007**, *46*, 1789.

9. Fujigaya, T.; Aida, T. *J. Am. Chem. Soc.*, **2003**, *125*, 14690.

10. (a) Seredyuk, M.; Gaspar, A. B.; Ksenofontov, V.; Reiman, S.; Galyametdinov, Y.; Haase, W.; Rentschler, E.; Gütlich, P. *Chem. Mater*. **2006**, *18*, 2513. (b) Seredyuk, M.; Gaspar, A. B.; Ksenofontov, V.; Galyametdinov, Y.; Verdaguer, M.; Villain, F.; Gütlich, P. *Inorg. Chem.*, **2008**, *47*, 10232. (c) Seredyuk, M.; Gaspar, A. B.; Ksenofontov, V.; Galyametdinov, Y.; Kusz, J.; Gütlich, P. *J. Am. Chem. Soc*. **2008**, *130*, 1431.

11. (a) Livingstone, S. E.; Oluka, J. E. *Transition Met. Chem.* **1978**, *3*, 261. (b) Gallego, M.; Garcia-Vargas, M.; Valcarcel, M. *Analyst* **1979**, *104*, 613. (c) Suarez Iha, M. E. V.; Pehkonen, S. O.; Hoffmann, M. R. *Environ. Sci. Technol.* **1994**, *28*, 2080. (d) Sangeetha, N. R.; Pal, S. *Polyhedron* **2000**, 19, 1593. (e) Fondo, M.; Sousa, A.; Bermejo, M. R.; Garcia-Deibe, A.; Sousa-Pedrares, A.; Hoyos, O. L.; Helliwell, M. *Eur. J. Inorg. Chem*. **2002**, *3*, 703. (f) He, Z.; He, C.; Wang, Z-M.; Gao, E-Q.; Liu, Y.; Yan, C-H. *Dalton Tran*s. **2004**, *4*, 502. (g) Gao, L-B; Kan, J.; Fan, Y.; Zhang, L-Y; Liu, S-H.; Chen, Z-N. *Inorg. Chem.* **2007**, *46*, 5651. (h) Chow, C-F.; Fujii, S.; Lehn, J-M. *Angew. Chem., Int. Ed.* **2007**, *46*, 5007. (i) He, C.; Lin, Z.; He, Z.; Duan, C.; Xu, C.; Wang, Z.; Yan, C. *Angew. Chem., Int. Ed.* **2008**, *47*, 877. (j) Mondal, S.; Naskar, S.; Dey, A. K.; Sinn, E.; Eribal, C.; Herron, S. R.; Chattopadhyay, S. K. *Inorg. Chim. Acta* **2013**, *398*, 98. (k) Vantomme, G.; Hafezi, N.; Lehn, J-M. *Chem. Sci.* **2014**, *5*, 1475. (l) Giri, C.; Topic, F.; Cametti, M.; Rissanen, K. *Chem. Sci.* **2015**, *6*, 5712. (m) Dey, M.; Dutta, S.; Sarma, B.; Deka, R. Ch.; Gogoi, N. *Chem. Commun.* **2016**, *52*, 753.

12. (a) Bernhardt, P. V.; Caldwell, L. M.; Chaston, T. B.; Chin, P.; Richardson, D. R. *J. Biol. Inorg. Chem.* **2003**, *8*, 866. (b) Bernhardt, P. V.; Chin, P.; Richardson, D. R. *Dalton Trans.* **2004**, *20*, 3342. (c) Lovejoy, D. B.; Sharpe, P. C.; Richardson, D. R.; Senaratne, D.; Kalinowski, D. S.; Islam, M.; Bernhardt, P. V. *J. Med. Chem.*, **2006**, *49*, 6510. (d) Kalinowski, D. S.; Yu, Y.; Sharpe, P. C.; Islam, M.; Liao, Y.-T., Lovejoy, D. B.; Kumar, N.; Bernhardt, P. V.; Richardson, D. R. *J. Med. Chem.* **2007**, *50*, 3716. (e) Bernhardt, P. V.; Sharpe, P. C.; Chin, P.; Richardson, D. R. *Dalton Trans.* **2007**, *30*, 3232. (f) Bernhardt, P. V.; Wilson, G. J.; Sharpe, P. C.; Kalinowski, D. S.; Richardson, D. R. *J. Biol. Inorg. Chem.* **2008**, *13*, 107. (g) Bernhardt, P. V.; Sharpe, P. C.; Islam, M.; Lovejoy, D. B.; Kalinowski, D. S.; Richardson, D. R. *J. Med. Chem*. **2009**, *52*, 407.

13. (a) Zhang, L.; Xu, G-C.; Xu, H-B.; Zhang, T.; Wang, Z-M.; Yuan, M.; Gao, S. *Chem. Comm.*, **2010**, *46*, 2554. (b) Zhang, L.; Xu, G-C; Xu, H-B; Mereacre, V.; Wang, Z-M.; Powell, A. K.; Gao, S. *Dalton Trans.* **2010**, *39*, 4856. (c) Zhang, L.; Xu, G-C.; Xu, H-B.; Wang, Z.-M.; Gao, S. *Eur. J. Inorg. Chem.*, **2013**, 1043. (d) Zhang, L.; Wang, J-J.; Xu, G-C.; Li, J.; Jia, D-Z.; Gao, S. *Dalton Trans.* **2013**, *42*, 8205. (e) Zhang, Y. *J. Chem. Phys.* **2014**, *141*, 214703/1.

14. Shongwe, M. S.; Al-Rahbi, S. H.; Al-Azani, M. A.; Al-Muharbi, A. A.; Al-Mjeni, F.; Matoga, D.; Gismelseed, A.; Al-Omari, I. A.; Yousif, A.; Adams, H.; Morris, M. J.; Mikuriya, M.; *Dalton Trans.* **2012**, *41*, 2500.

15. Romero-Morcillo, T.; Seredyuk, M.; Muñoz, M. C.; Real, J. A. *Angew. Chem. Int. Ed*., **2015**, *54*, 14777.

16. (a) Tamboura, F. B.; Diop, M.; Gaye, M.; Sall, A. S.; Barry, A. H.; Jouini, T. *Inorg. Chem. Commun*. **2003**, *6*, 1004. (b) He, C.; Wu, X.; Kong, J.; Liu, T.; Zhang, X.; Duan, C. *Chem. Commun.* **2012**, *48*, 9290. (c) Xue, S.; Chen, X-H.;

Zhao, L.; Guo, Y-N.; Tang, J. *Inorg. Chem*. **2012**, 51, 13264. (d) Xue, S.; Guo, Y-N.; Zhao, L.; Zhang, H.; Tang, J. *Inorg. Chem.* **2014**, *53*, 8165. (e) Batchelor, L. J.; Cimatti, I.; Guillot, R.; Tuna, F.; Wernsdorfer, W.; Ungur, L.; Chibotaru, L. F.; Campbell, V. E.; Mallah, T. *Dalton Trans.* **2014**, *43*, 12146. (f) Mondal, A. K.; Goswami, S.; Konar, S. *Dalton Trans.* **2015**, *44*, 5086.

17. Kaiba, A.; Shepherd, H J.; Fedaoui, D.; Rosa, P.; Goeta, A.E.; Rebbani, N.; Létard, J.-F.; Guionneau, P. *Dalton Trans.* **2010,** *39*, 2910.

18. Brooker, S. *Chem. Soc. Rev.* **2015**, *44*, 2880.

19. Gütlich, P; Gaspar, A. B.; Garcia, Y. *Beilstein J. Org. Chem.* **2013**, *9*, 342.

20. (a) König, E.; Madeja, K. *Inorg. Chem.* **1967**, *6*, 48. (b) König, E.; Madeja, K.; Watson, J. K. *J. Am. Chem. Soc.* **1968**, *90*, 1146.

21. Tao, J.; Wei, R-J .; Huang R-B.; Zheng, L-S. *Chem. Soc. Rev.* **2012**, *41*, 703.

22. Neville, S. M.; Leita, B. A.; Offermann, D. A.; Duriska, M. B.; Moubaraki, B.; Chapman, K. W.; Halder, G. J.; Murray, K. S. *Eur. J. Inorg. Chem.* **2007**, 1073.

23. Wei, R.-J.; Li, B.; Tao, J. Huang, R.-B.; Zheng, L.-S.; Zheng, Z. *Inorg. Chem.* **2011**, *50*, 1170.

24. Bartual-Murgui, C.; Codina, C.; Roubeau, O.; Aromí, G. *Chem. Eur. J.* **2016**, *22*, 12767.

25. Zhang, L. *Ph.D. Thesis*, Peking University, **2010**.

26. Zhang, Y. *J. Chem. Phys.* **2014**, *141*, 214703.

27. (a) Roux, C.; Zarembowitch, J.; Gallois, B.; Granier T.; Claude, R. *Inorg. Chem.* **1994**, *33*, 2273. (b) Reger, D. L.; Gardinier, J. R.; Smith, M. D.; Shahin, A. M.; Long, G. J.; Rebbouh L.; Grandjean, F. *Inorg. Chem.* **2005**, *44*, 1852. (c) Galet, A.; Muñoz, M. C.; Gaspar A. B.; Real, J. A. *Inorg. Chem.* **2005**, *44*, 8749. (d) Neville, S. M.; Leita, B. A.; Halder, G. J.; Kepert, C. J.; Moubaraki, B.; Létard, J.-F.; Murray, K. S. *Chem. Eur. J.* **2008**, *14*, 10123. (e) Haryono, M.; Heinemann, F. W.; Petukhov, K.; Gieb, K.; Müller, P.; Grohmann, A. *Eur. J. Inorg. Chem.* **2009**, 2136. (f) Agustí, G.; Muñoz, M. C.; Gaspar, A. B.; Real, J. A. *Inorg. Chem.* **2009**, *48*, 3371. (g) Luan, J; Zhou, J.; Liu, Z.; Zhu, B.; Wang, H.; Bao, X.; Liu, W.; Tong, M.-L. Peng, G.; Peng, H.; Salmon, L.; Bousseksou, A. *Inorg. Chem.* **2015**, *54*, 5145.

28. Hagiwara, H.; Okada, S. *Chem. Commun.* **2016**, *52*, 815.

29. (a) Hayami, S.; Shigeyoshi, Y.; Akita, M.; Inoue, K.; Kato, K.; Osaka, K.; Takata, M.; Kawajiri, R.; Mitani, T.; Maeda, Y. *Angew. Chem. Int. Ed.* **2005**, *44*, 4899. (b) Hayami, S.; Kato, K.; Komatsu, Y.; Fuyuhiro, A.; Ohba, M. *Dalton Trans.* **2011**, *40*, 2167. (c) Ohtani, R.; Egawa, S.; Nakaya, M.; Ohmagari, H.; Nakamura, M.; Lindoy, L. F.; Hayami S. *Inorg. Chem.*, **2016**, 55, 3332.

30. (a) Šalitroš, I.; Fuhr, O.; Eichhöfer, A.; Kruk, R.; Pavlik, J.; Dlháň, L.; Boča, R.; Ruben, M. *Dalton Trans.* **2012**, *41*, 5163. (b) Bushuev, M. B.; Daletsky, V. A.; Pishchur, D. P.; Gatilov, Y. V.; Korolkov, I. V.; Nikolaenkova, E. B.; Krivopalov, V. P. *Dalton Trans.* **2014**, *43*, 3906.

31. (a) Shatruk, M.; Phan, H.; Chrisostomo, B. A.; Suleimenova, A. *Coord. Chem. Rev.* **2015**, *289–290*, 62. (b) Ortega-Villar, N.; Muñoz, M. C.; Real, J. A. *Magnetochemistry* **2016**, *2*, 16.

32. (a) Terzis, A. F.; Vanakaras, A. G.; Photinos, D. J. *Mol. Cryst. Liq. Cryst.* **2000**, *352*, 265. (b) Crisanti, A.; Leuzzi, L. *Phys. Rev. Lett.* **2005**, *95*, 087201.

33. Mitcov, D. *Ph.D. Thesis*, University of Bordeaux, **2014**.

34. (a) He, Z.; He, C.; Wang, Z.-M.; Gao, E.-Q.; Liu, Y.; Yan C.-H. *Dalton Trans.* **2004**, 502. (b) Jia, L.; Xu, J.; Xu, X.-M.; Chen, L.-H.; Jiang, P.; Cheng, F.-X.; Lu, G.-N.; Wang, Q.; Wu, J.-C.; Tang, N. *Chem. Pharm. Bull.* **2010**, *58*, 1077. (c) Wu, J.; Zhao, L.; Guoab, M.; Tang, J. *Chem. Commun.* **2015**, *51*, 17317. (d) Giri, C.; Topić, F.; Cametti, M.; Rissanen, K. *Chem. Sci.*, **2015**, 6, 5712. (e) Wu, J.; Zhao, L.; Zhang,L.; Li, X.-L.; Guo, M.; Tang, J. *Inorg. Chem.* **2016**, *55*, 5514.

35. Wilson, B; Rosario-Amorin, D. and co-workers, unpublished results.

Chapter IV

Soft Materials based on Cyanido-Bridged $\{Fe^{III}_2(\mu\text{-}CN)_4M^{II}_2\}$ Molecular Squares

Table of Contents for Chapter IV:

IV.1. Introduction

The interest in cyanide-based single-molecule magnets (SMMs) and electron transfer (ET) systems is in direct line with the famous Prussian blue (PB) and its analogues. These systems have been intensively studied, in particular by the groups of Girolami,[1] Hashimoto,[2] Verdaguer[3] and Miller.[4] An experimental and detailed theoretical understanding of the magnetic interaction through bridging cyanide ligands has been achieved in the relation to the involved metal ions and structural/geometrical parameters. However, the reduced solubility of these inorganic compounds limit their potential applications and requires elaboration of strategies for nanoparticles design, to increase their solubility and to create multi-functionalities at nano-scale.[5] Since then, a new cyanide-metallate research started towards the synthesis and investigation of discrete PB analogues that have flexible molecular and electronic structures coupled with improved solubility. Several groups designed and studied molecular analogues of PB by rational choice of various capping ligands.[6-21] Many of these systems exhibited unusual properties such as single-molecule magnets,[7-9] spin crossover[10] and electron transfer.[11-21]

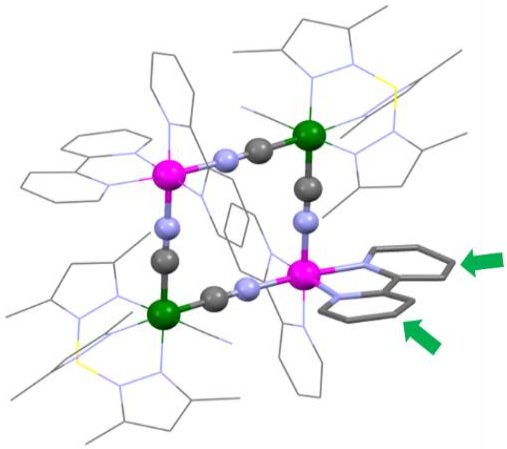

Figure IV-1. Schematic representation of $\{Fe^{III}_2M^{II}_2\}$. Color scheme: Fe green, M (Co or Ni) pink, B yellow, N blue, C grey. The green arrows represent the position chosen for the functionalization of the bipyridine ligand

Going further toward systems with easy processability, we proposed during this thesis to develop soft materials based on $\{[(Tp^*)Fe^{III}(CN)_3]_2[M^{II}(R,R\text{-bpy})_2]_2\}(A)_2$ (where Tp* = hydridotris(3,5-dimethylpyrazol-1-yl)borate; M^{II} = Ni^{II} or Co^{II}; R,R-bpy = 4,4'-disubstituent-2,2'-bipyridine derivative; A = monovalent anion) (Figure IV-1). These molecular squares are well-known to behave as single-molecule magnets[8,9] or display thermally and photo-induced electron transfer[15-19] in the case of Ni^{II} and Co^{II} analogues, respectively, and have been intensively studied by our team.[9,15,19] The aim of our study is to play on the ligand functionalization in order to promote liquid-crystal properties in the resulting materials or improve their solubility in usual organic solvents without altering significantly their intrinsic magnetic properties. This approach have been initiated during the PhD theses of D. Siretanu and D. Mitcov, during which bipyridine ligands were functionalized with alkyl chains (hexyl or tridecyl) and used for the preparation of $\{Fe_2Co_2\}$ squares.[19] This strategy brought interesting properties and appeared to be an efficient way to control thermally-induced ET properties in solution. However, the functionalization was not appropriate to induce

mesomorphic features, while spin switchable properties were not maintained in solid-state. During this PhD work, we applied the same approaches as used in previous chapters, which consisted to introduce additional strongly lipophilic substituents or calamitic smectogen units such as biphenyl and cyanobiphenyl groups in order to favor mesomorphic properties. This Chapter is divided in two parts dedicated to the two types of molecular squares. In the first part, we discuss on the synthetic approach for the preparation of bipyridine-based mesogenic ligands and $\{Fe_2Ni_2\}$ complexes, as well as the characterization of their thermotropic properties and preliminary investigations of their magnetic properties. The second part dedicated to $\{Fe_2Co_2\}$ systems, is mainly oriented toward their investigations in solution.

IV.2. Synthesis and characterization of $\{Fe_2Ni_2\}$ molecular squares

IV.2.1. Synthetic approach

In order to attach multiple mesogenic substituents onto bipyridine ligand, we tested several synthetic strategies. The first one consisted to deprotonate and alkylate the methyl positions of the 4,4'-dimethyl-2,2'-bipyridine (Scheme IV-1), as previously described for the preparation of analogues with hexyl and tridecyl alkyl chains.[19] As test reaction, we used the precursor 3,5-bis(dodecyloxy)benzyl bromide, which has been previously prepared in the lab by reduction of methyl 3,5-bis(dodecyloxy)benzoate with lithium aluminium hydride ($LiAlH_4$), followed by a bromination of the resulting alcohol with phosphorus tribromide (PBr_3). Unfortunately, this method was not very efficient. Even though the deprotonation was selective and complete, as verified by deuteration tests, the alkylation was not operating properly. Indeed, only traces of the expected compound were found in NMR spectra of the crude sample. This was explained by a major decomposition of the benzyl bromide derivative, which notably involves a breaking of the Ar-C bond.

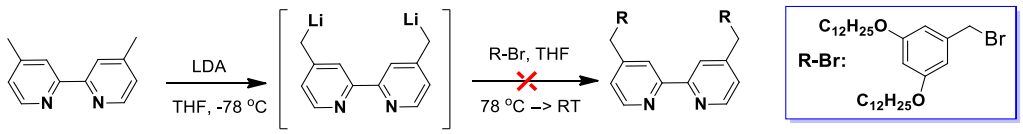

Scheme IV-1. Unsuccessful strategy to prepare mesogenic 2,2'-bipyridine ligand analogues.

Thereafter, we followed another strategy that involves an ether coupling reaction between 3,5-bis(dodecyloxy)benzyl bromide and 2,2'-bipyridine-4,4'-diyldimethanol **B** (Scheme IV-2). This latter was prepared by esterification of the 2,2'-bipyridine-4,4'-dicarboxylic acid, followed by a reduction of the resulting ester **A** using sodium borohydride ($NaBH_4$).

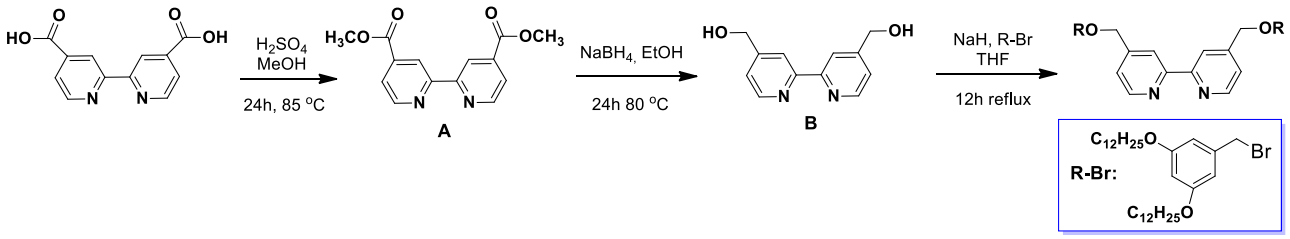

Scheme IV-2. Second strategy tested to introduce mesogenic substituent in 2,2-bipyridine ligand.

The ether coupling reaction was carried using sodium hydride (NaH) in slight excess (2.2 equivalents) under inert and anhydrous conditions. Even though the conversion of the reaction was acceptable (~ 40 %),

the product could not be isolated in good yield. Indeed, the purification of the desired compound by column chromatography was efficient since it has a very similar polarity with the mono-functionalized by-product.

The third approach proposed was to graft the mesogenic part through an ester link by reaction between **C**, obtained by bromination of **B**, and benzoic acid precursors $\mathbf{D^{1\text{-}6}}$ using tetrabutylammonium fluoride (TBAF) as mediator (Scheme IV-3). The non-commercial precursors $\mathbf{D^{1\text{-}6}}$ were prepared according to Chapter II. This procedure was found particularly efficient and we were able to produce four new ligands containing long dodecyl chains or smectogen units, $\mathbf{L^{3\text{-}6}}$, as well as two ligands containing short substituents, $\mathbf{L^{1\text{-}2}}$, which were used as model for our studies.

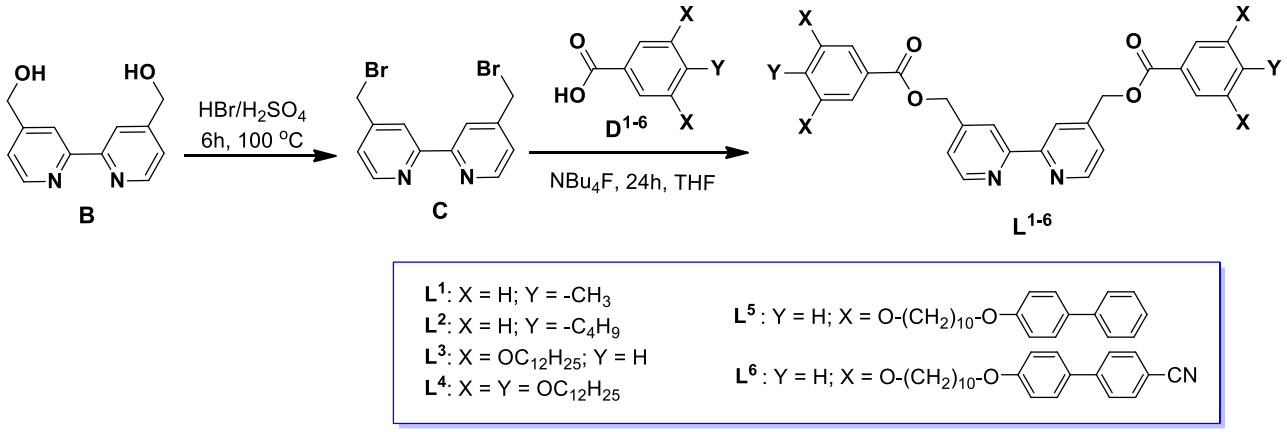

Scheme IV-3. Synthetic pathway for the preparation of $\mathbf{L^{1\text{-}6}}$ ligands

The general synthetic approach for preparation of molecular PB analogues is the combination between solvated metal cations and cyanido-metallate ions. In order to prevent from polymerization, it is necessary to employ capping ligands, which will limit the number of available binding sites on the metal ions.

Thus, the reaction of the tricyanido-metallate precursor (A)[(Tp*)Fe(CN)$_3$] (A = NEt$_4$ or PPh$_4$) with Ni(OTf)$_2$ in DMF lead spontaneously to the self-assembly of the square $\{[(Tp^*)Fe^{III}(CN)_3]_2[Ni^{II}(DMF)_4]_2\}(A)_2$ (Scheme IV-4).

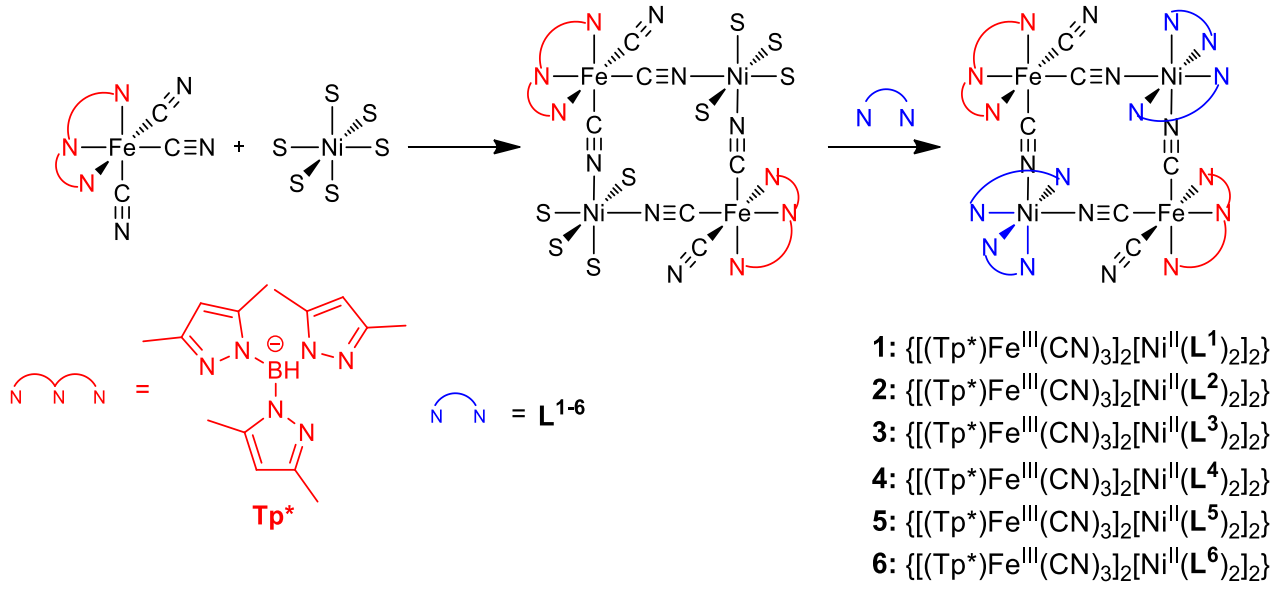

Scheme IV-4. Synthetic scheme of the approach used to obtain cyanido-bridged $\{Fe^{III}_2Ni^{II}_2\}$ molecular squares. Charges on metal ions and counter-ions omitted for clarity.

The DMF ligands from the Ni^{II} site are then subsituted by addition of the bipyridine-like ligands in CH_2Cl_2. This procedure was used to produce the two model complexes **1** and **2**, which were isolated as single-crystal by diethyl ether slow diffusion technique. The structures of these complexes are described later in Section 2.3. Due to the very poor solubility of $\mathbf{L}^{3\text{-}6}$ in DMF, the synthetic procedure was slightly modified and the reaction was performed in a mixture CH_2Cl_2/MeCN (4:1). Due to the presence of the flexible substituents, it was not reasonably possible to obtain single crystals of these materials. Consequently, at the end of the reaction, the solution was concentrated and the brownish-orange sticky residue was triturated with MeCN and MeOH in order to remove the PPh_4OTf salt formed during the reaction. Using these conditions, it was found that a minor impurity of 1D polymer or oligomer $\{[(Tp^*)Fe(CN)_3]_2[Ni(S)_2]\}_n$ (S = solvent) was formed during the reaction. Although not isolated, the evidence of this impurity was revealed by the presence of a characteristic χ'' signal around 15 K in zero *dc* field,[22,23] during our initial *ac* magnetic measurements. To prevent from its formation, attempts to optimize the reaction conditions were made, for example by using pre-formed $\{[(Tp^*)Fe^{III}(CN)_3]_2[Ni^{II}(DMF)_4]_2\}(A)_2$ square (using isolated single-crystals) or non-coordinating solvent (nitromethane). Unfortunately, none of these conditions were successful to give better results. Thus, the impurity was removed by size exclusion column chromatography, using Bio-Beads S-X3 beads (neutral, porous styrene divinylbenzene copolymer beads) as stationary phase.

IV.2.2. FTIR spectroscopic analyses

The stretching bands specific to cyanide groups ($\bar{\nu}_{CN}$) are sensitive to their coordination mode (bridging and terminal) and the oxidation states of the coordinated metal ions.[24] Thus, infrared spectroscopy is an efficient tool to study the self-assembly of Fe^{III}-based cyanide-containing building blocks. The FTIR spectroscopy of the tricyanido-metallate precursor, $(NEt_4)[(Tp^*)Fe(CN)_3]$, shows a strong $\bar{\nu}_{CN}$ stretching at 2115 cm^{-1} and another one of the medium intensity corresponding to $\bar{\nu}_{BH}$ at 2549 cm^{-1} (Figure S.IV-1, top).[15a] Selected FT-IR spectra are shown in Figure IV-2.

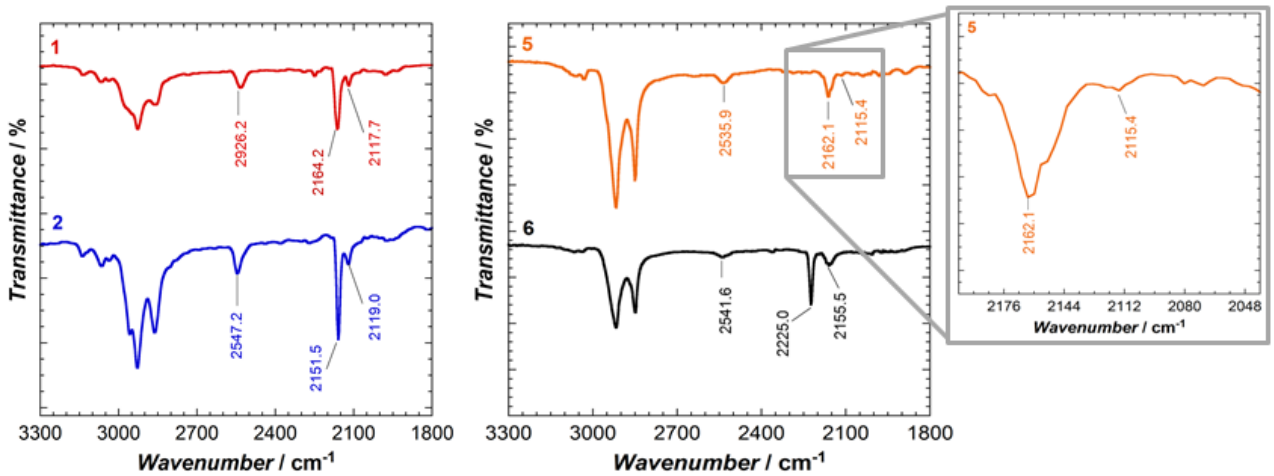

Figure IV-2. (left) FTIR spectra collected between 3300 and 1800 cm^{-1} at 290 K for the red crystals of **1**, **2** and (right) for red glass solids of **5** and **6**.

The stretching band of the cyanide groups in cyanido-bridged $\{Fe_2Ni_2\}$ molecular squares at room temperature is shifted to higher energies and divided into two bands: one at 2151 – 2164 cm^{-1} that is characteristic of bridging cyanides within $\{Fe^{III}_{LS}(\mu\text{-}CN)Ni^{II}_{HS}\}$ units and the second one around 2120 cm^{-1} corresponding to terminal cyanide.[8,9] For **6** the cyanido-bridged band around 2225 cm^{-1} is too high due to the presence of cyanide that is coming from ligand L^6. Furthermore, the presence of the B-H stretching band from the Tp* ligand at 2535 – 2926 cm^{-1} and the intense C-H bands at 2930 and 2859 cm^{-1} from the functionalized bipyridine ligands, confirms the formation of functionalized $\{Fe_2Ni_2\}$ molecular squares.

IV.2.3. Structural descriptions

IV.2.3.1. Structure of $\{[(Tp^*)Fe(CN)_3]_2[Ni(L^1)_2]_2\}(OTf)_2$ (1)

Single crystals of complex **1** were obtained by recrystallization of the raw powder. The compound was dissolved in acetonitrile, and slow diffusion of diethyl ether vapor was applied. The single-crystal X-ray diffraction analysis of the complex was performed at 120 K. A view of the structure is shown in Figure IV-3 and selected crystallographic data are gathered in Table IV-1. The compound crystallizes as structurally related squares[11h] in the triclinic *P-1* space group. The unit cell consists of a cyanido-bridged $\{Fe_2Ni_2\}$ square, two free trifluorometanesulfonate ions, one molecule of H_2O and two molecules of CH_3CN. Adjacent hexa-coordinated Fe and Ni ions consist in alternate corners and are linked by cyanide ligands to form {Fe(μ-CN)Ni} pairs. The Fe ions are coordinated with tridentate Tp* with facial configuration, while Co ions are coordinated with two bidentate bipyridine ligands (Figure IV-3). The asymmetric unit consists of a half of the complex cation, $[(Tp^*)Fe(CN)_3Ni(\mathbf{L^1})_2]$, a free trifluoromethanesulfonate ion and co-crystallized solvent molecules (H_2O and CH_3CN).

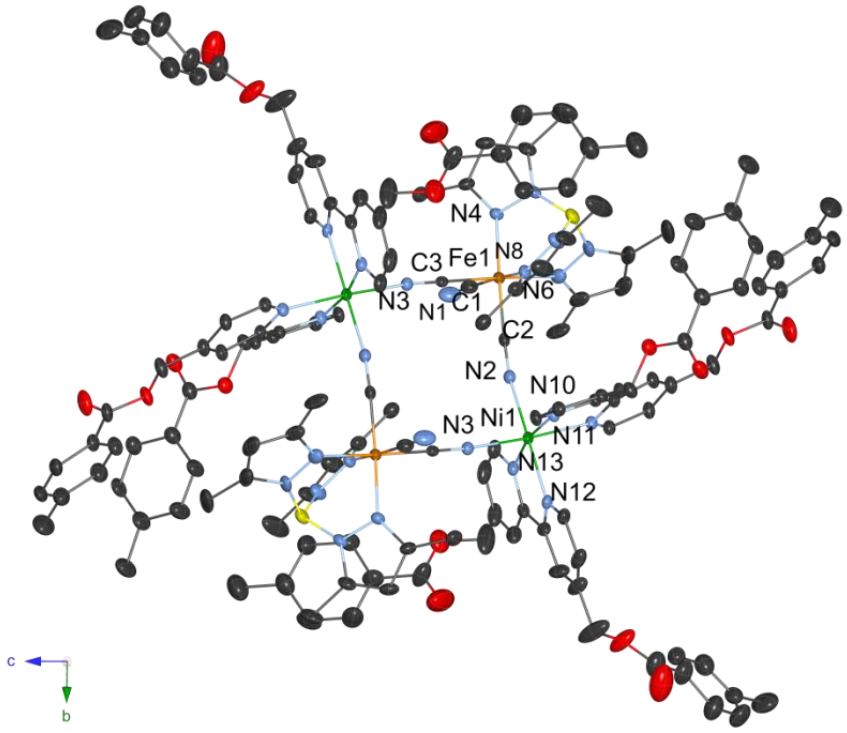

Figure IV-3. The structure of the complex cation of $\mathbf{1}\cdot H_2O\cdot 2CH_3CN$ at 120 K. Thermal ellipsoids are at 30 % of probability. All anions, lattice solvent molecules, and hydrogen atoms are omitted for clarity. Color scheme: Fe orange, Ni green, N blue, C grey, B yellow, O red

As expected, the average Ni-N bond length of 2.073 Å is characteristic for Ni^{II} in high-spin (HS) configuration, while the averages Fe-C (1.920 Å) and Fe-N (1.998 Å) bond distances (Table IV-1) are similar to those measured for Fe^{III} in low-spin (LS) configuration.[8,9] The $\{Fe_2(\mu\text{-}CN)_4Ni_2\}$ core adopts a distorted square geometry. Indeed, the cyanide bridges are significant bent especially on the nickel sites for which the two Ni-N-C angles were 165.5(4)° and 174.3(3)°, while the two Fe-C-N angles are 174.9(5)° and 176.5(4)° (Table IV-1). The distance for Fe-CN-Ni edge is 5.08 Å. The cationic cores are well-isolated and intercomplex Ni···Ni contacts of 7.21 Å are observed. The coordination sphere of the Ni^{II} site is less disordered than the one found in Fe^{III} site. The values of N-Ni-N angles (Table IV-1) in the coordination sphere of the HS Ni^{II} ion depart from orthogonality, as shown from the $\Sigma_{(N\text{-}Ni\text{-}N)}$ parameter of 46.9°, that is the sum of deviations from 90° of the 12 *cis* Φ angles in the coordination sphere of the nickel ion to estimate the distortion.[25]

Table IV-1. Crystallographic data for **1**·H_2O·$2CH_3CN$ at 120 K.

Temperature	**120 K**	**Selected bond distances (Å)**	
Crystal color	brownish-orange	Ni(1)-N(11)	2.097(4)
FW / g·mol^{-1}	3185.82	Ni(1)-N(13)	2.069(4)
Empirical formula	$C_{154}H_{146}B_2F_6Fe_2N_{28}Ni_2O_{23}S_2$	Ni(1)-N(12)	2.100(3)
Crystal system	Triclinic	Ni(1)-N(2)	2.057(3)
Space group	*P-1*	Ni(1)-N(10)	2.076(4)
a, Å	11.3229(8)	Ni(1)-N(3)	2.038(4)
b, Å	17.3355(22)	Fe(1)-N(8)	2.013(5)
c, Å	19.7033(13)	Fe(1)-N(6)	2.014(4)
α , °	88.590(3)	Fe(1)-N(4)	1.968(3)
β, °	86.991(3)	Fe(1)-C(2)	1.925(5)
γ , °	80.915(4)	Fe(1)-C(1)	1.932(6)
V, Å^3	3813.2(4)	Fe(1)-C(3)	1.904(4)
Z	2	**Selected bond angles (°)**	
ρ_{calcd}, g/cm^3	1.387	N(11)-Ni(1)-N(13)	93.3(1)
μ, 1/mm	0.542	N(11)-Ni(1)-N(12)	90.4(1)
$\theta_{min} - \theta_{max}$	0.919 ° - 25.461 °	N(11)-Ni(1)-N(2)	88.4(1)
Refl. Coll. / unique	9433 / 14034	N(11)-Ni(1)-N(10)	79.4(1)
Completeness to 2θ	0.994	N(13)-Ni(1)-N(12)	79.0(1)
R_{int}	0.1757	N(13)-Ni(1)-N(2)	95.8(1)
Refined param./restr.	1014 / 0	N(13)-Ni(1)-N(3)	92.9(1)
[a] R_1 ($I > 2\sigma(I)$)	0.0681	N(2)-Ni(1)-N(10)	92.0(1)
[b] wR_2 (all data)	0.2066	N(2)-Ni(1)-N(3)	90.0(1)
[c] *GoF*	1.051	N(12)-Ni(1)-N(10)	92.9(1)
		N(12)-Ni(1)-N(3)	91.9(1)
<Fe-C>, Å	1.920	N(10)-Ni(1)-N(3)	94.5(1)
<Fe-N>, Å	1.998	Ni(1)-N(2)-C(2)	165.4(4)
<Ni-N>, Å	2.073	Fe(1)-C(3)-N(3)	177.3(1)
Fe(1)···Ni(1), Å	5.084	Fe(1)-C(1)-N(1)	174.9(5)
Fe···Fe, Å	7.174	Fe(1)-C(2)-N(2)	176.5(4)
Ni···Ni , Å	7.206	C(1)-Fe(1)-C(3)	83.3(2)
Σ(N-Ni-N)[a], °	46.9	C(2)-Fe(1)-C(3)	89.5(2)
		C(2)-Fe(1)-C(1)	87.2(2)

[a] $I > 2\sigma(I)$, $R_1 = \Sigma||F_o| - |F_c||/\Sigma|F_o|$. [b] $wR_2 = \{\Sigma[w(F_o^2 - F_c^2)^2]/\Sigma[w(F_o^2)^2]\}^{1/2}$. [c] *GoF* (goodness of fit on F^2) = $\{\Sigma[w(F_o^2 - F_c^2)^2]/ (n\text{-}p)\}^{1/2}$, where n is the number of reflections and p is the total number of refined parameters.

In the crystal packing, strong intermolecular π-π type interactions between adjacent $\{Fe_2Ni_2\}$ complexes are present (2.97 and 2.63 Å, Figure IV-4, left). An hydrogen bond is also present between the

nitrogen atom N(1) from terminal cyanide ligand and lattice water molecule N(1)···O(12)w (2.93 Å, Figure IV-4, right).

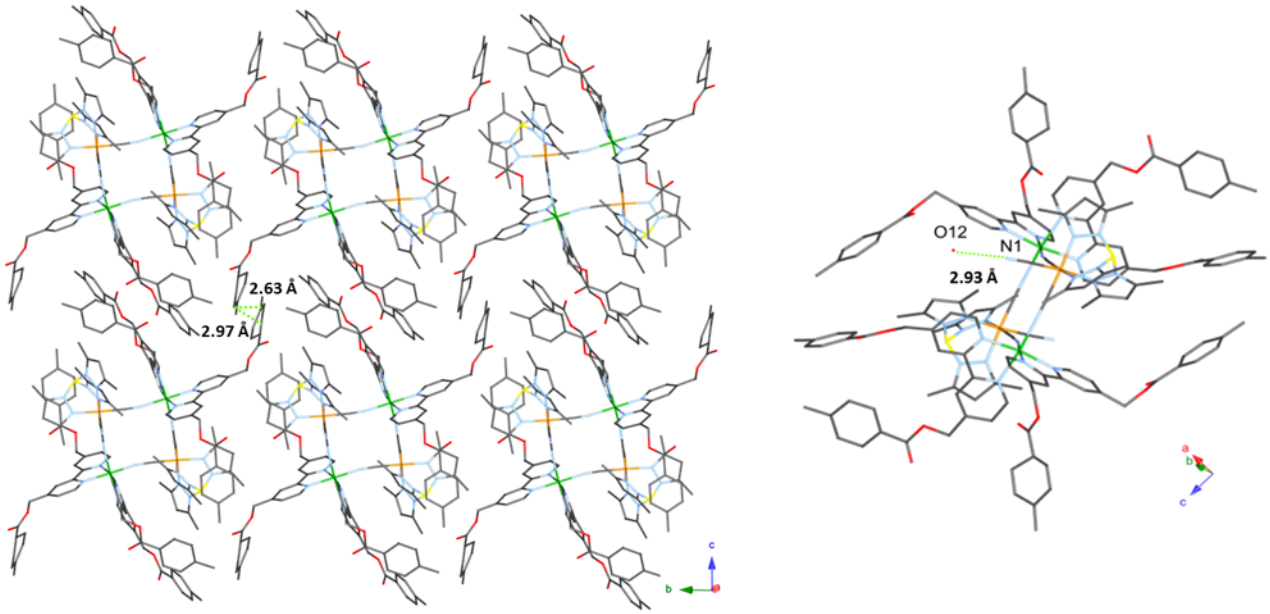

Figure IV-4. (left) Packing arrangements illustrating π-π interactions present between adjacent complexes of **1** along the crystallographic *a*-axis at 120 K. (right) View of the intermolecular short contacts in crystal packing of **1** at 120 K All anions, lattice solvent and hydrogen atoms are omitted for clarity. Color scheme: Fe orange, Ni green, N blue, C grey, B yellow, O red

IV.2.3.2. Structure of $\{[(Tp^*)Fe(CN)_3]_2[Ni(L^2)_2]_2\}(OTf)_2$ (2)

In contrast with **1**, complex **2** was directly crystallized from the mother liquor using slow diffusion of diethyl ether vapor. Single-crystal X-ray diffraction analysis of the complex was performed at 120 K. A view of the structure is shown in Figure IV-5 and selected crystallographic data are gathered in Table IV-2. Due to the strong agitation of carbon atoms corresponding to the alkyl chain the R_1 and wR_2 values are significantly high. Therefore, the structure is emphasized in ball and sticks (Figure IV-5). The compound was solved in monoclinic $P2_1/c$ space group. The unit cell is composed of a centro-symmetric cyanido-bridged $\{Fe_2Ni_2\}$ square, two free trifluorometanesulfonate ions, two water and four DMF molecules. The general structural features of **2** are quite similar to the analogue **1**. The asymmetric unit consists of a half of the complex cation $[(Tp^*)Fe(CN)_3Ni(\mathbf{L}^2)_2]$, a free trifluoromethanesulfonate ion and co-crystallized solvent molecules (H_2O and 2·DMF). The average Ni-N bond distances of 2.079 Å are in agreement with Ni^{II} in HS configuration, while the average of Fe-N and Fe-C bond distances of 1.965 and 1.933 Å respectively, suggest the LS configuration of Fe^{III} site (Table IV-2). The heterometallic cyanido-bridged core has a slightly distorted square shape, based on N(5)-Ni(1)-N(6) and C(70)-Fe(1)-C(69) bond angles of 88.9(2)° and 92.1(3)°, respectively. On the Ni^{II} sites, Ni-N-C angles are 163.9(6)° and 168.1(5)°, while the Fe-C-N angles range between 179.9(6)° and 175.6(7)°. The Fe-CN-Ni edges are identical and slightly shorter than those found in **1**: the Fe(1)···Ni(1) distance is 5.062 Å. The Fe···Fe and Ni···Ni distances are 7.008 and 7.313 Å, respectively (Table IV-2). The angular distortion parameter on the Ni sites has a value of 56.0° that is 10° higher compared to **1**.

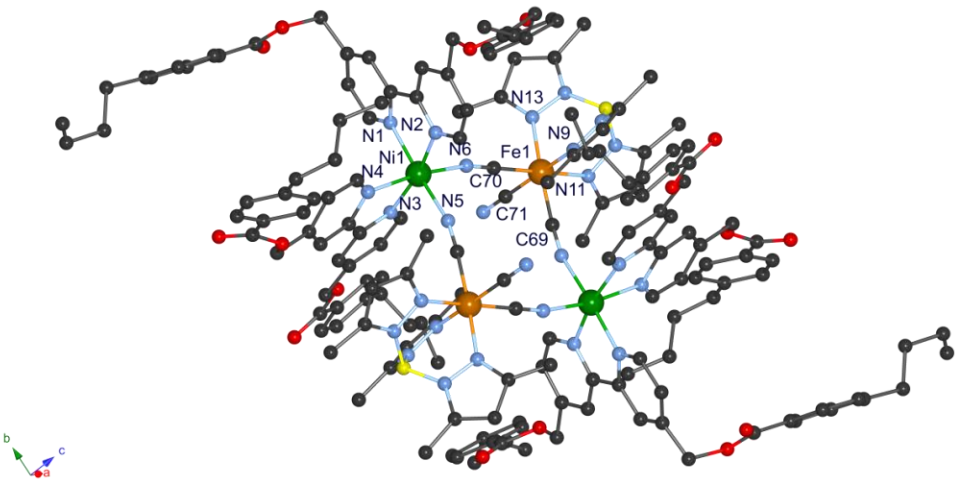

Figure IV-5. Structure of the cationic part of **2** at 120 K. Lattice solvents, anions, and hydrogen atoms are omitted for clarity. Color scheme: Fe orange, Ni green, B yellow, N blue, C grey.

Table IV-2. Crystallographic data for **2** at 120 K.

Temperature	**120 K**	**Selected bond distances (Å)**	
Crystal color	brownish-orange	Ni(1)-N(2)	2.101(5)
FW / g·mol^{-1}	3752.77	Ni(1)-N(1)	2.077(5)
Empirical formula	$C_{186}H_{220}B_2F_6Fe_2N_{30}Ni_2O_{28}S_2$	Ni(1)-N(3)	2.103(5)
Crystal system	Monoclinic	Ni(1)-N(4)	2.091(5)
Space group	$P2_1/c$	Ni(1)-N(5)	2.062(5)
a, Å	19.573(2)	Ni(1)-N(6)	2.042(5)
b, Å	22.319(2)	Fe(1)-N(9)	1.933(7)
c, Å	21.097(2)	Fe(1)-N(11)	1.980(6)
β, °	96.851(4)	Fe(1)-N(13)	1.984(5)
V, Å^3	9150.41	Fe(1)-C(69)	1.933(7)
Z	2	Fe(1)-C(71)	1.939(7)
ρ_{calcd}, g/cm^3	1.355	Fe(1)-C(70)	1.928(7)
μ, 1/mm	0.465	**Selected bond angles (°)**	
$\theta_{min} - \theta_{max}$	1.766 ° - 25.728 °	N(2)-Ni(1)-N(1)	78.7(2)
Refl. Coll. / unique	9736 / 17143	N(2)-Ni(1)-N(3)	92.8(2)
Completeness to 2θ	0.982	N(2)-Ni(1)-N(5)	94.4(2)
R_{int}	0.2581	N(2)-Ni(1)-N(6)	96.7(2)
Refined param./restr.	1198 / 193	N(1)-Ni(1)-N(3)	92.3(2)
[a]R_1 ($I > 2\sigma(I)$)	0.0978	N(1)-Ni(1)-N(4)	95.5(2)
[b]wR_2 (all data)	0.3243	N(1)-Ni(1)-N(6)	92.9(2)
[c]*GoF*	1.046	N(3)-Ni(1)-N(4)	78.0(2)
		N(3)-Ni(1)-N(5)	87.0(2)
<Fe-C>, Å	1.933	N(4)-Ni(1)-N(5)	91.1(2)
<Fe-N>, Å	1.965	N(4)-Ni(1)-N(6)	92.9(2)
<Ni-N>, Å	2.079	N(5)-Ni(1)-N(6)	88.9(2)
Fe(1)···Ni(1), Å	5.067	Ni(1)-N(5)-C(69)	163.9(6)
Fe···Fe, Å	7.008	Fe(1)-C(70)-N(6)	179.9(6)
Ni···Ni, Å	7.313	Fe(1)-C(69)-N(5)	175.6(6)
Σ(N-Ni-N)[a], °	56.0	Fe(1)-C(71)-N(7)	175.6(7)
		C(69)-Fe(1)-C(71)	87.2(3)
		C(70)-Fe(1)-C(69)	92.1(3)
		C(71)-Fe(1)-C(70)	84.4(3)

[a]$I > 2\sigma(I)$, $R_1 = \Sigma||F_o| - |F_c||/\Sigma|F_o|$. [b]$wR_2 = \{\Sigma[w(F_o^2 - F_c^2)^2]/\Sigma[w(F_o^2)^2]\}^{1/2}$. [c]GoF (goodness of fit on F^2) = $\{\Sigma[w(F_o^2 - F_c^2)^2]/ (n\text{-}p)\}^{1/2}$, where n is the number of reflections and p is the total number of refined parameters.

The packing shows weak intermolecular π-π interactions between benzoate moieties of two adjacent complexes (3.37 Å, Figure IV-6, left). Moreover, weak intermolecular C-H···π interactions between benzoate and pyrazole rings from Tp* are present along *b*-axis. H-bonds are also established between the nitrogen atom N(7) from terminal cyanide ligand, a water molecule and one DMF molecule (N(7)···O(1)w, 2.92 Å and O(1)w···$O(12)_{DMF}$, (2.84 Å, Figure IV-6, right).

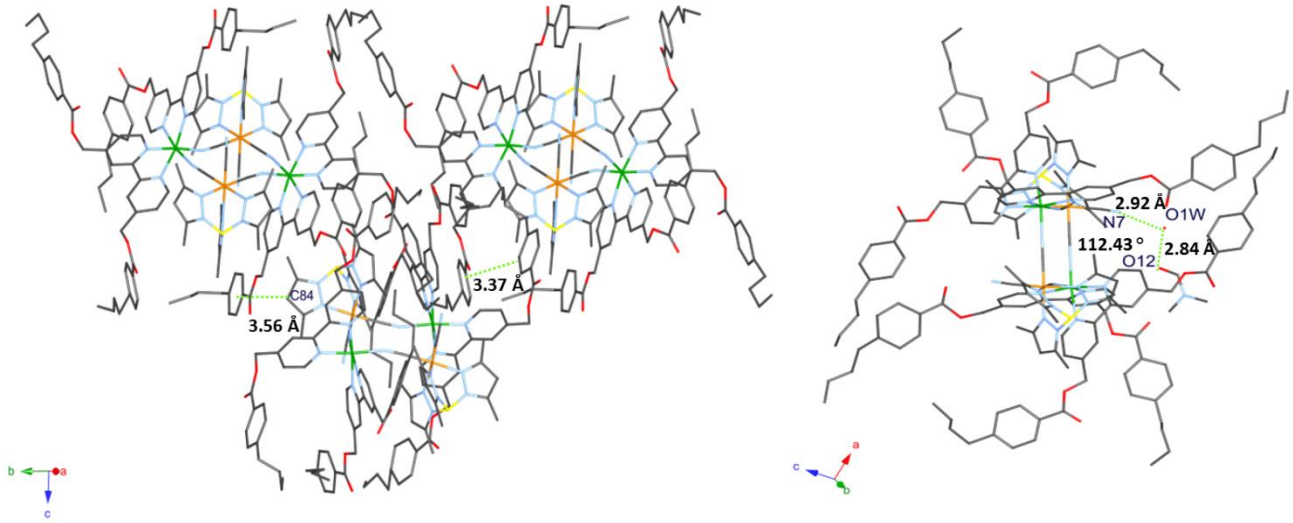

Figure IV-6. (left) Packing arrangements illustrating π-π interactions present between adjacent complexes of **2** along the crystallographic *a*-axis at 120 K. (right) View of the intermolecular short contacts in the crystal packing of **2** at 120 K. All anions, lattice solvent molecules and hydrogen atoms are omitted for clarity.

IV.2.4. Thermotropic properties

In order to investigate thermotropic properties on $\{Fe_2Ni_2\}$ squares, polarized optical microscopy (POM), differential scanning calorimetry (DSC) and small-angle X-ray scattering (SAXS) were performed. Preliminary investigations on complexes with ligand $\mathbf{L^3}$ and $\mathbf{L^4}$, (**3** and **4**, respectively) did not reveal any liquid crystalline behaviour. The two compounds melt into the liquid phase around 400 K based upon POM analysis, while the transition associated to the melting could not be clearly observed by DSC. On cooling, no birefringence texture could be detected down to room temperature, suggesting a poorly crystalline or amorphous behaviour. The SAXS profiles during the first heating displayed an intense reflection at 1.98 and 1.70 nm^{-1} for **3** and **4**, respectively, as well as very weak peaks in low and wide angle region, confirming a poorly crystalline behaviour (Figure S.IV-2). The sharp reflection in the low-angle region was attributed to the interlamellar distance imposed by the dodecyl chains and the values are 31.7 and 37.2 Å for **3** and **4**, respectively, indicating strong differences in the organization between the two compounds. On cooling, the intensity of reflections decreased significantly, indicating a slow-dynamic process for crystallization of the materials that solidify mainly as a glass as seen before in Chapter III. In contrast, the two squares containing $\mathbf{L^5}$ and $\mathbf{L^6}$ (**5** and **6**) were found to exhibit mesomorphism. The DSC and SAXS data for the two complexes are shown in Figure IV-7 and IV-8 and thermodynamic parameters are summarized in Table IV-3.

The DSC of **5** revealed an endothermic transition at 337 K, while the corresponding opposite peak is observed during the cooling at 326 K (Figure IV-7, left). SAXS measurements were performed to confirm the nature of the phases below and above the transition. From room temperature up to 338 K, only two sharp

reflections in the low reciprocal spacing region (q) and very diffuse halo around 14 nm^{-1} are observed as typically found in liquid-crystal materials (Figure IV-8, top).

Table IV-3. Phase transition temperatures and thermodynamic parameters for **5** and **6**

Compound	Transition[a]	T / K	ΔH / kJ·mol^{-1}
5	Sm-I	337.3	27.0
	I-Sm	325.9	29.2
6	Cr-Sm	315.1	98.0
	Sm-I	347.3	22.9

Cr = crystalline phase; I = isotropic liquid; Sm = smectic phase.

When heating further, a transition occurs between 338 and 343K and the two reflections disappear, indicating that the material reaches the isotropic liquid phase. The behaviour is perfectly reversible and the liquid crystalline organization is recovered at 328 K during the cooling. The two sharp reflections observed at 1.61 and 3.18 nm^{-1} are in ratio 1:2, showing that the molecules form a lamellar arrangement. The distance between the d_{001} and d_{002} layers is almost independent of the temperature and was calculated as 39.1 Å (Table IV-4). This value is in fair agreement to the expected distance separating the biphenyl groups from each side of the square (Figure IV-9). This result suggests that the material exhibits a bilayer lamellar organization as found before in Mn_{12} SMMs functionalized with biphenyl or cyanobiphenyl smectogen units (see in Chapter II). The DSC of **6** shows two reversible transitions (Figure IV-7, right). The first peak with the maximum of 315 K corresponds to a transition from a crystalline phase into smectic mesophase as evidenced by SAXS experiment. Upon further heating a second peak appears at 347 K and was attributed to the clearing into isotropic liquid phase based upon POM and SAXS measurements. Once again, the thermal behavior is reversible. Between the two transitions, SAXS profiles display only two sharp reflections that are in ration 1:2 as well as a broad and diffuse halo around 14 nm^{-1}, confirming the existence of a lamellar mesophase in the material (Figure IV-8, bottom). The interlamellar distance deduced from the two sharp reflections is almost temperature-independent and is 44.6 Å (Table IV-4). This value is higher than the one found in **5**, as depicted in other molecular systems previously described, and attributed to lower electrostatic interaction between biphenyl units.[19b,26]

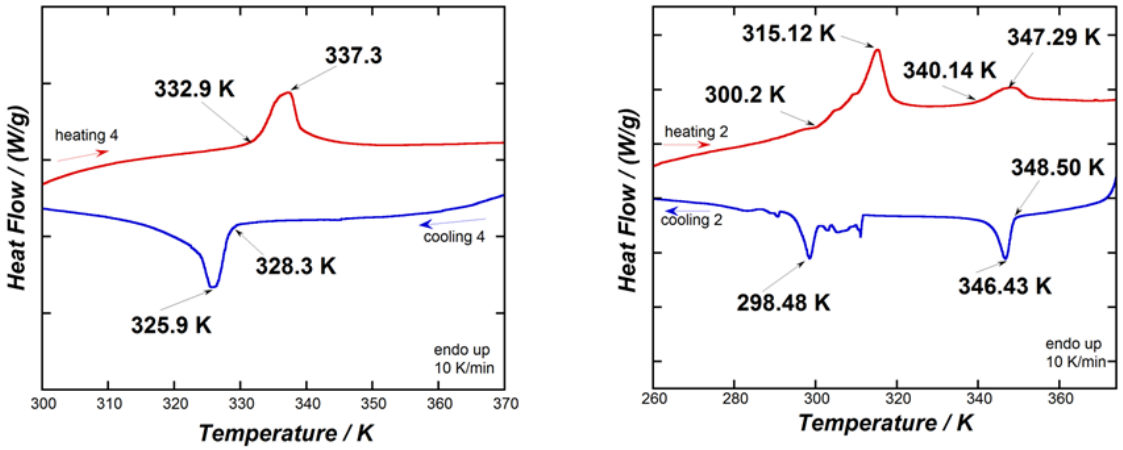

Figure IV-7. (left) DSC data for **5** recorded during the 2nd heating/cooling cycle between 300 and 370 K, (right) DSC data for **6** recorded during second heating/cooling cycle between 260 and 375 K

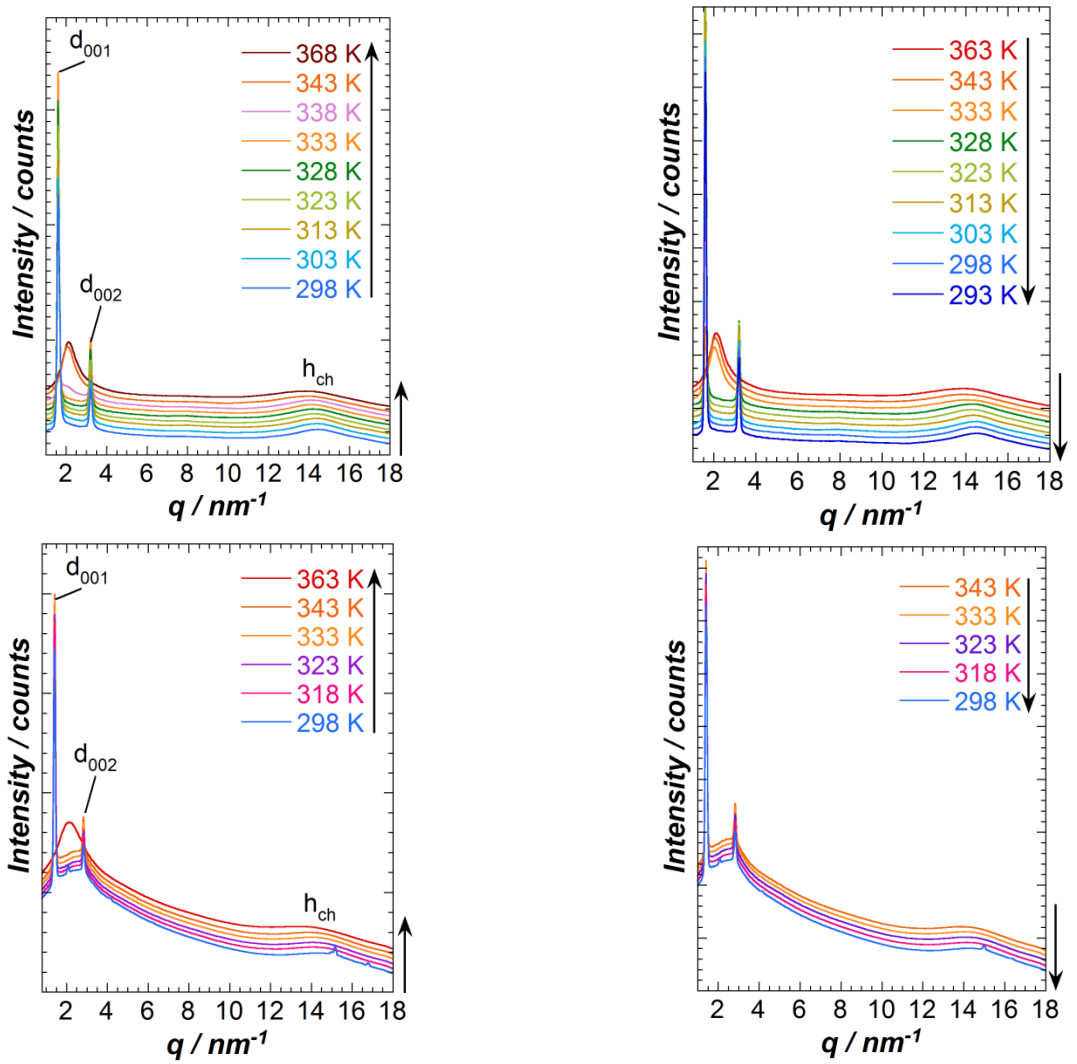

Figure IV-8. (top) SAXS profiles for **5** on 4th heating /cooling cycles between 293 and 368 K (bottom) SAXS profiles for **6** on 2nd heating/cooling cycle between 298 to 363 K.

Table IV-4. Indexation of SAXS profiles for **5** and **6**

5						**6**					
T / K	Peak number	$q_{(obs)}$ / nm^{-1}	$d_{(obs)}$ /Å	hkl	Interlamellar distance	T / K	Peak number	$q_{(obs)}$ / nm^{-1}	$d_{(obs)}$ /Å	hkl	Interlamellar distance
293	1	1.61	39.02	001		298	1	1.40	44.87	001	
	2	3.20	19.63	002			2	2.08	30.2	-	
303	1	1.61	39.02	001			3	2.83	22.20	002	
	2	3.20	19.63	002		318	1	1.41	44.56	001	
313	1	1.61	39.02	001			2	2.82	22.28	002	
	2	3.21	19.57	002		323	1	1.41	44.56	001	
323	1	1.60	39.26	001	d = 39.1		2	2.82	22.28	002	
	2	3.21	19.57	002		333	1	1.41	44.56	001	d = 44.6
328	1	1.60	39.26	001			2	2.82	22.28	002	
	2	3.19	19.69	002		343	1	1.41	44.56	001	
333	1	1.59	39.51	001			2	2.83	22.20	002	
	2	3.21	19.57	002							
338	1	1.61	39.02	001							
	2	3.21	19.57	002							

$q_{(obs)}$ is the observed/measured reciprocal spacing, $q = 4\pi \cdot sin\theta/\lambda$, where λ is the wavelength, 2θ is the diffraction angle, $d_{(obs)}$ is observed and calculated diffraction spacings: $d_{(obs)} = 2\pi/q_{(obs)}$, d is interlamellar distance $d = \frac{1}{n}\sum_{i=1}^{n} i \cdot d_{00i}$

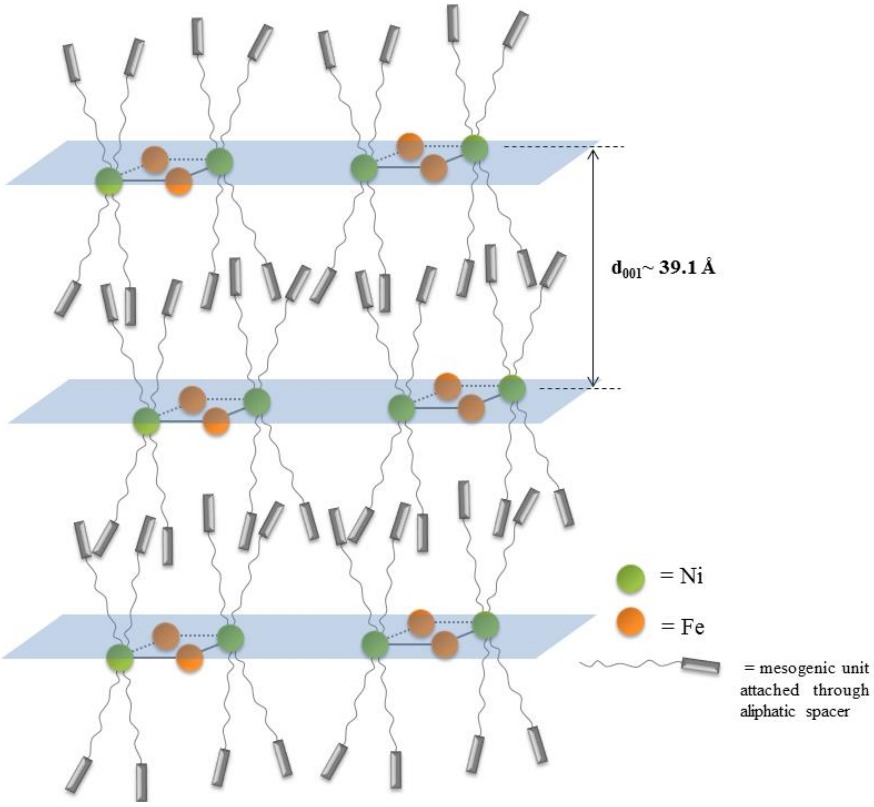

Figure IV-9. Schematic representation of the idealized intermolecular interactions leading to inter-planar distances in the mesophase observed for **5** complex.

IV.2.5. Magnetic properties

The two model complexes **1**, **2** and one mesomorphic analogue, **5**, were checked for SMM properties by magnetic susceptibility measurements in both *dc* and *ac* modes. The characteristic magnetic parameters extracted from these investigation are gathered in Tables IV-5 and results form dc and ac measurements are discussed in sections IV.2.5.1 and IV.2.5.2, respectively.

Table IV-5. Magnetic Properties for $\{Fe_2Ni_2\}$ square-based complexes.

Compound	*S*	*g*	*J*	τ_0 (s)	Δ_{eff}/k_B (K)	Optimum field, H (Oe)
1	3	2.14	9.7	1.6×10^{-7}	15	1500
2	3	2.16	9.6	2.8×10^{-8}	23	1000
5	3	2.19	10.6	2.5×10^{-7}	12	1500

S: spin ground state; *g*: Landé factor of ground state; Δ_{eff}: potential energy barrier; k_B: Boltzmann constant; τ_0: pre-exponential factor.

IV.2.5.1. Static magnetic measurements for 1, 2 and 5

The temperature dependence of the χT products of the $\{Fe_2Ni_2\}$ squares were collected in a static *dc* field of 0.1 T over a range of temperatures (1.8 – 300 K, Figure IV-10). For **1** and **2**, the measurements were performed on freshly filtered crystals. The χT values at room temperature (3.52, 3.20 and 3.89 $cm^3\ mol^{-1}\ K$, for **1, 2** and **5**, respectively), are in agreement with the presence of magnetically isolated Fe^{III}_{LS} (S = ½, g = 2.6 – 2.8) and Ni^{II} (S = 1, g = 2.2 – 2.3) ion in a 2:2 ratio, assuming that significant orbital contributions are present on Fe^{III}_{LS} ions.[8,9,27] With decreasing temperatures, the χT values gradually increase between 300 and

ca. 50 K suggesting that ferromagnetic interactions are operative. At lower temperatures, maximum values of 6.80, 6.96 and 8.12 $cm^3\ mol^{-1}$ K at 5.5 K are observed, which decrease slightly to 6.4, 6.7 and 7.6 $cm^3\ mol^{-1}$ K at 1.8 K for **1**, **2**, **5**, respectively.

Considering an idealized symmetrical square structure for these compounds, the magnetic data were initially modeled in the frame of an isotropic Heisenberg spin Hamiltonian:

$$H = -2J((S_{Ni} + S_{NiA}) \cdot (S_{Fe} + S_{FeA})) \qquad \textbf{(eq.1)}$$

where J is the average exchange interaction between Fe^{III}_{LS} and Ni^{II} sites through the cyanido-bridge, and S_i are the spin operators for each metal ions ($S_{Ni(II)} = 1$ and $S_{Fe(III)} = ½$).

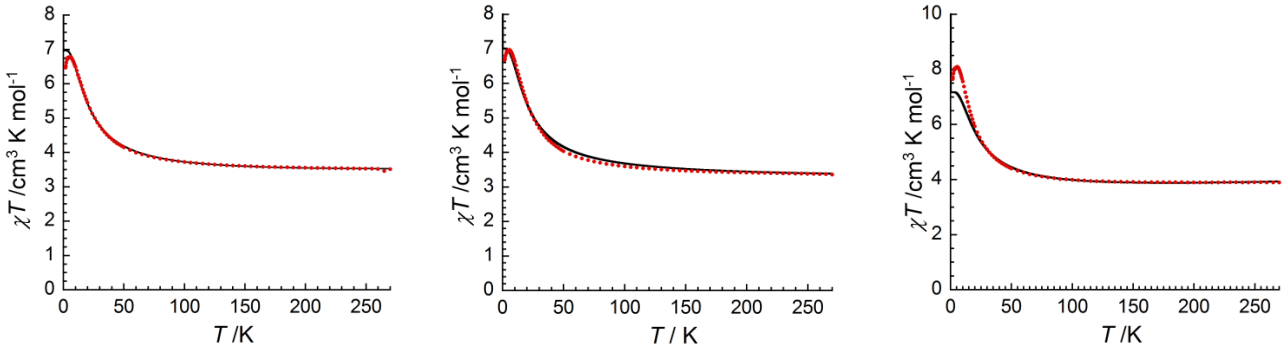

Figure IV-10. Temperature dependence of the χT product collected in an applied *dc* field of 0.1 T and the fitting (with black solid line) for: (left) **1** (center) **2** and (right) **5**.

Subsequent application of the van Vleck equation to Kambe's vector coupling scheme allowed for analytical expression (eq.2) of the magnetic susceptibility in the low field approximation:[28]

$$\chi = N\frac{2g_{av}^2\mu_B^2}{k_BT}\left\{\frac{14exp\left(\frac{10J}{k_BT}\right)+5exp\left(\frac{8J}{k_BT}\right)+7exp\left(\frac{6J}{k_BT}\right)+6exp\left(\frac{4J}{k_BT}\right)+1}{7exp\left(\frac{10J}{k_BT}\right)+5exp\left(\frac{8J}{k_BT}\right)+12exp\left(\frac{6J}{k_BT}\right)+8exp\left(\frac{4J}{k_BT}\right)+exp\left(\frac{2J}{k_BT}\right)+3}\right\} \qquad \textbf{(eq.2)}$$

Taking into account only data above 5 K to avoid the effects of intermolecular interactions and/or magnetic anisotropy, the best fit parameters J/k_B = 9.7, 9.6 and 10.6 K with g values of 2.14, 2.16, 2.19 for **1**, **2**, **5**, respectively. The intra-complex magnetic interactions lead to an $S_T = 3$ spin ground state.

The field dependence of the magnetization collected for three squares confirms that all the compounds exhibit significant magnetic anisotropy for cyanide-based SMMs (Figure S.IV-5). At 1.85 K the magnetization values found (5.5 μ_B for **1** and **2**, 5 μ_B for **5**) confirm that the S_T = 3 spin ground. This conclusion is consistent with previously described magnetic data (χT versus T data). Moreover, the M versus H/T data obtained for the $\{Fe_2Ni_2\}$ squares is confirming that significant magnetic anisotropy is present below 8 K. We note that no hysteresis is observed above 1.85 K in the M versus H data and is consistent with behavior reported for a variety of polynuclear cyanide-bridged complexes.[7-9,27]

IV.2.5.2. Dynamic magnetic measurements for 1, 2 and 5

In order to probe the magnetization dynamics of **1**, **2** and **5**, *ac* susceptibility measurements were first performed in the absence of a static *dc* magnetic field. The in-phase χ' and out-of-phase χ'' components of the ac susceptibility were measured as function of the temperature at various *ac* field frequencies (Figure S.IV-6). In all cases, the onset of frequency-dependent χ'' signal are observed below 4 K, while the maxima of the

peak could not be observed at low temperature, suggesting that slow relaxation of magnetization is only operative below 1.9 K. Therefore, it was not possible from these data to extract accurately the characteristic relaxation times. These results indicate that in absence of an applied field, the systems are not able to retain magnetization and relax fast above 1.9 K, as found previously in $\{Fe^{III}_2Ni^{II}_2\}$ analogues.[8,9] In these systems, slow relaxation processes in measurable temperature or frequency ranges can be activated by applying small static magnetic fields.[8,9] Thus to determine the optimal fields, *ac* susceptibility measurements were performed at 1.9 with applied *dc* magnetic fields ranging from 0 to 10000 Oe. (Figure IV-11). The three complexes show *ac* signals with relaxation modes lower than 10 kHz for *dc* field above 200 Oe. The maxima of the χ'' signals decrease in frequency with increasing *dc* field. Strong differences of this evolution were found between the three compounds. For example with an applied field of 1000 Oe, the maxima of the χ'' signals are found at about 80 Hz, 500 Hz and 1200 Hz for **2**, **1** and **5**, respectively, meaning that **2** is characterized by an higher energy barrier. From these data, the optimal *dc* fields were estimated to 1000 Oe for **2** and 1500 Oe for **1** and **5** complexes and were used for further investigations of the magnetization dynamics (Figure S.IV-4).

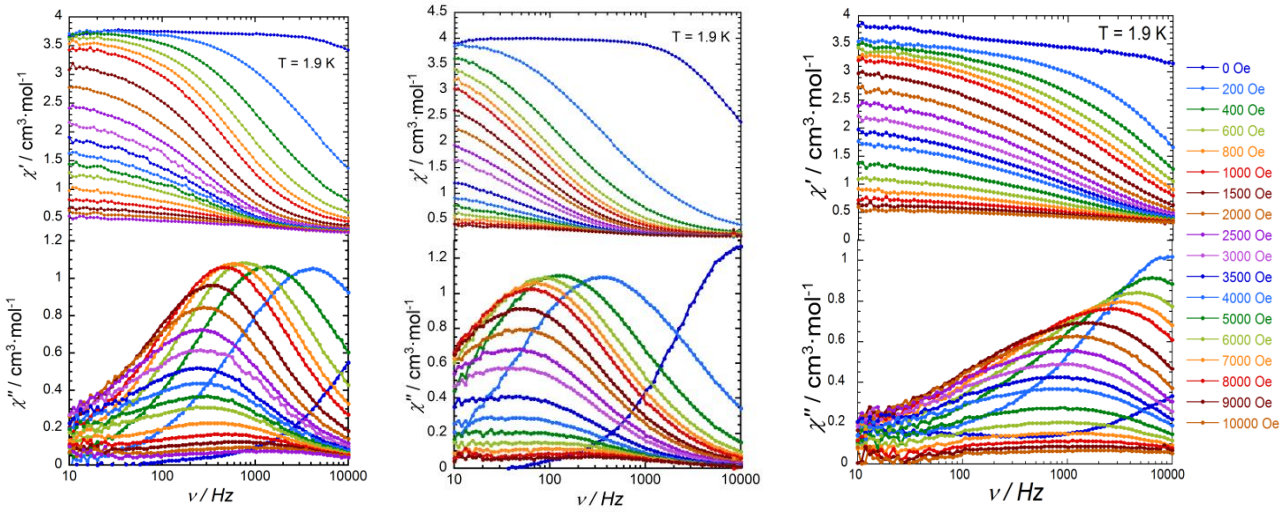

Figure IV-11. Plots of the in-phase (top), χ', and out-of-phase (bottom), χ'', components of the *ac* magnetic susceptibility *versus* the frequency, *ν*, of the oscillating field at 1.9 K between 0 to 10000 Oe of **1** (left), **2** (center) and **5** (right).

The temperature and frequency dependence of the *ac* susceptibility, recorded at 1.9 K with these optimal *dc* fields, are shown in Figure IV-12 and Figure S.IV-7, respectively. As expected, the maxima of the χ'' signals are shifted toward higher temperature as the operating frequency increases. At 10 kHz, the maxima are ca. 3.0, 3.4 and 2.8 K for **1**, **2** and **5**, respectively, confirming the better ability of **2** to retain magnetization. In contrast with **1** and **2** complexes, the χ'' signals displayed by **5** are quite broad, while a shoulder can be deduced at low operating frequencies (typically below 600 Hz). This result indicates that at least two relaxation mode are present, and can be explained slight sub-structural differences between molecules resulting from an inhomogeneous organization of the frozen liquid crystalline phase.

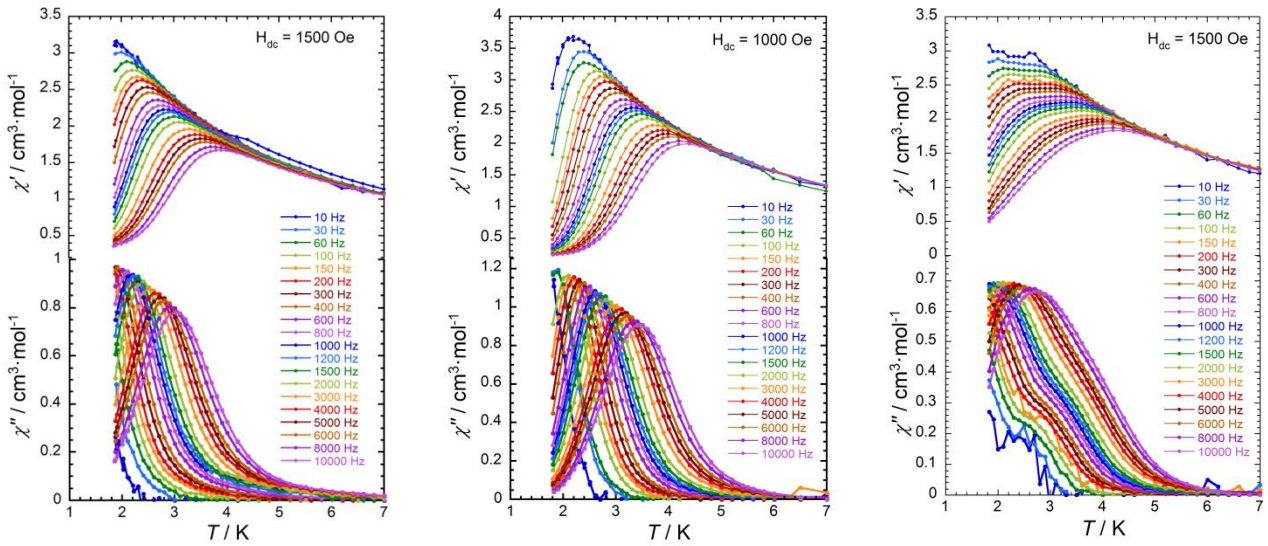

Figure IV-12. Plots of the in-phase (top), χ', and out-of-phase (bottom), χ'', components of the *ac* magnetic susceptibility *versus* the temperature , *T*, under an external optimal magnetic field at different frequency between 10 and 10000 Hz for the compound (left) **1** at 1500 Oe, (center) **2** at 1000 Oe and (right) **5** at 1500 Oe.

From the maxima of the χ'' signals, it was possible to extract the characteristic relaxation times τ at different temperature. In all cases, the relaxation time follows an Arrhenius law, where the ln(τ) versus *1/T* plots. From the linear regression fits, the energy barriers Δ_{eff}/k_B were estimated to 15, 23 K and 12 K respectively for **1**, **2** and **5** (Figure IV-13), which is in agreement with previous value found in $\{Fe^{III}_2Ni^{II}_2\}$ analogues.[8,9]

Hence, these investigations revealed the strong influence of the functionalization on the magnetic behavior, and confirmed the possibility to preserve SMM features on a mesomorphic complex **5**. Although, no measurement was performed so far for the other complexes functionalized with mesogenic substituents, we assume that this behavior will be maintained.

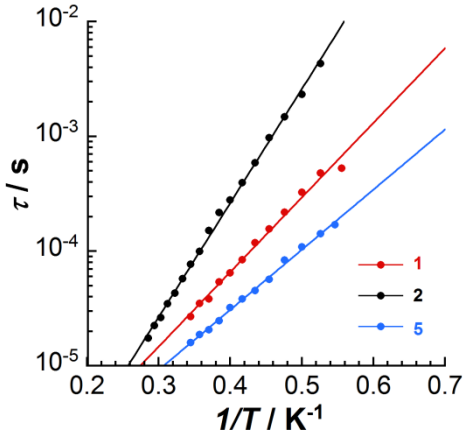

Figure IV-13. τ versus 1/*T* plot for **1**(red), **2** (black), and **5** (blue), in semi logarithmic scale.

IV.3. Synthesis and characterization of $\{Fe_2Co_2\}$ molecular squares

In the second part of this project, we have been interested in the functionalization of cyanido-bridged $\{Fe_2Co_2\}$ molecular squares with the aim to promote liquid crystal properties or at least to improve their solubility in usual organic solvents. Our initial strategy was to develop the analogues of $\{Fe_2Ni_2\}$ squares described earlier using the same ligands. Several of these complexes were prepared and our preliminary investigations confirmed remarkably the same liquid crystalline features when **L**^{5} and **L**^{6} are used, while no liquid crystal properties are observed with **L**^{3} and **L**^{4} ligands are employed. All the complexes were isolated as red powder or glassy solids which is the characteristic color for the paramagnetic phase. Unfortunately, upon cooling to liquid nitrogen temperature, none of them revealed change of color into green as expected for ET process. The absence of ET in solid state is not unusual,[16,19] and can be either explained by crystal packing effects, ie. the intermolecular interactions, or by the functionalization of the bipyridine ligands that changes the redox potential of the metal center, making the ET unfavourable. The first hypothesis was discarded since even in solution, no change of color could be detected. Hence, this preliminary study revealed that the functionalization proposed was successful to promote liquid crystalline properties in these molecular squares but was unfortunately inappropriate to obtain ET properties and highlighted the necessity to revise the design of our systems.

IV.3.1. Synthetic approach

In order to promote ET properties in $\{Fe_2Co_2\}$ squares, two strategies might be applied: First, by changing the ligand on the Fe^{III} building block and second, by changing the ligands on the Co^{II} center. During this work we were mainly focused on the second strategy. In particular, assuming that the change of the redox potential is mainly due to the presence of benzylic carbon functions, we looked for an alternative spacer between the bipyridine platform and the mesogenic part. Previous work in our team showed that $\{Fe_2Co_2\}$ molecular squares functionalized with 4,4' dimethoxy-2,2'-bipyridine exhibit ET in solid-state according to the nature of counter-anion and solvation.[19b] Taking into account this result, we proposed to synthetize two new ligands, **L**^{7} and **L**^{8}, containing mesogenic groups linked to the bipyridine through an ether function (Scheme IV-5).

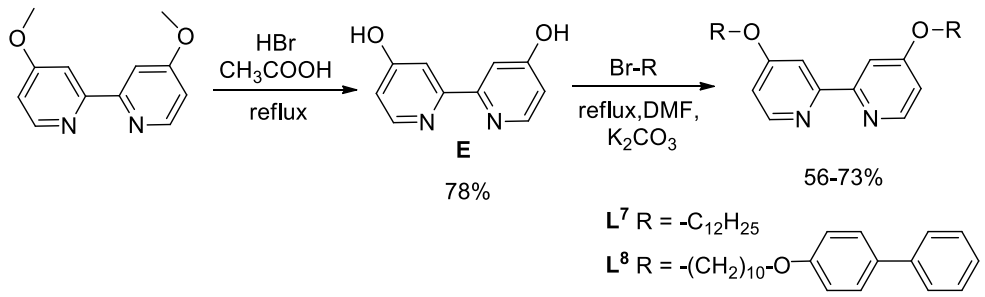

Scheme IV-5. Synthetic pathway for the preparation of **L**^{7} and **L**^{8}.

The ligands were prepared in two steps following the pathway described in Scheme IV-5. The precursor 4,4'-dimethoxy-2,2'-bipyridine was treated with a mixture of HBr/acetic acid and refluxed for 12

hours to produce **E**. The ligands were then obtained by Williamson reaction of precursor **E** with the corresponding alkyl bromide.

The $\{Fe_2Co_2\}$ molecular squares were prepared as previously described, by the self-assembly of $[(Tp^*)Fe^{III}(CN)_3][NEt_3]$ with $Co(OTf)_2$ in presence of $\mathbf{L^{7\text{-}8}}$ in a mixture of DMF/CH_2Cl_2. The clear solutions are red which is indicative for the molecule in their paramagnetic state, characterized by the $\{Fe^{III}_{LS}(\mu\text{-}CN)Co^{II}_{HS}\}_2$ squares. However, when the solution is concentrated and diethyl ether is added, a green precipitate is formed in agreement with formation of the diamagnetic phase corresponding to the $\{Fe^{II}_{LS}(\mu\text{-}CN)Co^{III}_{LS}\}_2$ squares. The raw powder samples were dissolved in MeOH and recrystallized by slow evaporation. Dark green single crystals (needles) were obtained for complex $\{[(Tp^*)Fe(CN)_3]_2[Co(\mathbf{L^7})_2]_2\}(OTf)_2$, which was found to co-crystallizes with six water molecules. Unfortunately, due to its low solubility in MeOH, only a green microcrystalline powder sample could be isolated for the complex $\{[(Tp^*)Fe(CN)_3]_2[Co(\mathbf{L^8})_2]_2\}(OTf)_2$. We also prepared analogues with hexafluorophosphate counter anion since this latter was found efficient to promote ET process in $\{Fe_2Co_2\}$ complexes with 4,4'-dimethoxy-2,2'-bipyridine.[19b] These were obtained by treating the $\{[(Tp^*)Fe(CN)_3]_2[Co(\mathbf{L^{7\text{-}8}})_2]_2\}(OTf)_2$ with an excess of Bu_4NPF_6 in methanol. In contrast with previous cases, both complexes were obtained as red microcrystalline samples, suggesting the paramagnetic phase.
The four prepared complexes will be thereafter referred as following:

7 - $\{[(Tp^*)Fe(CN)_3]_2[Co(\mathbf{L^7})_2]_2\}(OTf)_2\cdot 6H_2O$;

8 - $\{[(Tp^*)Fe(CN)_3]_2[Co(\mathbf{L^7})_2]_2\}(PF_6)_2$;

9 - $\{[(Tp^*)Fe(CN)_3]_2[Co(\mathbf{L^8})_2]_2\}(OTf)_2$;

10 - $\{[(Tp^*)Fe(CN)_3]_2[Co(\mathbf{L^8})_2]_2\}(PF_6)_2$.

IV.3.2. FTIR spectroscopic analyses

The oxidation state of the two set of complexes was confirmed by FTIR spectroscopy. In **7** and **9** complexes, the stretching vibration of cyanide ligands in bridging mode were spitted in two bands at ca. 2090 and 2057 cm^{-1}, while the stretching vibration corresponding to terminal cyanide is found around 2110 cm^{-1}. These values were similar to those previously found in the diamagnetic analogue $\{Fe^{II}_2Co^{III}_2\}$ (with 4,4'-dimethoxy-2,2'-bipyridine ligand and PF^{6-} counter anion).[19b] In both cases, a very weak band is observed around 2160 cm^{-1}, suggesting the presence of a small fraction of paramagnetic $\{Fe^{III}_2Co^{II}_2\}$ square in the sample. This latter was previously explained by solvent loss, which induce an irreversible ET into the paramagnetic phase.[19b]

In **8** and **10** complexes, the stretching vibrations for cyanide ligands in bridging mode are significantly shifted to higher energy, ca. 2160 cm^{-1}, as expected for the paramagnetic phase (Figure IV-14, right).[11b,15-19] The terminal cyanide band is almost unperturbed compared to **7** and **9**, and is found around 2120 cm^{-1} (Figure IV-14, left). In all complexes, the formation of expected complexes is also supported by the presence of the B-H stretching band from the Tp* ligand at 2506-2921 cm^{-1} and the intense double band at 2940 and 2930 cm^{-1} ascribed to C-H stretching vibration from the alkyl chains.

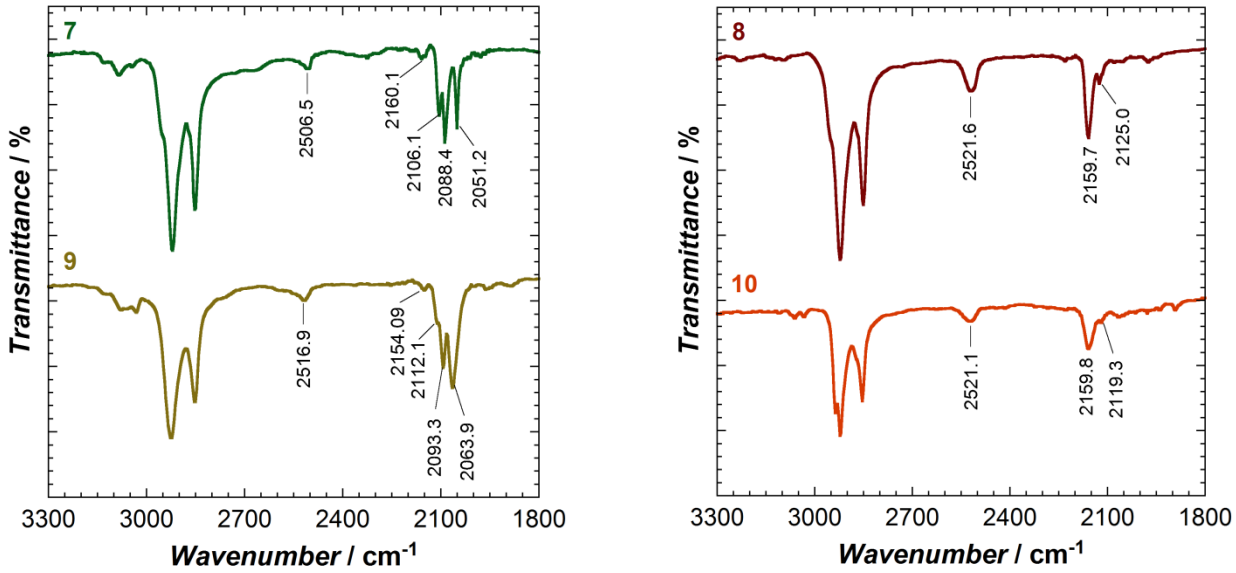

Figure IV-14. FTIR spectra collected between 3300 and 1800 cm^{-1} at room temperature: (left) for the **7** (green crystals) and **9** complexes (green powder); (right) for the **8** and **10** complexes (red powders).

IV.3.3. Structural description of $\{[(Tp^*)Fe(CN)_3]_2[Co(L^7)_2]_2\}(OTf)_2\cdot 6H_2O$ (7)

The crystals of **7** are green at room temperature, which is an indication for the diamagnetic configuration. When the crystal is kept outside the mother liquor, it remains stable (no loss of solvent) and no change of color could be perceived.

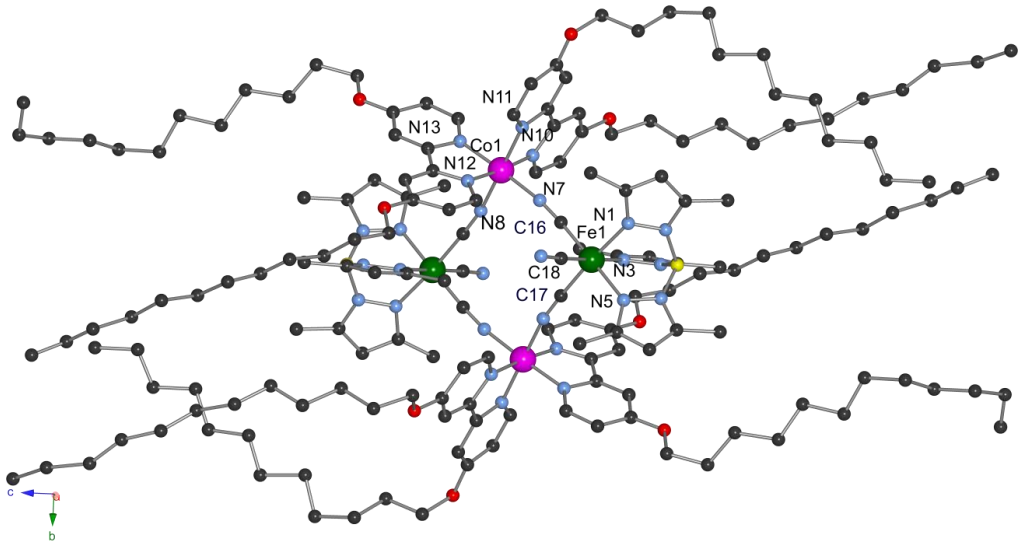

Figure IV-15. Structure of the cationic part of **7** at 120 K. Lattice solvents, anions, and hydrogen atoms are omitted for clarity. Color scheme: Fe green, Co pink, B yellow, N blue, C grey.

However, when the crystal is heated up to 320 K, the crystals turn irreversibly to red and lose crystallinity. Therefore, single-crystal X-Ray diffraction studies could not be performed at high temperatures. The crystal was collected at 120 K and showed that the compound crystallizes in triclinic *P-1* space group. The asymmetric unit is composed of one cationic $\{Fe_2(\mu\text{-}CN)_4Co_2\}$ molecular square, two trifluorosulfonate counter anions and six co-crystallized water molecules. The structure of the central fragment is essentially similar to those previously reported.[15-19] The central fragment is constituted from a square shaped core where Fe and Co ions are alternately bridged by cyanide ions. The tridentate Tp* ligands is facially coordinated to

the Fe ion, and the remaining coordination sites are occupied by the three cyanide ligands through the carbon atoms (Figure IV-15).

Table IV-6. Crystallographic data for **7** at 120 K.

Temperature	**120 K**	**Selected bond distances (Å)**	
Crystal color	green	Co(1)-N(7)	1.899(7)
FW / g·mol^{-1}	3473.46	Co(1)-N(8)	1.890(8)
Empirical formula	$C_{174}H_{280}B_2F_6Fe_2N_{26}Co_2O_{20}S_2$	Co(1)-N(10)	1.920(6)
Crystal system	Triclinic	Co(1)-N(11)	1.939(8)
Space group	*P-1*	Co(1)-N(12)	1.940(7)
a, Å	12.1561(9)	Co(1)-N(13)	1.926(7)
b, Å	17.2525(13)	Fe(1)-N(1)	2.034(8)
c, Å	23.0199(16)	Fe(1)-N(3)	2.037(7)
α, °	88.523(4)	Fe(1)-N(5)	2.036(7)
β, °	80.997(6)	Fe(1)-C(16)	1.867(7)
γ, °	73.821(4)	Fe(1)-C(17)	1.892(9)
V, Å^3	4631.69	Fe(1)-C(18)	1.893(8)
Z	1	**Selected bond angles (°)**	
ρ_{calcd}, g/cm^3	1.245	N(11)-Co(1)-N(10)	82.9(3)
μ, 1/mm	0.426	N(11)-Co(1)-N(7)	90.8(3)
$\theta_{min} - \theta_{max}$	1.229 ° - 25.565°	N(11)-Co(1)-N(12)	94.0(3)
Refl. Coll. / unique	16907 / 8393	N(11)-Co(1)-N(13)	90.8(3)
Completeness to 2θ	0.974	N(10)-Co(1)-N(7)	93.6(4)
R_{int}	0.1289	N(10)-Co(1)-N(13)	93.3(3)
Refined param./restr.	1054 / 165	N(10)-Co(1)-N(8)	94.6(3)
[a]R_1 ($I > 2\sigma(I)$)	0.2263	N(7)-Co(1)-N(12)	94.4(3)
[b]wR_2 (all data)	0.4277	N(7)-Co(1)-N(8)	90.7(3)
[c]GoF	1.398	N(12)-Co(1)-N(13)	83.0(3)
		N(12)-Co(1)-N(8)	88.4(3)
<Fe-C>, Å	1.884	N(13)-Co(1)-N(8)	87.8(3)
<Fe-N>, Å	2.035	Co(1)-N(11)-C(24)	114.2(6)
<Co-N>, Å	1.920	Co(1)-N(11)-C(28)	126.2(6)
Fe(1)···Co(1), Å	4.915	Fe(1)-C(17)-N(8)	177.6(7)
Fe···Fe, Å	6.969	Fe(1)-C(16)-N(7)	174.7(7)
Co···Co, Å	6.918	Fe(1)-C(18)-N(9)	176.3(7)
Σ(N-Co-N)[a], °	34.2	C(17)-Fe(1)-C(16)	90.1(3)
		C(18)-Fe(1)-C(17)	91.2(3)
		C(18)-Fe(1)-C(16)	85.8(3)

[a] $I > 2\sigma(I)$, $R_1 = \Sigma||F_o| - |F_c||/\Sigma|F_o|$. [b] $wR_2 = \{\Sigma[w(F_o^2 - F_c^2)^2]/\Sigma[w(F_o^2)^2]\}^{1/2}$. [c] GoF (goodness of fit on F^2) = $\{\Sigma[w(F_o^2 - F_c^2)^2]/ (n\text{-}p)\}^{1/2}$, where n is the number of reflections and p is the total number of refined parameters.

Two of the three cyanide ions from the Fe sites coordinate the Co ions in bridging mode, while the free cyanide groups adopt an *anti* orientation relative to the $\{Fe_2(\mu\text{-}CN)_4Co_2\}$ plane. The coordination sphere of Co ion is completed by two bidentate $\mathbf{L}^7$ ligands. The $\{Fe_2(\mu\text{-}CN)_4Co_2\}$ core is nearly planar as shown by Fe-C-N angles, which range between 174.7(7) and 177.6(7)°, while Co-N-C angles range between 114.2(6) and 126.2(6)° (Table IV-6, Figure IV-15). In addition, the C(17)-Fe(1)-C(16) angle (90.1(3)°), Fe···Fe (6.969 Å) and Co···Co (6.918 Å) distances indicate that **7** adopts an nearly ideal square structure (Figure IV-15, Table IV-6). The oxidation state of the molecular square, $\{Fe^{II}_2(\mu\text{-}CN)_4Co^{III}_2\}$ was unambiguously confirmed by the examination of the coordination sphere of the Co ion site. The Co-N bond distance range from 1.899 to 1.940 Å, which is in agreement with Co^{III} in its LS state (Table IV-6), and Fe^{II}_{LS} ion was therefore deduced to satisfy the charge balance. The Co^{III}_{LS} configuration is also supported by the relatively low distortion of the coordination sphere ($\Sigma_{(N\text{-}Co\text{-}N)} = 34.2°$).

The packing of **7** shows a layered structure (Figure IV-16). The molecular squares are arranged face to face in pairs along the *a*-axis in the (*ab*) plane. The alkyl chains of adjacent layers are strongly interdigitated, separating the layers by 23.020 Å, corresponding to *c* parameter of the unit cell. The aliphatic chains are packed and separated by approximately 5 Å. Because of the van der Waals interactions between the hydrocarbon chains, the thermal motion is increasing on entirely chain. Because of the strong agitation of carbon atoms corresponding to the long alkyl chain the R_1 and wR_2 values are significantly high (Table IV-6). Therefore, the structure is emphasized in ball and sticks (Figure IV-15). Furthermore, the water molecules form hydrogen bonds with terminal cyanide groups (Figure IV-17).

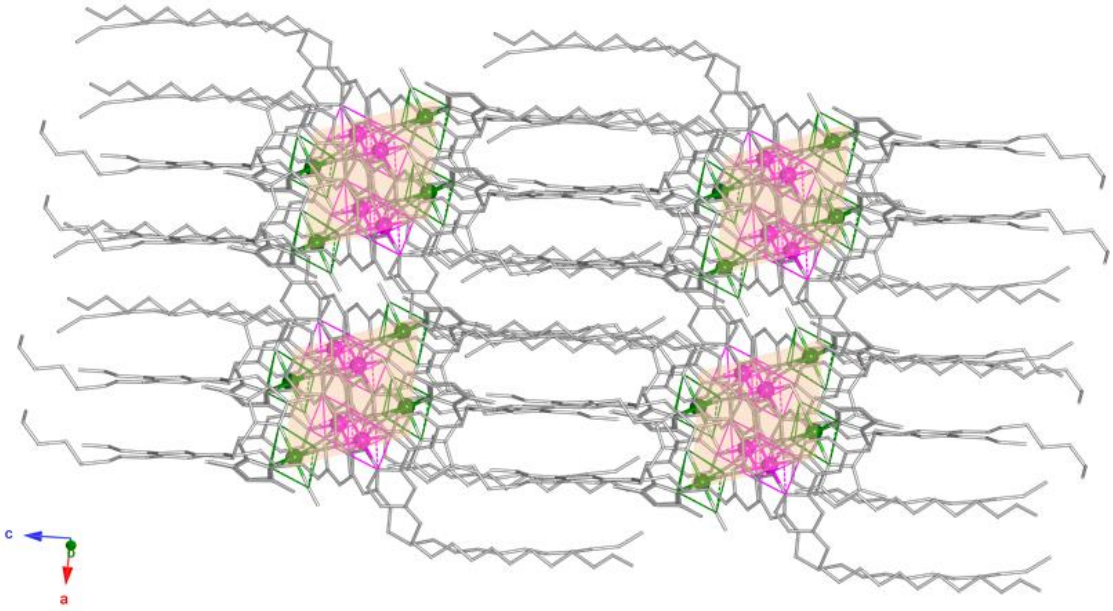

Figure IV-16. Packing diagram of **7** in the bc plane emphasizing one unit cell. Lattice solvent molecules, anions, and hydrogens are omitted for clarity. Color scheme: Fe green, Co pink, B, N and C grey.

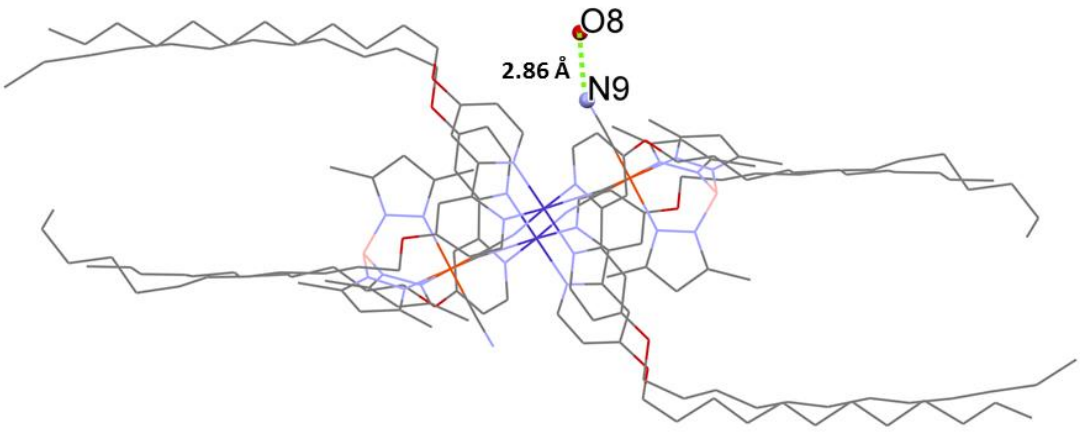

Figure IV-17. Packing diagram of **7** in the *ab* plane illustrating the H bonding between solvent molecules and terminal cyanide groups. Anions and hydrogen atoms are omitted for clarity. Color scheme: Fe orange, Co purple, B pink, N blue, C grey.

IV.3.4. Magnetic measurements in solid state

Magnetic susceptibility measurements confirmed that the **7** does not undergo reversible thermally induced ET (Figure IV-18). The χT value from 1.8 to 305 K is nearly constant with the value of 0.11 $cm^3 \cdot K/mol$ confirming that **7** is in a diamagnetic $\{Fe^{II}_2Co^{III}_2\}$ configuration as shown by XRD analysis and by its green color at room temperature. As the temperature increase from 306 to 336 K, the χT product increases abruptly up to 5.02 $cm^3 \cdot K/mol$, indicating the occurrence of thermally induced ET (Figure IV-18, red line). The χT product is lower than the expected value ~ 7 $cm^3 \cdot K/mol$ for two non-interacting Fe^{III}_{LS} (S = 1/2) and two Co^{II}_{HS} (S = 3/2) ions. The low value of the χT product may be explained by the presence of diamagnetic impurities such as free ligand. On cooling the reverse process is not observed and the material remains paramagnetic. This irreversible ET behavior is probably induced by the desolvation of the compound (MeOH), which is thereafter stabilized in the paramagnetic phase, as shown before in the analogue complex containing tridecyl substituents.[19] From 350 down to 240 K, the χT product slightly decreases from 5.11 to 4.21 $cm^3 \cdot K/mol$ due to the intrinsic spin orbit coupling of the cobalt centers. At lower temperatures, the χT values increase to ca. 4.55 $cm^3 \cdot K/mol$ at 7.7 K, suggesting the presence of intramolecular ferromagnetic interactions between Co^{II}_{HS} and Fe^{III}_{LS} centers. Below 5 K, the χT product drops to ca. 2.40 $cm^3 \cdot K/mol$ due to intermolecular antiferromagnetic interactions between adjacent molecular squares or zero-field splitting.

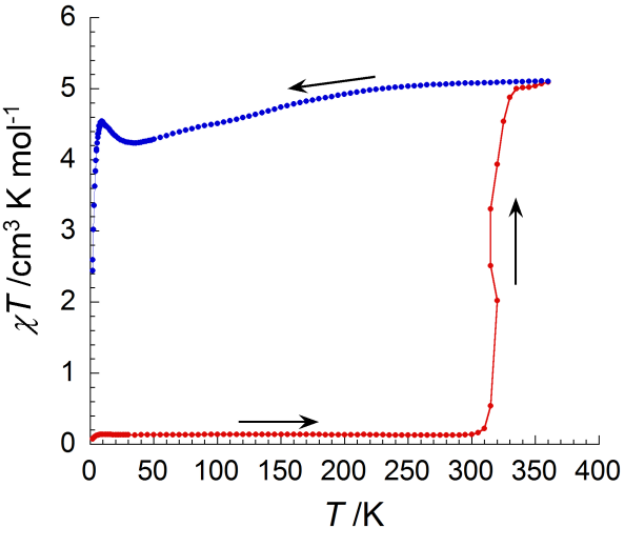

Figure IV-18. Temperature dependence of the χT product (with χ defined as the molar magnetic susceptibility and equal to M/H) for compound **7** collected in an applied *dc* field of 1 T.

Magnetic susceptibility studies for **8** and **10** were carried out between 1.8 and 280 K and confirmed the absence of thermally-induced ET process in these materials (Figure IV-19). The χT product for complex **8** is 7.1 $cm^3 \cdot K/mol$ at high temperature (Figure IV-19, left). This value is in agreement with the one expected for similar squares with low spin Fe^{III} ions (S = ½) and two high-spin Co^{II}_{HS} (S = 3/2) ions. Below 50 K, the χT product increases abruptly due to intramolecular ferromagnetic coupling between the Co^{II} and Fe^{III} ions through cyanide bridges. At 6 K, the curve reaches a maxima of 9.95 $cm^3 \cdot K/mol$, before decreasing rapidly

down to 9.40 $cm^3 \cdot K/mol$ at 1.8 K as the result of antiferromagnetic intermolecular interactions between adjacent molecules and/or magnetic anisotropy in Co^{II}_{HS} sites.

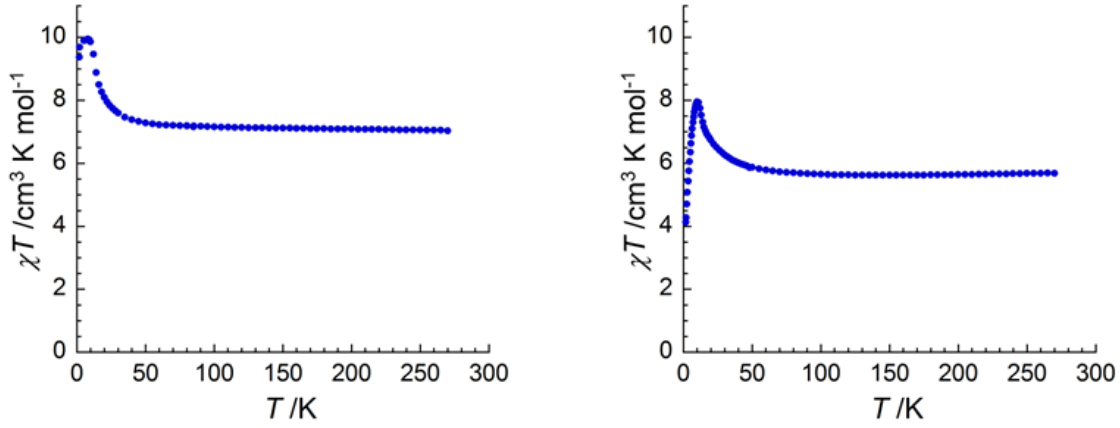

Figure IV-19. Temperature dependence of the χT product (with χ defined as the molar magnetic susceptibility and equal to M/H) for compound **8** (left) and of **10** (right) at 0.1 T.

Similarly, the temperature dependence of the χT product for complex **10** shows a value of 5.8 – 5.9 $cm^3 \cdot K/mol$ at high temperature (Figure IV-19, right), which is slightly lower than expected for the sum of two magnetically isolated low spin Fe^{III} ions (S = ½) and high-spin Co^{II} (S = 3/2) ions. Upon cooling the χT product remains roughly constant down to 50 K and then increases abruptly up to 8.0 $cm^3 \cdot K/mol$ at 10 K. Once again, the χT value decreases down to 4.15 $cm^3 \cdot K/mol$ at 1.8 K due to antiferromagnetic intermolecular interactions and/or the magnetic anisotropy of Co^{II}_{HS} ions.

For both samples, additional evidences for ferromagnetic exchanges between Fe^{III}_{LS} and Co^{II}_{HS} ions are found in the field-dependence of magnetization. At 1.8 K, the magnetization values are increasing constantly upon applying external *dc* fields (Figure S.IV-8), without presenting any S-shape curves that could be an indicative for the presence of antiferromagnetic interactions. For **10**, the magnetization curves show an absence of saturation presuming magnetic anisotropy of the Co^{II} site (Figure S.IV-8, right).

IV.3.5. Characterization of $\{Fe_2Co_2\}$ molecular squares in solution

The structural and magnetic studies showed that functionalized complexes **7-10** do not undergo reversible thermally (Figure S.IV-3) or photo-induced ET (according to reflectivity measurements) in solid state. By analogy, the previous analogues with 4,4-dimethoxy2,2'bipyridine ligands exhibited or not ET properties in solid-state depending on the nature of the counter anion and solvation, suggesting a strong influence of the packing on the redox phenomenon.[19b] To determine whether ET process, associated with switching of the magnetic and optical properties, is favorable for our complexes, we performed measurements in diluted solutions.

As expected, complex **7** containing bipyridine ligands functionalized with long alkyl chains is soluble in a broad range of organic solvents (Table IV-7). In most of the case, a change of color from red to green is observed upon cooling to 77 K (Figure IV-20), which is a clear indication for a conversion from the paramagnetic into the diamagnetic phase as the result of a thermally-induced ET process. Complex **9** was found poorly soluble in polar solvents and thus ET process occurs only in a limited number of solvents. For

the solutions where a change of color was observed, it is assumed that the $\{Fe_2Co_2\}$ molecules remain intact (no dissociation).

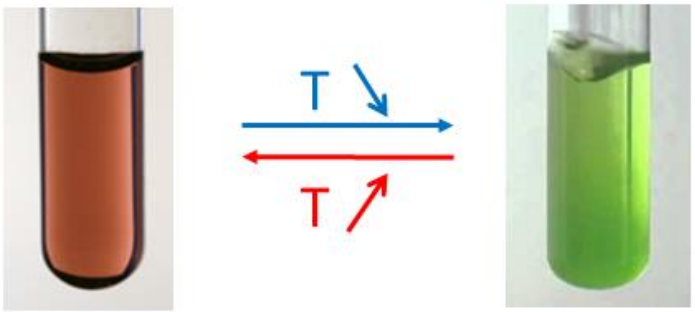

Figure IV-20. Change of color observed when a methanol solution of **7** is cooled from room temperature (left) and cooled down with liquid nitrogen (right).

Table IV-7. Solubility of **7** and **9** in various solvents and qualitative tests for electron-transfer in their solutions.

Solvents	**Polarity index (P')**	**7**	**9**
Water	9.0	×	×
Nitromethane	6.8	red - green	×
Methanol	6.6	red - green	×
Dimethyl sulfoxide	6.5	red	red
Dimethylformamide	6.4	red	red
Acetonitrile	6.2	red - green	×
Ethanol	5.2	red - green	×
Acetone	5.1	red - green	red - green
Butyronitrile	4.6	red - green	red - green
Ethyl acetate	4.3	red - green	×
Tetrahydrofuran	4.2	red - green	red - green
Chloroform	4.1	red - green	red
Dichloromethane	3.4	red - green	red - green
Diethyl Ether	2.9	red - green	×
Toluene	2.3	red - green	red - green
Hexane	0.0	×	×

× - insoluble at 298 K; ***red*** - color at all temperatures suggesting the absence of electron-transfer; ***red-green*** - colors at 290 and 77 K suggesting an electron-transfer process in solution.

The thermochromism observed in solutions of **7** and **9** was characterized by Vis/UV spectroscopy in three different solvents (methanol, butyronitrile and dichloromethane). The temperature-dependent Vis/UV spectra in butyronitrile are shown in Figure IV-21 (left) and those recorded in methanol and dichoromethane can be found in Figures S.IV-9 and S.IV-10. At high temperature, a broad absorption band is centered at 470 nm in addition to a small shoulder at approximately 560 nm (Figure IV-21, left). The intense absorption at 470 nm corresponds to a spin and Laporte-allowed ligand-to-metal charge-transfer (LMCT) transition, whereas the shoulder at 560 nm is attributed to a $Co^{II} \rightarrow Fe^{III}$ metal-to-metal charge-transfer (MMCT) transition.[15b,16b]

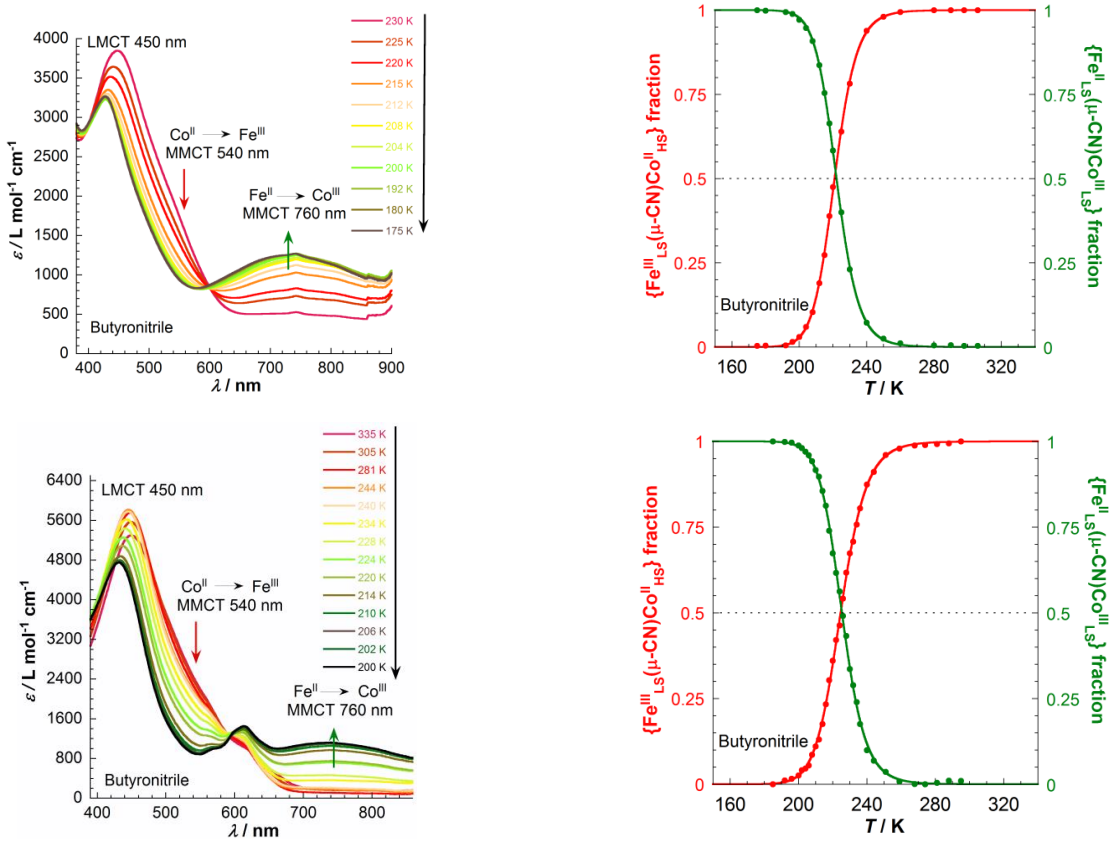

Figure IV-21. (left) UV-Vis spectra for **7** (top) and **9** (bottom) in butyronitrile on cooling mode from 298 to 170 K (at 0.2 to 0.3 K/min). (right) Temperature dependence of the $\{Fe^{III}_{LS}(\mu\text{-CN})Co^{II}_{HS}\}$ and $\{Fe^{II}_{LS}(\mu\text{-CN})Co^{III}_{LS}\}$ fractions estimated from the absorption intensities at the MMCT bands (≈ 540 nm and ≈ 760 nm) for **7** (top) and **9** (bottom) in butyronitrile, solid lines are fits to the ideal solution model.

As the temperature decreases the absorption band at 560 nm decreases progressively in intensity, while a new absorption band, characteristic of the a $Fe^{II} \rightarrow Co^{III}$ MMCT, where in the same time a band appears around 770 nm (Figure IV-21, left). Therefore, the spectroscopic data unambiguously demonstrate that the thermal conversion of $\{Fe^{III}_{LS}(\mu\text{-CN})Co^{II}_{HS}\}$ into $\{Fe^{II}_{LS}(\mu\text{-CN})Co^{III}_{LS}\}$ pairs occurs in solution. Furthermore, the isosbestic point at 600 nm strongly suggests that only two species are involved in the interconversion process. The $\{Fe^{III}_{LS}(\mu\text{-CN})Co^{II}_{HS}\}$ and $\{Fe^{II}_{LS}(\mu\text{-CN})Co^{III}_{LS}\}$ fractions can be deduced from the thermal variation of the absorptions at 540 and 760 nm, respectively, and plotted as function of the temperature (Figure IV-21, right and Figures S.IV-9 and S.IV-10). As expected, two fractions, cross each other at 0.5 defining the $T_{1/2}$ temperature at which $\{Fe^{III}_{LS}(\mu\text{-CN})Co^{II}_{HS}\}$ and $\{Fe^{II}_{LS}(\mu\text{-CN})Co^{III}_{LS}\}$ species are equally present. Since only two species are in equilibrium, we can fits these plots using the binary ideal solution model[29] described in Chapter I:

$$X = X_{LT} + \frac{X_{HT}+X_{LT}}{1+\exp\left(\frac{\Delta H}{R}\left(\frac{1}{T}+\frac{1}{T_{1/2}}\right)\right)} \qquad \textbf{(eq.3)}$$

for the two redox pairs, X is the {Fe(μ-CN)Co} fraction; X_{LT} and X_{HT} are low-temperature {Fe(μ-CN)Co} and high-temperature {Fe(μ-CN)Co} fractions, respectively; R is the ideal gas constant (8.314 $J \cdot K^{-1} \cdot mol^{-1}$) and ΔH is the enthalpy change. The calculated ΔH, $T_{1/2}$, and ΔS extracted for the fits are summarized in Table IV-8.

Table IV-8. Thermodynamic parameters obtained from the ideal solution model[20] fit of the UV-Vis data for **7** and **9** in different solvents.

	7			**9**		
	ΔH, kJmol^{-1}	$T_{1/2}$, K	ΔS, J·K^{-1}·mol^{-1}	ΔH, kJ·mol^{-1}	$T_{1/2}$, K	ΔS, J·K^{-1}·mol^{-1}
Methanol	58.7	267.8	219.1	-	-	-
Butyronitrile	61.8	221.0	279.9	55.4	224.7	246.6
Dichloromethane	63.0	207.8	302.3	58.3	208.3	280.6

For both compounds thermodynamic parameters are in the same ranges indicating that two distinct substituents (dodexyloxyl *vs.* 4-(decyloxy)-1,1'-biphenyl) have almost the same electronic effects on the Co-coordination sphere and thus only a minor influence of the redox process in solution. More interestingly, the $T_{1/2}$ is strongly solvent-dependent and is shifter to higher temperature with increasing polarity index, as shown previously with other square analogues (Figure IV-22).[15b,19] In the same respective solvents, the $T_{1/2}$ values were found slightly higher than those found for the analogue with methoxy substituents and significantly higher compared to the analogue with methyl substituents.[15b,19] This results can be explained by the higher electrodonating of the alkyoxy substituents which stabilize the diamagnetic species at higher temperature.

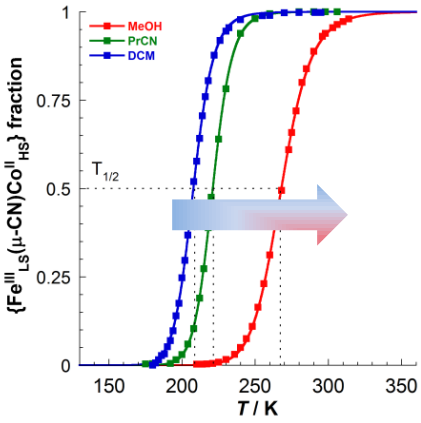

Figure IV-22. Temperature dependence of the $\{Fe^{III}_{LS}(\mu\text{-}CN)Co^{II}_{HS}\}$ fraction estimated from the absorption intensities at the MMCT band (≈ 540 nm) for **7** in dichloromethane $T_{1/2}$ = 207.8 K, butyronitrile $T_{1/2}$ = 221.0 K and methanol $T_{1/2}$ = 267.8 K. Solid lines are the fits to the ideal solution model.

IV.4. Conclusions and Perspectives

During this work, we were interested in the functionalization of magnetic complexes $\{Fe^{III}M^{II}\}_2$ (M = Co, Ni) molecular squares in order to promote liquid crystalline properties in these materials or improve their solubility in usual organic solvents. In the first part of the work, our strategy consisted to attach multiple lipophilic substituents onto the bipyridine platform or to graft smectogen units (biphenyl and cyanobiphenyl) through an aliphatic spacer. These second approach was found successful to obtain the desired liquid-crystal properties, since all the complexes exhibited such features. The $\{Ni_2Fe_2\}$ complexes 5 and 6 form bilayer lamellar mesophase in a large range of temperature as found before in one Mn_{12} complex described in Chapter II. Upon functionalization with mesogenic substituents, the magnetic behaviour of $\{Fe^{III}Ni^{II}\}$ squares seems slightly affected as shown by our initial magnetic investigations on complex **5**. Nonetheless, the study revealed the preservation of SMM behavior and the magnetic parameters were in the same ranges

to those obtained for the model complexes **1** and **2**. The *ac* magnetic susceptibilities of these three compounds revealed ferromagnetic coupling within the complex, giving a ground state $S = 3$. The complexes showed temperature dependence of *ac* susceptibility when a static *dc* field of 1000-1500 Oe is applied and effective barriers Δ_{eff}/k_B ranging from 12 to 23 K were deduced. Unfortunately, such functionalization was found inappropriate to promote ET features in the $\{Fe_2Co_2\}$ molecular squares and the complexes remains paramagnetic (red) in both solid-state and in solution. Thus, in the second part of this work, we attempt a new design strategy involving the grafting of mesogenic substituents onto the bipyridine ligand through an ether coupling. Four new tetranuclear new cyanido-bridged complexes, **7-10**, have been synthesized and their properties in solid state and in solutions have been described by structural, spectroscopic and magnetic methods. No evidence of reversible thermally-induced ET in solid-state could be deduced in these materials. In one case, complex **7**, an irreversible and incomplete ET was found probably induced by the loss of solvent.

Optical studies performed in solutions revealed that complexes undergo thermally-induced intramolecular ET. It was found that the ET characteristic temperatures $T_{1/2}$ are strongly dependent of the nature of the solvent, confirming the results obtained in the team for other $\{Fe_2Co_2\}$ analogues.[15b,19]

Even though no mesomorphic feature was deduced, the second approach seems more appropriate for $\{Fe_2Co_2\}$ squares since ET process was at least found in solution. These promising results should encourage us to tune the packing through the change of the solvation or counter anions in order to eventually promote ET in both solid and solution phase. We should also continue on the derivatization of this type of ligands by applying the same strategy as before (ie. grafting of additional greasy substituents and calamitic smectogens units) to promote mesomorphic features on the resulting materials.

IV.5. Supporting materials

IV.5.1. Experimental protocols

IV.5.1.1. Synthesis of the organic precursors and ligands

Solvents and starting materials were purchased from Acros, Alfa Aesar or Aldrich, and used without further purification unless otherwise stated. The non-commercial benzoic acid derivatives were prepared according to procedures described in Chapter II.

Preparation of 4,4'-dimethoxycarbonyl-2,2'-bipyridine A. To a suspension of 2,2'-bipyridine-4,4'-dicarboxylic acid (2,2 g, 8.1 mmol) in 200 ml methanol was added 4 ml of 87 wt% sulfuric acid and the mixture was refluxed for 24 h. Then clear solution was cooled to room temperature. Water (200 ml) was added and the excess of methanol removed under vacuum. The pH was adjusted to neutral with NaOH solution (2M) and the resulting precipitate was filtered, washed with water and dried under vacuum. The precursor **A** was isolated as a white powder: Yield 2.61 g (98 %). ^{1}H NMR (400 MHz) in $CDCl_3$ (δ, ppm): 8.95 (dd, *J* = 3.0 Hz, 2H), 8.66 (d, *J* = 5.0 Hz, 2H), 7.90 (dt, *J* = 5.1 Hz, 2H), 3.97 (s, 6H).

Preparation of 2,2'-bipyridine-4,4'-diyldimethanol B. Sodium borohydride (7.23 g, 19.2 mmol) was slowly added to a suspension of **A** (2.61 g, 9.6 mmol) in 180 ml of ethanol absolute. The mixture was refluxed for 3 hours and cooled to room temperature. Then, the excess of borohydride was quenched with 180 ml of saturated ammonium chloride solution. The ethanol was removed under vacuum and the precipitate was dissolved in a minimal amount of water. The resulting solution was extracted with ethyl acetate (5 x 180 ml), dried over anhydrous sodium sulfate, filtered and the solvent was removed under vacuum. The compound **B** was obtained as a white powder: Yield 1.26 g (75 %). ^{1}H NMR (400 MHz) in $CDCl_3$ (δ, ppm): 8.65 (d, *J* = 4.9 Hz, 2H), 8.36 (m, 2H), 7.36 (d, *J* = 4.8 Hz, 2H), 4.83 (q, *J* = 7.2 Hz, 4H). Elemental analysis – Calc. (Found) for $C_{12}H_{12}N_2O_2$: C, 66.65 (65.98), H, 5.59 (5.80), N, 12.96 (12.90).

Preparation of 4,4'-bis(bromomethyl)-2,2'-bipyridine C. The functionalized bipyridine ***B*** (1.26 g, 5.88 mmol) was dispersed in a mixture of 48 % HBr (25 ml) and concentrated sulfuric acid (9 ml) was add. The resulting solution was refluxed for 6 hours and then allowed to cool to room temperature. The reaction mixture is diluted with 50 ml of water and the pH was adjusted to pH = 7 with $NaHCO_3$. The product was extracted with chloroform (3 x 50 ml), dried over anhydrous sodium sulfate, filtered and evaporated to dryness. The compound **C** was isolated as a white powder: Yield 1.23 g (62 %). ^{1}H NMR (400 MHz) in $CDCl_3$ (δ, ppm): 8.66 (t, *J* = 7.2 Hz, 2H), 8.42 (d, *J* = 9.9 Hz, 2H), 7.36 (dd, *J* = 4.9 Hz, 2H), 4.47 (d, *J* = 11.2 Hz, 4H). Elemental analysis – Calc. (Found) for $C_{12}H_{10}Br_2N_2$: C, 42.14 (41.96); H, 2.95 (3.06); N, 8.19 (8.18). Selected FT-IR data (ATR, cm^{-1}): 3019 (m), 2968 (m), 1592 (s), 1554 (s), 1456 (s), 1373 (s), 1210 (s), 1119 (m), 990 (m), 903 (m), 851 (s), 832 (s), 742 (m), 637 (vs), 559 (vs).

Preparation of $L^{1\text{-}6}$ ligands. All the ligands were prepared in the same fashion and the general procedure is described for L^1. To a solution of **C** (0.349 g, 1.02 mmol) and 4-methylbenzoic acid (0.23 g,

1.68 mmol) in 20 ml of THF was added tetrabutylammonium fluoride (TBAF) (1 M in THF, 2.5 ml, 2.5 mmol). The mixture was stirred 24 hours at room temperature under Argon. The solvent was removed, and the sticky residue was dispersed in diethyl ether (80 ml) with vigorous stirring. After 3 hours, the white precipitate was collected by filtration, washed with water, cold methanol and dried under vacuum, leaving **L[1]** as a white powder: Yield 430 mg (95 %). Selected FT-IR data (ATR, cm^{-1}): 3065 (m), 3036 (m), 2951 (m), 2923 (m), 2857 (m), 1715 (vs), 1604 (s), 1437 (s), 1347 (s), 1277 (vs), 1180 (s), 1118 (s), 1021 (m), 847 (m), 812 (s), 701 (s), 590 (m). ^{1}H NMR (400 MHz) in $CDCl_3$ (δ, ppm): 8.68 (d, *J* = 10.8 Hz, 2H), 8.45 (d, *J* = 10.7 Hz, 2H), 8.00 (t, *J* = 8.9 Hz, 4H), 7.38 (d, *J* = 4.9 Hz, 2H), 5.44 (s, 4H), 2.41 (s, 6H). Elemental Analysis – Calc. (Found) for $C_{28}H_{24}N_2O_4$: C, 74.32 (73.91); H, 5.35 (5.68); N, 6.19 (6.18).

L[2]: Yield 76 %. Selected FT-IR data (ATR, cm^{-1}): 3065 (m), 3035 (m), 2952 (m), 2927 (m), 2854 (m), 1721 (vs), 1598 (s), 1455 (s), 1347 (m), 1269 (vs), 1178 (s), 1116 (s), 1020 (m), 847 (m), 812 (vs), 699 (s), 592 (m). ^{1}H NMR (400 MHz) in $CDCl_3$ (δ, ppm) for 8.67 (d, *J* = 5.0 Hz, 2H), 8.46 (s, 2H), 8.00 (d, *J* = 8.2 Hz, 4H), 7.39 (d, *J* = 5.0 Hz, 2H), 5.44 (s, 4H), 2.66 (m, 4H), 1.58 (t, *J* = 7.5 Hz, 6H), 1.37 (m, *J* = 7.4 Hz, 4H), 0.93 (t, *J* = 8.4 Hz, 6H). Elemental Analysis – Calc. (Found) for $C_{34}H_{36}N_2O_4$: C, 76.09 (76.07); H, 6.76 (7.05); N, 5.22 (5.21).

L[3]: Yield 71 %. Selected FT-IR data (ATR, cm^{-1}): 2915 (vs), 2848 (s), 1713 (s), 1599 (m), 1587 (m), 1501 (m), 1429 (s), 1358 (m), 1332 (s), 1215 (vs), 1118 (vs), 1036 (m), 841 (s), 812 (s), 760 (s), 719 (m). ^{1}H NMR (400 MHz) in $CDCl_3$ (δ, ppm) for 8.70 (d, *J* = 5.1 Hz, 2H), 8.49 (s, 2H), 7.42 (d, *J* = 4.6 Hz, 2H), 7.21 (d, *J* = 2.3 Hz, 4H), 6.65 (t, *J* = 2.3 Hz, 2H), 5.45 (s, 4H), 3.95 (t, *J* = 6.3 Hz, 8H), 1.76 (m, 8H), 1.43 (m, 8H), 1.31-1.19 (m, 64H), 0.87-0.83 (t, *J* = 6.9 Hz, 12H). Elemental Analysis – Calc. (Found) for $C_{74}H_{116}N_2O_8$: C, 76.51 (76.40); H, 10.06 (10.27); N, 2.41 (2.64).

L[4]: Yield 68 %. Selected FT-IR data (ATR, cm^{-1}): 2916 (vs), 2848 (s), 1713 (vs), 1600 (s), 1587 (m), 1501 (m), 1429 (s), 1388 (m), 1358 (m), 1332 (s), 1214 (vs), 1118 (vs), 811 (m), 759 (m), 719 (m). ^{1}H NMR (400 MHz) in $CDCl_3$ (δ, ppm): 8.65 (d, *J* = 5.1 Hz, 2H), 8.48 (s, 2H), 7.35 (d, *J* = 3.8 Hz, 2H), 7.31 (d, *J* = 1.9 Hz, 4H), 5.42 (s, 4H), 3.99 (d, *J* = 6.5 Hz, 4H), 1.77 (m, 12H), 1.59 (s, 8H), 1.43 (s, 8H), 1.23 (d, 96H), 0.86 (d, *J* = 7.5 Hz, 18H). Elemental Analysis – Calc. (Found) for $C_{98}H_{164}N_2O_{10}$: C, 76.91 (76.45); H, 10.80 (10.95); N, 1.82 (1.98).

L[5]: Yield 55%. Selected FT-IR data (ATR, cm^{-1}): 3032 (w), 2929(s), 2851 (s), 1719 (s), 1598 (s), 1521 (s), 1488 (s), 1466 (s), 1449 (s), 1250 (s), 1163 (s), 1028 (s), 831 (s), 759 (s), 691 (m). ^{1}H NMR (400 MHz) in $CDCl_3$ (δ, ppm): 8.689 (d, 2H), 8.472 (t, 2H), 7.553 (dd, 8H), 7.516 (dd, 8H), 7.413 (dd, 8H), 7.38 (d, 2H), 7.299 (t, 4H), 7.24 (d, 4H), 6.966 (d, 8H), 6.677 (t, 2H), 5.445 (s, 4H), 3.992 (m, 16H), 1.805 (m, 16H), 1.415 (m, 48H).

L[6]: Yield 90 %. Selected FT-IR data (ATR, cm^{-1}): 3035 (w), 2922(s), 2851 (s), 2225 (s, ν_{CN}), 1717 (s), 1600 (s), 1521 (s), 1494 (s), 1465 (s), 1444 (s), 1249 (s), 1165 (s), 1054 (s), 819 (s), 761 (s), 675 (m). ^{1}H NMR (400 MHz) in $CDCl_3$ (δ, ppm): 8.69 (d, 2H), 8.482 (t, 2H), 7.658 (dd, 16H,), 7.526 (d, 8H), 7.396 (d, 2H), 7.22 (d, 4H), 6.98 (d, 8H), 6.671 (t, 2H), 5.448 (s, 4H), 3.991 (t, 16H), 1.805 (m, 16H), 1.407 (m, 48H).

Preparation of 4,4'-diol-2,2'-bipyridine E. To a solution of 4,4'-dimethoxy-2,2'-bipyridine (0.288 g, 1.3 mmol) in acetic acid (12 mL) was added hydrobromic acid (48 wt%, 12 ml) and mixture was refluxed

overnight. After cooling to room temperature, the solution was diluted with water (100 mL) and neutralized with aqueous solution of NH_4OH. This resulting white powder was filtered, washed with water (2 x 20 mL) and ethanol (2 x 20 mL) and dried under vacuum: Yield 2.06 g (78 %). ^{1}H NMR (400 MHz) in CD_3OD (δ, ppm): 8.58 (d, *J* = 5.0 Hz, 2H), 8.25 (s, 2H), 7.41 (d, *J* = 5.0 Hz, 2H). Selected FT-IR data (ATR, cm^{-1}): 2535 (m), 1583 (vs), 1557 (vs), 1457 (vs), 1434 (s), 1389 (s), 1389 (s), 1289 (vs), 1029 (vs), 984 (s), 896 (vs), 813 (vs), 660 (m), 582 (s), 573 (s).

Preparation of 4,4'-bis(dodecyloxy)-2,2'-bipyridine (L^7). To a solution of **E** (0.25 g, 1.33 mmol) in 25 mL of dimethylformamide, anhydrous potassium carbonate (0.979 g, 6.65 mmol) was added. The mixture was heated to reflux and 1-bromododecane (0.73 g, 2.92 mmol) and a catalytic amount of potassium iodide were added. The reaction mixture was then refluxed for 24 hours. The solvent was removed and CH_2Cl_2 (50 mL) was added. The suspension was washed with water (3x50 mL). The organic layer was dried over anhydrous sodium sulfate, filtrated and concentrated. The obtained white vitreous solid was filtrated, washed with diethyl ether and dried under vacuum: Yield 340 mg (48 %). Elemental analysis – Calc. (Found) for $C_{34}H_{56}N_2O_2$: C, 77.81 (78.02); H, 10.76 (11.54); N, 5.34 (5.49). ^{1}H NMR (400 MHz) in $CDCl_3$ (δ, ppm): 8.45 (d, *J* = 5.7 Hz, 2H), 7.99 (d, *J* = 2.5 Hz, 2H), 6.84 (dd, *J* = 5.7 Hz, 2H), 4.14 (t, *J* = 6.5 Hz, 4H), 3.89 (m, 4H), 1.38 – 1.14 (m, 36H), 0.45 (t, *J* = 6.8 Hz, 6H). Selected FT-IR data (ATR, cm^{-1}): 2916 (vs), 2848 (vs), 1579 (vs), 1579 (vs), 1562 (s), 1393 (s), 1378 (s), 1296 (vs), 1243 (vs), 1021 (vs), 865 (m), 840 (vs), 717 (m), 578 (m).

Preparation of 4,4'-bis((10-([1,1'-biphenyl]-4-yloxy)decyl)oxy)-2,2'-bipyridine (L^8). To a solution of **E** (0.5 g, 2.66 mmol) in 25 mL of dimethylformamide, anhydrous potassium carbonate (0.979 g, 6.65 mmol), 4-((10-bromodecyl)oxy)-1,1'-biphenyl (2.28 g, 5.9 mmol) and a catalytic amount of potassium iodide were added. The reaction mixture was then refluxed for 24 hours. After evaporation of the solvent, the residue was dispersed in 150 mL of water and the product extracted with CH_2Cl_2 (3 x 30 mL). The organic layer was dried over anhydrous sodium sulfate, filtrated and the solvent removed under vacuum. The white vitreous solid was filtrated, washed with diethyl ether and dried under vacuum leaving $\mathbf{L^8}$ as a white solid: Yield 340 mg (56 %). Elemental analysis – Calc. (Found) for $C_{54}H_{64}N_2O_4$: C, 80.56 (80.05); H, 8.01 (8.34); N, 3.48 (2.95). ^{1}H NMR (400 MHz) in $CDCl_3$ (δ, ppm): 8.42 (m, 2H), 7.99 (s, 2H), 7.93 (t, *J* = 5.1 Hz, 2H), 7.50 (m, 8H) 7.40 (t, *J* = 7.6 Hz, 4H), 6.96 (m, 4H), 3.96 (t, *J* = 6.6 Hz, 4H), 1.81 (m, 6H), 1.46 (m, 8H), 1.33 (s, 16H). Selected FT-IR data (ATR, cm^{-1}): 2919 (vs), 2851(vs), 1581 (vs), 1562 (vs), 1394 (s), 1378 (m), 1297 (s), 1243 (vs), 1043 (s), 1003 (vs), 853 (s), 833 (s), 763 (s), 717 (m).

IV.5.1.2. Synthesis of metal ion precursors and complexes

Preparation of $M(OTf)_2{\cdot}6H_2O$ ($M = Co^{2+}, Ni^{2+}$). To a 10 mL of trifluoromethanesulfonic acid (0.5 g, 3.2 mmol) solution in water (30ml) were added slowly MCO_3 (0.2 g, 1.6 mmol). The mixture was stirred until CO_2 gas stopped to form. Then the solution was filtered and concentrated under reduced pressure. $Co(OTf)_2$ was precipitated as a pink solid and $Ni(OTf)_2$ as a green solid. The compounds were dried in vacuum at 110 °C. The yield were 2.3 g (82 %) for $Co(OTf)_2$ and 2.84 g (85 %) $Ni(OTf)_2$. Elemental analysis

– Calc. (Found) for $C_2H_{12}CoF_6O_{12}S_2$ ($Co(CF_3SO_3)_2\cdot 6H_2O$): C, 5.16 (5.87), H, 2.60 (2.74). Selected FT-IR data (ATR, cm^{-1}): 1648 (m), 1614 (m), 1230 (vs), 1188 (vs), 1033 (vs), 719 (m), 633 (s), 580 (s). Elemental analysis – Calc. (Found) for $C_2H_{12}NiF_6O_{12}S_2$ ($Ni(CF_3SO_3)_2\cdot 6H_2O$): C, 5.17 (5.86); H, 2.60 (2.74). Selected FT-IR data (ATR, cm^{-1}): 1634 (s), 1219 (vs), 1190 (vs), 1030 (vs), 693 (m), 625 (vs).

Preparation of $(NEt_4)[(Tp^*)Fe(CN)_3]$. KTp* (0.5 g, 1.48 mmol) dissolved in 2.5 mL of methanol was dropwise added to $Fe(acac)_3$ (0.5 g, 1.41 mmol) solution in 2.5 mL of methanol affording a dark brown mixture that was stirred for 2 hours. A reddish precipitate was isolated by filtration and dried. Afterwards it was re-dissolved in 5 mL of acetonitrile and treated with 0.6 g of $(NEt_4)CN$ (3.8 mmol) in 5 mL of acetonitrile. The mixture was stirred for 2 hours at 50°C. The excess of $(NEt_4)CN$ was removed by column chromatography (silica gel, CH_3CN). The compound was purified by recrystallization from methanol solution layered with diethyl ether. The yield was 0.23 g (55 %). Elemental analysis – Calc. (Found) for $1\cdot 2H_2O$, $C_{26}H_{46}BFeN_{10}O_2$: C, 52.28 (52.70); H, 7.76 (7.58); N, 23.45 (24.25). Selected FT-IR data (ATR, cm^{-1}): 2982 (m), 2934 (m), 2549 (m, ν_{BH}), 2115 (s, ν_{CN}), 1541 (vs), 1446 (vs), 1414 (vs), 1370 (vs), 1200 (vs), 1059 (vs), 1028 (m), 814 (vs), 773 (vs), 691 (s), 643 (vs).

Preparation of $\{[(Tp^*)Fe(CN)_3]_2[Ni(L^1)_2]_2\}[OTf]_2$ (1). $[NEt_4][(Tp^*)Fe(CN)_3]\cdot 2H_2O$ (17 mg, 0.03 mmol) was treated with $Ni(OTf)_2$ (18 mg, 0.04 mmol) in 3 ml of DMF to afford a red solution that was allowed to stir for 2 hours. Subsequently, $\mathbf{L^1}$ (30 mg, 0.06 mmol) in 2 ml of DCM was added and the mixture was stirred for 2 days at room temperature and then filtered. Red solution were evaporated affording a brownish-orange powder. Brownish-orange crystals of $\mathbf{1}\cdot H_2O\cdot 2CH_3CN$ were obtained by slow diffusion of diethyl ether into a solution of **1** in CH_3CN (3 mL): Yield 52 %. Elemental analysis – Calc. (Found) for $C_{154}H_{148}B_2Ni_2F_6Fe_2N_{28}O_{23}S_2$: C, 58.06 (58.50); H, 4.68 (4.69); N, 12.30 (11.71). Selected FT-IR data (ATR, cm^{-1}): 2926 (m), 2845 (m), 2533 (m, ν_{BH}), 2164 (s, ν_{CN}), 2117 (m, ν_{CN}), 1716 (vs), 1672 (s), 1611 (s), 1543 (s), 1446 (s), 1414 (s), 1371 (s), 1264 (vs), 1178 (s), 1147 (s), 1102 (s), 1062 (s), 1030 (s), 837 (s), 752 (vs).

Preparation of $\{[(Tp^*)Fe(CN)_3]_2[Ni(L^2)_2]_2\}[OTf]_2$.(2). $[NEt_4][(Tp^*)Fe(CN)_3]\cdot 2H_2O$ (17 mg, 0.03 mmol) was treated with $Ni(OTf)_2$ (18 mg, 0.04 mmol) in 3 ml of DMF to afford a red solution that was allowed to stir for 2 hours. Subsequently $\mathbf{L^2}$ (48 mg, 0.06 mmol) in 2 ml of DCM was added and the mixture was stirred for 2 days at room temperature and then filtered. Slow diffusion of diethyl ether vapor into the mother liquor at 5 °C afford brownish-orange crystal of $\mathbf{2}\cdot H_2O\cdot 2DMF$ after few days: Yield 68 %. Elemental analysis – Calc. (Found) for $C_{186}H_{220}B_2Ni_2F_6Fe_2N_{30}O_{28}S_2$: C, 59.94 (60.61); H, 5.76 (5.81); N, 10.87 (10.10). Selected FT-IR data (ATR, cm^{-1}): 2917 (s), 2926 (m), 2847 (m), 2533 (m, ν_{BH}), 2152 (s, ν_{CN}), 2119 (m, ν_{CN}), 1716 (s), 1672 (s), 1607 (s), 1611 (s), 1543 (s), 1446 (s), 1414 (s), 1371(s), 1264 (vs), 1178 (s), 1102 (s), 1030 (s), 837 (s), 752 (s), 691 (s).

Preparation of $[\{(Tp^*)Fe(CN)_3\}_2\{Ni(L^{3\text{-}6})_2\}_2][OTf]_2$ complexes. All the complexes were prepared in the same fashion and products were obtained as glassy solid with 56 to 85 % yields. The general procedure is given for $[\{(Tp^*)Fe(CN)_3\}_2\{Ni(\mathbf{L^5})_2\}_2][OTf]_2$. In a vial, a solution of $[PPh_4][(Tp^*)Fe(CN)_3]$ (23 mg, $2.9\cdot 10^{-5}$ mol) is dissolved in 5 mL MeCN, and $Ni(OTf)_2\cdot 6H_2O$ (13.5 mg, $2.9\cdot 10^{-5}$ mol) is added. The solution is

stirred for 10 minutes at RT and then a solution of **L**^{5} (100 mg, $5.8\cdot10^{-5}$ mol) in 20 mL of DCM is to the vial. The reaction mixture is stirred at room temperature for 24 hours. The clear solution is concentrated to about 3 mL during which a sticky solid precipitate. The product is removed and the remaining solid is washed several times with MeCN and MeOH. The brownish-orange residue is purified by size extrusion column chromatography (Bio-Beads S-X3 beads) using CH_2Cl_2 as eluent.

[{(Tp*)Fe(CN)$_3$}$_2${Ni(L^3)}$_2$][OTf]$_2$ (3): Yield 56 %. Selected FT-IR data (ATR, cm^{-1}): 2921 (s), 2851 (s), 2533 (w), 2161 (m), 1723 (s), 1593 (s), 1444 (s), 1220 (s), 1159 (s), 1030 (s), 841 (m), 761 (s), 636 (s)

[{(Tp*)Fe(CN)$_3$}$_2${Ni(L^4)}$_2$][OTf]$_2$ (4): Yield 82 % Elemental analysis – Calc. (Found) for $C_{430}H_{700}B_2Ni_2F_6Fe_2N_{26}O_{46}S_2$: C, 69.80 (69.04); H, 9.54 (9.63); N, 4.92 (4.72). Selected FT-IR data (ATR, cm^{-1}): 2920 (s), 2851 (s), 2530 (w, ν_{BH}), 2159 (m, ν_{CN}), 1718 (s), 1583 (s), 1429 (s), 1332 (s), 1202 (s), 1111 (s), 1029 (s), 760 (s), 637 (s)

[{(Tp*)Fe(CN)$_3$}$_2${Ni(L^5)}$_2$][OTf]$_2$ (5): Yield 75 % Elemental analysis – Calc. (Found) for $C_{494}H_{572}B_2Ni_2F_6Fe_2N_{26}O_{54}S_2$: C, 72.65 (71.92); H, 7.06 (7.09); N, 4.46 (4.42). Selected FT-IR data (ATR, cm^{-1}): 2917 (s), 2849 (s), 2536 (m, ν_{BH}), 2162 (m, ν_{CN}), 2120 (b, ν_{CN}), 1722 (s), 1607 (s), 1487 (s), 1471 (s), 1447 (s), 1222 (s), 1159 (vs), 1029(s), 1029 (vs), 831 (vs), 761 (vs), 695 (s), 636 (s).

[{(Tp*)Fe(CN)$_3$}$_2${Ni(L^6)}$_2$][OTf]$_2$ (6): Yield 85 %. Selected FT-IR data (ATR, cm^{-1}): 3029 (w), 2917 (s), 2849 (s), 2542 (w, ν_{BH}), 2225 (s, ν_{CN}), 2155 (m, ν_{CN}), 1722 (s), 1601 (s), 1523 (m), 1493 (s), 1465 (s), 1446 (s), 1248 (s), 1161 (s), 1029 (s), 820 (s), 763 (m), 636(s).

Preparation of {[(Tp*)Fe(CN)$_3$]$_2$[Co(L^7)$_2$]$_2$}[OTf]$_2$ (7). [NEt$_4$][(Tp*)Fe(CN)$_3$]·2H$_2$O (35 mg, 0.06 mmol) was treated with Co(OTf)$_2$ (36 mg, 0.08 mmol) in 3 ml of DMF to afford a red solution that was allowed to stir for 2 hours. Subsequently, **L**^{7} (63 mg, 0.12 mmol) in 3 ml of DCM was added, and the mixture was stirred for 2 days at room temperature and then filtered. The red solution obtained was evaporated, redissolved in 50 ml of MeOH and set for slow evaporation, after five days, resulting green needles are collected by filtration and washed with cold methanol (2 x 1 mL). Yield 30 %. Selected FT-IR data (ATR, cm^{-1}): 2921 (vs), 2852 (vs), 2506 (b, ν_{BH}), 2160 (b, ν_{CN}), 2106 (m, ν_{CN}), 2088 (s, ν_{CN}), 2051(s), 1611 (vs), 1559(m), 1599 (s), 1495 (s), 1452 (vs), 1334 (s), 1251 (vs), 1223 (s), 1155 (s), 1028 (vs), 861 (m). Elemental analysis – Calc. (Found) for **7**·6H$_2$O $C_{174}H_{280}B_2Co_2F_6Fe_2N_{26}O_{20}S_2$: C, 59.96 (60.75); H, 8.10 (8.03); N, 10.45 (9.97).

Preparation of {[(Tp*)Fe(CN)$_3$]$_2$[Co(L^8)$_2$]$_2$}[OTf]$_2$ (9). [NEt$_4$][(Tp*)Fe(CN)$_3$]·2H$_2$O (35 mg, 0.06 mmol) was treated with Co(OTf)$_2$ (36 mg, 0.08 mmol) in 3 ml of DMF to afford a red solution that was allowed to stir for 2 hours. Subsequently, **L**^{8} (96 mg, 0.12 mmol) in 3 ml of DCM was added and the mixture was stirred for 2 days at room temperature and then filtered. To the clear solution, diethyl ether (25 mL) was added, and the resulting green powder was collected by filtration and washed with methanol (3 x 5 mL): Yield 40 %. Selected FT-IR data (ATR, cm^{-1}): 2925 (s), 2853 (s), 2516 (b, ν_{BH}), 2154 (b, ν_{CN}), 2112 (m, ν_{CN}), 2093 (s, ν_{CN}), 2063 (s), 1668 (vs), 1609 (vs), 1558 (s), 1487 (s), 1450 (s), 1248 (s), 1251 (vs), 1223 (s), 1155 (s), 1028 (vs), 861 (m). Elemental analysis – Calc. (Found) for $C_{254}H_{300}B_2Co_2F_6Fe_2N_{26}O_{22}S_2$: C, 67.82 (66.10); H, 6.72 (6.49); N, 8.10 (7.80).

Preparation of $\{[(Tp^*)Fe(CN)_3]_2[Co(L^{7\text{-}8})_2]_2\}[PF_6]_2$. To a solution $Co(OTf)_2$ (36 mg, 0.08 mmol) in 2 ml of MeOH was added $\mathbf{L}^7$ (63 mg, 0.12 mmol) or $\mathbf{L}^8$ (96 mg, 0.12 mmol) in MeOH (7 ml) and the resulting pale yellow solution was stirred for 30 minutes at room temperature. Then, $[NEt_4][(Tp^*)Fe(CN)_3]\cdot 2H_2O$ (35 mg, 0.06 mmol) in CH_3OH (2 ml) and NBu_4PF_6 (46 mg, 0.12 mmol) were subsequently added and the reaction mixture was stirred for 2 days. The resulting red precipitate was collected by filtration and washed with cold methanol.

$\{[(Tp^*)Fe(CN)_3]_2[Co(L^7)_2]_2\}[PF_6]_2$ (8). Yield 45 %. Selected FT-IR data (ATR, cm^{-1}): 2922 (s), 2852 (s), 2521 (m, ν_{BH}), 2159 (s, ν_{CN}), 2125 (m, ν_{CN}), 1608 (s), 1562 (s), 1543 (s), 1494 (s), 1448 (s), 1324 (s), 1204 (vs), 1061 (s), 1027 (s), 831 (vs), 778 (s). Elemental analysis – Calc. (Found) for $C_{174}H_{268}B_2Co_2F_6Fe_2N_{26}O_8P_2$: C, 61.31 (60.34); H, 8.02 (7.78); N, 10.81 (11.11).

$\{[(Tp^*)Fe(CN)_3]_2[Co(L^8)_2]_2\}[PF_6]_2$ (10). Yield 40 %. Selected FT-IR data (ATR, cm^{-1}): 2921 (s), 2854 (s), 2521 (b, ν_{BH}), 2159 (s, ν_{CN}), 2119 (m, ν_{CN}), 1585 (s), 1545 (s), 1519 (s), 1450 (s), 1283 (s), 11242 (vs), 1191 (s), 1016 (s), 833 (s), 763 (vs), 696 (s), 600 (s). Elemental analysis – Calc. (Found) for $C_{252}H_{300}B_2Co_2F_6Fe_2N_{26}O_{16}P_2$: C, 67.40 (67.85); H, 6.73 (7.11); N, 8.11 (8.60).

IV.5.2. FTIR spectroscopic analyses

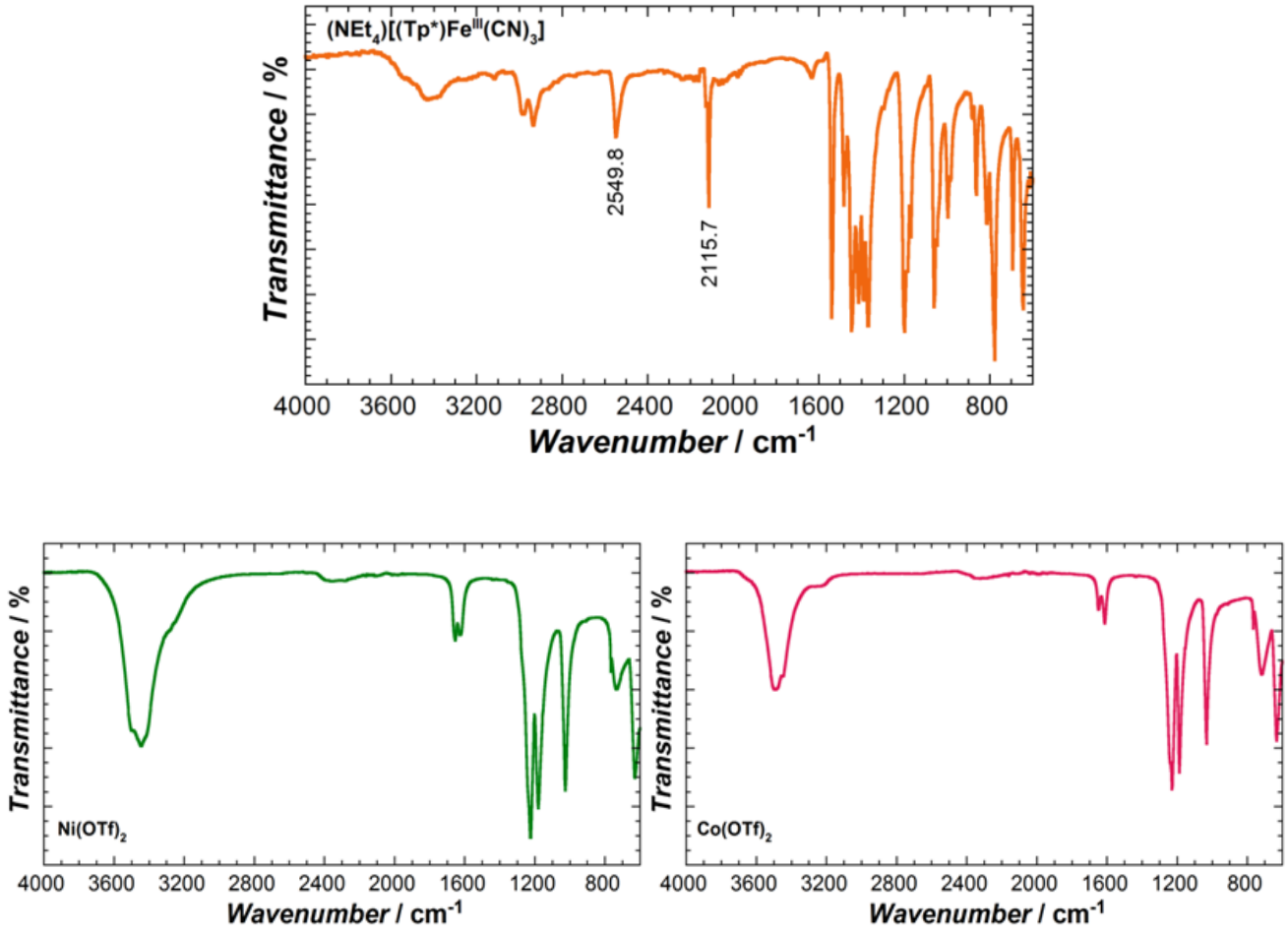

Figure S.IV-1. FTIR spectrum at room temperature for: (top) tricyanido-metallate precursor $(EtN_4)[(Tp^*)Fe(CN)_3]$, (bottom left) nickel trifluoromethanesulfonate and (bottom right) cobalt trifluoromethanesulfonate.

IV.5.3. Powder X-ray diffraction data

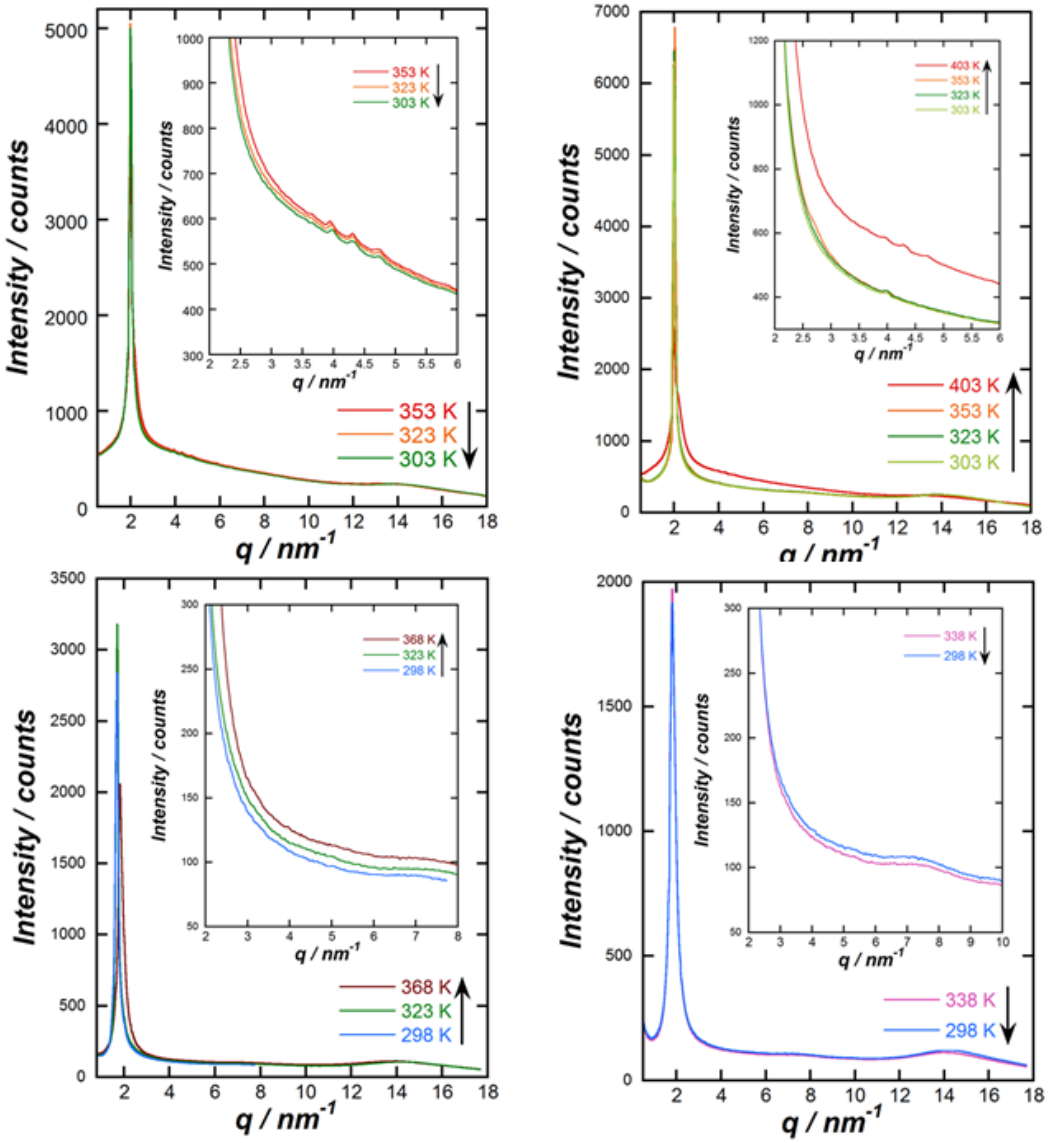

Figure S.IV-2. Small angle X-ray diffraction profiles (top) for **3** on 1st heating from 303 to 403 K (left) and on 1st cooling from 353 to 303 K (right); and bottom for **4** on 1st heating from 298 K to 368 K (left) and on 1st cooling from 338 to 298 K (right).

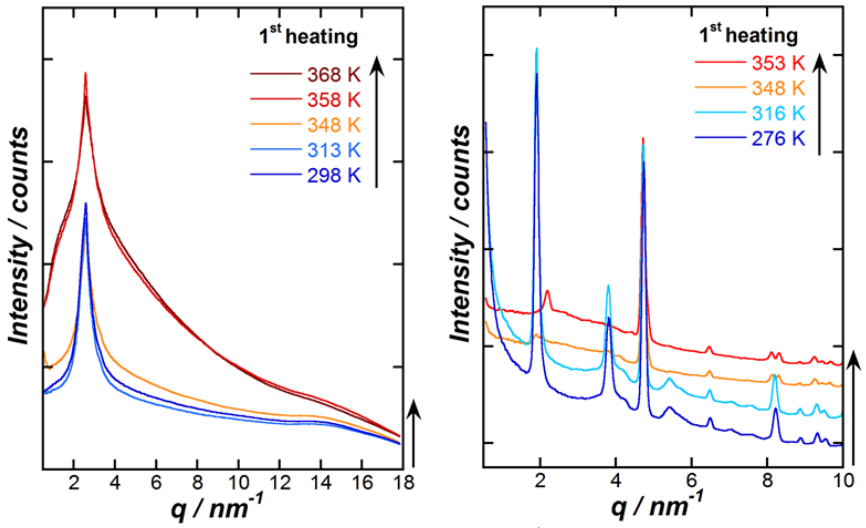

Figure S.IV-3. Small angle X-ray diffraction profiles (left) for **7** on 1st heating from 298 to 368 K and (right) for **9** on 1st heating from 276 K to 353 K.

IV.5.4. Magnetic measurements

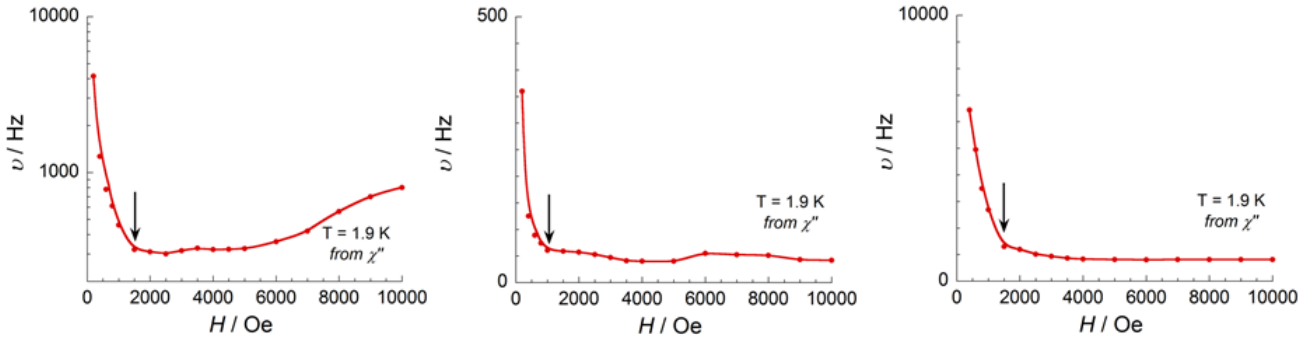

Figure S.IV-4. Field dependence of the characteristic frequency of the relaxation mode at 1.9 K for 1, 2 and 5 deduced from Figure IV-11.

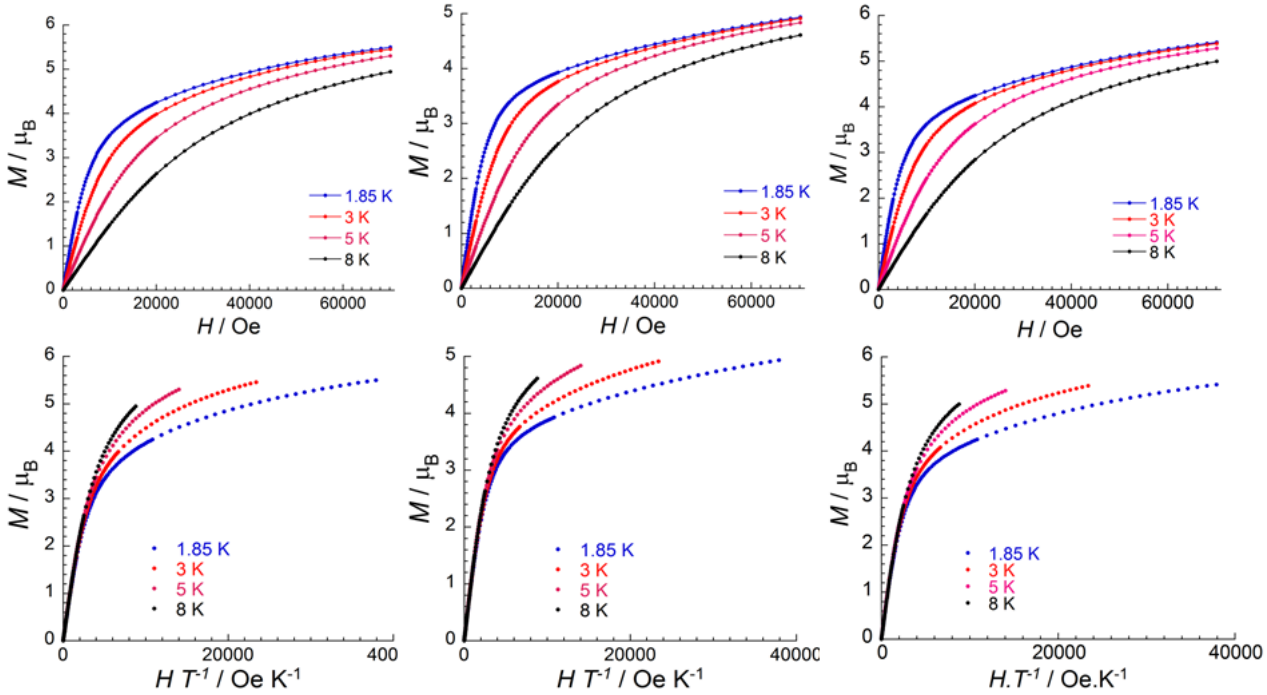

Figure S.IV-5. *M* vs *H* (top) and *M* vs *H/T* (bottom) data for: (left) **1,** (center) **2** and (right) **5** between 1.8 and 8 K with sweep-rates of 100-200 Oe/min.

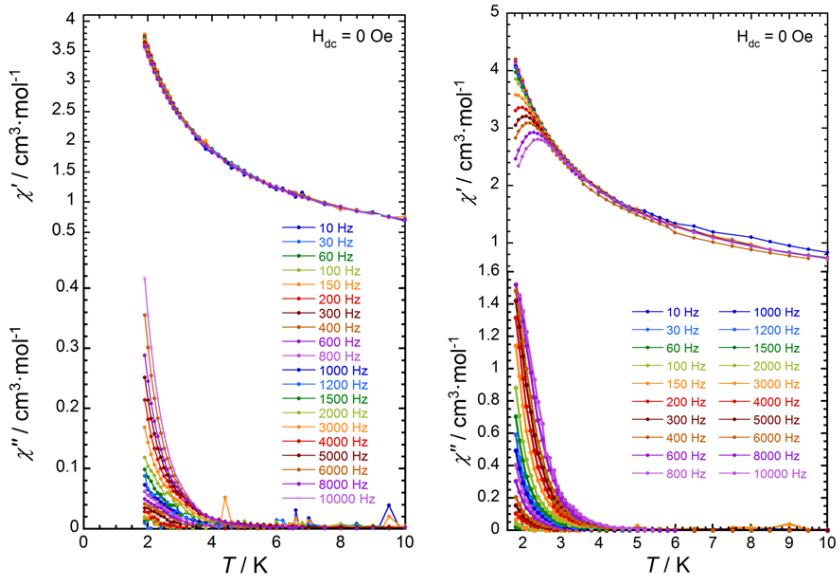

Figure S.IV-6. Plots of the in-phase (top), χ', and out-of-phase (bottom), χ'', components of the *ac* magnetic susceptibility versus temperature, *T*, under no external magnetic field at different frequencies between 10 and 10000 Hz of the compounds: (left) **1** and (right) **2**.

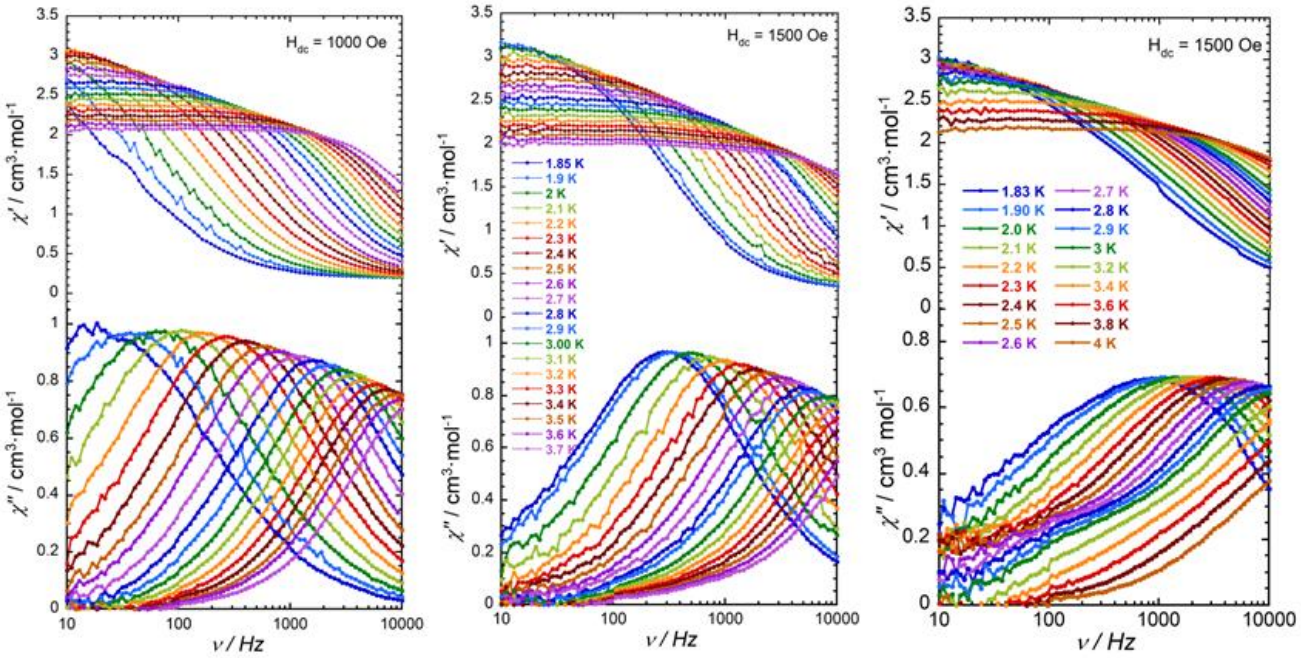

Figure S.IV-7. Plots of the in-phase (top), χ', and out-of-phase (bottom), χ'', components of the *ac* magnetic susceptibility versus frequency, ν, under an external magnetic field at different at the indicated temperatures: (left) **1** at 1500 Oe, (center) **2** at 1000 Oe and (right) **3** at 1500 Oe.

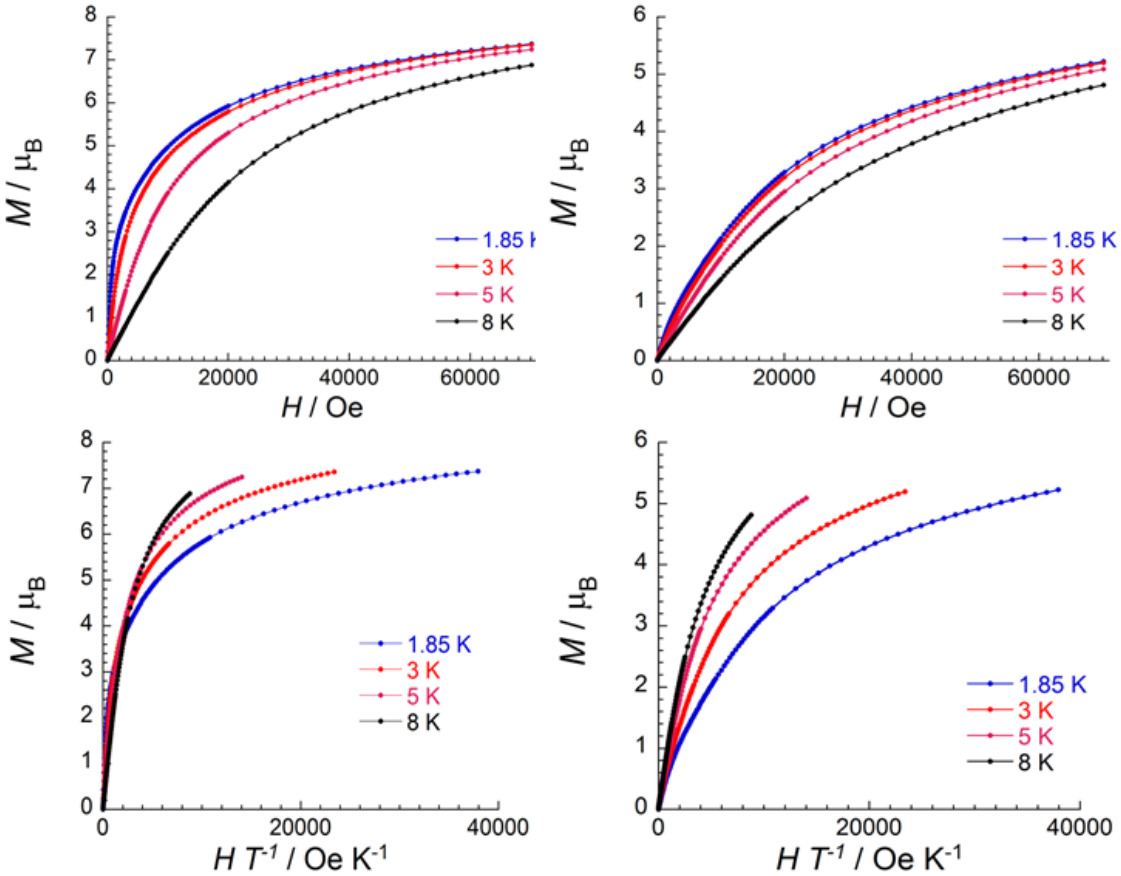

Figure S.IV-8. *M* vs *H* (top) and *M* vs *H/T* (bottom) data for: **8** (left) and of **10** (right) between 1.8 and 8 K with sweep-rates of 100-200 Oe/min.

IV.5.5. UV-Vis studies in diluted solution

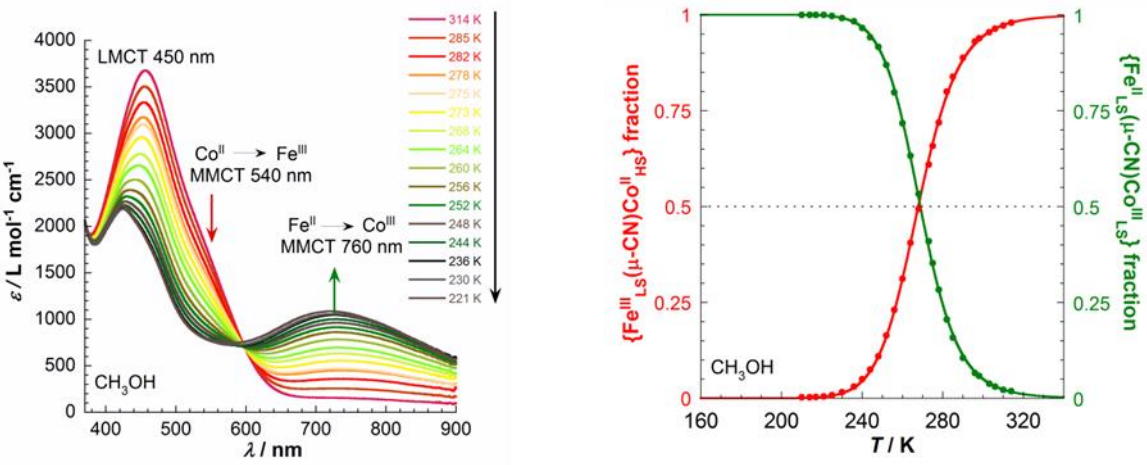

Figure S.IV-9. (left) UV-Vis spectra for **7** in methanol on cooling mode from 310 to 210 K (at 0.2 to 0.3 K/min) estimated from the absorption intensities at the MMCT bands (≈ 540 nm and ≈ 760 nm), solid lines are fits to the ideal solution model.

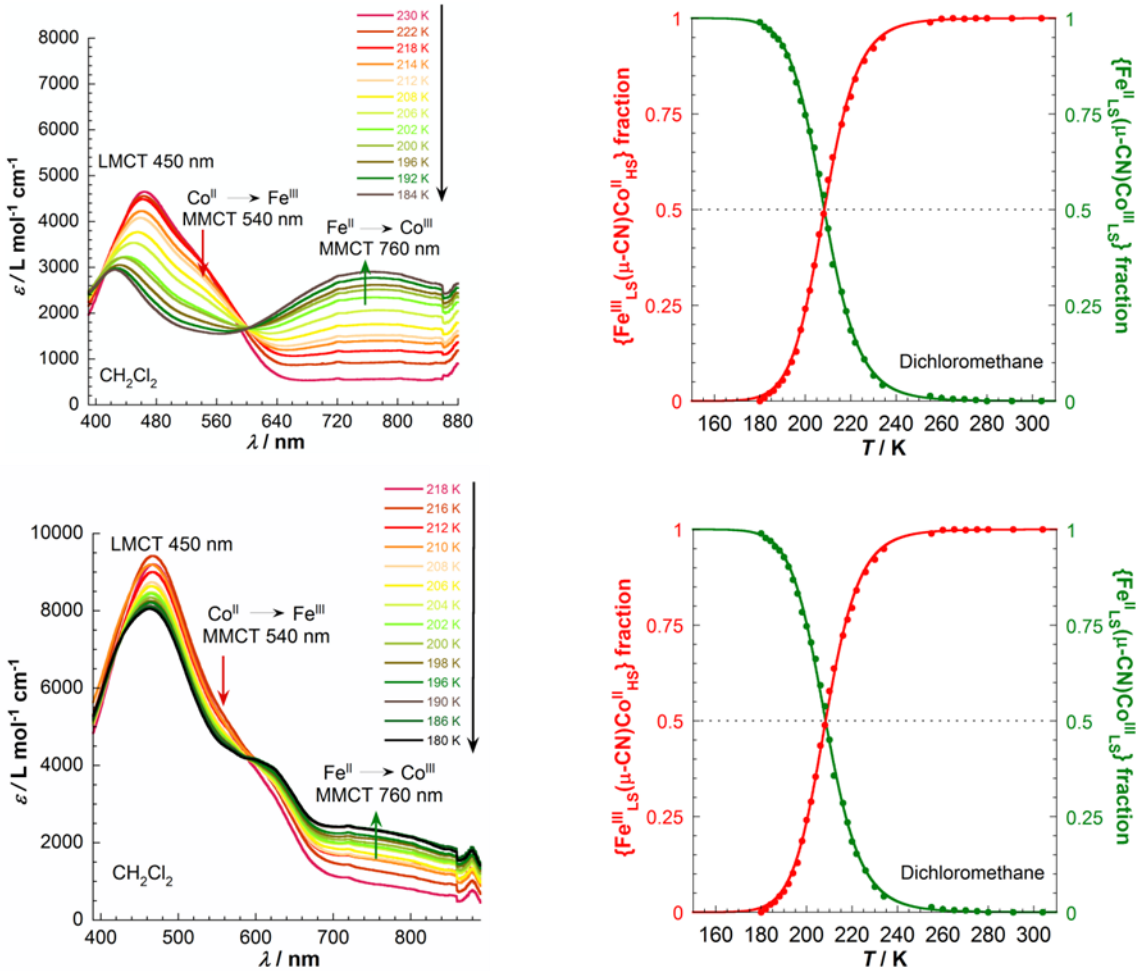

Figure S.IV-10. (left) UV-Vis spectra for **7** (top) and **9** (bottom) in dichloromethane on cooling mode from 218 to 180 K (at 0.2 to 0.3 K/min). (right) Temperature dependence of the $\{Fe^{III}_{LS}(\mu\text{-}CN)Co^{II}_{HS}\}$ and $\{Fe^{II}_{LS}(\mu\text{-}CN)Co^{III}_{LS}\}$ fractions estimated from the absorption intensities at the MMCT bands (≈ 540 nm and ≈ 760 nm) for **7** (top) and **9** (bottom) in dichloromethane, solid lines are fits to the ideal solution model.

IV.6. References

1. (a) Entley, W. R; Girolami, G. S. *Science* **1995**, *268*, 397. (b) Entley, W. R.; Treadway, R. W.; Girolami, G. S. *J. Am. Chem. Soc.* **1997**, *119*, 6251. (c) Holmes, S. M.; Girolami, G. S. *Mol. Cryst. Liq. Cryst*. **1997**, *305*, 279. (d) Awaga, K.; Sekine, T.; Okawa, M.; Fujita, W.; Holmes, S. M.; Girolami, G. S. *Chem. Phys. Lett.* **1998**, *293*, 352. (e) Verdaguer, M.; Girolami, G. S. "Magnetic Prussian Blue Analogues", in *Magnetism Molecules to Materials V*, **2005**, 283-346. (f) Holmes, S. M.; Whelpley, A. S.; Girolami, G. S. *Polyhedron* **2007**, *26*, 2291.

2. (a) Sato, O; Iyoda, T.; Fujishima, A.; Hashimoto, K. *Science* **1996**, *272*, 704. (b) Sato, O; Einaga, Y.; Fujishima, A.; Hashimoto, K. *Inorg. Chem*. **1999**, *38*, 4405. (c) Sato, O.; Tao, J.; Zhang, Y.-Z. *Angew. Chem*. **2007**, *119*, 2200. (d) Sato, O.; Tao, J.; Zhang, Y.-Z. *Angew. Chem., Int. Ed*. **2007**, *46*, 2152.

3. Verdaguer, M.; Bleuzen, A.; Marvaud, V.; Vaissermann, J.; Seuleiman, M.; Desplanches, C.; Scuiller, A.; Train, C.; Garde, R.; Gelly, G.; Lomenech, C.; Rosenman, I.; Veillet, P.; Cartier, C.; Villain, F.; *Coord. Chem. Rev.* **1999**, *192*, 1023.

4. Miller, J. S.; Manson, J. L. *Acc. Chem. Res*. **2001**, *34*, 563.

5. Catala, L.; Volatron, F.; Brinzei, D.; Mallah, T. *Inorg. Chem.* **2009**, *48*, 3360.

6. (a) Beltran, L. M. C.; Long, J. R. *Acc. Chem. Res.* **2005**, 38, 325. (b) Rebilly, J.-N.; Mallah, T. *Struct. Bonding* **2006**, *122*, 103. (c) Wang, S.; Ding, X.-H.; Zuo, J.-L.; You, X-Z.; Huang, W. *Coord. Chem. Rev.* **2011**, *255*, 1713. (d) Newton, G. N.; Nihei, M.; Oshio, H. *Eur. J. Inorg. Chem.* **2011**, 3031.

7. (a) Wang, S.; Zuo, J.-L.; Zhou, H.-C.; Choi, H. J.; Ke, Y.; Long, J. R.; You, X.-Z. *Angew. Chem., Int. Ed.* **2004**, *43*, 5940. (b) Li, D.; Parkin, S.; Wang, G.; Yee, G. T.; Prosvirin, A. V.; Holmes, S. M. *Inorg. Chem.* **2005**, *44*, 4903. (c) Li, D.; Parkin, S.; Wang, G.; Yee, G. T.; Clérac, R.; Wernsdorfer, W.; Holmes, S. M. *J. Am. Chem. Soc.* **2006**, *128*, 4214. (d) Schelter, E. J.; Karadas, F.; Avendano, C.; Prosvirin, A. V.; Wernsdorfer, W.; Dunbar, K. R. *J. Am. Chem. Soc*. **2007**, *129*, 8139. (e) Freedman, D. E.; Jenkins, D. M.; Iavarone, A. T.; Long, J. R. *J. Am. Chem. Soc.* **2008**, *130*, 2884. (f) Cao, L.; Tao, J.; Gao, Q.; Liu, T.; Xia, Z.; Li, D. *Chem. Commun.* **2014**, *50*, 1665.

8. (a) Liu, W.; Wang, C.-F.; Li, Y.-Z.; Zuo, J.-L.; You, X.-Z. *Inorg. Chem.* **2006**, *45*, 10058. (b) Wang, C.-F.; Liu, W.; Song, Y.; Zhou, X.-H.; Zuo, J.-L.; You, X.-Z. *Eur. J. Inorg. Chem.* **2008**, 717. (c) Wu, D.; Zhang, Y.; Huang, W.; Sato, O. *Dalton Trans.* **2010**, *39*, 5500. (d) Hoshino, N.; Sekine, Y.; Nihei, M.; Oshio, H. *Chem. Commun.* **2010**, *46*, 6117. (e) Peng, Y.-H.; Meng, Y.-F.; Hu, L.; Li, Q.-X.; Li, Y.-Z.; You, X.-Z. *Inorg. Chem.* **2010**, *49*, 1905. (f) Zhuang, P.-F.; Zhang, Y.-J.; Jiao, C.-Q.; Zhao, L.; Wang, J.-L.; He, C.; Duan, C.-Y.; Liu, T. *Dalton Trans.* **2015**, *44*, 3393.

9. (a) Li, D.; Clérac, R.; Parkin, S.; Wang, G.; Yee, G. T.; Holmes, S. M. *Inorg. Chem.*, **2006**, *45*, 5251-5253; (b) Li, D.; Clérac, R.; Wang, G.; Yee, G. T.; Holmes, S. M. *Eur. J. Inorg. Chem.* **2007**, 1341-1346. (c) Zhang, Y.; Mallik, U. P.; Clérac, R.; Rath, N. P.; Holmes, S. M. *Polyhedron*, **2013**, *52*, 115-121.

10. (a) Herchel, R.; Boca, R.; Gembicky, M.; Kozísek, J.; Renz, F. *Inorg. Chem.* **2004**, *43*, 4103. (b) Nihei, M.; Ui, M.; Yokota, M.; Han, L.; Maeda, A.; Kishida, H.; Okamoto, H.; Oshio, H. *Angew. Chem., Int. Ed.* **2005**, *44*, 6484. (c) Shatruk, M.; Dragulescu-Andrasi, A.; Chambers, K. E.; Stoian, S. A.; Bominaar, E. L.; Achim, C.; Dunbar, K. R. *J. Am. Chem. Soc.* **2007**, *129*, 6104. (d) Boldog, I.; Munoz-Lara, F. J.; Gaspar, A. B.; Munoz, M. C.; Seredyuk, M.; Real, J. A. *Inorg. Chem*. **2009**, *48*, 3710.

11. (a) Bleuzen, A.; Marvaud, V.; Mathonière, C.; Sieklucka, B.; Verdaguer, M. *Inorg. Chem.* **2009**, *48*, 3453. (b) Aguilà, D.; Prado, Y.; Koumousi, E. S.; Mathonière, C.; Clérac, R. *Chem. Soc. Rev.* **2016**, 45, 203.

12. (a) Herrera, J. M.; Marvaud, V.; Verdaguer, M.; Marrot, J.; Kalisz, M.; Mathonière, C., *Angew. Chem. Int. Ed*. **2004**, *43*, 5468. (b) Mathonière, C.; Podgajny, R.; Guionneau, P.; Labrugère, C.; Sieklucka, B., *Chem. Mater*. **2005**, *17*, 442. (c) Bleuzen, A.; Marvaud, V.; Mathonière, C.; Sieklucka, B.; Verdaguer, M., *Inorg. Chem.* **2009**, *48*, 3453. (d) Hilfiger, M.; Chen, M.; Brinzari, T.; Nocera, T.; Shatruk, M.; Petasis, D.; Musfeldt, J.; Achim, C.; Dunbar, K. R. *Angew. Chem., Int. Ed.* **2010**, *49*, 1410. (e) Mondal, A.; Chamoreau, L.-M.; Li, Y.; Journaux, Y.; Seuleiman, M.; Lescouëzec, R. *Chem. Eur. J.* **2013**, *19*, 7682.

13. (a) Berlinguette, C. P.; Dragulescu-Andrasi, A.; Sieber, A.; Galán-Mascarós, J. R.; Güdel, H.-U.; Achim, C.; Dunbar, K. R. *J. Am. Chem. Soc.* **2004**, *126*, 6222. (b) Berlinguette, C. P.; Dragulescu-Andrasi, A.; Sieber, A.; Güdel, H.-U.; Achim, C.; Dunbar, K. R. *J. Am. Chem. Soc.* **2005**, *127*, 6766. (c) Funck, K. E.; Prosvirin, A. V.; Mathonière, C.; Clérac, R.; Dunbar, K. R. *Inorg. Chem.* **2011**, *50*, 2782.

14. Li, D.; Clérac, R.; Roubeau, O.; Harté, E.; Mathonière, C.; Le Bris, R.; Holmes, S. M. *J. Am. Chem. Soc*. **2008**, *130*, 252.

15. (a) Zhang, Y.; Li, D.; Clérac, R.; Kalisz, M.; Mathonière, C.; Holmes, S. M. *Angew. Chem., Int. Ed.* **2010**, *49*, 3752. (b) Siretanu, D.; Li, D.; Buisson, L.; Bassani, D. M.; Holmes, S. M.; Mathonière, C.; Clérac, R. *Chem. Eur. J.* **2011**, *17*, 11704. (c) Zhang, Y.-Z.; Ferko, P.; Siretanu, D.; Ababei, R.; Rath, N. P.; Shaw, M. J.; Clérac, R.; Mathonière, C.; Holmes, S. M. *J. Am. Chem. Soc.* **2014**, *136*, 16854.

16. (a) Nihei, M.; Sekine, Y.; Suganami, N.; Oshio, H.; *Chem. Lett.* **2010**, 978. (b) Nihei, M.; Sekine, Y.; Suganami, N.; Nakazawa, K.; Nakao, A.; Nakao, H.; Murakami, Y.; Oshio, H. *J. Am. Chem. Soc.* **2011**, *133*, 3592. (c) Newton, G. N.; Nihei, M.; Oshio, H. *Eur. J. Inorg. Chem.* **2011**, *20*, 3031. (d) Sekine, Y.; Nihei, M.; Oshio, H. *Chem. Lett.* **2014**, 1029. (e) Sekine, Y.; Nihei, M.; Kumai, R.; Nakao, H.; Murakami, Y.; Oshio, H. *Inorg. Chem. Front.* **2014**, *1*, 540. (f) Sekine, Y.; Nihei, M.; Kumai, R.; Nakao, H.; Murakami, Y.; Oshio, H. *Chem. Commun.* **2014**, *50*, 4050. (g) Kitagawa, Y.; Asaoka, M.; Miyagi, K.; Matsui, T.; Nihei, M.; Oshio, H.; Okumura, M.; Nakano, M. *Inorg. Chem. Front.* **2015**, *2*, 771.

17. (a) Mercurol, J.; Li, Y.; Pardo, E.; Risset, O.; Seuleiman, M.; Rousselière, H.; Lescouëzec, R.; Julve, M. *Chem. Commun.* **2010**, *46*, 8995. (b) Mondal, A.; Li, Y.; Seuleiman, M.; Julve, M.; Toupet, L.; Buron-Le Cointe, M.; Lescouëzec, R. *J. Am. Chem. Soc.* **2013**, *135*, 1653.

18. (a) Cao, L.; Tao, J.; Gao, Q.; Liu, T.; Xia, Z.; Li, D. *Chem. Commun*. **2014**, *50*, 1665; (b) Zheng, C.; Xu, J.; Yang, Z.; Tao, J.; Li, D. *Inorg. Chem*. **2015**, 54, 9687.

19. (a) Siretanu, D. *PhD Thesis*, Univ. of Bordeaux 1, **2011**. 87. (b) Mitcov, D. *PhD Thesis*, Univ. of Bordeaux, **2014**.

20. (a) Jeon, I.-R.; Calancea, S.; Panja, A.; Piñero Cruz, D. M.; Koumousi, E. S.; Dechambenoit, P.; Coulon, C.; Wattiaux, A.; Rosa, P.; Mathonière, C.; Clérac, R. *Chem. Sci.* **2013**, *4*, 2463. (b) Jeon, I.-R. *PhD Thesis*, Univ. of Bordeaux, **2012**.

21. (a) Koumousi, E. S.; Jeon, I.-R.; Gao, Q.; Dechambenoit, P.; Merzeau, P.; Buisson, L.; Jia, B.; Li, D.; Woodruff, D. N.; Voltaron, F.; Mathonière, C.; Clérac, R. *J. Am. Chem. Soc*. **2014**, *136*, 15461. (b) Koumousi, E. S. *PhD Thesis*, Univ. of Bordeaux, **2015**.

22. Wen, H.-R.; Wang, C.-F.; Song, Y.; Gao, S.; Zuo, J.-L.; You, X.-Z. *Inorg. Chem*. **2006**, *45*, 8942.

23. Zhang, Y.-Z.; Mallik, U.P.; Clérac, R.; Rath, N.P.; Holmes, S. *Chem. Commun.* **2011**, *47*, 7194.

24. Nakamoto, K. *Infrared and Raman Spectra of Inorganic and Coordination Compounds*, 5th Ed. John Wiley and Sons: New York, **1997**.

25. Kaiba, A.; Shepherd, H. J; Fedaoui, D.; Rosa, P; Goeta, A.; Rebbani, N.; Létard, J. F.; Guionneau, P. *Dalton Trans.* **2010**, *39*, 2910.

26. (a) Molard, Y.; Dorson, F.; Cîrcu, V.; Roisnel, T.; Artzner, F.; Cordier, S. *Angew. Chem. Int. Ed*. **2010**, *49*, 3351. (b) Mocanu, A. S.; Amela-Cortes, M.; Molard, Y.; Cîrcu, V.; Cordier, S. *Chem. Commun.* **2011**, *47*, 2056.

27. (a) Zhang, Y.-Z.; Gao, S.; Sun, G. S.; Wang, Z. M.; Zhang, S. W. *Chem. Commun.* **2004**, *40*, 1906. (b) Park, K.; Holmes, S. *Phys. Rev.* **2006**, *B 74*, 224440. (c) Zhang, Y.-Z.; Mallik, U.P.; Rath, N.P.; Clérac, R.; Holmes, S. *Chem. Commun*. **2010**, *46*, 4953. (d) Zhang, Y.-Z.; Mallik, U.P.; Rath, N.P.; Clérac, R.; Holmes, S. *Inorg. Chem.* **2011**, *50*, 10537.

28. Kambe, K. *J. Phys. Soc. Jpn.* **1950**, *5*, 48.

29. Atkins, P.; De Paula, J. *Physical Chemistry*, 8th Ed., Oxford University Press, **2006**.

General Conclusions

At the end of this manuscript, we will recall the main results obtained during this thesis work.

In the first introduction chapter, we outline theoretical aspects of the single molecule magnets, spin cross-over and electron-transfer systems, to make the readers to understand the subsequent Chapters II to IV. Several examples have been described that show the richness of coordination chemistry. This literature summary emphasizes that hybrid systems are multifunctional materials. Towards this, we attempt to obtain hybrid materials in order to induce and organize magnetic materials by functionalizing with organic ligands.

Chapter II is dedicated on synthesis and characterization of new Mn_{12}-based SMMs towards hybrid liquid crystalline systems by applying a rational functionalization. In contrast with previous studies in which the sixteen acetate groups were replaced by mesogenic ligands, we alternatively introduced these ligands only on certain positions of the Mn_{12} core using the regioselective functionalization methodology. The four Mn_{12}-based complexes were successfully synthesized and fully characterized. All the complexes preserve SMM properties, confirming the versatility of these molecular systems to undergo ligand substitution without altering significantly the structure and properties of the magnetic core. The two complexes containing dodecyl chains present high-temperature clearing points, where the integrity of the complexes is not confirmed after annealing into the isotropic phase. Indeed, complexes self-organize into liquid crystalline cubic phases, indicating that no improvement on the overall structural anisotropy was achieved. This result may reflect the tendency of the flexible moieties to reorganize themselves all around the Mn_{12} core leading therefore to a pseudo-spherical geometry of the complex. For the compound containing two biphenyl moieties, no columnar mesophases was obtained. The complex self-organizes in the same fashion as its precursor (bilayer lamellar phase). Even though, the chosen strategy of functionalization did not reveal desired properties, this compound could be an interesting candidate for surface deposition.

In order to avoid of the reorganization of the flexible chains around the magnetic core as in our two first complexes, we should increase the separating distance between these moieties. One idea would be to add a rigid spacer between the anchoring part of the ligand (carboxylate) and the mesogenic one. In this respect, we can induce the columnar phases, by ordering this ligand in axial position of the Mn_{12}-core.

In Chapter III, we described the synthesis and characterization of functionalized spin cross-over systems based on $Fe^{II}L_2$ complexes with a N_4O_2 coordination sphere. In the first part of the chapter, five complexes containing non-mesogenic ligands containing donating groups were synthesized and characterized. According to this functionalization, we can conclude that the presence of methoxy functions on the benzohydrazide scaffold is not incompatible with SCO, since such features were emphasized for compounds [Fe($\mathbf{L^1}$)$_2$], [Fe($\mathbf{L^2}$)$_2$] and [Fe($\mathbf{L^3}$)$_2$] and their polymorphs. But an interesting achievement of this work is the presence of polymorphism in these molecular systems. Moreover, the three structures that feature the highest number of π-π contacts (β-{[Fe($\mathbf{L^1}$)$_2$]·MeOH}, α-[Fe($\mathbf{L^2}$)$_2$] and solvent-free [Fe($\mathbf{L^2}$)$_2$] complexes) do not exhibit SCO feature suggesting that proliferation of such interactions in the packing might create a

certain stress to the molecule. In the second part of the chapter, we described our attempts to promote liquid crystalline features on this molecular system by using strongly lipophilic ligands. Five complexes were synthesized and characterized magnetically, thermotropic and structurally. Thus, by increasing the chain length we could not induce liquid crystalline behavior, while was observed the presence of a liquid phase. Also, by multiplying the dodecyl chains, two compounds revealed same features as for the compound that contained one long alkyl chain. It was reported the formation of intermediate phase in which both LS and HS species coexist when a mono-alkylation (with dodecyl or octadecyl chains) is applied. This behavior observed in the three $[Fe(\mathbf{L}^{4\text{-}6})_2]$ complexes and was explained by a crystallographic symmetry breaking (CSB) that is occurring during the SCO process and has been unambiguously evidenced in one case. From the other side, we have seen that the introduction of multiple dodecyl chains gives access to soft materials with low-melting points.

As our functionalization was accompanied by unexpected reverse-SCO behavior, numerous studies might be realized in continuation to this work. One of the perspective is the preparation of solid solutions of $[Fe_xZn_{(1-x)}(\mathbf{L})_2]$. Also, the goal is still to obtain metallomesogens and several strategies to reach this are considered. Firstly, we can add the calamitic smectogen units (i.e. biphenyl, cyanobiphenyl), that have been applied successfully and lead to a bilayer lamellar mesophase for Mn_{12} SMM (see Chapter II). The other goal is to induce more geometrical constrains to the complex, especially by elaborating [2 x 2] grids in which the mesogenic substituents would be oriented perpendicular to the $[Fe_4L_4]$ core.

Chapter IV is reported the functionalization of cyanido-bridged molecular squares with general formula $\{[(Tp^*)Fe^{III}(CN)_3]_2[M^{II}(R,R\text{-bpy})_2]_2\}(A)_2$ (where Tp* = hydridotris(3,5-dimethylpyrazol-1-yl)borate; M^{II} = Ni^{II} or Co^{II}; R,R-bpy = 4,4'-disubstituent-2,2'-bipyridine derivative; A = monovalent anion). Three squares shaped $\{Fe^{III}(\mu\text{-}CN)Ni^{II}\}$ complexes functionalized were synthesized and their properties were investigated in solid, by structural, thermal and magnetic methods. The magnetic studies show intramolecular ferromagnetic coupling and appreciable magnetic anisotropy of the complexes. This functionalization gives the possibility to induce liquid crystalline behavior in case for two complexes **$\{[(Tp^*)Fe(CN)_3]_2[Ni(L^5)_2]_2\}(OTf)_2$** and **$\{[(Tp^*)Fe(CN)_3]_2[Ni(L^6)_2]_2\}(OTf)_2$**. These compounds showed a smectic mesophase and preserved the magnetic properties. For $\{Fe_2Co_2\}$ we attempt a new design strategy involving the grafting of mesogenic substituents onto the bipyridine ligand through an ether coupling. Four new tetranuclear new cyanido-bridged complexes, **7-10**, and have been synthesized and their properties in solid state and in solutions have been described by structural, spectroscopic and magnetic methods. By performing optical investigations was found that the ET characteristic temperatures $T_{1/2}$ are strongly dependent of the nature of the solvent, confirming the results obtained in the team for other $\{Fe_2Co_2\}$ analogues.

Many attempts was done to induce ET in solid-state in $\{Fe_2Co_2\}$ squares, unfortunately, all failed. These results confirmed the strong impact of crystal packing effects on the phenomenon. Even though, we should continue our investigations on the derivatization of this type of ligands by applying the same strategy as before to promote mesomorphic features on the resulting materials.

Annex

A1: Physico-chemical methods

✓ Elemental analysis (EA)

Elemental analyses (C, H and N) were performed following the classical Pregl−Dumas technique on a ThermoFischer Flash EA 1112 instrument at the Institut de Chimie de la Matière Condensée de Bordeaux (ICMCB). The results of this microanalysis are shown in mass fractions of each element in the compound.

✓ Thermogravimetric analyses (TGA)

Thermogravimetric analyses were carried out using samples of 10 – 20 mg, at 5 K/min in the nitrogen atmosphere using a thermogravimetric analyzer Setaram TAG 16.

✓ Fourier transformed infrared (FTIR) analysis

The FTIR spectra were recorded between 4000 and 550 cm^{-1} on a Thermal Scientific Nicolet™ 6700 ATR (attenuated total reflectance) spectrometer equipped with a Smart iTR diamond window.

✓ Electrospray Ionization Mass Spectrometry (ESI-MS) analysis

ESI-MS spectra were performed using an Electro Spray Ionization – time-of-light (TOF) mass spectrometer (LCQ Advantage; ThermoFicher) by analyzing positive ions.

✓ Nuclear magnetic resonance

^{1}H NMR and ^{19}F NMR spectra were collected with JEOL ECS 400 instrument at room temperature, using $CDCl_3$, CD_3CN, DCM or THF as solvent. Chemical shifts of ^{1}H NMR signals were quoted to internal standard TMS (δ = 0.00 ppm) and expressed as chemical shifts in ppm (δ), multiplicity, coupling constant (Hz), and relative intensity.

✓ Single crystal X-ray analysis

The X-ray diffraction data for the single crystals were collected with a Bruker APEX II diffractometer, using graphite monochromated MoK_α radiation (λ = 0.71073 Å). The program SAINT was used to integrate the data, which were thereafter corrected for absorption using SADABS.[1] The structure was solved by direct methods and refined by least squares on F^2 with SHELXL-97.[2] All non-hydrogen atoms were refined anisotropically. Hydrogen atoms were assigned to ideal positions using the appropriate HFIX command in SHELXL-97.

✓ X-ray Powder Diffraction (XRD)

The X-ray powder diffraction data for compounds were collected with Philips PW 1820 diffractometer with Bragg-Bentano geometry (λ = 1.5406 Å). The angular range extends from 5 to 60° in θ with a step acquisition of 1 or 10 seconds.

✓ Small angle X-ray scattering (SAXS)

X-Ray diffraction experiment at small and wide angle were performed on a home-made experimental set-up equipped with a Rigaku Nanoviewer (XRF microsource generator, MicroMax 007HF), with an 1200-W rotating anode (λ = 1.54180 Å) coupled to a confocal Max-FluxH Osmic mirror (Applied Rigaku Technologies) and a MAR345 image plate detector (Marresearch GmbH). The studied samples were mounted in glass capillaries of 1 mm diameter. Diffraction patterns were integrated with the FIT2D software.[3]

✓ Polarized optical microscopy

The thermal behavior and the optical textures of the compounds were studied with an Olympus BX51TRF polarizing microscope equipped with a Mettler Toledo FP82HT hot-stage.

✓ Differential scanning calorimetry

The transition temperatures and enthalpies changes were measured by differential scanning calorimetry with a Q2000 TA instrument. DCS traces were recorded at different scanning rates, from 1 to 10 K/min in a nitrogen environment. Measurements were carried out using closed Tzero aluminium pans. Calibration of temperature and melting enthalpy was performed with an indium and tin sample. Transition enthalpies changes were deduced by integration of the DSC peaks after polynomial baseline corrections.

✓ UV/Vis analysis

UV/Vis spectra were recorded between 350 and 1000 nm using a PerkinElmer UV-Vis/NIR recording spectrophotometer. Variable temperature UV/Vis data were obtained using an Oxford Liquid Nitrogen Cryostat Optistat^{ON} (static) equipped with an Oxford ITC502 controller operating between 77 and 300 K.

✓ Reflectivity analysis

Surface reflectivity measurements were performed on a home-built system at different temperatures ranging from 10 to 300 K using freshly filtered compounds. Heating and cooling rates were maintained at 4 K·min^{-1} during the measurements. This setup collects the light reflected by the sample (sum of direct and diffuse reflected light) that is analyzed by a high-sensitivity Hamamatsu 10083CA spectrometer between 500 and 1000 nm. The spectra are compared to a white reference obtained with a NIST traceable standard for reflectance (SphereOptics, ref SG3054). The background, collected with the light source switched off, is subtracted from all measurements. The reflectivity can be plotted as a function of temperature, time, or wavelength. Different light emitting diodes (LEDs) operating between 365 and 1050 nm and bought from Thorlabs were used for excitation measurements. As the samples are potentially photosensitive, the light exposure time was minimized during all the experiments keeping the samples in the dark except during the spectra measurements when white light is shined on the sample surface (P = 0.4 mW/cm^2). The temperature dependence of the reflectivity spectra was followed during a cycle of cooling−heating. For all the

excitation/de-excitation experiments performed at 10 K, the sample was initially placed at this temperature keeping the sample in the dark to avoid any excitation.

✓ Magnetic measurements

Magnetic susceptibility measurements were carried out on a Quantum Design SQUID magnetometer MPMS-XL (CRPP) operating between 1.8 and 400 K for applied dc fields ranging from -7 to 7 T. Measurements in solid state were performed on a microcrystalline samples that were filtered from its mother liquor and dried in air less than 2 minutes prior the use. Magnetic data was corrected for the sample holder and diamagnetic contributions for all magnetic measurements. Photomagnetic measurements were performed at ICMCB using a halogen-tungsten light source (Leica CLS 150 XD tungsten halogen source adjustable from 0.5 mW/cm^2 to 1 W/cm^2) coupled through an optical fiber directed into the magnetometer cavity. Samples of ca. 3 mg were packed into a thermoformed plastic straw placed about 3.5 cm from the optical fiber (the power of the irradiation light was chosen carefully to find a good compromise between minimizing thermal heating of the sample and maximizing the photoconversion efficiency). Sample temperatures were corrected for the light-induced heating (average ±2 K at 10 K under white light irradiation), and the calibration of experimental sample temperatures was referenced to the data collected in absence of light.

✓ Mössbauer spectroscopy

The Mössbauer measurements were carried out on Mössbauer spectrometer HALDER type (ICMCB) constant acceleration using as a radioactive source at room temperature. The spectra were performed at 298 K using a cryostat. The refinement of the spectrum was carried out taking into account the distribution of hyperfine parameters.

A2: List of abbreviations

0D	Zero-dimensional
1D	One-dimensional
2D	Two-dimensional
3D	Three-dimensional
ac	Alternating current
AcOH	Acetic acid
bik	bis(1-methylimidazol-2-yl)ketone
BN	Banana like mesophases
1,3-bpp	2-(pyrazol-1-yl)-6-(pyrazol-3-yl)-pyridine)
bpy	2,2’-bipyridine
C*n*-terpy	4'-alkyloxy-2,2':6',2''-terpyridine, n = 14, 16
Col	Columnar

Cr	Crystal/crystalline phase
CRPP	Centre de Recherche Paul Pascal
CSB	Crystallographic symmetry breaking
Cub	Cubic phase
dec	decomposition
dc	Direct current
DCM	Dichloromethane
diMebpy	4,4'-methyl,2,2'-bipyridine
DMA	N,N-dimethylacetamide
DMF	N,N-dimethylformamide
DSC	Differential scanning calorimetry
EA	Elemental analysis
ESI-MS	Electrospray Ionization Mass Spectrometry analysis
ET	Electron transfer
FR	Fast relaxing
FTIR	Fourier transform infrared spectroscopy
g	Glass solid
HS	High spin
HT	High temperature
I	Isotropic phase
JT	Jahn-Teller
LC	Liquid crystal
LED	Light emitting diode
LIESST	Light-Induced Excited Spin-State Trapping
LMCT	Ligand-to-metal charge transfer
LS	Low spin
LT	Low temperature
MeCN	Acetonitrile
MeOH	Methanol
MMCT	Metal-to-metal charge transfer
Mn_{12}-OAc	$[Mn_{12}O_{12}(O_2CCH_3)_{16}(H_2O)_4$ or Mn_{12}-OAc
$–N(CH_3)_2$	Dimethylamino group
NEt_4^+	Tetraethylammonium
NMR	Nuclear magnetic resonance
OTf^-	Trifluoromethanesulfonate ($CF_3SO_3^-$)
PB	Prussian blue
PBA	Prussian blue analogue

PF_6^-	Hexafuorophosphate
Ph	Phenyl
phen	1,10-Phenantroline
pK_a	Logarithmic acid dissociation constant
POM	Polarized optical microscopy
PrCN	Butyronitrile
ptol	p-toluene sulfonate anion
ptz	1-propyltetrazole
pyr	pyrazine
$pzCCH_2OH$	2,2,2-tris(pyrazolyl)ethanol
pzTp	Tetrapyrazolylborate
RT	Room temperature
R-trz	4-(alkyl)-1,2,4-triazole
sal	Salicylaldehyde
SAXS	Small angle X-ray scattering
SCO	Spin crossover
SCM	Single-chain magnet
Sm	Smectic phase
SMM	Single-molecule magnet
SR	Slow relaxing
S_T	Spin ground state
*t*Bu	*tert*-Butyl
T_C	Curie temperature
TGA	Thermogravimetric analysis
THF	Tetrahydrofurane
Tp	tri(pyrazol-1-yl)hydroborate
Tp*	tris(3,5-dimethylpyrazol-1-yl)hydroborate
tpa	tris(pyridylmethyl)amine)
trien	triethylenetetramine
trz	triazole
VSM	Vibrating Sample Magnetometer
XRD	X-ray diffraction

A3: Physical constants

	Symbol	Value	Units SI	CGS
Avogadro constant	N_A	6.02217	10^{23} mol^{-1}	
Boltzmann constant	k_B	1.38062	10^{-23} J·K^{-1}	10^{-21} erg·G^{-1}
Bohr magneton	μ_B	9.27410	10^{-24} J·T^{-1}	10^{-16} erg·K^{-1}
Electron volt	eV	1.60219	10^{-19} J	10^{-11} erg
Vacuum permeability	μ_0		$4\pi10^{-7}$ N·A^{-2}	1
Molar gas constant	R	8.31446	J·mol^{-1}·K^{-1}	10^{7} erg·mol^{-1}·K^{-1}

References

1. Sheldrick, G. M. *SADABS*, Version 2.03; Bruker Analytical X-Ray Systems: Madison, WI, **2000**.

2. Sheldrick, G. M. *Acta Cryst*. **2008**, *A64*, 112-122.

3. (a) Hammersley, A. P. *ESRF Internal Report, ESRF97HA02T*, **1997**; (b) www.esrf.eu/computing/scientific/FIT2D/

Résumé

Les matériaux magnétiques ont été à l'origine d'avancées technologiques majeures devenues indispensables à une société moderne. Les composants magnétiques sont omniprésents dans notre quotidien comme dans les générateurs électriques, les moteurs, les haut-parleurs, les microphones, les commutateurs, les capteurs, les disques durs, etc. Jusque dans les années 80, la majorité des systèmes magnétiques développés et étudiés sont des matériaux inorganiques basés sur des métaux purs, des alliages ou des oxydes métalliques. Cependant, le développement de nouveaux matériaux magnétiques basés sur des précurseurs moléculaires a connu un essor considérable au cours de ces dernières décennies. Les matériaux moléculaires présentent des avantages synthétiques par rapport aux analogues inorganiques puisqu'ils utilisent des précurseurs bien définis permettant un excellent contrôle de l'architecture, de la dimensionnalité des matériaux finaux et ainsi de leurs propriétés physiques. Par ailleurs, ces systèmes moléculaires sont accessibles par des voies souvent beaucoup plus douces et économe en énergie, impliquant la chimie de coordination ou chimie organométallique. Outre l'aspect synthétique, les propriétés magnétiques de ces matériaux moléculaires sont souvent rares ou inaccessible dans les matériaux inorganiques traditionnels. Ainsi, des systèmes moléculaires présentant des phénomènes de conversion de spin,[1] du photomagnétisme[2] ou encore des comportements de molécule-aimant[3] ou chaîne-aimant[4] ont été découverts. Ces matériaux sont d'autant plus attrayants que leurs propriétés magnétiques peuvent être modulées sur mesure en modifiant les précurseurs moléculaires qui les constituent. Même si les propriétés magnétiques sont les motivations principales de ce domaine de recherche, d'autres propriétés, qui font souvent défaut dans les matériaux inorganiques comme la transparence, le thermo- photochromisme, la biocompatibilité, la recyclabilité, peuvent être présentes dans ces systèmes moléculaires, offrant ainsi des solutions pratiques pour répondre aux nouveaux besoins technologiques.

Des efforts de recherche considérables ont été dédiés ces dernières décennies à la synthèse de systèmes à l'échelle nanométrique, afin par exemple de réduire la taille des unités magnétiques dans les dispositifs de stockage de l'information. Les matériaux moléculaires aux propriétés uniques pourraient répondre à cette attente en donnant l'opportunité de stocker l'information à l'échelle du nanomètre voir à l'échelle de la molécule. Toutefois, il reste un immense chemin à parcourir avant que ces matériaux moléculaires puissent être utilisés dans de telles applications et ceci impliquera des innovations et/ou améliorations aussi bien des systèmes moléculaires et technologies requises. Parmi cela, un des défis sera de développer des méthodes pour organiser et mettre en forme ces composés. A cet égard, d'intense recherches ont été dédiées aux dépôts de ces matériaux sur des surfaces et de nombreuses approches basées par exemples sur les monocouches auto-organisées (SAM : self-assembled monolayer), la lithographie, la sublimation ou les films Langmuir-Blodgett ont été explorées. Une autre alternative pour faciliter leur dépôt consiste à insérer ces composés au sein de phases molles telles que des gels ou des cristaux-liquides. La conception d'hybrides magnétiques est devenue une des principales activités de recherche du groupe Matériaux Moléculaires et Magnétisme (M_3) au Centre de Recherche Paul Pascal (CRPP). La stratégie mise en œuvre consiste à modifier des complexes magnétiques connus en fonctionnalisant leurs ligands organiques avec divers substituants permettant d'induire des propriétés liquide-cristalline, ou tout simplement, permettant d'améliorer leur solubilité dans des solvants usuels. Bien que cette approche puisse sembler évidente, elle est encore relativement peu

développée et seuls quelques groupes de recherche étudient actuellement cette stratégie pour créer de nouveaux matériaux hybrides. C'est dans cette philosophie que ce travail de thèse a été réalisé. Ainsi, nous nous sommes intéressé à divers systèmes moléculaires incluent des molécule-aimants, des complexes à conversion de spin et transfert d'électron avec pour premier objectif d'induire des propriétés de cristal-liquide par une fonctionnalisation rationnel de leur ligands. Diverses mesures physico-chimiques ont été réalisées afin de mieux comprendre l'effet de nos stratégies de fonctionnalisation aussi bien sur le comportement magnétique que sur l'auto-organisation des matériaux hybrides produits.

Ce manuscrit de thèse comprend quatre chapitres. Dans le premier chapitre, les concepts fondamentaux sur les comportements de molécule-aimant, de conversion de spin et transfert d'électron sont y sont résumés. Dans la deuxième partie de ce chapitre, une étude bibliographique fait un bref état de l'art des études menées sur des hybrides magnétiques, notamment possédant des propriétés de cristal-liquide, de gel ou des systèmes solubles.

Le chapitre II est consacré à la préparation et étude d'hybrides magnétiques basés sur le complexe dodecamanganèse $[Mn_{12}O_{12}(OAc)_{16}(H_2O)_4]$ (Mn_{12}-OAc, Figure R-1 (a)). Cette molécule est le premier exemple connus de molécule-aimant et demeure avec ses analogues celle qui est la plus étudiée à ce jour. D'autre part, c'est un des seules types de molécule-aimant ayant fait l'objet d'étude dans des systèmes cristal-liquides.[5] Dans les précédentes études,[5] des phases liquides cristallines ont pu être obtenues en remplacent les seize ligands acétate du complexe par des ligands benzoate porteurs de substituants mésogènes. Deux stratégies avaient ainsi été explorées: (a) la fonctionnalisation des ligands benzoate avec des groupements fortement lipophiles (longues chaînes alkyle), ou (b) le greffage de promoteurs smectogènes *via* des espaceurs aliphatiques. Dans le premier cas des phases cristallines ou mésophases cubiques ont été obtenues en raison de la forme globulaire des complexes tandis que des mésophases lamellaires ont été observées en utilisant la seconde approche. Dans la continuité de ces travaux, nous avons cherché à savoir s'il était possible de générer d'autres types d'organisation et d'améliorer les propriétés thermotropes de ces systèmes (en particulier, diminuer la température de clarification). A cet égard, nous avons proposé une nouvelle approche consistant à introduire des ligands mésogènes uniquement sur des positions spécifiques du complexe Mn_{12} en se basant sur une fonctionnalisation régiosélective. En effet, en modifiant la molécule par des ligands mésogènes sur les positions équatoriales, nous espérerions que la molécule adopte une structure de forme discotique qui serait, selon la cohésion intermoléculaire, favorable à la formation de mésophases nématiques ou colonnaires (Figure R-1 (b)). Dans le cas d'une fonctionnalisation des positions axiales par des ligands mésogènes, il peut être anticipé que la structure moléculaire soit de type calamitique, ce qui conduirait à une organisation lamellaire. Au cours de ce travail de thèse, nous nous sommes essentiellement focalisée sur la première option. Une fonctionnalisation régiosélective du complexe Mn_{12} est possible en raison de la différence de réactivité entre les ligands carboxylate présents sur les positions axiales et ceux occupant les positions équatoriales. Celle-ci peut s'expliquer par les élongations de Jahn Teller sur les ligands axiaux. De ce fait, les positions axiales sont stabilisées par des ligands de faible pK_a alors que des ligands plus basiques sont plus favorables pour les positions équatoriales.

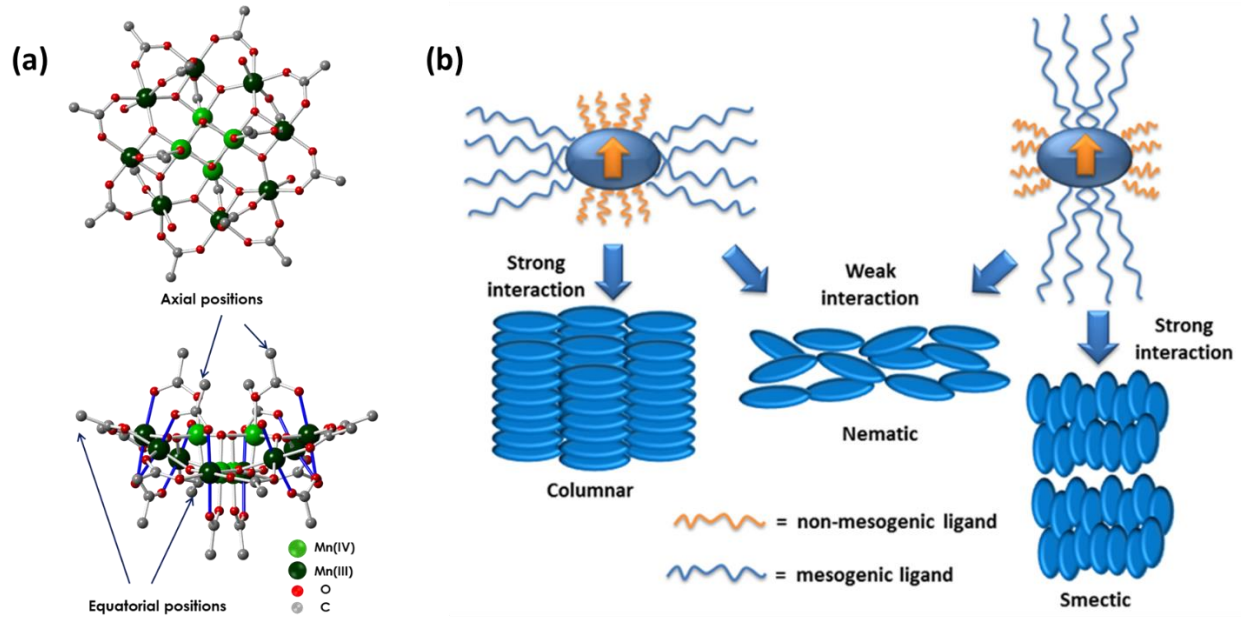

Figure R-1. (a) Structure cristallographique du complexe Mn_{12}-OAc. Les liaisons sujettes à une élongation de Jahn Teller sont montrées en bleu (b) Stratégies de fonctionnalisation envisagées pour obtenir des phases cristal-liquides.

Ainsi, pour occuper les positions axiales nous avons choisi le ligand trifluoroacétate (pK_a = 0.3), tandis que des ligands mésogènes de type benzoate ayant des pKa beaucoup plus élevés (pK_a ~ 4.2 – 4.4) ont été choisi pour fonctionnaliser les positions équatoriales. Afin de faire une comparaison directe avec les précédentes approches étudiées dans l'équipe, nous avons choisi les mêmes ligands mésogènes (Schéma R-1). Aussi, pour une meilleure compréhension et pour confirmer la méthode de synthèse, nous avons également préparé un complexe modèle avec le ligand non-mésogènique 4-methoxybenzoate (L^1; Schéma R-1). Les quatre complexes hétéroleptiques $[Mn_{12}O_{12}(CF_3COO)_8^{ax}(\mathbf{L^i})_8^{eq}(H_2O)_4]$ (i = 1-4) ont été préparés avec succès par réaction équimolaire entre les complexes homoleptique $[Mn_{12}O_{12}(CF_3COO)_{16}(H_2O)_4]$ et $[Mn_{12}O_{12}(L^1)_{16}(H_2O)_4]$. Ces derniers ont été obtenus comme précédemment décrit par une réaction d'échange de ligands en traitant le complexe Mn_{12}-OAc avec un excès de $\mathbf{HL^{1-4}}$ ou d'acide trifluoroacétique. La régiosélectivité de la réaction a été confirmée sans ambiguïté par la résolution de la structure du complexe modèle qui montre bien la présence des huit ligands trifluoroacetate sur les positions axiales et des huit ligands 4-methoxybenzoate sur les sites équatoriaux (Figure R-2).

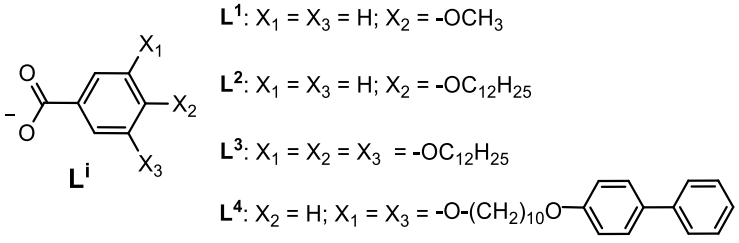

Schéma R-1. Structure chimique des ligands $\mathbf{L^{1-4}}$ utilisés pour la fonctionnalisation des sites équatoriaux du complexe Mn_{12}.

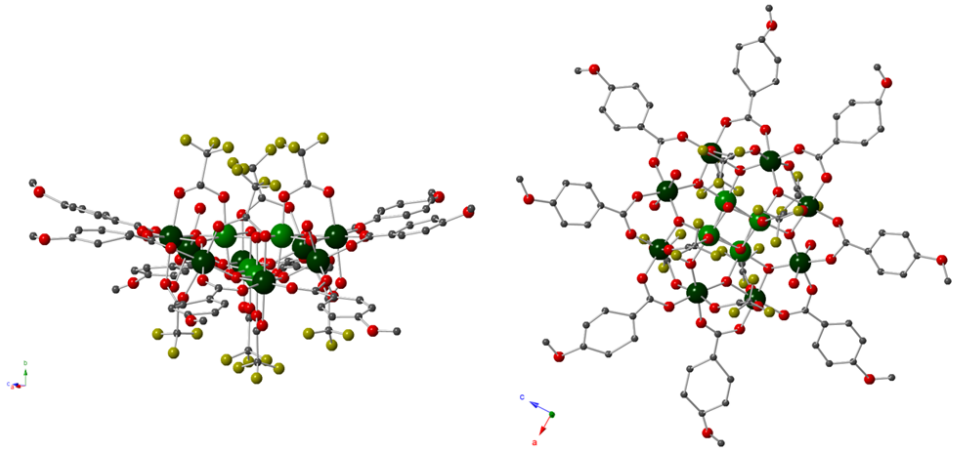

Figure R-2. Structure cristalline du complexe $[Mn_{12}O_{12}(CF_3COO)_8^{ax}(\mathbf{L^1})_8^{eq}(H_2O)_4]$ vue selon le plan *bc* (gauche) et plan *ac* (droite). Les atomes d'hydrogène sont omis pour plus de clarté. Couleur du schéma: Mn^{IV} vert clair, Mn^{III} vert fonce, O rouge, C gris, F jaune.

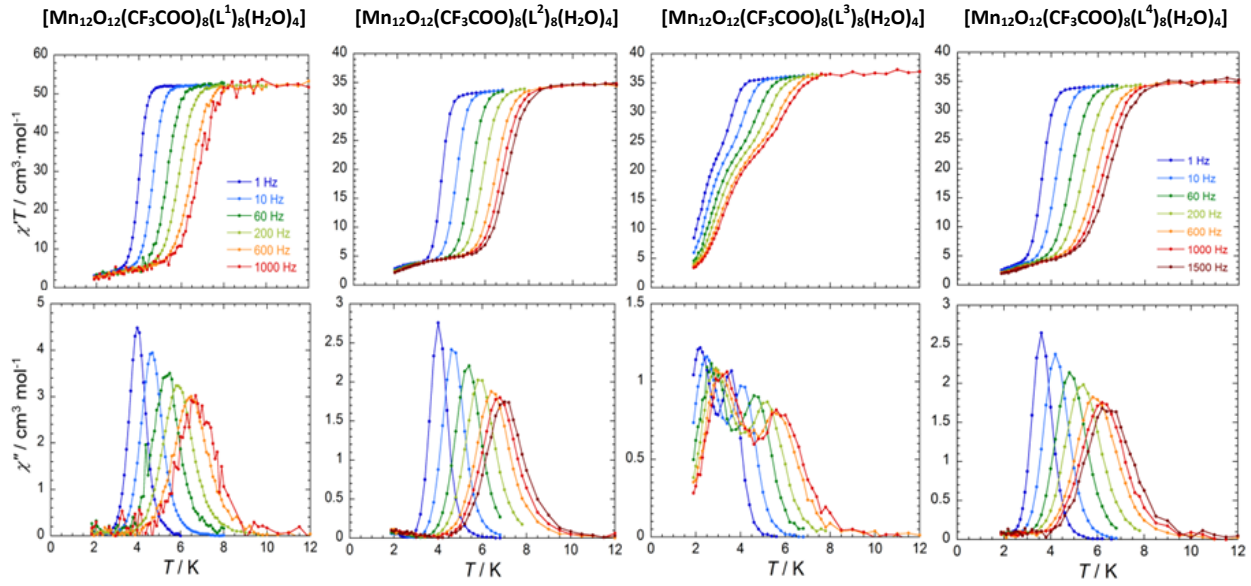

Figure R-3. Dépendance en température du $\chi'T$ et χ'' pour les complexes $[Mn_{12}O_{12}(CF_3COO)_8(\mathbf{L^{1\text{-}4}})_8(H_2O)_4]$ mesuréess pour des champs oscillants de différentes fréquences (1-1500 Hz) et sous un champ permanent H_{dc} nul.

Les propriétés magnétiques des quatre complexes ont entièrement été caractérisées et comparées à leur précurseurs homoleptiques. Comme attendu, tous les complexes préservent un comportement de molécule-aimant (Figure R-3), montrant ainsi la grande versatilité de ces systèmes pour subir des modifications sans affecter de manière significative les propriétés du cœur magnétique. Il est important de noter qu'a l'exception d'un cas, $[Mn_{12}O_{12}(CF_3COO)_8(\mathbf{L^3})_8(H_2O)_4]$, tous les complexes montrent un seul mode de relaxation entre 4 et 8 K dans les mesures de susceptibilité magnétique *ac*. Ceci indique que ces composés ne sont pas sujet a un isomérisme de Jahn-Teller (JT) alors que cela avait été systématiquement le cas pour les précurseurs homoleptiques $[Mn_{12}O_{12}(\mathbf{L^{1\text{-}4}})_{16}(H_2O)_4]$ et autres analogues.[5] Ceci suggère que la présence des ligands trifluoroacétate stabilise la forme isomérique classique dans laquelle tous les axes d'élongations de JT sont quasi parallèles les uns des autres et perpendiculaires au plan de la molécule (Figure R-1 (a)). Dans

le cas du complexe $[Mn_{12}O_{12}(CF_3COO)_8(\mathbf{L^3})_8(H_2O)_4]$, un second mode de relaxation (2 - 4 K) est observé et est attribué à la présence d'un second isomère dans lequel un des axes de JT est anormalement orienté.[5]

Les propriétés mésomorphes des complexes ont été étudiées par microscopie optique en lumière polarisée (POM : polarized optical microscopy), analyse enthalpique différentielle (DSC : differential scanning calorimetry) et diffraction des rayons X aux petits angles (SAXS: small-angle X-ray scattering). Les deux complexes fonctionnalisés par des ligands fortement lipophiles ($\mathbf{L^2}$ et $\mathbf{L^3}$) présentent le même comportement thermotrope que leur précurseurs homoleptiques, s'auto-organisant ainsi dans des phases cubiques. Ceci indique, que malgré l'absence de fonctions mésogènes sur les positions axiales, la géométrie du complexe demeure globulaire et suggère que les chaines alkyles viennent recouvrir l'ensemble de la molécule à la façon d'une pelote. De la même manière que son analogue homoleptique, le complexe contenant le ligand $\mathbf{L^3}$, forme une mésophase lamellaire, due aux des unités diphényle qui favorisent ce type d'organisation. Même si cette stratégie n'a pas permis d'obtenir des mésophases colonnaires ou nématiques comme nous l'espérions, ce dernier système est tout à fait prometteur d'un point de vue de la mise en forme. En effet celui-ci présente une température de clarification relativement basse et bien en dessous de la température de décomposition à l'inverse de la plupart des autres hybrides Mn_{12} précédemment décrits, ce qui nous permet d'envisager de former des films homogènes sur des surfaces.

Le chapitre III est dédié à nos travaux sur des hybrides magnétiques basé sur des complexes à conversion de spin. Nous avons proposé au cours de ces travaux de développer des métallomésogènes basé sur un complexe de Fe(II) mononucléaire contenant des ligands de type base de Schiff appartenant à la famille des pyridylaroylhydrazones (Schéma R-2).[6-8] Bien qu'aucune tentative pour produire des métallomésogènes n'avait été réalisée auparavant, ce système nous est apparue être un très bon candidat. En effet, la molécule a une géométrie coudée, ce qui est propice pour obtenir des mésophases lamellaires ou éventuellement de type banane (BN). D'autre part il est neutre, relativement stable en température et contre l'oxydation.

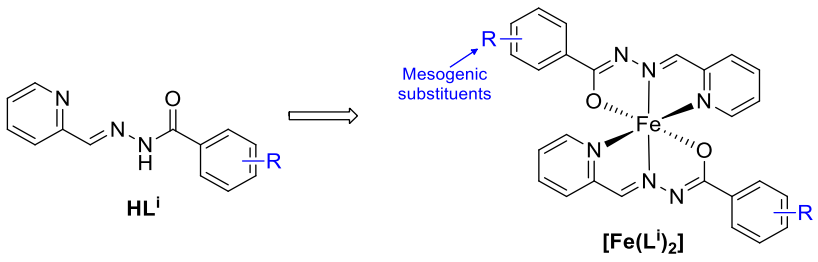

Schéma R-2. Structure générale du ligand pyridylbenzohydrazine $\mathbf{HL^i}$ et complexe $[Fe(\mathbf{L^i})_2]$.

Dans la première partie de ce chapitre nous nous sommes intéressés à la synthèse et étude de complexes présentant des ligands non-mésogènes. En effet il existe très peu d'exemples de complexes à conversion de spin basés sur ce système moléculaire et notre premier objectif a été de savoir si une modification du ligand, en particulier la fonctionnalisation avec des fonctions alkoxy, permettrait de

conserver des propriétés de commutation de spin. Trois nouveaux ligands porteurs de une à trois fonctions methoxy ainsi que les complexes correspondants ont été préparés (Schéma R-3 (a)).

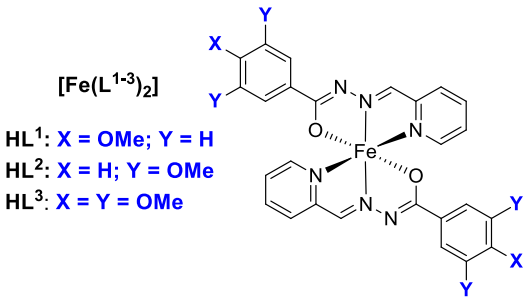

Scheme R-2. Structure chimiques des complexes [Fe($\mathbf{L}^{i}$)$_2$] avec des ligands non-mésogènes étudiés durant la thèse.

Cette étude a permis de démontrer que la modification du ligand par des groupes methoxy n'était pas incompatible avec des propriétés de conversion de spin, mais était fortement dépendante des conditions expérimentales qui régissent la manière dont les molécules sont organisées à l'état solide et l'état de solvatation. En effet, nous avons pu isoler de manière sélectives ces complexes sous forme de différents polymorphes et solvatomorphes et montré l'immense impact que cela a sur le comportement magnétique. Par exemple, le complexe [Fe($\mathbf{L}^{2}$)] a été isolé sous deux formes polymorphes, l'une étant purement paramagnétique tandis que la seconde présente une conversion de spin au-dessus de 400 K. Le complexe [Fe($\mathbf{L}^{3}$)] a également été obtenu sous deux différentes formes polymorphes: (a) par une voie directe par cristallisation ou (b) par désolvatation du complexe [Fe($\mathbf{L}^{3}$)]·MeOH. Dans ce cas aussi, seul un des polymorphes montre des propriétés de conversion de spin tandis que le second est diamagnétique. Le cas du complexe [Fe($\mathbf{L}^{1}$)$_2$] s'est avéré plus intéressant. En effet le complexe a été isolé sous forme de trois polymorphes et deux solvatomorphes [Fe($\mathbf{L}^{1}$)$_2$]·MeOH. Les trois formes non solvatées exhibent une transition de spin qui s'étale sur un domaine de température de près de 100 K (Figure R-4), montrant le fort impact des effets du réseau cristallin sur le processus de commutation de spin.

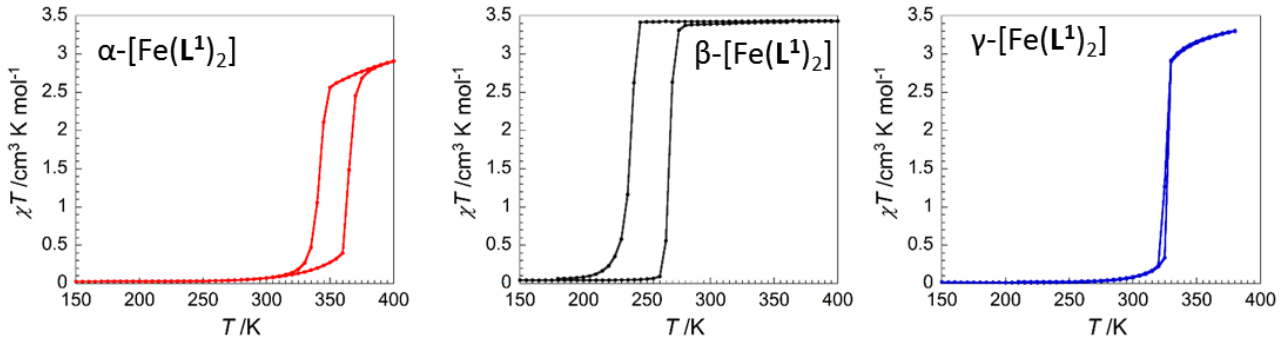

Figure R-4. Dépendance en température du produit χT pour les trois formes polymorphes du complexe [Fe($\mathbf{L}^{1}$)$_2$].

Dans la deuxième partie de ce chapitre, nous décrivons nos tentatives pour induire des propriétés mésomorphes. Notre stratégie s'est essentiellement focalisée sur la fonctionnalisation du ligand par une à trois chaines alkyles. Ainsi une série de nouveaux ligands et complexes ont été préparés avec succès (Schéma R-3).

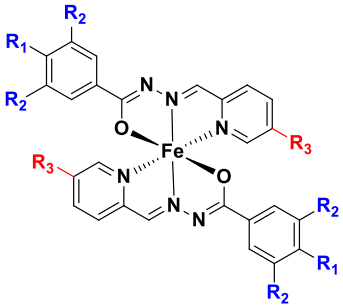

$[Fe(L^{4-8})_2]$

L^4: $R_1 = C_{12}H_{25}$; $R_2 = H$; $R_3 = H$
L^5: $R_1 = C_{12}H_{25}$; $R_2 = H$; $R_3 = Cl$
L^6: $R_1 = C_{18}H_{37}$; $R_2 = H$; $R_3 = H$
L^7: $R_1 = H$; $R_2 = C_{12}H_{25}$; $R_3 = H$
L^8: $R_1 = R_2 = C_{12}H_{25}$; $R_3 = H$

Schéma R-3. Structure chimiques des complexes $[Fe(\mathbf{L}^{i})_2]$ synthétisés en vue d'induire des propriétés cristal-liquides.

Bien que cette stratégie n'a permis en aucun cas d'obtenir les propriétés cristal-liquides désirées, la fonctionnalisation du ligand par des chaines alkyle a permis de mettre en évidence des effets intéressants sur le comportement magnétique des matériaux hybrides. Les complexes contenant les ligands $\mathbf{L}^4$-$\mathbf{L}^6$ (une seule chaine alkyle), montrent une transition de spin incomplète due à la formation d'une phase intermédiaire où les deux espèces Bas-Spin (BS) et Haut-Spin (HS) sont présentes. Par exemple, le complexe $[Fe(\mathbf{L}^4)_2]$ exhibe une transition entre la phase diamagnétique BS et la phase intermediaire BS-HS (Figure R-5, gauche). Ce phénomène a été directement attribué à la présence des chaines alkyle. En effet, la transition de spin est accompagnée par une augmentation de la distance interlamellaire (axe *b*) résultant du changement de la géométrie coudée du complexe (Figure R-5, droite). Par conséquent, afin de maintenir une interdigitation des chaines, ceci entraine une compression de la couche contenant les centres métalliques (plan *ac*), ce qui empêche la conversion complète de tous les sites Fe(II).

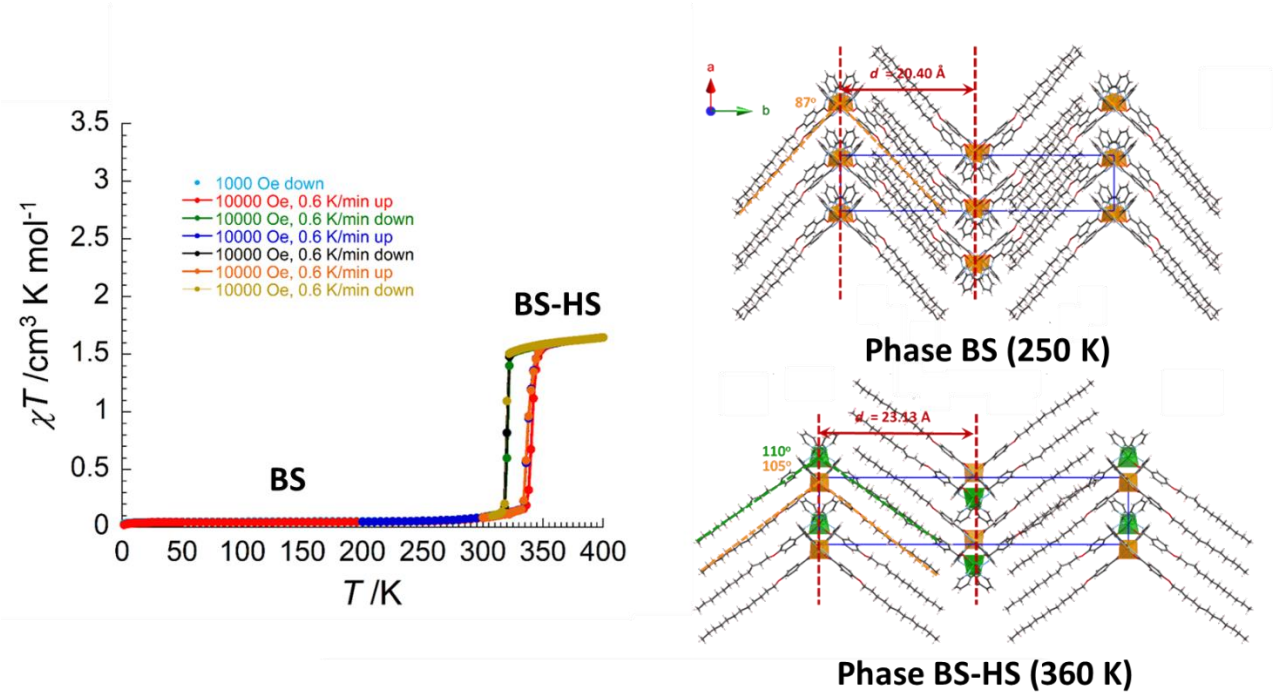

Figure R-4. (Gauche) Dépendance en température du produit χT pour $[Fe(\mathbf{L}^4)_2]$. (Droite) Structure cristallographique du complexe $[Fe(\mathbf{L}^4)_2]$ dans la phase BS et phase intermédiaire BS-HS. Les sites BS et HS sont respectivement représentés en orange et vert.

D'un autre cote, nous avons montré que l'augmentation du nombre de chaines alkyle permet de réduire considérablement la température de fusion des matériaux hybrides. La transition vers la phase liquide a un

impact direct sur la sphère de coordination du Fe(II) et entraine une conversion de spin inverse, qui bien que partielle, n'avait jamais été observée auparavant.

Le Chapitre IV est dédié à nos travaux sur les complexes tetranucléaires $\{[(Tp^*)Fe^{III}(CN)_3]_2[M^{II}(R,R\text{-}bpy)_2]_2\}(A)_2$ (où Tp* = hydridotris(3,5-dimethylpyrazol-1-yl)borate; M^{II} = Ni^{II} ou Co^{II}; R,R-bpy = 4,4'-disubstituant-2,2'-bipyridine; A = anion monovalent). Ces carrés moléculaires sont connus pour exhiber des comportements de molécule-aimant dans le cas où M = Ni^{II} [9] ou montrer des propriétés de commutation thermo ou photo-induites résultant d'un transfert d'électron intramoléculaire dans le cas où M = Co^{II}.[10-12, 5d-e] Comme précédemment notre objectif a été de modifier la structure des ligands afin d'induire des propriétés mésomorphes ou plus simplement d'accroitre la solubilité de ces systèmes dans des solvants organiques usuels. Le chapitre est divisé en deux parties qui recouvrent ces deux types de systèmes moléculaires.

Dans la première partie du chapitre nous décrivons les différentes stratégies de synthèse testées pour attacher des fonctions mésogènes sur le ligand bipyridine et celle retenue consiste à faire un couplage *via* une estérification. Cette méthode s'est avérée particulièrement efficace et nous a permis de préparer une série de ligands, **L**^{3}-**L**^{6}, contenant différents nombres et types de substituants mésogènes. Deux ligands, **L**^{1} et **L**^{2}, porteurs de substituants non-mésogènes ont également été synthétisés et utilisés pour la synthèse de complexe modèles.

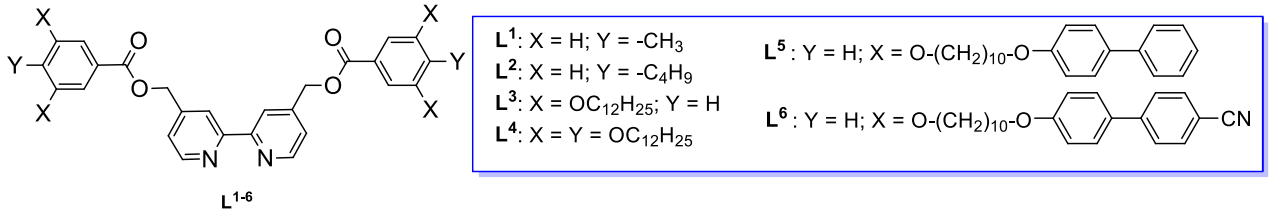

Scheme R-3. Structure chimique des ligands utilisés pour la synthèse des complexes $\{Fe_2Ni_2\}$.

Les complexes ont été obtenus comme décrit dans le Schéma R-4 par l'auto-assemblage entre le sel de Ni(II) et l'ion tricyanido-métallate, $(A)[(Tp^*)Fe(CN)_3]$ (avec A = NEt_4 ou PPh_4). Les molécules de solvant coordonnées sur les sites Ni(II) sont ensuite remplacées *in situ* par l'ajout du ligand bipyridine, **L**$^{1\text{-}6}$. La formation de ces carrés moléculaires a pu être vérifiée par analyse élémentaire, RMN, IR ainsi que par diffraction des rayons X sur monocristal dans le cas des complexes modèles **1** et **2**.

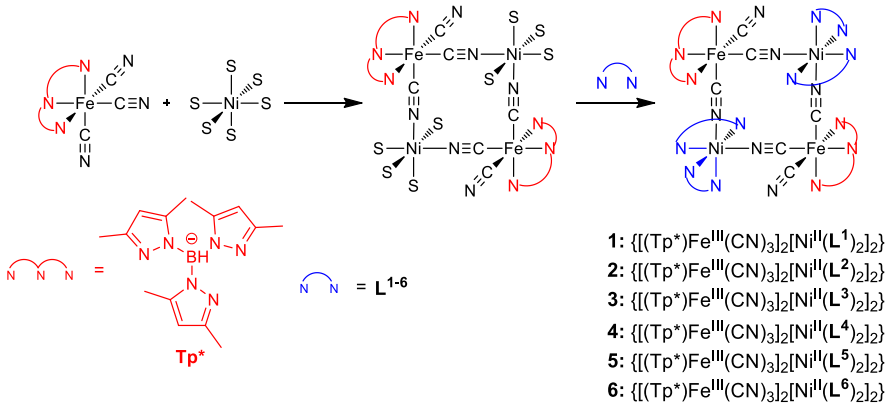

Scheme R-4. Schéma réactionnel pour la préparation des carrés $\{Fe^{III}_2Ni^{II}_2\}$. Les charges et contre-ions sont omis pour plus de clarté.

Les études complémentaires de POM, DSC et SAXS ont montré que les complexes contentant les ligands porteurs de chaines dodecyle n'exhibent pas de propriétés mésomorphes et se présentent sous forme de matériaux faiblement cristallins ou amorphes. En revanche, lorsque des ligands porteurs de fonction biphenyle ou cyanobiphenyle sont utilisés, les carrés $\{Ni_2Fe_2\}$ (**5** et **6)** forment des mésophases lamellaires dans un large domaine de température (Figure R-6). Ceci confirme, comme dans le cas du complexe Mn_{12}, que l'utilisation de ces unités pro-mésomorphes est une stratégie efficace pour générer des phases smectiques.

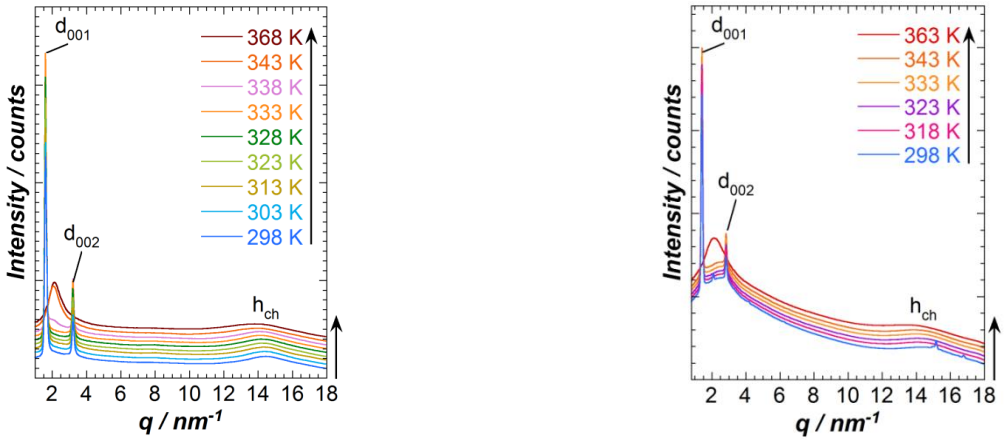

Figure R-6. Evolution des profils SAXS avec la température pour les complexes **5** (gauche) et **6** (droite).

Des mesures magnétiques en mode *dc* et *ac* ont été effectuées pour les deux complexes modèles **1** et **2** ainsi que pour le complexe **5**. Ces mesures ont confirmé dans tous les cas, une préservation du comportement de SMM et des propriétés magnétiques très similaires entre elles et avec celles des analogues déjà connus, montrant que la fonctionnalisation n'a pas d'impact significatif sur le comportement magnétique.

Nous avons par suite cherché à étendre cette étude aux carrés $\{Fe_2Co_2\}$ et nous avons ainsi préparé les complexes analogues avec les ligands $\mathbf{L^3}$-$\mathbf{L^6}$. Nous avons démontré que le remplacement du Ni(II) par Co(II) n'affecte pas l'architecture générale des complexes qui s'auto-organisent ainsi de la même manière que les analogues de Ni(II). Malheureusement, aucun de ces complexes ne montre du transfert d'électron intramoléculaire que ce soit à l'état solide ou en solution, indiquant que la fonctionnalisation des ligands bipyridine affecte le potentiel redox sur le site du Co(II). Ainsi, nous avons proposé de modifier le design des ligands en changeant le couplage ester pas un couplage éther. En effet, il a été précédemment montré que l'introduction de fonctions methoxy sur le ligand bipyridine était compatible pour obtenir des propriétés de transfert d'electron.[5e] Nous avons ainsi préparé deux nouveaux ligands, $\mathbf{L^7}$ et $\mathbf{L^8}$ selon la séquence synthétique décrite sur le Schéma R-5.

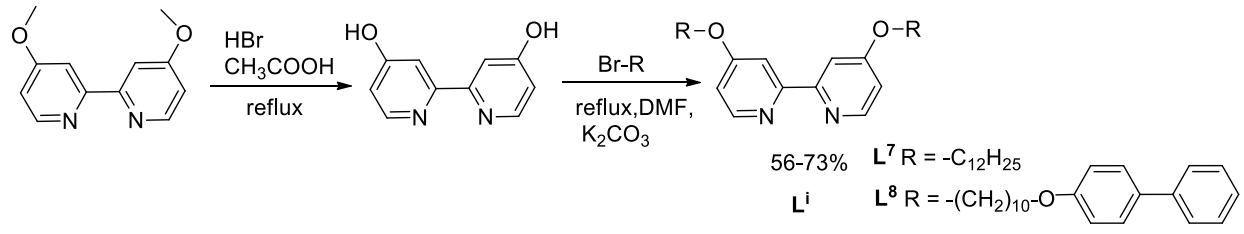

Schéma R-5. Schéma synthétique pour la préparation des ligands $\mathbf{L^7}$ et $\mathbf{L^8}$.

Les quatre complexes $\{Fe_2Co_2\}$ suivant, avec les contre-anions triflate et hexafluorophosphate ont été préparés :

7 - $\{[(Tp^*)Fe(CN)_3]_2[Co(\mathbf{L}^7)_2]_2\}(OTf)_2\cdot 6H_2O$;

8 - $\{[(Tp^*)Fe(CN)_3]_2[Co(\mathbf{L}^7)_2]_2\}(PF_6)_2$;

9 - $\{[(Tp^*)Fe(CN)_3]_2[Co(\mathbf{L}^8)_2]_2\}(OTf)_2$;

10 - $\{[(Tp^*)Fe(CN)_3]_2[Co(\mathbf{L}^8)_2]_2\}(PF_6)_2$.

Aucun de ces complexes ne présente un comportement réversible de transfert d'électrons. En revanche, en solution tous les complexes montrent un changement de couleur du rouge au vert après refroidissement, ce qui est caractéristique du processus de transfert d'électron. Le processus de transfert d'électron a été suivie par des mesures UV-vis dans différents solvants et ont confirmé une forte dépendance de la température caractéristique $T_{1/2}$ avec la nature du solvant ; celle-ci augmentant avec la polarité du solvant (Figure R-7).

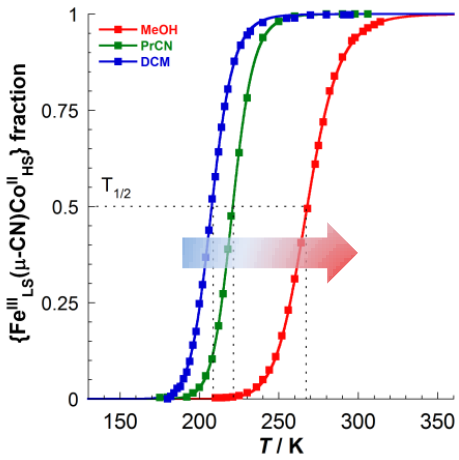

Figure R-7. Dépendance en température de la fraction $\{Fe^{III}_{LS}(\mu\text{-CN})Co^{II}_{HS}\}$ pour le complexe **7** dans du dichlorométhane, du butyronitrile et du méthanol. La fraction a été estimé par l'absorption sur la bande de transfert de charge intermétallique a 540 nm.

References

1. (a) Kahn, O. *Molecular Magnetism*, VCH, New York, **1993** (b) Gatteschi, D.; Sessoli, R.; Villain, J. *Molecular Nanomagnets*, Oxford University Press, **2006**. (c) .Bruce, D. W.; O'Hare, D.; Walton, R. I. *Molecular Materials*, Inorganic Materials Series, John Wiley and Sons, UK, **2010**.

2. Gütlich, P.; Goodwin, H. A. *Spin Crossover in Transition Metal Compounds*, Topics in Current Chemistry, Springer, Wien New York, vol. 233-235. **2004**.

3. (a) Descurtins, S.; Gütlich, P.; Köhler, C. P.; Spiering, H. *Chem. Phys. Lett.* **1984**, *105*, 1-4. (b) Sato, O.; Iyoda, T.; Fujishima, A.; Hashimoto, K. *Science*, **1996**, *272*, 704-705. (c) Sato, O.; Einaga, Y.; Fujishima, A.; Hashimoto, K. *Inorg. Chem.*, **1999**, *38*, 4405-4412.

4. (a) Coulon, C.; Miyasaka, H.; Clérac, R. *Struct. Bond.* **2006**, *122*, 163. (b) Ritter, S. K. Chem. Eng. News **2004**, *82*, 29.

5. (a) Terazzi, E.; Bourgogne, C.; Welter, R.; Gallani, J.-L.; Guillon, D.; Rogez, G.; Donnio, B. *Angew. Chem., Int. Ed.* **2008**, *47*, 490-495. (b) Terazzi, E.; Jensen, T. B.; Donnio, B.; Buchwalder, K.; Bourgogne, C.; Rogez, G.; Heinrich, B.; Gallani, J.-L.; Piguet, C. *Dalton Trans.*, **2011**, *40*, 12028-12032. (c) Terazzi, E.; Rogez, G.; Gallani, J.-L.; Donnio, B. *J. Am. Chem. Soc.*, **2013**, *135*, 2708-2722. (d) Siretanu, D. *PhD Thesis*, Univ. of Bordeaux 1, **2011**. (e) Mitcov, D. *PhD Thesis*, Univ. of Bordeaux, **2014**.

6. (a) Zhang, L.; Xu, G-C.; Xu, H-B.; Zhang, T.; Wang, Z-M.; Yuan, M.; Gao, S. *Chem. Comm*., **2010**, *46*, 2554. (b) Zhang, L.; Xu, G-C; Xu, H-B; Mereacre, V.; Wang, Z-M.; Powell, A. K.; Gao, S. *Dalton Trans.* **2010**, *39*, 4856. (c) Zhang, L.; Xu, G-C.; Xu, H-B.; Wang, Z.-M.; Gao, S. *Eur. J. Inorg. Chem*., **2013**, 1043. (d) Zhang, L.; Wang, J-J.; Xu, G-C.; Li, J.; Jia, D-Z.; Gao, S. *Dalton Trans.* **2013**, *42*, 8205. (e) Zhang, Y. *J. Chem. Phys.* **2014**, *141*, 214703/1.

7. Shongwe, M. S.; Al-Rahbi, S. H.; Al-Azani, M. A.; Al-Muharbi, A. A.; Al-Mjeni, F.; Matoga, D.; Gismelseed, A.; Al-Omari, I. A.; Yousif, A.; Adams, H.; Morris, M. J.; Mikuriya, M.; *Dalton Trans.* **2012**, *41*, 2500.

8. Romero-Morcillo, T.; Seredyuk, M.; Muñoz, M. C.; Real, J. A. *Angew. Chem. Int. Ed.*, **2015**, *54*, 14777.

9. (a) Li, D.; Clérac, R.; Parkin, S.; Wang, G.; Yee, G. T.; Holmes, S. M. *Inorg. Chem.*, **2006**, *45*, 5251-5253; c) Li, D.; Clérac, R.; Wang, G.; Yee, G. T.; Holmes, S. M. *Eur. J. Inorg. Chem.*, **2007**, 1341-1346; (h) Zhang, Y.; Mallik, U. P.; Clérac, R.; Rath, N. P.; Holmes, S. M. *Polyhedron*, **2013**, *52*, 115-121.

10. (a) Zhang, Y.; Li, D.; Clérac, R.; Kalisz, M.; Mathonière, C.; Holmes, S. M. *Angew. Chem., Int. Ed.* **2010**, *49*, 3752. (b) Siretanu, D.; Li, D.; Buisson, L.; Bassani, D. M.; Holmes, S. M.; Mathonière, C.; Clérac, R. *Chem. Eur. J.* **2011**, *17*, 11704. (c) Zhang, Y.-Z.; Ferko, P.; Siretanu, D.; Ababei, R.; Rath, N. P.; Shaw, M. J.; Clérac, R.; Mathonière, C.; Holmes, S. M. *J. Am. Chem. Soc.* **2014**, *136*, 16854.

11. (a) Nihei, M.; Sekine, Y.; Suganami, N.; Oshio, H.; *Chemistry Chem. Lett.* **2010**, 978. (b) (a) Nihei, M.; Sekine, Y.; Suganami, N.; Nakazawa, K.; Nakao, A.; Nakao, H.; Murakami, Y.; Oshio, H. *J. Am. Chem. Soc.* **2011**, *133*, 3592. (c) Newton, G. N.; Nihei, M.; Oshio, H. *Eur. J. Inorg. Chem.* **2011**, *20*, 3031. (d) Sekine, Y.; Nihei, M.; Oshio, H. *Chem. Lett.* **2014**, 1029. (e) Sekine, Y.; Nihei, M.; Kumai, R.; Nakao, H.; Murakami, Y.; Oshio, H. *Inorg. Chem. Front.* **2014**, *1*, 540. (f) Y Sekine, Y.; Nihei, M.; Kumai, R.; Nakao, H.; Murakami, Y.; Oshio, H. *Chem. Commun.* **2014**, *50*, 4050. (g) Kitagawa, Y.; Asaoka, M.; Miyagi, K.; Matsui, T.; Nihei, M.; Oshio, H.; Okumura,

12. (a) Cao, L.; Tao, J.; Gao, Q.; Liu, T.; Xia, Z.; Li, D. *Chem. Commun*. **2014**, *50*, 1665; (b) Zheng, C.; Xu, J.; Yang, Z.; Tao, J.; Li, D. *Inorg. Chem.* **2015**, 54, 9687.

Fonctionnalisation rationnelle de matériaux moléculaires: vers des liquides et des cristaux-liquides magnétiques

Développer des méthodes efficaces pour mettre en forme les matériaux moléculaires magnétiques demeure un enjeu majeur et représente une étape essentielle en vue de possible applications. A cet égard, l'élaboration d'hybrides magnétiques présentant des propriétés de cristaux-liquides ou des systèmes solubles apparait comme une approche prometteuse. Ce travail de thèse a été axé sur la conception, la synthèse et la caractérisation de nouveaux hybrides basé sur des molécule-aimants (SMMs), des complexes à conversion de spin (SCO) et systèmes à transfert d'électrons (ET). Le chapitre I contient des informations générales et concepts théoriques sur ces trois classes de complexes magnétiques (SMM, SCO et ET) ainsi qu'un aperçu bibliographique sur les hybrides magnétiques connus. Le chapitre II est axé sur nos travaux de fonctionnalisation de molécules-aimants basés sur le complexe Mn_{12}, en vue d'obtenir des phases cristaux-liquides. Dans le chapitre III, l'étude d'une série de complexes à conversion de spin de type Fe(II)-pyridylbenzohydrazone au sein de phases cristallines ou de phases molles est décrite. Le chapitre IV est dédié à l'étude de complexes tetranucléaire a pont cyanure de type $\{Fe_2M_2\}$ ($M = Co^{2+}$, Ni^{2+}), qui sont connus pour présenter des propriétés de transfert de charge ou SMM avec l'ion Co(II) et Ni(II), respectivement. Dans ces trois chapitres expérimentaux, l'influence de la fonctionnalisation des ligands sur l'auto-organisation et les propriétés thermiques et magnétiques des matériaux résultants est discutée en détail.

Mot clés: *magnétisme moléculaire ; cristal liquide ; molécule-aimant ; conversion de spin ; transfert d'électron ;*

Rational functionalization of molecular materials: towards magnetic liquids and liquid crystals

Developing efficient methods to process molecular magnetic materials remains a considerable challenge and constitutes one of the critical steps toward possible applications. In this scope, the development magnetic hybrids featuring liquid crystal properties or improved solubility appears as a promising approach. This thesis work aimed to design, synthetize and characterize new hybrid materials based on the single-molecule magnets (SMMs), spin crossover (SCO) and electron transfer (ET) complexes. Chapter I contains general information and theoretical concepts on these three classes of magnetic complexes (SMMs, SCO and ET complexes), followed by a bibliographic survey on hybrid magnetic materials. Chapter II, rational is focused on the functionalization of Mn_{12}-based SMM towards liquid crystalline phases. In Chapter III, a series of pyridylbenzohydrazone-based Fe(II) SCO complexes is investigated in both crystalline and soft-matter phase. Chapter IV is dedicated to the study of cyanido-bridged $\{Fe_2M_2\}$ molecular squares (M = Co(II), Ni(II)), which are known to exhibit SMM and thermally- or photo induced ET, respectively with Co(II) and Ni(II). In these three experimental chapters, the influence of ligand functionalization on self-organization, thermal and magnetic properties of the resulting materials is discussed in detail.

Keywords: *molecular magnetism; liquid crystal; single-molecule magnet; spin crossover; electron transfer.*

Thèse préparée au:
Centre de Recherche Paul Pascal UPR 8641 / CNRS - Université de Bordeaux
115 av. Albert Schweitzer, 33600 PESSAC (France)
http://www.crpp-bordeaux.cnrs.fr/